Beyond Color: Lattice Gauge Theory for Strongly-Coupled Physics

by

Patrick R. Oare
B.A. Physics, B.A. Mathematics, University of California, Berkeley (2019)

Submitted to the Department of Physics
in partial fulfillment of the requirements for the degree of
Doctor of Philosophy in Physics, Statistics, and Data Science
at the
MASSACHUSETTS INSTITUTE OF TECHNOLOGY
September 2024

Author:

Patrick R. Oare
Department of Physics
August 16th, 2024

Certified by:

Phiala E. Shanahan
Associate Professor, Thesis Supervisor

Accepted by:

Lindley Winslow
Associate Department Head of Physics

Beyond Color: Lattice Gauge Theory for Strongly-Coupled Physics

by

Patrick R. Oare

Submitted to the Department of Physics
on August 16th, 2024, in partial fulfillment of the
requirements for the degree of
Doctor of Philosophy in Physics, Statistics, and Data Science

Abstract

Quantum Chromodynamics (QCD) is the prototypical strongly interacting Quantum Field Theory (QFT). It is the interaction that yields the strong nuclear force that binds protons and neutrons together. The underlying mathematical picture of QCD is known exactly: it is an $SU(3)$ gauge theory coupled to six flavors of fermions (the quarks). Despite this, it remains difficult to compute QCD observables because QCD is strongly-coupled, and typical perturbative methods used in QFT only work in specific regimes of validity for QCD. The most successful *ab initio* method to study QCD is Lattice Gauge Theory (LGT). This computational formalism computes observables by discretizing spacetime to render the path integral tractable. The primary focus of LGT in the 40 years since its inception has been the study of QCD, as the theory has direct physical relevance to so much of our universe, and the desire to understand QCD has driven many conceptual breakthroughs and advancements in LGT. Despite the focus on QCD, lattice methods find significant utility in studying other strongly-coupled gauge theories related to and unrelated to QCD.

This thesis will focus on applying LGT to strongly-coupled physics inside and outside of QCD and on developing techniques within LGT that may be used to better understand said theories. First, the spectral function reconstruction problem in LGT is considered, and a new method for spectral function reconstruction in LGT is presented. Spectral functions describe the energy states of a theory: bound states, resonances, and continuum thresholds. The presented reconstruction method uses the analytic properties of the retarded Green's function to constrain the full set of spectral functions that may be reconstructed from LGT data using the Nevanlinna-Pick interpolation problem. Next, two theories will be numerically studied using LGT. The first is the Standard Model Effective Field Theory (SMEFT). The SMEFT process that is considered is neutrinoless double β ($0\nu\beta\beta$) decay, a hypothetical decay of two neutrons into two protons and two electrons. LGT is used to compute non-perturbative matrix elements for the unphysical $\pi^- \to \pi^+ e^- e^-$ transition, which contributes to nuclear $0\nu\beta\beta$ decay, and for the decay of the dinucleon $n^0 n^0 \to p^+ p^+ e^- e^-$. Connections to Effective Field Theory studies of $0\nu\beta\beta$ decay will also be discussed. Finally, adjoint QCD (QCD_2), the theory of a Majorana fermion coupled to a $SU(N)$ gauge

field in the adjoint representation in $1+1$ spacetime dimensions, will be studied using LGT. QCD_2 is a well-studied QCD-like theory whose properties have been crucial in the study of confinement. Lattice methods are used to compute the static quark potential, string tensions, and the low-lying spectrum of the theory, which will provide input that may be used to understand better QCD_2 and the confinement mechanism in general.

Thesis Supervisor: Phiala E. Shanahan
Title: Associate Professor

Acknowledgments

It takes support from all types of places to get through the process of writing a Ph.D. thesis. I've had a host of mentors throughout my time in academia that have made this dissertation possible. My love for the physical sciences began in the Chatham High School science wing under the instruction of David Bandel and James Cai. Both of you taught me so much about physics and chemistry and helped to nurture my ever-growing love of science. I wouldn't be here today without the support I found in high school. Second, the place where I went from a hopeful practitioner of the physical sciences to a researcher: the University of California, Berkeley. I did my undergraduate research in Laura Waller's Computational Imaging Lab, and Laura and the graduate students and postdocs in the lab took me under their wing and taught me so much about how to be a scientific researcher. Dan Shuldman, Zack Phillips, Nick Antipa, and Emrah Bostan were all instrumental mentors at various stages throughout my tenure in the Waller Lab. In fact, my first introduction to inverse problems (discussed in Chapter 4) was actually not in the field of physics, but in the Waller Lab, while working with Nick and Emrah on a project on computational photography.

Throughout graduate school, I have had a host of collaborators to whom I am immensely grateful. My advisor, Phiala Shanahan, who took in a student who knew nothing about the field of lattice gauge theory and taught me almost all of what I know about the field. Will Detmold, who has been my co-advisor in all but name, who was a huge source of guidance and advice throughout my Ph.D. Will Jay, who has had endless patience with me and been exactly the type of mentor and friend that I needed to get me to the finish line. Thank you all for the time and effort you have put in to turn me into the scientiest I am today. The other graduate students in the group have also been a huge source of support and knowledge for me, without which I could not have written this thesis: Artur Avkhadiev, Anthony Grebe, Çağin Yunus, Dimitra Pefkou, Josh Lin, Ryan Abbott, and Tej Kanwar.

Without the support from my family, I could not have gotten through any amount of school, let alone completing a Ph.D. degree. Mom and Dad, I know when I started this neither of you (nor me) knew what I was in for, but you've been unwaveringly by my side throughout the last five years, and for all the years I've had before that. I couldn't have asked for better parents. Adam and Kierra, we've watched one another grow up, and things weren't always pleasant. I'm so glad that we're friends now, and I'm so proud of the people you both have become. My grandparents: Nana Mom and

Nana Dad, and Gong-Gong: thank you for always loving and supporting me, and for teaching me so much about world. I wish Paw-Paw were here to see this in person, but I know she's been watching over me for the last 8 years.

There are so many friends that I consider family at this point. The Sordillos: Andrew and Ashley, John, Nancy, Nicky, and Ryan. Thank you for all the food you've fed me and all the vacations we've spent together over the years. My roommates and friends from Berkeley: Cade Hermeling, Caolan John, Dan Ferenc Segedin, Jackson Michalski, Nathan Cheng, Peter Baumbacher, Spencer Doyle, Teddy Yerxa, and Thomas McClave. All of you made Berkeley such a fun place to study physics and math, and I'm grateful to have such a great group of friends.

I've made a number of very important friends in graduate school who I would like to thank. Ben Reichelt, the first new person I met at MIT, who has become one of my closest friends throughout the last five years. I am so glad I helped you move that couch on that sweaty August morning in 2019. My Moral Support group: Wenzer Qin, Sam Alipour-fard, and Artur Avkhadiev. This has been such an important group to me: I don't know that anyone else knows exactly what my journey through graduate school was like as much as the three of you, and I'm so grateful to have had such a great support group when things got tough. Rahul Jayaraman and Nick Kamp, with whom I have spent so many hours gossiping and destressing in the climbing gym: thank you for helping me escape into moments of levity, but also being there for me when I needed more than that. I would be remiss to not mention Daniel Mayer and Kaliroë Pappas, who wrote their theses at essentially the same time as I did. It was so helpful having two people going through the same trials as me, and I'm glad to call you both my friends– we did it! To everyone mentioned, and all the other friends I've made at MIT, thank you for making MIT an amazing place to work and live. I will cherish the memories I've made here for the rest of my life.

My final and most important acknowledgement is to my partner, Emily Glazer. Without her constant support throughout the years, my journey throughout graduate school would have been infinitely harder. She has been my rock when times got tough, and has always been there for me with a smile. She's set an immensely high bar as a partner, and I hope that I can do the same for her as she continues her Ph.D. studies. Emily, thank you for all your support throughout my time at MIT. I know you always say that "[I] could have done without [you]", but I really do not think that is the case, at least without a significant increase in difficulty. Thank you for everything.

Contents

List of Figures

List of Tables

Chapter 1

Introduction

The development of the Standard Model of particle physics in the mid- to late-20$^{\text{th}}$ century was an incredible triumph for the high-energy physics community. The Standard Model describes the building blocks of nature: the quarks, leptons, gauge bosons, and the Higgs boson. The theory explains the interactions between all these particles in a way consistent with their symmetries and has remarkable predictive power. It is known that the Standard Model does not provide a Theory of Everything, as phenomena such as dark matter and neutrino masses have been observed that cannot be predicted within the context of the Standard Model. Nonetheless, the theory is remarkably useful and remains the theoretical description of nature that best matches the empirical evidence.

The specific component of the Standard Model that will be focused on in this thesis is Quantum Chromodynamics (QCD), the theory of the strong nuclear force that describes the interactions between quarks and gluons. QCD is a confining theory, meaning that lone quarks and gluons are not found in nature; instead, the rich structure of QCD manifests as hadronic states, composite particles made up of quarks and gluons. The theory describes the individual quarks and gluons themselves. Hadronic operators may be written down, but the complicated structure of QCD as a gauge theory makes the computation of hadronic observables impossible with conventional field-theoretic means like perturbation theory. The only systematically-improvable *ab initio* method for understanding QCD is lattice gauge theory (LGT), which computes QCD observables by discretizing spacetime to render the path integral finite-dimensional. LGT is an inherently numerical method based on Markov Chain Monte Carlo techniques for evaluating high-dimensional integrals. It provides a framework to compute estimators for QCD correlation functions in a systematically improvable way. These correlation functions may then be analyzed to extract estimators for underlying quantities of interest in the theory.

LGT was first formalized in the 1970s to study strongly-coupled field theories from a non-perturbative lens. As computational power has increased and more sophisticated algorithms for LGT have been developed [6, 7], it has become tractable to use LGT to study QCD directly. Since then, the LGT community has focused primarily on studying QCD because of the phenomenological value of the theory. However, there remains value in studying strongly-coupled theories that are not QCD using LGT. Such theories often provide a simpler setting to study interesting physics than full QCD, or allow one to focus their attention on the consequences that specific properties have on the structure of a field theory. The canonical example is the Schwinger model, the theory of a single Dirac fermion coupled to a $U(1)$ gauge field in $1+1$ spacetime dimensions [8], which provides a toy model of confinement that is easier to study analytically than four-dimensional $SU(3)$ Yang-Mills theory. Other examples include Beyond the Standard Model (BSM) theories, with many applications seeking to understand theories of supersymmetry [9] and dark matter [10]. My doctoral research at MIT has used LGT to understand the physics of strongly-coupled gauge theories both inside and outside of QCD, which will be outlined in Sections 1.1 and 1.2.

1.1 Publications

Throughout my PhD I have contributed to several publications, which I have listed below:

1. W. Detmold, M. Illa, D. Murphy, P. Oare, K. Orginos, P. Shanahan, M. Wagman, F. Winter, **Lattice QCD constraints on the parton distribution functions of ^{3}He**. Phys. Rev. Lett. **126**, 202001 (2021) [1].

2. W. Detmold, W. Jay, D. Murphy, P. Oare, P. Shanahan, **Neutrinoless Double Beta Decay from Lattice QCD: The Short-Distance $\pi^- \to \pi^+ e^- e^-$ Amplitude**. Phys. Rev. D **107** (2023) 9, 094501 [2].

3. T. Bergamaschi, W. Jay, P. Oare, **Hadronic Structure, Conformal Maps, and Analytic Continuation**, Phys. Rev. D **108** (2023) 7, 074516 [3].

4. D. Hackett, P. Oare, D. Pefkou, P. Shanahan, **Gravitational form factors of the pion from lattice QCD**, Phys. Rev. D **108** (2023) 11, 114504 [4].

5. Z. Davoudi, W. Detmold, Z. Fu, A. Grebe, W. Jay, D. Murphy, P. Oare, P. Shanahan, M. Wagman, **Long-Distance Nuclear Matrix Elements for**

Neutrinoless Double-Beta Decay from Lattice QCD, Phys. Rev. D **109** (2024) 11, 114514 [5].

Although most of my research contributions will be outlined in this thesis, I have left out a discussion of Refs. [1, 4]. My primary contribution to these works was the calculation of the renormalization of the quark energy-momentum tensor, which is described in each manuscript.

1.2 Outline

This thesis contains five content chapters. The first two are background chapters, first on QCD and the Standard Model (Chapter 2), and second on LGT (Chapter 3). These chapters should provide the tools to understand the following three chapters, which detail my research contributions. Each research chapter begins with a discussion of my specific contributions to each project.

Chapter 4 defines the notion of a spectral density in quantum field theory and the role that the spectral density plays in the theory of thermal Green's functions. The reconstruction of a spectral density from LGT data for correlation functions is an ill-posed inverse problem. This chapter presents a new method for the reconstruction of smeared spectral functions developed by Thomas Bergamaschi, William Jay, and myself [3], based on the Nevanlinna Analytical Continuation method of Ref. [11]. Our method is based on the analytic properties of retarded Green's functions and allows for constructing a rigorous bound on where the smeared spectral density may lie. The chapter presents simulations where the method is rigorously tested and concludes with a discussion of the application of our method to noisy Monte Carlo data.

Chapter 5 describes the calculation of neutrinoless double β ($0\nu\beta\beta$) decay matrix elements with LGT. $0\nu\beta\beta$ decay is a hypothesized decay mode of two down quarks into two up quarks and two electrons that is being searched for in experiments world-wide. If observed, $0\nu\beta\beta$ decay would have many interesting corollaries, including the definitive proof that the Standard Model neutrino is a Majorana particle. $0\nu\beta\beta$ decays generally fall into two categories: long-distance decays, mediated by the exchange of a light Majorana neutrino, and short-distance decays, mediated by heavy BSM physics. This chapter will outline LGT calculations of long- and short-distance matrix elements in two systems: $\pi^- \to \pi^+ e^- e^-$ and $n^0 n^0 \to p^+ p^+ e^- e^-$. It will present the current status of our work, which in particular has presented calculations of the short-distance $\pi^- \to \pi^+ e^- e^-$ decay [2][1] and the long-distance $n^0 n^0 \to p^+ p^+ e^- e^-$ decay [5].

[1]The long-distance $\pi^- \to \pi^+ e^- e^-$ decay calculation was performed by David Murphy and Will

Chapter 6 details an ongoing project studying two-dimensional adjoint QCD (QCD_2), the theory of a Majorana fermion coupled to an $SU(N)$ gauge field in the adjoint representation. QCD_2 has been a toy model for the study of confinement for the last 30 years, which, in particular, has provided numerous insights into the mechanism that underlies confinement. In particular, the rich symmetry structure of QCD_2 implies it confines when the Majorana fermion has mass but deconfines when the Majorana fermion is taken to be massless. The strongly-coupled nature of this theory makes it a natural candidate for a LGT calculation. We have computed the static quark potential, string tensions, and the ground state energy in the pseudoscalar sectors on ten ensembles drawing from a discretized QCD_2 action with $N = 2$ colors.

Detmold in Ref. [12].

Chapter 2

Quantum Chromodynamics and the Standard Model

Modern understanding of particle physics is encoded in the Standard Model, a renormalizable quantum field theory (QFT) that has proven remarkably robust in describing the universe. The Standard Model has yielded many celebrated predictions, including a prediction of the W and Z bosons [13, 14] and the top quark [15]. Despite the basic structure of the Standard Model having been mapped out in the 1960s and 1970s, the theory is still the subject of a large amount of active research today.

One particularly vibrant area of research is quantum chromodynamics (QCD), the sector of the Standard Model which describes the strong force that binds nuclei together. QCD is a challenging area of study because it is non-perturbative at the low energies (e.g., at nuclear energy scales) and cannot be studied with perturbation theory, the predominant tool used to study most QFTs. At these energies, QCD must instead be matched onto an effective field theory (EFT) or studied with non-perturbative means like lattice gauge theory (LGT). The LGT approach is the subject of this thesis and will be extensively detailed.

The Standard Model is a triumph of modern physics but has shortcomings. Many phenomena have been observed beyond the Standard Model (BSM)—i.e., neutrino oscillations [16], dark matter [17], and matter-antimatter asymmetry [18]—that cannot be described solely by the Standard Model. Furthermore, gravity cannot be added to the Standard Model in a renormalizable way, so although one can naïvely write down a quantum theory of gravity, it cannot be completely described by a finite number of input parameters. Whatever physical theory underlies the universe must answer all these questions. It is thus essential to identify possible channels for BSM physics and study these channels theoretically and experimentally to constrain whatever theory lies beyond the Standard Model.

2.1 The Standard Model

The Standard Model is a non-abelian gauge theory with gauge group $SU(3) \times SU(2) \times U(1)$. The different factors of this gauge group encode different physical phenomena with different dynamics. The $SU(3)$ factor describes QCD and is often called $SU(3)_c$ ("$SU(3)$-color"), while the $SU(2) \times U(1)$ describes the electroweak force, and is often called $SU(2)_L \times U(1)_Y$ ("$SU(2)$-left times $U(1)$-hypercharge"). Each factor of the gauge group has a corresponding gauge coupling, a set of generators that implement the symmetry, and a spin-1 gauge boson that transforms in the adjoint representation of its respective gauge group: $SU(3)_c$ has coupling g, generators $\{t^a\}_{a=1}^8$, and gauge bosons G_μ^a; $SU(2)_L$ has coupling g', generators $\{T^A\}_{A=1}^3$, and gauge bosons W_μ^A; and $U(1)$ has coupling g_Y, a single generator Y, and gauge boson B_μ.

The fermionic content of the Standard Model is contained in three generations of particles. Each generation contains five fields q_L, u_R, d_R, ℓ_L, and e_R, with transformation properties under $SU(3)_c \times SU(2)_L \times U(1)_Y$ and the Lorentz group $SO(1,3)$ given in Table 2.1. Across generations, particles transform in the same way and are only distinguished by their mass and couplings. Fermions that transform in the fundamental of $SU(3)_c$ (q_L, u_R, and d_R) are called quarks, and fermions that transform as a singlet of $SU(3)_c$ (ℓ_L and e_R) are called leptons. The last particle that makes up the Standard Model is the Higgs boson H. This scalar field only transforms non-trivially under the electroweak symmetry [19, 20], with charges given in Table 2.1.

Field	$SU(3)_c$	$SU(2)_L$	$U(1)_Y$	Lorentz
q_L	**3**	**2**	$1/6$	$(1/2,0)$
u_R	**3**	1	$2/3$	$(0,1/2)$
d_R	**3**	1	$-1/3$	$(0,1/2)$
ℓ_L	1	**2**	$-\frac{1}{2}$	$(1/2,0)$
e_R	1	1	-1	$(0,1/2)$
H	1	**2**	$1/2$	$(0,0)$

Table 2.1. Charges of each Standard Model fermion field in a given generation, and the Higgs boson. Note that only the left-handed fermion fields (the $(1/2,0)$ representation of the Lorentz group) transform non-trivially under $SU(2)_L$, hence the nomenclature "$SU(2)$-left".

We can express the Standard Model Lagrangian as the sum of four parts,

$$\mathcal{L}_{\text{SM}} = \mathcal{L}_{\text{Gauge}} + \mathcal{L}_{\text{Fermion}} + \mathcal{L}_{\text{Higgs}} + \mathcal{L}_{\text{Yukawa}}, \tag{2.1}$$

each of which can be written in terms of the defined fields. The **gauge sector** $\mathcal{L}_{\text{Gauge}}$ is simply a Yang-Mills Lagrangian for each of the respective gauge fields,

$$\mathcal{L}_{\text{Gauge}} = -\frac{1}{4}G^a_{\mu\nu}G^{\mu\nu a} - \frac{1}{4}W^A_{\mu\nu}W^{\mu\nu A} - \frac{1}{4}B_{\mu\nu}B^{\mu\nu}, \tag{2.2}$$

where here for each gauge boson $A_\mu \in \{G_\mu, W_\mu, B_\mu\}$ with coupling $g_A \in \{g, g', g_Y\}$ and structure constants[1] f^{abc}, the field strength is defined as $A^a_{\mu\nu} = \partial_\mu A^a_\nu - \partial_\nu A^a_\mu + g_A f^{abc} A^b_\mu A^c_\nu$. The indices a and A respectively parameterize the $SU(3)$ and $SU(2)$ generators, $a \in \{1, ..., 8\}$ and $A \in \{1, 2, 3\}$. The **fermion sector** $\mathcal{L}_{\text{Fermion}}$ describes the kinetic terms of each Standard Model fermion and will be expanded in terms of a QCD fermion sector and an electroweak fermion sector

$$\mathcal{L}_{\text{Fermion}} = i\sum_\psi \overline{\psi}\gamma^\mu D^{\text{SM}}_\mu \psi \equiv \mathcal{L}^{\text{QCD}}_{\text{Fermion}} + \mathcal{L}^{\text{EW}}_{\text{Fermion}} \tag{2.3}$$

where ψ sums over each fermion field in Table 2.1 (q_L, u_R, d_R, ℓ_L, and e_R) for each generation[2]. Here the gauge covariant derivative is defined as $D^{\text{SM}}_\mu = \partial_\mu - igG^a_\mu t^a - ig'W^A_\mu T^A - ig_Y Y$, and $\mathcal{L}^{\text{QCD}}_{\text{Fermion}}$ and $\mathcal{L}^{\text{EW}}_{\text{Fermion}}$ are defined as

$$\begin{aligned}
\mathcal{L}^{\text{QCD}}_{\text{Fermion}} &= i\sum_\psi \overline{\psi}\gamma^\mu(\partial_\mu - igG^a_\mu t^a)\psi \equiv i\sum_\psi \overline{\psi}\gamma^\mu D^{\text{QCD}}_\mu \psi, \\
\mathcal{L}^{\text{EW}}_{\text{Fermion}} &= i\sum_\psi \overline{\psi}\gamma^\mu(-ig'W^A_\mu T^A - ig_Y Y)\psi.
\end{aligned} \tag{2.4}$$

The advantage of this definition is that electroweak symmetry breaking (EWSB) will only affect $\mathcal{L}^{\text{EW}}_{\text{Fermion}}$ and leave $\mathcal{L}^{\text{QCD}}_{\text{Fermion}}$ untouched.

The **Higgs sector** $\mathcal{L}_{\text{Higgs}}$ is responsible for EWSB [19, 21, 22],

$$\mathcal{L}_{\text{Higgs}} = |D^{\text{SM}}_\mu H|^2 + \mu^2 H^\dagger H - \lambda(H^\dagger H)^2. \tag{2.5}$$

where μ, λ are couplings. The potential for the Higgs, $V(H) = -\mu^2 H^\dagger H + \lambda(H^\dagger H)^2$, is minimized when the Higgs field has norm $|\langle H\rangle| = v \equiv \frac{\mu^2}{\lambda}$, which induces EWSB. This is the vacuum expectation value (vev) for the Higgs. In nature, the electroweak symmetry breaking scale is $v = 247$ GeV. At energies are below v, $SU(2)_L \times U(1)_Y$

[1] The structure constants of a gauge group define its Lie algebra. For a Lie group generated by algebra elements $\{t^a\}$, the structure constants are defined as $[t^a, t^b] = f^{abc}t^c$.

[2] The fermion fields in Table 2.1 are Weyl fermions, although Dirac conjugation is only defined for Dirac fermions. This notation will be abused to embed Weyl fermions into Dirac spinors whenever necessary; for example, if $\psi = q_L$, one considers ψ to be the left-handed Dirac spinor $\begin{pmatrix} q_L \\ 0 \end{pmatrix}$.

is spontaneously broken to a subgroup $U(1)_{\text{EM}}$ generated by the electric charge Q

$$Q = Y + T^3. \tag{2.6}$$

The natural basis for the gauge fields after EWSB is the photon A_μ, the Z boson Z_μ, and the charged W bosons $W^\pm_\mu$, given by

$$\begin{pmatrix} A_\mu \\ Z_\mu \end{pmatrix} = \begin{pmatrix} \cos\theta_w & \sin\theta_w \\ -\sin\theta_w & \cos\theta_w \end{pmatrix} \begin{pmatrix} B_\mu \\ W^3_\mu \end{pmatrix} \qquad W^\pm_\mu = \frac{1}{\sqrt{2}}\left(W^1_\mu \mp iW^2_\mu\right) \tag{2.7}$$

where θ_w is the weak mixing angle, with value $\sin^2\theta_w \approx 0.223$ [23, 24]. The photon is the gauge boson corresponding to the unbroken subgroup $U(1)_{\text{EM}} \subset SU(2)_L \times U(1)_Y$, and hence remains massless at all energies, while the Z and W bosons are massive with masses given in Table 2.3.

After EWSB, the $SU(2)$ doublets q_L and ℓ_L are often written in terms of their individual components,

$$q_L = \begin{pmatrix} u_L \\ d_L \end{pmatrix} \qquad \ell_L = \begin{pmatrix} \nu_L \\ e_L \end{pmatrix}, \tag{2.8}$$

as the pairs (u_L, u_R), (d_L, d_R), and (e_L, e_R) have the same quantum numbers under the unbroken subgroup $SU(3)_c \times U(1)_{\text{EM}}$. In terms of these fields, the electroweak fermion Lagrangian $\mathcal{L}^{\text{EW}}_{\text{Fermion}}$ is recast as:

$$\begin{aligned} \mathcal{L}^{\text{EW}}_{\text{Fermion}} =& \frac{g}{\sqrt{2}} \sum_{i=1}^{3} \left(\overline{u}^i_L \not{W}^+ d^i_L + \nu^i_L \not{W}^+ e^i_L + \text{h.c.} \right) \\ &+ \frac{g}{\cos\theta_w} \sum_\psi \overline{\psi} \not{Z} (t^3 P_L - Q_\psi \sin^2\theta_w)\psi + e \sum_\psi Q_\psi \overline{\psi} \not{A} \psi \end{aligned} \tag{2.9}$$

where Q_ψ is the eigenvalue of $Q = Y + T^3$ acting on ψ, and can be read off from Table 2.1.

The **Yukawa sector** $\mathcal{L}_{\text{Yukawa}}$ couples the fermion fields to the Higgs and gives the fermions mass at energies $\ll v$,

$$\mathcal{L}_{\text{Yukawa}} = -y^e_{ij} \overline{\ell}^i_L H e^j_R - y^d_{ij} \overline{q}^i_L H d^j_R - y^u_{ij} \overline{q}^{ia}_L \epsilon_{ab} H^{*b} u^j_R + \text{h.c.}, \tag{2.10}$$

where y^e_{ij}, y^d_{ij}, and y^u_{ij} are the Yukawa couplings. The $SU(2)$ doublets q_L and ℓ_L are

often written in terms of their individual components,

$$q_L = \begin{pmatrix} u_L \\ d_L \end{pmatrix} \qquad \ell_L = \begin{pmatrix} \nu_L \\ e_L \end{pmatrix}, \tag{2.11}$$

as the pairs (u_L, u_R), (d_L, d_R), and (e_L, e_R) have the same quantum numbers under $SU(3)_c \times U(1)_{\text{EM}}$. After EWSB, the Higgs takes its vev $|\langle H \rangle| = v$, which induces Dirac masses for the fermions u, d, and e. To see this, the mass term from $\mathcal{L}_{\text{Yukawa}}$ may be expanded as

$$\mathcal{L}^{\text{mass}}_{\text{Yukawa}} \xrightarrow{E \ll v} -v \left(\overline{e}_L y^e e_R + \overline{d}_L y^d d_R + \overline{u}_L y^u u_R \right), \tag{2.12}$$

where generation indices are suppressed in favor of matrix-vector notation.

The matrices y^e, y^d, and y^u may be diagonalized by rotating the fermion fields,

$$\psi \to K_\psi \psi \tag{2.13}$$

where $\psi \in \{d_L, u_L, e_L, d_R, u_R, e_R\}$. This new (rotated) basis is called the **mass basis**, while the original basis is called the **flavor basis**. The remainder of this work will assume the fermion fields are written in the mass basis unless otherwise specified. In the mass basis, observe that the Yukawa terms induce Dirac masses for up-type quarks, down-type quarks, and electron-type leptons. Each mass m_ψ is related to the corresponding diagonal Yukawa coupling by $m_\psi = y_{\psi\psi} v/\sqrt{2}$, with y_ψ corresponding to the diagonal component of the Yukawa matrix for the fermion ψ, i.e. either $y^e_{\psi\psi}$, $y^d_{\psi\psi}$, or $y^u_{\psi\psi}$. These particles are interpreted as massive Dirac fermions u, d, and e at energies $\ll v$, while at high energies $\gtrsim v$, they are interpreted as massless left- or right-handed Weyl fermions. The generations and names of each fermion are listed in Table 2.2, and the mass of each massive Standard Model particle is given in Table. 2.3. Note that the only fermion that remains massless is the neutrino ν_L; the neutrino is known to be a massive particle because of neutrino oscillations [25], but the neutrino is massless within the context of the Standard Model. The role of the neutrino will be discussed further in Section 2.3.

The Standard Model Lagrangian is only affected by rotation from the flavor to the mass basis in one place: the couplings between the quarks and the W bosons, which are given by the first term in Eq. (2.9). Because K_{u_L} and K_{d_L} do not need to

Generation	u-type quark	d-type quark	e-type lepton	ν-type lepton
1	Up (u)	Down (d)	Electron (e)	Electron neutrino (ν_e)
2	Charm (c)	Strange (s)	Muon (μ)	Muon neutrino (ν_μ)
3	Top (t)	Bottom (b)	Tau (τ)	Tau neutrino (ν_τ)

Table 2.2. Standard Model fermion content after EWSB. Each generation consists of: an up-type quark (u, c, t); a down-type quark (d, s, b); an electron-type lepton (e, μ, τ); and a neutrino-type lepton (ν_e, ν_μ, ν_τ).

e	u	d	s	μ	c	τ	b	W	Z	H	t
511k	2.2M	4.7M	93M	110M	1.3G	1.8G	4.7G	80G	91G	125G	172G

Table 2.3. Mass hierarchy of the Standard Model. Units are listed in electron volts, i.e., 511k corresponds to 511 keV. Masses are sourced from the Particle Data Group's Review of Particle Physics [26]. Note that although neutrino oscillations prove neutrinos have mass, in the Standard Model, neutrinos do not have mass, hence m_ν is set to zero.

be the same, in the mass basis, this term transforms to

$$\mathcal{L}^{\text{EW}}_{\text{Fermion}} \supset \frac{g}{\sqrt{2}} \sum_{i=1}^{3} \left(\overline{u}^i_L \not{W}^+ V^{ij}_{\text{CKM}} d^j_L + \nu^i_L \not{W}^+ e^i_L + \text{h.c.} \right) \tag{2.14}$$

where V_{CKM} is the **Cabibbo-Kobayashi-Maskawa (CKM) Matrix** [27, 28], defined as

$$V_{\text{CKM}} \equiv K^\dagger_{u_L} K_{d_L}. \tag{2.15}$$

The CKM matrix mixes quark flavors, enabling flavor-changing processes like $d \to uW^-$, which will become important later when neutrinoless double beta decay is considered in Chapter 5. Note that there is no corresponding CKM-like matrix for the leptons (e, ν) in the Standard Model because the Standard Model neutrino is massless; hence, there is no need to rotate it between its flavor and mass bases. If neutrinos are given a mass, then a corresponding matrix mixes lepton flavors; this will be discussed in Chapter 2.3.

While the gauge symmetries of the Standard Model have been extensively discussed, its global symmetries are also important to consider. There are four **accidental symmetries**[3] in the Standard Model Lagrangian [29]: baryon number,

[3]These symmetries are called "accidental" because, unlike gauge symmetry, they are not imposed in the theory in its construction. Instead, the Standard Model Lagrangian just happens to have these symmetries; however, they are important to consider nonetheless.

electron number, muon number, and tau number. The accidental symmetry group is

$$U(1)_B \times U(1)_e \times U(1)_\mu \times U(1)_\tau, \tag{2.16}$$

and each subgroup is respectively generated by the operators B, L_e, L_μ, and L_τ. These generators act on Standard Model fields in the following way:

- $Bq = \frac{1}{3}q$, $B\overline{q} = -\frac{1}{3}\overline{q}$ for any quark field q. B annihilates any lepton field. Baryon number B is normalized so that baryons, composite states of three quarks, have charge +1.
- $L_e e = e$, $L_e \overline{e} = -\overline{e}$, where e is the electron field. L_e annihilates any other field.
- $L_\mu \mu = \mu$, $L_\mu \overline{\mu} = -\overline{\mu}$, where μ is the muon field. L_μ annihilates any other field.
- $L_\tau \tau = \tau$, $L_\tau \overline{\tau} = -\overline{\tau}$, where τ is the tau field. L_τ annihilates any other field.

Although each lepton number L_e, L_μ, and L_τ is separately conserved, only total baryon number B is conserved. This is because there is no CKM-like matrix for leptons in the Standard Model, as Standard Model neutrinos have no mass. When neutrino masses are added, separate lepton numbers are no longer conserved, and instead, only the total lepton number

$$L \equiv L_e + L_\mu + L_\tau \tag{2.17}$$

is conserved.

This story holds at the classical level but changes when quantum effects are included. Several mixed gauge-global anomalies affect the accidental symmetry group $U(1)_B \times U(1)_e \times U(1)_\mu \times U(1)_\tau$ [30]. The non-anomalous symmetries of the Standard Model are $B - L$, $L_e - L_\mu$, $L_\mu - L_\tau$, and $L_e - L_\tau$. When neutrino mixing is considered (Section 2.3), there is only a single remaining non-anomalous symmetry: baryon number minus lepton number, $B - L$.

2.2 Quantum Chromodynamics

QCD is the study of the strong force; more precisely, it is the study of the $SU(3)_c$ sector of the Standard Model gauge group. It is a simple theory to write down— six fermions (quarks) coupled to $SU(3)_c$ in the fundamental representation— but it boasts perhaps the richest dynamics of all the Standard Model sectors. This force

confounded scientists for decades, and it was the last of the three fundamental Standard Model forces (electromagnetic, weak, strong) to be understood as a quantum field theory. Quantum electrodynamics (QED), the quantum field theory describing the electromagnetic force, was primarily worked out in the 1940s by Feynman, Schwinger, and Tomonaga [31–33]. The weak force, although first understood as an effective theory by Fermi in 1934 [34], was unified with the electromagnetic force with contributions from Glashow, Weinberg, and Salam in the 1960s [23, 35, 36]. In 1962, Anderson proposed a mechanism for superconductivity based on spontaneous symmetry breaking that could give rise to the Meissner effect in superconductors [37]. This work was reformulated in a particle physics context in 1964, when three works– led by Higgs; Brout and Englert; and Guralnik, Hagen, and Kibble– proposed a variant of Anderson's mechanism, the Higgs mechanism, as a way to give the fermions mass in a gauge invariant way [19, 21, 38]. Note that although these theories were written down, they were not experimentally confirmed until later; the W and the Z bosons were not discovered until 1983 [13, 14, 39], and the Higgs until 2012 [20]. Although QCD was written down as a Yang-Mills theory in the 1960s, it was not understood as governing the strong force until the 1970s, when the discovery of asymptotic freedom [40, 41] led physicists to be able to interpret QCD as the description of the strong force. In the 2010s, LGT calculations had matured enough to reproduce the low-lying hadronic spectrum, which had previously only been known from experiment [42].

2.2.1 The Static Quark Potential and Confinement

A unique feature that distinguishes QCD from the other Standard Model sectors is **confinement**. QCD describes the interactions of gluons with quarks and antiquarks; however, unlike leptons like the electron or the muon, lone quarks have never been observed in nature. Instead, quarks are bound together in **hadrons**, composite particles made of constituent quarks. Anytime a quark is found in nature[4], it can be seen as a constituent particle of a hadron.

QCD is confining because of the nature of its potential, which is best explored in pure $SU(3)$ Yang-Mills theory. Unlike the QED potential $V(r) \propto 1/r$, the static quark potential in $SU(3)$ Yang-Mills theory has an additional linear term that dominates as r increases [44, 45]:

$$V_{\text{static quark}}(r) \supset \frac{a}{r} + \sigma r, \tag{2.18}$$

where a and σ are proportionality constants. The Coulomb part of the potential falls

[4]Except highly energetic scales where phases of matter like quark-gluon plasma can be found [43].

off as $r \to \infty$, but the linear part grows stronger. Consider two particles charged under a gauge theory, first with a Coulomb potential and second with a Coulomb + linear potential.

1. $V(r) \propto A/r$. As these particles are separated, they eventually become free and do not interact; the force between them scales as $1/r^2$, which goes to zero as they become infinitely far apart.

2. $V(r) \propto A/r + \sigma r$. As these particles are separated, they do not become free. Although the Coulomb part of the potential dies off, the linear part does not; the force between the particles stays constant. No matter how far these particles are separated, they still feel the influence of one another; there is a constant force between them.

Henceforth one only considers the Coulomb + linear case, which will describe specific regimes of the QCD potential.

In such a potential, the Coulombic piece dominates at short-distances, and the linear piece dominates at long-distances. In terms of the parameterization of Eq. (2.18), "short" and "long" mean relative to some inverse energy scale, which may be written in terms of a and σ[5]. This energy scale is called Λ_{QCD}: a mass scale generated by QCD that sets the scale of the hadronic interactions.

Quarks will interact strongly with one another, regardless of distance apart, unless they are **screened** by other quarks or antiquarks. As quarks transform in the fundamental representation $\mathbf{3}$ of $SU(3)$, tensoring together the appropriate copies of $\mathbf{3}$ and $\overline{\mathbf{3}}$ determines if a combination of quarks and antiquarks can produce a color-neutral singlet. Any such state is called a **hadron**. For example, consider a quark q and an antiquark $\overline{q}$, which are respectively in the $\mathbf{3}$ and $\overline{\mathbf{3}}$ representations of $SU(3)$. The composite $q\overline{q}$ state lies in the tensor product $\mathbf{3} \otimes \overline{\mathbf{3}}$, which can be decomposed as follows [46]:

$$\mathbf{3} \otimes \overline{\mathbf{3}} = \mathbf{1} \oplus \mathbf{8}. \tag{2.19}$$

The $q\overline{q}$ state can lie in a singlet under $SU(3)$ or in the adjoint representation of $SU(3)$. The color-neutral singlet forms a type of hadron called a **meson**, a hadron formed from a $q\overline{q}$ pair. Another useful color-neutral combination of quarks is to consider three quarks:

$$\mathbf{3} \otimes \mathbf{3} \otimes \mathbf{3} = \mathbf{3} \otimes (\overline{\mathbf{3}} \oplus \mathbf{6}) = \mathbf{1} \oplus \mathbf{8} \oplus \mathbf{8} \oplus \mathbf{10} \tag{2.20}$$

[5]In QCD, A may be computed in perturbation theory, and σ using LGT techniques that will be described later in this thesis.

The color-singlet combination qqq is called a **baryon**. Given three quark fields q_1, q_2, q_3, a baryon can be explicitly constructed with the Levi-Civita tensor ϵ as $\epsilon_{abc}\, q_1^a\, q_1^b\, q_1^c$.

The pieces may now be put together, which will be illustrated for the case of a $q\overline{q}$ pair in full QCD, for simplicity. Without an external force, the q and $\overline{q}$ will bind together into a color-neutral meson. Suppose now that the q and $\overline{q}$ particles are pulled apart from one another. The q and $\overline{q}$ will still strongly interact with one another because of the long-range nature of the QCD potential. This long-range interaction is mediated by gluons and is called a **flux tube**, or a **QCD string**[6], as depicted in Fig. 2.1. As the $q\overline{q}$ pair is separated further and further, eventually, it becomes energetically favorable for the QCD vacuum to pair-produce another quark-antiquark pair $q'\overline{q}'$ and create two mesons: q' and $\overline{q}$ form a meson, and q and $\overline{q}'$ form a meson. In this way, the **string breaks** and becomes two different color-neutral particles. Note this phenomenon does not occur in pure $SU(3)$ Yang-Mills theory, as this theory cannot pair produce fundamental matter. Classically, one can compute the distance R_q the string will break at, in terms of the mass m_q of the lightest meson containing a q quark, and the string tension σ_q of the $q\overline{q}$ pair:

$$2m_q = \sigma R_q \implies R_q = \frac{2m_q}{\sigma_q}. \tag{2.21}$$

R_q is an estimate for an inherently quantum quantity but Eq. (2.21) provides a useful back-of-the-envelope estimate to gain an intuition for the string-breaking scale.

When string breaking occurs, the q and $\overline{q}$ no longer feel the confining force between one another: each is screened by the respective particle that was created to bind it into a meson. The static quark potential is no longer in a linear regime but instead in a flat regime: after string breaking, the q and $\overline{q}$ will feel no force between one another. To summarize, the QCD potential acts qualitatively different in three regimes:

1. Short-range, $r \ll \Lambda_{\text{QCD}}^{-1}$. The Coulombic potential a/r dominates in this regime, and QCD is perturbative in this sector.

2. Mid-range, $\Lambda_{\text{QCD}}^{-1} \ll r \ll R_q$. The linear potential σr dominates in this regime. Here, $q\overline{q}$ pairs form flux tubes, and the theory is non-perturbative.

3. Long-range, $R_q \ll r$. The potential in this region is constant. This sector describes the potential after string breaking, where the individual quarks are

[6]This name for the flux tube originates from Effective String Theory, which describes QCD flux tubes as string degrees of freedom [47–49].

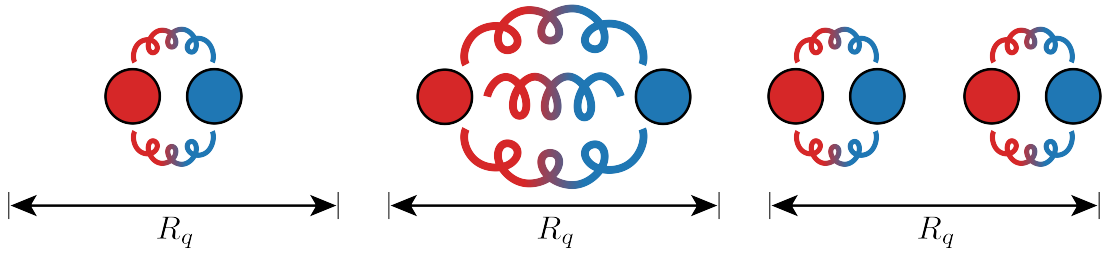

(a) Time t_1. **(b)** Time t_2. **(c)** Time t_3.

Figure 2.1. Cartoon depiction of string breaking. At time t_1 (Figure 2.1a), a $q\overline{q}$ pair is created and subsequently pulled apart. When the distance between the valence quarks is $< R_q$ (time t_2, Figure 2.1b), a flux tube of gluons and sea quarks (not depicted) is created between the valence quarks. As the distance between the quarks reaches R_q, the string breaks, and it is energetically favorable for the $q\overline{q}$ pair to split into two mesons (time t_3, Figure 2.1c).

screened and no longer interact with quarks outside their respective hadrons.

2.2.2 Asymptotic Freedom

The Minkowski space QCD action is

$$S_{\text{QCD}} = \int d^4x \left(-\frac{1}{4} G^a_{\mu\nu} G^{\mu\nu a} + i \sum_{q \in \{u,d,s,c,b,t\}} \overline{q} \gamma^\mu D^{\text{QCD}}_\mu q \right), \tag{2.22}$$

where D^{QCD}_μ is the QCD covariant derivative defined in Eq. (2.4). Correlation functions of local operators $\mathcal{O}_1(x), ..., \mathcal{O}_n(x)$ may be defined with respect to the QCD action via the path integral, which is a functional integral over the fields ψ, $\overline{\psi}$, G_μ defined as,

$$C_n(x_1, ..., x_n) \equiv \langle \mathcal{O}_1(x_1) ... \mathcal{O}_n(x_n) \rangle = \frac{1}{\mathcal{Z}} \int D\psi \, D\overline{\psi} \, DG_\mu \, e^{iS_{\text{QCD}}[\psi, \overline{\psi}, G]} \mathcal{O}_1(x_1) \cdots \mathcal{O}_n(x_n). \tag{2.23}$$

Here $\mathcal{Z}$ is the partition function of QCD, and the path integral measure $D\psi$ is formally the infinite-dimensional measure [50],

$$\int D\psi = \int \prod_{x \in \mathbb{R}^4} d\psi(x), \tag{2.24}$$

with equivalent definitions for $D\overline{\psi}$ and DG_μ[7]. Eq. (2.23) allows one to compute any information that is desired from the theory.

Despite the compact and deterministic form of Eq. (2.23), QCD is not a solved theory. One may write down the equation describing any correlation function, but explicitly evaluating the path integral that defines the correlator is often extremely difficult. A particularly well-studied way to evaluate the path integral (Eq. (2.23)) is by performing a perturbative expansion in the strong coupling,

$$\alpha_s = \frac{g^2}{4\pi}, \tag{2.25}$$

and computing Feynman diagrams to a given order M in perturbation theory in α_s. Perturbative approaches yield a solution for $C_n(x_1, ..., x_n)$ as an asymptotic series in α_s, truncated at order α_s^M. If $\alpha_s \ll 1$, this truncated perturbation series approximates the actual result. However, if $\alpha_s \not\ll 1$, then the perturbation expansion breaks down; either the perturbation series expansion converges too slowly and $C_n(x_1, ..., x_n)$ must be calculated to higher order M than is computationally tractable; or the perturbation series does not converge at all, and this technique does not allow for the calculation of $C_n(x_1, ..., x_n)$ at all.

After renormalization the strong coupling $\alpha_s(\mu)$ runs with energy scale, μ, with its running described by the QCD β-function β_s,

$$\mu \frac{d}{d\mu} \alpha_s(\mu) = \beta_s(\alpha_s). \tag{2.26}$$

The strong coupling $\alpha_s(\mu)$ is determined at all energies by $\beta_s(\alpha_s)$ and by its experimentally measured value at the Z boson mass m_Z [26, 51–54]

$$\alpha_s(m_Z) = 0.1179(9). \tag{2.27}$$

The QCD β-function was first computed independently by Gross and Wilczek [40] and Politzer [35] to one-loop in perturbation theory, with the result

$$\beta_s(\alpha_s) = -\frac{1}{2\pi}\left(\frac{11}{3}N_c - \frac{2}{3}N_f\right)\alpha_s^2, \tag{2.28}$$

where N_c is the number of colors ($N_c = 3$ for QCD) and N_f is the number of active quark flavors ($N_f = 6$ for QCD at high energies). As μ passes each quark mass

[7]For compactness an integral over the additional degrees of freedom in $\psi(x)$ is suppressed, i.e., $d\psi(x) = \prod_{\alpha,a} d\psi^a_\alpha(x)$ where α, a range over the spinor and color components of ψ.

threshold in Table 2.3, the respective quark is integrated out of the theory, and N_f decreases by one. For $N_f \leq 6$, observe that $\frac{11}{3}(3) - \frac{2}{3}N_f > 0$, hence[8]

$$\beta_s(\alpha_s) < 0. \tag{2.29}$$

As the scale μ increases, $\alpha_s(\mu)$ will grow smaller, while as μ decreases, $\alpha_s(\mu)$ will increase. This behavior can be seen in Fig. 2.2, which shows the strong coupling as a function of energy scale. This property of QCD is called **asymptotic freedom**. The QCD coupling is small at high energies $\mu \gg 1$ GeV, and the theory is perturbative at these scales. At lower energies $\mu \lesssim 1$ GeV, the coupling will become large and non-perturbative; for example, $\alpha_s(1\text{ GeV}) \approx 0.5$[9].

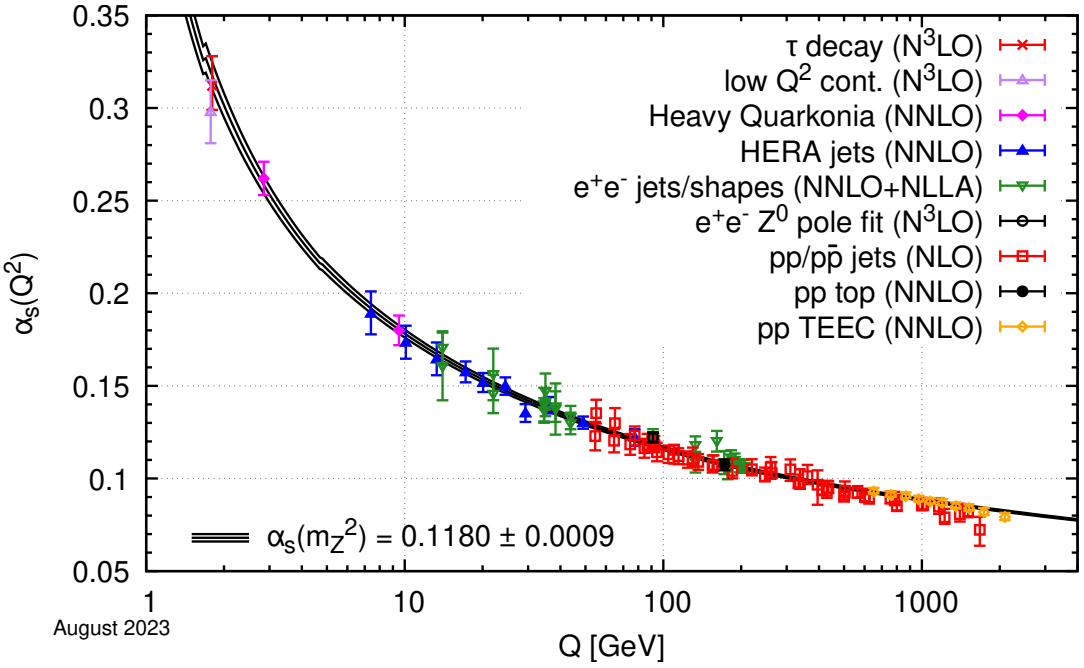

Figure 2.2. Status of determinations of the running coupling α_s as a function of the energy scale Q, as of August 2023. Each data point represents a method of determining α_s at a given energy scale, with the order of perturbation theory used in the extraction denoted in parentheses next to each method. This figure is taken from the Particle Data Group's 2024 Review of Particle Physics [26].

The renormalization group equations for $\alpha_s(\mu)$ imply that it will become infinite

[8]Note that although Eq. (2.28) is only calculated to one-loop, this statement is general and holds to all orders in perturbation theory.

[9]Throughout this thesis, strong coupling will be run to different scales using the RunDec 3 [55] package, which integrates the renormalization group equation for α_s (Eq. (2.26)) at 3-loop order from $\alpha_s(m_Z) = 0.1179(9)$ to the desired scale.

at some finite scale μ; it has a Landau pole. This scale μ is called Λ_{QCD}, and in $\overline{\text{MS}}$, has a numerical value of about $\Lambda_{\text{QCD}} \approx 200$ MeV [56]. This is called **dimensional transmutation**: QCD generates a new mass scale independent of the quark masses, which approximately sets the scale of hadronic interactions. For example, the mass of the rho meson, the lightest hadronic vector resonance, is 770 MeV, which is the same order of magnitude as Λ_{QCD}.

Understanding QCD, therefore, requires non-perturbative methods to compute QCD observables at low energies. This thesis will focus on one particular method, LGT, which discretizes QCD on a Euclidean spacetime lattice and evaluates the path integral numerically. LGT will be discussed in detail in Chapter 3.

2.3 Neutrino Physics

The Standard Model does not tell the entire story of the neutrino. In the Standard Model, neutrinos are forbidden from having a mass term because of gauge invariance: Standard Model masses are generated via the Higgs mechanism, and there is no gauge-invariant Higgs coupling to the lepton doublet that can produce a neutrino mass. However, it is experimentally known that neutrinos have mass, indicating that BSM physics must generate the neutrino mass. It is unknown whether the neutrino mass is Dirac or Majorana, or even how many of the Standard Model neutrinos are massive: all that is known is that some of these neutrinos have mass.

There are a host of other mysteries about the nature of the neutrino. It is the only chiral fermion in the Standard Model. Each other fermion has left- and right-handed species that couple to one another to produce a massive Dirac fermion, and the neutrino is the only particle with no such chiral partner. Every Standard Model neutrino is left-handed, and every Standard Model antineutrino is right-handed [57]. Many BSM theories postulate the existence of a right-handed neutrino that is not charged under $SU(3) \times SU(2)_L \times U(1)$ [58]. Such a particle is called **sterile**, as conventional Standard Model probes may not detect it.

2.3.1 Neutrino masses

The origin of neutrino masses is not known, but it is enlightening to briefly summarize a few mechanisms via which neutrino masses may be added to the Standard Model. Suppose three generations of sterile right-handed neutrinos ν_R^i are added to the Standard Model. As stated, the presence of ν_R cannot be detected under probes

other than gravity or the Higgs. The right-handed neutrinos can be added to the Standard Model Lagrangian via the Yukawa couplings:

$$\mathcal{L}_{\nu_R} \equiv i\overline{\nu}_R \gamma^\mu D_\mu^{\mathrm{SM}} \nu_R - y^\nu_{ij} \overline{\ell}^{ai} \epsilon_{ab} H^{\dagger b} \nu_R^j + \text{h.c.}\,. \tag{2.30}$$

After spontaneous symmetry breaking, Eq. (2.30) generates a Dirac mass term for the neutrino

$$\overline{\nu}_L m_\nu \nu_R + \text{h.c.} \tag{2.31}$$

where the generation matrix m_ν can be computed as usual in terms of the Yukawa y^ν and the Higgs vev v.

There are two types of Lorentz-invariant mass terms that a spinor may have: a Dirac mass term couples a fermion to its corresponding antifermion, and is invariant under all symmetries the fermion is charged under; a Majorana mass term couples a fermion to itself, and is not invariant under the symmetries the fermion is charged under. These masses are explained further in Appendix B.4. A Majorana mass term may be added to the Standard Model Lagrangian depending on the quantum numbers of the right-handed neutrino. If ν_R is charged under lepton number (if lepton number is conserved), then adding a Majorana mass term is forbidden, and the Lagrangian describing the theory is $\mathcal{L}_{\mathrm{SM}} + \mathcal{L}_{\nu_R}$. The neutrino is then a Dirac particle whose right-handed components are not charged under the Standard Model gauge group.

If, instead, the right-handed neutrino is not charged under lepton number, then a Majorana mass may be added to the theory

$$\mathcal{L}_M \equiv -M_{ij} \epsilon_{\dot{a}\dot{b}} \nu_R^{i\dot{a}} \nu_R^{j\dot{b}} + \text{h.c.}\,, \tag{2.32}$$

and the full theory is described by the Lagrangian $\mathcal{L}_{\mathrm{SM}} + \mathcal{L}_{\nu_R} + \mathcal{L}_M$. Here $\epsilon_{\dot{a}\dot{b}}$ is the 2×2 antisymmetric tensor, and the spinor dot notation is detailed in Appendix B.4. Embedding the Weyl spinors ν_L and ν_R into Dirac spinors

$$\nu_L \xrightarrow{\text{Dirac}} \begin{pmatrix} \nu_{La} \\ \epsilon^{\dot{a}\dot{b}} \nu^\dagger_{L\dot{b}} \end{pmatrix} \qquad \nu_R \xrightarrow{\text{Dirac}} \begin{pmatrix} \epsilon_{ab} \nu_R^{\dagger b} \\ \nu_R^{\dot{a}} \end{pmatrix} \tag{2.33}$$

makes it clear the effect that the Majorana mass term M has on the neutrino mass:

$$\begin{aligned}\mathcal{L}_{\nu_R} + \mathcal{L}_M &\supset -(\nu_{La} m_\nu \nu_R^{\dagger a} + \text{h.c.}) - \nu_R^{\dot{a}} M \nu_{R\dot{a}} \\ &= -\frac{1}{2}(\overline{\nu}_L m_\nu \nu_R + \overline{\nu}_R m_\nu \nu_L) - \overline{\nu}_R \frac{M}{2} \nu_R \\ &= -\frac{1}{2} \begin{pmatrix} \overline{\nu}_L & \overline{\nu}_R \end{pmatrix} \begin{pmatrix} 0 & m_\nu \\ m_\nu & M \end{pmatrix} \begin{pmatrix} \nu_L \\ \nu_R \end{pmatrix},\end{aligned} \tag{2.34}$$

where the generation indices are suppressed for brevity. When m_ν and M are diagonalized (the neutrinos are rotated into the mass basis), the light and heavy particles have masses on the order of:

$$m_{\nu,\text{light}} \approx \frac{m_\nu^2}{M} \qquad\qquad m_{\nu,\text{heavy}} \approx M \tag{2.35}$$

This is called the **seesaw mechanism**: the light mass eigenstates are the left-handed neutrinos which have been observed, and the heavy eigenstates are the sterile right-handed neutrinos [59, 60]. When the mass scale M increases, the heavy particle gets heavier, but the light particle gets lighter.

The seesaw mechanism provides an elegant solution to the naturalness problem of why the left-handed neutrinos have such light masses [61, 62]. M is naturally a large parameter: it is coupled to a dimension-3 operator sensitive to the theory's UV cutoff. The Yukawa couplings y^ν should naturally be expected to be on the same order of magnitude as the other Yukawa couplings y^e, y^d, and y^u, indicating that the masses of the neutrinos should be the same order of magnitude as the masses of the other Standard Model fermions. If the right-handed neutrinos were not sterile, or if they were charged under lepton number, it would not be possible to add a Majorana mass term to the Lagrangian, and the left-handed neutrinos would have mass of order m_ν. However, when a Majorana mass term is present, the mixing between the left- and right-handed neutrinos lowers the mass of the light neutrinos to be very small, in line with what is observed experimentally, and consistent with naturalness expectations.

Right-handed neutrinos do not need to be added to the Standard Model to describe neutrino masses. Left-handed neutrinos can still generate their mass from the dimension-5 **Weinberg operator** [63, 64]:

$$\Delta\mathcal{L}_{\text{SM}} = \frac{c_5}{\Lambda} \epsilon^{ij} (\epsilon_{ab} \ell_i^a H^b)(\epsilon_{cd} \ell_j^c H^d), \tag{2.36}$$

where ϵ^{ij} is the 2-dimensional antisymmetric tensor with $\epsilon^{12} \equiv -\epsilon^{21} \equiv 1$. The heavy scale Λ is the UV cutoff of the theory. It provides a natural reason for the light

neutrino mass: the order 1 Wilson coefficient c_5 is suppressed by the heavy scale Λ, as the neutrino mass will be proportional to $\frac{c_5}{\Lambda}$. The Weinberg operator is also generated by integrating heavy right-handed neutrinos out of the theory. In this case, the scale Λ is identified with the Majorana mass of the right-handed neutrinos, Eq. (2.32).

The existence of neutrino masses implies the **Pontecorvo-Maki-Nakagawa-Sakata (PMNS) matrix** [65, 66], the leptonic analog of the CKM matrix, is non-trivial, as it describes the difference in flavor eigenstates for electrons and neutrinos. In the Standard Model, the PMNS matrix is trivial because there is no barrier to rotating the neutrino flavors in the same way as the electron flavors, as Standard Model neutrinos have no mass coupling that prevents this. The PMNS matrix has the same physics as the CKM matrix and describes couplings between the electrons and the neutrinos but is conventionally defined differently than the CKM matrix. Recall the CKM matrix is defined as the difference in rotations between the mass and flavor eigenbases for the up and down quarks. In contrast, the PMNS matrix U is defined as simply the rotation that takes neutrinos into their mass eigenbasis:

$$|\nu_a\rangle = U_{ai}|\nu_i\rangle \tag{2.37}$$

where the $a \in \{e, \mu, \tau\}$ index denotes flavor and the $i \in \{1, 2, 3\}$ index denotes mass eigenstate. Note that the mass eigenbasis $\{|\nu_i\rangle\}_{i=1}^{3}$ is not necessarily ordered according to mass; the neutrino mass ordering is discussed next.

2.3.2 Neutrino oscillations

The smoking gun that proved the existence of non-zero neutrino masses was the observation of **neutrino oscillations** [67–69] by the Super-Kamiokande Collaboration [16] in 1998 and the Sudbury Neutrino Observatory (SNO) Collaboration [70] in 2002. Neutrino oscillations are flavor-mass eigenstate oscillations that neutrinos undergo as they propagate from one place to another. They are detected by studying a known source of a single neutrino type and seeing how these neutrinos interact with the same lepton type (i.e., a ν_e source interacting with electrons) after they have traveled a far distance; if some of the neutrinos have changed flavor, there will be fewer interactions with this lepton source than one would expect. A small but nonzero mass is needed for this phenomenon to occur because the neutrino's flavor eigenstates will differ from its mass eigenstates.

The frequency of neutrino oscillations is proportional to the mass-squared differ-

ence $\Delta m_{ij}^2 = m_i^2 - m_j^2$ between the neutrino mass eigenstates $|\nu_i\rangle$ and $|\nu_j\rangle$. The mass-squared differences are known through experiments and are known to be non-zero. This does not provide an absolute value for any neutrino mass, only a mass difference between the different mass eigenstates. Different neutrino sources allow experimental access to study the different mass-squared mixings, Δm_{ij}^2. There are two main types of natural neutrino sources.

1. Solar neutrinos [71] are predominantly electron neutrinos ν_e, produced from fusion reactions in the sun, $p^+p^+ \to d^+e^+\nu_e$ where d^+ is a deuteron. SNO first observed oscillations in solar neutrinos.

2. Atmospheric neutrinos [72] are produced from cosmic ray interactions and are primarily muon neutrinos ν_μ because of the decay $\pi^+ \to \mu^+\nu_\mu$. Super-Kamiokande first observed neutrino oscillations in atmospheric neutrinos.

Neutrino oscillation data for atmospheric and solar neutrinos is consistent with the initial neutrinos oscillating only into a single other flavor, not both remaining flavors (i.e., solar neutrino oscillations imply the electron neutrino oscillates primarily with either the muon neutrino or the tau neutrino, but not both), hence each corresponds to a single value of the mass-squared matrix Δm_{ij}^2. Two conventions are typically adopted in the definition of the mass eigenstates: first, that they are ordered so that the solar neutrino mass probes the mass difference Δm_{21}^2; and second, that $m_1 < m_2$, i.e., $\Delta m_{12}^2 > 0$. Atmospheric neutrino oscillations either correspond to Δm_{31}^2 or Δm_{32}^2; data shows that this splitting is much larger than Δm_{21}^2 [73]. This means that the neutrino masses have two possible hierarchies:

$$m_1 < m_2 \ll m_3 \qquad\qquad m_3 \ll m_1 < m_2. \tag{2.38}$$

The first hierarchy is called the **normal hierarchy** (NH), and the second is called the **inverted hierarchy** (IH) [74]. Estimates of Δm_{21}^2 and Δm_{31}^2 from Ref. [73] are given in Table 2.4.

Δm_{21}^2 (eV^2)	Δm_{31}^2 (eV^2), NH	Δm_{23}^2 (eV^2), IH
$7.50^{+0.19}_{-0.17} \times 10^{-5}$	$2.458^{+0.046}_{-0.047} \times 10^{-3}$	$2.448^{+0.047}_{-0.047} \times 10^{-3}$

Table 2.4. Mass splittings between the different neutrino mass eigenstates assuming a NH and IH. The mass splitting Δm_{21}^2 is independent of which hierarchy is assumed. Results are sourced from Ref. [73].

Many specifics about the nature of the neutrino remain unknown. The only way

to answer these questions is to experimentally understand the neutrino's properties. As such, many theoretical efforts to understand the neutrino focus on interpreting experimental results and establishing pipelines to determine the physics that can be extracted from hypothesized experimental results. Perhaps the largest such effort underway is the search for **neutrinoless double β ($0\nu\beta\beta$) decay**, a hypothetical decay that, if observed, would definitively prove that the neutrino is a Majorana particle. $0\nu\beta\beta$ decay has been a large focus of my thesis research, which will be discussed extensively in Chapter 5.

Chapter 3

Lattice Gauge Theory

Lattice gauge theory is a formalism that allows for the non-perturbative computation of matrix elements by explicitly evaluating the path integral numerically. This chapter will define LGT and discuss some of its fundamental features. The canonical example used throughout this section will be QCD. Section 3.1 introduces LGT and its degrees of freedom. Section 3.2 discusses discretizations of the fermion field. The fermion doubling problem will be introduced, and some basic actions that circumvent the doubling problem. Section 6.7 introduces the basics of spectroscopy in LGT, and Section 3.4 discusses sampling of gauge fields. This chapter concludes with a discussion of statistics in LGT calculations (Section 3.5).

3.1 Introduction to LGT

3.1.1 Discretization

Consider the path integral for an arbitrary QCD correlation function, Eq. (2.23),

$$C_n(x_1, ..., x_n) = \frac{1}{\mathcal{Z}} \int D\psi \, D\overline{\psi} DG_\mu \, e^{-S_{\text{QCD}}[\psi, \overline{\psi}, G_\mu]} \, \mathcal{O}_1(x_1) \cdots \mathcal{O}_n(x_n) \tag{3.1}$$

where S_{QCD} is the Euclidean action of the theory. This path integral is formalized in Euclidean space after Wick rotation[1] in order to use Euclidean geometry and have an exponentially decaying action $e^{-S_{\text{QCD}}}$. The remainder of this thesis will work in Euclidean space unless otherwise specified. The advantage of working in Euclidean space is that the density $\frac{1}{\mathcal{Z}} D\psi D\overline{\psi} DG_\mu \, e^{-S_{\text{QCD}}[\psi, \overline{\psi}, G_\mu]}$ becomes a probability density,

[1]Here Wick rotation means the redefinition of the time variable, $t \to i\tau$, in order to make the metric Euclidean. After this variable redefinition, the theory is defined via its analytic continuation from the imaginary axis to the real axis, hence the name "rotation". The variable t denotes Euclidean time unless otherwise specified.

and correlation functions become integrals against this probability distribution. The difficulty lies in the dimension of this distribution: as formulated, it is an integral over an uncountable number of dimensions (each point x_μ in spacetime, Eq. (2.24)) with no closed form solution.

To evaluate Eq. (3.1), lattice methods discretize Euclidean spacetime ($\mathbb{R}^4$) with a 4-dimensional lattice of spatial size $L \in \mathbb{Z}_+$ and temporal size $T \in \mathbb{Z}_+$, with isotropic lattice spacing a between the sites[2]:

$$\Lambda \equiv \{a(n_x, n_y, n_z, n_t) \in (a\mathbb{Z})^4 : 1 \leq n_x, n_y, n_z \leq L, 1 \leq n_t \leq T \}. \tag{3.2}$$

Note that Λ is equivalently indexed by $n \in \Lambda$ and $an \in \Lambda$; this notation will often be abused WLOG. LGT calculations primarily use **lattice units**, where the lattice spacing a defines the length scale and is set equal to 1. Upon discretization, the path integral measure becomes finite-dimensional:

$$\int D\psi \longrightarrow \int \prod_{an \in \Lambda} d\psi(n) \tag{3.3}$$

where $\psi(n)$ represents the value of the field at site $x = an \in \Lambda$. The correlation functions of interest (Eq. (3.1)) may now be explicitly computed with numerical methods like Markov Chain Monte Carlo (MCMC), which is explored in Section 3.4.

Note that the lattice theory simultaneously makes two approximations: the finite-volume approximation and the discretization approximation. As the box size $V \equiv \text{vol}(\Lambda) = L^3 \times T$ is made larger and the lattice spacing a is made smaller, the approximation to the continuum path integral becomes better. The tradeoff is that this increases the path integral's dimensionality, making it more difficult to compute.

The volume V and the lattice spacing a must be removed from the calculation to compute quantities in the continuum and infinite-volume limit[3]. To do this, the desired observables $\mathcal{O}(a, V)$ are explicitly computed in the discretized theory, at several different values for the lattice volume and spacing[4]. These different samples are then

[2]This thesis will only consider isotropic lattice geometries, where the lattice spacing in the spatial direction equals the lattice spacing in the temporal direction. Anisotropic and random geometries have also been studied and are discussed in Refs. [75, 76].

[3]Additional parameters like the quark mass are often modified in the lattice action as well, and extrapolated to their physical values at the end of the calculation alongside a and V.

[4]Note that lattice simulations on a computer are inherently dimensionless and work with lattice units $a = 1$. In order to compare to experiment or other lattice calculations, the scale a is determined by comparison of a chosen observable to experiment or theory. This is discussed further in Section 3.3.4.

used to extrapolate the result to the continuum, infinite-volume limit,

$$\lim_{V\uparrow\infty}\lim_{a\downarrow 0}\mathcal{O}(a,V), \tag{3.4}$$

which defines the infinite-volume, continuum limit observable that one could extract if the path integral of Eq. (3.1) could be computed analytically.

3.1.2 Lattice Degrees of Freedom

The degrees of freedom one considers in LGT differ slightly from those of continuum theory. For concreteness, consider continuum QCD, which has three fields of interest: the quark field $\psi(x)$, the anti-quark field $\overline{\psi}(x)$, and the gauge field $G_\mu(x)$. The quark field $\psi(x)$ and antiquark field $\overline{\psi}(x)$ transform respectively in the fundamental and antifundamental representation of $SU(3)$ under gauge transformation $\Omega \in SU(3)$ as,

$$\psi(x) \to \Omega(x)\psi(x), \qquad\qquad \overline{\psi}(x) \to \overline{\psi}(x)\Omega^\dagger(x). \tag{3.5}$$

The gauge field acts as a connection and allows one to parallel transport the quark field to different positions with the Wilson line:

$$W(x,y) = \mathrm{P}\exp\left(i\int_x^y dz_\mu\, G_\mu(z)\right). \tag{3.6}$$

The Wilson line transforms under a gauge transformation $\Omega(x) \in SU(3)$ as $W(x,y) \to \Omega(x)W(x,y)\Omega^\dagger(y)$, which ensures that a quantity like $W(x,y)\psi(y)$ transforms under $SU(3)$ like $\psi(x)$.

On the lattice, it is advantageous to instead consider an analog of the Wilson line as the fundamental degree of freedom for the gauge field, as this is easier to work with and makes gauge invariance more manifest. Because the lattice spacing a provides a natural unit of length and a finite number of directions that are traversable from each point on the lattice, we work with the **link variables** $U_\mu(n)$:

$$U_\mu(n) \equiv W(an, a(n+\hat{\mu})) \tag{3.7}$$

where $\hat{\mu} \in \{\hat{0},\hat{1},\hat{2},\hat{3}\}$ is the unit vector in the μ direction. Link variables transform under the gauge transformation $\Omega(n) \equiv \Omega(x = an) \in SU(3)$ as

$$U_\mu(n) \xrightarrow{\Omega} \Omega(n)U_\mu(n)\Omega^\dagger(n+\hat{\mu}). \tag{3.8}$$

Note that when evaluating lattice-valued fields, notation will be abused and indexing the field at n will correspond to indexing the continuum field at $x = an$. One can likewise define a negative orientation for the link variables,

$$U_{-\mu}(n) \equiv W(an, an - a\hat{\mu}) = U_\mu^\dagger(n - \hat{\mu}), \tag{3.9}$$

which satisfies the gauge transformation property $U_{-\mu}(n) \xrightarrow{\Omega} \Omega(n)U_{-\mu}(n)\Omega^\dagger(n - \hat{\mu})$, as one would expect. The relation $U_{-\mu}(n) = U_\mu^\dagger(n-\hat{\mu})$ implies that $U_\mu(n)$ and $U_{-\mu}(n)$ are not independent gauge fields; rather, $U_{-\mu}(n)$ is simply a variable redefinition of $U_\mu(n)$ that is often used for convenience. The field $U_\mu(n)$ is referred to as the **gauge field**, as it contains the same information as $G_\mu(an)$; they are related as

$$U_\mu(n) = \mathrm{P}\exp\left(i\int_{an}^{an+a\hat{\mu}} dz_\mu G_\mu(z)\right) \xrightarrow{a\downarrow 0} e^{ia\,G_\mu(an)} = 1 + ia\,G_\mu(an) \tag{3.10}$$

where the equality on the right-hand side is only valid in the $a \downarrow 0$ limit.

The natural gauge-invariant quantity one can construct from the gauge field is the **plaquette**, the ordered product of the links around each square on the lattice,

$$\begin{aligned}\mathcal{P}_{\mu\nu}(n) &\equiv U_\mu(n)U_\nu(n+\hat{\mu})U_{-\mu}(n+\hat{\mu}+\hat{\nu})U_{-\nu}(n+\hat{\nu}) \\ &= U_\mu(n)U_\nu(n+\hat{\mu})U_\mu^\dagger(n+\hat{\nu})U_\nu^\dagger(n).\end{aligned} \tag{3.11}$$

The plaquette is defined on each square in the lattice, and the set of all plaquettes is $\{\mathcal{P}_{\mu\nu}(n) : n \in \Lambda, \mu < \nu\}$. Each plaquette measures the circulation of the gauge field around each closed loop, which has the appealing interpretation as the gauge flux through each loop on the lattice,

$$\mathcal{P}_{\mu\nu}(n)\Big|_{a\downarrow 0} = e^{ia^2\,F_{\mu\nu}(an)+\mathcal{O}(a^3)}. \tag{3.12}$$

The plaquette contains information about the continuum field strength. The simplest action for a gauge field is the **Wilson gauge action** [77],

$$S_g[U] = \beta\sum_{n\in\Lambda}\sum_{\mu<\nu}\left(1 - \frac{1}{N}\mathrm{Re}\,\mathrm{Tr}\,\mathcal{P}_{\mu\nu}(n)\right). \tag{3.13}$$

To summarize, fermion fields live on the links of the lattice and are much the same as their continuum counterparts. However, the algebra-valued continuum gauge field $G_\mu(an)$ is replaced on the lattice with the group-valued gauge field $U_\mu(n)$, which lives

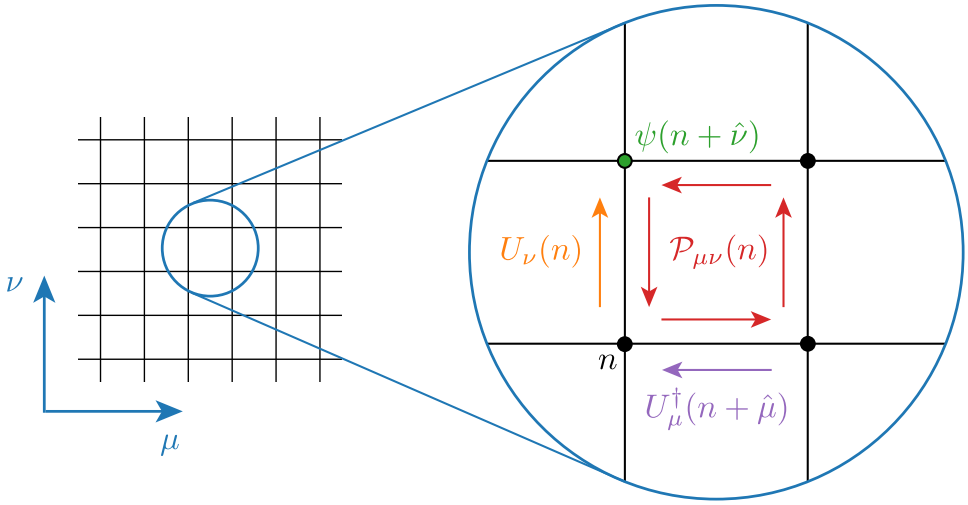

Figure 3.1. Lattice gauge theory setup. Here $\psi(n)$ (green) is the fermion field that lives on the sites of the lattice, $U_\mu(n)$ (orange, magenta) is the gauge field which lives on the links of the lattice, and $\mathcal{P}_{\mu\nu}(n)$ (red) is the plaquette and lives on the faces of the lattice.

on the links of the lattice. The continuum field strength $F_{\mu\nu}(an)$ is likewise replaced with the plaquette $\mathcal{P}_{\mu\nu}(n)$, which lives on each square of the lattice. The lattice setup is depicted in Figure 3.1.

3.2 Discretizing the QCD action

Now that the degrees of freedom have been introduced, the QCD action must be discretized. The basic ideas of discretization can be found in a simpler example: discretizing the derivative of a field ϕ. Recall the definition of the derivative in the continuum:

$$\partial_\mu \phi(x) = \lim_{a \downarrow 0} \frac{\phi(x + a\hat{\mu}) - \phi(x)}{a}. \tag{3.14}$$

A discretization of the derivative is defined as any operator $\partial_\mu^{(a)}$ that has the correct continuum limit:

$$\lim_{a \downarrow 0} \partial_\mu^{(a)} \phi(n) \Big|_{n=x} = \partial_\mu \phi(x). \tag{3.15}$$

The simplest possible discretization of ∂_μ removes the limit in Eq. (3.14) and defines the derivative at finite lattice spacing as

$$\partial_\mu^{(a)} \phi(n) \equiv \frac{\phi(n + \hat{\mu}) - \phi(n)}{a}. \tag{3.16}$$

This is a valid discretization of the derivative because it has the correct continuum limit.

The definition of the discretized derivative, Eq. (3.16), is not unique. This can be immediately seen because the symmetric derivative,

$$\tilde{\partial}_\mu^{(a)}\phi(n) \equiv \frac{\phi(n+\hat{\mu}) - \phi(n-\hat{\mu})}{2a}, \tag{3.17}$$

has the correct continuum limit and does not equal Eq. (3.16). There are an infinite number of discretizations of $\partial_\mu\phi(n)$ because given a valid discretization, one can arbitrarily add additional terms to the discretization as long as they go to zero in the continuum limit[5].

Although there are infinite possible discretizations of ∂_μ, there are usually reasons to prefer one definition. Although all discretizations approach the continuum definition as $a \downarrow 0$, each discretization (and each observable for a given discretization of the action) approaches this limit differently. Some definitions approach the continuum limit quickly, while others take much longer. Choosing a definition that approaches the continuum limit quickly is often beneficial because it means that the $a \downarrow 0$ extrapolation will be simpler to perform and that the results of a calculation at finite lattice spacing may look more directly like the continuum calculation.

Consider the difference between $\partial_\mu^{(a)}\phi(n)$ and $\tilde{\partial}_\mu^{(a)}\phi(n)$ as $a \downarrow 0$. Each definition may be Taylor expanded to determine its approach to the continuum limit. For the forward derivative, one determines the corrections to the continuum definition of $\partial_\mu\phi$ by Taylor expanding the definition:

$$\partial_\mu^{(a)}\phi(n) = \frac{(\phi(n) + a\partial_\mu\phi(n) + \frac{1}{2}a^2\partial_\mu^2\phi(n) + \mathcal{O}(a^3)) - \phi(n)}{a} = \partial_\mu\phi(n) + \mathcal{O}(a). \tag{3.19}$$

The $\frac{1}{2}a^2\partial_\mu^2\phi(n)$ term is the first correction to the derivative and enters as an $\mathcal{O}(a)$ correction to the continuum definition. However, upon performing the same expansion with the symmetric derivative, observe that the corrections to the continuum

[5]For example, for $n \in \mathbb{Z}_{>0}$ and $c \in \mathbb{C}$, the operator

$$\partial_\mu^{(a)} + c\,a^n \tag{3.18}$$

is a discretization of ∂_μ, because as $a \downarrow 0$ the polynomial terms in a vanish.

derivative begin to appear at higher order in a:

$$\begin{aligned}\tilde{\partial}_\mu^{(a)}\phi(n) &= \frac{(\phi(n)+a\partial_\mu\phi(n)+\frac{1}{2}a^2\partial_\mu^2\phi(n))-(\phi(n)-a\partial_\mu\phi(n)+\frac{1}{2}a^2\partial_\mu^2\phi(n))+\mathcal{O}(a^3)}{2a}\\ &= \partial_\mu\phi(n)+\mathcal{O}(a^2).\end{aligned} \tag{3.20}$$

The $\frac{1}{2}a^2\partial_\mu^2\phi(n)$ terms cancel out, so the leading order corrections to the continuum definition enter at $\mathcal{O}(a^2)$. This definition is $\mathcal{O}(a^2)$**-improved**; for small a, the symmetric derivative provides a better discretization than the forward derivative. One can extend this argument to higher-order in a and define a derivative improved to a given order in the lattice spacing.

The same ideas hold when discretizing the QCD action. There are infinitely many possible discretizations, which will have advantages and drawbacks. This thesis will explore the naïve discretization of the QCD action, then two types of discretizations: Wilson and Wilson-Clover.

3.2.1 A First Discretization: the Doubling Problem

The first discretization of the QCD action that is considered is the **naïve discretization**, obtained by simply discretizing the covariant derivative with a symmetric difference and the integral with a discrete sum,

$$\begin{aligned}D_\mu\psi(x) &\xrightarrow{x=an} \frac{U_\mu(n)\psi(n+\hat{\mu})-U_\mu^\dagger(n-\hat{\mu})\psi(n-\hat{\mu})}{2a},\\ \int d^4x &\xrightarrow{x=an} a^4\sum_{n\in\Lambda}.\end{aligned} \tag{3.21}$$

The gauge fields $U_\mu(n)$ appear in order to enforce that the derivative is well-defined and that $D_\mu\psi(x)$ transforms covariantly as $\psi(x)$. With these replacements, the discretized fermion action $\overline{\psi}(\gamma^\mu D_\mu+m)\psi$ becomes

$$\begin{aligned}S_{\text{naive}} &= a^4\sum_{n\in\Lambda}\left(\overline{\psi}(n)\gamma^\mu\frac{U_\mu(n)\psi(n+\hat{\mu})-U_\mu^\dagger(n-\hat{\mu})\psi(n-\hat{\mu})}{2a}+m\overline{\psi}(n)\psi(n)\right)\\ &= a^4\sum_{n,m\in\Lambda}\overline{\psi}_\alpha^a(n)\mathcal{D}_{\alpha\beta}^{ab}(n,m)\psi_\beta^b(m).\end{aligned} \tag{3.22}$$

The operator $\mathcal{D}^{ab}_{\alpha\beta}(n,m)$ is the **Dirac operator** for the naïve discretization. It is the kernel that allows the action to be written as a bilinear in ψ and $\overline{\psi}$, which explicitly allows the fermions to be integrated out of the theory in LGT calculations (this will be discussed further in Section 6.7). Each discretization will have its own Dirac operator, vital to implementing the calculation.

It is illuminating to Fourier transform the Dirac operator and study its momentum-space behavior:

$$\tilde{\mathcal{D}}(p,q) \equiv \sum_{an,am} e^{-ia(p\cdot n - q\cdot m)}\mathcal{D}(n,m) = \delta^{(4)}(p-q)\tilde{\mathcal{D}}(p) \tag{3.23}$$

where $\mathcal{D}(p)$ is the result after splitting off the δ-function,

$$\tilde{\mathcal{D}}(p) = m + \frac{i}{a}\sum_{\mu}\gamma^{\mu}\sin(ap_{\mu}). \tag{3.24}$$

Periodicity of the position-space Dirac operator implies periodicity of the momentum-space Dirac operator: the domain of the momentum-space Dirac operator is called the **Brillouin zone**. For antiperiodic boundary conditions on a $L^3 \times T$ lattice, the Brillouin zone is [78]

$$p_{\mu} \in \Lambda_p \equiv \left\{ \left(\frac{2\pi}{aL_{\mu}}(k_{\mu} + b_{\mu}) \right)_{\mu} \in \mathbb{R}^4 : k_{\mu} \in \left\{ -\frac{L_{\mu}}{2} + 1, ..., L_{\mu} - 1, L_{\mu} \right\} \right\} \tag{3.25}$$

where $L_{\mu} = (L, L, L, T)$ and the vector $b_{\mu} = (0, 0, 0, \frac{1}{2})$ accounts for the antiperiodic boundary conditions in time. The inverse of the Dirac operator is the **propagator** $S(p)$; poles in the propagator give particle masses in the theory (not considering mass renormalization), which are equivalently zeroes of the Dirac operator.

Consider the massless Dirac operator. When p_{μ} takes a value of either 0 or π in any component, $\sin(ap_{\mu})$ vanishes identically. This implies that at any of the 16 values

$$p_{\mu} \in \left\{ \left(0,0,0,0\right), \left(0,0,0,\frac{\pi}{a}\right), \left(0,0,\frac{\pi}{a},0\right), ..., \left(\frac{\pi}{a},\frac{\pi}{a},\frac{\pi}{a},\frac{\pi}{a}\right) \right\}, \tag{3.26}$$

the Dirac operator (Eq. (3.24)) has a zero, and this represents a particle in the theory. The analysis begins in the continuum case with only a single massless particle (corresponding to a pole at $(0,0,0,0)$ in momentum space) which thence produces 15 additional particles. These extra particles are called **doublers**, and they are an

artifact of the discretization of the theory. Despite attempting to write down a theory with a single particle, the periodicity of the lattice has yielded these extra unphysical modes.

3.2.2 Wilson and Wilson-Clover Fermions

The Wilson discretization of the QCD action removes the doublers from the theory by explicitly gapping them out: this can be done by augmenting the Dirac operator $\tilde{\mathcal{D}}(p)$ with an additional term that removes the zero at each of the 15 unphysical modes. Explicitly, one adds the **Wilson term** to the naïve Dirac operator to form the Wilson-Dirac operator [77],

$$\mathcal{D}_W(n,m) \equiv \mathcal{D}(n,m) - \frac{ar}{2}\frac{1}{2a^2}\sum_\mu \left(U_\mu(n)\delta_{n+\hat{\mu},m} - 2\delta_{n,m} + U_\mu^\dagger(n-\hat{\mu})\delta_{n-\hat{\mu},m}\right), \quad (3.27)$$

where here $r \in (0,1]$ is a free parameter. The Wilson term is a discretization of the covariant Laplacian,

$$-\frac{ar}{2}\overline{\psi}D^2\psi \quad (3.28)$$

which is an irrelevant operator that may be added to a lattice action without affecting the continuum limit. The corresponding momentum-space Dirac operator is

$$\tilde{\mathcal{D}}_W(p) = m + \frac{i}{a}\sum_\mu \gamma^\mu \sin(ap_\mu) + \frac{r}{a}\sum_\mu (1-\cos(ap_\mu)). \quad (3.29)$$

Observe the effect the Wilson term has on the theory: it lifts the degeneracy of the doublers. In the massless theory, the 15 doubler modes with $p_\mu^{\text{double}} \neq (0,0,0,0)$ and $p_\mu^{\text{double}} \equiv (0,0,0,0) \mod \frac{\pi}{a}$ no longer specify a zero of the Dirac operator: instead, $\tilde{\mathcal{D}}_W(p^{\text{double}})$ is non-zero. The Wilson action describes only a single particle rather than 16 particles.

The Wilson action finds utility in its simplicity: it is easy to implement and understand and efficiently removes the doublers from the theory. However, it does leave several properties to be desired. The Wilson term explicitly breaks chiral symmetry, even for $m = 0$. The naïve massless Dirac operator $\mathcal{D}$ couples left-handed quarks to left-handed quarks, and vice versa for right-handed quarks:

$$\overline{\psi}\mathcal{D}\psi = \overline{\psi}_L\mathcal{D}\psi_L + \overline{\psi}_R\mathcal{D}\psi_R. \quad (3.30)$$

For the Wilson-Dirac operator, this symmetry breaks. Expand $\mathcal{D}_W = \mathcal{D} + \delta\mathcal{D}_W$,

where $\delta\mathcal{D}_W$ is the discretization of the covariant Laplacian given in Eq. (3.27). This term couples together left-handed quarks with right-handed quarks,

$$\overline{\psi}\delta\mathcal{D}_W\psi = \overline{\psi}_L\delta\mathcal{D}_W\psi_R + \overline{\psi}_R\delta\mathcal{D}_W\psi_L, \tag{3.31}$$

which breaks chiral symmetry. In general, it remains a difficult problem to formulate a discretization of QCD with chiral symmetry and remove the doublers from the theory because of the Nielsen-Ninomiya no-go theorem [79]. The theorem states that it is impossible to have a fermion action on a four-dimensional lattice that respects chiral symmetry, is local, and has no doublers. Attempts to introduce a fermion discretization that respects chiral symmetry must circumvent one of the assumptions of the no-go theorem. A clear example of this is the **domain-wall** fermion discretization, which realizes four-dimensional chiral fermions as edge states living on a five-dimensional bulk space [80, 81]. Domain-wall fermions will be used in Chapter 5 because of their chiral symmetry properties.

The Wilson action is not improved: corrections to the continuum QCD action enter at $\mathcal{O}(a)$. From the Wilson action, one can construct a $\mathcal{O}(a)$-improved action: it is known as the **Wilson-Clover action**. Two additional dimension-5 operators can be added to the Wilson action to remove the $\mathcal{O}(a)$ discretization artifacts: $\overline{\psi}\not{D}\not{D}\psi$, and the Pauli operator $\overline{\psi}\sigma_{\mu\nu}F^{\mu\nu}\psi$. The first term provides no additional information, as $\not{D}\not{D} = D^2 + \frac{1}{2}\sigma_{\mu\nu}F^{\mu\nu}$, hence to improve the action, one thus must consider adding a discretization of $\overline{\psi}\sigma_{\mu\nu}F^{\mu\nu}\psi$ with the appropriate coefficient to remove the $\mathcal{O}(a)$ artifacts.

The field strength $F_{\mu\nu}$ can be discretized with the **clover term** $Q_{\mu\nu}(n)$,

$$F_{\mu\nu}(x) \longrightarrow -\frac{i}{8a^2}\left(Q_{\mu\nu}(n) - Q_{\nu\mu}(n)\right). \tag{3.32}$$

The clover term is a sum of plaquettes oriented in a "clover" geometry around the site n,

$$Q_{\mu\nu}(n) = \mathcal{P}_{\mu,\nu}(n) + \mathcal{P}_{\nu,-\mu}(n) + \mathcal{P}_{-\mu,-\nu}(n) + \mathcal{P}_{-\nu,\mu}(n). \tag{3.33}$$

The clover term is depicted in Figure 3.2.

The full $\mathcal{O}(a^2)$ improved action yielded by the addition of the Pauli operator is the **Wilson-Clover action**, with Dirac operator

$$\mathcal{D}_{\mathrm{WC}}(n,m) = \mathcal{D}_W(n,m) - \frac{i}{8a}c_{\mathrm{sw}}\sum_{\mu<\nu}\frac{1}{2}\sigma_{\mu\nu}\left(Q_{\mu\nu}(n) - Q_{\nu\mu}(n)\right). \tag{3.34}$$

The coupling c_{sw} is called the **Sheikholeslami-Wohlert coefficient** [82]. It is chosen to eliminate the $\mathcal{O}(a)$ term in the Taylor expansion of the continuum action to yield a $\mathcal{O}(a^2)$-improvement.

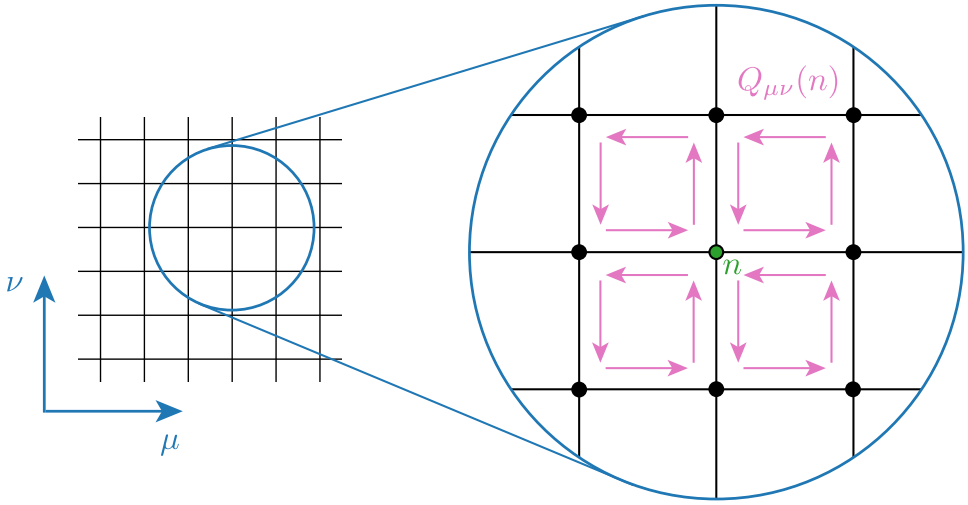

Figure 3.2. The clover term (pink) at $n \in \Lambda$ (green), $Q_{\mu\nu}(n) = \mathcal{P}_{\mu,\nu}(n) + \mathcal{P}_{\nu,-\mu}(n) + \mathcal{P}_{-\mu,-\nu}(n) + \mathcal{P}_{-\nu,\mu}(n)$ (Eq. (3.33)). The clover term is a sum of the positive-oriented plaquettes around the point n and acts as a discretization of the field strength tensor $F_{\mu\nu}$, as in Eq. (3.32).

3.3 Spectroscopy

The remainder of the thesis will use lattice units, where a is set to unity, unless otherwise specified. This choice will be discussed further in Section 3.3.4.

Lattice gauge theory provides a framework to non-perturbatively calculate the correlation functions of operators. The correlation functions of a theory encode all the information about the theory and can be used to compute observables of interest. This section will discuss the calculation of correlation functions and work through the explicit example of mass spectroscopy.

3.3.1 Extracting the Energy Spectrum

Let $\{|n\rangle\}$ denote the energy eigenstates of a theory, and let $|0\rangle$ denote the interacting ground state. The charges of an operator under the symmetries of a theory are called its **quantum numbers**. For example, if $q = \begin{pmatrix} u \\ d \end{pmatrix}$ is the quark isospin doublet, the

quantum numbers of the operator

$$\chi_5(x) \equiv \overline{q}(x)\gamma_5 q(x) \tag{3.35}$$

are spin zero, charge zero, parity odd, and isospin zero. Let $|0\rangle$ denote the vacuum state of the interacting theory. The operator $\mathcal{O}(x)$ may be used to determine information about the energy states of the theory with the same quantum numbers: the matrix element $\langle n|\mathcal{O}^\dagger(x)|0\rangle$ may only be non-zero if the state $|n\rangle$ has the same quantum numbers as $\mathcal{O}(x)$, where $|n\rangle$ is the n^{th} energy state of the theory. The state $\mathcal{O}^\dagger(x)|0\rangle$ is thus a superposition of states in the theory with the same quantum numbers as $\mathcal{O}(x)$[6].

The operator $\chi_5(x)$ (Eq. (3.35)) is an example of an **interpolating operator** [83]. In a given LGT calculation, one typically wants to study a specific state or set of states with given quantum numbers, denoted by $\{|k\rangle\}$. An interpolating operator is any operator that excites the desired set of states. There is freedom to choose between different interpolating operators, and the best interpolator to use to study the states $\{|k\rangle\}$ is the interpolator $\chi(x)$ that maximizes the overlap onto these states, $\langle k|\chi^\dagger(x)|0\rangle$.

One is typically interested in states of definite three-momentum $\mathbf{p}$, as this represents a particle with definite momentum and energy (note that $\mathbf{p} = \mathbf{0}$ denotes a particle in its rest frame). To excite states with momentum $\mathbf{p}$, one **momentum projects** the interpolator $\chi(x)$:

$$\tilde{\chi}_{\mathbf{p}}(t) \equiv \frac{1}{\sqrt{L^3}} \sum_{\mathbf{x}} e^{-i\mathbf{p}\cdot\mathbf{x}} \chi(\mathbf{x}, t). \tag{3.36}$$

The state $\tilde{\chi}_{\mathbf{p}}(t)|0\rangle$ is interpreted as a combination of states with the same quantum numbers as the operator χ, all at time t with definite momentum $\mathbf{p}$.

To explicitly see the interplay of the different components, recall the resolution of the identity,

$$1 = \sum_n \frac{1}{2E_n} |n\rangle\langle n| \tag{3.37}$$

where $\{|n\rangle\}$ denotes all the energy eigenstates in the theory, and the eigenstates are relativistically normalized according to $\langle n|n'\rangle = 2E_n\delta_{n,n'}$. The resolution of the identity allows us to spectrally decompose any state or correlation function in the

[6]Note that although any state $|n\rangle$ with the same quantum numbers can potentially be excited by $\mathcal{O}^\dagger(x)$, it does not have to be; such a state could have zero, or very small, overlap with the operator $\mathcal{O}^\dagger(x)$, i.e., $\langle n|\mathcal{O}^\dagger(x)|0\rangle \approx 0$.

basis $\{|n\rangle\}$ of energy eigenstates:

$$\tilde{\chi}^\dagger_{\mathbf{p}}(t)|0\rangle = 1\tilde{\chi}^\dagger_{\mathbf{p}}(t)|0\rangle = \sum_n \frac{1}{2E_n}|n\rangle\langle n|\tilde{\chi}^\dagger_{\mathbf{p}}(t)|0\rangle. \tag{3.38}$$

The overlap factor $Z_{n,\mathbf{p}} \equiv \langle n|\tilde{\chi}^\dagger_{\mathbf{p}}(t)|0\rangle$ is the weight of the state $|n\rangle$ in the decomposition of the state $\tilde{\chi}^\dagger_{\mathbf{p}}(t)|0\rangle$. To study a specific state, one chooses an interpolator that maximizes its overlap with said state. The decomposition of Eq. (3.38) also clarifies that operators only excite states with the same quantum numbers. If $|n\rangle$ and $\tilde{\chi}_{\mathbf{p}}(t)$ have different quantum numbers, the matrix element $\langle n|\tilde{\chi}^\dagger_{\mathbf{p}}(t)|0\rangle$ vanishes identically, hence $|n\rangle$ will not be present in the superposition of states $\tilde{\chi}^\dagger_{\mathbf{p}}(t)|0\rangle$.

Two-point correlation functions will provide the basic ingredient to determine the spectrum of a theory. Consider the two-point function of the interpolator $\tilde{\chi}_{\mathbf{p}}(t)$, separated by time t:

$$C_2(t;\mathbf{p}) \equiv \langle 0|\tilde{\chi}_{\mathbf{p}}(t)\tilde{\chi}^\dagger_{\mathbf{p}}(0)|0\rangle \tag{3.39}$$

$C_2(t;\mathbf{p})$ is a function of t at fixed $\mathbf{p}$. Recall that in Euclidean space, the Heisenberg picture evolution of an operator (with spatial indices suppressed) is:

$$\mathcal{O}(t) = e^{Ht}\mathcal{O}(0)e^{-Ht}, \tag{3.40}$$

where H is the Hamiltonian. Inserting a resolution of the identity into $C_2(t;\mathbf{p})$ yields (denoting by E_n the energy of state $|n\rangle$),

$$\begin{aligned} C_2(t;\mathbf{p}) &= \sum_n \frac{1}{2E_n}\langle 0|\tilde{\chi}_{\mathbf{p}}(t)|n\rangle\langle n|\tilde{\chi}^\dagger_{\mathbf{p}}(0)|0\rangle \\ &= \sum_n \frac{1}{2E_n}\langle 0|e^{Ht}\tilde{\chi}_{\mathbf{p}}(0)e^{-Ht}|n\rangle\langle n|\tilde{\chi}^\dagger_{\mathbf{p}}(0)|0\rangle \\ &= \sum_n \frac{1}{2E_n}\left|\langle n|\tilde{\chi}^\dagger_{\mathbf{p}}(0)|0\rangle\right|^2 e^{-E_n t} \\ &= \sum_n \frac{|Z_{n,\mathbf{p}}|^2}{2E_n}e^{-E_n t} \end{aligned} \tag{3.41}$$

The spectral decomposition of $C_2(t;\mathbf{p})$ shows that it is a sum of decaying exponentials in t, each weighted by the energy of the corresponding state in the tower.

Suppose that the states are labeled in terms of energy, i.e., $E_0 < E_1 < E_2 < ...$ (with no degeneracies, for simplicity). Although the sum in Eq. (3.41) has an infinite number of terms, as $t \to \infty$ the lowest-lying states dominate the correlator because

higher-energy terms are exponentially suppressed:

$$\lim_{t\to\infty} C_2(t;\mathbf{p}) = \frac{|Z_{0;\mathbf{p}}|^2}{2E_0} e^{-E_0 t}. \tag{3.42}$$

This is an explicit parameterization of the large-time behavior of $C_2(t;\mathbf{p})$ in terms of the system's ground state energy E_0. Computing and analyzing the correlator $C_2(t;\mathbf{p})$ in the large-time limit allows one to estimate the ground state energy E_0 from the exponential decay rate. One can also fit additional exponential corrections to the model of Eq. (3.42) to model excited-state dependence; this will be discussed further in Chapter 5.

A simple way to extract the ground state energy E_0 from a two-point correlator $C(t)$ (here the $\mathbf{p}$ dependence is suppressed) is to construct the correlator's **effective mass**, defined as

$$m_{\text{eff}}(t) \equiv \log\left(\frac{C(t)}{C(t+1)}\right). \tag{3.43}$$

In a correlator satisfying the asymptotic limit of Eq. (3.42), the effective mass asymptotes to the desired value, E_0, as $t \to \infty$. When there is a gap Δ between the ground state and first excited state such that $\Delta/E_0 \not\ll 1$ (i.e., the ground state and first excited state may be well-distinguished), Monte Carlo data for $m_{\text{eff}}(t)$ will plateau when $0 \ll t \ll T/2$. The value of this plateau is an estimator for E_0. The effective mass is a useful heuristic, but it may be improved by considering boundary conditions. When the spectral decomposition (Eq. (3.42)) is applied with finite temporal boundary conditions, a backward-propagating state becomes apparent when $t \not\ll T$,

$$\lim_{t\to\infty} C_2(t;\mathbf{p}) = \frac{|Z_{0;\mathbf{p}}|^2}{2E_0}\left(e^{-E_0 t} \pm e^{-E_0(T-t)}\right). \tag{3.44}$$

The sign $\pm$ depends on the system (see Section 4.3 for further discussion). This sign modifies the behavior of the effective mass, and from the decomposition of Eq. (3.44), the proper quantity to compute for a symmetric $(+)$ correlator is the **cosh-corrected effective mass**,

$$m_{\text{eff}}^{\cosh}(t) \equiv \operatorname{arccosh}\left(\frac{C(t+1)+C(t-1)}{C(t)}\right). \tag{3.45}$$

This variant of the effective mass correctly accounts for the boundary conditions in the system.

The calculation of $C_2(t;\mathbf{p})$ is a simple example but illustrates the general principle

that LGT uses to extract observable quantities from the theory. To calculate an observable, one decides on a set of correlation functions to compute and shows that in specific limits, a combination (often a ratio) of these correlation functions asymptotes to the desired observable. The next thing to consider is the computation of correlation functions in LGT.

3.3.2 Calculating Correlators in LGT

Let $\{U_\mu^{(i)}(x)\}_{i=1}^N$ be an ensemble of N gauge field configurations that sample the Boltzmann distribution for some lattice QCD gauge action, and suppose that one wishes to compute correlation functions on each gauge configuration. This computation begins with the partition function to illustrate the basic ideas and then computes an arbitrary n-point correlation function.

Let $\mathcal{D}[U]$ be the discretized Dirac operator, so the full action S may be expanded in terms of a fermion piece and a gauge part $S_g[U]$:

$$S[\psi, \overline{\psi}, U] = \int d^4x\, d^4y\, \overline{\psi}(x)\mathcal{D}[U](x,y)\psi(y) + S_g[U] \tag{3.46}$$

Recall that the Dirac operator $\mathcal{D}[U] = \mathcal{D}[U]^{ab}_{\alpha\beta}(x,y)$ is a matrix in spin-color space, as well as on the discrete spacetime[7]. The advantage of the representation of the fermion action as $\overline{\psi}\mathcal{D}[U]\psi$ is that the path integral is explicitly a Gaussian integral over the Grassmann-valued fields ψ and $\overline{\psi}$, which may be explicitly evaluated before integrating over the gauge degrees of freedom. This yields a fermion determinant,

$$\mathcal{Z} = \int DU\, D\psi D\overline{\psi}\, e^{-\int d^4x\, d^4y\, \overline{\psi}(x)\mathcal{D}[U](x,y)\psi(y) - S_g[U]} = \int DU\, e^{-S_g[U]}\, \mathrm{Det}[\mathcal{D}[U]], \tag{3.48}$$

where Det denotes a functional determinant. The main takeaway is that the fermion degrees of freedom may be explicitly integrated out of the path integral, reducing the path integral to an integral solely over the gauge degrees of freedom. The gauge integral may be computed numerically with Markov Chain Monte Carlo (MCMC) [84]. Explicit implementation details for MCMC in LGT will be discussed in Section 3.4.

When operators are inserted into the path integral, expressions become more complicated. Still, the core idea holds: evaluate the fermion path integral analytically,

[7] Note that these inner products will often be abbreviated with matrix-vector notation, for example

$$\overline{\psi}\mathcal{D}[U]\psi = \int d^4x\, d^4y\, \overline{\psi}^a_\alpha(x)\mathcal{D}[U]^{ab}_{\alpha\beta}(x,y)\psi^b_\beta(y). \tag{3.47}$$

then use MCMC to numerically estimate the path integral over the gauge degrees of freedom. Suppose one wishes to compute the correlation function $\langle \mathcal{O}_1(x_1)...\mathcal{O}_k(x_k)\rangle$. As before, this may be reduced down to an integral over gauge degrees of freedom:

$$\begin{aligned}\langle \mathcal{O}_1(x_1)...\mathcal{O}_k(x_k)\rangle &= \int DU\, D\psi D\overline{\psi}\, e^{-\int d^4x\, d^4y\, \overline{\psi}(x)\mathcal{D}[U](x,y)\psi(y) - S_g[U]}\, \mathcal{O}_1(x_1)...\mathcal{O}_k(x_k) \\ &= \int DU\, e^{-S_g[U]}\, (\mathrm{Det}\, \mathcal{D}[U])\, \langle \mathcal{O}_1(x_1)...\mathcal{O}_k(x_k)\rangle_F[U].\end{aligned} \tag{3.49}$$

Here, Eq. (3.49) introduces the notation $\langle\cdot\rangle_F[U]$ to denote the fermion expectation value of an expression:

$$\langle \mathcal{O}_1(x_1)...\mathcal{O}_k(x_k)\rangle_F[U] \equiv \frac{1}{\mathrm{Det}\, \mathcal{D}[U]} \int D\psi\, D\overline{\psi}\, e^{-\int d^4x\, d^4y\, \overline{\psi}(x)\mathcal{D}[U](x,y)\psi(y)}\, \mathcal{O}_1(x_1)...\mathcal{O}_k(x_k). \tag{3.50}$$

Splitting the integral into these two pieces clarifies how the computation proceeds. The fermion expectation value is first evaluated analytically, and then the resulting path integral over gauge degrees of freedom is evaluated with MCMC.

When the operators $\mathcal{O}_i(x)$ are polynomials in $\overline{\psi}(x)$ and $\psi(x)$, the fermion expectation value can be evaluated with **Wick's theorem** [85] since Eq. (3.50) computes the moments of a Gaussian path integral. Wick's theorem says that the fermion path integral may be computed by summing over all possible Wick contractions in an expression:

$$\langle \mathcal{O}_1(x_1)...\mathcal{O}_k(x_k)\rangle_F[U] = \sum_{(a,b,...,c,d)\in \mathrm{Wick}} \mathcal{D}^{-1}_{ab}[U]...\mathcal{D}^{-1}_{cd}[U]. \tag{3.51}$$

Here, the indices $(a, b, ..., c, d)$ are multi-indices that package together each inverse Dirac operator's spin, color, and spacetime indices. A Wick contraction is any way to connect a field with its anti-partner. For example, if q is a quark field, the expression $\langle q\overline{q}\rangle$ has one possible Wick contraction: there is one way to connect q with $\overline{q}$. This is denoted by $\langle \overline{q}q\rangle$. In the more complicated example of $\mathcal{O}_1 = \mathcal{O}_2 = \mathcal{O}_3 = \overline{q}q$, there are six possible Wick contractions (the spacetime argument is written as a subscript to avoid clutter):

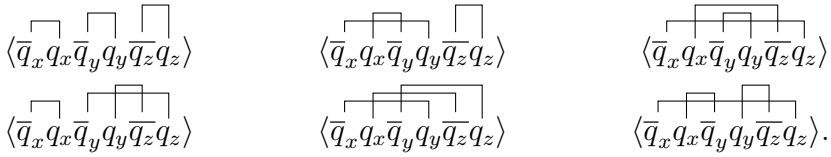

(3.52)

Here the Wick contraction $\langle \overline{q}_x ... q_z ... \rangle$ denotes that the field $\overline{q}_x$ should be contracted with the field q_z, (anti)commuting all necessary fields in order to form the propagator $\langle q_z \overline{q}_x ... \rangle = \mathcal{D}_{zx}^{-1}[U]\langle ... \rangle$. As an explicit example,

$$\langle \overline{q}_x q_x \overline{q}_y q_y \overline{q}_z q_z \rangle = (-1)^2 \langle q_z \overline{q}_x q_x \overline{q}_z q_y \overline{q}_y \rangle = \mathcal{D}_{zx}^{-1}[U]\mathcal{D}_{xz}^{-1}[U]\mathcal{D}_{yy}^{-1}[U], \tag{3.53}$$

where the two factors of -1 come from anticommuting q_y past $\overline{q}_y$, and q_z past each other field in the correlator. Computing the correlation function $\langle \mathcal{O}_1(x)\mathcal{O}_2(y)\mathcal{O}_3(z)\rangle$ hence requires six different contractions of $\mathcal{D}^{-1}$, each corresponding to one set of Wick contractions. Fields can only contract with anti-partners of the same type. For example, there is only one Wick contraction of $\langle \overline{u}u\overline{d}d\rangle$, which results from contracting u with $\overline{u}$, and d with $\overline{d}$. The inverse of the Dirac operator is called a **propagator**, often denoted by S. Propagators describe the probability amplitude for a particle to propagate between x and y. Note that in the case where some subset of the operators $\mathcal{O}_i(x)$ contain the gauge field (for example, $\mathcal{O}_1(x) = \sum_{\mu<\nu}\sum_x P_{\mu\nu}(x)$, or $\mathcal{O}(x) = \sum_x \overline{\psi}(x)U_\mu(x)\psi(x+\hat{\mu})$), one simply factors these gauge factors out of the fermion expectation value $\langle ... \rangle_F$, as the fermionic path integral can be evaluated without considering gauge observables. So, for example,

$$\left\langle \sum_x \overline{\psi}(x)U_\mu(x)\psi(x+\hat{\mu}) \right\rangle_F [U] = -\sum_x \mathcal{D}_{x+\hat{\mu},x}[U]U_\mu(x). \tag{3.54}$$

After computing the Wick contractions for the given correlation function and factoring out the pure gauge observables, the correlation function is obtained by taking the gauge average over $\langle \mathcal{O}_1 ... \mathcal{O}_k \rangle_F[U]$. Naïvely, one would do this by using a Markov chain to sample $\{U^{(i)}\} \sim DU\, e^{-S_g[U]}$, compute $\operatorname{Det}\mathcal{D}[U^{(i)}]\langle \mathcal{O}_1(x_1)...\mathcal{O}_k(x_k)\rangle_F[U^{(i)}]$ on each sample, then average this quantity over all samples. The problem with this is the fermion determinant, $\operatorname{Det}\mathcal{D}[U^{(i)}]$. Computing the determinant of a $n \times n$ matrix is a $\mathcal{O}(n^3)$ operation. This is prohibitively expensive for even modest lattice sizes (e.g., $16^3 \times 48$).

Instead of direct evaluation of the determinant of the Dirac operator, one absorbs the fermion determinant into the definition of the probability measure. Rather than sampling gauge configurations from the density $DU\, e^{-S_g[U]}$, one samples configurations from the density

$$\{U^{(i)}\} \sim DU\, e^{-S_g[U]} \operatorname{Det}\mathcal{D}[U]. \tag{3.55}$$

The exact details of how this sampling is implemented and its limitations are described

in Section 3.4. Once the configurations $\{U^{(i)}\}$ are generated, the fermion expectation value $\langle \mathcal{O}_1(x_1)...\mathcal{O}_k(x_k)\rangle_F[U^{(i)}]$ is computed on each configuration and averaged over configurations. All work described in this thesis will use dynamical fermions.

To summarize, the workflow to calculate a correlation function $\langle \mathcal{O}_1(x_1)...\mathcal{O}_k(x_k)\rangle$ in LGT is thus as follows.

1. Specify an action and set of correlation functions to compute.

2. Generate an ensemble of gauge configurations corresponding to the desired action.

3. Compute the fermion expectation value $\langle \mathcal{O}_1(x_1)...\mathcal{O}_k(x_k)\rangle_F[U]$ of each correlation function by performing all possible Wick contractions and factoring out factors of the gauge field.

4. Compute $\langle \mathcal{O}_1(x_1)...\mathcal{O}_k(x_k)\rangle_F[U]$ on each gauge configuration in the ensemble to determine a Monte Carlo estimate of $\langle \mathcal{O}_1(x_1)...\mathcal{O}_k(x_k)\rangle$.

3.3.3 Dirac Operators and Propagators

Given a Dirac operator $D^{ab}_{\alpha\beta}(x,y)$, the propagator is defined as its inverse $S^{ab}_{\alpha\beta}(x,y)$,

$$\sum_{z\in\Lambda} D^{ac}_{\alpha\gamma}(x,z)S^{cb}_{\gamma\beta}(z,y) = \sum_{z\in\Lambda} S^{ac}_{\alpha\gamma}(x,z)D^{cb}_{\gamma\beta}(z,y) = \delta_{\alpha\beta}\delta^{ab}\delta^{(4)}(x-y) \tag{3.56}$$

On the lattice, the Dirac operator $D^{ab}_{\alpha\beta}(x,y)$ is explicitly a $(N_c \times N_s \times L^3 \times T) \times (N_c \times N_s \times L^3 \times T)$ dimensional matrix, so theoretically the matrix can be inverted numerically. However, the size of a matrix in a large-scale LGT calculation almost always makes direct inversion of $D^{ab}_{\alpha\beta}(x,y)$ prohibitively expensive; for example, a QCD Dirac fermion in $d = 4$ on a lattice of size $48^3 \times 96$ has a Dirac operator matrix of size $\approx 10^8 \times 10^8$, which is much too large to invert or store numerically.

Conventional LGT methods circumvent this problem in a variety of ways. In addition to being the inverse of the Dirac operator, the propagator also has an appealing interpretation as a two-point function of the quark field:

$$S^{ab}_{\alpha\beta}(x,y) = \langle 0|T\{q^a_\alpha(x)\overline{q}^b_\beta(y)\}|0\rangle. \tag{3.57}$$

Eq. (3.57) shows that $S^{ab}_{\alpha\beta}(x,y)$ is the amplitude for a particle to propagate from the multi-index (y,β,b) (the **source**) to the multi-index (x,α,a) (the **sink**). The

full propagator is called an **all-to-all propagator** because it contains propagation amplitudes from all sources to all sinks.

The Wick contractions describing a given correlation function (e.g., Eq. (3.51)) deconstruct a given correlation function into a superposition of propagator components that connect specific source and sink points that are compatible with the symmetries of the desired correlation function and underlying theory. As such, for a given correlation function, the full all-to-all propagator is not necessary to compute: one can instead focus on computing propagation amplitudes between specific source and sink points, which significantly reduces the computational complexity of the problem: in simpler terms, it is easier to compute a row or column of a matrix inverse than to perform the full matrix inversion.

The discrete system has **translation invariance** in the limit of infinite statistics. One can use translation invariance to reduce the number of inversions required for the calculation by fixing the source or sink to the time-slice at 0. Computing $S((\mathbf{x}, t); (\mathbf{y}, 0))$ instead of $S((\mathbf{x}, t); (\mathbf{y}, s))$ reduces the number of inversions by a factor of T, which can speed up the computation greatly. One can likewise use symmetries to reduce the number of propagator inversions. For example, if one considers an amplitude describing the interaction between two parity-even particles, only the parity-even components of the propagator need to be computed.

A particularly important symmetry of the Dirac operators considered in this thesis is **γ_5-hermicity**. A Dirac operator $\mathcal{D}(n, m)$ is γ_5-hermitian if

$$\gamma_5 \mathcal{D}(n, m) \gamma_5 = \mathcal{D}^\dagger(m, n). \tag{3.58}$$

Here, $\cdot^\dagger$ is applied to the color-spin blocks of the Dirac operator so that the right-hand side may be regarded as a full Hermitian conjugate over the full set of color, spin, and spacetime indices. A useful property of γ_5-hermicity is that it relates a forward-moving propagator to a backward-moving propagator: this can significantly cut down on the number of inversions required to compute a correlation function.

To compute a specific superposition of propagator components, one first chooses a **source** $\sigma^a_\alpha(x)$ to invert the propagator on. The source describes the initial state of the system before propagation. The following linear system is solved for $M^b_\beta(y)$,

$$\sum_{b,\beta,y} \mathcal{D}^{ab}_{\alpha\beta}(x, y) M^b_\beta(y) = \sigma^a_\alpha(x), \tag{3.59}$$

which is a specific superposition of propagator components dictated by σ:

$$M_\alpha^a(x) = \sum_y (\mathcal{D}^{-1})_{\alpha\beta}^{ab}(x,y)\sigma_\beta^b(y) = \sum_y S_{\alpha\beta}^{ab}(x,y)\sigma_\beta^b(y). \tag{3.60}$$

Eq. (3.59) is typically solved using a numerical inversion algorithm like the Conjugate Gradient Method [86].

Several important sources will be considered in this thesis, each of which corresponds to specific initial states. This list is not exhaustive; any field $\sigma_\alpha^a(x)$ can be used as a source.

- A **point source** at (γ, c, z):

$$\sigma_\alpha^a(x) = \delta_{\alpha\gamma}\delta^{ac}\delta_{xz} \qquad M_\alpha^a(x) = S_{\alpha\gamma}^{ac}(x,z). \tag{3.61}$$

  Inverting from a point source isolates the column of the propagator corresponding to the index (γ, c, z); the field $M_\alpha^a(x)$ contains the propagation amplitude for a particle to propagate from the source (γ, c, z) to any sink (α, a, x) on the lattice.

- A **three-dimensional wall source** at time t_0 with momentum $\mathbf{p}$:

$$\sigma_\alpha^a((\mathbf{x},t)) = e^{i\mathbf{p}\cdot\mathbf{x}}\delta_{t,t_0} \qquad M_\alpha^a(x) = \sum_{\beta,b,\mathbf{y}} e^{i\mathbf{p}\cdot\mathbf{y}} S_{\alpha\beta}^{ab}(x,(\mathbf{y},t_0)) \tag{3.62}$$

  The three-dimensional wall source describes a particle with fixed momentum $\mathbf{p}$ at time t_0. It can also be used with a Dirac and color structure to excite specific Dirac and color components to this momentum.

- A **four-dimensional wall source**, with four-momentum p:

$$\sigma_\alpha^a(x) = e^{-ip\cdot x} \qquad M_\alpha^a(x) = \sum_{\beta,b,y} S(x,y)e^{-ip\cdot y} \tag{3.63}$$

  The four-dimensional wall source projects the source to definite four-momentum p and is conventionally used in non-perturbative renormalization calculations.

3.3.4 Lattice Units and Scale Setting

The inputs to a LGT calculation are the couplings, masses, and the lattice size $L^3 \times T$. The lattice spacing a is not an input parameter to the calculation; on the lattice, all

dimensionful quantities come in factors of lattice units. The spacing a cannot be measured directly on the lattice but can only be determined by comparison to a benchmark. In the case of Standard Model field theories, this benchmark can be taken to be a physical quantity that has been experimentally measured. This may not always be possible in lattice field theories other than QCD, as there may be no experimental measurements to compare to. This will be discussed in Chapter 6 in the case of 2-dimensional adjoint QCD.

On a given ensemble, lattice quantities are computed at fixed spacing a, and the scale is set by matching a dimensionful observable M (e.g., the proton mass m_p) computed on the lattice to its experimental value [87]. Let aM_{lat} be the value of M computed on the lattice, and M_{exp} the experimentally known value of M. The lattice spacing is determined as

$$a_M \equiv \frac{aM_{\text{lat}}}{M_{\text{exp}}}. \tag{3.64}$$

Note that different choices of M will yield different values for the lattice spacing. Depending on the precision that aM_{lat} and M_{exp} are known to, the statistical precision that a_M is known to will vary.

There are many important considerations when choosing an observable M to set the scale. The lattice spacing a should have as little statistical and systematic error as possible, as it enters every calculation that has a mass scale. Thus, M should be chosen as a quantity that can be computed to high precision on the lattice, and is known to high precision through the experiment. The computational cost of computing aM_{lat} should also be factored into the choice of M: cheaper quantities are preferred over more expensive ones. Finally, all LGT calculations are done at finite lattice spacing and volume, and many are performed at unphysically heavy quark masses. One should pick an observable for M that has little dependence on the lattice spacing, volume, and quark mass. Useful choices for scale setting to experiment are the pion decay constant f_π, the proton mass m_p, and the Ω baryon mass m_Ω [88].

Comparison to experiment is not always needed: it is often useful to only compare the lattice spacing between different ensembles, without regard for the absolute physical scale. This is called indirect scale setting. In this case, other observables can be used to set the scale that are not experimentally measurable, but can be measured precisely and cheaply in a lattice calculation. Often, these observables are solely functions of the gauge fields and do not require the inversion of quark propagators, like f_π or baryon masses. The various projects discussed in this thesis will use two different scale-setting parameters: the Sömmer parameter r_0[89, 90], and the Wilson

flow scale w_0 [91].

3.4 Generating Gauge Configurations

One important bottleneck in LGT calculations is sampling the desired probability distribution on the space of gauge fields. The gauge fields must be generated according to the probability distribution $\mathbb{P}$ specified by the desired choice of action, and they must be independent and identically distributed (iid):

$$\{U^{(i)}\} \overset{\text{iid}}{\sim} \mathbb{P}. \tag{3.65}$$

Gauge fields will be sampled from this distribution with a **Markov Chain**, which is a chain of configurations $U^{(0)} \to U^{(1)} \to U^{(2)} \to ...$ that are sampled from the law $\mathbb{P}$. The variable i is called the **computer time**, and this specifies the number of iterations the chain has been run for.

Given a configuration $U^{(i)}$, the Markov Chain describes how to compute the next state in the chain $U^{(i+1)}$. The Markov Chain requires an initial configuration $U^{(0)}$ to begin; once it is seeded with this configuration, it can be run to produce more samples. Typically, the initial configuration is either randomly sampled from the space of gauge fields (a **hot start**) or set equal to the identity field (a **cold start**). The law of the chain at small computer time will depend on the initial configuration $U^{(0)}$, and as such, will not obey the desired distribution $\mathbb{P}$. However, after a sufficiently long time, the law of the chain will converge to the measure $\mathbb{P}$ [84], regardless of where the chain was started. This process is known as **thermalization**. The **thermalization time** τ_{therm} of the chain is the computer time required to make the law of $\{U^{(i)}\}_{i \geq \tau_{\text{therm}}}$ equal $\mathbb{P}$ in distribution. One can compute τ_{therm} by performing a hot and cold start and seeing when the distribution of the two Markov chains appear equal. Once τ_{therm} is computed, one drops all configurations generated with computer time $i \leq \tau_{\text{therm}}$.

Depending on the updating scheme, the configurations in the chain may not be independent over short computer time separations: configuration $U^{(i+1)}$ is typically highly correlated with configuration $U^{(i)}$. These correlations must be removed to generate independent configurations. To determine the **correlation length**, one picks a set of gauge observables $\{\chi\}$ that is easy to compute on each configuration (for example, the sum of all plaquettes and the topological charge). For each observable χ, one computes the **autocorrelation** $\text{Corr}[\chi(U^{(i)}), \chi(U^{(i+\delta)})]$, which can be shown

to decay as an exponential in the computer time separation δ

$$\text{Corr}[\chi(U^{(i)}), \chi(U^{(i+\delta)})] \propto e^{-\delta\tau_\chi} \tag{3.66}$$

The maximum value of τ_χ over all observables (rounded up to the next integer) is the **correlation length** of the system

$$\tau \equiv \sup_\chi \tau_\chi. \tag{3.67}$$

This is the computer time that must separate configurations if they are to be sampled with little or no autocorrelation. To generate independent configurations, one subsamples all configurations $\{U^{(i)}\}$ and only uses configurations that are at least τ apart in computer time: that is, the set

$$\{U'^{(k)}\} \equiv \{U^{(k\tau)}\} \tag{3.68}$$

for $k \in \mathbb{Z}_{>0}$. The configurations $U'^{(k)}$ produce the desired iid distribution after thermalization. The $'$ superscript on U will be dropped, and this thesis will only refer to the original, non-independent links if the gauge generation process is being discussed.

Any Markov chain is characterized by a transition probability T,

$$T[U|U'] \equiv \mathbb{P}\left[U^{(i)} = U | U^{(i-1)} = U'\right] \tag{3.69}$$

which is the probability of the chain evolving to the configuration U from configuration U'[8]. The transition probabilities are chosen to make the desired probability measure $\mathbb{P}$ an **invariant measure** for the Markov chain. Once the law of the Markov chain becomes $\mathbb{P}$ (after the chain thermalizes), further transitions within the Markov chain will continue to have the law $\mathbb{P}$. This is encoded in the definition of the invariant measure as the eigenvectors of the transition matrix with unit eigenvalue [92]:

$$\mathbb{P}[U] = \sum_{U'} \mathbb{T}[U|U']\mathbb{P}[U'] \tag{3.70}$$

The transition probabilities are constrained to satisfy a **balance equation** that determines there is no net probability flux. In other words, the probability of transi-

[8]Note the Markov property implies that chain is completely characterized by its current state: the transition probabilities only depend on the configurations they connect, not on the computer time each configuration was sampled at.

tioning into a state equals the probability of transitioning out of a state. The balance equation is:

$$\sum_{U'} T[U|U']\mathbb{P}[U'] = \sum_{U'} T[U'|U]\mathbb{P}[U]. \tag{3.71}$$

Here, the left-hand side represents the probability of transition from any state into U, and the right-hand side represents the probability of transition from U into any state. If the balance equation is satisfied, the invariant measure of the Markov chain will be $\mathbb{P}$. Typically, in LGT, the stronger condition of **detailed balance** is imposed, in which the balance equation holds configuration-by-configuration:

$$T[U|U']\mathbb{P}[U'] = T[U'|U]\mathbb{P}[U]. \tag{3.72}$$

Any transition probability satisfying Eq. (3.72) will fulfill Eq. (3.71), the balance equation, although it is not a necessary condition to satisfy the detailed balance equation.

State-of-the-art LGT calculations with dynamical fermions use Hamiltonian Monte Carlo (HMC) [93, 94] to construct a Markov chain satisfying the detailed balance equation. The general principles behind HMC will be discussed in Section 6.4.3 in generating gauge configurations for two-dimensional adjoint QCD.

3.5 Statistics for LGT

At the heart of LGT lies the statistical analysis of Monte Carlo data. LGT calculations generate correlated[9] Monte Carlo samples for correlation functions: these samples must be fit to different models to extract estimators of physical quantities. Assume that one has an ensemble of n_{cfgs} gauge field configurations $U^{(i)}$ and a family of correlation functions $\{C_k^{(i)}(t)\}$ computed on each configuration. Here $k \in [K]$ indexes the number of correlation functions that are computed, and $t \in \mathcal{T}$ parameterizes each correlation function, where $\mathcal{T}$ is a finite indexing set[10]. Note that for any $n \in \mathbb{N}$, this work adopts the notation

$$[n] \equiv \{1, ..., n\}. \tag{3.73}$$

[9]Note that here "correlated" refers to correlations between different correlation functions. For a given correlation function, the Monte Carlo samples are independent, as one assumes that the Markov Chain $U^{(i)}$ is sampling independent samples.

[10]This suggestive notation is picked because the parameter t is often the time separation of the correlation function, in which case $\mathcal{T} = [T]$ indexes all the time-slices on the lattice. However, the general techniques in this section can be applied to any parameterization of correlation functions, particularly in cases like non-perturbative renormalization (NPR) where t is a four-momentum and $\mathcal{T}$ is the set of all four-momenta accessible on the lattice.

This gives us an ensemble of correlation functions

$$\left\{C_k^{(i)}(t) : i \in [n_{\text{cfgs}}],\, k \in [K],\, t \in \mathcal{T}\right\}, \tag{3.74}$$

which is the starting point for LGT data analysis. Furthermore, the samples $C_k^{(i)}(t)$ are assumed to be independent in i because the gauge fields $U^{(i)}$ are all separated by a computer time of at least the autocorrelation length in the original generation of the Markov chain.

3.5.1 Resampling and the Bootstrap

Resampling methods generate new samples from the existing data measurements: they provide an efficient way to compute statistical estimators when given a correlated data set. There are two primary advantages of resampling the data, both of which are beneficial in the context of a LGT calculation [95]:

1. Resampling makes it very simple to track correlations.

2. Resampling allows one to compute standard errors of statistical estimators with simulation without an explicit closed form for the estimator.

This work will primarily consider a resampling method called the **bootstrap** [96], although the jackknife method [97] is also often used in LGT calculations.

For simplicity, fix k and t and consider only the samples for one part of one correlation function, $C^{(i)} \equiv C_k^{(i)}(t)$; this will extended to the full set of correlators later. The best guess of the distribution from which $C^{(i)}$ is drawn is the **empirical distribution** of $C^{(i)}$, which evenly distributes mass at each observed sample. The empirical distribution has PDF

$$f_{\text{emp}}(c) \equiv \frac{1}{n_{\text{cfgs}}} \sum_{i=1}^{n_{\text{cfgs}}} \delta\left(c - C^{(i)}\right). \tag{3.75}$$

A **bootstrap sample** C^b is the average of n_{cfgs} samples drawn from the empirical distribution. In practice, this means that C^b is constructed by uniformly sampling with replacement n_{cfgs} times from $C^{(i)}$ and averaging these samples together. This procedure is repeated independently B times to form a bootstrap distribution $\{C^b\}_{b=1}^B$, where B is the size of the resampled distribution. B is a hyperparameter in the analysis and is typically chosen to be the same order of magnitude as n_{cfgs}, but can be increased or decreased depending on the specifics of the calculation.

To extend the bootstrap to the full set of correlation functions $\{C_k^{(i)}(t)\}$, one generates a bootstrap ensemble for each correlation function $C_k(t)$. Note that the correlation between $C_k(t)$ and $C_\ell(s)$ must be preserved for each choice of k, ℓ, t, and s: as such, each bootstrap sample must be drawn in a correlated way. For each bootstrap $b \in [B]$, one thus draws n_{cfgs} samples with replacement $\{i_1, ..., i_{\text{ncfgs}}\}$ from the set $[n_{\text{cfgs}}]$, and $C_k^b(t)$ is the average

$$C_k^b(t) = \frac{1}{n_{\text{cfgs}}} \sum_{j=1}^{n_{\text{cfgs}}} C_k^{(i_j)}(t). \tag{3.76}$$

This retains the correlation between the measurements and constructs the bootstrap distribution $\{C_k^b(t)\}$.

One computes several important estimators from the bootstrap distribution. One first defines the sample mean of a bootstrap distribution:

$$\widehat{\mathbb{E}}[C_k(t)] \equiv \overline{C}_k(t) \equiv \frac{1}{B} \sum_{b=1}^{B} C_k^b(t). \tag{3.77}$$

This notation is used interchangeably: first, to emphasize that this quantity is an estimator of the mean of the random variable $C_k(t)$; and second, to emphasize that this quantity is the sample mean over bootstraps of $C_k(t)$. The unbiased sample covariance of the distribution is also defined,

$$\widehat{\text{Cov}}[C_k(t), C_\ell(s)] \equiv \frac{1}{B-1} \sum_{b=1}^{B} \left(C_k^b(t) - \overline{C}_k(t)\right) \left(C_\ell^b(s) - \overline{C}_\ell(s)\right). \tag{3.78}$$

The diagonal elements of the covariance matrix are the variance of the respective random variables $\overline{C}_k(t)$,

$$\widehat{\text{Var}}[C_k(t)] = \frac{1}{B-1} \sum_{b} \left(C_k^b(t) - \overline{C}_k(t)\right)^2 = \text{Cov}[C_k(t), C_k(t)]. \tag{3.79}$$

3.5.2 Fitting correlated data

Suppose one measures correlation functions $C_k(t)$, and that B bootstrap samples $\{C_k^b(t)\}_{b=1}^B$ are constructed from the data. Each correlation function $C_k(t)$ must be fit to a model $f_k(t; \mathbf{p}_k)$. The models f_k are determined by analytic methods, for example, the spectral decomposition of a correlator, or derived in EFT, and the $\mathbf{p}_k$ are undetermined parameters for the k^{th} model determined through the fit procedure.

Let α_k be the number of parameters in model k, i.e. $||\mathbf{p}_k|| = \alpha_k$, and let $\alpha \equiv \sum_{k=1}^{K} \alpha_k$ denote the total number of fit coefficients. For example, for a 3-state multi-exponential fit to a single correlation function $C(t)$, one has six unknown parameters, $\mathbf{p} = (\mathcal{Z}_1, E_1, \mathcal{Z}_2, E_2, \mathcal{Z}_3, E_3)$, with

$$f(t; \mathbf{p}) = \sum_{k=1}^{3} \mathcal{Z}_k e^{-E_k t}, \tag{3.80}$$

where the interpretation is that this model describes a theory with three energy states of energy $\{E_k\}$ and with ground state overlaps of the interpolating operator $\{\mathcal{Z}_k\}$. Typically, one assumes that the data obeys the given model for some range $t \in \mathcal{T}_{\text{sub}} \subseteq \mathcal{T}$ and not for the entire domain $\mathcal{T}$, as many models are only valid for a subset of the entire fit range consistent with assumptions on the theory in which they were derived[11]

The fitting question asks how to determine posteriors on the parameters $\{\mathbf{p}_k\}$ that are consistent with the statistical fluctuations on the input data $\{C_k^b(t)\}$. One typically assumes that the full vector of coefficients $\mathbf{p} \equiv (\mathbf{p}_1, ..., \mathbf{p}_K)$ follows a normal distribution, $\mathbf{p} \sim \mathcal{N}(\mu_k, \Sigma_k)$, where $\mu_\mathbf{p}$ is the mean of the distribution and $\Sigma_\mathbf{p}$ is the $\alpha \times \alpha$ covariance matrix. The goal is to estimate $\mu_\mathbf{p}$ and $\Sigma_\mathbf{p}$ from the $\{C_k^b(t)\}$, along with a metric of "how consistent" the final statistical model is with the input data.

Given a model $f_k(t; \mathbf{p}_k)$ and data with mean $\overline{C}_k(t)$ and covariance $\widehat{\text{Cov}}[C_k(t), C_\ell(s)]$ (Eqs. (3.77) and (3.78)), the χ^2 goodness-of-fit parameter [98] is defined as

$$\chi^2(\mathbf{p}) \equiv \sum_{t,s} \sum_{k,\ell} \delta_k(t; \mathbf{p}_k) \, \widehat{\text{Cov}}^{-1}[C_k(t), C_\ell(s)] \, \delta_\ell(s, \mathbf{p}_\ell). \tag{3.81}$$

Here $\delta_k(t; \mathbf{p}_k)$ is the difference between the mean of the data and the model, evaluated at a given set of parameters $\mathbf{p}_k$,

$$\delta_k(t; \mathbf{p}_k) = \overline{C}_k(t) - f_k(t; \mathbf{p}_k). \tag{3.82}$$

The parameters $\mathbf{p}^*$ which best fit the data, equivalently the coefficients that best estimate the mean μ_k of the distribution obeyed by the parameters $\mathbf{p}$, are the minimizers of the χ^2 [99]

$$\mathbf{p}^* = \underset{\mathbf{p}}{\text{argmin}} \, \chi^2(\mathbf{p}), \tag{3.83}$$

[11] Many models are derived from EFT. The validity of such a model breaks down when the power-counting parameters in the EFT become large, for example, in chiral EFT at large values of the quark mass.

while the covariance $\Sigma_{\mathbf{p}}$ is estimated from the data as the derivative of the χ^2,

$$\hat{\Sigma}_{\mathbf{p}}(\mathbf{p}_k^a, \mathbf{p}_\ell^b) = \frac{\partial^2}{\partial \mathbf{p}_k^a \partial \mathbf{p}_\ell^b}\bigg|_{\mathbf{p}=\mathbf{p}^*} \chi^2(\mathbf{p}). \tag{3.84}$$

Various packages exist to perform this minimization numerically; the one I primarily used throughout my Ph.D. research is Peter Lepage's lsqfit package [100].

When the measurement errors are assumed to be normally distributed, the χ^2 test statistic (Eq. (3.81)) follows a χ^2 distribution with d degrees of freedom [101]. The degrees of freedom of a fit is defined to be the difference in the number of data points and the number of fit parameters,

$$d \equiv |\mathcal{T}| - K. \tag{3.85}$$

This distribution is denoted χ^2_d, formally defined as the distribution resulting from summing the squares of d iid standard normal random variables. The p-value of the fit is then obtained from the χ^2_d distribution,

$$p = \int_{\chi^2(\mathbf{p}^*)}^{\infty} dx\, \chi^2_d(x) \tag{3.86}$$

where $\chi^2_d(x)$ denotes the PDF of the χ^2_d distribution. The p-value tests the null hypothesis $H_0 : \{\text{The data is drawn from the model } f_k\}$.

The p-value does not tell the entire story because it cannot detect overfitting. The **reduced** χ^2 (χ^2 per degree of freedom) for the best-fit parameters $\mathbf{p}^*$,

$$\chi^2_r(\mathbf{p}^*) \equiv \frac{1}{d}\chi^2(\mathbf{p}^*) \tag{3.87}$$

is a test statistic that can be used to roughly estimate the fit's quality. A "good fit" has a $\chi^2_r(\mathbf{p}^*)$ of around 1: this means that the (normalized) deviations of the data from the model are order one and are due to statistical noise, not due to a model mismatch. If $\chi^2_r(\mathbf{p}^*) \gg 1$, there are large deviations between the model predictions and the data that are unlikely to be unaccounted for by statistical fluctuation. This is called **underfitting**. The other case is when $\chi^2(\mathbf{p}^*) \ll 1$. Naïvely, this seems like the desired case because the model almost perfectly predicts the data measurements. However, because the data is randomly sampled from the model with some amount of error, $\chi^2(\mathbf{p}^*) \ll 1$ represents a case where the model fits the data too well: the statistical fluctuations that one would expect if the data were sampled from the model

are not present. This case is called **overfitting**. Figure 3.3 depicts the three possible cases of underfitting, overfitting, and a good fit.

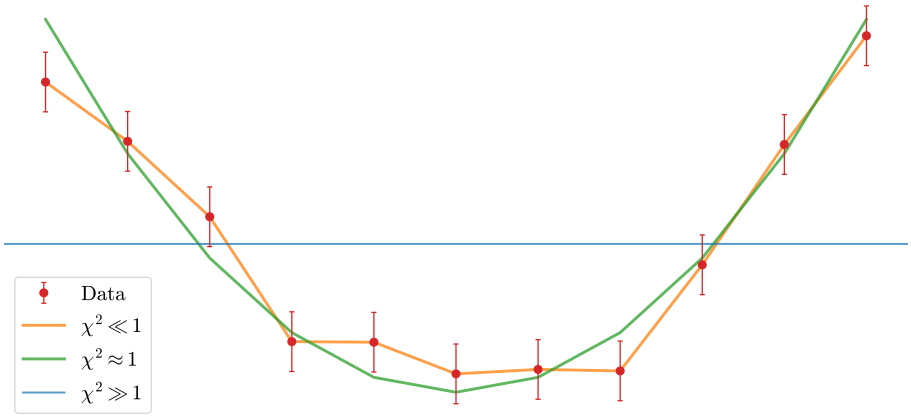

Figure 3.3. Example of underfitting, overfitting, and a good fit. Generated data with 1σ error bars are shown in red. The orange curve is overfit: the curve's value at each point exactly equals the mean of the data and is not consistent with statistical fluctuations in the data. The green curve is well fit, with $\chi^2_d \approx 1$. In this case, the residuals from the fit are relatively small but are consistent with the error bars on the data. The final case of the blue curve is underfit: the model does not account for the fluctuations in the data, even considering that the measurements are drawn from a statistical distribution with non-trivial variance.

It is often the case that one wishes to select the "best model" from a set of N models $\mathcal{M}$ for a fit to the data. The "best model" should minimize the χ^2_d of the fit, but not at the expense of overcomplicating the fit; it is therefore desirable to reduce the χ^2_d with the simplest (least number of parameters) model possible[12]. This condition is encapsulated in the **Akaike Information Criterion** (AIC) [102]. Given a model m, the AIC of m is defined as

$$\mathrm{AIC}(m) \equiv \chi^2(m) + 2K(m) \tag{3.88}$$

where $\chi^2(m)$ is the minimum of the χ^2 (previously denoted $\chi^2(\mathbf{p}^*)$) for the model m, and $K(m)$ is the number of parameters in m. Suppose WLOG that $\mathcal{M}$ is parameter-

[12] To see why, suppose the set of models is the set of polynomial models, indexed by degree $n \in \mathbb{N}$. For a finite data set as $n \to \infty$, the Stone-Weierstrauss theorem implies that the data can be perfectly fit once sufficiently many polynomial terms are included, so infinitely many models have $\chi^2_d = 0$. These high-order polynomial models completely overfit the data available, so they should not be chosen as the "best model" despite fitting the data perfectly.

ized by $[N]$ in order of complexity,

$$\mathcal{M} = \{m_n : n \in [N] \text{ s.t. } k \leq \ell \implies K(m_k) \leq K(m_\ell)\}. \tag{3.89}$$

The AIC is used to select the best model from $\mathcal{M}$. The model with the largest grading (m_N) will have the lowest χ^2_d, as it has the most parameters. However, one wishes to select the simplest model that fits the data well. The best model is denoted m^*. To iteratively construct this model, initialize $m^* \leftarrow m_1$ to be the first model. For $k \in \{2, 3, ..., N\}$, accept model m_k as the current best model if and only if

$$\text{AIC}(m_k) - \text{AIC}(m^*) < -\mathcal{A}\, d(m_k), \tag{3.90}$$

in which case $m^* \leftarrow m_k$ and the iteration continues. The iteration is terminated when the next model is not accepted, or all models are exhausted. In Eq. (3.90), $d(m_{k+1})$ is the number of degrees of freedom of model $k+1$ and $\mathcal{A} \in [0, 1]$ is a hyperparameter. Larger values of $\mathcal{A}$ emphasize simpler models, as it takes a larger reduction in the AIC to accept the next model.

Chapter 4

Spectral Functions from Lattice Gauge Theory

This chapter discusses spectral function reconstruction from LGT and presents a novel method for spectral function reconstruction. I worked on this project with William Jay and Thomas Bergamischi. Will had the idea for this project in 2022, which was to take a technique recently developed in the Condensed Matter Theory community, called Nevanlinna Analytical Continuation [11], and use it in LGT calculations. We began working together to understand the theory and, along the way, learned that other aspects of the Nevanlinna-Pick theory could be brought to field theory. This work culminated in the Wertevorrat (Section 4.5.5), which is the capstone of our method and distinguishes it from all other spectral reconstruction methods. Along with developing the theory with Will, I also wrote the majority of the code base for the project, which can be found in the Github repository here.

This chapter begins with a general introduction to spectral densities in QFT (Section 4.1) and then presents analytic properties of thermal Green's functions (Sections 4.2 and 4.3). Section 4.5 details a new method for spectral reconstruction, the Nevanlinna-Pick Spectral Reconstruction method [3], which is tested via simulation in Section 4.6. Section 4.7 discusses applying this method to noisy Monte Carlo data, which is an active area of research: the problem is precisely formulated, and one potential solution is presented.

4.1 Introduction: the R-Ratio

The spectral functions of a quantum field theory encode a wealth of information about the structure of energy states in the theory. The conventional approach to spectral functions is through current-current correlators in inclusive processes, where an inclusive process is defined as any scattering process where the final states are summed over. The canonical example of such a process is inclusive e^+e^- scattering,

$$e^+e^- \to \text{hadrons}. \tag{4.1}$$

This process is typically studied through the hadronic polarization tensor $\rho_{\mu\nu}(q)$, defined as a momentum-projected commutator of two electromagnetic currents,

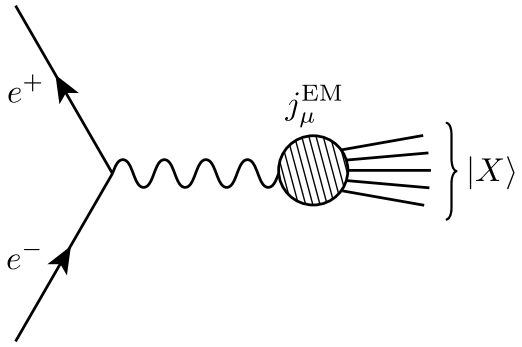

Figure 4.1. Inclusive $e^+e^- \to$ hadrons scattering. Here, $|X\rangle$ denotes any final hadronic state and is summed over. The hatched circle denotes the hadronic interaction with the electromagnetic current j^μ_{EM}, which is defined non-perturbatively through the matrix element of Eq. (4.2).

$$\rho_{\mu\nu}(q) = \frac{1}{2\pi}\int d^4x\, e^{iq\cdot x}\langle 0|[j_\mu^{\text{EM}}(x), j_\nu^{\text{EM}}(0)]|0\rangle. \tag{4.2}$$

Here, $|0\rangle$ denotes the vacuum state of the interacting theory. The tensor $\rho_{\mu\nu}$ describes the hadronic interaction with the electromagnetic current and can be expanded in terms of a scalar structure function $\rho(q^2)$ multiplying a tensor structure dictated by symmetry,

$$\rho_{\mu\nu}(q) = (q_\mu q_\nu - q^2 g_{\mu\nu})\rho(q^2). \tag{4.3}$$

The function $\rho(q^2)$ is called the **spectral function** of the process.

The cross-section of this process is conventionally defined in terms of the R-ratio [103, 104], which is the ratio of the inclusive cross-section to the tree-level $e^+e^- \to \mu^+\mu^-$ cross-section at center-of-mass energy $\sqrt{s}$,

$$R(s) \equiv \frac{\sigma(e^+e^- \to \text{hadrons})}{\sigma_{\text{tree}}(e^+e^- \to \mu^+\mu^-)} = 12\pi^2\rho(s). \tag{4.4}$$

The R-ratio encodes the same information as the spectral function $\rho(s)$. Experimental

data for $R(s)$ is shown in Figure 4.2. The $R(s)$ data shows resonances near the vector mesons ρ, ω, ϕ, and J/ψ and its excited states. Clear steps in $R(s)$ can also be seen: for example, the step in $R(s)$ between 4 and 5 GeV is due to the $c\bar{c}$ creation threshold.

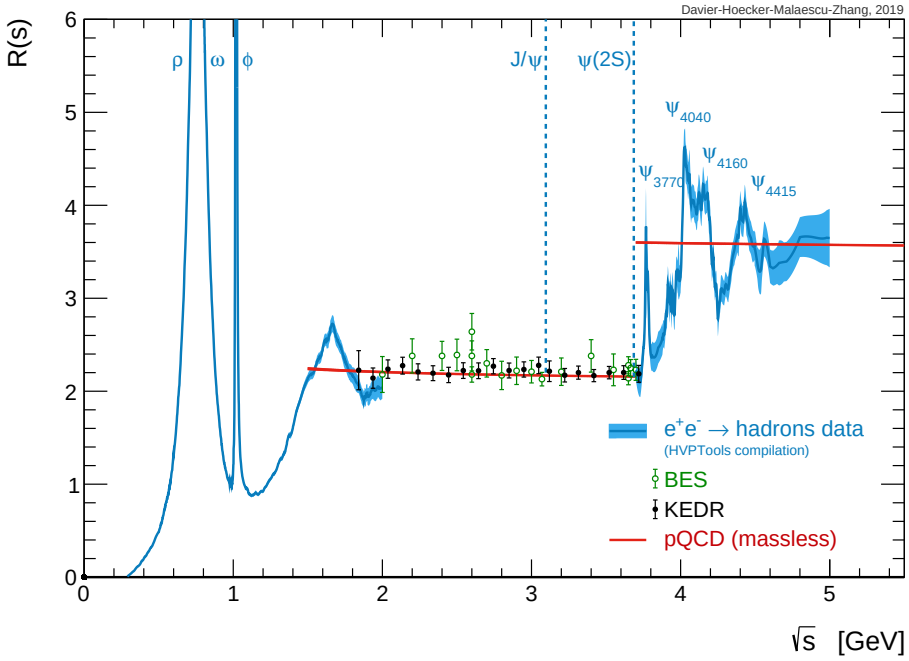

Figure 4.2. Experimental data for the R-ratio $R(s)$, compiled in Ref. [105].

Any inclusive process has a spectral function that similarly encodes its hadronic information. Delta functions in the spectral function correspond to bound states in the theory; extended peaks correspond to resonances, with the width of the peak proportional to the particle's decay width; and steps in the spectral function correspond to kinematic thresholds. The spectral function contains all the kinematic information about the inclusive process at hand, and as such, it is vital to understand how to compute spectral functions. Computation of the spectral function in non-perturbative QFTs requires the use of lattice gauge theory, where a zero-temperature Euclidean time correlation function $\mathscr{G}_E(\tau)$ is related to a corresponding spectral density $\rho(\omega)$ by the Laplace transformation [106],

$$\mathscr{G}_E(\tau) = \int_0^\infty d\omega\, e^{-\omega\tau} \rho(\omega). \tag{4.5}$$

Given $\rho(\omega)$, solving for $\mathscr{G}_E(\tau)$ requires inverting the Laplace transformation. This is an ill-posed inverse problem: the Euclidean correlator $\mathscr{G}_E(\tau)$ is known at a finite number of points, whereas the spectral function $\rho(\omega)$ is a function, defined at an uncountable number of points. There is no analytic inversion method to solve Eq. (4.5), and many

LGT groups are working on different methods to solve this inverse problem [107–113].

4.2 Thermal Green's Functions

The formal definition of the spectral density is in terms of the thermal Green's functions of the theory, which is now reviewed from Ref. [106]. Consider a QFT at finite temperature $1/\beta$ with Hamiltonian $\mathcal{H}$. The density matrix describing this theory is,

$$\hat{\rho} = \frac{1}{\mathcal{Z}} \exp\left(-\beta \mathcal{H}\right), \tag{4.6}$$

where $\mathcal{Z}$ is the partition function of the theory. Operator expectation values are formally defined with respect to $\hat{\rho}$ as

$$\langle \mathcal{O}_1 ... \mathcal{O}_n \rangle \equiv \text{Tr}\left[\hat{\rho}\, \mathcal{O}_1 ... \mathcal{O}_n\right]. \tag{4.7}$$

For an operator $A(t)$, define the following correlation functions,

$$\mathscr{G}(t) \equiv \langle A(t) A(0) \rangle \qquad\qquad \mathscr{G}_{\pm}(t) \equiv i \langle \{A(t), A(0)\}_{\pm} \rangle \tag{4.8}$$

where $\{\cdot,\cdot\}_+$ ($\{\cdot,\cdot\}_-$) is the anticommutator (commutator) which arises for fermionic (bosonic) operators $A(t)$. The Euclidean Green's function of Eq. (4.5) is defined in terms of the Green's function $\mathscr{G}(t)$ by evaluation on the imaginary axis,

$$\mathscr{G}_E(\tau) \equiv \mathscr{G}(-i\tau). \tag{4.9}$$

Note that $\tau \in \mathbb{R}$ is the real-valued Euclidean time, although it evaluates $\mathscr{G}(t)$ at an imaginary time. The Fourier coefficients of the Euclidean correlator are computed as

$$G_E^{(\ell)} \equiv \int_0^\beta d\tau\, e^{i\omega_\ell \tau}\, \mathscr{G}_E(\tau), \tag{4.10}$$

where ω_ℓ are the Matsubara frequencies of the system,

$$\omega_\ell \equiv \begin{cases} \frac{2\ell\pi}{\beta} & \text{bosons} \\ \frac{(2\ell+1)\pi}{\beta} & \text{fermions} \end{cases}, \tag{4.11}$$

defined for $\ell \in \mathbb{Z}$. The notation used for the Greens functions in this thesis is summarized in Table 4.1.

Symbol	Description	Definition
$\mathscr{G}_\pm(t)$	Real-time Green function	Eq. (4.8)
$\mathscr{G}_E(\tau)$	Euclidean-time Green function	Eq. (4.9)
$G_\pm(\omega)$	Retarded Green function, $\omega \in \mathbb{R}$	Eq. (4.12)
$G_\pm(z)$	Retarded Green function, $z \in \mathbb{C}^+$	Eq. (4.12)
$\mathcal{G}_\pm(\zeta)$	Retarded Green function, $\zeta \in \mathbb{D}$	Eqs. (4.55, 4.58)

Table 4.1. Notation for the Green's functions appearing in this thesis. Bosonic and fermionic Green's functions are distinguished by the sign $\pm$ of the commutator or anti-commutator.

The retarded, or causal, correlator is the Fourier transform of $\mathscr{G}_\pm(t)$,

$$G_\pm(\omega) \equiv \int_0^\infty dt\, e^{i\omega t}\, \mathscr{G}_\pm(t), \tag{4.12}$$

for $\omega \in \mathbb{R}$. This definition is analytically continued to the upper half-plane

$$\mathbb{C}^+ \equiv \{z \in \mathbb{C} : \operatorname{Im} z > 0\} \tag{4.13}$$

to define a map $G_\pm(z)$, evaluated at complex energies $z \in \mathbb{C}^+$. The maps $G_\pm(\omega)$ and $G_\pm(z)$ will both be referred to as the retarded correlator, with the domain understood from context. Viewed as a map on $\mathbb{C}^+$, $G_\pm$ is an analytic function

$$G_\pm : \mathbb{C}^+ \to \Omega_\pm \subseteq \mathbb{C}^+ \tag{4.14}$$

with image $\Omega_\pm$, which will be specified shortly. This object lies at the heart of the theory of spectral functions. It is related to the Fourier coefficients of the Euclidean correlator, Eq. (4.10), by evaluation on the imaginary axis,

$$G_E^{(l)} = G_\pm(i\omega_\ell) \qquad (\ell \neq 0), \tag{4.15}$$

which will be explicitly derived in the next section. One regards $G_\pm(z)$ as the analytic continuation of the Fourier coefficients $G_E^{(\ell)}$ to the entire upper half-plane[1]. From the

[1]Note that because $G_E^{(\ell)}$ is only defined at a finite number of points, its analytic continuation to an open subset of $\mathbb{C}$ is not uniquely defined: it has infinitely many analytic continuations. Carlson's theorem [114] may be used to define a unique analytic continuation to an open domain given the function values on a countable subset of $\mathbb{C}$ along with growth constraints on the function. However, one would still require knowledge of $G_E^{(\ell)}$ at an infinite number of points. Section 4.4.2 will discuss these mathematical details further.

retarded correlator, one defines the spectral function as the Fourier transform of $\mathscr{G}_{\pm}(t)$,

$$\begin{aligned}\rho_{\pm}(\omega) &\equiv \frac{1}{2\pi i}\int_{-\infty}^{\infty} dt\, e^{i\omega t}\,\mathscr{G}_{\pm}(t) \\ &= \frac{1}{2\pi i}\left(G_{\pm}(\omega) - G_{\pm}(\omega)^*\right) \\ &= \frac{1}{\pi}\mathrm{Im}\left[G_{\pm}(\omega)\right]\end{aligned} \tag{4.16}$$

for $\omega \in \mathbb{R}$, which is proportional to $\mathrm{Im}\left[G_{\pm}(\omega)\right]$. The equality $\rho_{\pm}(\omega) = \frac{1}{\pi}\mathrm{Im}\left[G_{\pm}(\omega)\right]$ is conceptually very useful and is depicted in Figure 4.3 for an example spectral function.

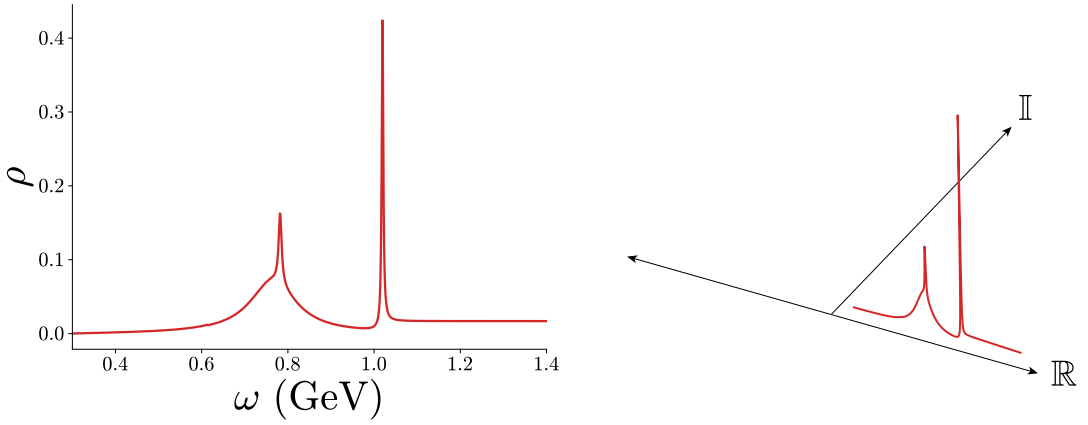

(a) Example spectral function. **(b)** Spectral function in the complex plane.

Figure 4.3. Example spectral function viewed (left, Fig. 4.3a) as a function of energy, and viewed (right, Fig. 4.3b) in the complex energy plane. The spectral function is related to the imaginary part of the retarded Green's function by evaluation on the real axis, $\rho_{\pm}(\omega) = \frac{1}{\pi}\mathrm{Im}\left[G_{\pm}(\omega)\right]$. The specific form of this spectral function is from the parameterization of the R-ratio, Eq. (4.120), from Ref. [104].

4.3 Green's Functions in Finite Volume

Section 4.2 made no assumptions about the underlying QFT other than the finite-temperature assumption. Consider now the case where the QFT of interest is defined in a finite box of spatial volume $V = L^3$. In finite volume, the spectrum of the theory becomes discrete, and the resolution of the identity is given by Eq. (3.37). Inserting

Eq. (3.37) into the definition of $\mathscr{G}_{\pm}(t)$ (Eq. (4.8)) yields[2]

$$\mathscr{G}_{\pm}(t) = \frac{i}{\mathcal{Z}} \sum_{n,m} \frac{e^{-iE_{nm}t}|A_{mn}|^2}{4E_m E_n} \left(e^{-\beta E_m} \pm e^{-\beta E_n}\right), \tag{4.17}$$

where $E_{nm} \equiv E_n - E_m$ is the energy gap between states $|n\rangle$ and $|m\rangle$, and the operator matrix elements are $A_{mn} \equiv \langle m|A|n\rangle$. Likewise, using the identity

$$\int_0^\infty dt\, e^{izt} e^{-iE_{nm}t} = \frac{i}{z - E_{nm}} \tag{4.18}$$

for $E_{mn} \in \mathbb{R}$ and $z \in \mathbb{C}^+$, the finite-volume retarded correlator may be expanded as,

$$G_{\pm}(z) = \frac{1}{\mathcal{Z}} \sum_{n,m} \frac{|A_{mn}|^2}{4E_m E_n} \left(e^{-\beta E_m} \pm e^{-\beta E_n}\right) \frac{-1}{z - E_{nm}}. \tag{4.19}$$

The retarded correlator is a sum of poles at each energy gap in the theory and is analytic on $\mathbb{C}^+$.

The finite-volume spectral density may be determined by expanding $G_{\pm}(z)$ near the imaginary axis as $z \downarrow \mathbb{R}$. Let $\epsilon > 0$ be given, and let $z = \omega + i\epsilon$ with $\omega \in \mathbb{R}$. The pole term in Eq. (4.19) becomes,

$$\frac{1}{\pi}\mathrm{Im}\, \frac{-1}{(\omega + i\epsilon) - E_{nm}} = \frac{1}{\pi} \frac{\epsilon}{(\omega - E_{nm})^2 + \epsilon^2} \tag{4.20}$$

$$\equiv \delta_\epsilon(\omega - E_{nm}), \tag{4.21}$$

where $\delta_\epsilon(\omega - E_{nm})$ is the Poisson kernel [115], which smoothly approximates the Dirac δ distribution,

$$\lim_{\epsilon \downarrow 0} \delta_\epsilon(x) = \delta(x), \tag{4.22}$$

where the convergence is understood to be as a sequence of distributions [116]. Expanding the poles in Eq. (4.19) yields the representation of the finite-volume spectral

[2]This thesis has adopted the relativistic normalization of states, $1 = \sum_n \frac{1}{2E_n}|n\rangle\langle n|$, Eq. (3.37). Much of the presentation of the Green's function formalism (i.e. [106]) uses the normalization $1 = \sum_n |n\rangle\langle n|$, hence these equations presented in this thesis may differ from external sources by factors of $1/2E_n$. This does not affect any conclusions of the work and is purely cosmetic.

function as a sum of poles,

$$\begin{aligned}\rho_\pm(\omega) &= \frac{1}{\mathcal{Z}}\sum_{n,m}\frac{|A_{mn}|^2}{4E_mE_n}\left(e^{-\beta E_m} \pm e^{-\beta E_n}\right)\delta(\omega - E_{nm}) \\ &\overset{\beta\to\infty}{=} \sum_n \frac{|A_{0n}|^2}{4E_0E_n}\big(\delta(\omega - E_n) \pm \delta(\omega + E_n)\big).\end{aligned} \tag{4.23}$$

Note the parity of $\rho_\pm$, which is independent of the system's temperature: the spectral function is even for fermionic systems and odd for bosonic systems. The second line of Eq. (4.23) is the zero-temperature spectral function. In this case, the fermionic and bosonic spectral functions only differ by a relative sign between each pair of poles (although the energy levels E_n may shift between different fermionic and bosonic systems).

The Poisson kernel (Eq. (4.21)) defines a natural smearing kernel for the spectral function,

$$\rho^\epsilon_\pm(\omega) = \int d\omega' \delta_\epsilon(\omega - \omega')\rho_\pm(\omega'). \tag{4.24}$$

The smeared spectral function $\rho^\epsilon_\pm(\omega)$ is now a well-defined function rather than a distribution like the original, unsmeared spectral function. Integrating δ_ϵ in Eq. (4.24) against the finite-volume representation of $\rho_\pm$ (Eq. (4.23)) yields the identity,

$$\rho^\epsilon_\pm(\omega) = \frac{1}{\pi}\mathrm{Im}\, G_\pm(\omega + i\epsilon), \tag{4.25}$$

which holds for arbitrary $z = \omega + i\epsilon \in \mathbb{C}^+$. The smeared spectral function $\rho^\epsilon_\pm(\omega)$ thus has the interpretation as the imaginary part of the retarded correlator, evaluated on the shifted real axis $\mathbb{R} + i\epsilon = \{\omega + i\epsilon : \omega \in \mathbb{R}\}$. Observe that ϵ does not need to be small for Eq. (4.25) to be valid; this identity holds for arbitrary $\epsilon > 0$.

To reconstruct the spectral function from a Euclidean correlation function, one expands the Euclidean correlator $\mathscr{G}_E(\tau)$ (Eq. (4.9)) and the Fourier coefficients $G_E^{(\ell)}$ (Eq. (4.10)) in finite volume,

$$\mathscr{G}_E(\tau) = \frac{1}{\mathcal{Z}}\sum_{n,m}\frac{e^{-\beta E_m}e^{-E_{nm}\tau}\,|A_{mn}|^2}{4E_mE_n}, \qquad G_E^{(\ell)} = G_\pm(i\omega_\ell). \tag{4.26}$$

This confirms the identity of Eq. (4.15) and shows that the retarded correlator $G_\pm(z)$ is the analytic continuation of the Fourier coefficients $G_E^{(\ell)}$, evaluated at the Matsubara frequencies $\{i\omega_\ell\}$, to the upper half-plane. Furthermore, note that Eq. (4.26) may be

expanded in terms of the finite-volume spectral function (Eq. (4.23)) as

$$\begin{aligned}\mathscr{G}_E(\tau) &= \int_0^\infty d\omega\, \rho_\pm(\omega) \left[\frac{e^{-\omega\tau} + e^{-\omega(\beta-\tau)}}{1 \pm e^{-\omega\beta}}\right] \\ &\overset{\beta\to\infty}{=} \int_0^\infty d\omega\, \rho_\pm(\omega) e^{-\omega\tau}.\end{aligned} \tag{4.27}$$

This provides an explicit derivation of Eq. (4.5): the Euclidean Green's function is the Laplace transformation of the spectral function at zero temperature. At finite temperature for a fermionic (bosonic) system, $\mathscr{G}_E(\tau)$ is given by integrating $\rho_\pm(\omega)$ against a Fermi-Dirac (Bose-Einstein) distribution.

The image $\Omega_\pm$ of $G_\pm(z)$ is crucial to understanding the analytic structure of $G_\pm$. From Eqs. (4.19, 4.21), one immediately sees that the fermionic retarded correlator G_+ has strictly positive imaginary part, $\operatorname{Im} G_+(z) > 0$ for each $z \in \mathbb{C}^+$. This implies that Ω_+, the image of G_+, is the upper half of the complex plane,

$$\Omega_+ = \mathbb{C}^+. \tag{4.28}$$

An analytic map from $\mathbb{C}^+ \to \mathbb{C}^+$ is called a **Nevanlinna function**, named for the mathematician Rolf Nevanlinna, who pioneered the study of such functions in the early 20th century [117, 118]. In contrast, the image of the bosonic Green's function G_- is not a Nevanlinna function. It is an odd function, and the expansion of Eq. (4.19) shows that its imaginary part is positive in quadrant I and negative in quadrant II of $\mathbb{C}^+$. Symmetry implies that $\operatorname{Im} G_-$ can only vanish on the positive imaginary axis, $\mathbb{I}^+$. Note that for $y > 0$, $\operatorname{Re} G_-(iy) > 0$, hence on this half-axis G_- only takes positive real values. This makes it clear that the image of G_- is all of $\mathbb{C}$, except for the negative real axis $\mathbb{R}^- \equiv \{x \in \mathbb{R} : x < 0\}$, hence

$$\Omega_- = \mathbb{C} \setminus \mathbb{R}^-. \tag{4.29}$$

The method presented in Section 4.5 will reconstruct the smeared spectral function $\rho_\pm^\epsilon$ by explicitly mapping the retarded correlator $G_\pm$ to the unit disk

$$\mathbb{D} \equiv \{z \in \mathbb{C} : |z| < 1\}. \tag{4.30}$$

Knowledge of the image $\Omega_\pm$ is essential in order to define the maps into $\mathbb{D}$.

4.3.1 Preparing the Fourier Coefficients $G_E^{(\ell)}$ from LGT Data

It is useful to discuss the computation of the Euclidean Fourier coefficients $G_E^{(\ell)}$ (Eq. (4.26)) from the correlation function $\mathscr{G}_E(\tau)$. Naïvely, one would expect to simply evaluate $G_E^{(\ell)}$ via a discrete Fourier transform of $\{\mathscr{G}_E(\tau)\}_{\tau=0}^{\beta-1}$,

$$\int_0^\beta d\tau\, e^{i\omega_\ell \tau}\mathscr{G}_E(\tau) \overset{?}{\approx} \sum_{t=0}^{\beta-1} e^{i\omega_\ell \tau}\mathscr{G}_E(\tau). \tag{4.31}$$

While this approximation works well in some instances, it is not always the best way to prepare $G_E^{(\ell)}$ from lattice data.

To illustrate this, consider a bosonic Euclidean Green's function for a single state of mass m,

$$\mathscr{G}_E(\tau) = e^{-m\tau} + e^{-m(T-\tau)}. \tag{4.32}$$

The discrete Fourier transform of this correlator is

$$\sum_{\tau=0}^{\beta-1} e^{i\omega_\ell \tau}\mathscr{G}_E(\tau) = \frac{\left(1-e^{-\beta m}\right)\sinh(ma)}{\cosh(ma)-\cos(\omega_l a)}, \tag{4.33}$$

where factors of the lattice spacing a have explicitly been included. The right-hand side immediately presents a problem if it is directly interpreted as $G_+(i\omega_\ell)$. It is not analytic in the upper half-plane, as required of the retarded correlator. In addition to the expected pair of poles at $\omega_\ell = \pm m$, there are additional poles at $\pm m + 2\pi i a\mathbb{Z}$ due to the periodicity of the cosine. Regardless, the continuum limit has the correct analytic structure,

$$\lim_{a\to 0} a\frac{\left(1-e^{-\beta m}\right)\sinh(ma)}{\cosh(ma)-\cos(\omega_\ell a)} = \frac{2m}{m^2+\omega^2}. \tag{4.34}$$

This suggests a better method to construct the Fourier coefficients than Eq. (4.10), namely to perform a Fourier transform closer to the continuum limit than the naïve LGT data $\mathscr{G}_E(\tau)$. Because the Euclidean correlator $\mathscr{G}_E(t)$ (Eq. (4.32)) is smooth (in the sense that data is drawn from a smooth curve in the continuum) and monotonic for $t \in \mathbb{R}$, it can be interpolated, and this interpolation can be evaluated on a finer grid and Fourier transformed to produce the Fourier coefficients $G_E^{(\ell)}$. In practice, this is done by fitting a polynomial spline to $\log \mathscr{G}_E(\tau)$, as $\log \mathscr{G}_E(\tau)$ varies much slower than $\mathscr{G}_E(\tau)$. This interpolation procedure is shown in Figure 4.4 for a grid refinements with $N \in \{1, 2, 5, 25\}\beta/a$ points. As expected, finer refinements yield results for the

Fourier coefficients $G_E^{(\ell)}$ that agree much more closely with the continuum correlation function. This is expected to hold for any finite-volume system as the refinement becomes infinitely fine, as spectral densities in finite-volume are the sum of poles.

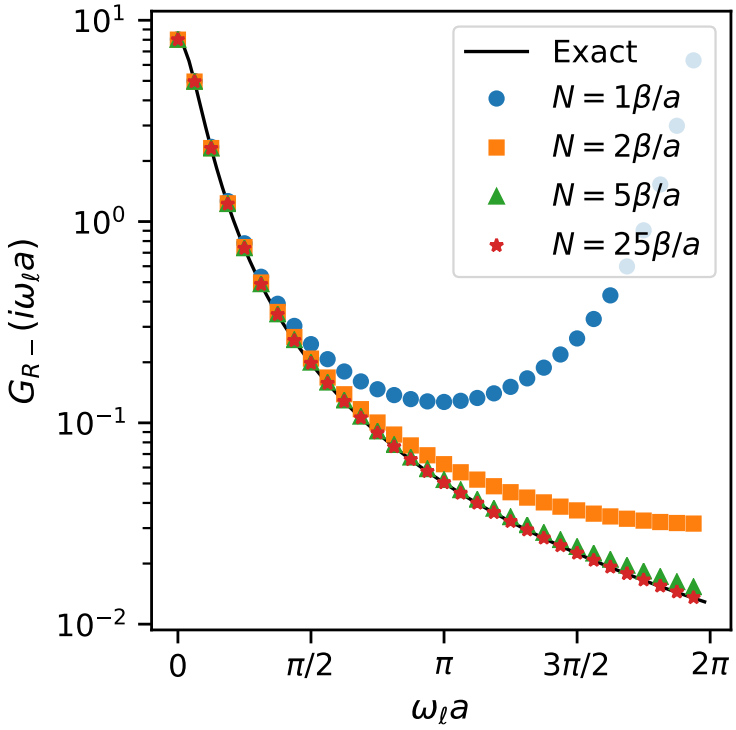

Figure 4.4. Numerical evaluation of the Fourier coefficients $G_E^{(\ell)}$ using different interpolation densities, using a Euclidean correlator $G_E(\tau) = e^{-m\tau} + e^{-m(\beta-\tau)}$ (Eq. (4.32)) with $\beta = 96$ and $m = 0.25$. Results are shown for every third Matsubara frequency, and the different marker types show different interpolation refinements. The blue circles show the coarsest refinement, which directly evaluates the discrete Fourier transform (Eq. (4.33)). These agree well with the exact Green's function for small ω_ℓ but deviate as $a\omega_\ell$ approaches the boundary of the Brillouin zone. The red stars depict the Fourier coefficients obtained from the finest refinement of $\mathscr{G}_E(\tau)$, $N = 25\beta/a$. These results agree with the exact continuum results to the sub-percent level.

4.4 Spectral Reconstruction from Euclidean Correlation Functions

4.4.1 Infinite-Volume Spectral Reconstruction from LGT

The ultimate goal of LGT calculations is to extract continuum and infinite-volume physics. It is thus important to consider how the finite-volume spectral densities reconstructed on a finite Euclidean lattice relate to their infinite-volume counterparts. In the infinite-volume continuum, the momentum space for each field is indexed by a continuous variable $\boldsymbol{p} \in \mathbb{R}^3$, the three-momentum of the particle. Suppose one discretizes a continuum theory onto a spatially isotropic lattice with L spatial sites in each direction. Momentum space becomes discretized, and the continuous $\boldsymbol{p}$ becomes a discrete variable,

$$\boldsymbol{p}_{\boldsymbol{n}} = \frac{2}{a} \sin\left(\frac{\pi \boldsymbol{n}}{L}\right) \equiv \frac{2}{a} \sin \boldsymbol{k}_{\boldsymbol{n}} \tag{4.35}$$

where $\boldsymbol{n} \in \mathbb{Z}^3$. The momentum space is $\{\boldsymbol{p}_{\boldsymbol{n}} : \boldsymbol{n} \in (\mathbb{Z} \cap [0, 2L))^3\}$, and in particular is a discrete, finite variable that takes $(2L-1)^3$ values, as Eq. (4.35) is periodic in $\boldsymbol{n}$. Let the set of possible energies arising from this discrete momentum space be denoted $\{\omega_i\}_{i=1}^K$, where K is the total number of unique energies allowed in finite-volume[3].

Let $\rho(\omega)$ be an extended spectral feature to be discretized[4]. Upon discretization, $\rho(\omega)$ becomes a δ-train,

$$\rho(\omega) \mapsto \rho_L(\omega) \equiv \sum_{i=1}^{K} w_i \delta(\omega - \omega_i) \tag{4.36}$$

i.e., a sum of δ-functions placed at each finite-volume energy ω_i with weight w_i. Note the dependence of $\widetilde{\rho}_L$ on the spatial size L is made explicit, while the energy modes ω_i implicitly carry a dependence on L. The weights w_i are chosen so that the finite-volume feature $\widetilde{\rho}_L$ converges in distribution to the infinite-volume feature ρ,

$$\rho_L \xrightarrow{d} \rho, \tag{4.37}$$

[3]Each finite-volume momentum $\boldsymbol{p}_{\boldsymbol{n}}$ yields an energy via the dispersion relation $\omega(\boldsymbol{p})$, for example the single-particle dispersion $\omega(\boldsymbol{p}) = \boldsymbol{p}^2 + m^2$. One reindexes $\{\omega(\boldsymbol{p}_{\boldsymbol{n}}) : \boldsymbol{n} \in \mathbb{Z}^3\} = \{\omega_i\}$ to avoid duplicates that arise when $\boldsymbol{p}_{\boldsymbol{n}}^2 = \boldsymbol{p}_{\boldsymbol{m}}^2$ for $\boldsymbol{n} \neq \boldsymbol{m}$.

[4]For example, a square root cut starting at a mass threshold or a Breit-Wigner peak describing a resonance.

where convergence in distribution means that for any smooth test function f,

$$\int \rho_L(dx)\, f(x) \xrightarrow{L\to\infty} \int \rho(dx)\, f(x), \tag{4.38}$$

where $\rho_L(dx)$, $\rho(dx)$ are the measures respectively induced by the push-forward of the Lebesgue measure dx on $\mathbb{R}$ from the distributions ρ_L, ρ.

The convergence of Eq. (4.37) is defined in distribution but is not defined almost surely (a.s.) or in measure. Indeed, this is clear because the locations of each δ function in $\rho_L(\omega)$ moves as L increases, although the density of the δ functions increases. The set

$$\{\omega \in \mathbb{R} : \rho_L(\omega) \not\to \rho(\omega) \text{ as } L \longrightarrow \infty\} \tag{4.39}$$

certainly does not have measure zero since there is no point-wise convergence of ρ_L to ρ *anywhere*. A similar argument holds to show that ρ_L does not converge to ρ in measure.

Consider now the numerical procedure that one would use to extract $\rho(\omega)$ from data $\rho_L(\omega)$ at a finite number of spatial sizes L. One would ideally define $\rho(\omega)$ as the point-wise limit of $\rho_L(\omega)$,

$$\rho(\omega) \overset{?}{\equiv} \lim_{L\to\infty} \rho_L(\omega). \tag{4.40}$$

But, ρ_L does not converge almost surely to ρ, so in practice, this would not work, as this limit is not defined anywhere. It is possible to choose the spatial sizes L so that the existing energy modes ω_i do not move, for example, $L = 2^n$ for $n \in \mathbb{N}_{>0}$, where $\mathbb{N}_{>0}$ is the natural numbers (originating at 1 to avoid confusion). In this case, the point-wise limit will formally exist on the dense subset $\{\frac{k}{2^n} : n \in \mathbb{N}_{>0}, k \in \mathbb{Z}\} \subset \mathbb{R}$ and can be continued to a continuous function. However, this would not work in practice, as the lattice's spatial size cannot be taken to be arbitrarily large because of computational reasons; even lattices with $L = 64$ or $L = 128$ are extremely costly to generate.

A more efficient and stable way to achieve the desired infinite-volume limit via a point-wise extrapolation is to **smear** the finite-volume spectral function. Let $\delta_\epsilon(\omega)$ be a smearing kernel, defined to be a positive function $\delta_\epsilon \geq 0$ with normalization one which converges to the δ function in distribution,

$$\delta_\epsilon \xrightarrow{d} \delta \text{ as } \epsilon \downarrow 0. \tag{4.41}$$

The parameter ϵ is called the smearing width of the kernel. A popular smearing kernel

is the centered Gaussian with variance ϵ^2,

$$\frac{1}{\sqrt{2\pi}\epsilon}\exp\left(-\frac{\omega^2}{2\epsilon^2}\right) \tag{4.42}$$

but the kernel can generally be any normalized bump form [119]. The smearing kernel primarily used throughout the remainder of the chapter will be the Poisson kernel defined in Eq. (4.21) because of its relation to the analytic continuation of the thermal Green's function.

Given a smearing kernel δ_ϵ, one defines a smeared finite-volume spectral density as

$$\rho_L^\epsilon(\omega) = (\delta_\epsilon * \rho_L)(\omega) = \sum_{i=1}^{K} w_k \delta_\epsilon(\omega - \omega_i), \tag{4.43}$$

where $*$ denotes convolution. This definition "smears out" the finite-volume spectral density; the divergences caused by the δ train have been regulated, and ρ_L^ϵ is much better behaved than ρ_L. In particular, at finite smearing width ϵ, it converges a.s. to the smeared, infinite-volume spectral density ρ_∞^ϵ,

$$\rho_L^\epsilon \xrightarrow{a.s.} \rho_\infty^\epsilon \text{ as } L \to \infty. \tag{4.44}$$

The well-behaved limiting behavior of the smeared spectral density, Eq. (4.44), makes it desirable to formulate the infinite-volume extrapolation of the spectral density as follows. First, Eq. (4.44) implies that the definition,

$$\rho^\epsilon(\omega) \equiv \lim_{L\to\infty} \rho_L^\epsilon(\omega), \tag{4.45}$$

is well-defined almost surely. This limit is numerically stable and can be used to extract the smeared infinite-volume spectral density. The smeared, infinite-volume spectral densities are then used to extract $\rho(\omega)$ [112],

$$\rho(\omega) = \lim_{\epsilon\downarrow 0} \lim_{L\to\infty} \rho_L^\epsilon(\omega). \tag{4.46}$$

The order of the limits is important; if they are interchanged, one will be left with all the problems discussed above.

Reconstructions of the spectral function in LGT focus on extracting smeared, finite-volume spectral densities from the Euclidean correlator data. As the targets of LGT calculations are infinite-volume theories, it does not matter if one does not know the exact finite-volume spectral density. Rather, the smeared finite-volume

spectral density is computed at various values of L and ϵ, then extrapolated to the infinite-volume limit using Eq. (4.46). In practice, it is also easier to reconstruct smeared finite-volume spectral densities rather than unsmeared finite-volume spectral densities.

4.4.2 The Inverse Problem: Mathematical Considerations

The inverse problem of extracting the smeared spectral density $\rho^\epsilon(\omega)$ from Euclidean correlator data $G_E^{(\ell)}$ is one of analytic continuation. Given data $(i\omega_\ell, G_E^{(\ell)})$, the spectral density is obtained by analytic continuation of $(i\omega_\ell, G_E^{(\ell)})$ to a thermal Green's function $G(z)$ on $\mathbb{C}^+$, whose evaluation on the shifted contour $\{\omega + i\epsilon : \omega \in \mathbb{R}\}$ yields $\rho^\epsilon(\omega)$.

The difficult part of this prescription is the analytic continuation $(i\omega_\ell, G_E^{(\ell)}) \to G(z)$. Suppose a complex-valued holomorphic function f_Ω is defined on a subset $\Omega \subseteq \mathbb{C}^+$. The analytic continuation of f_Ω on $\mathbb{C}^+$ is any holomorphic function $f : \mathbb{C}^+ \to \mathbb{C}$ which extends f to $\mathbb{C}^+$, i.e.,

$$f|\Omega = f_\Omega. \tag{4.47}$$

It is commonly known that when Ω is an open subset of $\mathbb{C}^+$, the analytic continuation of f_Ω is a well-defined mathematical concept: there is a *unique* analytic continuation of f_Ω to $\mathbb{C}^+$.

The assumption that Ω is open is too strong. This can be lifted in many cases; for example, for $\Omega = \mathbb{R}$, there is a unique analytic continuation of $f_\mathbb{R}(x) \equiv e^x$ to $\mathbb{C}$ given by $f(z) = e^z$ (the complex exponential). However, this is not true in general: unless Ω and f_Ω are chosen with specific properties, an arbitrary subset $\Omega \subseteq \mathbb{C}^+$ is not guaranteed to support a unique analytic continuation of f_Ω to $\mathbb{C}^+$. One may consider the space of holomorphic functions on $\mathbb{C}^+$ that restrict to f_Ω on Ω; this space will typically have cardinal greater than one.

The discussion will now be restricted to the case when Ω is a discrete subset of the positive imaginary numbers, $\mathbb{I}^+ \equiv i\mathbb{R}_{\geq 0}$, as is the case for the analytic continuation of Euclidean correlation function data. Carlson's theorem [114, 120] is a uniqueness relation about analytic continuation that may be applied if f_Ω, formally stated[5] as follows:

Theorem 4.4.1 (Carlson)**.** Suppose that f_Ω has an analytic continuation f on $\mathbb{C}$ and

[5]Note that Carlson's theorem applies to $\mathbb{C}$, not $\mathbb{C}^+$. However, the identical theorem holds for analytic continuations to $\mathbb{C}^+$ by analytic continuation from $\mathbb{C}^+$ to the entirety of $\mathbb{C}$. Suppose that $f_{\mathbb{C}^+}$ is an analytic continuation of f_Ω to $\mathbb{C}^+$ satisfying Eqs. (4.48, 4.49), with $\mathbb{C}$ replaced by $\mathbb{C}^+$. Then $f_{\mathbb{C}^+}$ may be analytically continued to f on $\mathbb{C}$ satisfying Eqs. (4.48, 4.49), and Carlson's theorem implies this is unique.

that the following assumptions hold.

1. $\exists C, \tau \in \mathbb{R}$ such that for each $z \in \mathbb{C}$,

$$|f(z)| \leq Ce^{\tau|z|}. \tag{4.48}$$

   In this case, one says f is of exponential type [121].

2. $\exists \tau' < \pi$ such that for each $y \in \mathbb{R}$,

$$|f(iy)| \leq Ce^{\tau'|y|}. \tag{4.49}$$

3. $\Omega = i\mathbb{N}_{>0}$.

Then, the analytic continuation of f_Ω to $\mathbb{C}$ is unique.

Carlson's theorem heuristically says that if the function's value is known on $i\mathbb{N}_{>0}$ and the function does not grow too fast at infinity (sub-exponentially), then a unique analytic continuation of this function exists. This is useful when considering spectral reconstructions, as the spectral density and thermal Green's function can be shown to grow polynomially at infinity [122]. This implies that if the Euclidean Green's function is known at each point in $i\mathbb{N}_{>0}$, then it may be uniquely analytically continued, and it corresponds to a unique spectral density[6].

When Ω is a finite subset of $\mathbb{I}^+$ (as in the case of spectral function reconstruction), Carlson's theorem does not apply, and no analog of the theorem implies a unique analytic continuation of the data. Nonetheless, Carlson's theorem provides valuable information about the structure of the problem. As the number of Matsubara frequencies increases (i.e., by increasing the number of sites in the temporal direction), the number of solutions to the spectral reconstruction problem decreases. In the limit where the correlator is evaluated at infinitely many Matsubara frequencies, a unique spectral function that is consistent with the Euclidean data exists. Carlson's theorem has also been used as the basis for a novel method of spectral function reconstruction, as in Refs. [124, 125].

There are infinite solutions to the spectral reconstruction problem for a given Euclidean correlation function computed in LGT, even if the points are known to infinite precision. Any inverse problem with this property is called **ill-posed**: such problems

[6]The assumptions in Carlson's theorem are overly stringent and can be lifted slightly, as done by Rubel [123]. One technically only requires Ω to be an unbounded, infinite subset of $i\mathbb{N}_{>0}$ (e.g., Ω must provide information about the function's value as it tends towards infinity).

are ubiquitous in physical sciences and extremely difficult, even impossible, to solve, because the formal problem statement lacks a unique solution [126, 127], with applications in fields ranging from astrophysics [128] to computational photography [129]. That such a problem does not have a unique solution means that one must impose priors onto the solution space to determine a "best" solution to the problem. Different methods often incorporate different priors, leading to entirely different approaches to solving the inverse problem. Given the same input data, different approaches will thus typically produce solutions that are not equal numerically. One therefore hopes that the qualitative features of the solutions from different methods are similar, rather than the exact numerical details. In the case of spectral function reconstruction, examples of features that one would ideally like to reconstruct faithfully are the location of peaks, number of peaks, and shape of extended spectral features such as thresholds.

4.5 Nevanlinna-Pick Spectral Reconstruction

The work presented in this thesis (Ref. [3]) will reconstruct the spectral density $\rho_\pm(\omega)$ from the Euclidean correlation function $G_E^{(\ell)}$ by exploiting the analytic relations between $\rho_\pm(\omega)$, $G_\pm(z)$, and $G_E^{(\ell)}$ that have been hitherto discussed in Section 4.3. As opposed to directly inverting the Laplace transform in Eq. (4.27), this method presents an algorithm that takes as input the Fourier coefficients $G_E^{(\ell)}$ (which may be computed in LGT) and constructs all possible analytic continuations $G_\pm(z)$ which are consistent with this input data. The smeared spectral function $\rho_\pm^\epsilon(\omega)$ is then constrained by evaluating each possible analytic continuation on the contour $\mathbb{R} + i\epsilon$. For the reader's convenience, the existing Green's function definitions have been summarized in Table 4.1. This method is called **Nevanlinna-Pick Spectral Reconstruction (NPSR)**, for reasons that will be discussed shortly.

To state the spectral reconstruction problem, assume that one has precisely[7] computed N Euclidean Fourier coefficients $\{G_E^{(\ell)}\}_{\ell=1}^N$ at the Matsubara frequencies $\{\omega_\ell\}_{\ell=1}^N$. The reconstruction algorithm will be presented assuming that the Euclidean correlator is known at the first N Matsubara frequencies; however, the algorithm remains valid when the inputs $\{\omega_\ell\}_{\ell=1}^N$ and $\{G_E^{(\ell)}\}_{\ell=1}^N$ are replaced with data taken at an arbitrary cardinal M subset of the Matsubara frequencies $\{\omega_{\ell_j}\}_{j=1}^M$ and $\{G_E^{(\ell_j)}\}_{j=1}^M$. The spectral reconstruction problem is to reconstruct the set $\Lambda(\{G_E^{(\ell)}\})$ of all possible

[7] The presentation of this method assumes there is no statistical error on the inputs, even though any LGT calculation for $\{G_E^{(\ell)}\}$ will have finite statistical errors. The extension of this algorithm to LGT data with finite statistics is underway. The current state of this work will be detailed in Section 4.7.

analytic continuations $G_\pm(z)$ for the data $\{G_E^{(\ell)}\}$: in other words, to construct the space of analytic functions consistent with $\{(i\omega_\ell, G_E^{(\ell)})\}_{\ell=1}^N$,

$$\Lambda(\{G_E^{(\ell)}\}) \equiv \left\{ G_\pm : \mathbb{C}^+ \to \Omega_\pm \text{ analytic} \,\middle|\, \forall \ell \in [N],\, G_\pm(i\omega_\ell) = G_E^{(\ell)} \right\}. \tag{4.50}$$

Let $\epsilon > 0$ be a smearing parameter. The function space $\Lambda(\{G_E^{(\ell)}\})$ is then used to construct the space $\mathrm{SF}_\epsilon(\{G_E^{(\ell)}\})$ of all spectral functions consistent with the data,

$$\mathrm{SF}_\epsilon(\{G_E^{(\ell)}\}) \equiv \left\{ \omega \mapsto G_\pm(\omega + i\epsilon) : G_\pm \in \Lambda(\{G_E^{(\ell)}\}) \right\}. \tag{4.51}$$

The spaces $\Lambda(\{G_E^{(\ell)}\})$ and $\mathrm{SF}_\epsilon(\{G_E^{(\ell)}\})$ were first parameterized in fermionic condensed matter systems in the seminal work by Fei, Yeh, and Gull [11, 130]. The NPSR uses an identical approach to parameterize $\Lambda(\{G_E^{(\ell)}\})$ and $\mathrm{SF}_\epsilon(\{G_E^{(\ell)}\})$ for fermionic systems, but presents a novel approach to parameterize these spaces in bosonic systems. The following sections will keep precise the contributions of Ref. [11] and emphasize where the NPSR method differs from this reconstruction method. Moreover, the NPSR also allows one to construct an explicit bound $(\rho_\pm^{\min}(\omega), \rho_\pm^{\max}(\omega))$ on the space of smeared spectral functions, in the sense that

$$\rho_\pm^{\min} \leq \rho_\pm \leq \rho_\pm^{\max} \text{ almost everywhere} \tag{4.52}$$

for each $\rho_\pm \in \mathrm{SF}_\epsilon(\{G_E^{(\ell)}\})$. This is in contrast to conventional spectral function reconstruction methods that choose some "best" spectral density $\rho_{\text{best}} \in \mathrm{SF}_\epsilon(\{G_E^{(\ell)}\})$, where "best" means that ρ_{best} extremizes a heuristically chosen loss function [107–113].

The NPSR method is based on the formative work of Rolf Nevanlinna [131, 132] and Georg Pick [133] in the early 20th century, who first studied an analogous interpolation problem, named the Nevanlinna-Pick problem, in the unit disk $\mathbb{D}$. The Nevanlinna-Pick problem will be rigorously defined in the following sections. Much of the modern understanding of the mathematics behind the interpolation problem has been presented by Arthur Nicolau [134], whose notation is adopted in this work whenever possible. Additional detail about the underlying complex analysis can be found in Refs. [135, 136].

4.5.1 Mapping the problem to the unit disk

The NPSR method relies on the properties of the finite-volume retarded correlator $G_\pm(z)$ (Eq. (4.19)), which are used to map the analytic continuation problem onto a

well-studied interpolation problem on the open unit disk $\mathbb{D}$. Recall the image of $G_\pm$ is $\Omega_\pm$, computed in Eqs. (4.28, 4.29),

$$\Omega_+ = \mathbb{C}^+ \qquad\qquad \Omega_- = \mathbb{C} \setminus \mathbb{R}_{\leq 0}. \tag{4.53}$$

The **Cayley transform** $C : \mathbb{C}^+ \to \mathbb{D}$ is a conformal bijection between $\mathbb{C}^+$ and $\mathbb{D}$:

$$C(z) = \frac{z-i}{z+i} \qquad\qquad C^{-1}(\zeta) = -i\left(\frac{\zeta+1}{\zeta-1}\right). \tag{4.54}$$

To clarify the domains, z will refer to a variable in $\mathbb{C}^+$, while ζ will be used for variables in $\mathbb{D}$. The Cayley transform is used to lift the fermionic Green's function from $\mathrm{Hol}(\mathbb{C}^+)$ to the $\mathrm{Hol}(\mathbb{D})$, where $\mathrm{Hol}(S)$ denotes the space of holomorphic functions on a domain $S \subseteq \mathbb{C}$. One defines the map $\mathcal{G}_+ : \mathbb{D} \to \mathbb{D}$,

$$\mathcal{G}_+(\zeta) = (C \circ G_+ \circ C^{-1})(\zeta). \tag{4.55}$$

which is clear from the commutative diagram,

$$\begin{array}{ccc} \mathbb{C}^+ & \xrightarrow{G_+} & \mathbb{C}^+ \\ {\scriptstyle C}\downarrow & & \downarrow{\scriptstyle C} \\ \mathbb{D} & \xrightarrow{\mathcal{G}_+} & \mathbb{D}. \end{array} \tag{4.56}$$

The Cayley transform is represented pictorially in Figure 4.5a.

For the bosonic Green's function with image $\Omega_- = \mathbb{C} \setminus \mathbb{R}^-$, one can likewise define an associated conformal bijection $\widetilde{C} : \mathbb{C} \setminus \mathbb{R}^- \to \mathbb{D}$,

$$\widetilde{C}(z) = \frac{\sqrt{z}-1}{\sqrt{z}+1}, \qquad\qquad \widetilde{C}^{-1}(\zeta) = \left(\frac{1+\zeta}{1-\zeta}\right)^2. \tag{4.57}$$

The Green's function G_- maps $\mathbb{C}^+$ onto $\mathbb{C} \setminus \mathbb{R}^-$, so defines the associated map $\mathcal{G}_-$ on $\mathrm{Hol}(\mathbb{D})$ by lifting the domain of G_- with C^{-1} and projecting the image with $\widetilde{C}$,

$$\mathcal{G}_-(\zeta) = (\widetilde{C} \circ G_- \circ C^{-1})(\zeta), \tag{4.58}$$

which is shown in the commutative diagram,

$$\begin{array}{ccc} \mathbb{C}^+ & \xrightarrow{G_-} & \mathbb{C} \setminus \mathbb{R}^- \\ {\scriptstyle C}\downarrow & & \downarrow{\scriptstyle \widetilde{C}} \\ \mathbb{D} & \xrightarrow{\mathcal{G}_-} & \mathbb{D}, \end{array} \tag{4.59}$$

and depicted in Figure 4.5b.

To streamline notation, one packages together the C and $\widetilde{C}$ transforms into a single transform $\mathscr{C}_\pm$,

$$\mathscr{C}_\pm : \Omega_\pm \to \mathbb{D} \qquad \begin{cases} \mathscr{C}_+ \equiv C \\ \mathscr{C}_- \equiv \widetilde{C} \end{cases}, \tag{4.60}$$

with the analogous definition for $\mathscr{C}_\pm^{-1}$. With this notation, the transformed Green's function may be written in both cases as

$$\mathcal{G}_\pm(\zeta) = (\mathscr{C} \circ G_\pm \circ C^{-1})(\zeta), \tag{4.61}$$

and summarized in the diagram,

$$\begin{array}{ccc} \mathbb{C}^+ & \xrightarrow{G_\pm} & \Omega_\pm \\ {\scriptstyle C}\downarrow & & \downarrow{\scriptstyle \mathscr{C}} \\ \mathbb{D} & \xrightarrow{\mathcal{G}_\pm} & \mathbb{D}. \end{array} \tag{4.62}$$

The transformed Green's functions $\mathcal{G}_\pm$ are elements of the **Schur class** of analytic functions,

$$\mathscr{S} = \{f : \mathbb{D} \to \overline{\mathbb{D}} : f \text{ is analytic}\}, \tag{4.63}$$

where $\overline{\mathbb{D}}$ denotes the closure of $\mathbb{D}$, the closed unit disk. The Schur class comprises constant functions on $\mathbb{D}$ and non-constant, analytic functions $\mathbb{D} \to \mathbb{D}$. Further details about the mathematical structure of the interpolation problem are discussed in Appendix E.

To reframe the reconstruction problem entirely on the unit disk, one must also

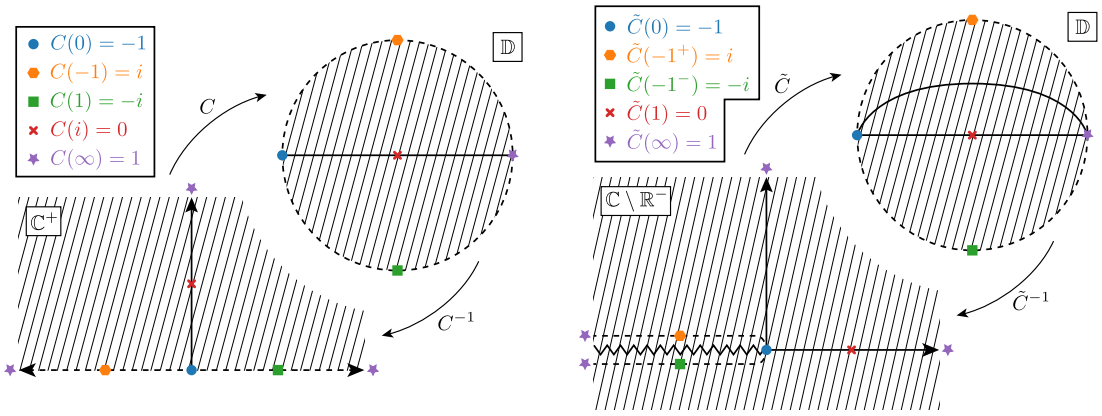

(a) Cayley Transform $C : \mathbb{C}^+ \to \mathbb{D}$. **(b)** $\widetilde{C}$ Transform $\widetilde{C} : \mathbb{C} \setminus \mathbb{R}^- \to \mathbb{D}$.

Figure 4.5. Diagrammatic representation of the Cayley transform $C : \mathbb{C}^+ \to \mathbb{D}$ and the inverse transform $C^{-1} : \mathbb{D} \to \mathbb{C}^+$. The real line is mapped to the boundary of the unit disk, while the upper half-plane is mapped to its interior.

map the inputs $\{i\omega_\ell\} \subseteq \mathbb{C}^+$, $\{G_\pm(i\omega_\ell)\} \subseteq \Omega_\pm$ to corresponding points $\{\zeta_\ell\}, \{w_\ell\} \subseteq \mathbb{D}$,

$$\begin{aligned} \mathbb{D} \ni \zeta_\ell &\equiv C(i\omega_\ell) \\ \mathbb{D} \ni w_\ell &\equiv \mathscr{C}_\pm(G_\pm(i\omega_\ell)), \end{aligned} \tag{4.64}$$

with the transform $\mathscr{C}_\pm$ defined in Eq. (4.60). The interpolation problem is now to determine the space of all possible functions $\mathcal{G}_\pm \in \mathscr{S}$ (Eq. (4.63)) consistent with the input data,

$$\mathcal{G}_\pm(\zeta_\ell) = w_\ell. \tag{4.65}$$

For given $\epsilon > 0$, each $\mathcal{G}_\pm$ yields a transformed smeared spectral function by evaluation on the contour $C(\{\omega + i\epsilon : \omega \in \mathbb{R}\}) \subset \mathbb{D}$, which is then lifted to the corresponding $\rho^\epsilon_\pm(\omega)$ with the inverse $\mathscr{C}_\pm$ transform,

$$\rho^\epsilon_\pm(\omega) = \mathscr{C}_\pm^{-1}\left(G_\pm(C(\omega + i\epsilon))\right). \tag{4.66}$$

This reformulates the interpolation problem as an interpolation problem on the unit disk $\mathbb{D}$. The setting for the Matsubara frequencies and the evaluation axis is summarized in Figure 4.6. The Matsubara frequencies $\{i\omega_\ell\}$ and their images in $\mathbb{D}$, $\{\zeta_\ell\}$, are depicted in red, and the transformed evaluation axis $\{C(\omega + i\epsilon) : \omega \in \mathbb{R}\}$ is depicted in blue.

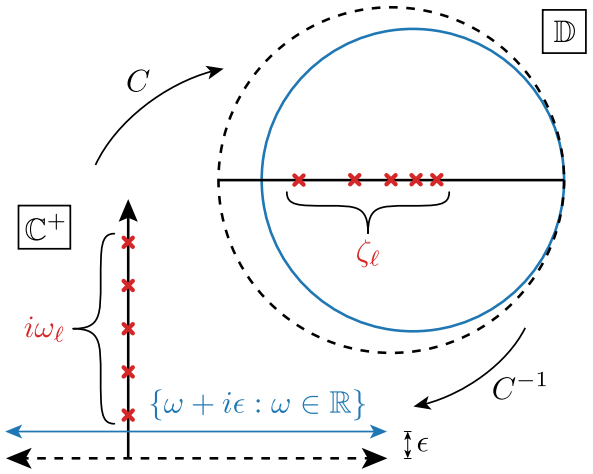

Figure 4.6. Analytic structure of the interpolation problem. The Cayley transform (Eq. (4.54)) maps the Matsubara frequencies $\{i\omega_\ell\} \subseteq \mathbb{C}^+$ to $\{\zeta_\ell\} \subset \mathbb{D}$ (depicted in red), and maps the evaluation contour for the smeared spectral function $\mathbb{R} + i\epsilon = \{\omega + i\epsilon : \omega \in \mathbb{R}\}$ to the contour $\{C(\omega + i\epsilon) : \omega \in \mathbb{R}\}$ (depicted in blue). The same mapping to the disk has been considered in Refs [130, 137] (cf. Fig 1 in Ref. [137]) for fermionic correlators.

4.5.2 The Nevanlinna-Pick Problem

The preceding section (Section 4.5.1) mapped the objects of interest for the interpolation problem to the unit disk $\mathbb{D}$. The problem now remains to construct a valid interpolation function for the data $\{(\zeta_\ell, w_\ell)\}_{\ell=1}^N \subseteq \mathbb{D}^2$; that is, to construct an analytic function f that interpolates these points,

$$f : \mathbb{D} \to \mathbb{D} \qquad\qquad f(\zeta_\ell) = w_\ell. \tag{4.67}$$

The space of all such interpolants f immediately yields the space $\Lambda(\{G_E^{(\ell)}\})$ by pulling each function back to a map between the domains $\mathbb{C}^+ \to \Omega_\pm$, using the inverse transformation to Eq. (4.61). This function f is a member of the Hardy space H^∞, defined as the space of functions f on $\mathbb{D}$ whose sup-norm is finite,

$$||f||_\infty = \sup_{z\in\mathbb{D}} |f(z)| < \infty. \tag{4.68}$$

Additional information about Hardy spaces are given in Appendix E.1, with more detail given in Ref. [138]. This interpolation problem is known as the **Nevanlinna-Pick interpolation problem**, first considered independently by mathematicians Rolf Nevanlinna and Georg Pick. Nevanlinna's contribution to the problem was the

construction of a valid interpolation function that parameterizes the space of all possible solutions in H^∞ [131, 132]. In contrast, Pick studied the *existence* of an interpolating function, given an arbitrary set of input data [133]. Both approaches provide valuable insight into the structure and solution to this interpolation problem. When appropriate, the problem of constructing a solution f to Eq. (4.67) is referred to as the *Nevanlinna problem*, and the problem of determining if such an f exists as the *Pick problem*.

The Nevanlinna construction of an interpolant is formulated in terms of Blaschke products. For $a \in \mathbb{D} \setminus \{0\}$, the **Blaschke factor centered at** a is defined to be the analytic map $b_a : \mathbb{D} \to \mathbb{D}$ given by

$$b_a(\zeta) = \frac{|a|}{a} \frac{a - \zeta}{1 - a^* \zeta}, \tag{4.69}$$

and conventionally define $b_0 \equiv \mathrm{id}_{\mathbb{D}}$. A product of Blaschke factors is known as a Blaschke product. Blaschke products play a privileged role in the theory of complex function interpolation because of the properties they satisfy. First, for any $a \in \mathbb{D}$, the Blaschke factor $b_a \in \mathrm{Aut}(\mathbb{D})$, where $\mathrm{Aut}(\mathbb{D})$ denotes the automorphism ring of the unit disk. Second, Eq. (4.69) clearly implies that $b_a(a) = 0$. These facts may be applied in conjunction with the maximum modulus principle [139] to "factor out" the zeros of a function. Suppose that $g : \mathbb{D} \to \mathbb{D}$ is analytic and has a zero at $a \in \mathbb{D}$. The maximum modulus principle then implies that g may be written as

$$g(\zeta) = b_a(\zeta) \widetilde{g}(\zeta) \tag{4.70}$$

where $\widetilde{g} : \mathbb{D} \to \mathbb{D}$ is another analytic function on $\mathbb{D}$. This fact will be used to construct the Nevanlinna interpolant for the problem. Further properties of Blaschke products and visualizations are presented in Appendix E.3.

The following will provide a convenient notation for continued fraction composition,

$$\begin{pmatrix} a(\zeta) & b(\zeta) \\ c(\zeta) & d(\zeta) \end{pmatrix} h(\zeta) \equiv \frac{a(\zeta)h(\zeta) + b(\zeta)}{c(\zeta)h(\zeta) + d(\zeta)}. \tag{4.71}$$

Here, a, b, c, d, and h are analytic functions on $\mathbb{D}$. This matrix-vector notation coincides nicely with the composition of continued fractions: two continued fraction expansions correspond to matrix multiplication, and inverting a continued fractions expansion corresponds to matrix inversion. Further details and proofs of these prop-

erties are in Appendix E.2.

4.5.3 Solving the Nevanlinna Problem: The Schur Algorithm

Nevanlinna's approach to constructing an interpolation function expanded on ideas from Issai Schur [140] published in 1918. As such, the interpolation algorithm to solve the Nevanlinna problem is called the **Schur algorithm**. The Schur algorithm's central pillar is using Eq. (4.70) to strip off each zero and iteratively construct a solution. To build intuition, consider the Nevanlinna-Pick problem with $N = 1$. Suppose that $f : \mathbb{D} \to \mathbb{D}$ is a solution to Eq. (4.67), which simply means $f(\zeta_1) = w_1$. The function $\zeta \mapsto \frac{f(\zeta)-w_1}{1-w_1^* f(z)}$ has a zero at ζ_1 (the normalization guarantees this function has codomain $\mathbb{D}$), hence Eq. (4.70) implies that this function may be written as

$$\frac{f(\zeta) - w_1}{1 - w_1^* f(\zeta)} = b_{\zeta_1}(\zeta) f_1(\zeta) \tag{4.72}$$

where $f_1 \in H^\infty$ is an arbitrary function. Solving for $f(\zeta)$ yields the expansion,

$$f(\zeta) = \frac{b_{\zeta_1}(\zeta) f_1(\zeta) + w_1}{w_1^* b_{\zeta_1}(\zeta) f_1(\zeta) + 1} \equiv U_1(\zeta) f(\zeta) \quad U_1(\zeta) \equiv \frac{1}{\sqrt{1 - |w_1|^2}} \begin{pmatrix} b_{\zeta_1}(\zeta) & w_1 \\ w_1^* b_{\zeta_1}(\zeta) & 1 \end{pmatrix}, \tag{4.73}$$

where the matrix-vector notation is used in the equality $f(\zeta) = U_1(\zeta) f_1(\zeta)$. The normalization of $U_1(\zeta)$ by $1/\sqrt{1 - |w_1|^2}$ is conventional and guarantees $\det U_1(\zeta) = b_{\zeta_1}(\zeta)$, with no effect on the continued fractions expansion (c.f. Appendix E.2). This expansion makes it clear that any function $f_1 \in H^\infty$ will yield a valid interpolating function $f(\zeta)$ defined by Eq. (4.73) since $f_1(\zeta)$ is always multiplied by a Blaschke factor $b_{\zeta_1}(\zeta)$ which vanishes at ζ_1.

The general solution to the Nevanlinna problem for N points is a generalization of this idea. To fix $f(\zeta_2) = w_2$, one continues to expand $f(\zeta)$ as a continued fraction. Using the expansion of Eq. (4.73), the interpolation condition $f(\zeta_2) = w_2$ yields,

$$w_2 = f(\zeta_2) = \frac{b_{\zeta_1}(\zeta_2) f_1(\zeta_2) + w_1}{w_1^* b_{\zeta_1}(\zeta_2) f_1(\zeta_2) + 1} \tag{4.74}$$

which is rearranged for $f_1(\zeta_2)$ to yield,

$$f_1(\zeta_2) = \frac{1}{b_{\zeta_1}(\zeta_2)} \frac{w_2 - w_1}{1 - w_1^* w_2} \equiv w_2^{(1)}. \tag{4.75}$$

Imposing the interpolation condition $f(\zeta_2) = w_2$ enforces a constraint on f_1. The zero at ζ_2 in the function $\frac{f_1(\zeta)-w_2^{(1)}}{1-w_2^{(1)*}f_1(\zeta)}$ can again be factored out using Eq. (4.70) to strip off a Blaschke factor,

$$\frac{f_1(\zeta) - w_2^{(1)}}{1 - w_2^{(1)*} f_1(\zeta)} = b_{z_2}(\zeta) f_2(\zeta) \iff f_1(\zeta) = \frac{b_{\zeta_2}(\zeta) f_2(\zeta) + w_2^{(1)}}{w_2^{(1)*} b_{\zeta_2}(\zeta) f_2(\zeta) + 1} \tag{4.76}$$

where $f_2 \in H^\infty$ is an arbitrary function. As before, any $f_2 \in H^\infty$ will yield a valid interpolant $f(\zeta)$, and in fact any analytic $f : \mathbb{D} \to \mathbb{D}$ that interpolates (ζ_1, w_1) and (ζ_2, w_2) must be able to be expanded as Eq. (4.76).

The extension to the N-point Nevanlinna problem becomes clear by formulating the expansion for the zero at ζ_2 in terms of the matrix-vector notation of Eq. (4.71). The first interpolation point yields $f(\zeta) = U_1(\zeta) f_1(\zeta)$, where f_1 is an arbitrary function and U_1 is defined in Eq. (4.73). The interpolation constraint $f(\zeta_2) = w_2$ can be expanded with this notation,

$$w_2 = f(\zeta_2) = U_1(\zeta_2) f_1(\zeta_2) \implies f_1(\zeta_2) = U_1(\zeta_2)^{-1} w_2 \tag{4.77}$$

where w_2 is considered as the column vector $\begin{pmatrix} w_2 \\ 1 \end{pmatrix}$. Note that this is indeed the definition of $w_2^{(1)}$, and one can confirm that $U_1(\zeta_2)^{-1} w_2$ indeed equals Eq. (4.77) by computing the matrix inverse and matrix-vector product. The key point is that the matrix-vector notation simplifies the complicated continued fractions expansion for $w_2^{(1)}$ (the value f_1 takes at ζ_2) into the compact expression of Eq. (4.77). The zero in $f_1(\zeta) - w_2^{(1)}$ can then be factored out with a Blaschke product to produce the expansion in Eq. (4.76). The expansion for f_1 of Eq. (4.76) yields,

$$f_1(\zeta) = U_2(\zeta) f_2(\zeta) \qquad U_2(\zeta) \equiv \frac{1}{\sqrt{1 - |w_2^{(1)}|^2}} \begin{pmatrix} b_{\zeta_2}(\zeta) & w_2^{(1)} \\ w_2^{(1)*} b_{\zeta_2}(\zeta) & 1 \end{pmatrix}. \tag{4.78}$$

This is the same form as $U_1(\zeta)$, with $\zeta_1 \mapsto \zeta_2$ and $w_1 \mapsto w_2^{(1)}$. The matrix-vector notation makes it simple to expand f in terms of f_2,

$$f(\zeta) = U_1(\zeta) U_2(\zeta) f_2(\zeta) \tag{4.79}$$

as continued fraction composition corresponds to matrix multiplication.

The general case is clear: the function

$$f(\zeta) = U_1(\zeta)...U_N(\zeta)f_N(\zeta) \tag{4.80}$$

solves the N-point Nevanlinna problem, with $f_N \in H^\infty$ an arbitrary function, where for each $\ell \in \{1, ..., N\}$, the matrix $U_\ell(\zeta)$ is defined as

$$U_\ell(\zeta) \equiv \frac{1}{\sqrt{1 - |w_\ell^{(\ell-1)}|^2}} \begin{pmatrix} b_{\zeta_\ell}(\zeta) & w_\ell^{(\ell-1)} \\ w_\ell^{(\ell-1)*} b_{\zeta_\ell}(\zeta) & 1 \end{pmatrix}. \tag{4.81}$$

Here $w_\ell^{(\ell-1)} \in \mathbb{D}$ are defined recursively in terms of the previously defined $f_\ell \in H^\infty$ as

$$w_k^{(\ell)} = f_\ell(\zeta_k), \tag{4.82}$$

defined for $1 \leq \ell < k$. The explicit value of $w_k^{(\ell)}$ is computed in terms of w_k and the values $U_1(\zeta_k), ..., U_n(\zeta_k)$,

$$\begin{aligned} w_k = f(\zeta_k) &= U_1(\zeta_k)...U_n(\zeta_k)w_k^{(\ell)} \\ \implies w_k^{(\ell)} &= U_\ell^{-1}(\zeta_k)U_{\ell-1}^{-1}(\zeta_k)\cdots U_1^{-1}(\zeta_k)w_k. \end{aligned} \tag{4.83}$$

Moreover, Eq. (4.80) not only solves the Nevanlinna problem but also any solution to the Nevanlinna problem may be written in this form for some $f_N \in H^\infty$. It is conventional to define the **Nevanlinna coefficients** $P_N, Q_N, R_N, S_N : \mathbb{D} \to \mathbb{D}$ as

$$\begin{pmatrix} P_N(\zeta) & Q_N(\zeta) \\ R_N(\zeta) & S_N(\zeta) \end{pmatrix} \equiv U_1(\zeta)U_2(\zeta)...U_N(\zeta). \tag{4.84}$$

The Nevanlinna coefficients are analytic functions on $\mathbb{D}$ and contain all the information about the interpolation problem $\{(\zeta_\ell, w_\ell)\}_{\ell=1}^N$. They will be discussed further in Section 4.5.5.

To prove the previous claim, one proceeds by strong induction on N, which has already been shown for $N = 1, 2$. Suppose that $f(\zeta) = U_1(\zeta)...U_N(\zeta)f_N(\zeta)$. To include a point (ζ_{N+1}, w_{N+1}) into the interpolation, one expands

$$w_{N+1} = f(\zeta_{N+1}) = U_1(\zeta_{N+1})...U_N(\zeta_{N+1})f_N(\zeta_{N+1}). \tag{4.85}$$

This immediately yields $w_{N+1}^{(N)} = f_N(\zeta_{N+1}) = U_N(\zeta_{N+1})^{-1}...U_1(\zeta_{N+1})^{-1}w_{N+1}$. Note that $w_{N+1}^{(N)}$ is constructible from the current data, as the $U_1(\zeta), ..., U_N(\zeta)$ are assumed

to have already been computed. As before, Eq. (4.70) is used to expand

$$\frac{f_N(\zeta) - w_{N+1}^{(N)}}{1 - w_{N+1}^{(N)*} f_N(\zeta)} = b_{z_{N+1}}(\zeta) f_{N+1}(\zeta) \iff f_N(\zeta) = U_{N+1}(\zeta) f_{N+1}(\zeta) \tag{4.86}$$

with $U_{N+1}(\zeta)$ defined as in Eq. (4.81) and $f_{N+1} \in H^\infty$ an arbitrary function. It is clear that this implies $f(\zeta) = U_1(\zeta)...U_N(\zeta)U_{N+1}(\zeta)f_{N+1}(\zeta)$ as claimed. Conversely, any such interpolating function must likewise satisfy these identities because of the interpolation condition $f(\zeta_{N+1}) = w_{N+1}$, so any such $f(\zeta)$ solving the $N+1$-point interpolation problem can be parameterized in this way. This completes the induction and proves the claim.

The Schur interpolation algorithm is specified by Eqs. (4.80–4.83). The algorithm iteratively constructs the $U_n(\zeta)$, and therefore $w_n^{(n-1)}$, in terms of $U_k(\zeta)$ for $1 \leq k \leq n-1$. The expansion of $f(\zeta) = U_1(\zeta)...U_N(\zeta)f_N(\zeta)$ (Eq. (4.80)) parameterizes the full space of analytic functions $\mathbb{D} \to \mathbb{D}$ that interpolate the points $\{(\zeta_n, w_n)\}_{n=1}^N$. This presents an explicit parameterization of $\Lambda(\{G_E^{(\ell)}\})$ and $\mathrm{SF}_\epsilon(\{G_E^{(\ell)}\})$ (Eqs. (4.50, 4.51) by the Hardy space H^∞. The parameterization for $\Lambda(\{G_E^{(\ell)}\})$ is

$$\Lambda(\{G_E^{(\ell)}\}) = \left\{\mathscr{C}^{-1} \circ (U_1...U_N f_N) \circ C : f_N \in H^\infty\right\} \tag{4.87}$$

where the matrices $U_n(\zeta)$ are constructed as stated, and the function $(U_1(\zeta)...U_N f_N)(\zeta) = U_1(\zeta)...U_N(\zeta)f_N(\zeta)$, which yields the corresponding parameterization for $\mathrm{SF}_\epsilon(\{G_E^{(\ell)}\})$

$$\mathrm{SF}_\epsilon(\{G_E^{(\ell)}\}) = \left\{\omega \mapsto (\mathscr{C}^{-1} \circ (U_1...U_N f_N) \circ C)(\omega + i\epsilon) : f_N \in H^\infty\right\}. \tag{4.88}$$

This parameterization is the first result of the NPSR method, which was first written down by Fei, Yeh, and Gull in Ref. [11] for fermionic systems. The NPSR method extends their work to bosonic systems by introducing the transform $\mathscr{C} : \Omega_\pm \to \mathbb{D}$.

That the space of analytic continuations $\Lambda(\{G_E^{(\ell)}\})$ is parameterized by the function space H^∞ shows that the inverse problem is ill-posed. Given a set of data $\{(i\omega_\ell, G_E^{(\ell)})\}$, there are an infinite number of possible analytic continuations of this data to a retarded correlator $G_\pm(z)$ that is consistent with the analytic properties of Section 4.3 (Eq. (4.87)). However, the interpolation problem constrains the set of solutions to the problem: although $f_N \in H^\infty$ is an arbitrary function, the matrices $U_1(\zeta), ..., U_N(\zeta)$ (equivalently the Nevanlinna coefficients $P_N(\zeta), Q_N(\zeta), R_N(\zeta), S_N(\zeta)$) contain the information about the interpolation problem, and constrain the behavior of the interpolant $U_1(\zeta)...U_N(\zeta)f_N(\zeta)$ regardless of the choice of $f_N(\zeta)$. This param-

eterization may be used to determine a "best" spectral function that satisfies the interpolation data, which will be discussed in the next section.

This parameterization is theoretically sound, but it does not immediately tell one about the behavior of an arbitrary spectral function $\rho^\epsilon_\pm(\omega)$ that is consistent with the data. Section 4.5.5 will present the second part of the NPSR method, which will construct an envelope that any reconstructed smeared spectral function must be found in. Such an envelope is more valuable than a parameterization of $\mathrm{SF}_\epsilon(\{G_E^{(\ell)}\})$ because it yields information about the geometry of the entire space rather than a specific element in the space.

4.5.4 Optimization of f_N

As discussed, the connection between spectral reconstruction and Nevanlinna-Pick interpolation was first made explicit by Fei, Yeh, and Gull [11]. Here the method of spectral reconstruction presented in Ref. [11] is summarized, which involves searching the space $\mathrm{SF}_\epsilon(\{G_E^{(\ell)}\})$ of all possible smeared spectral functions for a "best" smeared spectral function $(\rho^\epsilon_\pm)_*(\omega)$ by extremizing a cost functional. This section will suppress the $\pm$ subscript on $\rho^\epsilon_\pm(\omega)$, and denote the "best" smeared spectral function as $\rho^\epsilon_*(\omega)$.

To formalize this, one chooses a cost functional that is consistent with the properties desired by the reconstructed spectral function. The most immediate example of this is to enforce that $\rho^\epsilon(\omega)$ is smooth and non-oscillatory, which is equivalent to the second derivative $(\rho^\epsilon)''(\omega)$ having a small L^2 norm. Consider, for example, the cost functional,

$$F_\lambda[\rho] = \left(1 - \int d\omega\, \rho(\omega)\right)^2 + \lambda \int d\omega\, \left(\rho''(\omega)\right)^2, \tag{4.89}$$

where $\lambda \ll 1$ is a regulator that enforces the relative importance of the second term that damps oscillations, $\int (\rho'')^2$, compared to the first term that enforces normalization of the spectral function, $(1 - \int \rho)^2$. The "best" spectral function ρ^ϵ_* is chosen to minimize $F_\lambda[\rho]$

$$\rho^\epsilon_* = \operatorname*{argmin}_{\rho^\epsilon \in \mathrm{SF}_\epsilon(\{G_E^{(\ell)}\})} F_\lambda[\rho^\epsilon]. \tag{4.90}$$

Note that the reconstructed spectral density ρ^ϵ_* is implicitly a function of the specified cost functional F_λ. The cost functional $F_\lambda[\rho]$ is arbitrary and, as mentioned, can be modified to include whatever properties of ρ^ϵ one wants to enforce. Eq. (4.89) uses a Tikhonov regularization [141, 142] on ρ'' to enforce the output spectral density is

smooth. Ideally, one would desire ρ_*^ϵ to be independent of the choice of F_λ, but in practice, this is not the case; the reconstructed spectral density can heavily depend on F_λ, indicating this reconstruction method may rely too heavily on heuristics.

There are many additional choices of F_λ that would impose different properties on the spectral density. A physically well-informed constraint that may be used as a regulator comes from sum rules [143] that the spectral density is known to satisfy analytically. Sum rules constrain the moments of the spectral density; an arbitrary sum rule has the form,

$$\int d\omega\, \rho^n(\omega) = I^{(n)}, \tag{4.91}$$

where n and I_n are known analytically [144]. Enforcing this constraint amounts to adding the term,

$$F_\lambda[\rho] \supset \xi_n \left(I^{(n)} - \int d\omega\, \rho^n(\omega) \right)^2, \tag{4.92}$$

to the cost functional, where $0 < \xi_n \ll 1$ is a hyperparameter. Note that here the deviation between the n^{th} moment of ρ and I_n is squared in order to make the term differentiable. One can add an arbitrary number of sum rules to the cost functional, but additional regulator terms increase the complexity of the optimization problem. In particular, as each regulator has its own hyperparameter, tuning the hyperparameters may bottleneck the calculation if a large number of sum rules are enforced. Given a set of input Euclidean correlation function data $\{G_E^{(\ell)}\}$, the full space $\text{SF}_\epsilon(\{G_E^{(\ell)}\})$ is not mathematically guaranteed to satisfy the sum rules, and in general, one should only consider the subset of $\text{SF}_\epsilon(\{G_E^{(\ell)}\})$ that is consistent with all applicable sum rules for a given system.

The optimization of Eq. (4.90) can be simplified in terms of the Hardy space H^∞. Recall that any $\rho^\epsilon \in \text{SF}_\epsilon(\{G_E^{(\ell)}\})$ may be expanded as

$$\rho^\epsilon[f_N](\omega) = \mathscr{C}^{-1}\left(U_1(\omega + i\epsilon)...U_N(\omega + i\epsilon) f_N(\omega + i\epsilon)\right) \tag{4.93}$$

for $f_N \in H^\infty$. The domain of the optimization problem is hence reduced to searching over the Hardy space H^∞,

$$f_N^* = \underset{f_N \in H^\infty}{\text{argmin}}\, F_\lambda\left[\rho^\epsilon[f_N]\right]. \tag{4.94}$$

Note that because $H^\infty \subseteq H^p$ for $1 \leq p < \infty$[8], moments of $f_N(\zeta)$ and its derivatives are well-defined. The optimization of Eq. (4.94) is a functional optimization over

[8]The p^{th} Hardy space H^p is defined as the space of holomorphic functions on $\mathbb{D}$ whose angular

the full Hardy space H^∞ and is hard to implement generally because the dimension of H^∞ is countably infinite. Computationally, the simplest way to implement this optimization is to instead restrict the optimization to a finite-dimensional subspace of H^∞. One expands f_N in a basis for this finite-dimensional subspace and optimizes the finite number of basis coefficients, turning the problem into a tractable convex optimization in Euclidean space.

In order to define a square-integrable norm that can be optimized, f_N is considered as an element of the Hardy space[9] H^2. A basis for H^2 is $\{g_k, g_k^*\}_{k=1}^\infty$ (the functions g_k and their complex conjugates) given by [145],

$$g_k(\zeta) \equiv \frac{i}{2\sqrt{\pi}}(\zeta - 1)\zeta^k. \tag{4.96}$$

with $k \in \{0, 1, 2, ...\}$. The function $f_N(\zeta)$ is expanded with the first $2M$ elements of the Hardy basis and is written as

$$f_N(\zeta) = \sum_{k=0}^{M} (\alpha_i g_k(\zeta) + \beta_i g_k^*(\zeta)) \tag{4.97}$$

This expansion reduces the functional $\rho^\epsilon[f_N]$ to a function $\rho^\epsilon(\{(\alpha_k, \beta_k)\}_{k=0}^M)$ of $2M+2$ real parameters $\{(\alpha_k, \beta_k)\}_{k=0}^M$, which recasts the optimization problem into a problem on finite-dimensional Euclidean space $\mathbb{R}^{2M+2}$ with cost function (note $\epsilon > 0$ is fixed and not optimized over)

$$\begin{aligned} F_\lambda(\{(\alpha_k, \beta_k)\}_{k=0}^M; \epsilon) = &\left(1 - \int d\omega\, \rho^\epsilon(\{(\alpha_k, \beta_k)\}_{k=0}^M)(\omega)\right)^2 \\ &+ \lambda \int d\omega\, \left(\rho^\epsilon(\{(\alpha_k, \beta_k)\}_{k=0}^M)''(\omega)\right)^2. \end{aligned} \tag{4.98}$$

The solution to this optimization is not the "best" choice of f_N over the space of

integral

$$\sup_{r\in[0,1)} \left(\int_{S^1} \frac{d\theta}{2\pi} |f(re^{i\theta})|^p\right)^{\frac{1}{p}} \tag{4.95}$$

is finite; for more details, refer to Appendix E.1.

[9]Note that the mathematical formalism presented thus far has considered $f_N \in H^\infty$, while Ref. [11] considers $f_N \in H^2$. Although $H^\infty \subseteq H^2$, it is my view that $f_N \in H^\infty$ is a necessary constraint for the resulting interpolating function f to be a valid analytic map $\mathbb{D} \to \mathbb{D}$. Expanding f_N in a basis for H^2 may produce results of the Nevanlinna interpolation that are not analytic functions $\mathbb{D} \to \mathbb{D}$, since elements in $H^2 \setminus H^\infty$ may not necessarily satisfy the constraints in the Schur algorithm. The resulting functions $f(\zeta)$ will still interpolate the correct points, but they may have image$(f) \not\subseteq \mathbb{D}$. This is likely a small concern, as the elements in $H^\infty \setminus H^2$ are pathological.

all functions $f_N \in H^\infty$, but rather the "best" choice of f_N in the space spanned by $\{g_0, g_0^*, ..., g_M, g_M^*\}$, which is a subspace of H^2.

4.5.5 Nevanlinna Coefficients and the Wertevorrat

Recall the functions $P_N, Q_N, R_N, S_N : \mathbb{D} \to \mathbb{C}$ defined in Section 4.5.3 are called Nevanlinna coefficients. They lie in the Smirnov class of functions (see Appendix E.1 for more details) and determine the possible solutions to the Schur interpolation problem.

The Nevanlinna coefficients satisfy many properties directly from their definition (Eq. (4.84)) [146, 147], which are stated here for convenience. The functions $P_N(\zeta), Q_N(\zeta), R_N(\zeta), S_N(\zeta)$ are rational functions by construction, and they have poles at $1/\zeta_\ell$. The Nevanlinna coefficient matrix satisfies a constraint on its determinant,

$$P_N(\zeta)S_N(\zeta) - Q_N(\zeta)R_N(\zeta) = B_N(\zeta), \tag{4.99}$$

where $B_N(\zeta)$ is the Blaschke product $B_N(\zeta) = \prod_{i=1}^N b_{\zeta_i}(\zeta)$ (Appendix E.3). This result is immediate because each $U_j(\zeta)$ is normalized to satisfy $\det U_j(\zeta) = b_{\zeta_j}(\zeta)$ (Eq. (4.81)), hence $\det(\prod_i^N U_i(\zeta)) = \prod_i^N \det U_i(\zeta)$ yields the result. Additionally, for $\zeta \in \mathbb{D}$, one has the following relations between the sizes of the coefficients,

$$|S_N(\zeta)| \geq 1, \qquad |S_N(\zeta)| \geq \max\{P_N(\zeta), Q_N(\zeta), R_N(\zeta)\}, \tag{4.100}$$

and the following constraints on the coefficients themselves,

$$P_N(\zeta) = B_N(\zeta)S_N^*(1/\zeta^*), \qquad Q_N(\zeta) = B_N(\zeta)R_N^*(1/\zeta^*). \tag{4.101}$$

Eqs. (4.100, 4.101) are proved in Ref. [134].

A remarkable fact about the Nevanlinna coefficients is that they may be used to compute an explicit bound on the output interpolation function $f(\zeta)$ for arbitrary $f_N(\zeta)$, which in turn extends to a rigorous bound on the values that the smeared spectral function $\rho_\pm^\epsilon(\omega)$ can take. Recall that for any $f_N \in H^\infty$, the function

$$f(\zeta) = \frac{P_N(\zeta)f_N(\zeta) + Q_N(\zeta)}{R_N(\zeta)f_N(\zeta) + S_N(\zeta)} \tag{4.102}$$

solves the Nevanlinna-Pick interpolation problem (Eqs. (4.80, 4.84). Conversely, any solution to the Nevanlinna-Pick interpolation problem may be parameterized as Eq. (4.102) for some choice of $f_N \in H^\infty$. Varying f_N over all possible functions

in H^∞ gives an envelope for f containing all possible solutions to the interpolation problem.

The **Wertevorrat**[10] is defined for each $\zeta \in \mathbb{D}$ as

$$\Delta_N(\zeta) \equiv \{f(\zeta) : f \in H^\infty \text{ s.t. } \forall \ell \in \{1, ..., N\},\, f(\zeta_\ell) = w_\ell\}\,, \tag{4.103}$$

which is a closed subset of $\mathbb{D}$. In other words, the Wertevorrat at ζ is the set of all possible values an interpolating function consistent with the input data can take at ζ. Knowledge of the Wertevorrat directly quantifies how ill-posed the inverse problem is. If the Wertevorrat can be computed, the uncertainty associated with the inverse problem can be precisely constrained.

The key to the NPSR method is that $\Delta_N(\zeta)$ can be directly quantified in terms of the Nevanlinna coefficients and the N-point Blaschke product,

$$B_N(\zeta) = \prod_{\ell=1}^{N} b_{\zeta_\ell}(\zeta). \tag{4.104}$$

Let $\zeta \in \mathbb{D}$ be fixed. To compute the Wertevorrat $\Delta_N(\zeta)$, the main idea will be to vary $f_N(\zeta)$ in the expansion of Eq. (4.102), since $|f_N(\zeta)| \leq 1$. The Wertevorrat may be rewritten as,

$$\Delta_N(\zeta) = \{T_{N,\zeta}(w) : w \in \mathbb{D}\}, \tag{4.105}$$

where $T_{N,\zeta} : \mathbb{D} \to \mathbb{D}$ is defined as

$$T_{N,\zeta}(w) = \frac{P_N(\zeta)w + Q_N(\zeta)}{R_N(\zeta)w + S_N(\zeta)}, \tag{4.106}$$

because $f_N(\zeta) \in \mathbb{D}$ can take on an arbitrary value in the disk as f_N is varied over all of H^∞. The map $w \mapsto T_{N,\zeta}(\zeta)$ is a Möbius transformation [148], which has the property that it maps circles to circles. Hence, $\Delta_N(\zeta)$ must be a disk.

It remains to compute the center and radius of this disk. To compute the center of this disk, note that $T_{N,\zeta}(-S_N(\zeta)/R_N(\zeta)) = \infty$ in the extended complex plane. The reflection property of Möbius transformations implies that $T_{N,\zeta}$ maps $-(R_N(\zeta)/S_N(\zeta))^*$

[10] The codomain of a function $f : A \to B$ is called the "Wertevorrat" in German. The terminology is meant to evoke the codomain of a function, as the Wertevorrat is the space of values that the analytic continuation can possibly take on.

to the center of $\Delta_N(\zeta)$, hence the disk is centered at

$$c_N(\zeta) = \frac{P_N(\zeta)\left(-R_N(\zeta)/S_N(\zeta)\right)^* + Q_N(\zeta)}{R_N(\zeta)\left(-R_N(\zeta)/S_N(\zeta)\right)^* + S_N(\zeta)} \tag{4.107}$$

$$= \frac{Q_N(\zeta)S_N^*(\zeta) - P_N(\zeta)R_N^*(\zeta)}{|S_N(\zeta)|^2 - |R_N(\zeta)|^2}. \tag{4.108}$$

The radius of the disk is given by the distance between any point $T_{N,\zeta}(e^{i\theta})$ on the boundary of $\Delta_N(\zeta)$ and the enter $c_N(\zeta)$, which evaluates to

$$r_N(\zeta) = \frac{|B_N(\zeta)|}{|S_N(\zeta)|^2 - |R_N(\zeta)|^2}, \tag{4.109}$$

where the Blaschke product is the result of the Nevanlinna determinant, Eq. (4.99).

To summarize, at fixed $\zeta \in \mathbb{D}$, the Wertevorrat is a Euclidean disk $\Delta_N(\zeta) \subseteq \mathbb{D}$ with center $c_N(\zeta)$ (Eq. (4.108)) and radius $r_N(\zeta)$ (Eq. (4.109)). This is a remarkable result: it means one has a direct measure of how "ill-posed" the reconstruction problem is via the Wertevorrat. When the radius $r_N(\zeta)$ of the Wertevorrat is small compared to its center $c_N(\zeta)$, the reconstructed smeared spectral function is easily resolvable, and any reconstruction that singles out a specific Poisson-smeared spectral function must lie in the Wertevorrat. In this way, the Wertevorrat itself can be used as a proxy for the reconstructed spectral function.

4.5.6 Constraining $\rho^{\epsilon}_{\pm}(\omega)$ from $\Delta_N(\zeta)$

The Wertevorrat $\Delta_N(\zeta) \subseteq \mathbb{D}$ is inherently a subset of the unit disk $\mathbb{D}$. For physical interpretation, it must be pulled back to the correct domain and codomain wherein the smeared spectral function resides. Given an interpolating function $\mathcal{G}_{\pm} : \mathbb{D} \to \mathbb{D}$, one maps $\mathcal{G}_{\pm}$ back to a retarded correlator with the transform $\mathscr{C}_{\pm}$ (Eq. (4.60))

$$\begin{aligned} &G_{\pm} : \mathbb{C}^+ \to \Omega_{\pm} \\ &G_{\pm}(z) = (\mathscr{C}_{\pm}^{-1} \circ \mathcal{G}_{\pm} \circ C)(z) \end{aligned} \tag{4.110}$$

The Wertevorräte[11] are pulled back to the upper half-plane in a similar manner,

$$\mathcal{D}_N(z) \equiv (\mathscr{C}_{\pm}^{-1} \circ \Delta_N \circ C)(z). \tag{4.111}$$

[11] Everything I have learned about how to pluralize German words comes from my collaborator and friend William Jay.

For each $z \in \mathbb{C}^+$, the retarded correlator $G_{\pm}(z)$ must lie inside the domain $\mathcal{D}_N(z) \subseteq \Omega_{\pm}$ to be a valid interpolating function for the Nevanlinna-Pick problem. The set $\mathcal{D}_N(z)$ is indeed a domain (an open, connected subset of $\mathbb{C}$) because it is the preimage of an open, connected set (a disk). Recall that for any interpolating function $G_{\pm}(z)$, one extracts the spectral density via evaluation on the shifted real axis,

$$\rho^{\epsilon}_{\pm}(\omega) = \frac{1}{\pi}\mathrm{Im}\, G_{\pm}(\omega + i\epsilon). \tag{4.112}$$

The uncertainty in the reconstruction of $\rho^{\epsilon}_{\pm}(\omega)$ induced by the ill-posed inverse problem is, therefore, the size of the Wertevorrat, mapped back to the correct domain and pulled back through Eq. (4.112), which is the full width of the imaginary part of $\mathcal{D}_N(\omega + i\epsilon)$,

$$\delta\rho^{\epsilon}_{\pm}(\omega) = \frac{1}{\pi}\left[\sup \mathrm{Im}\, \partial\mathcal{D}_N(\omega + i\epsilon) - \inf \mathrm{Im}\, \partial\mathcal{D}_N(\omega + i\epsilon)\right], \tag{4.113}$$

where $\partial\mathcal{D}_N(z)$ denotes the boundary of $\mathcal{D}_N(z)$. The computation of $\delta\rho^{\epsilon}_{\pm}(\omega)$ is summarized in Figure 4.7. Numerically, $\delta\rho^{\epsilon}_{\pm}(\omega)$ is computed by uniformly sampling the circle $\partial\Delta_N(C(\omega + i\epsilon))$ at 1,000 points, pulling each point back through the transformations of Eqs. (4.111, 4.113), and computing the maximum and minimum of these samples.

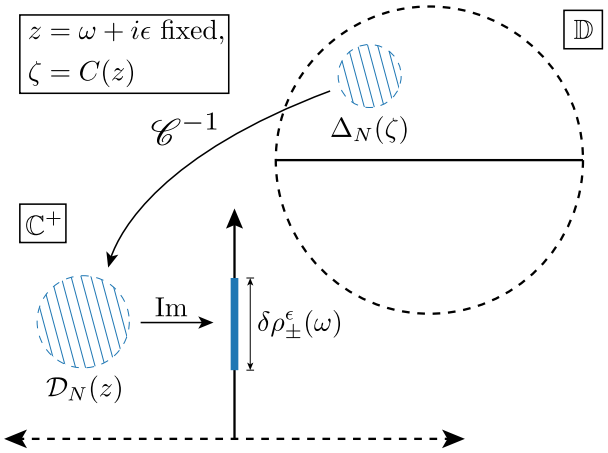

Figure 4.7. Interpretation of the Wertevorrat $\Delta_N(\zeta)$ as the uncertainty on the smeared spectral function $\rho^{\epsilon}_{\pm}(\omega)$. The Wertevorrat is mapped back to $\mathbb{C}^+$ with the transform $\mathscr{C}^{-1}$ and then projected onto its imaginary component. The resulting projection is proportional to the uncertainty in the smeared spectral density $\delta\rho^{\epsilon}_{\pm}(\omega)$.

It is insightful to study the behavior of the Wertevorrat $\mathcal{D}(\omega+i\epsilon)$ as one approaches the real axis from above, $\epsilon \downarrow 0$, which is equivalent to studying $\Delta_N(\zeta)$ as $\zeta \to \partial\mathbb{D}$. The following lemma, proved in Ref. [3], is helpful.

Lemma 4.5.1. Let $w, z \in \mathbb{C}$ with $w^*z \neq 1$. If $|z| < 1$ and $|w| < 1$, then $|\frac{w-z}{1-w^*z}| < 1$. If $|z| = 1$ or $|w| = 1$, then $|\frac{w-z}{1-w^*z}| = 1$.

This implies that when $|\zeta| = 1$, the Wertevorrat is the full unit disk $\Delta_N(\zeta) = \overline{\mathbb{D}}$. As $\mathscr{C}_\pm^{-1}(\overline{\mathbb{D}}) = \overline{\Omega_\pm}$, this means that as the smearing ϵ approaches 0, the spectral function is unconstrained by the interpolation,

$$\delta\rho_\pm^\epsilon(\omega)\Big|_{\epsilon\downarrow 0} = \infty. \tag{4.114}$$

This means the unsmeared spectral density cannot be directly reconstructed from the interpolation data, even with analytic guarantees on $G_\pm(z)$. The smaller the smearing width ϵ, the larger the Wertevorrat will grow, until it eventually fills the entire space, at which point the interpolation procedure yields no information.

4.5.7 Summary of the NPSR method

The NPSR method presented in this section takes the following steps to reconstruct a smeared spectral function.

1. From Euclidean correlator data $\mathscr{G}_E(\tau)$, compute the Fourier coefficients $G_E^{(\ell)}$ for each desired Matsubara frequency ω_ℓ via Eq. (4.10) and the discussion in Section 4.3.1. The pairs $\{(i\omega_\ell, G_E^{(\ell)})\}$ are the input data to the algorithm.

2. Transform the data $\{(i\omega_\ell, G_E^{(\ell)})\}$ to $\mathbb{D}$ with $\zeta_\ell = C(i\omega_\ell)$ and $w_\ell = \mathscr{C}_\pm(G_E^{(\ell)})$ (Eq. (4.64)).

3. Construct the Nevanlinna coefficients $P_N(\zeta), Q_N(\zeta), R_N(\zeta), S_N(\zeta)$ from the data using the Schur algorithm, Eqs. (4.80–4.83). Use the Nevanlinna coefficients to compute the center $c_N(\zeta)$ and the radius $r_N(\zeta)$ of the Wertevorrat, Eqs. (4.108, 4.109).

4. Pull back the Wertevorrat to $\mathcal{D}_N(z)$, evaluated on the domain of interest $\Omega_\pm$ for the system at hand, using Eq. (4.111).

5. Compute the space of smeared spectral functions $\delta\rho_\pm^\epsilon(\omega)$ using Eq. (4.113). The true smeared spectral function is rigorously guaranteed to lie within $\delta\rho_\pm^\epsilon(\omega)$.

The presented algorithm treats the bosonic and fermionic cases exactly the same, other than the transforms that are applied to map the data to the disk ($\mathscr{C}_\pm$), and where the Matsubara frequencies $i\omega_\ell \in \mathbb{C}^+$ lie (Eq. (4.11)). This can be exploited in the zero-temperature limit, where the finite-volume spectral function (Eq. (4.23)) satisfies the relation,

$$\rho_+(\omega) = \mathrm{sgn}(\omega)\rho_-(\omega). \tag{4.115}$$

This implies that the fermionic and bosonic smeared spectral densities must converge to the same result as the smearing parameter $\epsilon \downarrow 0$,

$$\lim_{\epsilon\to 0} \rho_+^\epsilon(\omega) = \mathrm{sgn}(\omega) \lim_{\epsilon\to 0} \rho_-^\epsilon(\omega). \tag{4.116}$$

The fermionic and the bosonic reconstructions contain the same information at zero temperature as the smearing goes to zero, and the choice of which to use is a question of ease. These methods can be used in conjunction to take the zero-smearing limit, as they both converge to the same unsmeared spectral density (up to $\mathrm{sgn}(\omega)$). Section 4.6.2 explores this idea in a numerical example.

It is illuminating to discuss the differences between the NPSR method and other recent work in this area, namely with the Nevanlinna Analytical Continuation (NAC) approach to spectral reconstruction developed by Fei, Yeh, and Gull [11], which heavily influenced many of the ideas in the NPSR method. The NAC method uses the Nevanlinna property of fermion correlation functions $G_+(z)$ to map the problem to the disk using the Cayley transform $C : \mathbb{C}^+ \to \mathbb{D}$ (Eq. (4.54)). While the NPSR method uses the same approach for fermionic correlators, it is generalizable to bosonic correlators via the map $\widetilde{C} : \mathbb{C} \setminus \mathbb{R} \to \mathbb{D}$ (Eq. (4.57)). Our perspective is that the unique property of fermionic correlators is not that they are Nevanlinna but rather that they can be conformally mapped to the unit disk. The prerequisite for the NPSR is that a conformal map exists between the image of the retarded correlator and the unit disk to apply the theory of Nevanlinna-Pick interpolation. A follow-up to Ref. [11] is the work of Nogaki and Shinaoka [149] in 2023, which uses the "hyperbolic tangent trick" to transform a bosonic system to a system of auxiliary fermions, at which point the method of Fei, Yeh, and Gull can be applied to the system.

Another essential difference between the NPSR and the NAC is the existence of the Wertevorrat, which allows the NPSR to rigorously constrain the full space of smeared spectral functions consistent with the data. The algorithms of Refs. [11, 149, 150] output a single smeared spectral function $\rho_*^\epsilon(\omega)$ that extremizes some chosen cost

functional (c.f. Section 4.5.4). In contrast, the NPSR method outputs the full space $\delta\rho^{\epsilon}_{\pm}(\omega)$ that the smeared spectral function is rigorously guaranteed to lie in. While the optimization step of the NAC outputs a spectral function with nicer properties than the naïve reconstruction resulting from choosing $f_N \in H^\infty$ to be some random element of the Hardy space, to our knowledge there is no rigorous field-theoretic reason why the smeared spectral function should extremize the cost functional of Eq. (4.89). One can modify this cost functional to add in desired properties of the output smeared spectral function, and in particular, one can add in constraints from field theoretic identities like sum rules [143]. The authors of Ref. [11] added constraints on the moments of the retarded correlator to the cost functional [144] and did not find any significant improvement to the reconstruction. Our perspective is that choosing a cost functional to filter through the space of possible smeared spectral functions induces an uncontrolled systematic into the reconstruction problem. For LGT calculations, statistical error and uncertainty must be precisely controlled, which is not possible via the optimization step of the NAC. The advantage of the Wertevorrat is that it can be identified with the reconstruction error and allows for a conservative estimate of the unavoidable error induced by the inverse problem.

The interpretation of $G_{\pm}(\omega + i\epsilon)$ as a Poisson-smeared spectral function is appealing in that the smeared spectral function is directly computable from the main analytic object of the study, the retarded Green's function. However, a downside of this method compared to other works like the Hansen-Lupo-Tantalo (HLT) method [112, 113] is that the smearing kernel cannot be chosen and manipulated: it is fixed to a Poisson kernel. While the Poisson kernel is a valid smearing kernel, dealing with other kernels like the standard Gaussian is mathematically more challenging. For example, the moments of the Poisson kernel are infinite, while other distributions behave better. While this does not influence the reconstruction of the smeared spectral function, the presence of a non-negligible amount of mass far away from the center of the distribution may make it harder to extrapolate the smeared spectral function to the infinite-volume limit.

One intriguing possibility for infinite-volume spectral reconstruction currently being explored by T. Blum, W. Jay, L. Jin, and D. Stewart is the possibility of "triangulating" the unsmeared infinite-volume spectral function using different smearing kernels. Each smearing kernel will have a different trajectory to the infinite-volume spectral density, but the limit should be independent of which smearing kernel is used. This idea would allow the NPSR method to be used in conjunction with the HLT method [112, 113], which takes the desired smearing kernel as input and jointly

extrapolates the smeared spectral densities to the infinite-volume limit. One potential difficulty with this idea is that, as mentioned previously, the HLT method only produces a single smeared spectral function consistent with the data; it does not yield a Wertevorrat-like object that specifies where the reconstruction can lie. As a result, it is difficult to quantify the error of the spectral reconstruction due to the nature of the inverse problem. Hence, errors from the extrapolation in the HLT method may undershoot the true error.

4.6 NPSR Method Simulations

The NPSR method (Section 4.5) is tested on simulated data to establish proof-of-concept when the Euclidean correlation function, Eq. (4.9), is known precisely. Even when known exactly, the nature of the inverse problem implies that there is not a unique smeared spectral function $\rho^{\epsilon}_{\pm}(\omega)$ corresponding to the input data, but an entire family of possible solutions. The goal of the simulations is to provide numerical evidence of the claim that the Wertevorrat indeed rigorously bounds the smeared spectral function when the $\mathscr{G}_E(\tau)$ is known precisely.

Simulation data is generated by fixing a ground truth finite-volume spectral function, which extends uniquely to a retarded correlator $G_{\pm}(z)$ by analytic continuation once either a fermionic or bosonic system is specified. Both systems will be considered in each simulation. The spectral density is expanded using its finite-volume decomposition, Eq. (4.23). In the case with extended features, this representation will be on a discrete mesh with mesh size ΔE. The corresponding spectral weights are

$$|A_{0n}|^2 = \int_{E_n}^{E_n+\Delta E} d\omega\, \rho(\omega), \tag{4.117}$$

where E_n are the energies in the mesh. The retarded Green's function $G_{\pm}(z)$ is then computed via Eq. (4.19), and the Euclidean Fourier coefficients $G_E^{(\ell)}$ follow from the evaluation of $G_{\pm}(z)$ at the Matsubara frequencies $i\omega_\ell$. These coefficients, along with the Matsubara frequencies, are then input into the NPSR method.

Simulations were run in four different representative systems: a discrete sum of three poles (Section 4.6.1), a sum of Gaussians (Section 4.6.2), a parameterization of the R-ratio (Section 4.6.3), and an example from a toy theory of interacting scalars [112, 113] (Section 4.6.4). This section concludes by discussing numerical precision in Section 4.6.5.

4.6.1 Simulation 1: Isolated poles

Consider a fermionic spectral density with three poles placed at $\{a\omega_n\} = \{0.2, 0.5, 0.8\}$,

$$\rho(\omega) = \delta(\omega - 0.2) + \delta(\omega - 0.5) + \delta(\omega - 0.8). \tag{4.118}$$

The corresponding Euclidean Green's function is computed at $\beta = 64$ Matsubara frequencies $i\omega_\ell$, both in the fermionic and bosonic cases. Figure 4.8 depicts the reconstructed Wertevorrat and the exact smeared spectral density in both cases for smearing widths $\epsilon \in \{0.06, 0.08, 0.1, 0.12\}$. The upper (lower) panel shows the fermionic (bosonic) reconstruction result. In all cases, the exact smeared spectral density rigorously lies within the Wertevorrat; in the fermionic case, the Wertevorrat is so small that it is difficult to see visually. Observe that as the smearing width is made smaller (as one approaches the real axis from above, in evaluating $G_\pm(\omega + i\epsilon)$), the size of the Wertevorrat increases. This is also seen in the remainder of the numerical simulations (Sections 4.6.2, 4.6.3, and 4.6.4) and is the expected behavior from the discussion surrounding Eq. (4.114).

4.6.2 Simulation 2: Gaussian Peaks

The next considered example tests the NPSR method against extended spectral features. Although finite-volume spectral functions are discrete delta trains, nothing in the formalism of the NPSR method prevents one from considering a continuous spectral density. The spectral density considered is the sum of two Gaussians,

$$\rho(\omega) = \sum_i \frac{1}{\sqrt{2\pi}\sigma_i} \exp\left(-\frac{(\omega - \mu_i)^2}{2\sigma_i^2}\right), \tag{4.119}$$

with $\mu = \{0.25, 0.75\}$ and $\sigma = \{0.1, 0.1\}$. Euclidean Fourier coefficients are generated as discussed at $\beta = 48$ Matsubara frequencies and input to the NPSR algorithm.

Reconstructions from the simulated data are again performed for the fermionic and bosonic methods at smearing widths $\epsilon \in \{0.08, 0.1, 0.12, 0.14\}$. Fermionic (bosonic) reconstructions are shown in the upper (lower) panel of Figure 4.9. The fermionic and bosonic reconstructions are also extrapolated at fixed ω ($a\omega = 0.16$) using a polynomial model to the $\epsilon \downarrow 0$ limit (Eq. (4.116)). The results of this extrapolation are shown in Figure 4.10 with the fermionic extrapolation in orange, the bosonic extrapolation in blue, and the exact value of the unsmeared spectral density at $\omega = 0.16$ denoted with a star. Jointly extrapolating both sets of data to the unsmeared

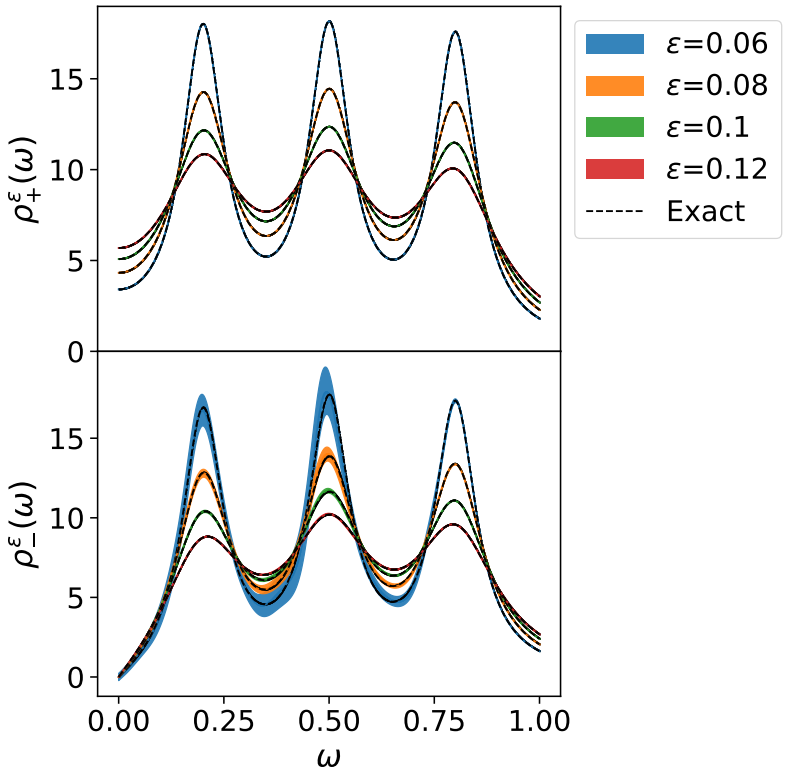

Figure 4.8. Results from the simulated reconstruction of the three-pole spectral density, Eq. (4.118), with $\beta = 64$. The fermionic (bosonic) reconstruction is shown in the upper (lower) panel. The smearing parameter ϵ is varied in $\{0.06, 0.08, 0.1, 0.12\}$ as shown in the legend. In each reconstruction, the exact smeared spectral function (dashed line) lies rigorously within the bound provided by the Wertevorrat. In the top panel, the thickness of the Wertevorrat is comparable to the thickness of the dashed line.

limit helps to reduce the error on the extrapolation.

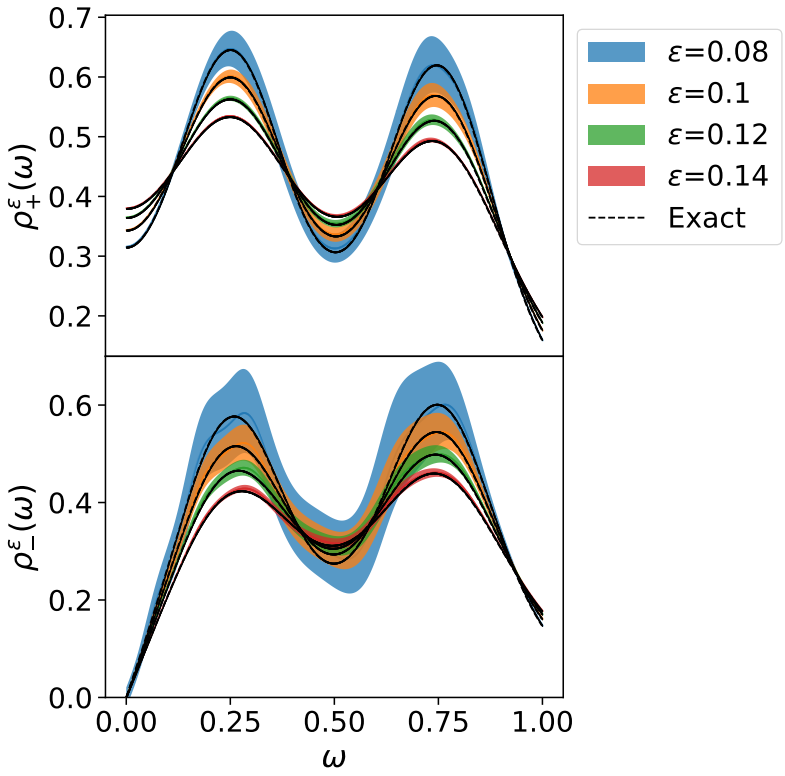

Figure 4.9. Results from the simulated reconstruction of the Gaussian spectral density, Eq. (4.119), with $\beta = 48$. The fermionic (bosonic) reconstruction is shown in the upper (lower) panel. The smearing parameter ϵ is varied in $\{0.08, 0.1, 0.12, 0.14\}$ as shown in the legend. In each reconstruction, the exact smeared spectral function (dashed line) lies rigorously within the bound provided by the Wertevorrat.

4.6.3 Simulation 3: The R-Ratio

A parameterization of the R-ratio data (Figure 4.2) is presented in Ref. [104] in terms of a phase space factor (with a non-trivial branch cut) and a sum of Breit-Wigner curves with parameters chosen to match the data in the PDG's Review of Particle Physics. The formula for $R(s)$ is

$$R(s) = \theta(\sqrt{s} - 2m_\pi)\theta(4.4m_\pi - \sqrt{s})\frac{1}{4}\left[1 - \frac{4m_\pi^2}{s}\right]^{3/2}(0.6473 + f_0(\sqrt{s}))\theta(\sqrt{s} - 4.4m_\pi)$$
$$\times\,\theta(M_3 - \sqrt{s})\left(\sum_{i=1}^{2} f_i(\sqrt{s})\right) + f_3(\sqrt{s}) + 3\left((\tfrac{2}{3})^2 + 2(\tfrac{1}{3})^2\right)\theta(\sqrt{s} - M_3) \tag{4.120}$$

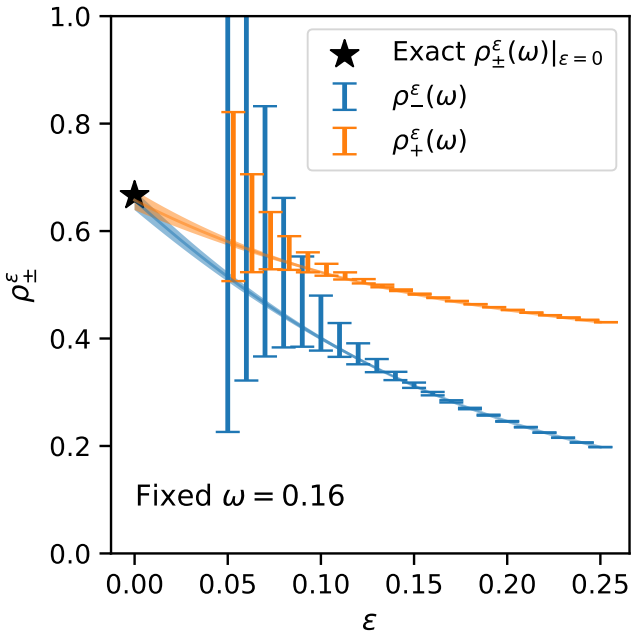

Figure 4.10. Joint extrapolation at fixed $\omega = 0.16$ to the unsmeared $\epsilon \downarrow 0$ limit for the fermionic (orange) and bosonic (blue) reconstructions of the Gaussian spectral density, Eq. (4.119). The curve shows the result of a polynomial fit to the $\epsilon > 0$ data, and the black star denotes the exact value of the unsmeared spectral density at $\omega = 0.16$.

with $f_i(\sqrt{s}) = C_i\Gamma_i^2/\left(4(\sqrt{s}-M_i)^2+\Gamma_i^2\right)$ simulating a resonance centered at M_i with width Γ_i and relative height C_i. Here for $i \in \{0,1,2,3\}$, M_i, Γ_i, C_i are parameters that are determined by fits to experimental data, with explicit values given in Table 1 of Ref. [104].

Numerical data for $G_E^{(\ell)}$ was computed for this spectral density using the methods described above with $\beta = 96$ Euclidean data points. The energy range of the parameterization was rescaled to fit in the unit interval, which places the peak of the $\rho(770)$ resonance at $a\omega \approx 0.25$. This corresponds to a lattice spacing of $a \approx 0.07$ fm, a typical value of a that appears in recent calculations of the anomalous magnetic moment of the muon [151–160].

The reconstructions are shown for several smearing widths ϵ in Figure 4.11, for both fermionic (top panel) and bosonic (bottom panel) reconstructions. The bosonic reconstruction is physical, and the fermionic reconstruction is used as an additional test case, as one can define an exact fermionic system with the R-ratio as its spectral density for positive ω. The peaks from the $\rho(770)/\omega(782)$ and from the $\phi(1020)$ resonances are clearly identifiable in both cases. In all cases, the exact smeared spectral densities lie within the Wertevorrat.

4.6.4 Simulation 4: Toy Model of Interacting Scalars

The final proof-of-concept simulation is a toy model of scalar fields π, ϕ, and K from Refs. [112, 113]. These fields have masses $3m_\pi < 2m_K < m_\phi$ and interact via the Lagrangian

$$\mathcal{L} = \frac{g_\pi}{6}\phi(x)\pi^3(x) + \frac{g_K}{m_\phi}2\phi(x)K^2(x), \tag{4.121}$$

where g_π and g_K are couplings. A correlation function in Ref. [112] was computed with associated finite-volume spectral density,

$$\begin{aligned}\rho_L(E) = &\frac{g_K^2 m_\phi^2}{2(m_\pi L)^3}\sum_{\boldsymbol{p}}\frac{\delta(E-2E_K(\boldsymbol{p}))}{4E_K^2(\boldsymbol{p})} \\ &\frac{g_\pi^2}{48m_\pi^3L^6}\sum_{\boldsymbol{p},\boldsymbol{q}}\frac{\delta(E-E_\pi(\boldsymbol{p})-E_\pi(\boldsymbol{q})-E_\pi(\boldsymbol{p}+\boldsymbol{q})}{E_\pi(\boldsymbol{p})E_\pi(\boldsymbol{q}))E_\pi(\boldsymbol{p}+\boldsymbol{q}))},\end{aligned} \tag{4.122}$$

with $E_\pi^2 = m_\pi^2 + \boldsymbol{p}^2$ (similarly for E_K) and L the number of spatial sites in the lattice. The sum on momenta runs over each finite-volume mode $\boldsymbol{p} = \frac{2\pi}{L}\boldsymbol{n}$ with $\boldsymbol{n} \in \mathbb{N}^3$. In the infinite-volume limit, the discrete poles converge (distributionally) to a continuum spectral density with kinematic factors involving multi-particle branch cuts (i.e., the

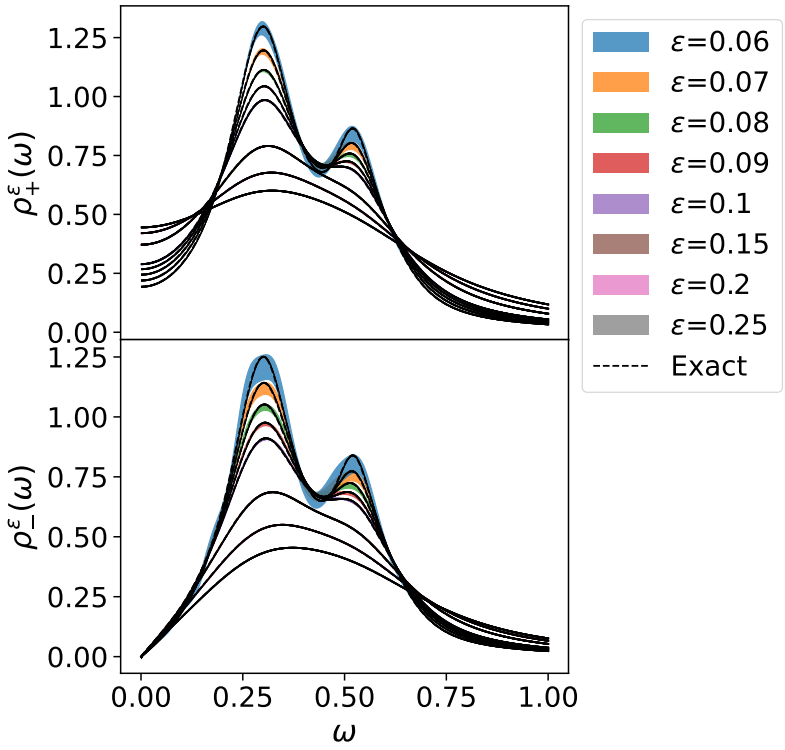

Figure 4.11. Results from the simulated reconstruction of the R-ratio, Eq. (4.119), with $\beta = 96$. The fermionic (bosonic) reconstruction is shown in the upper (lower) panel. The smearing parameter ϵ is varied in $\{0.06, 0.07, 0.08, 0.09, 0.1, 0.15, 0.2, 0.25\}$ as shown in the legend. In each reconstruction, the exact smeared spectral function (dashed line) lies rigorously within the bound provided by the Wertevorrat. The peaks from the $\rho(770)/\omega(782)$ and from the $\phi(1020)$ resonances are clearly identifiable in both the fermionic and the bosonic reconstructions at sufficiently small smearing.

first sum of Eq. (4.122) is proportional to $\sqrt{1-4m_K^2/E^2}\theta(E-2m_K)$). The explicit infinite-volume limit of Eq. (4.122) is given in Refs. [112, 113].

To simulate the theory, the particle masses are chosen to be $m_\pi = 0.066$, $m_K = 3.55m_\pi$, and $m_\phi = 7.3m_\pi$, as in Ref. [112]. The volume is taken to be $L = 64$, and $\beta = 2L$ points are sampled. Three-particle interactions are neglected ($g_\pi = 0$) as they are volume-suppressed, and the coupling g_K is set to unity; the input spectral density is hence the first line $\rho_L(E)$ in Eq. (4.122).

This reconstruction only considers the bosonic case because this is a theory of interacting bosons. The smearing widths are taken to be $\epsilon \in \{0.2, 0.225, 0.25\}$, and the reconstructions are shown in Figure 4.12. The finite-volume energy levels of the system (corresponding to the sum of Eq. (4.122)) are denoted by vertical lines on the plot with height proportional to the corresponding spectral weight. As in all previous examples, the exact smeared spectral function rigorously lies within the Wertevorrat for each smearing width.

4.6.5 An Aside: Numerical Precision

The mathematical identities satisfied by the Nevanlinna coefficients (Eqs. (4.99–4.101) provide insight into the numerical stability of the algorithms. Many spectral function reconstruction methods rely on extended-precision floating point numbers to perform the reconstruction because of the poor condition number of the Laplace kernel, as discussed in Section 4.4. This section uses an example of a spectral reconstruction from two isolated poles at $a\omega \in \{0.05, 0.1\}$,

$$\rho(\omega) = \delta(\omega - 0.05) + \delta(\omega - 0.1), \tag{4.123}$$

to provide further context on why extended-precision floating point arithmetic must be used in the NPSR method.

Recall that the Nevanlinna coefficients $P_N(\zeta), Q_N(\zeta), R_N(\zeta), S_N(\zeta)$ of the theory, Eq. (4.84) satisfy a number of identities. The Nevanlinna determinant identity, $P_N(\zeta)S_N(\zeta) - Q_N(\zeta)R_N(\zeta) = B_N(\zeta)$, Eq. (4.99), relates the determinant of the Nevanlinna coefficient matrix to the Blaschke product $B_N = \prod_{\ell=1}^{N} b_{\zeta_\ell}$, and must be satisfied by the Nevanlinna coefficients. Simulated data is computed from the spectral density at double precision, Eq. (4.123), as described previously in this section, and computed at $\beta = 48$ Euclidean points. The first 20 nonzero Matsubara frequencies and their corresponding Euclidean correlator values are input to the NPSR algorithm, but identical results are obtained if all 48 data points are input to the algorithm.

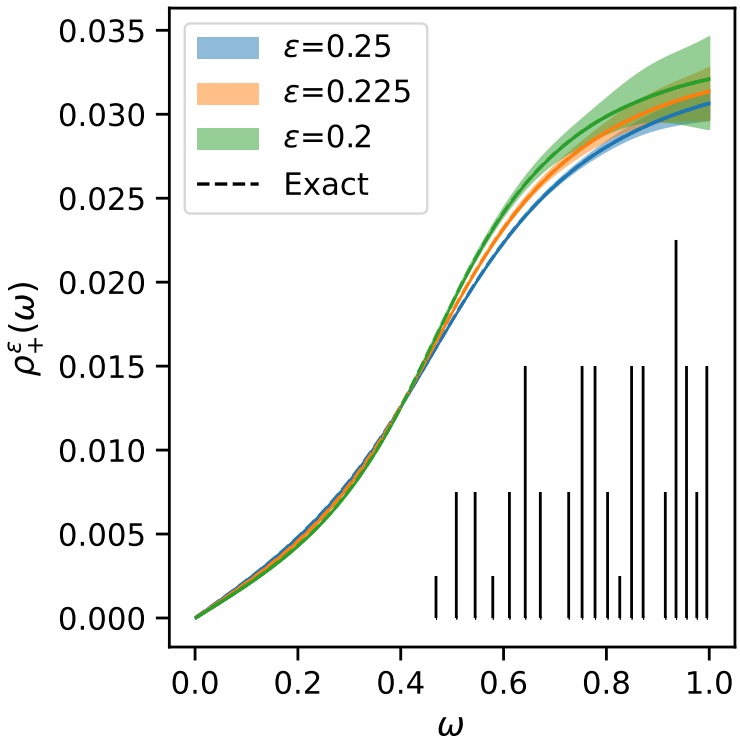

Figure 4.12. Results from the simulated bosonic reconstruction of the scalar toy model spectral density, Eq. (4.122), with $\beta = 96$. The smearing parameter ϵ is varied in $\{0.2, 0.225, 0.25\}$. The finite-volume energy levels of the system are denoted by the vertical black lines, with height proportional to the spectral weight of the corresponding state. In each reconstruction, the exact smeared spectral function (dashed line) lies rigorously within the bound provided by the Wertevorrat.

The resulting Nevanlinna determinant $P_N(\zeta)S_N(\zeta)-Q_N(\zeta)R_N(\zeta)$, computed with the NPSR algorithm using double-precision floats, is shown in Figure 4.13 in red, and the exact value of $B_N(\zeta)$ is denoted by the dashed black line. Both curves are plotted on the contour $\zeta(\omega) = C(\omega + i\epsilon)$ for $\omega \in \mathbb{R}$ and $\epsilon = 0.01$, with $\omega \in [0, 0.2]$. At small ω, the identity is confirmed precisely by the data for the Nevanlinna determinant. However, at large ω, there is a discrepancy, and the Nevanlinna coefficient begins to rapidly fluctuate off its predicted value of $B_N(\zeta(\omega))$.

The rapid fluctuations in the Nevanlinna determinant in Figure 4.13 are numerical artifacts due to truncation error for the floating point numbers used in the computation. This can be confirmed by computing the Nevanlinna determinant for this problem to extended precision. In this case, 128 bits of precision were used, implemented with the GNU MPC library [161]. Identical input data at double precision to the previous case was used for this reconstruction: these double precision inputs were padded with zeros to create extended precision inputs. The results of this computation are shown in Figure 4.14. The rapid fluctuations in the Nevanlinna determinant data are gone, and the curve lies directly on top of its predicted value of $B_N(\zeta(\omega))$.

The result of this experiment indicates that extended precision is needed for the mathematical guarantees of the NPSR method to hold. Despite using identical input data, the double-precision arithmetic used in the reconstruction introduces enough round-off error into the algorithm that the mathematical identity of Eq. (4.99) did not hold. It is important to stress that this error is not due to double-precision input data, as the algorithm was run on identical input data. Although the double-precision data does not equal the analytic value of the correlator at arbitrary precision, the reconstruction with double-precision input is still mathematically a well-posed problem, and the mathematical guarantees of the NPSR method will hold if the Nevanlinna coefficients are computed at sufficiently high precision. This suggests a necessary[12] check to see if the Nevanlinna coefficients have been constructed to high enough precision: namely, anytime a new set of Nevanlinna coefficients are computed, to verify they satisfy Eqs. (4.99, 4.101).

[12]But not sufficient, as there is a chance other mathematical identities or guarantees require higher precision in the calculation.

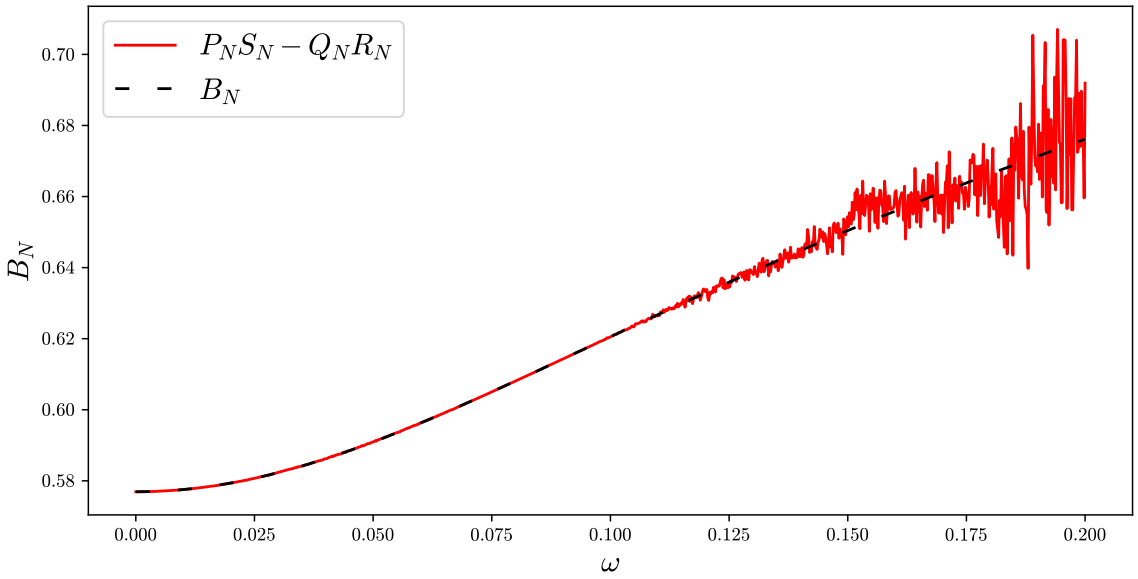

Figure 4.13. Evaluation of the determinant of the Nevanlinna coefficients, $P_N(\zeta)S_N(\zeta) - Q_N(\zeta)R_N(\zeta)$, plotted against the theoretical value of the determinant, $B_N(\zeta)$, on the contour $\{C(\omega + i\epsilon) : \omega \in \mathbb{R}\}$ with $\epsilon = 0.01$. These Nevanlinna coefficients were determined at double precision using simulated data generated from a spectral function $\rho(\omega) = \delta(\omega - m_1) + \delta(\omega - m_2)$ with $am_1 = 0.05$ and $am_2 = 0.1$, using a lattice with temporal extent $\beta = 48$, and the first 20 nonzero Matsubara frequencies as input to the reconstruction algorithm. At large ω ($\omega \gtrsim 0.1$), the computed Nevanlinna determinant deviates from its theoretical value due to round-off error.

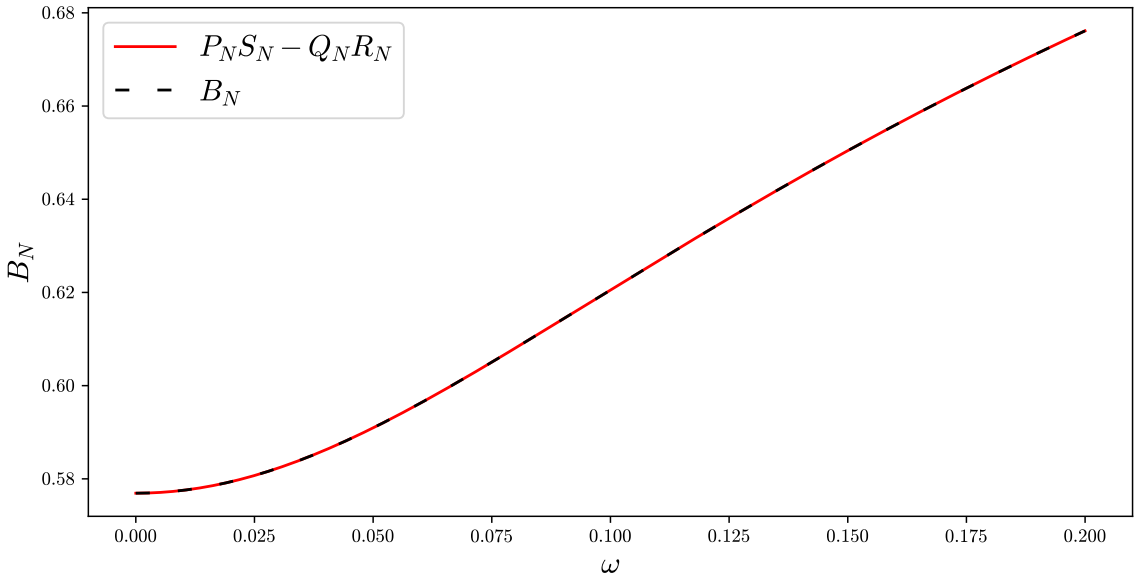

Figure 4.14. Same setup as Fig. 4.13, but for 128-bits of precision. In this case, the Nevanlinna determinant $P_N(\zeta)S_N(\zeta) - Q_N(\zeta)R_N(\zeta)$ agrees with its predicted value of $B_N(\zeta)$. The extra precision is required to verify Eq. (4.99) numerically, and the large deviations at $\omega \gtrsim 0.1$ due to round-off error are no longer observed, as in Figure 4.13.

4.7 Outlook: Monte Carlo Data and The Pick Criterion

As discussed, the simulations performed in this work were done at extended precision with the input data known precisely. For practical use in LGT calculations, the NPSR method must be robust enough to handle uncertainties in the input data that arise from the Monte Carlo calculation. This is an ongoing area of research, the basis of which will be detailed in this section.

4.7.1 The Pick Criterion

Section 4.5 has discussed solving the Nevanlinna problem at length, but this is only half the story. The **Pick problem** asks the following question: given data $\{(\zeta_\ell, w_\ell)\}_{\ell=1}^N \subset \mathbb{D}^2$, when does there exist an interpolating function $f \in \mathscr{S}$? Indeed, not every data set has a valid interpolating solution, illustrated in a simple example from Ref. [136]. Consider the Schwarz Lemma from complex analysis [162].

Lemma 4.7.1 (Schwarz)**.** Let $f \in \mathscr{S}$ s.t. $f(0) = 0$. Then $|f(z)| \leq z$ for each $z \in \mathbb{D}$.

Suppose an interpolant $f \in \mathscr{S}$ solves the Pick problem for $N = 2$ points: $(0, 0)$,

and (ζ_2, w_2). Then the Schwarz Lemma implies that $|w_2| \leq |\zeta_2|$. This constraint on the values of ζ_2 and w_2 shows that not every data set will satisfy the Pick problem, even in the simplest possible case. In a sense, the Schur class $\mathscr{S}$ is extremely well-behaved, so members of $\mathscr{S}$ cannot take on arbitrary values: this is encoded in the constraint $|w_2| \leq |\zeta_2|$ for this specific example.

Georg Pick generalized this idea to the full Pick problem in 1915 [133], where he proved an existence condition for the full problem with an arbitrary number of points $\{(\zeta_\ell, w_\ell)\}_{\ell=1}^N$. The **Pick matrix** is the $N \times N$ matrix defined from the data as

$$\mathcal{P}_{ij} \equiv \frac{1 - w_i w_j^*}{1 - \zeta_i \zeta_j^*} \tag{4.124}$$

Pick proved that there is an interpolating function $f \in \mathscr{S}$ if and only if the Pick matrix is positive semi-definite,

$$\mathcal{P} \geq 0, \tag{4.125}$$

i.e. if $\mathcal{P}$ has only non-negative eigenvalues. Furthermore, there is a unique interpolant if and only if the Pick matrix has a zero eigenvalue, equivalently

$$\det \mathcal{P} = 0. \tag{4.126}$$

The conditions of Eqs. (4.125, 4.126) constitute the **Pick criterion**. Note that the Schur algorithm does not assume the Pick matrix is positive semi-definite. As presented, the algorithm will always construct a valid interpolating function for the data regardless of whether the data satisfies the Pick criterion. The key is that the presented interpolant will only lie in the Schur class $\mathscr{S}$ if the Pick criterion is satisfied by the data. If the Pick criterion is not satisfied, the image of the interpolant will not be contained in $\mathbb{D}$.

For physical problems, it is expected that the Pick criterion always holds, at least if the input data is specified to sufficient precision, because the existence of a retarded Green's function satisfying the constraints of Section 4.2 should always yield a valid interpolating function in the Schur class for the data (once $G_\pm(z)$ is mapped to the correct domain). However, the Pick criterion need not be satisfied for LGT calculations with noisy Monte Carlo data, which was also observed in Refs. [11, 130]. If the data is specified to arbitrary precision, the Pick criterion must be satisfied, but with finite statistical error bars, the data need not satisfy Eq. (4.125). In this case, the mathematical guarantees of the NPSR method need not hold, and the constructed interpolating function may not have the correct codomain. Numerical

examples suggest that the Wertevorrat still provides guidance on where the smeared spectral density lies, even when the data does not satisfy the Pick criterion; however, it is not formally guaranteed.

4.7.2 Reformulations of the Pick Criterion

It is insightful to explore the Pick criterion through different lenses. This section will consider two different perspectives on the Pick criterion: first, through the Wertevorrat, and second, through the interpolation parameters $w_k^{(k-1)}$ of Eq. (4.82).

Recall the Wertevorrat $\Delta_N[w_1, ..., w_n](\zeta)$ defined in Eq. (4.103)[13] is the full space of solutions to the Nevanlinna-Pick problem. The Pick matrix and the Wertevorrat both tell us about the existence of solutions to the problem. Clearly, if (ζ_ℓ, w_ℓ) does not satisfy the Pick criterion, there must exist $\zeta \in \mathbb{D}$ such that $\Delta_N[w_1, ..., w_n](z) = \emptyset$. If the data satisfies the Pick criterion, then $\Delta_N[w_1, ..., w_n]$ is non-empty everywhere and can be computed from the Nevanlinna coefficients defined in Eq. (4.84). If the problem is extremal ($\det \mathcal{P} = 0$), then the Wertevorrat only contains a single point at each $\zeta \in \mathbb{D}$, i.e., $|\Delta[w_1, ..., w_n](\zeta)| = 1$. The correspondence is summarized in Table 4.2.

The second perspective to consider is through the coefficients $w_\ell^{(\ell-1)}$, defined in the Schur algorithm in Eq. (4.82). When a Nevanlinna interpolant exists, it is clear that

$$w_\ell^{(\ell-1)} \in \overline{\mathbb{D}} \tag{4.128}$$

as $w_\ell^{(\ell-1)} = f_{\ell-1}(\zeta_\ell)$ and $f_{\ell-1}$ has image contained in $\overline{\mathbb{D}}$. The converse holds as well.

Lemma 4.7.2. There exists a Nevanlinna interpolant for the interpolation problem with points (ζ_ℓ, w_ℓ) if and only if $w_\ell^{(\ell-1)} \in \overline{\mathbb{D}}$ for each $1 \leq \ell \leq n$.

Proof. The forward direction is immediate from the Nevanlinna theorem: given data that satisfies the Pick criterion, Nevanlinna proved the existence of the interpolant (Eq. (4.80)), which in particular constrains $w_\ell^{(\ell-1)} \in \mathbb{D}$. The backward direction is also straightforward: suppose that $w_\ell^{(\ell-1)} \in \overline{\mathbb{D}}$. Regardless of the assumption that

[13] This section will make the dependence of the Wertevorrat on the input data $\{w_\ell\}$ explicit with the notation $\Delta_N[w_1, ..., w_n](\zeta)$. Note that the Matsubara frequencies $\{\zeta_\ell\}$ are assumed to be fixed, hence Δ_N is only considered a function of the $\{w_\ell\}$. Likewise, the pullback of the Wertevorrat to the $\Omega_\pm$ domain, $\mathcal{D}_N$, is denoted

$$\mathcal{D}_N[G_1, ..., G_n](z) := \mathscr{C}_\pm^{-1}(\Delta_N[\mathscr{C}_\pm(G_1), ..., \mathscr{C}_\pm(G_n)](C(z))). \tag{4.127}$$

$w_\ell^{(\ell-1)} \in \overline{\mathbb{D}}$, the function $f(\zeta) = U_1(\zeta)...U_n(\zeta)f_n(\zeta)$ will always be a valid interpolant of the points $\{(\zeta_\ell, w_\ell)\}$; it remains to show that when $w_\ell^{(\ell-1)} \in \mathbb{D}$, this interpolant maps $\mathbb{D} \to \mathbb{D}$.

To prove this, consider the following claim: if $w_\ell^{(\ell-1)} \in \mathbb{D}$ and $a(\zeta) \in \overline{\mathbb{D}}$, then $U_\ell(\zeta)a(\zeta) \in \overline{\mathbb{D}}$, where $U_\ell(\zeta)a(\zeta)$ denotes the continued fractions matrix multiplication of Eq. (4.71). Note that proving this claim will complete the proof because this fact can inductively be applied, first to $f_k(\zeta) \in \overline{\mathbb{D}}$, then to $U_\ell(\zeta)$ acting on the iterated product $U_{\ell+1}(\zeta)...U_k(\zeta)f_k(\zeta)$, for any $1 \leq \ell < k \leq N$. The proof now proceeds by direct computation:

$$\begin{aligned} |U_\ell(\zeta)a(\zeta)|^2 &= \left| \frac{b_{\zeta_\ell}(\zeta)a(\zeta) + w_\ell^{(\ell-1)}}{\overline{w}_\ell^{(\ell-1)} b_{\zeta_\ell}(\zeta)a(\zeta) + 1} \right|^2 \\ &= \frac{b_{\zeta_\ell}(\zeta)a(\zeta) + w_\ell^{(\ell-1)}}{\overline{w}_\ell^{(\ell-1)} b_{\zeta_\ell}(\zeta)a(\zeta) + 1} \frac{\overline{b_{\zeta_\ell}}(\zeta)\overline{a}(\zeta) + \overline{w}_\ell^{(\ell-1)}}{w_\ell^{(\ell-1)} \overline{b_{\zeta_\ell}}(\zeta)\overline{a}(\zeta) + 1} \\ &= \frac{|b_{\zeta_\ell}(\zeta)a(\zeta)|^2 + 2\mathrm{Re}[\overline{w}_\ell^{(\ell-1)} b_{\zeta_\ell}(\zeta)a(\zeta)] + |w_\ell^{(\ell-1)}|^2}{|w_\ell^{(\ell-1)}|^2 |b_{\zeta_\ell}(\zeta)a(\zeta)|^2 + 2\mathrm{Re}[\overline{w}_\ell^{(\ell-1)} b_{\zeta_\ell}(\zeta)a(\zeta)] + 1} \end{aligned} \tag{4.129}$$

This is ≤ 1 iff the numerator is less than the denominator: in other words, iff

$$\begin{aligned} & |b_{\zeta_\ell}(\zeta)a(\zeta)|^2 + |w_\ell^{(\ell-1)}|^2 \leq |w_\ell^{(\ell-1)}|^2 |b_{\zeta_\ell}(\zeta)a(\zeta)|^2 + 1 \\ \iff & |w_\ell^{(\ell-1)}|^2 (1 - |b_{\zeta_\ell}(\zeta)a(\zeta)|^2) \leq 1 - |b_{\zeta_\ell}(\zeta)a(\zeta)|^2 \\ \iff & |w_\ell^{(\ell-1)}|^2 \leq 1. \end{aligned} \tag{4.130}$$

We have now reduced this to the assertion that $w_\ell^{(\ell-1)} \in \overline{\mathbb{D}}$: this proves the claim and completes the proof of the theorem. □

Lemma 4.7.2 and the Nevanlinna theorem now imply three equivalent ways to reformulate the Pick criterion. This correspondence is also explicitly summarized in Table 4.2.

Theorem 4.7.3. Let $(w_\ell) \in \mathbb{D}^n$. The following are equivalent:

1. (w_ℓ) satisfies the Pick criterion, i.e. the Pick matrix $\mathcal{P}$ is positive semi-definite.
2. The Wertevorrat $\Delta_N[w_1, ..., w_N](\zeta)$ is non-empty for each $\zeta \in \mathbb{D}$.
3. The $w_\ell^{(\ell-1)}$ defined recursively in the construction of the Nevanlinna interpolant, Eq. (4.82), satisfy
$$w_\ell^{(\ell-1)} \in \overline{\mathbb{D}}. \tag{4.131}$$

Nevanlinna-Pick Solution?	$\det \mathcal{P}$	$\Delta_N(\zeta)$	$w_k^{(k-1)}$
No solution	$\det \mathcal{P} < 0$	$\exists \zeta \in \mathbb{D}$ s.t. $\Delta(\zeta) = \emptyset$	$\exists k$ s.t. $w_k^{(k-1)} \notin \overline{\mathbb{D}}$
Unique solution	$\det \mathcal{P} = 0$	$\lvert\Delta(\zeta)\rvert = 1$	$\exists k$ s.t. $w_k^{(k-1)} \in \partial\mathbb{D}$
Infinite solutions	$\det \mathcal{P} > 0$	$\lvert\Delta(\zeta)\rvert = \infty$	$\forall k$, $w_k^{(k-1)} \in \mathbb{D}^o$

Table 4.2. Correspondence between the Pick criterion, the Wertevorrat, and the $w_k^{(k-1)}$ parameters. Note that the dependence of the Wertevorrat on the input interpolation points has been suppressed, i.e., $\Delta_N(z)$ represents $\Delta_N[w_1, ..., w_k](z)$ for some fixed $w_1, ..., w_k \in \mathbb{D}$.

4.7.3 Monte Carlo Data and the Pick Space

To solve the Nevanlinna-Pick problem in the presence of numerical noise, it is crucial to understand the space of valid inputs to the Nevanlinna-Pick theorem. In the NPSR reconstruction problem, the Cayley-transformed Matsubara frequencies (ζ_ℓ) are fixed, and the reconstruction takes the transformed correlator data (w_ℓ) as input. Each possible input to the problem is a vector $(w_\ell) \in \mathbb{D}^n$, and the space of inputs that are compatible with the Pick criterion is defined as

$$\mathbb{P} := \{(w_k) \in \mathbb{D}^n : \mathcal{P}[w_1, ..., w_n] \geq 0\}. \tag{4.132}$$

In other words, $\mathbb{P}$ is the set of input transformed correlator data that satisfies the Pick criterion and can be viewed as a subset $\mathbb{P} \subseteq \mathbb{D}^n$. The space $\mathbb{P}$ is called the **Pick space** in $\mathbb{D}^n$.

The general approach to inputting Monte Carlo data to the NPSR method will be to "project" the Monte Carlo data onto the Pick space. The sample mean of the Euclidean Fourier coefficients $(\overline{w}_\ell)$ will typically not lie in the Pick space, as it is not required to because of the statistical fluctuation. However, in the infinite-statistics limit $(\overline{w}_\ell)$ should approach $\mathbb{P}$. Rather, $(\overline{\omega}_\ell)$ will be an element of $\mathbb{D}^n \setminus \mathbb{P}$. Using the NPSR method with this Monte Carlo data first requires valid input to the method: the best input is the projection $(\overline{w}'_\ell)$ of $(\overline{w}_\ell)$ onto $\mathbb{P}$,

$$(\overline{w}'_\ell) \equiv \text{proj}_{\mathbb{P}}(\overline{w}_\ell) \in \mathbb{P}. \tag{4.133}$$

The projected data $(\overline{w}'_\ell)$ can then be input to the NPSR algorithm. Defining the projection operator $\text{proj}_{\mathbb{P}} : \mathbb{D}^n \to \mathbb{P}$ is the difficult part of the problem: one may

abstractly write down $\text{proj}_{\mathbb{P}}$ as the L^2 projection,

$$\text{proj}_{\mathbb{P}}(\overline{w}_\ell) \equiv \min_{(\overline{w}'_\ell)\in\mathbb{P}} ||(\overline{w}_\ell) - (\overline{w}'_\ell)||_2^2, \tag{4.134}$$

but without a numerical understanding of the Pick space, the projection is impossible to implement.

Current ideas on defining the projection operator rely on convex optimization to search the Pick space for the element with minimal L^2 norm to the data. Fortunately, the Pick space $\mathbb{P}$ is convex due to the convexity of the underlying space $\mathbb{D}^n$. To prove this, let $(w_\ell), (v_\ell) \in \mathbb{P}$, and $t \in [0, 1]$. One must show that the convex combination $(tw_\ell + (1-t)v_\ell) \in \mathbb{P}$. Note that this implies that there exist Nevanlinna interpolants $f, g : \mathbb{D} \to \mathbb{D}$ such that

$$f(\zeta_\ell) = w_\ell \qquad\qquad g(\zeta_\ell) = v_\ell. \tag{4.135}$$

Because $\mathbb{D}$ is convex, note that the function

$$h(\zeta) := tf(\zeta) + (1-t)g(\zeta) \tag{4.136}$$

maps $\mathbb{D} \to \mathbb{D}$. In particular, h is a Nevanlinna interpolant of $(tw_\ell + (1-t)v_\ell)$:

$$h(\zeta_k) = tf(\zeta_\ell) + (1-t)g(\zeta_\ell) = tw_\ell + (1-t)v_\ell. \tag{4.137}$$

This implies that $(tw_\ell + (1-t)v_\ell) \in \mathbb{P}$, which completes the proof.

For numerical implementation, a specific projection operator $\text{proj}_{\mathbb{P}}$ to the Pick space must be defined. This is the crux of the difficulty of handling Monte Carlo data; the Pick space is non-parametric, so defining such an operator is a difficult problem. Research is ongoing into defining such an operator, which will allow the NPSR method to be extended to handle noisy Monte Carlo data.

4.8 Conclusion

This chapter has presented a novel method for spectral density reconstruction in LGT. Reconstructing a finite-volume spectral density from a Euclidean correlator is an ill-posed inverse problem: given (infinitely precise) data for the Euclidean correlation function at the Matsubara frequencies, there are an infinite number of spectral functions that are consistent with the Euclidean correlator. Spectral reconstruction

methods in LGT typically focus on reconstructing the smeared finite-volume spectral density. This problem is still ill-posed but numerically much easier than naïvely attempting to reconstruct the full spectral function.

Spectral density reconstruction has many mathematical difficulties, but it is an extremely useful tool worth understanding. Typical spectroscopic methods in LGT only allow for the extraction of the low-lying spectrum of a theory and assume a parametric dependence of the correlation function on the energy levels of the theory (i.e., Eq. (3.41)). Spectral reconstruction techniques instead are non-parametric methods to extract the LGT spectrum which aim to reconstruct the full spectrum. Computation of the spectrum from *ab initio* QFT is desirable (even required in many cases) input for many theoretical and experimental research programs, as the full spectrum encodes all information about the bound states, resonances, and thresholds for a given process.

The R-ratio (Section 4.1) reveals the hadronic structure of QCD (c.f., Figure 4.2) and is a necessary ingredient to understand the anomalous magnetic moment of the muon from first principles [103]. A first-principles calculation of the R-ratio with LGT requires reconstructing a spectral density from the two-point correlator of the electromagnetic current, Eq. (4.2). A computation of the smeared R-ratio has been presented in Ref. [163], using the HLT method with a Gaussian smearing kernel of various widths. The computation is in mild tension with experimental results for the smeared R-ratio [164] but is still remarkable given the difficulties of spectral function reconstruction on the lattice. The tension between the theoretical LGT results and the experimental results is likely due to the ill-posed nature of the inverse problem (Section 4.4.2).

The systematic error that results from the ill-posed inverse problem has not been precisely quantifiable until now with the development of the Nevanlinna-Pick Spectral Reconstruction method (Section 4.5). The NPSR method provides a unique tool to analytically constrain the values the resulting smeared spectral density can take, as it is the only method that allows for accurate computation of the systemic errors in the ill-posed problem (the Wertevorrat). We hope to apply the NPSR method to reconstruct the R-ratio reconstruction in the future, both to augment the existing calculation of Ref. [163] (see Section 4.5.7 for ideas about "triangulating" the resulting spectral density in the infinite-volume limit) and to demonstrate the use the Wertevorrat has in constraining the systematic error of the spectral reconstruction.

The NPSR method has been developed and simulated (Section 4.6) without Monte Carlo noise. For applications to LGT, the technique must robustly handle Monte

Carlo error on the input Euclidean correlation function. We are developing an algorithm to apply the NPSR method to noisy Monte Carlo data. Once these algorithms are mature, we plan to calculate the smeared R-ratio from first principles. The main hurdle in such a calculation is the Pick criterion (Section 4.7), which encodes the analytic structure of the thermal Green's function. Any physical correlator must satisfy the Pick criterion, and the NPSR method assumes an input correlator that satisfies this criterion. However, noisy Monte Carlo data need not fulfill the Pick criterion. Understanding the interplay of the Pick criterion with the analytic structure of LGT correlators may lead to future techniques for denoising correlators because physical correlation functions must reside in the Pick space (Eq. (4.132)).

The smeared R-ratio is the first target for many spectral reconstruction methods because the R-ratio has been experimentally measured to high precision. Inclusive e^+e^- scattering is a rich sandbox that can be used to test theoretical predictions by verifying they match experimental data. The long-term goal of spectral reconstruction is to theoretically compute spectral densities that cannot be experimentally measured to the requisite precision. One such spectral density is the axial structure function of the nucleon, $F_A(q^2)$ [165]. This form factor is necessary input for neutrino oscillation experiments like the Deep Underground Neutrino Experiment (DUNE) [166], which seeks to understand the nature of the neutrino. DUNE, and other long-baseline neutrino experiments [167], have backgrounds that require $F_A(q^2)$ to be known at the percent-level to meet the precision goals of the experiment [168]. The axial structure function is poorly constrained from experimental data [169]; hence, theoretical methods must be used to extract $F_A(q^2)$ in the absence of new neutrino scattering experiments.

Lattice gauge theory is the natural candidate for such a calculation because it is systematically improvable; such a calculation can be performed as a reconstruction of spectral density from the Euclidean correlator $\langle N(x) j_5^\mu(y) \overline{N}(y) \rangle$, where N is the nucleon interpolator and j_5 is the axial current. The form factor $G_A(q^2)$ has been computed with LGT [170, 171] by fitting correlation functions to a z-expansion, but LGT results are in tension with results from experimental data [172]. These LGT techniques must be further developed to produce reliable extractions of spectral densities and form factors, especially to meet the precision goals of DUNE and other neutrino experiments. The NPSR method provides a significant step toward this goal by increasing understanding of the nature of the spectral reconstruction problem in LGT and providing a new algorithm for spectral reconstruction.

Chapter 5

Neutrinoless Double β Decay from Lattice QCD

This chapter will summarize the general theory of $0\nu\beta\beta$ decay and the LGT computation of inputs for $0\nu\beta\beta$ decay. A classification of $0\nu\beta\beta$ decay mechanisms into long- and short-distance mechanisms will be outlined in Section 5.2. The remaining sections will detail the LGT $0\nu\beta\beta$ decay calculations that I was involved in during my Ph.D., culminating in two papers, Refs. [2, 5], with a third paper expected to be completed soon.

Our LGT calculations of $0\nu\beta\beta$ decay considered two systems: the unphysical $\pi^- \to \pi^+ e^- e^-$ transition, and the decay $n^0 n^0 \to p^+ p^+ e^- e^-$. Only the short-distance contribution for the $\pi^- \to \pi^+ e^- e^-$ transition is considered (Section 5.3), as the long-distance $\pi^- \to \pi^+ e^- e^-$ matrix elements have been computed in LGT in Refs. [12, 173]. Our calculation [2] was the second LGT calculation of these matrix elements and found different results than the first calculation by the CalLat collaboration [174]; differences between the results and the methodology of the two calculations will be considered in Section 5.3. Both the long- and short-distance contributions to the $n^0 n^0 \to p^+ p^+$ decay are computed (Sections 5.4, 5.6) on a single gauge field ensemble. These are the first computations of $0\nu\beta\beta$ decay in a nuclear system, and they provide proof-of-principle of the calculation methodology. Finally, operator renormalization for the short-distance operators will be discussed in Section 5.5.

David Murphy began this research program at MIT shortly before I arrived in 2019 and, along with Will Detmold, performed the initial calculation of the long-distance $\pi^- \to \pi^+ e^- e^-$ transition [12]. David initially led the calculation of the short-distance $\pi^- \to \pi^+ e^- e^-$ transition (Section 5.3), and I became involved with the project through the renormalization of the short-distance operators (Section 5.5). David left the project after the two- and three-point functions were computed (Eqs. (5.19

and 5.20), and I inherited and finished the remainder of the calculation. The calculations of $0\nu\beta\beta$ decay in the $n^0n^0 \to p^+p^+e^-e^-$ system were led by Anthony Grebe in an extremely impressive computational effort. The long-distance $n^0n^0 \to p^+p^+e^-e^-$ section in this thesis is primarily added for additional context: I was involved in the calculation through discussions and performing cross-checks for the EFT matching but did not contribute to the numerical calculation. For the short-distance $n^0n^0 \to p^+p^+e^-e^-$ project, I identified and Fierzed the vector operator basis and performed the non-perturbative renormalization of the scalar and vector operators, in addition to performing some numerical cross-checks on the fits to the bare matrix elements.

5.1 Neutrinoless Double β Decay

$0\nu\beta\beta$ decay is the hypothetical decay inside a nucleus of two neutrons n^0 into two protons p^+ and two electrons e^-,

$$n^0n^0 \to p^+p^+e^-e^-. \tag{5.1}$$

At the quark level, the decay is induced by the decay of two down quarks into two up quarks and two electrons, $dd \to uuee$. This process is depicted in Figure 5.1 at the hadronic level, with the quark-level process colored in blue.

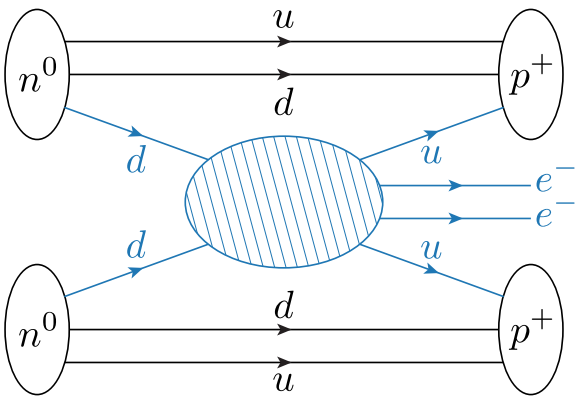

Figure 5.1. Diagram depicting nuclear $0\nu\beta\beta$ decay ($n^0n^0 \to p^+p^+e^-e^-$). The solid lines denote fermions, and the hatched circle denotes the quark-level process that induces $0\nu\beta\beta$ decay. The quark-level process mediating the decay, $dd \to uuee$, is depicted in blue.

There are a variety of different BSM mechanisms that may induce $0\nu\beta\beta$ decay. The best-understood mechanism is light Majorana neutrino exchange, depicted in Figure 5.2. This is very similar to the neutrinoful double β ($2\nu\beta\beta$) diagram, the rarest Standard Model process, except that the neutrinos annihilate one another because they are Majorana fermions and thus their own particles. Such a transition is induced by the dimension-5 Weinberg operator $\epsilon^{ij}(\epsilon_{ab}\ell_i^a H^b)(\epsilon_{cd}\ell_j^c H^d)$[1], Eq. (2.36), which violates lepton number by two units. Any mechanism induced by light Majorana neutrino exchange is called a long-distance mechanism. The different classes of mechanisms for $0\nu\beta\beta$ decay will be discussed further in Section 5.2.

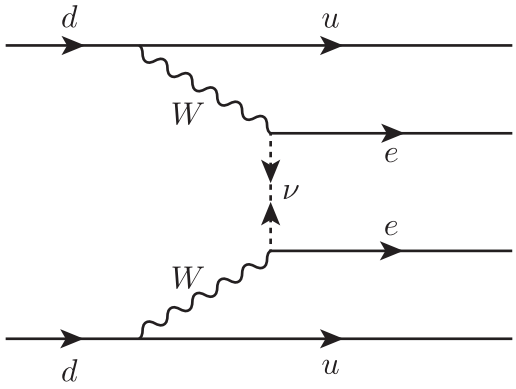

Figure 5.2. Example $0\nu\beta\beta$ decay induced through light Majorana neutrino exchange. Long-distance decays are mediated by a light Majorana neutrino ν, denoted with a dashed line.

Depending on the specifics of the observed $0\nu\beta\beta$ decay, it may also yield insights into the neutrino mass hierarchy (Section 2.3.2). The **effective Majorana neutrino mass** $m_{\beta\beta}$ is defined as

$$m_{\beta\beta} = \sum_k |U_{ek}|^2 m_k. \tag{5.2}$$

where U is the PMNS matrix (Eq. (2.37)) and m_k are the neutrino masses. The effective Majorana neutrino mass appears in the diagram of Figure 5.2 from the annihilation of the massive Majorana neutrino. Constraints on the neutrino mass-squared differences allow one to put constraints on the region of parameter space for which $0\nu\beta\beta$ decay may be observed, in terms of $m_{\beta\beta}$ and the lightest neutrino mass, m_{lightest}. Note that Eq. (2.38) implies that $m_{\text{lightest}} = m_1$ for the normal hierarchy and m_3 for the inverted hierarchy.

Either hierarchy can be used to produce an exclusion plot for the detection of $0\nu\beta\beta$ decay in $(m_{\text{lightest}}, m_{\beta\beta})$ space, which is depicted in Figure 5.4 [175]. The two hierarchies exclude very similar regions of parameter space for values of $m_{\text{lightest}} \gtrsim 0.01$ eV. If m_{lightest} lies in this region, then the discovery of $0\nu\beta\beta$ decay will not be able to distinguish between the normal hierarchy and the inverted hierarchy. However,

[1]Note that the Higgs takes on its vev v the energy scale of $0\nu\beta\beta$ decay, with the two factors of the Higgs vev being absorbed into the Majorana mass of the neutrino.

if $m_{\text{lightest}} \lesssim 0.01\,\text{eV}$, then the observation of $0\nu\beta\beta$ decay and measurement of these parameters can be used to determine the mass hierarchy of the three Standard Model neutrinos.

The existence of a Majorana mass term for the Standard Model neutrino implies $0\nu\beta\beta$ decay through the diagram of Figure 5.2. This statement may be made stronger, into an if and only if: any $0\nu\beta\beta$ decay mechanism will induce a Majorana mass for the neutrino, regardless of how exotic the underlying physics behind the decay is. This is the **Schechter-Valle Black-Box Theorem** [176]. The existence of $0\nu\beta\beta$ decay allows one to draw the diagram in Figure 5.3, which generates a Majorana mass for the neutrino. It does not matter how $0\nu\beta\beta$ decay is induced or the underlying mechanism, only that the decay is possible. In this sense, the decay is a "black box": the box's contents do not matter, only that the box exists and induces $0\nu\beta\beta$ decay.

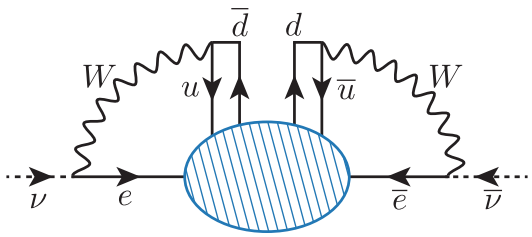

Figure 5.3. The Schechter-Valle diagram. The blue hatched circle denotes $0\nu\beta\beta$ decay (the "black box") and radiatively generates a Majorana mass for the neutrino.

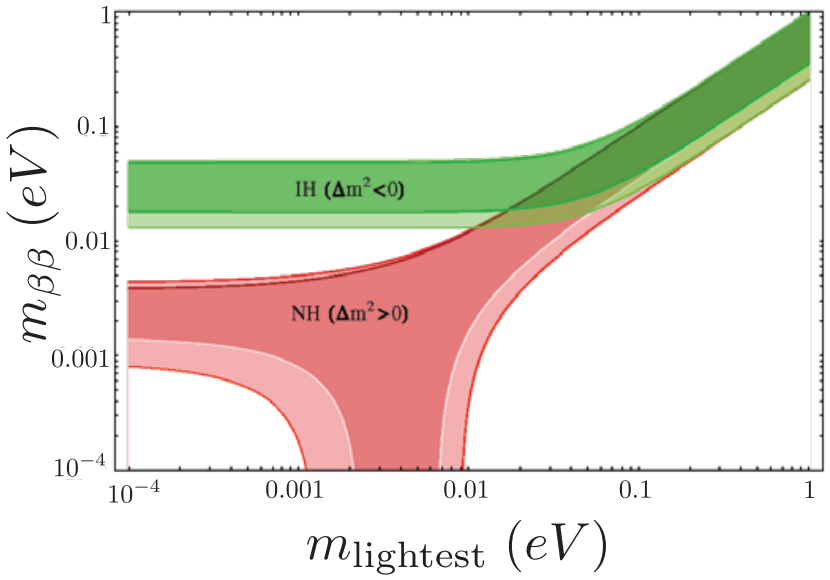

Figure 5.4. Regions of parameter space $(m_{\text{lightest}}, m_{\beta\beta})$ where $0\nu\beta\beta$ decay is kinematically possible if the neutrino masses follow a normal hierarchy (red) or an inverted hierarchy (green). This figure and its $0\nu\beta\beta$ decay bounds are sourced from Ref. [175].

5.2 Matrix Elements for $0\nu\beta\beta$ Decay

Mechanisms that induce $0\nu\beta\beta$ decay can be split into two broad classes [177]. As discussed in Section 5.1, the first class is called **long-distance mechanisms**, in which $0\nu\beta\beta$ decay is induced by a non-local interaction mediated by a light particle of mass much less than the hadronic scale [178, 179]. The standard example of this mechanism is light Majorana neutrino exchange, shown in Figure 5.2 (although other scenarios have been considered [180–183]) and discussed in Section 5.1.

The other mechanism class that may induce $0\nu\beta\beta$ decay is a **short-distance mechanism**, which is mediated by heavy BSM physics [184]. An exotic example of this is the supersymmetric exchange of two squarks and a gluino in R-parity-violating supersymmetry (RPV SUSY) [185–188], depicted in Figure 5.5. Here, the gluino $\tilde{g}$ is a heavy supersymmetric particle and can be integrated out of the theory at the $0\nu\beta\beta$ decay scale. Bounds on $0\nu\beta\beta$ decay can be used to impose bounds on the Wilson coefficients of RPV SUSY. Wilson coefficients are the couplings for effective operators in EFT which determine the strength of the corresponding effective interaction.

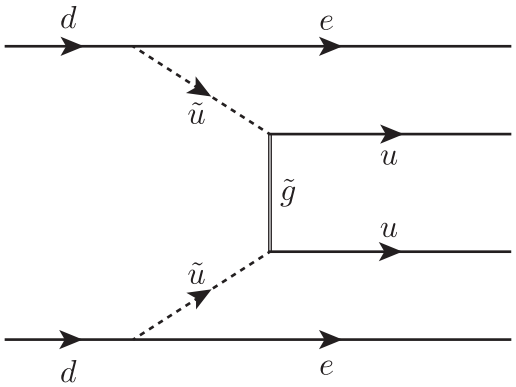

Figure 5.5. Example short-distance $0\nu\beta\beta$ decay. Short-distance decays are mediated by heavy BSM physics. In this case, this comes in the form of two heavy squarks $\tilde{u}$ (denoted by dashed lines) and one heavy gluino $\tilde{g}$ (denoted by a double line) in this example in RPV SUSY.

5.2.1 Long-Distance Mechanisms

At the energy scale of the decay, the W bosons in Figure 5.2 can be integrated out, and the theory can be matched to a four-Fermi effective theory [189, 190]. In the four-

Fermi theory, the decay is mediated by two insertions of the electroweak Hamiltonian,

$$\mathcal{H}_W = 2\sqrt{2} G_F V_{\text{CKM}}^{ud} \left(\overline{e}\gamma^\mu P_L \nu_e\right) j_\mu, \qquad\qquad j_\mu = \overline{u}\gamma_\mu P_L d. \tag{5.3}$$

Here $G_F = 1.16 \times 10^{-5}$ GeV^{-2} is the Fermi coupling constant, V_{CKM} is the CKM matrix (Eq. (2.15)), and j_μ is the electroweak charge current. The resulting diagram from matching to the four-Fermi theory is depicted in Figure 5.6a, with the electroweak Hamiltonian insertion denoted by the green crossed circle. The lowest-order contribution to the amplitude in Figure 5.6a between an initial hadronic state $|i\rangle$ and a final state $|fee\rangle$ (here $|f\rangle$ is the hadronic final state) is the second-order matrix element [191],

$$\begin{aligned} \langle f|S^{(2)}|i\rangle &\equiv \int d^4x\, d^4y\, \langle f|T\{\mathcal{H}_W(x)\mathcal{H}_W(y)\}|i\rangle \\ &= -4m_{\beta\beta} G_F^2 V_{ud}^2 \mathcal{N}_{e_1}\mathcal{N}_{e_2} \int d^4x\, d^4y\, H_{\alpha\beta}(x,y) L^{\alpha\beta}(x,y), \end{aligned} \tag{5.4}$$

where $S^{(2)}$ is the S matrix at second order in perturbation theory and $\mathcal{N}_{e_i}$ is the normalization of the outgoing electron states, which are put at rest for computational simplicity. This factors into the convolution of a leptonic tensor $L_{\alpha\beta}$ with a hadronic tensor $H_{\alpha\beta}(x,y)$,

$$L_{\alpha\beta}(x,y) \equiv \Gamma_{\alpha\beta} S_\phi(x,y) \qquad\qquad H_{\alpha\beta}(x,y) \equiv \langle N_f|T\{j_\alpha(x) j_\beta(y)\}|N_i\rangle. \tag{5.5}$$

Here $|N_i\rangle$ and $|N_f\rangle$ are the initial and final hadronic states with momenta p_i and p_f, respectively. The leptonic tensor $L_{\alpha\beta}$ is comprised of a massless scalar propagator $S_\phi(x,y)$ and a spinor $\Gamma_{\alpha\beta} \equiv \overline{u}_1(p_1)\gamma_\alpha\gamma_\beta(1+\gamma_5)u_2^C(p_2)$, where $u_1(p_1)$, $u_2(p_2)$ are the Dirac spinors corresponding to the outgoing electrons, and $u(p)^C = C\,\overline{u}^T(p)$ is the charge-conjugated electron spinor, with charge conjugation operator $C = -i\gamma_0\gamma_2$ (Eq. (C.7)). Note that the momenta of the two electrons, p_1 and p_2, have vanishing spatial components, $\boldsymbol{p}_1 = \boldsymbol{p}_2 = \boldsymbol{0}$. The propagator S_ϕ arises from the neutrino propagator,

$$\frac{\not{q} + m_{\beta\beta}}{q^2 + m_{\beta\beta}} = \frac{\cancel{\not{q}}}{\cancel{q^2 + m_{\beta\beta}}} + \frac{m_{\beta\beta}}{q^2 + m_{\beta\beta}} \longrightarrow \frac{m_{\beta\beta}}{q^2} \tag{5.6}$$

because the term proportional to $\not{q}$ has the wrong chirality to contribute to the decay, and in the remaining term, the neutrino mass $m_{\beta\beta} \ll \sqrt{q^2}$. The hadronic tensor $H_{\alpha\beta}(x,y)$ is inherently non-perturbative, and its convolution with $L_{\alpha\beta}$ can be computed within the context of LGT to yield the long-distance $0\nu\beta\beta$ decay amplitude

between given initial and final hadronic states $|N_i\rangle$ and $|N_f\rangle$.

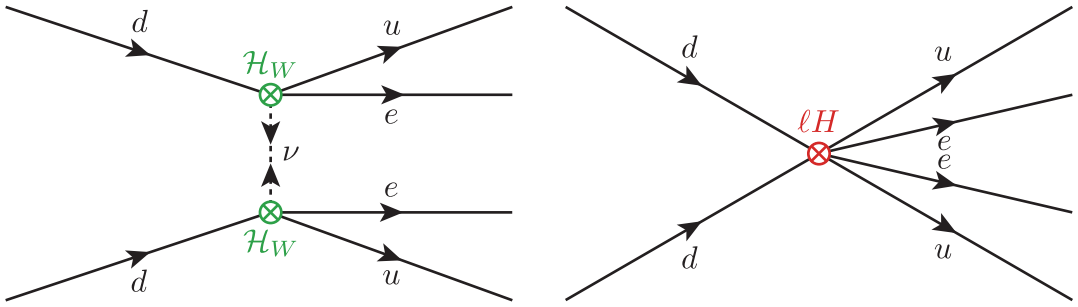

(a) Four-Fermi theory for long-distance decay. **(b)** SMEFT for short-distance decay.

Figure 5.6. EFT treatment of the two classes of $0\nu\beta\beta$ decay. In the long-distance case (Figure 5.6a), the W boson is integrated out and the decay is matched onto the four-Fermi EFT, where the decay $d \to ue\nu$ is mediated by an insertion of the electroweak Hamiltonian $\mathcal{H}_W$, denoted in green. The heavy BSM physics is integrated out of the theory in the short-distance case (Figure 5.6b). The short-distance contribution is matched onto the SMEFT where the decay $dd \to uuee$ is mediated by a product of leptonic contact operators ℓ and four-quark contact operators H, denoted in red, regardless of the physics inducing the decay at the microscopic level.

One can rewrite Eq. (5.4) as [5]

$$\langle f|S^{(2)}|i\rangle = i(2\pi)^4\delta^4(p_f - p_i + p_1 + p_2)\,\mathcal{M}^{i\to f}, \tag{5.7}$$

with

$$\mathcal{M}^{i\to f} = 4G_F^2 V_{ud}^2 m_{\beta\beta}\mathcal{N}_{e_1}\mathcal{N}_{e_2}\sum_n \left.\frac{\Gamma^{\mu\nu}\left(\langle N_f|j_\mu(0)|n\rangle\langle n|j_\nu(0)|N_i\rangle + \mu\leftrightarrow\nu\right)}{4\tilde{E}_n|\boldsymbol{q}|(|\boldsymbol{q}| + \tilde{E}_n - E_i + m_e)}\right|_{\boldsymbol{q}=\boldsymbol{p}_i-\tilde{\boldsymbol{p}}_n}. \tag{5.8}$$

It is useful to normalize the matrix element $\mathcal{M}^{i\to f}$ by stripping off the prefactors in Eq. (5.8). Defining the amplitude $\mathcal{A}^{i\to f}$ as

$$\mathcal{A}^{i\to f} \equiv \frac{\mathcal{M}^{i\to f}}{4G_F^2 V_{ud}^2 m_{\beta\beta}\mathcal{N}_{e_1}\mathcal{N}_{e_2}}, \tag{5.9}$$

this amplitude simplifies to,

$$\mathcal{A}^{i\to f} = \sum_n \frac{\langle N_f|j_\mu(0)|n\rangle\langle n|j^\mu(0)|N_i\rangle}{2\tilde{E}_n|\boldsymbol{q}|(|\boldsymbol{q}|+\tilde{E}_n-E_i+m_e)}\bigg|_{\boldsymbol{q}=\boldsymbol{p}_i-\tilde{\boldsymbol{p}}_n} . \tag{5.10}$$

The quantity $\mathcal{A}^{i\to f}$ is the subject of the LGT calculation in Ref. [5]; it contains all the non-perturbative physics in the long-distance decay, and its calculation in LGT is described in Section 5.6.

5.2.2 Short-Distance Mechanisms

For an arbitrary short-distance mechanism, the heavy mediating particle can be integrated out in Standard Model EFT (SMEFT) to generate contact interactions [184]. In the SMEFT framework, the Standard Model enters as the renormalizable sector of a non-renormalizable theory [192]. Potential short-distance contributions to $0\nu\beta\beta$ decay are induced by physics at the scale $\Lambda_{\rm LNV} \gtrsim v$, where $v = 247$ GeV is the electroweak scale set by the Higgs vacuum expectation value, and described in the SMEFT by operators with mass dimension greater than 4. Any SMEFT operator contributing to $0\nu\beta\beta$ decay must induce the process $dd \to uuee$ at the quark level. Every such operator must therefore contain at least six fermion fields, and so have mass dimension $d \geq 9$, with contributions to the $\pi^- \to \pi^+ e^- e^-$ decay power-suppressed by a factor of $\Lambda_{\rm LNV}^{d-4}$. The dimension-9 lepton-number violating operators thus contribute to the decay at leading-order (LO) in inverse powers of $\Lambda_{\rm LNV}$.

There are fourteen $SU(3)_c \times U(1)_{\rm EM}$-invariant dimension-9 SMEFT operators which violate lepton number and may contribute to the decays $\pi^- \to \pi^+ e^- e^-$ and $n^0 n^0 \to p^+ p^+ e^- e^-$; they can be factorized into a 4-quark operator multiplying a leptonic operator. Of these operators, four have corresponding 4-quark operators that transform as Lorentz 4-vectors and therefore match to the chiral EFT (χEFT) operator $\pi(\partial^\mu\pi)\bar{e}\gamma_\mu\gamma_5 e^{\rm c} + \text{h.c.}$, where the superscript c denotes charge conjugation and π and e represent the pion and electron fields. Integration by parts shows that pionic matrix elements of this operator are proportional to one power of the electron mass and give sub-leading contributions to the decay $\pi^- \to \pi^+ e^- e^-$. However, they are not necessarily suppressed in $0\nu\beta\beta$ decays of nuclear systems like $n^0 n^0 \to p^+ p^+ e^- e^-$. Of the remaining ten operators, five have corresponding 4-quark operators with positive parity and contribute to $\pi^- \to \pi^+ e^- e^-$ and $n^0 n^0 \to p^+ p^+ e^- e^-$, while the five operators containing 4-quark operators of negative parity do not contribute. Consequently,

at LO, these decays are described with the Lagrangian [193]

$$\begin{aligned}\mathcal{L}^{\pi\to\pi ee}_{\text{SMEFT}} &= \frac{G_F^2}{\Lambda_{\text{LNV}}}\overline{e}e^{\text{c}}\sum_k c_k\mathcal{O}_k,\\ \mathcal{L}^{nn\to ppee}_{\text{SMEFT}} &= \frac{G_F^2}{\Lambda_{\text{LNV}}}\left(\overline{e}e^{\text{c}}\sum_k c_k\mathcal{O}_k + \overline{e}\gamma^\mu\gamma_5 e^{\text{c}}\sum_p \widetilde{c}_p\mathcal{V}^\mu_p\right),\end{aligned} \tag{5.11}$$

where G_F is the Fermi coupling constant and c_k and $\widetilde{c}_p$ are dimensionless Wilson coefficients. The scalar operator basis $\{\mathcal{O}_k(x)\}$ is

$$\begin{aligned}\mathcal{O}_1(x) &= (\overline{q}_L(x)\tau^+\gamma^\mu q_L(x))[\overline{q}_R(x)\tau^+\gamma_\mu q_R(x)]\\ \mathcal{O}_2(x) &= (\overline{q}_R(x)\tau^+ q_L(x))[\overline{q}_R(x)\tau^+ q_L(x)] + (\overline{q}_L(x)\tau^+ q_R(x))[\overline{q}_L(x)\tau^+ q_R(x)]\\ \mathcal{O}_3(x) &= (\overline{q}_L(x)\tau^+\gamma^\mu q_L(x))[\overline{q}_L(x)\tau^+\gamma_\mu q_L(x)] + (\overline{q}_R(x)\tau^+\gamma^\mu q_R(x))[\overline{q}_R(x)\tau^+\gamma_\mu q_R(x)]\\ \mathcal{O}_{1'}(x) &= (\overline{q}_L(x)\tau^+\gamma^\mu q_L(x)][\overline{q}_R(x)\tau^+\gamma_\mu q_R(x))\\ \mathcal{O}_{2'}(x) &= (\overline{q}_R(x)\tau^+ q_L(x)][\overline{q}_R(x)\tau^+ q_L(x)) + (\overline{q}_L(x)\tau^+ q_R(x)][\overline{q}_L(x)\tau^+ q_R(x)),\end{aligned} \tag{5.12}$$

with $k \in \{1, 2, 3, 1', 2'\}$, and the vector operator basis $\{\mathcal{V}^\mu_p(x)\}$ is

$$\begin{aligned}\mathcal{V}^\mu_1(x) &= (\overline{q}_L(x)\gamma^\mu\tau^+ q_L(x))[\overline{q}_L(x)\tau^+ q_R(x)] + (\overline{q}_R(x)\gamma^\mu\tau^+ q_R(x))[\overline{q}_R(x)\tau^+ q_L(x)]\\ \mathcal{V}^\mu_2(x) &= (\overline{q}_L(x)\gamma^\mu\tau^+ q_L(x))[\overline{q}_R(x)\tau^+ q_L(x)] + (\overline{q}_R(x)\gamma^\mu\tau^+ q_R(x))[\overline{q}_L(x)\tau^+ q_R(x)]\\ \mathcal{V}^\mu_{1'}(x) &= (\overline{q}_L(x)t^a\gamma^\mu\tau^+ q_L(x))[\overline{q}_L(x)t^a\tau^+ q_R(x)] + (\overline{q}_R(x)t^a\gamma^\mu\tau^+ q_R(x))[\overline{q}_R(x)t^a\tau^+ q_L(x)]\\ \mathcal{V}^\mu_{2'}(x) &= (\overline{q}_L(x)t^a\gamma^\mu\tau^+ q_L(x))[\overline{q}_R(x)t^a\tau^+ q_L(x)] + (\overline{q}_R(x)t^a\gamma^\mu\tau^+ q_R(x))[\overline{q}_L(x)t^a\tau^+ q_R(x)]\end{aligned} \tag{5.13}$$

with $p \in \{1, 2, 1', 2'\}$ [186, 193]. Here $q_L(x)$ and $q_R(x)$ are the left and right-handed components of the quark field isospin doublet, respectively, t^a are the generators of $SU(3)$, and

$$\tau^+ = \begin{pmatrix}0 & 1\\ 0 & 0\end{pmatrix} \tag{5.14}$$

is the isospin-raising operator. The round and square brackets in Eq. (5.12) denote color contraction: for arbitrary Dirac matrices Γ_1 and Γ_2, the operators $\mathcal{O}_1(x)$, $\mathcal{O}_2(x)$, and $\mathcal{O}_3(x)$ factor into products of color singlets, $(\overline{u}\Gamma_1 d)[\overline{u}\Gamma_2 d] \equiv (\overline{u}^a\Gamma_1 d^a)(\overline{u}^b\Gamma_2 d^b)$, whereas the operators $\mathcal{O}_{1'}(x)$ and $\mathcal{O}_{2'}(x)$ mix color between the two Dirac bilinear terms, $(\overline{u}\Gamma_1 d][\overline{u}\Gamma_2 d) \equiv (\overline{u}^a\Gamma_1 d^b)(\overline{u}^b\Gamma_2 d^a)$, where a, b are color indices. The vector operators $\mathcal{V}^\mu_1(x)$ and $\mathcal{V}^\mu_2(x)$ likewise factor into color singlets, while the operators $\mathcal{V}^\mu_{1'}(x)$

and $\mathcal{V}^{\mu}_{2'}(x)$ mix color between the Dirac bilinears because of the t^a insertions[2], which will be discussed in Section 5.5. The operator bases $\{\mathcal{O}_k(x)\}$ (Eq. (5.12)) and $\{\mathcal{V}^{\mu}_p(x)\}$ (Eq. (5.13)) are named the BSM bases and are typically used in phenomenological calculations of $0\nu\beta\beta$ decay [193].

Chiral EFT is useful for studying $0\nu\beta\beta$ decay in systems with approximate chiral symmetry. Although the $\pi^- \to \pi^+ e^- e^-$ transition is unphysical, it has phenomenological importance as it is an input for calculations of nuclear $0\nu\beta\beta$ decay with χEFT [194]. In particular, the two-nucleon decay $n^0 n^0 \to p^+ p^+ e^- e^-$ is induced in χEFT by the diagrams in Fig. (5.7) and has LO contributions from the $\pi\pi$ and NN vertices [181, 193].[3] The associated effective Lagrangian relevant for $\pi^- \to \pi^+ e^- e^-$ (i.e., omitting NN and πN operators which do not contribute) is [174],

$$\mathcal{L}^{\pi\to\pi ee}_{\chi\text{EFT}} = \overline{e} e^{\text{c}} \frac{G_F^2}{\Lambda_{\text{LNV}}} \frac{\Lambda_\chi^4}{(4\pi)^2} \frac{f_\pi^2}{8} \left(c_1\beta_1 \mathcal{O}^\chi_1 - \frac{c_2\beta_2}{2}\mathcal{O}^\chi_2 - c_3\beta_3\mathcal{O}^\chi_3 + c_{1'}\beta_{1'}\mathcal{O}^\chi_{1'} - \frac{c_{2'}\beta_{2'}}{2}\mathcal{O}^\chi_{2'} \right). \tag{5.15}$$

Here, f_π is the pion decay constant in the chiral limit, $\Lambda_\chi^2 \equiv 8\pi^2 f_\pi^2$ is the scale of chiral symmetry breaking, and $\mathcal{O}^\chi_k$ denote the leading χEFT operators corresponding to $\mathcal{O}_k$ [195]. Note that the operators $\mathcal{O}^\chi_k$ are normalized to be dimensionless. The χEFT low energy constants (LECs) β_k determine the $\pi\pi$ coupling and are also an essential input to study the nuclear decay. The β_k can be determined by evaluating the pion matrix elements of the $\mathcal{O}_k$ in LQCD and matching them to the corresponding matrix elements of $\mathcal{O}^\chi_k$ in Eq. (5.15).

Lattice calculations of short-distance $0\nu\beta\beta$ decay aim to compute the matrix elements,

$$\langle f|\mathcal{O}_k|i\rangle, \qquad\qquad \langle f|\mathcal{V}^\mu_p|i\rangle, \tag{5.16}$$

where $|i\rangle$ and $|f\rangle$ are, respectively, the decay's initial and final hadronic states. These matrix elements are essential inputs for EFT and may only be computed theoretically using LGT. They must be renormalized to make contact with phenomenology, which is conventionally done in the $\overline{\text{MS}}$ scheme. Explicit calculations of these matrix elements in the $\pi^- \to \pi^+ e^- e^-$ and $n^0 n^0 \to p^+ p^+ e^- e^-$ systems are detailed in Sections 5.3

[2]The correspondence between the color-mixing in $\{\mathcal{O}_{1'}(x), \mathcal{O}_{2'}(x)\}$ and $\{\mathcal{V}^\mu_{1'}(x), \mathcal{V}^\mu_{2'}(x)\}$ is due to color Fierz identities, which allow products $t^a \otimes t^a$ to be recast as color-mixed Takahashi brackets. See Appendix D for more detail.

[3]Earlier work using the Weinberg power counting suggested the $\pi\pi$ contribution dominates, but subsequently, Weinberg power counting was found to be incorrect in this channel [186] and other contributions to $n^0 n^0 \to p^+ p^+ e^- e^-$ are equally important.

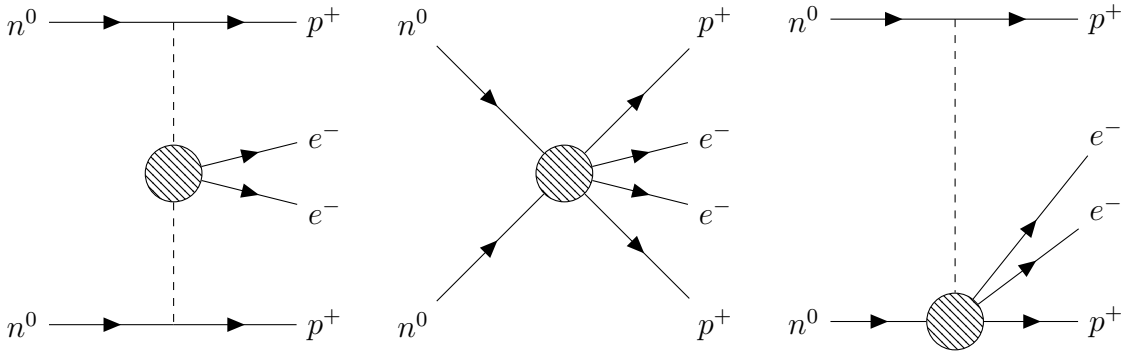

(a) $\pi\pi$ vertex. **(b)** NN vertex. **(c)** πN vertex.

Figure 5.7. Diagrams illustrating short-distance contributions to the $n^0n^0 \to p^+p^+e^-e^-$ $0\nu\beta\beta$ decay in χEFT. The solid lines denote nucleons or electrons, and the dotted lines denote pions. The hatched circles represent EFT operators built from hadronic fields, which at LO for the $\pi\pi$ vertex diagram, Fig. (5.7a), are determined by $\mathcal{O}_k^\chi$ in Eq. (5.15). The $\pi\pi$ (Fig. (5.7a)) and NN (Fig. (5.7b)) diagrams are the LO χEFT contributions to $n^0n^0 \to p^+p^+e^-e^-$.

and 5.4, and the renormalization of these matrix elements is presented in Section 5.5.

5.2.3 Relative Contributions and Λ_{LNV}

The numerical value of amplitudes of different $0\nu\beta\beta$ decay diagrams will depend on the specific mechanism of the decay and the exact value of the Wilson coefficients in the theory. Still, general order-of-magnitude estimates can be made to compare the contribution of long-distance mechanisms to short-distance mechanisms [196, 197]. Let $\mathcal{A}_{\text{LD}}$ denote the amplitude for a general long-distance process and $\mathcal{A}_{\text{SD}}$ the amplitude for a general short-distance process. One obtains a ratio of these amplitudes by power counting in EFT with the estimate [185]

$$\frac{\mathcal{A}_{\text{SD}}}{\mathcal{A}_{\text{LD}}} \approx \frac{m_W^4 q^2}{m_{\beta\beta}\Lambda_{\text{LNV}}}, \tag{5.17}$$

where $m_W \approx 80\,\text{GeV}$ is the W boson mass (Table 2.3), $q^2 \approx (50\text{ MeV})^2$ is the typical virtuality of the exchanged light Majorana neutrino, $m_{\beta\beta}$ is the effective Majorana neutrino mass (Eq. (5.2)), on the order of 1 eV, and Λ_{LNV} is the lepton number violating scale. As Λ_{LNV} is an unknown parameter, the value of Λ_{LNV} will determine the relative short-distance and long-distance contributions, if both are present in nature, as displayed in Table 5.1. If $\Lambda_{\text{LNV}} \gg 10$ TeV, then long-distance mechanisms will dominate [198], whereas if $\Lambda_{\text{LNV}} \ll 1$ TeV, then short-distance mechanisms will

dominate [194, 199]. In the intermediate regime $\Lambda_{\rm LNV} \sim 1 - 10$ TeV, both types of $0\nu\beta\beta$ decay mechanisms are roughly comparable. Both cases must be understood to draw conclusions about the underlying BSM physics from any experimental detection of $0\nu\beta\beta$ decay.

$\Lambda_{\rm LNV}$	Relative contribution
$\ll 1$ TeV	Short-distance dominates
$\sim 1 - 10$ TeV	Short-distance and long-distance are comparable
$\gg 10$ TeV	Long-distance dominates

Table 5.1. Effect of $\Lambda_{\rm LNV}$ on the dominance of different $0\nu\beta\beta$ decay mechanisms. As $\Lambda_{\rm LNV}$ increases, short-distance effects become further suppressed.

5.3 The short-distance $\pi^- \to \pi^+ e^- e^-$ amplitude

The pion matrix elements of each of the SMEFT operators in Eq. (5.12) are computed in LGT using gauge-field ensembles with $N_f = 2 + 1$ quark flavors generated by the RBC/UKQCD collaboration [200, 201], with parameters given in Table 5.2. Each ensemble uses the Shamir kernel [202] for the domain-wall fermion action [80] and the Iwasaki action [203] for the gauge field. The parameters of each ensemble are detailed in Table 5.2, and additional details regarding the ensemble generation can be found in Refs. [200, 201, 204]. The scale is set using the Wilson flow scale w_0 [205]. The pion mass, m_π, the pion decay constant, f_π, and the axial-vector renormalization constant, $\mathcal{Z}_A$, for each ensemble were determined in Ref. [12]. In the conventions used here, the physical pion decay constant [26] is $f_\pi^{(\rm phys)} = 130.2$ MeV. The vector renormalization constant, $\mathcal{Z}_V$, for these ensembles was computed in the chiral limit in Refs. [205, 206], and is approximately equal to $\mathcal{Z}_A$, indicating the ensembles exhibit approximate chiral symmetry. For more discussion on the vector and axial-vector renormalization coefficients, see Appendix H.

The short-distance contribution to the $\pi^- \to \pi^+ e^- e^-$ transition is encoded in the matrix elements

$$\langle \pi^+ | \mathcal{O}_k | \pi^- \rangle, \tag{5.18}$$

where the operators $\{\mathcal{O}_k\}$ are the five dimension-6 scalar operators in the BSM basis the contribute to $\pi^- \to \pi^+ e^- e^-$ at LO (Eq. (5.12)). The bare matrix elements are computed on each ensemble (Section 5.3.1) and renormalized in $\overline{\rm MS}$ at the scale 3 GeV (Section 5.5). Results for these matrix elements are presented after extrapolation to the chiral, continuum, and infinite-volume limit (Section 5.3.2).

Label	am_l	am_s	β	$L^3 \times T$	a [fm]	m_π [MeV]	f_π [MeV]	$\mathcal{Z}_A$
24I	0.01	0.04	2.13	$24^3 \times 64$	0.1106(3)	432(1)	163.7(6)	0.7167(2)
	0.005					340(1)	151.6(6)	
32I	0.008	0.03	2.25	$32^3 \times 64$	0.0828(3)	411(2)	162.0(9)	0.7448(2)
	0.006					360(1)	154.3(7)	
	0.004					302(1)	147.5(8)	

Table 5.2. Parameters of the gauge field ensembles used in the $\pi^- \to \pi^+ e^- e^-$ computation. Each ensemble was generated with two degenerate light quark flavors of mass m_ℓ and one heavy quark flavor of mass m_s. The lattice volumes are $L^3 \times T \times L_s$, with the fifth dimension having $L_s = 16$ sites. Derived quantities are computed in Ref. [12] (the pion mass m_π, the pion decay constant f_π, and the axial current renormalization $\mathcal{Z}_A$) and Refs. [205, 206] (the inverse lattice spacing a^{-1}).

5.3.1 LGT Calculation of Bare Matrix Elements

On each ensemble used in the $\pi^- \to \pi^+ e^- e^-$ calculation (Table 5.2), the time-averaged two-point function

$$\mathcal{C}_{2\text{pt}}(t) = \frac{1}{T} \sum_{t_-=0}^{T-1} \sum_{\boldsymbol{x},\boldsymbol{y}} \langle 0 | \chi_\pi(\boldsymbol{x}, t + t_-) \chi_\pi^\dagger(\boldsymbol{y}, t_-) | 0 \rangle \tag{5.19}$$

and three-point functions

$$\mathcal{C}_k(t_-, t_x, t_+) = \sum_{\boldsymbol{x},\boldsymbol{y},\boldsymbol{z}} \langle 0 | \chi_\pi^\dagger(\boldsymbol{x}, t_+) \mathcal{O}_k(\boldsymbol{z}, t_x) \chi_\pi^\dagger(\boldsymbol{y}, t_-) | 0 \rangle, \tag{5.20}$$

where the pion interpolating operator $\chi_\pi(x) = \overline{u}(x)\gamma_5 d(x)$ has the quantum numbers of the π^- and $t_+ \geq t_x \geq t_-$, are computed for each operator $\mathcal{O}_k(x)$ in the BSM basis (Eq. (5.12)). Wall-source propagators are computed at each available time slice on each configuration, where "wall" denotes projection to vanishing three-momentum in the Coulomb gauge (Section 3.3.3). Note that wall sources are not gauge-invariant; hence, there is a need for gauge fixing. The two-point functions (Eq. (5.19)) are constructed using a wall source propagator at t_- and a wall sink at $t + t_-$, and the three-point functions (Eq. (5.20)) are constructed using wall source propagators at t_- and t_+ and a point (local) sink at t_x. The explicit Wick contractions are given in Appendix F.

The bare pion matrix elements in lattice units

$$\langle \mathcal{O}_k \rangle \equiv a^4 \langle \pi^+ | \mathcal{O}_k(\boldsymbol{p} = \boldsymbol{0}) | \pi^- \rangle = a^4 \sum_{\mathbf{x}} \langle \pi^+ | \mathcal{O}_k(\boldsymbol{x}, 0) | \pi^- \rangle \tag{5.21}$$

are extracted from the effective matrix elements

$$O_k^{\text{eff}}(t) \equiv 2m_\pi \frac{\mathcal{C}_k(0,t,2t)}{\mathcal{C}_{2\text{pt}}(2t) - \frac{1}{2}\mathcal{C}_{2\text{pt}}(T/2)e^{m_\pi(2t-T/2)}}. \tag{5.22}$$

Subtracting $\frac{1}{2}\mathcal{C}_{2\text{pt}}(T/2)e^{m_\pi(2t-T/2)}$ in the denominator of Eq. (5.22) isolates the backward-propagating state in the two-point function, and in the $0 \ll t \ll T$ limit $O_k^{\text{eff}}(t)$ asymptotes to $\langle \mathcal{O}_k \rangle$. The effective matrix elements are computed on between 33 and 53 gauge field configurations for each ensemble (details in Appendix G, Table G.1), resampled using a bootstrap procedure with $n_b = 50$ bootstrap samples. The spectral decomposition of $O_k^{\text{eff}}(t)$ up to and including the first excited state with energy $m_\pi + \Delta$,

$$O_k^{\text{eff}}(t) = \frac{\langle \mathcal{O}_k \rangle + \mathcal{N}_1^{(k)} e^{-\Delta t} + \mathcal{N}_2^{(k)} e^{-(m_\pi+\Delta)(T-2t)}}{1 + \mathcal{N}_3^{(k)} e^{-2\Delta t} + \mathcal{N}_4^{(k)} e^{-(m_\pi+\Delta)T+2(2m_\pi+\Delta)t}}, \tag{5.23}$$

parameterizes the ground and excited-state contributions to $O_k^{\text{eff}}(t)$, where the coefficients $\mathcal{N}_i^{(k)}$ are constants determined by the spectral content of the theory. Eq. (5.23) can be Taylor expanded to first order in $\mathcal{N}_3^{(k)}$ and $\mathcal{N}_4^{(k)}$, yielding

$$\begin{aligned} f_k(t; \langle \mathcal{O}_k \rangle, m^{(k)}, \Delta^{(k)}, A_i^{(k)}) \equiv \langle \mathcal{O}_k \rangle &+ A_1^{(k)} e^{-\Delta^{(k)} t} + A_2^{(k)} e^{-(m^{(k)}+\Delta)(T-2t)} \\ &- A_3^{(k)} e^{-2\Delta^{(k)} t} - A_4^{(k)} e^{-(m^{(k)}+\Delta)T+2(2m^{(k)}+\Delta^{(k)})t}. \end{aligned} \tag{5.24}$$

This function is used to model the temporal dependence of $O_k^{\text{eff}}(t)$, treating $\langle \mathcal{O}_k \rangle$, $m^{(k)}$, $\Delta^{(k)}$, and $A_i^{(k)}$ as free parameters.

Fits of $O_k^{\text{eff}}(t)$ to the model of Eq. (5.24) are performed using a correlated least-squares fit. Each fit is performed over a given range $[t_{\text{min}}, t_{\text{max}}]$, with the covariance matrix obtained from the bootstrapped sample covariance matrix via linear shrinkage with parameter λ; the hyperparameters are varied, with $t_{\text{min}} \in [6, 11]$, $t_{\text{max}} \in [30, 32]$, and $\lambda \in \{0.1, 0.2, 0.3, 0.4\}$. Bayesian priors are placed on the model parameters, informed by the results of a two-state fit to $C_{2\text{pt}}(t)$. The priors on the spectral coefficients are set to $A_k^{(i)} = 0.0 \pm 0.1$, where $\mu \pm \sigma$ denotes the normal distribution with mean μ and width σ. To enforce positivity, log-normal priors are chosen for the mass $m_\pi^{(k)}$ and excited state gap $\Delta^{(k)}$ such that $m^{(k)} = m_\pi \pm \delta m_\pi$, where m_π (δm_π) is the mean (standard deviation) of the pion mass (Table 5.2), and $\Delta^{(k)} = 2m_\pi \pm m_\pi$. Statistically indistinguishable results are obtained for $\langle \mathcal{O}_k \rangle$ under variation of all hyperparameters within the ranges described above, and when widths of the priors are inflated by a factor of 2, hence fiducial values of the hyperparameters are chosen as $[t_{\text{min}}, t_{\text{max}}] = [6, 32]$ and $\lambda = 0.1$[4]. Posterior values for $A_3^{(k)}$ and $A_4^{(k)}$ are found to be $\ll 1$, thus the Taylor expansion in Eq. (5.24) is valid. The fits have χ^2/dof between 0.10 and 0.73. Fit results and the complete set of fits for each operator on each ensemble with the fiducial hyperparameters are shown in Appendix G. Illustrative fits to data from the 32I, $am_\ell = 0.004$ ensemble with the fiducial hyperparameters are shown in Fig. (5.8).

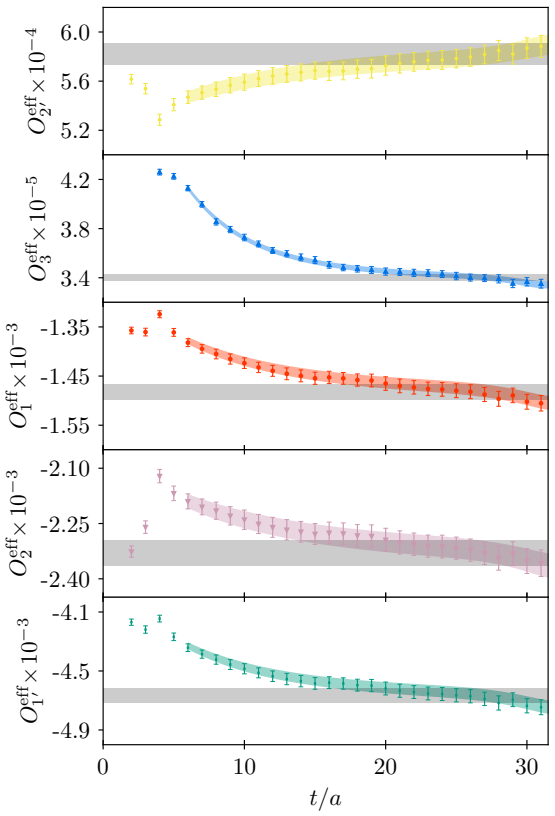

Figure 5.8. Effective matrix elements $O_k^{\text{eff}}(t)$ (Eq. (5.22)) computed on the 32I, $am_\ell = 0.004$ ensemble. Colored bands denote the best-fit band for the corresponding excited-state fit to the model of Eq. (5.24), with $[t_{\text{min}}, t_{\text{max}}] = [6, 32]$ and $\lambda = 0.1$. The grey band in each panel denotes the extracted value of $\langle \mathcal{O}_k \rangle$ (Eq. (5.24)).

Before extrapolation to the chiral, continuum, and infinite-volume limit, the bare

[4]This choice for λ is statistically the most conservative within the range, as $\lambda = 0$ corresponds to no shrinkage.

Operator		$\mathcal{O}_1$	$\mathcal{O}_2$	$\mathcal{O}_3$	$\mathcal{O}_{1'}$	$\mathcal{O}_{2'}$
Label	am_ℓ	$O_k(m_\pi, f_\pi, a, L)$				
24I	0.01	-0.0190(11)	-0.0467(15)	0.001602(59)	-0.0850(32)	0.01556(50)
	0.005	-0.0162(11)	-0.0391(15)	0.000815(28)	-0.0733(32)	0.01305(45)
32I	0.008	-0.0204(15)	-0.0436(18)	0.001383(57)	-0.0863(39)	0.01393(66)
	0.006	-0.0179(13)	-0.0387(14)	0.000937(39)	-0.0771(36)	0.01239(50)
	0.004	-0.0160(15)	-0.0347(16)	0.000569(24)	-0.0696(37)	0.01115(60)
		Extrapolated $O_k(m_\pi^{(\text{phys})}, f_\pi^{(\text{phys})}, 0, \infty)$				
O_k (GeV^4)		-0.0127(16)	-0.0245(22)	0.0000869(80)	-0.0535(48)	0.00757(75)
β_k		-1.21(17)	-2.37(23)	0.606(66)	-5.17(51)	0.735(80)
α_k (fm^{-2})		-0.27(31)	0.33(23)	0.13(22)	-0.04(23)	0.58(26)
c_k		-0.6(1.4)	-1.17(98)	8.6(1.4)	-1.18(98)	-1.5(1.0)
χ^2/dof		0.02	0.03	0.22	0.08	0.03

Table 5.3. Renormalized pion matrix elements $O_k(m_\pi, f_\pi, a, L)$, Eq. (5.61), of each operator $\mathcal{O}_k$ in the BSM basis computed on each of the ensembles (upper), and the results of chiral continuum extrapolation (lower). The parameters α_k, β_k, and c_k are the χEFT LECs, Eq. (5.25), and $\langle\pi^+|\mathcal{O}_k^{\overline{\text{MS}}}|\pi^-\rangle$ is the extrapolated matrix element in the continuum and infinite volume limit at physical quark masses in the $\overline{\text{MS}}$ scheme at $\mu = 3$ GeV.

matrix elements must be renormalized. Renormalization coefficients $\mathcal{Z}^{\overline{\text{MS}}}$ are computed in $\overline{\text{MS}}$ at scale $\mu = 3\,\text{GeV}$ for each of the five scalar operators $\mathcal{O}_k$ for each ensemble. The calculation of $\mathcal{Z}^{\overline{\text{MS}}}$ is presented in Section 5.5, with results shown in Tables 5.7 and 5.8.

5.3.2 Chiral Extrapolation

Computation of the non-perturbative renormalization coefficients necessary to renormalize the scalar operators on the five ensembles used in this calculation is described in Section 5.5. The renormalized matrix elements $O_k(m_\pi, f_\pi, a, L)$, Eq. (5.61), computed on each ensemble, are extrapolated to the continuum and infinite volume limit and physical pion mass using χEFT at NLO; the relevant expressions have been derived in Ref. [174] using the Lagrangian in Eq. (5.15). The chiral models $\mathcal{F}_k$ for O_k

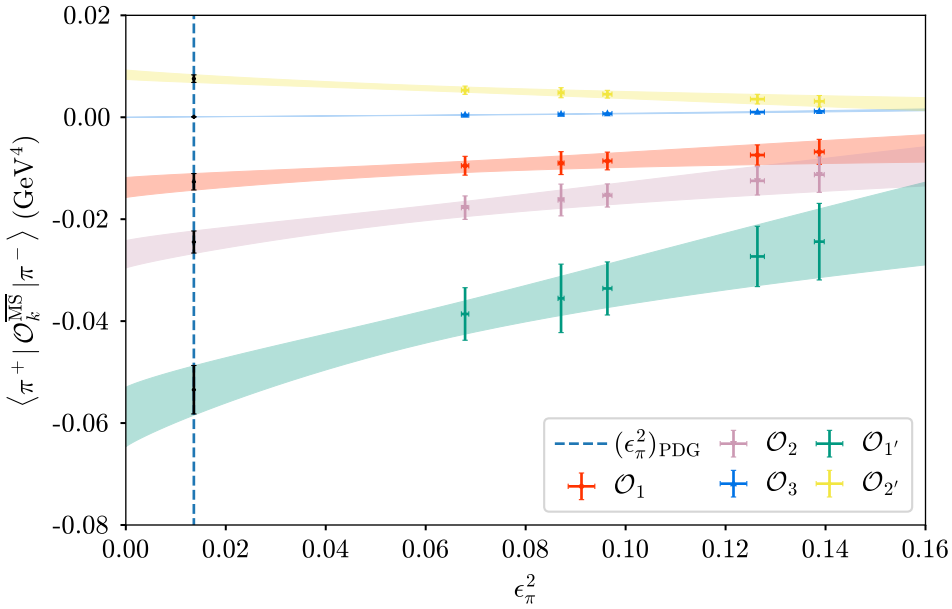

Figure 5.9. Chiral extrapolation of renormalized matrix elements. The LQCD results are shown at $\epsilon_\pi^2 = m_\pi^2/(8\pi^2 f_\pi^2)$ calculated using the pion mass of each ensemble and the physical value of f_π, and the values of $O_k(m_\pi, f_\pi, a, L)$ have been shifted by $-\mathcal{F}_k(m_\pi, f_\pi, a, L; \alpha_k, \beta_k, c_k) + \mathcal{F}_k(m_\pi, f_\pi^{(\rm phys)}, 0, \infty; \alpha_k, \beta_k, c_k)$, where α_k, β_k, c_k are the best-fit coefficients given in Table 5.3. The dashed line denotes the physical pion mass.

are given by

$$\begin{aligned}
&\mathcal{F}_1(m_\pi, f_\pi, a, L; \alpha_1, \beta_1, c_1) = \\
&\qquad \frac{\beta_1 \Lambda_\chi^4}{(4\pi)^2}\left[1 + \epsilon_\pi^2(\log \epsilon_\pi^2 - 1 + c_1 - f_0(m_\pi L) + 2 f_1(m_\pi L)) + \alpha_1 a^2\right], \\
&\mathcal{F}_2(m_\pi, f_\pi, a, L; \alpha_2, \beta_2, c_2) = \\
&\qquad \frac{\beta_2 \Lambda_\chi^4}{(4\pi)^2}\left[1 + \epsilon_\pi^2(\log \epsilon_\pi^2 - 1 + c_2 - f_0(m_\pi L) + 2 f_1(m_\pi L)) + \alpha_2 a^2\right], \\
&\mathcal{F}_3(m_\pi, f_\pi, a, L; \alpha_3, \beta_3, c_3) = \\
&\qquad \epsilon_\pi^2 \frac{\beta_3 \Lambda_\chi^4}{(4\pi)^2}\left[1 - \epsilon_\pi^2(3 \log \epsilon_\pi^2 + 1 - c_3 + f_0(m_\pi L) + 2 f_1(m_\pi L)) + \alpha_3 a^2\right],
\end{aligned} \tag{5.25}$$

where $\epsilon_\pi^2 = m_\pi^2/\Lambda_\chi^2$ is a power-counting parameter for χEFT, β_k are the LO LECs defined in Eq. (5.15), and α_k and c_k are the additional NLO LECs. The matrix elements $O_{1'}$ and $O_{2'}$ have the same chiral behavior as O_1 and O_2 and are modeled

by $\mathcal{F}_1$ and $\mathcal{F}_2$, respectively, but with different LECs, $\alpha_{1'}, \beta_{1'}, c_{1'}$ and $\alpha_{2'}, \beta_{2'}, c_{2'}$. The functions

$$\begin{aligned} f_0(mL) &= -2 \sum_{|\boldsymbol{n}|\neq 0} K_0(mL|\boldsymbol{n}|), \\ f_1(mL) &= 4 \sum_{|\boldsymbol{n}|\neq 0} \frac{K_1(mL|\boldsymbol{n}|)}{mL|\boldsymbol{n}|}, \end{aligned} \tag{5.26}$$

are sums of modified Bessel functions $K_i(z)$ arising from one-loop, finite volume χEFT in the p-regime.

The models are fit to the data in Table 5.3, using least-squares minimization including the correlations between O_k, m_π, and f_π on each ensemble. The final extrapolated results for the matrix elements and corresponding LECs are given in Table 5.3. The resulting fits are shown in Fig. (5.9), where to isolate the pion-mass dependence of the matrix elements, ϵ_π^2 has been rescaled by $(f_\pi^{(\text{lat})}/f_\pi^{(\text{phys})})^2$ and the values of $O_k(m_\pi, f_\pi, a, L)$ have been shifted by $-\mathcal{F}_k(m_\pi, f_\pi, a, L; \alpha_k, \beta_k, c_k) + \mathcal{F}_k(m_\pi, f_\pi^{(\text{phys})}, 0, \infty; \alpha_k, \beta_k, c_k)$, where α_k, β_k, c_k are the best-fit coefficients given in Table 5.3. The extrapolation bands for each $\mathcal{O}_k$ depict the functional form for the model $\mathcal{F}_k(m_\pi, f_\pi^{(\text{phys})}, 0, \infty; \alpha_k, \beta_k, c_k)$. The results for $\langle \pi^+ | \mathcal{O}_k^{\overline{\text{MS}}} | \pi^- \rangle$ obey the same hierarchy as the chiral $SU(3)$ estimates [207], and are consistent with these results within two standard deviations.

The results for the renormalized, extrapolated, matrix elements differ from the results of Ref. [174] by about 2.0 to 5.0 standard deviations. Several differences between the two calculations may account for the discrepancy. The present calculation was performed with the same domain-wall action for the valence and sea-quarks and is thus unitary, while that of Ref. [174] used a mixed action where unitarity is only restored in the continuum limit. Using the domain-wall action for valence and sea quarks yields matrix elements with a mild dependence on the lattice spacing. In contrast, the mixed action results appear to have a larger dependence on the lattice spacing. However, the analysis of Ref. [174] was performed on nine ensembles with pion masses $m_\pi \lesssim 310$ MeV, including one ensemble with pion mass below the physical point, which allows for an interpolation to the physical point. Ref. [174] also uses three lattice spacings as opposed to the two used in this computation, which allows for higher control of discretization artifacts in the non-perturbative renormalization and the chiral and continuum extrapolation.

5.4 The short-distance $n^0n^0 \to p^+p^+e^-e^-$ amplitude

The calculation of the short-distance $n^0n^0 \to p^+p^+e^-e^-$ matrix elements proceeds similarly to the short-distance $\pi^- \to \pi^+e^-e^-$ matrix elements, with a few notable differences. First, to excite the desired states, one requires nucleon interpolating operators,

$$\begin{aligned}\chi_p^\rho(x) &\equiv \epsilon_{abc}[u_a^\alpha(x)(P_+C\gamma_5)^{\alpha\beta}d_b^\beta(x)](P_+u(x))_c^\rho,\\ \chi_n^\rho(x) &\equiv \epsilon_{abc}[d_a^\alpha(x)(P_+C\gamma_5)^{\alpha\beta}u_b^\beta(x)](P_+d(x))_c^\rho,\end{aligned} \tag{5.27}$$

where ρ is a free spinor index, ϵ_{abc} is the $SU(3)_c$ Levi-Civita tensor, C is the charge conjugation operator, and the projector $P_+ \equiv \frac{1+\gamma_0}{2}$ projects the operator to positive parity. Each nucleon interpolator $\chi_N^\rho(x)$ with $N \in \{n, p\}$ is used to construct a dinucleon interpolator,

$$\chi_{NN}(x) \equiv \chi_N^\alpha(x)(C\gamma_5)^{\alpha\beta}\chi_N^\beta(x). \tag{5.28}$$

Second, because only a single ensemble (Table 5.4) is used, no extrapolation is performed on the renormalized, finite-volume matrix elements computed at $m_\pi \approx 806\,\text{MeV}$, and these finite-volume matrix elements constitute the final results as a proof-of-concept of the calculation. Finally, because the vector operators are not suppressed in the $n^0n^0 \to p^+p^+e^-e^-$ decay, hadronic matrix elements of both the scalar operators $\langle pp|\mathcal{O}_k|nn\rangle$ (Eq. (5.12)) and the vector operators $\langle pp|\mathcal{V}_p|nn\rangle$ (Eq. (5.13)) are computed and presented. To condense notation, let

$$\{H_i\}_{i=1}^9 = \{\mathcal{O}_1, \mathcal{O}_2, \mathcal{O}_3, \mathcal{O}_{1'}, \mathcal{O}_{2'}, \mathcal{V}_1, \mathcal{V}_2, \mathcal{V}_{1'}, \mathcal{V}_{2'}\} \tag{5.29}$$

denote the set of operators that can induce the short-distance contribution to $n^0n^0 \to p^+p^+e^-e^-$, where the vector indices are suppressed.

The nucleon matrix elements of the SMEFT operators in Eqs. (5.12, 5.13) are computed in LGT on a gauge-field ensemble at the $SU(3)$ flavor symmetric point with $m_\pi \approx 806$ MeV [208], with parameters given in Table 5.4. The ensemble uses a clover fermion action and a tadpole-improved Lüscher-Weisz gauge action [209]. The lattice spacing a is set with the Υ spectrum [210], and the renormalization coefficients $\mathcal{Z}_A$ and $\mathcal{Z}_V$ are calculated in the RI/sMOM scheme [211, 212].

am_q	β	$L^3 \times T$	a [fm]	m_π [MeV]	$\mathcal{Z}_A$	$\mathcal{Z}_V$	n_{cfg}
-0.2450	6.1	$32^3 \times 48$	0.1453(16)	806.9(8.9)	0.879(12)	0.802(22)	12,139

Table 5.4. Parameters of the gauge field ensemble used in the $n^0n^0 \to p^+p^+e^-e^-$ computation. The ensemble was generated at the $SU(3)$-flavor symmetric point where $m_u = m_d = m_s \equiv m_q$. The lattice volume is $L^3 \times T$, and n_{cfg} configurations were used. Derived quantities are computed in Ref. [208] (the pion mass m_π and the lattice spacing a) and Refs. [213] (the axial current renormalization $\mathcal{Z}_A$, the vector current renormalization $\mathcal{Z}_V$).

On this ensemble, two-point functions for the dinucleon

$$\mathcal{C}^{\text{nn}}_{\text{2pt}}(t) = \langle 0|\chi_{nn}(t)\chi^\dagger_{nn}(0)|0\rangle, \tag{5.30}$$

and three-point functions

$$\mathcal{C}^{\text{nnpp}}_i(t,\tau) = \langle 0|\chi_{pp}(t)H_i(\tau)\chi^\dagger_{nn}(0)|0\rangle, \tag{5.31}$$

are constructed. The two-point function $\mathcal{C}^{\text{nn}}_{\text{2pt}}(t)$ are constructed with a wall source and point sink, and the three-point functions $\mathcal{C}^{\text{nnpp}}_i(t,\tau)$ are constructed with a wall source, point operator, and point sink (Section 3.3.3).

The two-point function is used to extract the dinucleon mass by fitting $\mathcal{C}^{\text{nn}}_{\text{2pt}}(t)$ to a constant am_{eff}. The fits are performed over a range of windows $[t_{\text{min}}, t_{\text{max}}]$ with $t_{\text{min}} \in \{9, 10, ..., 13\}$ and $t_{\text{max}} = 16$ with multi-exponential models,

$$f_n(t) = \sum_{k=0}^{n} \mathcal{Z}_n e^{-E_k t}, \tag{5.32}$$

with $n \in \{0, 1, 2\}$. In practice for $n \geq 1$, fits are performed by imposing log-normal priors on the energy gaps $E_k - E_{k-1}$, which must be positive by the assumption that E_k monotonically increases. The best fit for a given window is selected via the AIC (Eq. (3.90)), and fits across all windows are averaged according to the procedure in Section 5.3.1. The fit results are shown in Figure 5.10. The displayed effective mass am_{eff} is the cosh-corrected effective mass (Eq. (3.45)) constructed from $\mathcal{C}^{\text{nn}}_{\text{2pt}}(t)$ and the resulting posterior for aE_0 is shown in Figure 5.10, with the result,

$$aE_0 = 2.3930(40). \tag{5.33}$$

This result is consistent with other studies on this ensemble that used different inter-

polating operators to compute the dineutron mass [214–217]. The level of precision with which aE_0 was extracted is not enough to determine if the dinucleon is a bound state or a scattering state at the set of parameters that define this gauge field ensemble (Table 5.4).

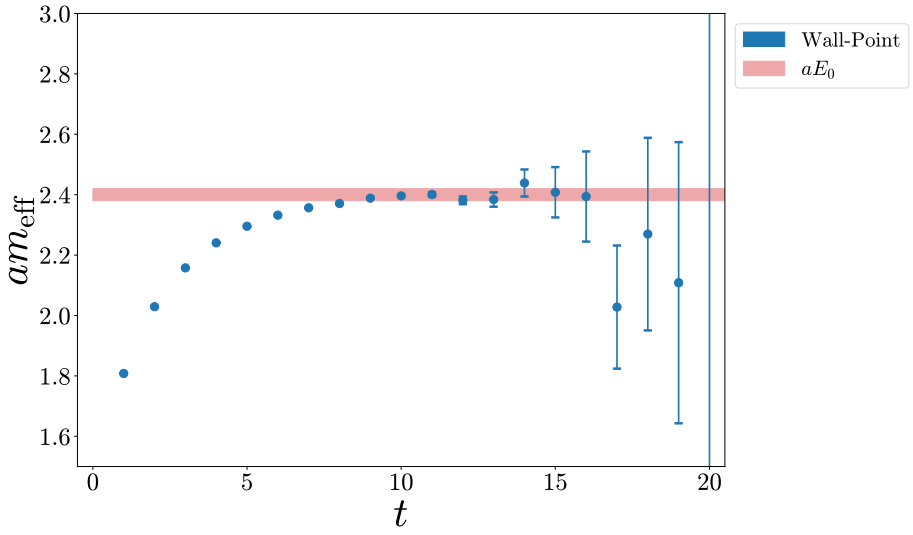

Figure 5.10. Data for the effective mass am_{eff} (Eq. (3.45)) is shown in blue, and the result of the averaged multi-exponential fit to $\mathcal{C}^{\text{nn}}_{\text{2pt}}(t)$ is depicted by the red band. The data is fit with a series of multi-exponential models (Eq. (5.32)), and the best fit is selected with the AIC (Eq. (3.90)). Fit ranges are averaged according to the procedure described in Section 5.3.1, and the averaged fit result yields a value of $aE_0 = 2.3930(40)$.

These correlators are used to form the ratio,

$$R_i(t,\tau) \equiv \frac{\mathcal{C}_i^{\text{nnpp}}(t,\tau)}{\mathcal{C}^{\text{nn}}_{\text{2pt}}(t)}, \tag{5.34}$$

which in the $0 \ll \tau \ll t \ll T$ limit asymptotes to $2E_0\langle pp|H_i|nn\rangle$. The data is observed to have minor excited state contamination, hence is fit to the model,

$$f(t,\tau) = A + Be^{-\delta\tau} + Ce^{-\delta(t-\tau)}. \tag{5.35}$$

Here δ corresponds to the excited state gap $E_1 - E_0$. The A coefficient corresponds to the desired quantity $2E_0\langle pp|H_i|nn\rangle$. Fits are performed over windows with the minimum sink-operator separation $t-\tau$ and operator-source separation τ in $\{3, ..., 8\}$, and averaged using the prescription in Section 5.3.1. Figure 5.11 shows the data for the effective matrix elements for each operator and the resulting posterior for A. The

χ^2/dof for the fits were very good, with most fits having a χ^2/dof between 0.5 and 1.4, although a few exceptional ranges had low χ^2/dof values between 0.2 and 0.5.

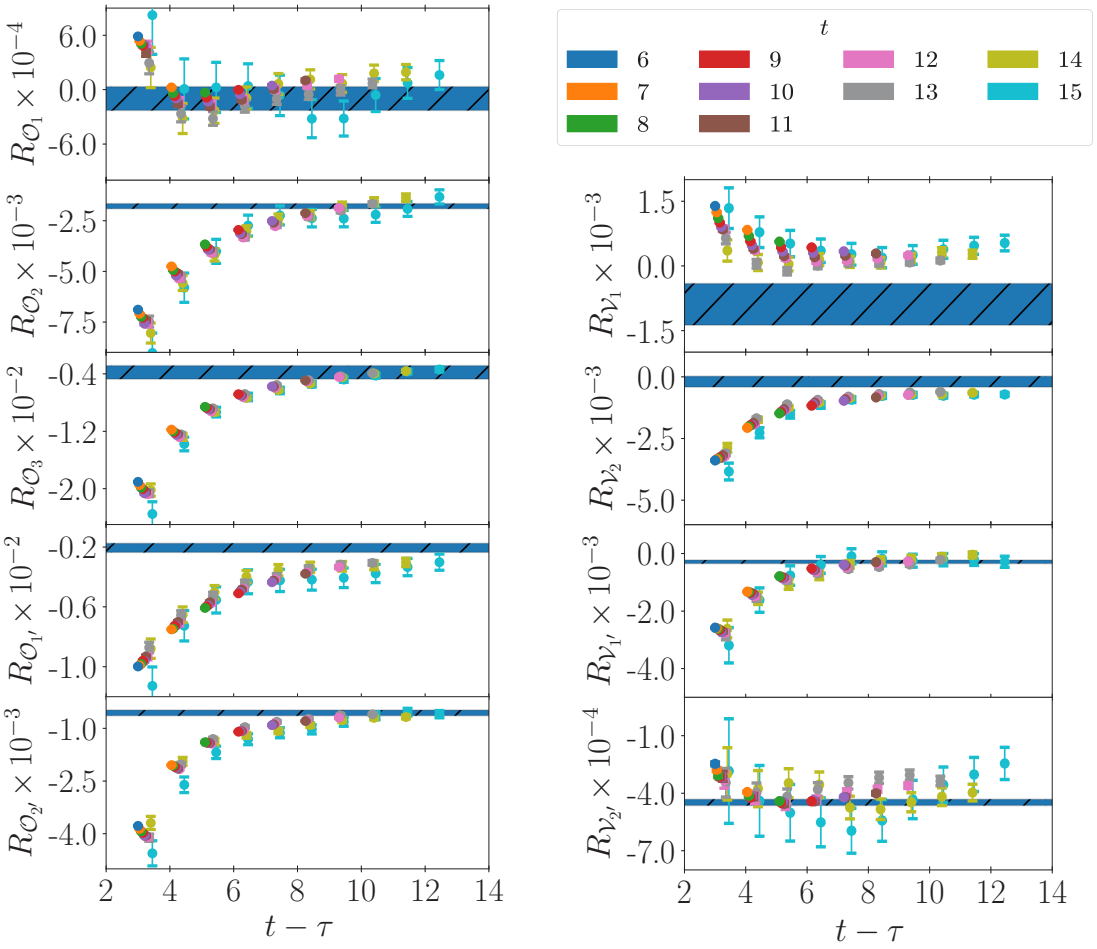

Figure 5.11. Data and fit results for the 9 effective matrix elements $R_i(t)$ (Eq. (5.34)) for the scalar operator basis $\mathcal{O}_k$ (left, Eq. (5.12)) and the vector operator basis (right, Eq. (5.12)), plotted against the sink-operator separation $t-\tau$. Note that each operator is labeled by $\mathcal{O}_k$ or $\mathcal{V}_p$ instead of H_i. The color of each point corresponds to the operator-source separation t, given in the legend. The fit is performed to the single-exponential model $f(t,\tau)$ given in Eq. (5.35), and the blue hatched band denotes the posterior on the A coefficient for the fit for each effective matrix element. The value of A extracted from each fit corresponds to $2E_0\langle pp|H_i|nn\rangle$.

The operator bases $\{\mathcal{O}_k\}$ and $\{\mathcal{V}_p\}$ must be renormalized to make contact to phenomenology. The operator renormalization calculation is described in Section 5.5. The renormalization coefficients are computed in $\overline{\text{MS}}$ at scale $\mu = 3$ GeV. The computation for the scalar operator basis yields the results presented in Tables 5.7–5.9. The vector operator renormalization is still ongoing, so the bare vector matrix

elements will be presented. An upcoming paper will present the full renormalized vector matrix elements when the renormalization calculation has been completed.

The results for the renormalized scalar matrix elements $\langle pp|\mathcal{O}_k^{\overline{\text{MS}}}|nn\rangle$ are shown in Table 5.5, and the results for the bare vector matrix elements $\langle pp|\mathcal{V}_p^{\mu;\,(0)}|nn\rangle$ are shown in Table 5.6. The diagonal renormalization factors are expected to be $O(1)$, with the off-diagonal renormalization factors suppressed relative to the diagonal ones. Therefore, although the vector operator results are bare, the relative magnitudes of the vector and scalar matrix elements may be roughly compared. There are two items of particular note in the results. First, that the contributions of the vector and scalar matrix elements to $n^0n^0 \to p^+p^+e^-e^-$ are roughly the same order of magnitude. Unlike the $\pi^- \to \pi^+e^-e^-$ case where the vector operators are suppressed, they should not be neglected in the $n^0n^0 \to p^+p^+e^-e^-$ calculation. Second, the result for $\langle pp|\mathcal{O}_3|nn\rangle$ is of the same order of magnitude, or even larger, than the other scalar operators. In the $\pi^- \to \pi^+e^-e^-$ case, this operator was suppressed in the chiral power counting, evident in the final extrapolated results for the renormalized $\pi^- \to \pi^+e^-e^-$ matrix elements (Table 5.3).

Operator	$\mathcal{O}_1$	$\mathcal{O}_2$	$\mathcal{O}_3$	$\mathcal{O}_{1'}$	$\mathcal{O}_{2'}$
$\langle\mathcal{O}_k\rangle$ (GeV^4)	-0.00033(44)	-0.00606(43)	-0.0129(32)	-0.0070(10)	-0.00190(27)

Table 5.5. Results for the $n^0n^0 \to p^+p^+e^-e^-$ short-distance matrix elements for the scalar operators, $\langle\mathcal{O}_k\rangle \equiv \langle pp|\mathcal{O}_k|nn\rangle$, renormalized in $\overline{\text{MS}}$ at $\mu = 3$ GeV.

5.5 Renormalization of short-distance operators

To make contact with phenomenological calculations, lattice-regulated matrix elements must be renormalized in the $\overline{\text{MS}}$ scheme. The renormalization calculation proceeds identically for the two short-distance decays considered here, $\pi^- \to \pi^+e^-e^-$ and $n^0n^0 \to p^+p^+e^-e^-$. The only difference is the ensembles used for each calculation and that the vector operator renormalizations (Eq. (5.13)) must also be considered for the case of $n^0n^0 \to p^+p^+e^-e^-$.

Operator	$\mathcal{V}_1$	$\mathcal{V}_2$	$\mathcal{V}_{1'}$	$\mathcal{V}_{2'}$
$\langle\mathcal{V}_p^\mu\rangle$ (GeV^4)	-0.0030(16)	-0.00066(74)	-0.00098(21)	-0.001523(55)

Table 5.6. Results for the bare $n^0n^0 \to p^+p^+e^-e^-$ short-distance matrix elements for the vector operators, $\langle\mathcal{V}_p^\mu\rangle \equiv \langle pp|\mathcal{V}_p^\mu|nn\rangle$. The calculation for the vector renormalization coefficients is still ongoing and described in Section 5.5.

In this calculation, the renormalization coefficients are computed non-perturbatively in the RI/sMOM-(γ^μ, γ^μ) (abbreviated as RIγ) scheme [211, 212] and perturbatively matched to $\overline{\text{MS}}$. In terms of the operator basis $\{\mathcal{O}_k(x)\}$ (Eq. (5.12)), the renormalized matrix elements can be expressed as

$$\begin{aligned}\mathcal{O}_k^{\overline{\text{MS}}}(x;\mu^2,a) &= \mathcal{Z}_{k\ell}^{\overline{\text{MS}};\mathcal{O}}(\mu^2,a)\mathcal{O}_\ell(x;a) \\ &= \mathcal{C}_{kj}^{\overline{\text{MS}}\leftarrow\text{RI}\gamma;\mathcal{O}}(\mu^2,a)\mathcal{Z}_{j\ell}^{\text{RI}\gamma;\mathcal{O}}(\mu^2,a)\mathcal{O}_\ell(x;a),\end{aligned} \tag{5.36}$$

where sums over repeated indices are implied. Here $\mathcal{O}_\ell(x;a)$ denotes the bare operator at lattice spacing a, and

$$\mathcal{C}_{kj}^{\overline{\text{MS}}\leftarrow\text{RI}\gamma;\mathcal{O}}(\mu^2,a) \equiv \mathcal{Z}_{ki}^{\overline{\text{MS}};\mathcal{O}}(\mu^2,a)\left[\mathcal{Z}^{\text{RI}\gamma;\mathcal{O}}(\mu^2,a)\right]_{ij}^{-1} \tag{5.37}$$

is the multiplicative matching coefficient from the RIγ to $\overline{\text{MS}}$ schemes, computed at one-loop in perturbation theory in the strong coupling $\alpha_s(\mu)$ [212, 218]. The vector operator renormalization coefficients $\mathcal{Z}_{k\ell}^{\overline{\text{MS}};\mathcal{V}}$ and matching coefficients $\mathcal{C}_{kj}^{\overline{\text{MS}}\leftarrow\text{RI}\gamma;\mathcal{V}}(\mu^2,a)$ are defined identically in terms of the basis $\{\mathcal{V}_k^\mu\}$ (Eq. (5.13)). Note that each renormalization coefficient is mass-independent and defined in the chiral limit.

The scalar operator renormalization coefficients, Eq. (5.36), are conventionally computed in the Non-Perturbative Renormalization (NPR) operator basis, $\{Q_n(x)\}$, which contains different linear combinations of operators than the BSM basis of Eq. (5.12). Correlation functions involving the color-mixed operators $\mathcal{O}_{1'}(x), \mathcal{O}_{2'}(x)$ may be rewritten with Fierz identities (Appendix D) as combinations of color-unmixed quark bilinears, which simplifies the calculation. The NPR basis is defined in terms of the quark bilinears:

$$\begin{aligned}SS(x) &= (\overline{u}(x)d(x))(\overline{u}(x)d(x)), \\ PP(x) &= (\overline{u}(x)\gamma_5 d(x))(\overline{u}(x)\gamma_5 d(x)), \\ VV(x) &= (\overline{u}(x)\gamma_\mu d(x))(\overline{u}(x)\gamma^\mu d(x)), \\ AA(x) &= (\overline{u}(x)\gamma_\mu\gamma_5 d(x))(\overline{u}(x)\gamma^\mu\gamma_5 d(x)), \\ TT(x) &= \sum_{\mu<\nu}(\overline{u}(x)\gamma_\mu\gamma_\nu d(x))(\overline{u}(x)\gamma^\mu\gamma^\nu d(x)),\end{aligned} \tag{5.38}$$

as

$$\begin{pmatrix} Q_1(x) \\ Q_2(x) \\ Q_3(x) \\ Q_4(x) \\ Q_5(x) \end{pmatrix} \equiv \begin{pmatrix} VV(x) + AA(x) \\ VV(x) - AA(x) \\ SS(x) - PP(x) \\ SS(x) + PP(x) \\ TT(x) \end{pmatrix}. \tag{5.39}$$

This basis is related to the positive-parity projection of the BSM basis, Eq. (5.12), as

$$\begin{pmatrix} Q_1(x) \\ Q_2(x) \\ Q_3(x) \\ Q_4(x) \\ Q_5(x) \end{pmatrix} = \begin{pmatrix} 0 & 0 & 2 & 0 & 0 \\ 4 & 0 & 0 & 0 & 0 \\ 0 & 0 & 0 & -2 & 0 \\ 0 & 2 & 0 & 0 & 0 \\ 0 & 2 & 0 & 0 & 4 \end{pmatrix} \begin{pmatrix} \mathcal{O}_1(x) \\ \mathcal{O}_2(x) \\ \mathcal{O}_3(x) \\ \mathcal{O}_{1'}(x) \\ \mathcal{O}_{2'}(x) \end{pmatrix}. \tag{5.40}$$

The space spanned by $\{Q_n(x)\}$ splits into three irreducible subspaces under chiral symmetry, with bases $\{Q_1(x)\}$, $\{Q_2(x), Q_3(x)\}$, and $\{Q_4(x), Q_5(x)\}$. As both the $\overline{\text{MS}}$ and RIγ schemes obey chiral symmetry, the renormalization coefficients $\mathcal{Z}_{nm}^{\overline{\text{MS}};Q}(\mu^2; a)$ and $\mathcal{Z}_{nm}^{\text{RI}\gamma;Q}(\mu^2; a)$, which satisfy analogous equations to Eqs. (5.36) and (5.37), each factorize into a direct sum of three block diagonal matrices, each of which spans an irreducible subspace. This is particularly notable for the domain-wall ensembles (Table 5.2), as they have approximate chiral symmetry. For the Wilson-Clover ensemble (Table 5.4), one expects mixing between the different irreducible chiral subspaces because the ensemble does not respect chiral symmetry.

One can likewise define a NPR basis $\{\mathcal{W}_p^\mu\}$ for the vector operators in terms of the vector bilinears

$$\begin{aligned} V^\mu S(x) &\equiv (\overline{u}(x)\gamma^\mu d(x))[\overline{u}(x)d(x)] \\ A^\mu P(x) &\equiv (\overline{u}(x)\gamma^\mu\gamma_5 d(x))[\overline{u}(x)\gamma_5 d(x)] \\ T^{\mu\nu}V^\nu(x) &\equiv (\overline{u}(x)\gamma^\mu\gamma^\nu d(x))[\overline{u}(x)\gamma^\nu d(x)] \\ i\epsilon^{\mu\nu\alpha\beta}A^\nu T^{\alpha\beta}(x) &\equiv i\epsilon^{\mu\nu\alpha\beta}(\overline{u}(x)\gamma^\nu\gamma_5 d(x))[\overline{u}(x)\gamma^\alpha\gamma^\beta d(x)]. \end{aligned} \tag{5.41}$$

as

$$\begin{pmatrix} \mathcal{W}_1^\mu(x) \\ \mathcal{W}_2^\mu(x) \\ \mathcal{W}_3^\mu(x) \\ \mathcal{W}_4^\mu(x) \end{pmatrix} \equiv \begin{pmatrix} V^\mu S(x) - A^\mu P(x) \\ V^\mu S(x) + A^\mu P(x) \\ \frac{i}{2}\epsilon^{\mu\nu\alpha\beta} A^\nu T^{\alpha\beta}(x) + T^{\mu\nu} V^\nu(x) \\ \frac{i}{2}\epsilon^{\mu\nu\alpha\beta} A^\nu T^{\alpha\beta}(x) - T^{\mu\nu} V^\nu(x) \end{pmatrix}. \tag{5.42}$$

Color and Dirac Fierz identities (Appendix D) allow the BSM basis of vector operators to be rewritten as linear combinations of the NPR basis,

$$\begin{pmatrix} \mathcal{W}_1^\mu(x) \\ \mathcal{W}_2^\mu(x) \\ \mathcal{W}_3^\mu(x) \\ \mathcal{W}_4^\mu(x) \end{pmatrix} = \begin{pmatrix} \frac{1}{2} & 0 & 0 & 0 \\ 0 & \frac{1}{2} & 0 & 0 \\ \frac{1}{4} & 0 & \frac{1}{4} & 0 \\ 0 & \frac{1}{4} & 0 & \frac{1}{4} \end{pmatrix} \begin{pmatrix} \mathcal{V}_1^\mu(x) \\ \mathcal{V}_2^\mu(x) \\ \mathcal{V}_{1'}^\mu(x) \\ \mathcal{V}_{2'}^\mu(x) \end{pmatrix}. \tag{5.43}$$

The space of vector operators splits into two irreducible subspaces under chiral symmetry, with bases $\{\mathcal{W}_1^\mu(x), \mathcal{W}_3^\mu(x)\}$ and $\{\mathcal{W}_2^\mu(x), \mathcal{W}_4^\mu(x)\}$. As in the scalar operator case, this implies that $\mathcal{Z}_{pq}^{\overline{\text{MS}};\mathcal{W}}(\mu^2; a)$ and $\mathcal{Z}_{pq}^{\text{RI}\gamma;\mathcal{W}}(\mu^2; a)$ will factor as a direct sum of two 2×2 matrices, each spanning one irreducible subspace. For ease of notation, let $\{\mathcal{H}_q\}_{q=1}^9$ denote the set of NPR basis operators,

$$\{\mathcal{H}_q\}_{q=1}^9 = \{Q_1, Q_2, Q_3, Q_4, Q_5, \mathcal{W}_1, \mathcal{W}_2, \mathcal{W}_3, \mathcal{W}_4\} \tag{5.44}$$

where the vector index on $\mathcal{W}_p$ is suppressed. This is the equivalent definition to the BSM basis $\{H_i\}_{i=1}^9$, presented in Eq. (5.29), for the NPR basis.

To renormalize the NPR basis operators, the four-point functions

$$\begin{aligned}(G_q)_{abcd}^{\alpha\beta\gamma\delta}(q; a, m_\ell) \equiv \frac{1}{V} \sum_x \sum_{x_1,\ldots,x_4} & e^{i(p_1\cdot x_1 - p_2\cdot x_2 + p_1\cdot x_3 - p_2\cdot x_4 + 2q\cdot x)} \\ & \times \langle 0 | \overline{d}_d^\delta(x_4) u_c^\gamma(x_3) \mathcal{H}_q(x) \overline{d}_b^\beta(x_2) u_a^\alpha(x_1) | 0 \rangle \end{aligned} \tag{5.45}$$

are computed on each ensemble, where $V = L^3 \times T$ is the lattice volume and $q = p_2 - p_1$. Latin letters a, b, c, d denote color indices, while Greek letters $\alpha, \beta, \gamma, \delta$ denote Dirac indices. All correlation functions used for the renormalization are computed in the Landau gauge with momentum sources [219] using ten configurations for each ensemble, as the V^2 averaging from the momentum sources significantly reduces noise.

The momenta are chosen subject to the symmetric constraint,

$$p_1^2 = p_2^2 = q^2 = \mu^2, \tag{5.46}$$

with the particular choice

$$p_1 = \frac{2\pi}{aL}(-j, 0, j, 0) \qquad\qquad p_2 = \frac{2\pi}{aL}(0, j, j, 0), \tag{5.47}$$

with $q = p_2 - p_1$ and $j \in \mathbb{Z}$. The kinematic configuration corresponding to $G_n(q; a, m_\ell)$ is depicted in Fig. (5.12). Note that with this choice of momentum, each value of q corresponds to a unique value of p_1 and p_2. Hence, functions of (p_1, p_2, q) are labeled as functions of q for conciseness. The four-point functions are amputated,

$$(\Lambda_q)^{\alpha\beta\gamma\delta}_{abcd}(q) \equiv (S^{-1})^{\alpha\alpha'}_{aa'}(p_1)(S^{-1})^{\gamma\gamma'}_{cc'}(p_1)(G_q)^{\alpha'\beta'\gamma'\delta'}_{a'b'c'd'}(q)(S^{-1})^{\beta'\beta}_{b'b}(p_2)(S^{-1})^{\delta'\delta}_{d'd}(p_2), \tag{5.48}$$

where

$$S(p; a, m_\ell) = \frac{1}{V}\sum_{x,y} e^{ip\cdot(x-y)}\langle 0|q(x)\overline{q}(y)|0\rangle \tag{5.49}$$

is the Landau-gauge momentum-projected quark propagator. The (a, m_ℓ) dependence of $\Lambda_n(q)$, $G_n(q)$, and $S(p)$ has been suppressed in Eq. (5.48) for clarity.

Projectors $(\mathcal{P}_q)^{\beta\alpha\delta\gamma}_{badc}$ are introduced to project $(\Lambda_r)^{\alpha\beta\gamma\delta}_{abcd}$ onto the NPR basis for RIγ to yield a matrix of projected four-point functions with components

$$\mathcal{F}_{rq}(q; a, m_\ell) \equiv (\mathcal{P}_q)^{\beta\alpha;\delta\gamma}_{ba;dc}(\Lambda_r)^{\alpha\beta;\gamma\delta}_{ab;cd}(q; a, m_\ell). \tag{5.50}$$

The projection matrix splits as a direct sum,

$$\mathcal{P} = P^{(Q)} \oplus P^{(\mathcal{W})}, \tag{5.51}$$

where $P^{(Q)}_{mn}$ and $P^{(\mathcal{W})}_{qp}$ are respectively a 5×5 and 4×4 projection matrix for the scalar and vector NPR bases. This is because these operator bases do not mix under renormalization; in other words, the projectors for the scalar and vector bases may be written separately, and these bases are treated independently. This likewise allows $\mathcal{F}$ to be written as a direct sum,

$$\mathcal{F} = F^{(Q)} \oplus F^{(\mathcal{W})}, \tag{5.52}$$

where $F^{(Q)}$, $F^{(\mathcal{W})}$ are the matrix of projections for the scalar and vector NPR operator

bases. It is also useful to introduce the matrix of tree-level projected vertex functions $\mathcal{F}^{(\text{tree})} = F^{(Q;\,\text{tree})} \oplus F^{(\mathcal{W};\,\text{tree})} = \mathcal{P}\Lambda^{(\text{tree})}$, where $\Lambda^{(\text{tree})}$ are the tree-level vertex functions for the operators $\mathcal{H}$, which will be required to state the renormalization condition.

The scalar projectors P^Q and the tree-level projections $F^{(Q;\,\text{tree})}$ are given in Ref. [212]. For the vector operators, the projectors $P^{(\mathcal{W})}$ and tree-level values $F^{(\mathcal{W})}$ have not been previously computed. In the (γ^μ, γ^μ) scheme,

$$\begin{aligned}
\left(P^{(\mathcal{W})}_{1,\,\mu}\right)^{\beta\alpha;\sigma\gamma}_{ba;dc} &= \gamma_\mu^{\beta\alpha}\delta^{\sigma\gamma}\delta^{ba}\delta^{dc} \\
\left(P^{(\mathcal{W})}_{2,\,\mu}\right)^{\beta\alpha;\sigma\gamma}_{ba;dc} &= (\gamma_\mu\gamma_5)^{\beta\alpha}\gamma_5^{\sigma\gamma}\delta^{ba}\delta^{dc} \\
\left(P^{(\mathcal{W})}_{3,\,\mu}\right)^{\beta\alpha;\sigma\gamma}_{ba;dc} &= \sum_\nu (\gamma_\mu\gamma_\nu)^{\beta\alpha}\gamma_\nu^{\sigma\gamma}\delta^{ba}\delta^{dc} \\
\left(P^{(\mathcal{W})}_{4,\,\mu}\right)^{\beta\alpha;\sigma\gamma}_{ba;dc} &= \epsilon^{\mu\nu\zeta\eta}(\gamma_\nu\gamma_5)^{\beta\alpha}(\gamma_\zeta\gamma_\eta)^{\sigma\gamma}\delta^{ba}\delta^{dc}
\end{aligned} \tag{5.53}$$

and,

$$\begin{aligned}
\left(\Lambda^{(\text{tree};\,\mathcal{W})}_{1,\,\mu}\right)^{\alpha\beta;\gamma\sigma}_{ab;cd} &= 2\left[\gamma_\mu^{\alpha\beta}\delta^{\gamma\sigma} - (\gamma_\mu)^{\alpha\sigma}\delta^{\beta\gamma}\right]\delta^{ab}\delta^{cd} \\
\left(\Lambda^{(\text{tree};\,\mathcal{W})}_{2,\,\mu}\right)^{\alpha\beta;\gamma\sigma}_{ab;cd} &= 2\left[(\gamma_\mu\gamma_5)^{\alpha\beta}\gamma_5^{\gamma\sigma} - (\gamma_\mu\gamma_5)^{\alpha\sigma}\gamma_5^{\beta\gamma}\right]\delta^{ab}\delta^{cd} \\
\left(\Lambda^{(\text{tree};\,\mathcal{W})}_{3,\,\mu}\right)^{\alpha\beta;\gamma\sigma}_{ab;cd} &= 2\sum_\nu\left[(\gamma_\mu\gamma_\nu)^{\alpha\beta}\gamma_\nu^{\gamma\sigma} - (\gamma_\mu\gamma_\nu)^{\alpha\sigma}\gamma_\nu^{\beta\gamma}\right]\delta^{ab}\delta^{cd} \\
\left(\Lambda^{(\text{tree};\,\mathcal{W})}_{4,\,\mu}\right)^{\alpha\beta;\gamma\sigma}_{ab;cd} &= 2\,\epsilon^{\mu\nu\zeta\eta}\left[(\gamma_\nu\gamma_5)^{\alpha\beta}(\gamma_\zeta\gamma_\eta)^{\gamma\sigma} - (\gamma_\nu\gamma_5)^{\alpha\sigma}(\gamma_\zeta\gamma_\eta)^{\beta\gamma}\right]\delta^{ab}\delta^{cd}.
\end{aligned} \tag{5.54}$$

The remaining quantities that are computed non-perturbatively on each ensemble (Tables 5.2 and 5.4) are the RIγ quark-field renormalization

$$\left(\frac{\mathcal{Z}_q^{\text{RI}\gamma}}{\mathcal{Z}_V}\right)(\mu^2; a, m_\ell)\Big|_{q^2=\mu^2} = \frac{1}{48}\text{Tr}[\gamma_\mu\Lambda_V^\mu(q)], \tag{5.55}$$

and the vector and axial-vector renormalizations, $\mathcal{Z}_V(\mu^2; a, m_\ell)$ and $\mathcal{Z}_A(\mu^2; a, m_\ell)$, whose computation is described in Appendix H. Here $\Lambda_V^\mu(q) = S^{-1}(p_1)G_V^\mu(q)S^{-1}(p_2)$ is the amputated vector three-point function, where

$$G_V^\mu(q; a, m_\ell) = \frac{1}{V}\sum_{x,x_1,x_2} e^{i(p_1\cdot x_1 - p_2\cdot x_2 + q\cdot x)}\langle 0|u(x_1)V^\mu(x)\overline{d}(x_2)|0\rangle \tag{5.56}$$

is the vector three-point function, with $V^\mu(x) = \overline{u}(x)\gamma^\mu d(x)$ the vector-current.

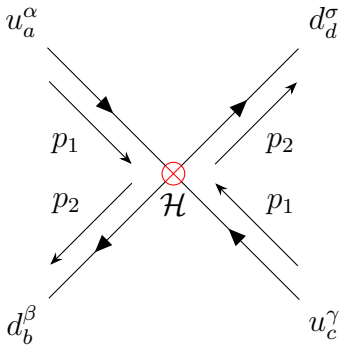

Figure 5.12. Kinematics for operator renormalization. The red crossed circle denotes the operator $\mathcal{H}$, which injects momentum $2q$ into the vertex, while the solid lines denote up quarks, with momentum p_1 into the vertex, and down quarks, with momentum p_2 out of the vertex. The momenta are chosen subject to the symmetric constraint, Eq. (5.46).

The renormalization coefficients for the $\pi^- \to \pi^+ e^- e^-$ calculation are defined in the chiral limit at fixed lattice spacing. In contrast, the renormalization coefficients for the $n^0 n^0 \to p^+ p^+ e^- e^-$ calculation are defined at fixed quark mass and fixed lattice spacing. This is because the computation was performed on multiple ensembles for each of the two lattice spacings ($a = 0.11$ fm, $a = 0.08$ fm) that the $\pi^- \to \pi^+ e^- e^-$ calculation was performed on, while for the $n^0 n^0 \to p^+ p^+ e^- e^-$ calculation, only one ensemble in total was used.

For the $\pi^- \to \pi^+ e^- e^-$ calculation, the quantities $Z \in \{\mathcal{Z}_q^{\mathrm{RI}\gamma}/\mathcal{Z}_V, F_{nm}\}$ display mild dependence on quark mass, and are extrapolated to the chiral limit via a joint fit over ensembles with different masses to the model

$$Z(\mu^2; a, m_\ell) = Z(\mu^2; a) + \tilde{Z}(\mu^2; a) m_\ell \tag{5.57}$$

where $Z(\mu^2; a)$ and $\tilde{Z}(\mu^2; a)$ are fit coefficients, and $Z(\mu^2; a)$ is understood as the chiral limit of $Z(\mu^2; a, m_\ell)$. Correlations between $\mathcal{Z}_q^{\mathrm{RI}\gamma}/\mathcal{Z}_V$ and F_{nm} on each ensemble are retained in the fits, and the covariance matrix is block-diagonal as data from different ensembles is uncorrelated. Fitted values of $Z(\mu^2; a)$ are statistically consistent when a constant model $Z(\mu^2; a, m_\ell) = Z(\mu^2; a)$ is used in place of the linear model of Eq. (5.57). The full set of extrapolations for $(\mathcal{Z}_q^{\mathrm{RI}\gamma}/\mathcal{Z}_V)(\mu^2; a)$ and $F_{mn}(q; a)$ for both the $a = 0.11$ fm and $a = 0.08$ fm ensembles is shown in Appendix I.

With the definitions above, the NPR-basis renormalization coefficients in the RIγ

scheme can be computed as

$$\frac{\mathcal{Z}_{qr}^{\mathrm{RI}\gamma;\,\mathcal{H}}}{\mathcal{Z}_V^2}(\mu^2;a)\bigg|_{\mathrm{sym}} = \left(\frac{\mathcal{Z}_q^{\mathrm{RI}\gamma}(\mu^2;a)}{\mathcal{Z}_V}\right)^2 \left[\mathcal{F}_{qs}^{(\mathrm{tree})}\mathcal{F}_{sr}^{-1}(q;a)\right] \tag{5.58}$$

where the notation $|_{\mathrm{sym}}$ denotes evaluation at the symmetric kinematic point, Eq. (5.46). Note that for the $n^0n^0 \to p^+p^+e^-e^-$ renormalization, there is an additional dependence of $\mathcal{Z}_{qr}^{\mathrm{RI}\gamma;\mathcal{H}}$ and $\mathcal{Z}_q^{\mathrm{RI}\gamma}(\mu^2;a)$ on the quark mass am_q which is suppressed in Eq. (5.58) for clarity.

The renormalization coefficients must be perturbatively matched to $\overline{\mathrm{MS}}$. For the vector operators for $n^0n^0 \to p^+p^+e^-e^-$, the computation of the anomalous dimension $\gamma^{\mathrm{RI}\gamma;\,\mathcal{V}}$ and matching factor $\mathcal{C}_{kj}^{\overline{\mathrm{MS}}\leftarrow\mathrm{RI}\gamma;\mathcal{V}}(\mu^2,a)$ is still ongoing. Hence, the perturbative matching will be presented only for the scalar operators $\{Q_n\}$. The vector operator matching will follow an identical procedure once $\gamma^{\mathrm{RI}\gamma;\,\mathcal{V}}$ and $\mathcal{C}_{kj}^{\overline{\mathrm{MS}}\leftarrow\mathrm{RI}\gamma;\mathcal{V}}(\mu^2,a)$ are computed. The renormalization coefficients $\mathcal{Z}_{nm}^{\mathrm{RI}\gamma;Q}(\mu^2;a)/\mathcal{Z}_V^2$ are only computed non-perturbatively at scales $\mu_j = \frac{2\pi}{aL}||(j,j,0,0)||$ corresponding to the lattice momenta given in Eq. (5.47), where $||\cdot||$ denotes the Euclidean norm of the lattice vector. However, the matching coefficients $\mathcal{C}_{nm}^{\overline{\mathrm{MS}}\leftarrow\mathrm{RI}\gamma;Q}(\mu^2,a)$ in Eq. (5.36) have been computed at $\mu = M \equiv 3$ GeV [212, 218], and therefore the renormalization coefficients must be perturbatively evolved from μ_j to M. To minimize the artifacts from truncating the perturbative expansion of the matching coefficients, the closest scale μ_{j*} to M which lies in the Rome-Southampton window [220, 221],

$$\Lambda_{\mathrm{QCD}} \ll \mu_{j*} \ll \left(\frac{\pi}{a}\right), \tag{5.59}$$

which also satisfies $\mu_{j*} \leq M$ to minimize discretization artifacts, is chosen as a starting point for perturbative evolution to M. In practice, the scale μ_4 is used for renormalization at both $a = 0.11$ fm and $a = 0.08$ fm, as this is the nearest available scale to M satisfying these constraints, and μ_5 is used for the clover ensemble. Numerically, these scales are $\mu_4 = 2.64\,\mathrm{GeV}$ for the $a = 0.11$ fm ensemble, $\mu_4 = 2.65$ GeV for the $a = 0.08$ fm ensemble, and $\mu_5 = 1.88$ GeV for the clover ensemble. Scale evolution from μ_{j*} to M is performed by integrating the evolution equation,

$$\begin{aligned}\left(\frac{\mathcal{Z}_{nm}^{\mathrm{RI}\gamma;Q}}{\mathcal{Z}_V^2}\right)(M;a) &= \left(\frac{\mathcal{Z}_{nm}^{\mathrm{RI}\gamma;Q}}{\mathcal{Z}_V^2}\right)(\mu_{j*};a) \\ &+ \int_{\mu_{j*}}^{M}\frac{d\mu}{\mu}\gamma_{np}^{\mathrm{RI}\gamma;Q}(\alpha_s(\mu))\left(\frac{\mathcal{Z}_{pm}^{\mathrm{RI}\gamma;Q}}{\mathcal{Z}_V^2}(\mu;a)\right),\end{aligned} \tag{5.60}$$

where the NPR basis anomalous dimensions $\gamma_{nm}^{\mathrm{RI}\gamma;Q}(\alpha_s(\mu))$ have been computed at two-loop order in $\alpha_s(\mu)$ in Ref. [222]. Statistically consistent results for $(\mathcal{Z}_{nm}^{\mathrm{RI}\gamma;Q}/\mathcal{Z}_V^2)(M)$ are obtained when μ_3 is instead used as μ_{j*} in Eq. (5.60) for the 24I and 32I ensembles, and when μ_4 is used for μ_{j*} for the clover ensemble.

The results for the NPR basis renormalization coefficients, computed at $\mu = 3$ GeV in $\overline{\mathrm{MS}}$, are shown in Tables 5.7–5.9. The components corresponding to transitions between operators in different irreducible chiral representations are consistent with $|\mathcal{Z}_{nm}^{\overline{\mathrm{MS}};Q}/\mathcal{Z}_V^2| < 10^{-5}$ for the 24I and 32I results, and thus not shown. This is expected since all five ensembles used in the extrapolations were domain-wall fermions with approximate chiral symmetry. For the $n^0n^0 \to p^+p^+e^-e^-$ renormalization, non-chirally suppressed renormalization coefficients were not consistent with zero and are shown in Figure 5.9. This is also expected, as the fermion action does not have approximate chiral symmetry and has heavy quarks ($m_\pi \approx 806\,\mathrm{MeV}$). The renormalization coefficients for the 24I and 32I geometries have been computed for the NPR operator basis (Eq. (5.39)) in Ref. [212] using s quarks in place of d quarks. The results in Ref. [212] agree with Table 5.7 and 5.8 at the percent level, and deviations between the results are likely due to perturbative truncation errors, as Ref. [212] used non-perturbative step-scaling [220, 221].

Ensemble	$\mathcal{Z}_{11}/\mathcal{Z}_V^2$	$\mathcal{Z}_{22}/\mathcal{Z}_V^2$	$\mathcal{Z}_{33}/\mathcal{Z}_V^2$	$\mathcal{Z}_{44}/\mathcal{Z}_V^2$	$\mathcal{Z}_{55}/\mathcal{Z}_V^2$
24I	0.90746(43)	1.04052(14)	0.95333(75)	0.91775(71)	1.13952(35)
32I	0.92625(51)	1.03941(31)	0.85916(82)	0.84035(87)	1.19362(57)
Clover	1.05286(50)	1.14953(86)	1.01262(59)	1.23365(87)	1.13916(11)

Table 5.7. Diagonal $\overline{\mathrm{MS}}$ renormalization coefficients for the scalar NPR basis $\{Q_n\}$, computed with the RI/sMOM renormalization condition, Eq. (5.58), and perturbatively matched at scale 3 GeV. The renormalization coefficients for the 24I and 32I ensembles are defined at finite lattice spacing in the chiral limit (extrapolation shown in Appendix (I)) for the $\pi^- \to \pi^+e^-e^-$ calculation. In contrast, the renormalization for the "Clover" ensemble is defined at finite lattice spacing and quark mass and used for the $n^0n^0 \to p^+p^+e^-e^-$ calculation.

Ensemble	$\mathcal{Z}_{23}/\mathcal{Z}_V^2$	$\mathcal{Z}_{32}/\mathcal{Z}_V^2$	$\mathcal{Z}_{45}/\mathcal{Z}_V^2$	$\mathcal{Z}_{54}/\mathcal{Z}_V^2$
24I	0.26154(56)	0.05286(12)	-0.02367(13)	-0.28140(66)
32I	0.27661(50)	0.04203(67)	-0.01061(40)	-0.29928(71)
Clover	$8.73722(66) \times 10^{-3}$	-0.17768(41)	$9.17662(12) \times 10^{-3}$	0.0236114(20)

Table 5.8. Same as Figure 5.7, but for the chirally allowed, off-diagonal $\overline{\mathrm{MS}}$ renormalization coefficients for the scalar NPR basis $\{Q_n\}$ at 3 GeV.

$\mathcal{Z}_{12}/\mathcal{Z}_V^2$	$\mathcal{Z}_{13}/\mathcal{Z}_V^2$	$\mathcal{Z}_{14}/\mathcal{Z}_V^2$	$\mathcal{Z}_{15}/\mathcal{Z}_V^2$
-0.0531075(43)	-0.0301354(27)	-0.0229017(46)	0.00574317(11)
$\mathcal{Z}_{21}/\mathcal{Z}_V^2$	$\mathcal{Z}_{24}/\mathcal{Z}_V^2$	$\mathcal{Z}_{25}/\mathcal{Z}_V^2$	$\mathcal{Z}_{31}/\mathcal{Z}_V^2$
$9.58158(80) \times 10^{-3}$	-0.121115(95)	-0.0363164(61)	-0.151727(13)
$\mathcal{Z}_{34}/\mathcal{Z}_V^2$	$\mathcal{Z}_{35}/\mathcal{Z}_V^2$	$\mathcal{Z}_{41}/\mathcal{Z}_V^2$	$\mathcal{Z}_{42}/\mathcal{Z}_V^2$
0.0123607(13)	0.0402692(29)	-0.0855981(83)	-0.17768(14)
$\mathcal{Z}_{43}/\mathcal{Z}_V^2$	$\mathcal{Z}_{51}/\mathcal{Z}_V^2$	$\mathcal{Z}_{52}/\mathcal{Z}_V^2$	$\mathcal{Z}_{53}/\mathcal{Z}_V^2$
-0.0122713(12)	$2.69506(82) \times 10^{-3}$	$9.63359(40) \times 10^{-3}$	$4.61145(34) \times 10^{-3}$

Table 5.9. Chirally disallowed, off-diagonal $\overline{\text{MS}}$ renormalization coefficients for the scalar NPR basis $\{Q_n\}$ at 3 GeV for the "clover" ensemble (Table 5.4) used in the $n^0n^0 \to p^+p^+e^-e^-$ calculation. Note that in the 24I and 32I renormalization coefficient calculation, these matrix elements were all consistent with zero, which indicates approximate chiral symmetry.

The NPR basis renormalization coefficients are converted to the BSM basis using the change of basis matrix, Eq. (5.40), and combined with the bare matrix elements to form renormalized matrix elements,

$$O_k(m_\pi, f_\pi, a, L) \equiv \langle \pi^+ | \mathcal{O}_k^{\overline{\text{MS}}}(\boldsymbol{p} = \boldsymbol{0}) | \pi^- \rangle (m_\pi, f_\pi, a, L). \tag{5.61}$$

On a given ensemble, the renormalization coefficients and bare matrix elements are computed on different configurations, as the former are only computed on a subset of 10 configurations used to compute the matrix elements on each ensemble. As such, they are combined as an uncorrelated product, and their errors are added in quadrature. Table 5.3 shows the renormalized matrix elements for the $\pi^- \to \pi^+e^-e^-$ calculation.

5.6 The long-distance $n^0n^0 \to p^+p^+e^-e^-$ amplitude

5.6.1 LGT methodology for long-distance $0\nu\beta\beta$

As discussed in Section 5.2.1, the non-perturbative dynamics of the long-distance decay are encoded in the amplitude $\mathcal{A}^{i\to f}$ defined in Eq. (5.10). To extract $\mathcal{A}^{i\to f}$ for the initial state $|i\rangle = |nn\rangle$ and the final state $|f\rangle = |pp\rangle$, one computes the four-point

function

$$\mathcal{C}_4^{i\to f}(t_{\text{snk}}, t, t_{\text{src}}) \equiv \int d^3\boldsymbol{x}_f\, d^3\boldsymbol{x}\, d^3\boldsymbol{y}\, D(x-y)\langle 0|\chi_f(\boldsymbol{x}_f, t_f) j_\mu(x) j_\mu(y) \chi_i^\dagger(\mathbf{0}, t_i)|0\rangle. \tag{5.62}$$

Here χ_i and χ_f are interpolators that excite the dineutron and diproton, respectively (Eq. (5.28)). Translation invariance implies that the correlators only depend on the relative time separations,

$$t_{\text{src}} \equiv \min\{t_x, t_y\} - t_i \qquad t \equiv t_x - t_y \tag{5.63}$$

$$t_{\text{snk}} \equiv t_f - \max\{t_x, t_y\} \qquad t' \equiv t_f - t_i, \tag{5.64}$$

where $t_{\text{src}}, t_{\text{snk}} > 0$. Note that $t' = t_{\text{src}} + t_{\text{snk}} + |t|$. Each correlator is defined in Euclidean space, projected to zero three-momentum via the integration over spatial coordinates, and accessible through LGT calculations in a compact, discrete space-time.

The spectral decomposition of the matrix element in Eq. (5.62) yields,

$$\begin{aligned}
&\langle 0|\chi_f(\boldsymbol{x}_f, t_f) j_\mu(\boldsymbol{x}, t_x) j^\mu(\boldsymbol{y}, t_y) \chi_i^\dagger(\mathbf{0}, t_i)|0\rangle = \\
&\qquad \int \frac{d^3\boldsymbol{p}_i}{(2\pi)^3} \frac{d^3\boldsymbol{p}_f}{(2\pi)^3} \frac{\langle 0|\mathcal{O}_f(\boldsymbol{x}_f)|N_f(\boldsymbol{p}_f)\rangle \langle N_i(\boldsymbol{p}_i)|\mathcal{O}_i^\dagger(\mathbf{0})|0\rangle}{2E_0} e^{-E_0(t_f - t_i)} \\
&\qquad \times \sum_n \frac{\langle N_f(\boldsymbol{p}_f)|J_\mu(\boldsymbol{x})|n\rangle \langle n|J^\mu(\boldsymbol{y})|N_i(\boldsymbol{p}_i)\rangle}{(2E_0)(2\widetilde{E}_n)} \\
&\qquad \times e^{-\Delta\widetilde{E}_{n0}|t|} \left(1 + Ae^{-\Delta E_{10} t_{\text{src}}} + Be^{-\Delta E_{10} t_{\text{snk}}} + Ce^{-\Delta E_{10}(t_{\text{snk}} + t_{\text{src}})} + \cdots\right),
\end{aligned} \tag{5.65}$$

where $\Delta E_n \equiv E_n - E_0$ is the energy gap between the n^{th} excited state and the ground state excited by the interpolator χ_i, and $\Delta\tilde{E}_n \equiv \tilde{E}_n - E_0$ is the gap between the n^{th} excited state of the intermediate hadronic system and the ground state. The coefficients A, B, and C are expressible in terms of matrix elements of excited states of the system, and the explicit form of these coefficients is not required for the calculation.

To extract the amplitude $\mathcal{A}^{i\to f}$ (Eq. (5.10)), consider the spectral decomposition

of the two-point function $\mathcal{C}_2(t)$, defined in Eq. (5.30),

$$\langle \chi_i(\boldsymbol{x}_f, t_f)\chi_i^\dagger(\mathbf{0}, t_i)\rangle = \int \frac{d^3\boldsymbol{p}_i}{(2\pi)^3} \frac{\langle 0|\chi_i(\boldsymbol{x}_f)|N_i(\boldsymbol{p}_i)\rangle\langle N_i(\boldsymbol{p}_i)|\chi_i^\dagger(\mathbf{0})|0\rangle}{2E_0} e^{-E_0(t_f-t_i)}\left(1 + De^{-\Delta E_{10}(t_f-t_i)} + \cdots\right), \tag{5.66}$$

where D is another coefficient constructed from excited-state matrix elements. One constructs the ratio between the four-point function and $\mathcal{C}_2^{nn}(t)$, which has the decomposition,

$$R^{i\to f}(t_{\text{snk}}, t, t_{\text{src}}) \equiv \frac{\mathcal{C}_4^{i\to f}(t_{\text{snk}}, t, t_{\text{src}})}{\mathcal{C}_2^{nn}(t_{\text{snk}} + |t| + t_{\text{src}})} \tag{5.67}$$

$$= \sum_n \frac{\langle f|J_\mu(0)|n\rangle\langle n|J^\mu(0)|i\rangle}{(2E_0)(2\tilde{E}_n)(2|\boldsymbol{q}|)} e^{-(|\boldsymbol{q}|+\Delta\tilde{E}_{n0})|t|}\Big|_{\boldsymbol{q}=-\tilde{\boldsymbol{p}}_n} \left(1 + Ae^{-\Delta E_{10}t_{\text{src}}} + Be^{-\Delta E_{10}t_{\text{snk}}} + Ce^{-\Delta E_{10}(t_{\text{snk}}+t_{\text{src}})} - De^{-\Delta E_{10}t'} + \cdots\right). \tag{5.68}$$

Comparison to the definition of $\mathcal{A}^{i\to f}$ reveals that the large-time limit of $R^{i\to f}(t_{\text{snk}}, t, t_{\text{src}})$ is the desired amplitude,

$$\mathcal{A}^{i\to f} = 2E_0 \int_{-\infty}^{\infty} dt \lim_{\substack{t_{\text{src}}\to\infty \\ t_{\text{snk}}\to\infty}} R^{i\to f}(t_{\text{snk}}, t, t_{\text{src}}). \tag{5.69}$$

These asymptotics are used to extract the amplitude $\mathcal{A}^{i\to f}$ with a LGT calculation.

5.6.2 LGT calculation of long-distance $n^0n^0 \to p^+p^+e^-e^-$

The correlation functions $\mathcal{C}_2^{nn}(t)$ and $\mathcal{C}_4^{i\to f}(t_{\text{snk}}, t, t_{\text{src}})$, Eqs. (5.30, 5.62), are computed on the Wilson-Clover ensemble of Table 5.4 on 12,139 configurations. The two-point function $\mathcal{C}_2^{nn}(t)$ is constructed with a wall source and a point-sink, and the spectral analysis of this correlator is described in the short-distance $n^0n^0 \to p^+p^+e^-e^-$ analysis, Section 5.4. For the four-point function, propagators were constructed from the operator insertion positions x and y, where $\boldsymbol{x}$ and $\boldsymbol{y}$ range over a sparsened spatial grid of 4^3 point sources (a sparsening factor of $32/4 = 8$) on every 8^{th} timeslice on each configuration[5]. On each configuration, 432 quark propagators were computed.

[5] As shown in Ref. [223], sparsening the spatial grid does not change the low-energy spectrum of the theory.

The computational details of the quark propagator computation and the contractions are described in Refs. ([5, 224]). In particular, Anthony Grebe's thesis (Ref. [224]) details the extraordinary computational effort to compute these propagators and contractions. Without many of the optimizations he made (for the computation of the three-point functions described in Section 5.4 as well), this project would realistically not have been feasible from a computational point of view. A total of 576 quark contractions were formed to construct each measurement of $\mathcal{C}_4^{i\to f}(t_{\text{snk}}, t, t_{\text{src}})$, and a heuristic depiction of a single quark contraction is shown in Figure 5.13.

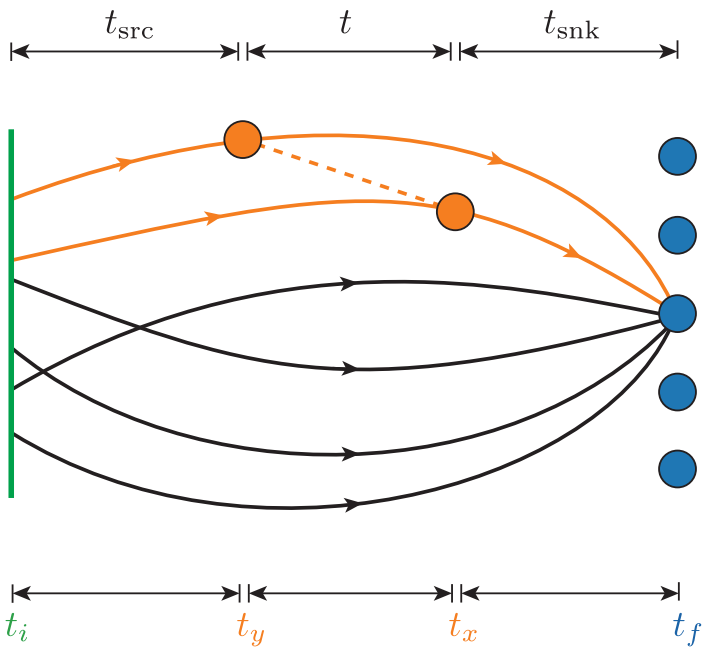

Figure 5.13. Heuristic depiction of the four-point contractions for the long-distance $n^0n^0 \to p^+p^+e^-e^-$ computation. Quark propagators are denoted by solid lines from a zero-momentum wall source with point sinks that are summed over the sparse grid. The interacting quarks for each contraction are denoted in orange, with the current insertions at time t_x and t_y denoted by the orange circles. The orange dashed line denotes the neutrino propagator between the two current insertions (Eq. (5.70)). The blue circles denote the sparse point grid of sinks, and the relevant times of interest (Eq. (5.64)) are explicitly labeled in the diagram.

The scalar propagator used for the neutrino, $S_\phi(x, y)$, is defined in finite-volume

by subtracting the zero-mode out from the propagator,

$$S_\phi(x,y) = \frac{1}{2L^3} \sum_{\boldsymbol{q} \in \frac{2\pi}{L}\mathbb{Z}^3 \setminus \{\mathbf{0}\}}^{|\mathbf{q}| \leq \pi/a} \frac{1}{|\boldsymbol{q}|} e^{i\boldsymbol{q}\cdot(\boldsymbol{x}-\boldsymbol{y})} e^{-|\boldsymbol{q}||t|}. \tag{5.70}$$

The propagator is defined in this way to ease the matching to the nuclear EFT [225]. An advantage of this particular choice of regulator is that all intermediate states in the calculation are now at higher energy than the initial and final hadronic states. In the long-distance $\pi^- \to \pi^+e^-e^-$ calculations [12, 173], degenerate intermediate states caused the four-point function to grow exponentially with operator separation time and had to be removed carefully. This regulation of the scalar propagator with zero-mode subtraction means that this does not apply in this calculation.

The electroweak currents $j^\mu(x)$ that define the four-point function require renormalization. This current is proportional to the difference in a left-handed vector current and a left-handed axial current, which renormalize via the vector renormalization $\mathcal{Z}_V$ and the axial-vector renormalization $\mathcal{Z}_A$, respectively. These renormalization coefficients are given in Table 5.4. This yields the renormalized current,

$$j_\mu^{ren}(x) = \frac{1}{2}\overline{u}(x)\gamma_\mu(\mathcal{Z}_V - \mathcal{Z}_A\gamma_5)d(x), \tag{5.71}$$

which is used in calculations of the four-point function.

To extract $\mathcal{A}^{i\to f}$ from $R(t_{\text{snk}}, t, t_{\text{src}})$, the limit of Eq. (5.68) must be taken carefully to avoid excited-state contamination. A two-step procedure will be followed. First, at fixed operator separations t, the Euclidean time dependence of $R(t_{\text{snk}}, t, t_{\text{src}})$ is modeled as a function of $(t_{\text{snk}}, t_{\text{src}})$ to extract the limit,

$$R^{i\to f}(t) \equiv \lim_{\substack{t_{\text{src}}\to\infty \\ t_{\text{snk}}\to\infty}} R^{i\to f}(t_{\text{snk}}, t, t_{\text{src}}). \tag{5.72}$$

while removing excited-state contamination. Next, $R^{i\to f}(t)$ must be integrated over t (Eq. (5.69)) to evaluate $\mathcal{A}^{i\to f}$. The spectral decomposition of $\mathcal{A}^{i\to f}$ reveals that $R^{i\to f}(t)$ decays as $\sum_{\boldsymbol{q},n} e^{-(|\boldsymbol{q}|+\Delta E_{n0})|t|}$. As shown below, this sum can be well-approximated to the present level of statistical precision by an exponential,

$$R^{i\to f}(t) \approx A^{(R)} e^{-E^{(R)}|t|}, \tag{5.73}$$

where $E^{(R)}$ and $A^{(R)}$ are an effective energy gap and amplitude associated with the asymptotic ratio $R^{i\to f}(t)$. Additional terms from the spectral decomposition will

make this approximation invalid at small temporal separations. However, because these additional excited-state terms cannot be resolved at the current lattice spacing, the integral defining $\mathcal{A}^{i\to f}$ (Eq. (5.69)) can be approximated as,

$$\mathcal{A}^{i\to f} = 2E_0 \int_{-\infty}^{\infty} dt\, R^{i\to f}(t) \approx 4E_0 \frac{A^{(R)}}{E^{(R)}}\,. \tag{5.74}$$

The measurements of $R^{i\to f}(t_{\text{snk}}, t, t_{\text{src}})$ on this ensemble are shown in Figure 5.14 as a function of the separation t between operator insertions (Eq. (5.63)). The dependence of $R^{i\to f}(t_{\text{snk}}, t, t_{\text{src}})$ on t_{snk} is shown through the color-coding of the plot, while its dependence on t_{src} is demonstrated through the data's offset at fixed (t, t_{snk}). Another view of the data is depicted in Figure 5.15, which depicts the ratio data at fixed $t/a = 3$ as t_{snk} and t_{src} are varied.

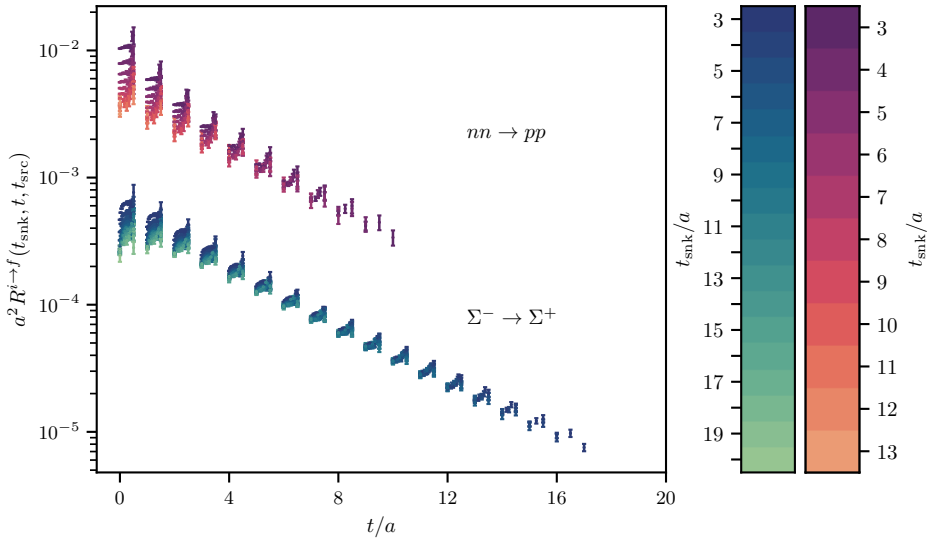

Figure 5.14. The ratio $R^{i\to f}(t_{\text{snk}}, t, t_{\text{src}})$ between the four- and two-point functions, Eq. (5.67), plotted as a function of the separation t (Eq. (5.63)) between the operator insertions. The points are color-coded according to the sink-operator separation t_{snk} as given in the legend. Points at fixed (t, t_{snk}) have been slightly offset proportional to t_{src} to make the dependence of the data on t_{src} more clear. Note that this Figure was taken from Ref. [5], which also computed the long-distance matrix elements for the $\Sigma^- \to \Sigma^+ e^- e^-$ transition, although this work has only described the calculation for $n^0n^0 \to p^+p^+e^-e^-$.

The first stage of fits extracts $R^{i\to f}(t)$ from $R^{i\to f}(t_{\text{snk}}, t, t_{\text{src}})$ by fitting the data to the spectral decomposition of Eq. (5.68). Inspection of the data (Figure 5.14) reveals that there is no statistically significant dependence of $R^{i\to f}(t_{\text{snk}}, t, t_{\text{src}})$ on t_{src}, hence only the terms dependent on t_{snk} in Eq. (5.68) are kept in the model. The model,

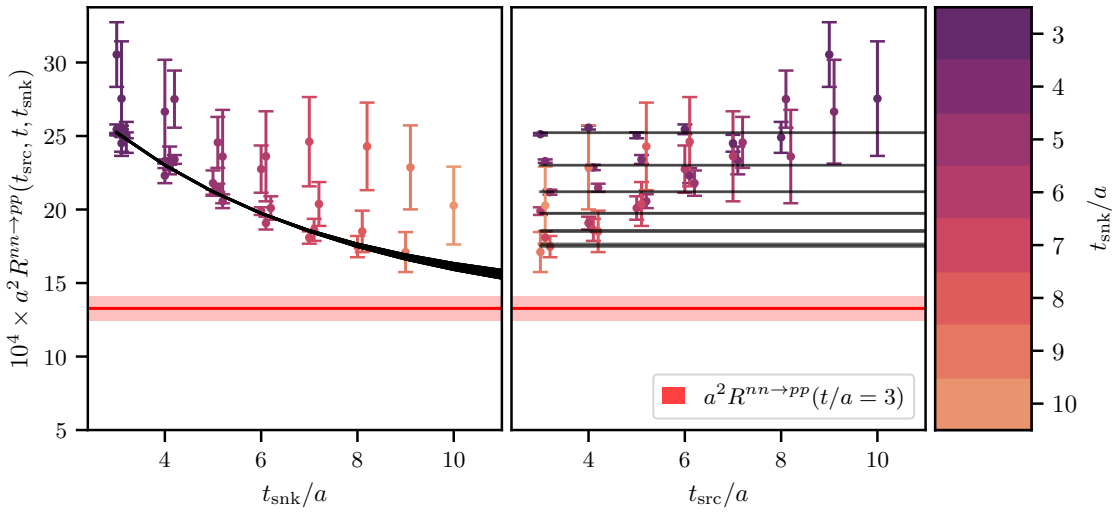

Figure 5.15. The ratio $R^{i\to f}(t_{\rm snk}, t, t_{\rm src})$ (Eq. (5.67)) computed at fixed operator separation $t/a = 3$. The left (right) subplot shows the dependence of $R^{i\to f}(t_{\rm snk}, t, t_{\rm src})$ on the sink-operator (operator-sink) separation $t_{\rm snk}/a$ ($t_{\rm src}$). The data in each panel is identical: to make this clearer, identical points across the two plots have the same color. The black curve shows the result of a correlated fit to the displayed data. In each row, the value of $R^{i\to f}(t)$ determined by the fit (Eq. (5.72)) is depicted by the red horizontal line, which is shared between both plots.

therefore, has two unknown parameters, B and ΔE_{10}. Figure 5.15 shows these fits' results at a single value of $t/a = 3$. The black curves show the best-fit curve from a correlated fit to the data, and the extracted value of $R^{i\to f}(t)$ from $R^{i\to f}(t_{\rm snk}, t, t_{\rm src})$ is shown by the horizontal red line. The χ^2/dof for the joint fit is 1.15, with 72 degrees of freedom, indicating a high-quality fit. This procedure is repeated for all operator separations t, and the result for $R(t)$ is shown in Figure 5.16.

At each t, the stability of the fit is determined by varying the domains of $(t_{\rm snk}, t_{\rm src})$ that the fit is performed over. The minimum values of $t_{\rm snk}$ and $t_{\rm src}$ are varied independently in $\{3, 4, 5, 6\}$, and the resulting values for $R^{i\to f}(t)$ from this variation are depicted as a cluster of colored points in Figure 5.16 at fixed t. Results at fixed t are combined by model averaging with AIC weights (Section 3.5.2), with the final results depicted by the black points in Figure 5.16.

The second stage of fits extracts the amplitude $\mathcal{A}^{i\to f}$ from the ratio $R^{i\to f}(t)$. As the ratio $R^{i\to f}(t)$ decreases linearly on a logarithmic scale (Figure 5.16), the single exponential model (Eq. (5.73)) is expected to describe the data well. Figure 5.17

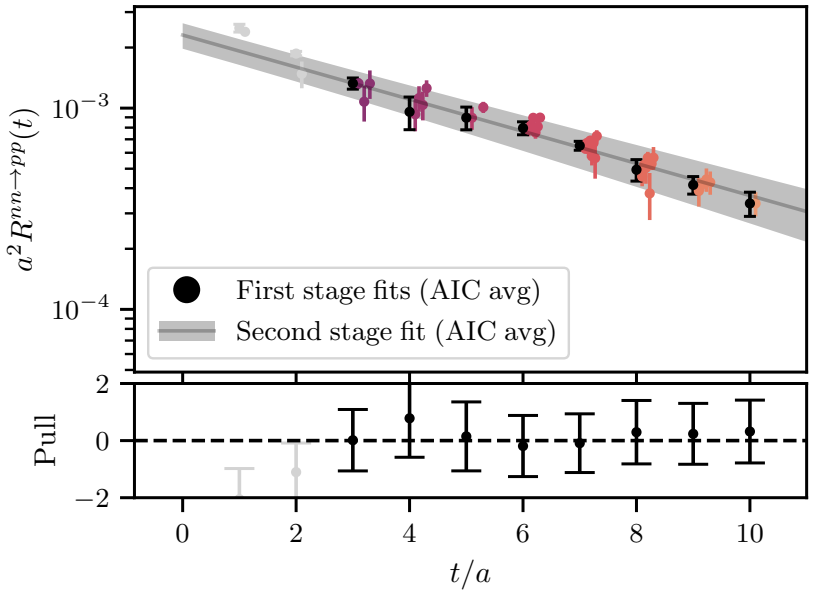

Figure 5.16. The ratio $R^{i\to f}(t)$ (Eq. (5.72)) shown on a logarithmic scale. Each cluster of colored points represents the fit results at the given value of t by varying the minimum t_{src} and t_{snk} of the fit: each point represents a different fit. The results at each fixed t are combined using model averaging with weights based on the AIC to yield the black points. The gray line and error band depict the result of the second stage of fits, which model the dependence of $R^{i\to f}(t)$ on the operator separation t for $t/a \geq 3$ (data for $t/a \leq 2$ appear in light gray and are not included in the second-stage analysis). The bottom panel denotes the difference between the fit and the data in units of the uncertainty of the fit, which is called the pull of the fit at time t.

shows the effective ratios,

$$aE_{\text{eff}}^{(R)}(t) \equiv \ln\left(\frac{R^{i\to f}(t)}{R^{i\to f}(t+a)}\right), \tag{5.75}$$

$$A_{\text{eff}}^{(R)}(t) \equiv R^{i\to f}(t)e^{E_{\text{eff}}^{(R)}(t)\,t}, \tag{5.76}$$

which are defined from the single-exponential model. Both quantities plateau at intermediate times, which indicates that a single exponential well describes the data. The data for $R^{i\to f}(t)$ are fit to Eq. (5.73), varying $t^{\text{min}} \in \{3, 4, \ldots, 7\}$ and $t^{\text{max}} \in \{t^{\text{min}}+3, t^{\text{min}}+4, \ldots, t_{\text{max}}^{\text{max}}\}$ to check for stability, where the variations in t^{max} extend to $t_{\text{max}}^{\text{max}} = 10$. Results are again combined using AIC weights, and the final posterior values for $E^{(R)}$ and $A^{(R)}$ are denoted by the horizontal bands in Figure 5.17. The grey band in Figure 5.16 depicts the results of the fit against the data $R^{i\to t}(t)$.

The integral of Eq. (5.74) can thus be evaluated by using the fit posteriors for $E^{(R)}$ and $A^{(R)}$. The resulting amplitude is,

$$a^2\mathcal{A}^{nn\to pp} = 0.078(16)\,. \tag{5.77}$$

Uncertainties on this result include statistical uncertainties from the Monte Carlo data and systematic uncertainties from the model averaging procedure. They also include uncertainties on the value of $\mathcal{Z}_V$ used (Table 5.4) in the renormalization of the currents j^μ.

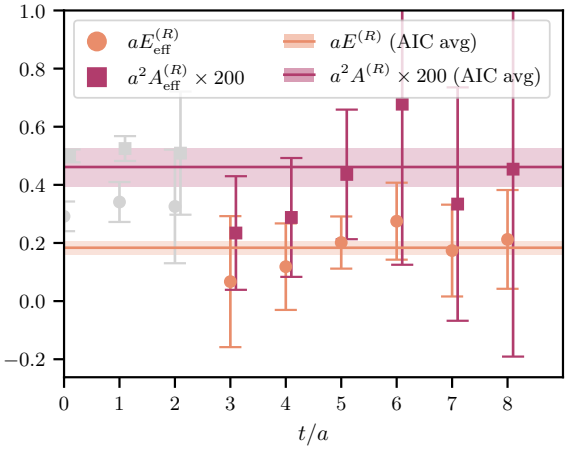

Figure 5.17. Effective energy $E_{\text{eff}}^{(R)}$ and amplitude $A_{\text{eff}}^{(R)}$ from fits to the ratio $R^{nn\to pp}(t)$. The horizontal lines and error bands show the final posterior results from fits to the exponential decay in Eq. (5.73). The amplitudes have been re-scaled by arbitrary factors for ease of visualization.

The determination of the amplitude $a^2\mathcal{A}^{nn\to pp}$ is physically useful as input to nuclear EFT. As discussed in Section 5.2, LGT calculations of $0\nu\beta\beta$ decay matrix elements in phenomenologically relevant nuclei are unfeasible given the factorial increase in computational complexity with the number of quarks in the system. LGT calculations are hence performed in simpler systems and used to extract LECs of nuclear EFTs which can be used to study systems with larger atomic number. The amplitude $a^2\mathcal{A}^{nn\to pp}$ can be studied in pionless EFT ($\not\pi$EFT) [226–228], an EFT that provides a framework to study low-energy nucleon-nucleon interactions by integrating out the pions, which are much heavier than the scale of typical low-energy nuclear processes. The $\not\pi$EFT describes dynamical nucleon fields which interact via contact interactions. The relevant interaction for $0\nu\beta\beta$ decay is the four-nucleon two-electron coupling $g_\nu^{nn}(\mu)$, which describes the strength of the interaction $nn \to ppee$. The matching procedure from the finite-volume, Euclidean space amplitude $a^2\mathcal{A}^{nn\to pp}$ to the infinite-volume, Minkowski space LEC $g_\nu^{nn}(\mu)$ at $m_\pi \approx 800\,\text{MeV}$ is described in Ref. [229] and implemented in Ref. [5].

The matching calculation takes additional input from LGT in the form of the low-lying two-nucleon spectrum and various scattering observables (the scattering length and effective range), which have been computed independently in two ways. The first method constructs asymmetric correlation functions and indicates that the dinucleon is deeply bound on the parameters given in the ensemble used in this work (Table 5.4) [230–233]. Note that at the resulting value of the finite-volume two-nucleon ground state energy determined from these works, $\not\pi$EFT converges poorly when the corresponding values of the scattering length and effective range are used, indicating alternative power counting schemes must be considered to rigorously constrain the LEC $g_\nu^{nn}(\mu)$. The second method constructs symmetric nucleon correlators and uses a variational method to bound the low-lying two-nucleon spectrum [234–236]. These results are consistent with the dinucleon being less deeply bound, or even a weakly attractive but unbound state, at the parameter values on this ensemble. However, the non-linearity in the matching relations between the variational bounds on the low-lying spectrum and the resulting LEC $g_\nu^{nn}(\mu)$ makes matching these results to the EFT difficult as well.

The resulting values for $g_\nu^{nn}(\mu)$ using the results from both of the described methods differ by about a factor of four. Both results have the same order of magnitude as the estimate of $g_\nu^{nn}(\mu)$ computed from a dispersive analysis in Ref. [237]. To better constrain $g_\nu^{nn}(\mu)$ from LGT, the finite-volume two-nucleon spectrum at $m_\pi \approx 800\,\text{MeV}$ and at lighter quark mass must be better constrained, as the dis-

agreement between the two extracted values of $g_\nu^{nn}(\mu)$ indicates uncontrolled systematics in the calculation. Looking towards the future, constraining $a^2\mathcal{A}^{nn\to pp}$ and the finite-volume two-nucleon spectrum closer to the physical quark masses would be the most useful LGT inputs for phenomenological studies of long-distance $0\nu\beta\beta$ decay, as knowledge of g_ν^{nn} at the physical point is essential input for nuclear many-body calculations of $0\nu\beta\beta$ decay. However, the $m_\pi \approx 800\,\text{MeV}$ systems must first be understood in the hopes that resolving the discrepancies in the calculations of the finite-volume spectrum will yield insight into the calculation at smaller values of the quark masses.

5.7 Conclusion

Neutrinoless double β decay is a hypothesized BSM decay that has garnered significant interest in the high-energy and nuclear physics community because of its implications for the nature of the neutrino. In particular, observation of $0\nu\beta\beta$ decay would imply the neutrino is a Majorana particle and that $B-L$ is not a conserved quantum number beyond the Standard Model. Numerous experiments around the world are currently searching for experimental signatures of $0\nu\beta\beta$ decay, with next-generation experiments planned to come online in the coming decade. If $0\nu\beta\beta$ decay is ever observed, the decay and its possible mechanisms must be understood theoretically to link experimental measurements with an underlying theoretical framework. This chapter has detailed the different classes of $0\nu\beta\beta$ decay mechanisms and computed the short-distance contribution to the $\pi^- \to \pi^+ e^- e^-$ transition and the long- and short-distance contributions to the $n^0 n^0 \to p^+ p^+ e^- e^-$ transition.

Lattice gauge theory provides the only framework to compute *ab initio* $0\nu\beta\beta$ decay matrix elements in a systematically improvable way. However, LGT calculations in nuclear systems are very expensive computationally, even in the smallest nuclear systems (i.e., the dinucleon decay, Sections 5.4 and 5.6). Computational cost scales factorially with the number of quarks in the system, making LGT calculations of $0\nu\beta\beta$ decay in heavy nuclei unfeasible without further algorithmic and computational developments. In order to study $0\nu\beta\beta$ decay in nuclear systems, nuclear many-body methods must be used. The models used in these methods are derived with EFT, and they require LGT input in the form of LECs.

The $\pi^- \to \pi^+ e^- e^-$ transition is an essential building block to understanding full nuclear EFT (c.f., Figure 5.7). The long-distance contribution to the $\pi^- \to \pi^+ e^- e^-$ amplitude has been previously computed in Refs. [12, 173]. This thesis (Section 5.3) has computed the leading-order short-distance matrix elements. These ma-

trix elements are renormalized in $\overline{\text{MS}}$ at $\mu = 3\,\text{GeV}$ and are extracted to the chiral, continuum, and infinite-volume limit to extract the χEFT LECs β_k. These LECs are the primary input from the calculation to nuclear EFT models; they have also been computed in a separate LGT calculation (Ref. [174]), and a mild tension between the two calculations still needs to be resolved.

This thesis also presents the first LGT calculation of $0\nu\beta\beta$ decay in a nuclear system (Sections 5.4 and 5.6). The long- and short-distance contributions to the $n^0n^0 \to p^+p^+e^-e^-$ decay are computed on a single ensemble at the $SU(3)$-flavor symmetric point, corresponding to $m_\pi \approx 806$ MeV, with ensemble parameters given in Table 5.4. The long-distance contribution is complete and provides the first determination of a long-distance $0\nu\beta\beta$ decay in a nuclear system. The calculation of the short-distance $0\nu\beta\beta$ decay is ongoing. Bare matrix elements have been computed for each of the nine operators, and renormalization coefficients in $\overline{\text{MS}}$ at 3 GeV have been calculated for five of these nine operators (the scalar operator basis). Calculation of the remaining renormalization coefficients is underway, with results expected to be published soon.

To improve understanding of short-distance nuclear $0\nu\beta\beta$ decay, NLO matrix elements in χEFT should also be computed. This includes both the NN vertex (Figure 5.7b) and the πN vertex (Figure 5.7c). For both of these diagrams, matrix elements of the scalar operators $\{\mathcal{O}_k\}$ (Eq. (5.12)) and the vector operators $\{\mathcal{V}_p^\mu\}$ (Eq. (5.13)) must be computed. Preliminary calculation of the NN vertex is underway on the ensemble with parameters given in Table 5.4. When the operator renormalization is complete, the result of this calculation will be presented at finite lattice spacing, finite volume, and heavy quark mass. The pion mass of $m_\pi \approx 800\,\text{MeV}$) explicitly breaks chiral symmetry on this ensemble (also encoded in the fact that $\mathcal{Z}_V \neq \mathcal{Z}_A$), and hence values of the matrix elements should not be matched to χEFT. To extract the NN LECs for χEFT, further calculations must be performed on a variety of ensembles closer to the physical point; in particular, with lighter quark masses and with discretizations that approximately preserve chiral symmetry, i.e., a domain-wall or overlap action. The algorithmic advances presented in the calculation performed in this work will provide a stepping stone for future LGT calculations of the $n^0n^0 \to p^+p^+e^-e^-$ decay.

The πN vertex in Figure 5.7c has not been computed in LGT at any set of couplings or parameters and should be a target for future LGT calculations. The corresponding LECs must be computed to understand the full behavior of short-distance nuclear $0\nu\beta\beta$ decay in χEFT. The matrix elements to compute take the

form $\langle \pi p^+ | H_i | n^0 \rangle$ (Figure 5.7c), where $\{H_i\}$ is the full basis of dimension-6 scalar and vector operators given in Eq. (5.29). The leading-order contributions to this vertex come from the operators $\{\mathcal{O}_3, \mathcal{V}_1^\mu, \mathcal{V}_2^\mu, \mathcal{V}_{1'}^\mu, \mathcal{V}_{2'}^\mu\}$ [193]. As the matrix element only has a single nucleon in the initial and final state, it is computationally simpler to access the dinucleon matrix elements and should be accessible closer to the physical point than the existing dinucleon calculation.

The neutrino is the most poorly understood particle in the Standard Model. It has been experimentally observed to have non-zero mass, but the nature of the mass term is unknown; it may be a Majorana mass or Dirac mass. If the former holds, then $(B-L)$ is not conserved in whatever theory of physics lies beyond the Standard Model. The smoking gun for a Majorana mass term for the neutrino is $0\nu\beta\beta$ decay. The importance of this decay has made it a central focus of experimental particle physics in the 21$^{\text{st}}$ century, with proposed next-generation experiments like CUPID [238] and LEGEND-1000 [239] that will soon be able to probe regions of parameter space that are predicted to contain $0\nu\beta\beta$ decay if the three Standard Model neutrinos obey an inverted mass hierarchy. If $0\nu\beta\beta$ decay exists in this universe, it may be discovered in the coming decades, in which case theoretical input will be required to interpret experimental signatures of the decay. Simply observing the decay is not enough; to understand the nature of the neutrino, nuclear $0\nu\beta\beta$ decay must be understood on theoretical grounds to make sense of any observed experimental data.

Although LGT calculations are not yet sophisticated enough to perform *ab initio* calculations of $0\nu\beta\beta$ decay in phenomenologically relevant nuclei, they still provide valuable input about the decay in simpler systems. As discussed in this chapter, these techniques work hand-in-hand with EFT and nuclear many-body methods in order to further understand $0\nu\beta\beta$ decay in complex nuclear systems. Neutrinoless double β decay can only be understood theoretically with each of these three communities continuing to work hand-in-hand with the same goal in mind. The calculations presented in this chapter are a step on the way toward a theoretical understanding of $0\nu\beta\beta$ decay.

Chapter 6

Confinement and Two-Dimensional Adjoint QCD

This chapter details my involvement with a project simulating two-dimensional adjoint QCD (QCD_2), a QCD-like theory which will be defined in Section 6.2, with LGT. I have worked on this project with my collaborators William Jay, Manki Kim, Phiala Shanahan, and Neill Warrington. I synthesized an idea for this project in Spring 2023 and have been working on it for about a year. I have been the main driver of the project, deciding which observables to calculate and writing the code to compute these observables. This chapter will detail the theory and preliminary results of an in-progress LGT calculation of QCD_2. Section 6.1 provides a mathematical overview of the confinement problem and how confining theories are studied with LGT. Section 6.2 defines and reviews QCD_2 and will detail two explicit examples of observables that will be studied numerically. Sections 6.3 and 6.4 discuss the lattice implementation of QCD_2. The numerical calculation is detailed in Section 6.5, and preliminary numerical results are presented in Sections 6.6 and 6.7.

6.1 Confinement in Lattice Gauge Theory

As discussed in Chapter 2, QCD confines quarks: the bound states of QCD are color-neutral, and lone quarks are not observed in nature outside of hadrons[1]. All of hadronic physics and the rich tapestry of emergent phenomena arising from hadronic interactions is due to confinement. However, the confinement mechanism itself is not well understood. In particular, pure $SU(3)$ Yang-Mills theory (QCD without quarks) confines and has been postulated to have a mass gap that arises because of

[1]Specifically, this is below the Hagedorn temperature [240]. Above the Hagedorn temperature, quarks are found in quark-gluon plasma.

the confining nature of the theory (the emergence of glueballs) [241]. This mass gap has been shown through numerical studies of QCD like LGT calculations but has not been proven mathematically [242, 243]. One of the long-standing Clay Millennium Problems is to prove the existence of a mass gap in QCD [244].

The study of confinement in gauge theories has spurred much interest in recent decades. It is a deeply interesting problem where formal and numerical quantum field theory meet. This section will provide some mathematical background about the structure of the confinement mechanism for a gauge theory with gauge group $SU(N)$. Many of the ideas in this section are taken from Ref. [245], which provides a well-written introduction to the basics of the confinement problem.

In Section 2.2.1, the confinement of quarks in QCD was discussed. The indicator of a confinement-like mechanism in QCD was the linear part of the QCD potential: as two test charges are pulled apart, a flux tube is formed between them, creating this linear potential. This part of the potential implies that the force between them stays constant. These charges attract one another to minimize this force and form bound states (hadrons) with neutral color charge (color singlets). Because hadrons have no net color charge, they are not influenced by external, far-away quarks.

In QCD, the static quark potential eventually stops being linear at large r because of string breaking (Figure 2.1). This is not a feature of pure $SU(3)$ gauge theory but is a feature of QCD because it has matter coupled to the gauge field in the fundamental representation (quarks). Any theory with fundamental matter will have string breaking, as will be discussed later.

The simplest definition of a confining theory is one that has a linear potential between two static test charges in the fundamental representation of the gauge group. With this definition, QCD is not actually a confining theory. It shares many properties of confining theories (it is a "confinement-like theory"), but string breaking makes the QCD potential plateau at large r, hence the theory does not satisfy this criterion. In contrast, pure $SU(3)$ gauge theory (QCD without quarks) is confining and has a linear potential that does not plateau asymptotically as $r \to \infty$. Flux tubes in pure $SU(3)$ gauge theory do not break like those in QCD. This definition of a confining theory is the starting point for the study of confinement.

The definition of the confining phase of a gauge theory as one with an asymptotically linear static quark potential is too strict in many cases, and should be considered with additional context. For example, by this definition QCD is not confining, as in the string-breaking regime the potential of the theory plateaus. As QCD is the canonical example of a confining theory, it is important to keep in mind that there

is more to the confinement mechanism than whether or not a theory satisfies this binary condition. Nonetheless, a key feature of confinement is that in some regime, the potential is linear (in QCD it is at distance scales below the string breaking distance). In $SU(N)$, this behavior is induced by gluons, which transform in the adjoint representation. The transformation properties of adjoint particles are essential to understanding why theories confine.

6.1.1 Scaling of the Wilson Loop

The confinement picture is often formulated on a discrete Euclidean spacetime lattice so that the definitions can be made rigorously. A key object that indicates if a gauge theory is confining is the fundamental Wilson loop $W_{\mathcal{C}}$ around some particular closed curve $\mathcal{C}$, which is simply the Wilson line (Eq. (3.6)) evaluated on $\mathcal{C}$. Consider a rectangular loop $\mathcal{C}$ on a Euclidean lattice of spatial size r and temporal size t, with corresponding Wilson loop by $W(r,t)$. From a LGT perspective, this is simply the product of the gauge links $U_\mu(x)$ around $\mathcal{C}$. The expectation value of the Wilson loop takes the form [78],

$$\langle W(r,t)\rangle \propto e^{-V(r)t}\left(1+\mathcal{O}(e^{-t\Delta E})\right), \tag{6.1}$$

as $t\to\infty$, where $V(r)$ is the static quark potential and ΔE is the energy gap between $V(r)$ and the first excited state of a $q\overline{q}$ pair. The static quark potential thus informs the behavior of Wilson loops, and vice versa: the behavior of the Wilson loop is often used to determine the phase a theory is in, as discussed below. Wilson loops will subsequently be considered in the $t\gg r$ limit, called the large Wilson loop limit.

There are many possible forms the static quark potential can take, but this section will restrict to a few specific examples. In a confining phase, the potential is linear, $V(r)=\sigma r+V_0$, where σ is the string tension and V_0 is some arbitrary scale. This yields,

$$\langle W(r,t)\rangle \xrightarrow{r\gg V_0/\sigma,\, t\to\infty} \exp\left(-\sigma r t\right) = \exp\left(-\sigma \mathrm{Area}(\mathcal{C})\right), \tag{6.2}$$

where $\mathrm{Area}(\mathcal{C})$ is the area of the domain bounded by $\mathcal{C}$. The behavior of the large Wilson loop in Eq. (6.2) is called an **area law** because the Wilson loop decays as the exponential of the area bounded by $\mathcal{C}$. Area law falloff is a key indicator of a confining theory and can be taken to be an equivalent definition of a confining theory in a discrete Euclidean spacetime, as the converse holds: area law decay of large Wilson loops implies the static quark potential is asymptotically linear.

Suppose that the theory is in a deconfining phase and the potential is instead Coulomb, $V(r)=\alpha(r)/r+2V_0$, where $\alpha(r)$ is the renormalized coupling and V_0 is

again an arbitrary scale. The behavior of a large Wilson loop with this potential is,

$$W(r,t) \xrightarrow{r\gg V_0^{-1}, t\to\infty} \exp\left(-2V_0 t\right) \approx \exp\left(-V_0 \text{Perim}(\mathcal{C})\right) \tag{6.3}$$

where the perimeter of the loop $\mathcal{C}$ is $\text{Perim}(\mathcal{C}) = 2(t+r) \approx 2t$ in the large Wilson loop limit. This scaling is called a **perimeter law** because the decay of the Wilson loop is dictated by its perimeter. Perimeter vs. area law scaling is a key indicator of whether or not a gauge theory is confining.

6.1.2 Adjoint Matter and N-ality

The N-ality of a representation r is the number of boxes in its Young tableau mod N. N-ality allows one to rigorously examine the effect of the dimension of a representation on the confining structure of the theory. Gluons, and in general any adjoint field, have N-ality 0. They may bind to particles with N-ality k to produce a charge in a representation with a lower dimension of the same N-ality k. If a field binds to a test charge, one says the test charge is **screened** by the field: in this case, color screening of a test charge by gluons produces a charge with the same N-ality. A similar phenomenon will hold if any adjoint field screens a test charge: screening by adjoint fields cannot change the N-ality of a test charge, only the dimension of the representation.

Pure $SU(N)$ Yang-Mills theory only has fields in the adjoint representation, as it only contains a gluon. Consider a pair of $q\overline{q}$ test charges that interact with this theory in the fundamental representation of $SU(N)$. Gluons screen this $q\overline{q}$ pair, but gluon screening cannot change the N-ality of the representation, only the dimension of the representation[2]. Although gluons screen the $q\overline{q}$ pair, this pair will still feel a constant non-zero force (linear potential) due to its color charge. The physical picture to keep in mind is that even when a cloud of gluons screens the quark and antiquark, these gluons cannot completely remove the interaction of the quarks from their charge. A similar situation arises when the $SU(N)$ gauge field is coupled to fermions in the adjoint representation. Adjoint fermions can screen a $q\overline{q}$ pair of test charges, but if the pair has non-zero N-ality, this screening does not change the potential between these particles.

This behavior changes when considering full QCD instead of pure $SU(3)$ Yang-Mills theory or, in general, with any gauge theory coupled to matter in a representa-

[2]In this case, gluons cannot even change the representation of the $q\overline{q}$ charges, as the fundamental representation is the lowest-dimensional irrep with N-ality 1.

tion with non-zero N-ality. This change leads to the string-breaking phenomenon. In QCD, quarks and antiquarks are coupled to the gauge field in representations of non-zero N-ality (the fundamental and anti-fundamental representations, respectively). Consider a $q\overline{q}$ pair of test charges in the fundamental representation of $SU(3)$ interacting with full QCD. In addition to screening by gluons (which cannot change the potential between q and $\overline{q}$), the $q\overline{q}$ pair can now be screened by quarks and antiquarks. These quarks and antiquarks can bind to the q and $\overline{q}$ and produce two color singlets that feel no force between one another. This is illustrated in Figure 2.1 and is a restatement of the string-breaking mechanism.

To summarize, an $SU(N)$ theory coupled to matter with non-zero N-ality will have string-breaking and deconfine because the static quark potential is asymptotically flat, not linear. One expects pure gauge $SU(N)$, or $SU(N)$ coupled to adjoint matter, to be confining, as adjoint fields cannot break strings in representations with non-zero N-ality. However, when $SU(N)$ is coupled to adjoint matter, there are specific examples where the theory can become deconfining, as will be seen in Section 6.2.

6.1.3 String tension

The string tension of a $q\overline{q}$ pair only depends on the N-ality k of the representation that the matter q is charged under, as gluons can bind to a q and modify its charge to the representation of the same N-ality with the lowest dimension. The k-string tension σ_k is the string tension of a $q\overline{q}$ pair when q ($\overline{q}$) in the representation with N-ality k ($N-k$) of the lowest dimension. The string tension σ_1 of fundamental matter will often be denoted as $\sigma \equiv \sigma_1$, for example, the string tension of the flux tube between a quark-antiquark pair in QCD.

The scaling of k-string tensions is a question of interest in the study of confinement of $SU(N)$ gauge theories, as different classes of theories that confinement yield different analytic predictions for the scaling of the k-string tension σ_k as a function of k. Of the postulated scalings, two have found particular relevance. The first is Casimir scaling,

$$\frac{\sigma_k}{\sigma} = \frac{k(N-k)}{N-1}, \tag{6.4}$$

Casimir scaling was first postulated in the weak-coupling limit of two-dimensional gauge theory [246, 247] and is thought to extend to more intricate systems via dimensional reduction [248]. The second scaling of interest is the sine-law,

$$\frac{\sigma_k}{\sigma} = \frac{\sin(\pi k/N)}{\sin(\pi N)}, \tag{6.5}$$

which arises in the study of supersymmetric gauge theories [249].

6.1.4 Center Symmetry and Polyakov Loops

An important question about confinement is whether a symmetry or order parameter distinguishes a confined phase of a gauge theory from a deconfined phase. Indeed, there is, and the modern understanding of such a symmetry is through higher-form symmetries [250–252]. Loosely speaking, higher-form symmetries allow one to act a symmetry on a higher-dimensional object. Ordinary global symmetries are called 0-form symmetries: they act on 0-dimensional submanifolds of spacetime (points). For $0 \leq p \leq d$, where d is the dimension of spacetime, a p-form symmetry acts on p-dimensional operators defined on p-dimensional submanifolds of spacetime. Each p-form symmetry yields a conserved $(d-1-p)$-dimensional charge. For example, a 0-form symmetry yields a conserved spatial charge through Noether's theorem [253], a $(d-1)$-dimensional charge.

The particular p-form symmetry of interest in the study of confinement is called **center symmetry**, which is a 1-form symmetry and hence acts on line operators. In LGT, line operators are Wilson lines and are products of the gauge field $U_\mu(x)$. Recall the center of a group G is the set of elements in G that commute with all other elements of G, $\text{center}(G) \equiv \{g \in G : \forall h \in G,\, [g,h] = 0\}$. The center elements of $SU(N)$ are the N^{th} roots of unity,

$$\text{center}(SU(N)) = \{z_i 1_N : i = 0, 1, ..., N-1\} \qquad z_i \equiv \exp\left(\frac{2\pi i n}{N}\right), \tag{6.6}$$

where 1_N is the identity element of $SU(N)$. Center symmetry acts on gauge fields $U_\mu(x)$ by rotating every time-like link at fixed spatial slice $t = t_0$ with an element of $z_i \in \text{center}(SU(N))$,

$$U_0(\boldsymbol{x}, t_0) \mapsto z_i U_0(\boldsymbol{x}, t_0) \tag{6.7}$$

while leaving the links $U_\mu(x,t)$ for $\mu \neq 0$ or $t \neq t_0$ unaffected. This is a 1-form symmetry of the Wilson action, as the only place this can modify the action is through a time-like plaquette at time t_0, $\mathcal{P}_{0i}(\boldsymbol{x}, t_0)$ (Eq. (3.11)). This transforms as,

$$\begin{aligned} \mathcal{P}_{0i}(\boldsymbol{x}, t_0) &= U_0(\boldsymbol{x}, t_0) U_i(\boldsymbol{x}, t_0 + 1) U_0^\dagger(\boldsymbol{x} + \hat{i}, t_0) U_i^\dagger(\boldsymbol{x}, t_0) \\ &\xrightarrow{z_i} (z_i U_0(\boldsymbol{x}, t_0)) U_i(\boldsymbol{x}, t_0 + 1)(z_i^\dagger U_0^\dagger(\boldsymbol{x} + \hat{i}, t_0)) U_i^\dagger(\boldsymbol{x}, t_0) = \mathcal{P}_{0i}(\boldsymbol{x}, t_0) \end{aligned} \tag{6.8}$$

where i is a spatial index. Because $z_i \in \text{center}(SU(N))$, it commutes through each link, and $z_i z_i^\dagger = 1$, which implies the plaquette is unchanged. Thus, center symmetry leaves the gauge action invariant.

Center symmetry is crucial to understanding confinement because matter fields of non-zero N-ality break center symmetry. Suppose ψ is a fermion coupled to $SU(N)$ in representation $\mathcal{R}$ with N-ality $k \neq 0$. The matter field couples to U_μ through a coupling of the form $\overline{\psi}(x)\mathcal{R}(U_\mu(x))\psi(x+\hat{\mu})$. Under center symmetry, this term does not leave the action invariant, which is evident by transforming the term on the time-slice t_0 in the $\hat{0}$ direction,

$$\overline{\psi}(\boldsymbol{x},t_0)\mathcal{R}(U_0(\boldsymbol{x},t_0))\psi(\boldsymbol{x},t_0+1) \xrightarrow{z_i} \overline{\psi}(\boldsymbol{x},t_0)z_i^k\mathcal{R}(U_0(\boldsymbol{x},t_0))\psi(\boldsymbol{x},t_0+1). \tag{6.9}$$

For $k \in \{1,2,...,N-1\}$, the phase factor z_i^k cannot be unity if z_i is a fundamental N^{th} root of unity (i.e., if i and N are coprime), hence coupling to matter fields of non-zero N-ality must break center symmetry.

This, therefore, identifies that if a system breaks center symmetry, it must not be confining: it must have string breaking, and the asymptotic potential cannot be linear. If the system instead respects center symmetry, it is confining and will have an asymptotically linear potential. An equivalent definition of a confining theory is, therefore, whether or not the system respects the 1-form center symmetry.

An order parameter that detects the existence of center symmetry is the **Polyakov loop** [254], which is a closed loop winding around the temporal direction of the lattice,

$$P(\boldsymbol{x}) = \prod_t U_0(\boldsymbol{x},t). \tag{6.10}$$

The Polyakov loop transforms non-trivially under center symmetry, as for center symmetry acting on time-slice t_0, the link $U_0(\boldsymbol{x},t_0) \xrightarrow{z_i} z_i U_0(\boldsymbol{x},t_0)$. This makes clear that

$$P(\boldsymbol{x}) \xrightarrow{z_i} z_i P(\boldsymbol{x}) \tag{6.11}$$

under center symmetry acting on *any* time-slice of the lattice. The Polyakov loop thus provides an order parameter to determine if the theory is in a confining or deconfining phase. If $\langle P(\boldsymbol{x})\rangle = 0$ is zero, then the system respects center symmetry and is confining, whereas if $\langle P(\boldsymbol{x})\rangle \neq 0$, then the system does not respect center symmetry and is deconfining.

The Polyakov loop is related to the free energy of a lone quark. Let F_q denote the difference in free energy between a gauge theory containing a single static quark and

a gauge theory without a static quark. The free energy difference satisfies [255]

$$\langle P(\boldsymbol{x})\rangle \propto e^{-\beta F_q}, \tag{6.12}$$

where β is the inverse temperature of the system, $\beta = T$, the temporal size of the lattice. If the Polyakov loop vanishes, the free energy F_q must be infinite. In this case, isolated quarks cannote exist because they would have infinite energy, i.e., the theory is in a confining phase. The two-point correlator of the Polyakov loop is,

$$\langle P(\boldsymbol{x})P^\dagger(\boldsymbol{y})\rangle = e^{-V(r)T}\left(1+\mathcal{O}(e^{-T\Delta E})\right), \tag{6.13}$$

where $V(r)$ is the static quark potential at distance $r = |\boldsymbol{x}-\boldsymbol{y}|$. This is an alternative way to extract $V(r)$ without computing large Wilson loops, as in Eq. (6.1).

6.2 Two-Dimensional Adjoint QCD

It is a question of great interest to know what properties of QCD are a result of the confining structure of the theory, and if these properties can be found in an arbitrary confining QFT. A particular example of this is the Yang-Mills mass gap conjecture discussed in Section 6.1. The conjecture asks one to prove that a general confining theory, for example a pure $SU(N)$ gauge theory, has a mass gap in its spectrum. The conjecture can be better understood by studying the spectrum of confining gauge theories, which should contain only massive bound states. The spectrum of a theory can also reveal other hints of the confining structure of a theory; namely, it can be used to distinguish between confining theories and confinement-like theories that have string breaking. If a theory has an asymptotically linear static quark potential (if it is confining in the sense of the definition provided in Section 6.1), the spectrum is discrete, whereas if the theory has a linear static quark potential which is asymptotically flat (QCD-like), then the spectrum is discrete at low energies with a branch cut at some kinematic threshold [256].

To provide insight into the confinement mechanism, other confining theories must be studied in addition to QCD. It is often advantageous to consider simpler theories, whether that is with fewer fields or in a lower number of dimensions, because there are more field theoretic tools available to study such theories. Different methods can provide insights into different aspects of the theory and how the physics behaves in different regions of parameter space. The closest cousin to QCD is pure four-dimensional $SU(N)$ gauge theory, i.e., QCD without quarks. Pure $SU(N)$ allows

one to study the dynamics of the gauge sector without string breaking. The theory exhibits an asymptotically linear potential and is confining. In the context of pure $SU(N)$, the Yang-Mills conjecture asks if the glueball mass has a lower bound, a topic that has been studied using lattice gauge theory (LGT) [243] but not definitively proven. A salient feature of pure gauge $SU(N)$ is that the only propagating degrees of freedom are the gauge fields $A^a_\mu(x)$, which transform in the adjoint representation of $SU(N)$. As discussed in Section 6.1.2, adjoint fields can screen test charges in a given representation of $SU(N)$, but in most cases leave the confining structure of the theory unchanged because they cannot change the N-ality of the test charge's representation.

An even simpler theory than four-dimensional $SU(N)$ gauge theory is two-dimensional adjoint QCD (QCD_2), the theory of a single Majorana fermion $\psi(x)$ in $(1+1)$ spacetime dimensions coupled to an $SU(N)$ gauge field in the adjoint representation,

$$S_{\text{QCD}_2}[\psi, G] = \int d^2x \,\text{Tr}\left[\frac{1}{2g^2}\, G_{\mu\nu}(x)G^{\mu\nu}(x) + \overline{\psi}(x)(i\gamma^\mu D_\mu - m)\psi(x)\right] \tag{6.14}$$

where $G_{\mu\nu}$ is the $SU(N)$ field strength, D_μ is the covariant derivative, g is the coupling, and m is the fermion mass. The fermion field $\psi(x)$ has adjoint indices,

$$\psi(x) = \psi^a(x)t^a \tag{6.15}$$

where a ranges from 1 to $d_N \equiv N^2 - 1$, the dimension of the adjoint representation of $SU(N)$. In two spacetime dimensions, pure $SU(N)$ gauge theory is solvable and does not have propagating local degrees of freedom [257], hence matter must be coupled to the theory to generate interesting dynamics.

Many studies of QCD_2 set the fermion mass $m = 0$. However, the massive and massless theories both contain interesting dynamics, and the mass will be kept as a free parameter in this work. When the adjoint fermion is massive, the theory confines. Interestingly enough, when the adjoint fermion is massless, the theory deconfines, counter to the intuition that the adjoint particles should screen, not shield, test charges [258, 259]. This deconfinement transition is related to the symmetry structure of the problem: when the Majorana fermion is massless, the theory boasts a non-invertible 1-form symmetry that can be shown to produce a perimeter law for a fundamental Wilson loop. This non-invertible symmetry is not present when the Majorana fermion is massive, hence yielding an area law for the Wilson loop.

The two dimensional setting of the theory allows for many non-perturbative tech-

niques to be used to study the theory, and is a toy model for confinement and how adjoint fields can influence the confining structure of a theory. In the last 30 years, there has been significant progress using tools like lightcone quantization [260, 261], supersymmetry [262], and bosonization [263] to understand the structure of QCD_2. Specific limits have been mapped out: the large N limit [264–266], and the large fermion mass limit [267, 268]. These studies of QCD_2 have revealed a rich dynamical structure with higher-form and non-invertible symmetries influencing the dynamics of the theory.

The spectrum of QCD_2 is known in a number of specific cases. The low-lying spectrum was first computed in 't Hooft's $N \to \infty$ limit [265, 269]. More recently, the spectrum has been computed with Discretized Lightcone Quantization (DLCQ) for $N = 2, 3, 4$ [261]. The results of Ref. [261] indicate that the spectrum approaches the large N limit quickly. The $N = 2$ case is qualitatively different than $N > 2$, and for $N = 3, 4$, the spectrum is very close to its predicted value for large N. In other words, the spectrum approaches the $N \to \infty$ limit rapidly. The light dependence of the spectrum on N has been observed in other $SU(N)$ gauge theories, in particular in the glueball spectrum of three- and four-dimensional $SU(N)$ gauge theories [242, 243, 270].

Many of the methods used to compute the spectrum of QCD_2 are employable only in a specific regime of validity; analytical computations in QCD_2 at arbitrary m, g, and N are not always possible because the theory is strongly coupled, and an *ab initio* understanding of the theory in all sectors does not currently exist. Lattice gauge theory (Chapter 3) provides a systematically improvable framework to non-perturbatively compute correlation functions of QCD_2 in Euclidean space when the Majorana fermion is massive. Lattice gauge theory was first used to study QCD_2 in 2011 [271], and more recently [272] has been used to extract the static quark potential $V(r)$ (Section 6.1.1), string tension σ (Section 6.1.3), and Polyakov loop expectation value $\langle P \rangle$ (Section 6.1.4) for a number of different choices of g, m, and N.

6.2.1 The String Tension in QCD_2

The k-string tension of QCD_2 has been computed analytically in two cases [259]. First is the $m \to \infty$ limit, where the Majorana fermion is integrated from the theory, leaving only pure $SU(N)$ gauge theory in 2 dimensions. In this case, the k-string

tension obeys Casimir scaling (Eq. (6.4)),

$$\sigma_k\Big|_{m\uparrow\infty} = Cg^2k(N-k) \tag{6.16}$$

where the constant of proportionality C is independent of the representation k. Note that the string tension vanishes in the adjoint representation ($k = N$).

The second limiting case where the string tension has been computed is the small mass limit for $N \leq 5$, where the theory is perturbed about the massless theory. Computations have only been performed for $N \leq 5$ because the relevant technique does not scale well to arbitrary N [259]. With these assumptions, non-invertible symmetries may be used to compute the behavior of the string tension. The behavior is observed to follow a sine-law (Eq. (6.5)),

$$\sigma_k\Big|_{m\downarrow 0,\, N\leq 5} = C'g|m|\sin\left(\frac{\pi k}{N}\right) \tag{6.17}$$

where as in Eq. (6.16), C' is a representation-independent coefficient. The mass dependence of this relation agrees with expectation, as at $m = 0$, the theory becomes deconfining and should have zero string tension, and at finite m, the string tension vanishes for adjoint lines.

LGT provides a framework for the direct computation of k-string tensions, as shown in Ref. [273] for pure $SU(N)$ gauge theory. Although LGT calculations cannot definitively prove the existence of the sine law for all N, these calculations may be used to strengthen the existing hypotheses and determine the relevant coefficients of proportionality. Depending on the outcome of the calculation, such calculations may also disprove a class of scaling behaviors. Such calculations may also provide insight into the mass scales at which a crossover from sine-law scaling to Casimir scaling would occur at in QCD_2. Calculation of this crossover would give insight into how the adjoint fermions influence the dynamics of the pure gauge theory, as the adjoint fermions are the degrees of freedom that cause the theory to shift from Casimir scaling in the pure gauge case to the sine-law prediction of adjoint QCD with $m \to 0$. The string tension of QCD_2 is computed in Section 6.6 for a number of different parameters (m, g) for $N = 2$ colors. For this number of colors, there is no way to distinguish between Casimir scaling and sine-law scaling. Future work will extend the calculation to larger numbers of colors and probe the difference between the two scaling regimes.

6.2.2 The QCD_2 Spectrum

The first calculation of the spectrum of QCD_2 at finite m and N was performed in 1998 using Discretized Lightcone Quantization (DLCQ) in the Hamiltonian formalism [274]. The calculation extracted the masses of the lowest-lying boson and fermion states but was not extendable to the entire spectrum. DLCQ computes the spectrum of the theory by discretizing and numerically diagonalizing the theory's Hamiltonian. The discrete Hamiltonian is constructed with a momentum cutoff proportional to an integer K: DLCQ computes the spectrum at finite K, then extrapolates the results to remove the cutoff, $K \to \infty$. Increasing K increases the number of states accessible in the discretization, making the Hamiltonian larger and more numerically intensive to diagonalize.

Recent developments have allowed this calculation to be extended to compute the spectrum of small N QCD_2 ($N = 2, 3, 4$) in the massive and massless case and, in particular, determine the continuum threshold for the theory in these cases [261]. The breakthrough of this work was using the Cayley-Hamilton theorem to determine and remove the null states of the theory from the overcomplete basis in which the Hamiltonian was computed and diagonalized. As the cutoff K increases, the number of null states grows significantly. Without removing the null states, it is intractable to compute the finite N spectrum for even moderate values of K. Removal of these null states allowed the study of a much larger part of the low-lying spectrum at finite K. This method was able to access $K = 60$ for $N = 2$, $K = 30$ for $N = 3$, and $K = 25$ for $N = 4$, and then extrapolate the results at finite K to $K \to \infty$. The results of Ref. [261] numerically found the supersymmetric point in the theory, $\pi m^2 = g^2 N$, and verified the equivalence of the bosonic and fermionic spectrum at this point. They also found that the spectrum received very small $1/N^2$ corrections, and the results at $N = 3$ and $N = 4$ are very close to the $N \to \infty$ results and determined the number of bound states that were found below the continuum threshold.

The DLCQ has been extremely useful in computing the spectrum of QCD_2. Still, because the DLCQ computes the spectrum at finite K, the extrapolation required means that there is a systematic uncertainty on the final result from the extrapolation. Many extrapolated states have a very light dependence on $1/K$, indicating a controlled extrapolation to $1/K \to 0$. However, the range of the values of $1/K$ for which there is data is significantly smaller than the size of the extrapolation. This is not necessarily a problem and, indeed, is a required part of the method, but additional methods of computing the spectrum would provide valuable cross-checks on these extrapolations

and allow for the reduction of systematic errors that are associated with the $K \to \infty$ extrapolation.

Lattice gauge theory allows for a calculation of the low-lying spectrum of QCD_2 in a systematically improvable way that can be used to study the QCD_2 spectrum from an alternative perspective, the Lagrangian formulation of the theory. The scaling of the computation with N is quadratic, and a priori, there is no barrier to accessing the spectrum for larger values of N, i.e., $N = 10$ or $N = 20$. LGT calculations may only study QCD_2 at finite mass, so exploring the theory at $m = 0$ must be done via a chiral extrapolation. In addition, using a lattice regulator instead of the cutoff K in the DLCQ approach suffers from the same problems, requiring an extrapolation to the continuum limit, $a \to 0$. This may be viewed as complementary to the DLCQ approach. Both methods have finite errors, and if they are computed at the same areas of parameter space, they can constrain existing results further. The calculation of the low-lying spectrum and preliminary results are presented in Section 6.7 at finite lattice spacing for a number of values of (m, g) with $N = 2$ colors.

6.3 Discretizing QCD_2

6.3.1 The Dirac operator

The first step to studying QCD_2 with LGT is discretizing the action. This work uses the Wilson action for Majorana fermions coupled to $SU(N)$ in the adjoint representation [275],

$$\begin{aligned} S_W^F[\psi, V] &= \frac{1}{2}\sum_{x,y\in\Lambda} \psi^T(x)\mathcal{D}_W(x,y)\psi(y) \\ &= \frac{1}{2}\sum_{x\in\Lambda}\Big\{\overline{\psi}^a(x)\psi^a(x) - \kappa\sum_{\mu=1}^{4}[\overline{\psi}^a(x+\hat{\mu})V_\mu^{ab}(x)(1+\gamma_\mu)\psi^b(x) \\ &\qquad + \overline{\psi}^a(x)(V_\mu^{ab})^T(x)(1-\gamma_\mu)\psi^b(x+\hat{\mu})\Big\}. \end{aligned} \tag{6.18}$$

Here κ is the hopping parameter for the theory and encodes the bare fermion mass m, and $\psi(x) = \psi^a(x)t^a$ is the adjoint fermion field, which transforms under gauge transformations $\Omega(x) \in SU(N)$ as

$$\psi(x) \mapsto \Omega(x)\psi(x)\Omega^\dagger(x) \tag{6.19}$$

where $V_\mu(x)$ are the adjoint links of the theory, defined in terms of the fundamental links $U_\mu(x)$ (Eq. (3.7)) as,

$$V_\mu^{ab}(x) = 2\mathrm{Tr}[U_\mu^\dagger(x) t^a U_\mu(x) t^b], \tag{6.20}$$

and $\mathcal{D}_W(x,y)$ is the Dirac operator for the Wilson discretization,

$$(\mathcal{D}_W)_{\alpha\beta}^{ab}(x,y) = \delta^{ab}\delta_{\alpha\beta}\delta_{x,y} - \kappa \sum_{\mu=1}^{2} \left[V_\mu^{ab}(x)(1-\gamma_\mu)_{\alpha\beta}\delta_{x+\hat{\mu},y} + (V_\mu^T)^{ab}(y)(1+\gamma_\mu)_{\alpha\beta}\delta_{x-\hat{\mu},y} \right]. \tag{6.21}$$

The Dirac operator $\mathcal{D}_W$ will often be denoted as either a function of the adjoint links $\mathcal{D}_W[V]$, or the fundamental links $\mathcal{D}_W[U]$, depending on what is more convenient, as the adjoint links may be constructed from the fundamental links by Eq. (6.20). Note that the adjoint links are real,

$$(V_\mu^{ab})^*(x) = 2\mathrm{Tr}[(t^b)^\dagger U_\mu^\dagger(x)(t^a)^\dagger U_\mu(x)] = 2\mathrm{Tr}[U_\mu^\dagger(x) t^a U_\mu(x) t^b] = V_\mu^{ab}(x), \tag{6.22}$$

and satisfy similar properties to the fundamental links,

$$V_{-\mu}(x) = V_\mu^T(x-\hat{\mu}) = V_\mu^\dagger(x-\hat{\mu}). \tag{6.23}$$

The Dirac operator satisfies the usual fermionic boundary conditions, periodic in space and antiperiodic in time. These boundary conditions manifest themselves as the 2-vector

$$b = \begin{pmatrix} 1 \\ -1 \end{pmatrix}. \tag{6.24}$$

With the boundary conditions b_μ, the Dirac operator with fermionic boundary conditions can be expanded as,

$$(D_W)_{\alpha\beta}^{ab}(x,y) = \delta^{ab}\delta_{\alpha\beta}\widetilde{\delta}_{x,y} - \kappa \sum_{\mu=1}^{2} \left[V_\mu^{ab}(x)(1-\gamma_\mu)_{\alpha\beta}\widetilde{\delta}_{x+\hat{\mu},y} + (V_\mu^T)^{ab}(y)(1+\gamma_\mu)_{\alpha\beta}\widetilde{\delta}_{x-\hat{\mu},y} \right]$$

$$\widetilde{\delta}_{x,y} = \begin{cases} 1 & x = y \\ b_0 & (x_0 \equiv y_0 \mod L) \text{ and } x_1 = y_1 \\ b_1 & x_0 = y_0 \text{ and } (x_1 \equiv y_1 \mod T) \end{cases} \tag{6.25}$$

The augmented spacetime δ function $\widetilde{\delta}$ ensures that anytime the fermion hops across

the boundary of the lattice, it incurs the appropriate sign change. Note that $x \pm \hat{\mu}$ takes values in the discrete box $[-1, L+1] \times [-1, T+1]$ to account for the boundaries in the definition.

The Wilson action is used for the fundamental gauge field,

$$S_W^g[U] = \beta \sum_{x \in \Lambda} \sum_{\mu < \nu} \left(1 - \frac{1}{N} \mathrm{Re}\, \mathrm{Tr}\, \mathcal{P}_{\mu\nu}(x) \right) \tag{6.26}$$

where $\mathcal{P}_{\mu\nu}$ is the plaquette in direction (μ, ν) at $x \in \Lambda$. For $d = 2$, this reduces to,

$$S_W^g[U] = \beta \sum_{x \in \Lambda} \left(1 - \frac{1}{N} \mathrm{Re}\, \mathrm{Tr}\, \mathcal{P}(x) \right) \tag{6.27}$$

where $\mathcal{P}(x) \equiv \mathcal{P}_{01}(x)$ is the only direction of plaquette that can be formed on a 2d lattice. Note that the gauge action is written in terms of the fundamental gauge links $U_\mu(x)$; one could equivalently rewrite S_W^g as a functional of the adjoint links $V_\mu(x)$, but the conventions adhered to here will use $U_\mu(x)$ as the basic degrees of freedom, as the adjoint links V_μ are functions of U_μ.

A particularly important property for the Dirac operator to satisfy is γ_5-hermicity. Recall a Dirac operator $\mathcal{D}(x, y)$ is γ_5-hermitian (Eq. (3.58)) if $\gamma_5 \mathcal{D}_W \gamma_5 = \mathcal{D}_W^\dagger$, where $\cdot^\dagger$ is taken over all spin, color, and spacetime indices on $\mathcal{D}_W$. This property is verified by direct computation,

$$\begin{aligned}
&\gamma^5 \mathcal{D}_W(x, y) \gamma^5 \\
&\quad = \gamma^5 \left(1_s 1_c \delta_{x,y} - \kappa \sum_{\mu=1,2} \left[V_\mu(x)(1_s - \gamma_\mu)\delta_{x+\hat{\mu},y} + V_\mu^T(y)(1_s + \gamma_\mu)\delta_{x-\hat{\mu},y} \right] \right) \gamma^5 \\
&\quad = 1_s 1_c \delta_{x,y} - \kappa \sum_{\mu=1,2} \left[V_\mu(x)(1_s + \gamma_\mu)\delta_{x+\hat{\mu},y} + V_\mu^T(y)(1_s - \gamma_\mu)\delta_{x-\hat{\mu},y} \right] \\
&\quad = 1_s 1_c \delta_{x,y} - \kappa \sum_{\mu=1,2} \left[(V_\mu^T)^\dagger(x)(1_s + \gamma_\mu)^\dagger \delta_{x+\hat{\mu},y} + V_\mu^\dagger(y)(1_s - \gamma_\mu)^\dagger \delta_{x-\hat{\mu},y} \right] \\
&\quad = \left(1_s 1_c \delta_{x,y} - \kappa \sum_{\mu=1,2} \left[V_\mu^T(x)(1_s + \gamma_\mu)\delta_{y,x+\hat{\mu}} + V_\mu(y)(1_s - \gamma_\mu)\delta_{y,x-\hat{\mu}} \right] \right)^\dagger \\
&\quad = \left(1_s 1_c \delta_{x,y} - \kappa \sum_{\mu=1,2} \left[V_\mu(y)(1_s - \gamma_\mu)\delta_{y+\hat{\mu},x} + V_\mu^T(x)(1_s + \gamma_\mu)\delta_{y-\hat{\mu},x} \right] \right)^\dagger \\
&\quad = \mathcal{D}_W(y, x)^\dagger.
\end{aligned} \tag{6.28}$$

Using γ_5-hermicity, one defines the Hermitian Dirac operator Q as

$$Q = \gamma_5 \mathcal{D}_W, \tag{6.29}$$

which satisfies $Q^\dagger = Q$ by definition. Note that the charge conjugation matrix is $C = \gamma_5$, so Q can equivalently be defined as $Q = C\mathcal{D}_W$. Importantly, this operator is also skew-symmetric,

$$Q^T = -Q. \tag{6.30}$$

The skew-symmetry of Q means that it has a Pfaffian $\mathrm{Pf}\, Q$, which will be important for Monte Carlo calculations involving the Dirac operator of Eq. (6.21).

6.3.2 Implementation of the Dirac Operator

The Dirac operator must be implemented efficiently for computations in this theory to be tractable. Observe that in the definition of the Wilson-Dirac operator (Eq. (6.21)), the $\delta_{x,y}$ and $\delta_{x,y\pm\hat{\mu}}$ functions imply that the Dirac operator only couples nearest-neighbor sites together. Therefore, the best way to construct the Dirac operator is in spin-color blocks, where the Dirac operator will be identically zero across most spin-color blocks. One first needs to vectorize the Dirac operator and the Dirac fermion fields as a $d_N N_s LT \times d_N N_s LT$ matrix, where:

$$D_{ij} = (D_W)^{ab}_{\alpha\beta}(x^\mu, y^\mu) \tag{6.31}$$

where i and j are multi-indices encoding (a, α, x^μ) and (b, β, y^μ), respectively. Here $d_N = N^2 - 1$ is the dimension of the adjoint representation of $SU(N)$, and $N_s = 2$ is the number of spin degrees of freedom. Note that here $x^\mu = (x, t)$ and $y^\mu = (y, s)$ are the two-positions corresponding to the scalar coordinates x, t and y, s. For a natural spacetime blocking, these multi-indices traverse first in color, then in spin, then in the spatial dimension, and finally in the temporal direction. The multi-index (a, α, x, t) is flattened with

$$i = a + d_N \alpha + d_N N_s x + d_{N_c} N_s L t. \tag{6.32}$$

Likewise, given a flattened index $i \in \{0, 1, ..., d_N N_s LT\}$, one recovers the corresponding multi-index (a, α, x, t) with the procedure,

$$\begin{aligned} \mathrm{t} &\rightarrow \mathrm{i} \;//\; (d_N N_s L) \\ \mathrm{i} &= \mathrm{i} - \mathrm{t} * (d_N N_s L) \\ \mathrm{x} &\rightarrow \mathrm{i} \;//\; (d_N N_s) \end{aligned}$$

$$
\begin{aligned}
\mathrm{i} &= \mathrm{i} - \mathrm{x} * (d_N N_s) \\
\alpha &\to \mathrm{i} \;//\; d_N \\
\mathrm{a} &\to \mathrm{i} - d_N \alpha
\end{aligned}
$$

which divides out by the correct block sizes for each step in the process.

The specific sparse representation of the Dirac operator used in this work is the Block Sparse Row (BSR) format [276]. The BSR format stores each dense subarray, along with a pointer to where the dense subarray may be found in the full matrix. For concrete visualization, for $N = 2$ colors the spin-color Dirac matrix blocks are,

$$
\mathcal{D}(x,y) = \begin{pmatrix}
\mathcal{D}^{00}_{00}(x,y) & \mathcal{D}^{01}_{00}(x,y) & \mathcal{D}^{02}_{00}(x,y) & \mathcal{D}^{00}_{01}(x,y) & \mathcal{D}^{01}_{01}(x,y) & \mathcal{D}^{02}_{01}(x,y) \\
\mathcal{D}^{10}_{00}(x,y) & \mathcal{D}^{11}_{00}(x,y) & \mathcal{D}^{12}_{00}(x,y) & \mathcal{D}^{10}_{01}(x,y) & \mathcal{D}^{11}_{01}(x,y) & \mathcal{D}^{12}_{01}(x,y) \\
\mathcal{D}^{20}_{00}(x,y) & \mathcal{D}^{21}_{00}(x,y) & \mathcal{D}^{12}_{00}(x,y) & \mathcal{D}^{20}_{01}(x,y) & \mathcal{D}^{21}_{01}(x,y) & \mathcal{D}^{22}_{01}(x,y) \\
\mathcal{D}^{00}_{10}(x,y) & \mathcal{D}^{01}_{10}(x,y) & \mathcal{D}^{02}_{10}(x,y) & \mathcal{D}^{00}_{11}(x,y) & \mathcal{D}^{01}_{11}(x,y) & \mathcal{D}^{02}_{11}(x,y) \\
\mathcal{D}^{10}_{10}(x,y) & \mathcal{D}^{11}_{10}(x,y) & \mathcal{D}^{12}_{10}(x,y) & \mathcal{D}^{10}_{11}(x,y) & \mathcal{D}^{11}_{11}(x,y) & \mathcal{D}^{12}_{11}(x,y) \\
\mathcal{D}^{20}_{10}(x,y) & \mathcal{D}^{21}_{10}(x,y) & \mathcal{D}^{12}_{10}(x,y) & \mathcal{D}^{20}_{11}(x,y) & \mathcal{D}^{21}_{11}(x,y) & \mathcal{D}^{22}_{11}(x,y)
\end{pmatrix} \tag{6.33}
$$

with the whole Dirac matrix D_{ij} decomposed as,

$$
D = \begin{pmatrix}
\mathcal{D}(\vec{0},\vec{0}) & \mathcal{D}(\vec{0},\vec{1}) & 0 & \dots \\
\mathcal{D}(\vec{1},\vec{0}) & \mathcal{D}(\vec{1},\vec{1}) & \mathcal{D}(\vec{1},\vec{2}) & \dots \\
0 & \mathcal{D}(\vec{2},\vec{1}) & \mathcal{D}(\vec{2},\vec{2}) & \dots \\
\dots & \dots & \dots & \dots
\end{pmatrix} \tag{6.34}
$$

where $\vec{1} \equiv \hat{0} = (1,0)$, $\vec{2} \equiv 2\hat{0}$ are respectively the first and second vector traversed in the spacetime indices. Blocks that are not nearest neighbors (i.e., $\mathcal{D}(\vec{0},\vec{2})$) are not coupled and are set to zero.

6.4 Markov Chain Monte Carlo for QCD_2

6.4.1 The "Sign" Problem for Majorana Fermions

MCMC calculations with Majorana fermions build on the formalism built up in Chapter 3, with one important difference. When ψ is a Majorana fermion,

$$
\mathcal{Z} = \int DU\, D\psi D\overline{\psi}\, e^{-\int d^2x\, d^2y\, \overline{\psi}(x)\mathcal{D}_W[U](x,y)\psi(y) - S_g[U]} = \int DU\, e^{-S_g[U]}\, \mathrm{Pf}[\mathcal{D}_W[U]], \tag{6.35}
$$

where $\mathrm{Pf}[A]$ is the Pfaffian [277] of the skew-symmetric $2n \times 2n$ dimensional matrix A,

$$\mathrm{Pf}[A] \equiv \frac{1}{2^n n!} \sum_{\sigma \in S_{2n}} \mathrm{sgn}(\sigma) \prod_{i=1}^{n} A_{\sigma(2i-1),\sigma(2i)}. \tag{6.36}$$

In this case, $n = (N^2-1)N_s LT/2$ is the dimension of the Dirac operator. Here S_{2n} denotes the symmetric group on $2n$ letters. The Pfaffian satisfies the identity $\mathrm{Pf}[A]^2 = \mathrm{Det}[A]$ and is often considered the square root of the determinant. Eq. (6.35) should be compared to Eq. (3.48) for the fermion path integral over a Dirac fermion field, which produces a determinant $\mathrm{Det}[\mathcal{D}_W[U]]$ of the Dirac operator.

The replacement of the determinant with the Pfaffian can introduce a sign problem into the theory. To compute dynamical Dirac fermions, the fermion determinant is absorbed into the probability measure $D\mathbb{P}\, e^{-S_g[U]} \mathrm{Det}\, \mathcal{D}_W[U]$, and in many situations of interest[3] can be taken to be real and positive. The Pfaffian $\mathrm{Pf}\, \mathcal{D}_W[U]$ does not need to be real and positive, and although it is constrained to have norm $\sqrt{\mathrm{Det}\, \mathcal{D}_W[U]}$, there is no such constraint on its phase. Any non-trivial phase factor makes it impossible to absorb into an effective gauge field probability measure fully.

This problem is treated using a procedure called **reweighting**, which has successfully been applied to sign problems in many areas of LGT, including thermodynamic systems at finite chemical potential [275, 278–284]. The idea behind reweighting is to absorb any non-trivial phase for the Pfaffian into the observable. One expands $\mathrm{Pf}\, \mathcal{D}[U]$ in polar coordinates as,

$$\mathrm{Pf}\, \mathcal{D}_W[U] = e^{i\alpha[U]} \left|\mathrm{Pf}\, \mathcal{D}_W[U]\right| \qquad \alpha[U] \equiv \arg \mathrm{Pf}\, \mathcal{D}_W[U], \tag{6.37}$$

where $\alpha[U] \in [0, 2\pi)$ and $|\mathrm{Pf}\, \mathcal{D}_W[U]|$ is manifestly non-negative. This parameterization of $\mathrm{Pf}\, \mathcal{D}_W[U]$ now allows for the definition of a valid probability measure, called the **partially quenched** measure, as

$$D\mathbb{P}_{\mathrm{pq}} \equiv DU e^{-S_g[U]} \left|\mathrm{Pf}\, \mathcal{D}_W[U]\right|. \tag{6.38}$$

Note that Eq. (6.35) may now be recast in terms of $D\mathbb{P}_{\mathrm{pq}}$,

$$\mathcal{Z} = \int D\mathbb{P}_{\mathrm{pq}}\, e^{i\alpha[U]}. \tag{6.39}$$

[3]The most common of these situations is the assumption that there are two degenerate light quarks u and d, which allows $(\mathrm{Det}\, \mathcal{D}^u_W[U])(\mathrm{Det}\, \mathcal{D}^d_W[U])$ to be written as $(\mathrm{Det}\, \mathcal{D}^u_W[U])^2$, which is an inherently positive quantity. If $\mathrm{Det}\, \mathcal{D}_W[U]$ is not real and positive, which it is typically not, then the calculation must also be reweighted, as will be discussed here for the Pfaffian case.

Reweighting provides a framework for the calculation of correlation functions of arbitrary operators. Consider the n-point correlator $\langle \mathcal{O}_1(x_1)...\mathcal{O}_n(x_n)\rangle$. This is rewritten in terms of $D\mathbb{P}_{\text{pq}}$ as

$$\begin{aligned}\langle \mathcal{O}_1(x_1)...\mathcal{O}_n(x_n)\rangle &= \frac{1}{\mathcal{Z}}\int DU\,D\psi D\overline{\psi}\,e^{-\int d^2x\,d^2y\,\overline{\psi}(x)\mathcal{D}_W[U](x,y)\psi(y)-S_g[U]}\mathcal{O}_1(x_1)...\mathcal{O}_n(x_n)\\ &= \frac{1}{\mathcal{Z}}\int DU\,e^{-S_g[U]}\text{Pf}\,\mathcal{D}_W[U]\,\langle \mathcal{O}_1(x_1)...\mathcal{O}_n(x_n)\rangle_F\\ &= \frac{1}{\mathcal{Z}}\int D\mathbb{P}_{\text{pq}}\,\langle e^{i\alpha[U]}\mathcal{O}_1(x_1)...\mathcal{O}_n(x_n)\rangle_F\\ &= \frac{\langle e^{i\alpha[U]}\mathcal{O}_1(x_1)...\mathcal{O}_n(x_n)\rangle_{\text{pq}}}{\langle e^{i\alpha[U]}\rangle_{\text{pq}}}\end{aligned} \tag{6.40}$$

where $\langle\cdot\rangle_F[U]$ denotes the fermionic expectation value, Eq. (3.50), and $\langle\cdot\rangle_{\text{pq}}$ denotes the partially-quenched expectation value,

$$\langle \mathcal{O}(x_1,...,x_k)\rangle_{\text{pq}} \equiv \frac{1}{\mathcal{Z}_{\text{pq}}}\int D\mathbb{P}_{\text{pq}}\,\mathcal{O}(x_1,...,x_k) \qquad \mathcal{Z}_{\text{pq}} \equiv \int D\mathbb{P}_{\text{pq}}. \tag{6.41}$$

Thus, one can compute the correlator $\langle \mathcal{O}_1(x_1)...\mathcal{O}_n(x_n)\rangle$ via the partially-quenched measure as long as the denominator of Eq. (6.40), $\langle e^{i\alpha[U]}\rangle_{\text{pq}}$, is never zero. Configurations are thus generated with respect to the partially-quenched measure $\mathbb{P}_{\text{pq}}$. On each configuration, the phase of the Dirac operator's Pfaffian, $e^{i\alpha[U]}$, is computed and used to evaluate $\langle e^{i\alpha[U]}\rangle_{\text{pq}}$. The closer the phase is to zero, the more difficult the sign problem in the theory is to remove.

6.4.2 Pseudofermions and the Rational Approximation

The Dirac operator Pfaffian of Eq. (6.40) is computationally prohibitive to compute in a sampling algorithm. Instead, sampling the desired probability density $\mathbb{P}_{\text{pq}}$ proceeds via the introduction of pseudofermions [285] to rewrite the norm of the Pfaffian as

$$\begin{aligned}|\text{Pf}\,\mathcal{D}[U]| &= |\text{Det}\,\mathcal{D}[U]|^{1/2} = (\text{Det}[\mathcal{D}^\dagger[U]\mathcal{D}[U]])^{1/4}\\ &\propto \int D\Phi D\Phi^\dagger \exp\left[-\Phi^\dagger(\mathcal{D}^\dagger[U]\mathcal{D}[U])^{-1/4}\Phi\right]\\ &\equiv \int D\Phi\,D\Phi^\dagger e^{-\Phi^\dagger K^{-1/4}[U]\Phi}\end{aligned} \tag{6.42}$$

where here, Φ and $\Phi^\dagger$ are bosonic pseudofermion fields that carry adjoint gauge, Dirac, and spacetime indices, $\Phi^a_\alpha(n)$. The kernel $K[U]$ is defined as

$$K[U] \equiv \mathcal{D}^\dagger[U]\mathcal{D}[U] = Q^\dagger[U]Q[U] \tag{6.43}$$

where $Q[U]$ is the Hermitian Dirac operator, Eq. (6.29).

Numerical evaluation of $K^{-1/4}[U]$ is very expensive. Instead of direct evaluation, a rational approximation $r^{(-1/4)}(K)$ to $K^{-1/4}$ is used,

$$K^{-1/4} \approx r^{(-1/4)}(K). \tag{6.44}$$

The choice of this function $r^{(-1/4)}$ is the heart of Rational HMC (RHMC). Rational approximations work well when the eigenvalues λ of $K[U]$ fall within a given window $[\lambda^{(-1/4)}_{\text{low}}, \lambda^{(-1/4)}_{\text{high}}]$, so K is scaled dynamically by multiplication with a constant to make its eigenvalues fall within that range [286]. For a given configuration U, its minimum and maximum eigenvalues of $K[U]$, $\lambda_{\min}(U)$ and $\lambda_{\max}(U)$, must therefore fall within the domain of convergence,

$$\lambda^{(-1/4)}_{\text{low}} < \lambda_{\min}(U) \ll \lambda_{\max}(U) < \lambda^{(-1/4)}_{\text{high}}. \tag{6.45}$$

This must be monitored as the simulation progresses to ensure no dynamic rescaling is needed. This is cheaper to monitor than the Pfaffian and can be monitored using algorithms such as those found in the PReconditioned Iterative Multi-Method Eigensolver (PRIMME) library [287].

The specifics of the approximation can be found in the Remez Algorithm [288], which also provides the coefficients for the following expansion of K^q for $q \in (-1, 1) \cap \mathbb{Q}$ in terms of P partial fractions:

$$K^q \approx r^{(q)}(K) \equiv \alpha^{(q)}_0 + \sum_{i=1}^{P} \frac{\alpha^{(q)}_i}{K + \beta^{(q)}_i}. \tag{6.46}$$

Note here that this is an operator-valued equation, so $\beta^{(q)}_i$ is really $\beta^{(q)}_i \text{id}$, with the same shape as K. This approximation will be used for $q = -1/4$ to approximate the integral kernel and $q = 1/8$ to initialize the pseudofermions Φ, which will be discussed in Section 6.4.3. For a given range $[\lambda^{(q)}_{\text{low}}, \lambda^{(q)}_{\text{high}}]$, the Remez algorithm allows us to deterministically compute the $(\alpha^{(q)}_i, \beta^{(q)}_i)$ parameters, and provides a bound on the error of the rational approximation, provided the eigenvalues of $K[U]$ lie within

the spectral bound $[\lambda_{\text{low}}^{(q)}, \lambda_{\text{high}}^{(q)}]$[4].

6.4.3 Rational Hamiltonian Monte Carlo (RHMC)

To sample gauge fields from the desired probability distribution (Eq. (6.35)), one simultaneously draws both gauge fields U and pseudofermion fields Φ from the Boltzmann distribution

$$U, \Phi \sim e^{-S_{\text{eff}}[U,\Phi]}, \tag{6.49}$$

with the effective action given by,

$$S_{\text{eff}}[U,\Phi] = S_g[U] + \underbrace{\Phi^\dagger r^{(-1/4)}(K)\Phi}_{S_F[U,\Phi]}. \tag{6.50}$$

Here $S_g[U]$ is the Wilson gauge action (Eq. (3.13)) and $r^{(-1/4)}(K)$ is the rational approximation to $K^{-1/4}[U]$, Eq. (6.46).

Sampling will be performed with the HMC algorithm[5] [290]. The degrees of freedom in the initial problem are the pseudofermion fields $\Phi(n)$ and the gauge fields $U_\mu(n)$, which are parameterized in terms of the $\mathfrak{su}(N)$ algebra as

$$U_\mu(n) = \exp\left(i\omega_\mu^a(n)t^a\right). \tag{6.51}$$

where $\omega_\mu(n) = \omega_\mu^a(n)t^a \in \mathfrak{su}(n)$. HMC introduces an auxiliary momentum variable for the gauge field and simulates the system via Hamiltonian evolution. It is most convenient to implement the sampling in terms of the $d_N = N^2 - 1$ real variables $\omega_\mu^a(n)$, as opposed to the $SU(N)$-valued variables $U_\mu(n)$. The conjugate momenta to $\omega_\mu^a(n)$ have coordinates $\Pi_\mu^a(n)$, with $\Pi_\mu(n) = \Pi_\mu^a(n)t^a \in \mathfrak{su}(N)$ and $e^{i\Pi_\mu(n)} \in SU(N)$ the conjugate momenta to the fundamental links $U_\mu(n)$. The effective Hamiltonian

[4]Another common convention for $r^{(q)}(K)$ is called the Zolotarev rational approximation [285], which is cited here for completeness,

$$r^{(q)}(K) = a_0^{(q)} \prod_{k=1}^{P} \frac{K + a_{2k-1}^{(q)}}{K + a_{2k}^{(q)}}. \tag{6.47}$$

The Zolotarev approximation is equivalent to Eq. (6.46) with the identifications,

$$a_0^{(q)} = \alpha_0^{(q)} \qquad a_{2k}^{(q)} = \beta_k^{(q)} \qquad \frac{\alpha_k^{(q)}}{\alpha_0^{(q)}} = \frac{\prod_{\ell=1}^{P}(-a_{2k}^{(q)} - a_{2\ell-1}^{(q)})}{\prod_{\ell\neq k}^{P}(-a_{2k}^{(q)} - a_{2\ell}^{(q)})}. \tag{6.48}$$

[5]The RHMC algorithm describes anytime HMC is used with a rational expansion of the kernel K^{-p} for $0 < p < 1$ [289].

is,

$$\begin{aligned} H[U,\Pi,\Phi] &= \frac{1}{2}\sum_{n\in\Lambda}\mathrm{Tr}[\Pi_\mu(n)^2] + S_{\text{eff}}[U,\Phi] \\ &= \frac{1}{2}\sum_{n}\mathrm{Tr}[\Pi_\mu(n)^2] + S_g[U] + \Phi^\dagger K^{-1/4}[U]\Phi. \end{aligned} \tag{6.52}$$

where the notation $H[\omega,\Pi,\Phi]$ is used interchangeably with $H[U,\Pi,\Phi]$.

The degrees of freedom for the problem must be initialized, which is performed as follows at computer time $s=0$.

- $\Pi_\mu(n;s=0)$: The conjugate momenta at time $s=0$ is distributed to a random Gaussian [285],

$$f(\Pi_\mu) = e^{-\mathrm{Tr}[\sum_{n\in\Lambda}\Pi_\mu(n)^2]} = e^{-\mathrm{Tr}[\frac{1}{2}\sum_{n\in\Lambda}(\Pi^a_\mu(n))^2]}. \tag{6.53}$$

- $U_\mu(n;s=0)$: There are two general methods to initialize $U_\mu(n)$, which both must agree after thermalization (Section 3.4). One either uses a **hot start** and initializes $U_\mu(n;s=0)$ to a random $SU(N)$ gauge field, or a **cold start** and initializes $U_\mu(n;s=0)$ to the identity link field.

- $\Phi(n;s=0)$: Pseudofermions at $s=0$ are distributed according to

$$f(\Phi) \propto e^{-\Phi^\dagger K^{-1/4}\Phi}. \tag{6.54}$$

  The choice of the distribution $f(\Phi)$ as well as a practical implementation for sampling from $f(\Phi)$ are discussed below.

Computer-time evolution of $\Phi(n;s)$, $U_\mu(n;s)$, and $\Pi_\mu(n;s)$ proceeds via Hamilton's equations for the system governed by the effective Hamiltonian, Eq. (6.52),

$$\begin{aligned} \delta_s\Pi^a_\mu(n) &= -\delta_{\omega^a_\mu(n)}H = -\left(\frac{\delta S_g[\omega]}{\delta\omega^a_\mu(n)} + \Phi^\dagger\frac{\delta K[\omega]^{-1/4}}{\delta\omega^a_\mu(n)}\Phi\right) \equiv -F^a_\mu(n)[\omega,\Phi] \\ \delta_s\omega^a_\mu(n) &= \delta_{\Pi^a_\mu(n)}H = \Pi^a_\mu(n) \end{aligned} \tag{6.55}$$

where the derivative is the force driving the conjugate momenta update,

$$F^a_\mu(n)[\omega,\Phi] = \frac{\delta S_g[\omega]}{\delta\omega^a_\mu(n)} + \Phi^\dagger\frac{\delta K[\omega]^{-1/4}}{\delta\omega^a_\mu(n)}\Phi \equiv (F_g)^a_\mu(n)[\omega] + (F_{\text{pf}})^a_\mu(n)[\omega,\Phi]. \tag{6.56}$$

Note that these forces depend functionally on ω and Φ, but in terms of indices, they

have an adjoint color, Lorentz, and spacetime index (a, μ, n). The explicit form for each force is computed in Appendix K.

It is often useful to recast the evolution equations to algebra-valued equations,

$$\begin{aligned}\delta_s \Pi_\mu(n) &= -\delta_{\omega_\mu(n)} H = -\left(\frac{\delta S_g[\omega]}{\delta \omega_\mu(n)} + \Phi^\dagger \frac{\delta K[\omega]^{-1/4}}{\delta \omega_\mu(n)} \Phi\right) \equiv -F_\mu(n)[\omega, \Phi] \\ \delta_s \omega_\mu(n) &= \delta_{\Pi_\mu(n)} H = \Pi_\mu(n)\end{aligned} \tag{6.57}$$

where here $\Pi_\mu(n) = \Pi_\mu^a(n) t^a \in \mathfrak{su}(N)$ and $\omega_\mu(n) = \omega_\mu^a(n) t^a \in \mathfrak{su}(N)$. The algebra representation is more compact in certain cases, which will specified if this is the case.

Hamilton's equations (Eqs. (6.55, 6.57)) are used to evolve the fields in computer time via leapfrog integration, a symplectic integrator [291]. Let $\Phi_0 \equiv \Phi(s)$, $\omega_0 \equiv \omega(s)$, and $\Pi_0 \equiv \Pi(s)$ denote the values of the fields at computer time s. Evolution of these fields to computer time $s+1$ consists of $n_{\text{inner}} \geq 1$ inner iterations with step size ϵ which proceed as follows:

1. (Initialize pseudofermions) Draw a pseudofermion Φ from the distribution

$$f(\Phi) \propto e^{-\Phi^\dagger K^{-1/4} \Phi}. \tag{6.58}$$

In practice, this is done by defining,

$$\Psi(\Phi) = K^{-1/8}[U]\Phi \qquad\qquad \Phi(\Psi) = K^{1/8}[U]\Psi \tag{6.59}$$

reducing the probability density to,

$$\tilde{f}(\Psi) = f(\Phi)\left(\text{Det}\frac{\partial \Phi}{\partial \Psi}\right)^{-1} = \text{Det}\left(K^{-1/8}[U]\right) e^{-\Psi^\dagger \Psi}. \tag{6.60}$$

The $\text{Det}\left(K^{-1/8}[U]\right)$ is a constant normalization independent of Ψ, hence one samples Ψ from the $2 \times (N_c^2 - 1)$-dimensional Gaussian distribution and constructs $\Phi(n)$ from Eq. (6.59) using the rational approximation $r^{(1/8)}(K)$ to $K^{1/8}$,

$$\Phi \approx r^{(1/8)}(K)\Psi. \tag{6.61}$$

2. (Initial inner update) $\Pi_{1/2} \leftarrow \Pi_0 - \frac{\epsilon}{2} F[\omega_0, \Phi]$.

3. (Intermediate inner updates) For $k = 1, 2, ..., n_{\text{inner}} - 1$, update $\omega_k \leftarrow \omega_{k-1} + \epsilon\, \Pi_{k-1/2}$ and $\Pi_{k+1/2} \leftarrow \Pi_{k-1/2} - \epsilon F[\omega_k, \Phi]$.

4. (Final inner update) $\omega_n \leftarrow \omega_{n-1} + \epsilon\,\Pi_{n-1/2}$ and $\Pi_n \leftarrow \Pi_{n-1/2} - \frac{\epsilon}{2}F[\omega_n, \Phi]$.

5. (Accept-reject step) Accept the new trajectory (ω_n, Π_n) only if a random $r \sim \text{Unif}[0,1]$ satisfies,

$$r < \exp\left(H[\omega_0, \Pi_0, \Phi] - H[\omega_n, \Pi_n, \Phi]\right) \tag{6.62}$$

   where H is the effective Hamiltonian for the system, Eq. (6.52).

The updated fields are then defined as either $(\omega(s+1), \Pi(s+1) \leftarrow (\omega_n, \Pi_n)$ is the accept-reject condition (Eq. (6.62)) holds, or $(\omega(s+1), \Pi(s+1) \leftarrow (\omega_0, \Pi_0)$ if not (i.e. the fields are not updated in this case).

The number of inner iterations n_{inner} and the step size ϵ must be tuned for the set of parameters the theory is simulated at. The more inner iterations performed, the better the accuracy of the leapfrog integrator. However, the cost of updating a configuration will scale linearly with n_{inner}, so it cannot be taken to be too large, or the computation will be prohibitively expensive. The simulations performed in this project typically use n_{inner} to be about 10 to 25. The step size ϵ is chosen to make the accept-reject rate close to 50%. If ϵ is large, each update will cover a large amount of field space but is more likely to be rejected.

6.5 Lattice Gauge Theory Setup

The data and figures presented throughout this section will be for the set of ensembles shown in Table 6.1. Each ensemble is generated with $N = 2$ colors, although it is planned to generate configurations at larger N ($N = 3, 4, 5$) to explore the N dependence of the spectrum. Representative plots shown in the remaining sections will be of the $L \times T = 20 \times 20$ ensemble, which has a large enough lattice size that the physics is representative of the other ensembles, with sufficient statistics such that the signal-to-noise ratio is small. The values of β and κ are chosen to fix the one-loop fermion mass.

All code for this project (RHMC implementation, correlator measurements, and fitting) is implemented in Python and can be found in the adjoint_qcd Github repository. The ensembles of Table 6.1 were generated on personal computers. Ensembles are now being generated using MIT's SuperCloud computing cluster [292].

To test that the RHMC code was sampling the correct distribution, two ensembles were generated for each set of parameters in Table 6.1. For each set of parameters,

L	T	β	κ	N_{cfgs}
10	10	3.125	0.138889	90
12	12	4.5	0.15	90
14	14	6.125	0.159091	90
16	16	8.0	0.166667	90
18	18	10.125	0.173077	90
20	20	12.5	0.178571	90
22	22	15.125	0.183333	90
24	24	18.0	0.1875	76
26	26	21.125	0.191176	58
28	28	24.5	0.194444	45

Table 6.1. Parameters for the lattice ensembles used in this study. Each study was performed on a 2-dimensional lattice with size $L \times T$ with $N = 2$ adjoint colors. The gauge coupling is β, and the fermion hopping parameter is κ. The total number of independent configurations (after thermalization) generated on each ensemble is N_{cfgs}.

the first ensemble was seeded with a cold start ($U_\mu(s = 0) = 1_N$), and the second ensemble was seeded with a hot start ($U_\mu(s = 0)$ taken to be a random $SU(N)$ matrix at each link). Four gauge observables were monitored on each configuration: the plaquette expectation value,

$$\langle \mathcal{P} \rangle \equiv \frac{1}{LT} \sum_{x \in \Lambda} \langle \mathcal{P}(x) \rangle, \tag{6.63}$$

and the expectation value of the 2×1, 3×1, and 2×2 Wilson loops $\langle W(2,1) \rangle$, $\langle W(3,1) \rangle$, and $\langle W(2,2) \rangle$, where $W(r,t)(x)$ is the Wilson loop formed around a $l \times t$ rectangle starting at $x \in \Lambda$,

$$\begin{aligned} W(r,t) = &\left(\prod_{k=0}^{r-1} U_0(x + k\,\hat{0}) \right) \left(\prod_{k=0}^{t-1} U_1(x + r\,\hat{0} + k\,\hat{1}) \right) \\ &\left(\prod_{k=1}^{r} U_0(x + (r-k)\,\hat{0} + t\,\hat{1}) \right)^\dagger \left(\prod_{k=1}^{t} U_1(x + (t-k)\,\hat{1}) \right)^\dagger . \end{aligned} \tag{6.64}$$

Note that $W(1,1)(x) = \mathcal{P}(x)$. For each set of ensembles, the hot start and cold start for all three observables converged to the same value, indicating that the same distribution is being sampled regardless of where the Markov chain is started.

Data for the volume-averaged plaquette $\langle \mathcal{P} \rangle$ is shown in Figure 6.1 and used to determine the Markov chain's thermalization time and correlation length. The total

number of configurations generated for each ensemble is given by N_{total} in Table 6.1. The thermalization time for each ensemble is about 1,000 samples, which may be seen from when each trajectory in Figure 6.1 approaches its plateau value. Only the configurations sampled after the thermalization time are used in the analysis. The correlation length τ_P of $\langle \mathcal{P} \rangle$ is between 50 and 100 units of computer time on each ensemble, computed as [293],

$$\tau_P(M) = 1 + 2 \sum_{s=1}^{M} \hat{\rho}_P(s). \tag{6.65}$$

Here $\hat{\rho}_P(s)$ is the normalized autocorrelation function for $\{P_i\}$, defined as $\hat{\rho}_P(s) \equiv c(s)/c(0)$, where $c(s)$ is the autocorrelation function with lag s,

$$c(s) \equiv \frac{1}{N_{\text{cfgs}} - s} \sum_{n=1}^{N_{\text{cfgs}}-s} (P_i - \langle P \rangle)(P_{i+s} - \langle P \rangle), \tag{6.66}$$

and $M < N_{\text{cfgs}}$ is a cutoff on the lag of the autocorrelation function because large values of s will be statistically noisy. In practice, one chooses $M \ll N_{\text{cfgs}}$ to be the smallest value such that $M > C\tau_P(M)$, for a constant $C \approx 5$ which is empirically determined by the data. The plaquette values in Figure 6.1 are shown in units of 100 samples, so that each point is an approximately independent measurement. The set of ensembles shown in Table 6.1 has a relatively weak coupling, as the free-field value of $\langle \mathcal{P} \rangle$ is 1. Additional ensembles of parameters are currently being run with larger values of β to sample the theory in the strongly-coupled regime.

The Pfaffian of the Dirac operator has been measured with the pfapack Python library [294] on each configuration to determine if the calculation must be reweighted (Section 6.4.1). Figure 6.2 shows determined to be real and positive, with $\operatorname{Im} \operatorname{Pf} \mathcal{D}[U] < 10^{-15}$. An example of this is shown in Figure 6.2 for the 20×20 ensemble. This indicates there is no need to reweight the observables on these configurations. However, this is not an exhaustive proof that the Pfaffian is real and positive. Every configuration sampled must have the phase of the Pfaffian computed to determine if the observables must be reweighted during the computation.

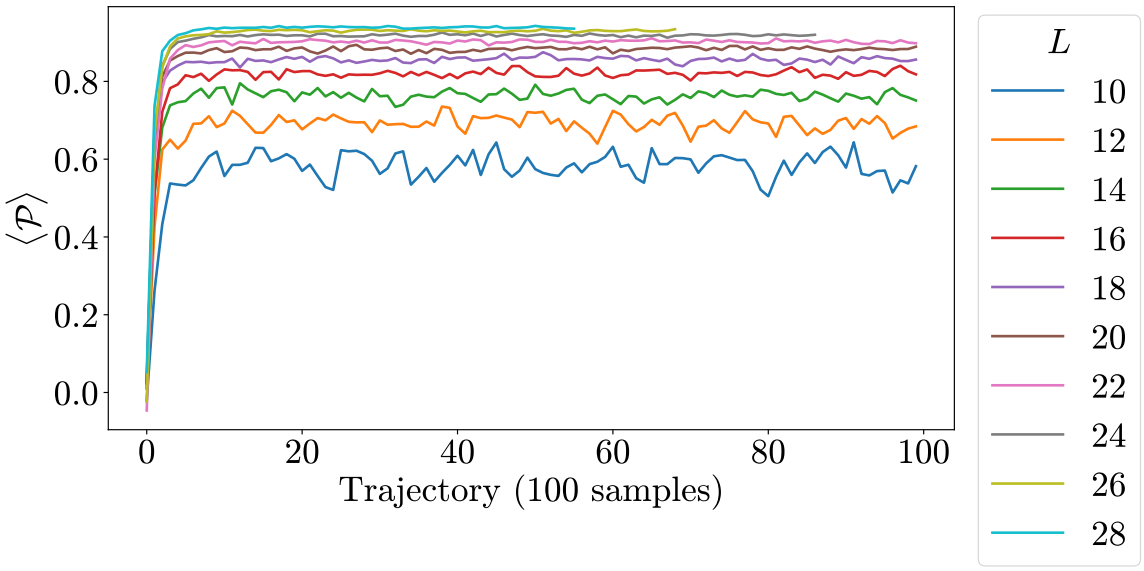

Figure 6.1. Volume-averaged plaquette $\langle \mathcal{P} \rangle$ (Eq. (6.63)) on each ensemble. Each colored curve corresponds to an ensemble in Table 6.1. The correlation length on each ensemble is between 50 and 100 units of computer time, hence each point shows an independent sample. Because fewer configurations are generated for the larger values of L (24, 26, 28), the plaquette streams stop earlier. Note that after 10 samples, $\langle \mathcal{P} \rangle$ has thermalized on all ensembles.

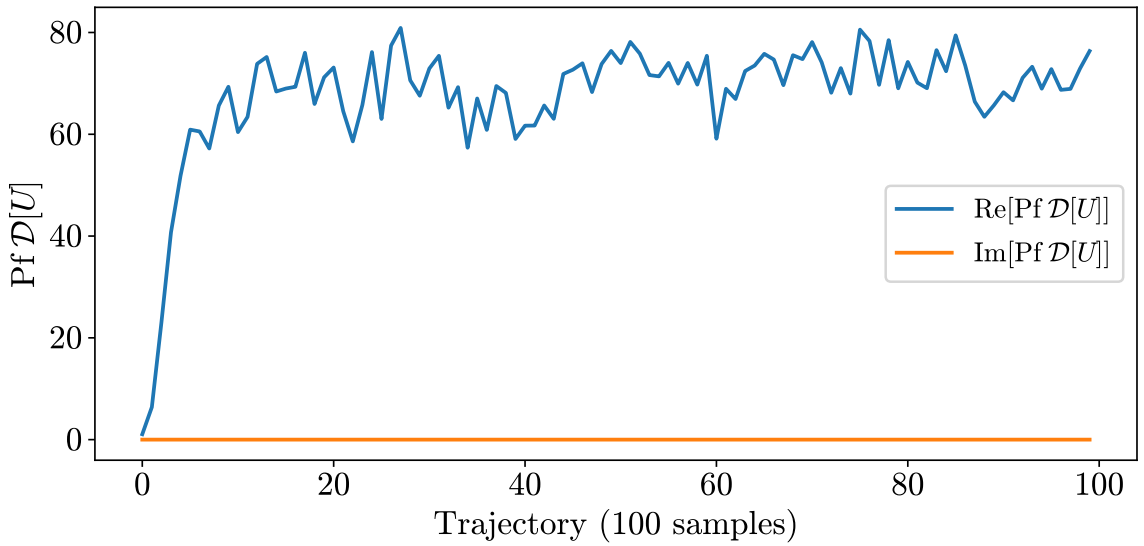

Figure 6.2. The Pfaffian of the Dirac operator, measured on the N_{cfgs} independent configurations for the $L \times T = 20 \times 20$ ensemble. The real part of the Pfaffian is denoted in blue, and the imaginary part is in orange. The magnitude of $\operatorname{Im} \operatorname{Pf} \mathcal{D}[U]$ is less than 10^{-14}, indicating that the Pfaffian is purely real and there is no need to reweight the calculation on these configurations.

6.6 The Static Quark Potential and String Tension

The static quark potential $V(r)$ is computed through the asymptotic form for the fundamental Wilson loop as $t \to \infty$,

$$\langle W(r,t) \rangle = Ce^{-V(r)t}, \tag{6.67}$$

given in Eq. (6.1), where C is a constant independent of r and t. Corrections to this equation occur at $\mathcal{O}(e^{-t\Delta E})$, where ΔE is the gap between $V(r)$ and the first excited $q\bar{q}$ state. The large t limit of the Wilson loop hence allows for an extraction of the static quark potential $V(r)$. The static quark potential for a confining theory may be parameterized as a linear term plus a Coulomb term,

$$V(r) \sim A + \sigma r + \frac{B}{r}, \tag{6.68}$$

where A, B are coefficients and σ is the string tension. Note that Eq. (6.68) is in lattice units; units will be restored to this equation later in this section to set the scale.

The static quark potential is defined for a fundamental fermion. In general, one can compute the static quark potential between fermions in a representation $\mathcal{R}$ with N-ality k, $V_{\mathcal{R}}(r)$, by using the $\mathcal{R}$-Wilson line $W_{\mathcal{R}}(r,t)$. An explicit formula for $W_{\mathcal{R}}(r,t)$ can be obtained by replacing U_μ in the definition of the fundamental line $W(r,t)$, Eq. (6.64), with its image under $\mathcal{R}$,

$$\begin{aligned} W_{\mathcal{R}}(r,t) = &\left(\prod_{k=0}^{r-1} \mathcal{R}(U_0)(x + k\,\hat{0})\right)\left(\prod_{k=0}^{t-1} \mathcal{R}(U_1)(x + r\,\hat{0} + k\,\hat{1})\right) \\ &\left(\prod_{k=1}^{r} \mathcal{R}(U_0)(x + (r-k)\,\hat{0} + t\,\hat{1})\right)^\dagger \left(\prod_{k=1}^{t} \mathcal{R}(U_1)(x + (t-k)\,\hat{1})\right)^\dagger. \end{aligned} \tag{6.69}$$

The static quark potential in representation $\mathcal{R}$ is extracted from the $\mathcal{R}$-Wilson loop identically to the fundamental case, Eq. (6.1), as $\langle W_{\mathcal{R}}(r,t) \rangle \xrightarrow{t\to\infty} e^{-V_{\mathcal{R}}(r)t}$. This $\mathcal{R}$-potential has an analogous parameterization to Eq. (6.68) with k-dependent coefficients A_k, B_k, and σ_k. The linear coefficient σ_k is the k-string tension.

On each configuration in each ensemble of Table 6.1, all possible Wilson loops are calculated. This is not computationally intensive because the lattice sizes are relatively small; for larger lattices, all Wilson loops up to a given maximum spatial

and temporal size will be computed: it is not necessary to keep every Wilson loop, as the signal-to-noise degrades with the size of the loop. The data is bootstrapped with $n_b = 100$ bootstrap samples drawn on each ensemble. Figure 6.3 shows measurements of all volume-averaged Wilson loops $W(r,t)$ on the 20×20 ensemble.

The set of all Wilson loops on the 20×20 ensemble, $\langle W(r,t)\rangle$, is shown in Figure 6.3. For each fixed r, the static quark potential $V(r)$ is extracted by performing a correlated fit to the data with the exponential model,

$$f_r(t) = Ce^{-V(r)t} \tag{6.70}$$

The model has unknown parameters C and $V(r)$ and models the lowest-order term in the expansion of Eq. (6.1). The data for $\langle W(r,t)\rangle$ becomes too noisy to constrain the fit around $t = 10$: when this data is included, it does not shift the fit at all, and its contribution to the χ^2 function is very small because of its large uncertainty. As a result, fits are performed over the range $t \in [1, 10]$. Correlations in $\langle W(r,t)\rangle$ are propagated to correlations in $V(r)$ fitting each bootstrap to extract an ensemble $\{V_b(r)\}_{b=1}^{n_b}$. The statistical error on the bootstrap ensemble $\{V_b(r)\}_b$ is consistent with the error on $V(r)$ from the fit.

The best-fit bands on the 20×20 ensemble are shown in Figure 6.4. The fits for low r (on this ensemble, $r \leq 4$) have χ^2/dof between 0.5 and 1.5, which degrades as r increases and the signal-to-noise ratio becomes smaller. The fit results for the static quark potential $V(r)$ are plotted against r in Figure 6.5 for the 20×20 ensemble. The trend in the data is linear, which indicates a confining potential. A correlated fit is performed of the potential $V(r)$ to a linear model $A + \sigma r$ (Eq. (6.68) with $B = 0$), as the data does not appear to have a Coulomb term. Adding the Coulomb term B/r to the model causes overfitting— identified as the posterior value of B being significantly larger than the posterior values of A and σ— which drastically changes the behavior of the functional form fit to the data. The simulated ensembles are likely too coarse to see the appearance of such a term, as it dominates at short distances. Only the first 4 points in $V(r)$ are used for the fit, as extracting $V(r)$ is difficult at higher r: the resulting fits have $\chi^2/\text{dof} \gg 1$, indicating a poor goodness of fit. Figure 6.5 shows the resulting static quark potential, with the fit band overlaid onto the data. Although the fit band underestimates $V(r)$ for $r \geq 5$, this is likely due to the difficulty of extracting $V(r)$ at these values of r. As seen in Figure 6.4, there are only a small number of resolved points for the Wilson loop $\langle W(r,t)\rangle$ at these values, which makes the fits performed to extract $V(r)$ unreliable. The posterior on σ is the

string tension for the given ensemble in lattice units. The extracted values of the string tension for each ensemble are shown in Table 6.2.

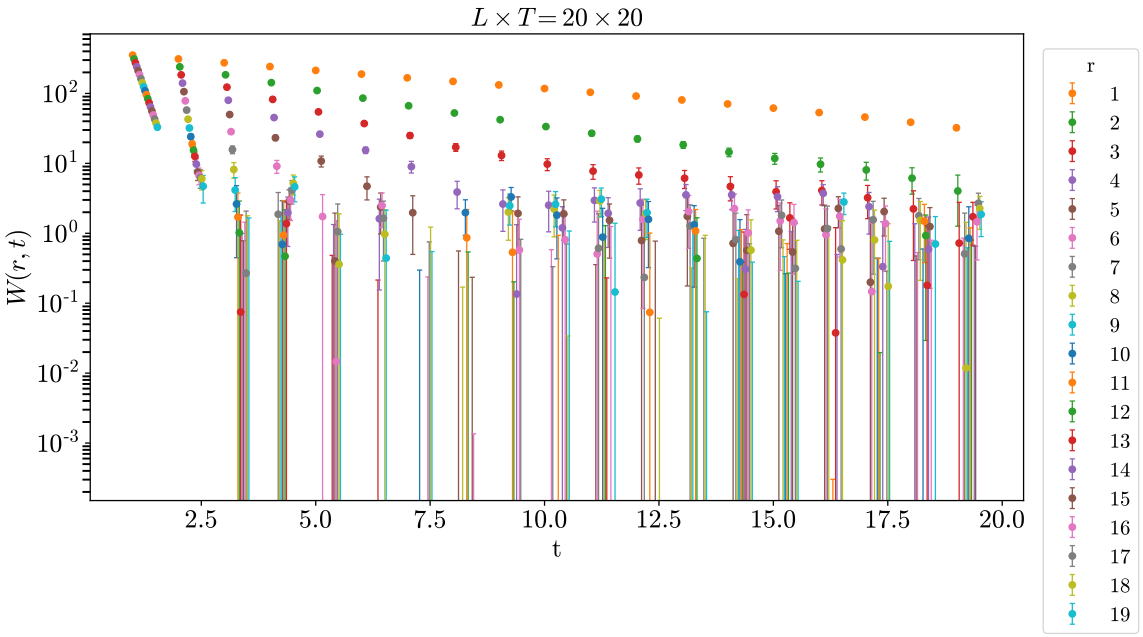

Figure 6.3. All volume-averaged Wilson loops $\langle W(r,t)\rangle$ for the 20×20 ensemble, plotted on a logarithmic scale as a function of the temporal size t. The color of each point denotes its spatial size r, which is further emphasized in the plot by offsetting points with different values of r. At fixed r, the slope of the log plot roughly corresponds to the static quark potential $V(r)$.

The string tension is used to set the scale of each ensemble. The general methodology behind scale setting in LGT is reviewed in Section 3.3.4. QCD_2 is not a physical theory, hence there are no experimental measurements of observables that one can match to set the scale. The scale must, therefore, be set with a relative scale setting scheme: scales between different ensembles are meaningful, but the absolute magnitude of a scale is not meaningful. The scheme adopted in this calculation hence measures the lattice spacing in units of σ^{-1}, where σ is the physical value of the constant string tension across ensembles. This implies that the lattice spacing may be computed as,

$$a = a\sigma \ [\sigma^{-1}] \tag{6.71}$$

where the quantity $a\sigma$ is tabulated in Table 6.2. The scale of each ensemble is plotted in Figure 6.6 in units of σ^{-1}.

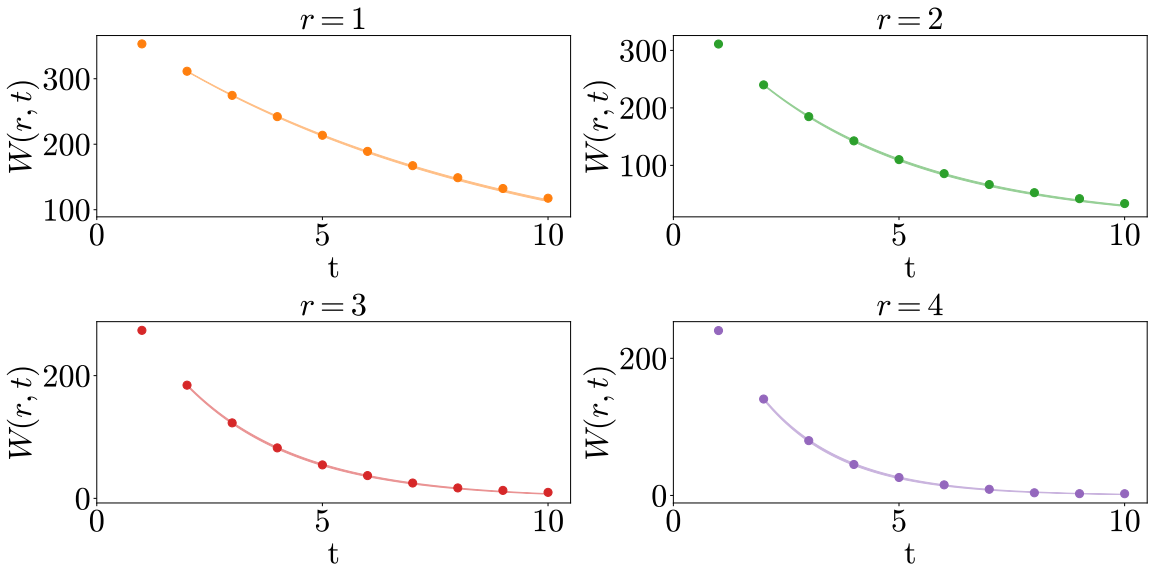

Figure 6.4. Volume-averaged Wilson loops $\langle W(r,t)\rangle$ for the 20×20 ensemble with $r \leq 4$, plotted against the temporal extent t of the loop for $t \leq 10$. The shaded colored band on each plot denotes the best-fit band from an exponential fit (Eq. (6.70)). The single-exponential model fits the data well, with χ^2/dof values between 0.5 and 1.5.

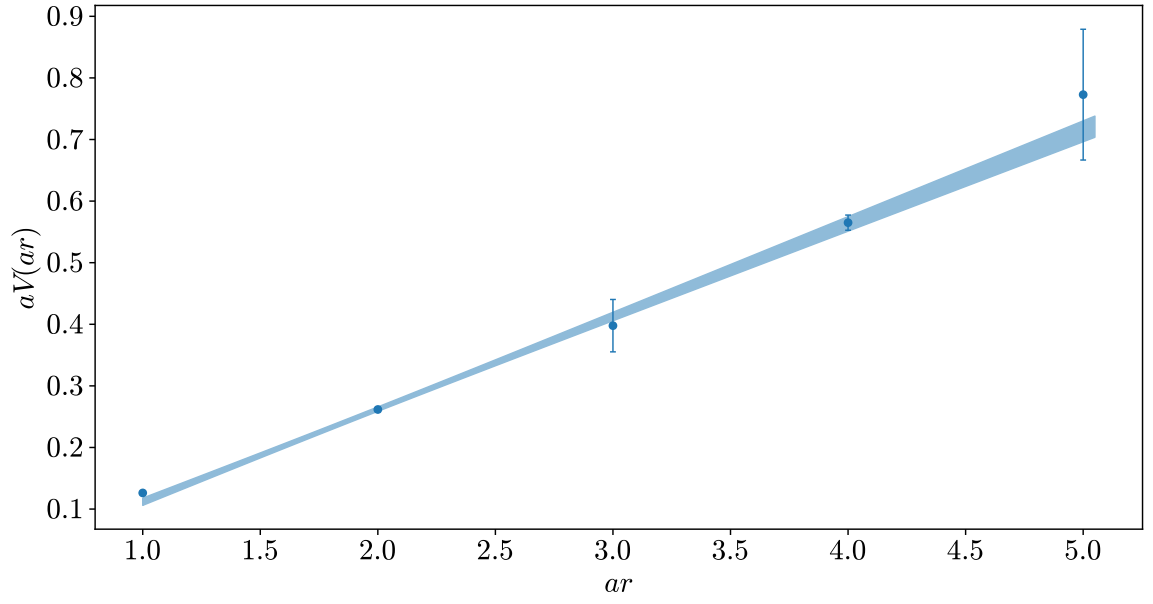

Figure 6.5. Static quark potential for the 20×20 ensemble, computed for $r \leq 5$. The static quark potential is fit to the linear model $V(r) \sim A + \sigma r$ to determine the string tension σ. Results for the string tension on each ensemble are given in Table 6.2.

Ensemble	$a\sigma$
10	0.534(33)
12	0.389(13)
14	0.2614(50)
16	0.2029(33)
18	0.1518(24)
20	0.1347(16)
22	0.1029(15)
24	0.0818(10)
26	0.083(46)
28	0.06640(78)

Table 6.2. Numerical results for the string tension (and lattice scale a) for each adjoint QCD ensemble in Table 6.1. The string tension is computed by fitting the static quark potential $V(r)$ to a linear model. The scale is then set by the string tension, and the lattice spacing of each ensemble equals $a\sigma$ in units of σ^{-1}.

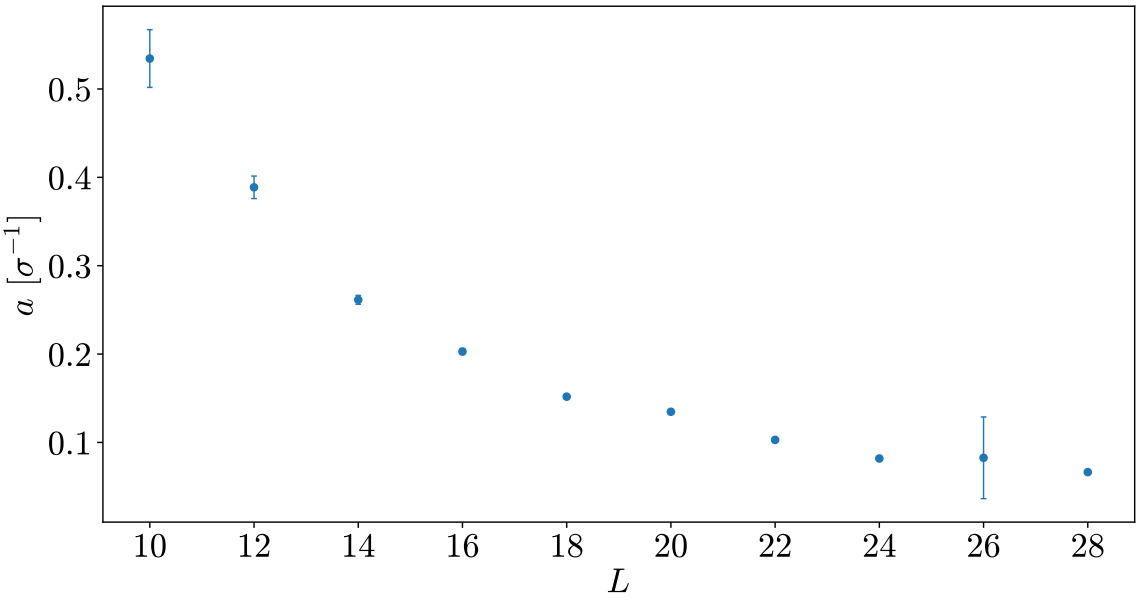

Figure 6.6. Scales for each ensemble set by the string tension, in units of σ^{-1}. Note the value on the vertical axis is simply the dimensionless string tension $a\sigma$ of Table 6.2.

6.7 Spectroscopy

6.7.1 Wick's Theorem for Majorana Fermions

Wick's theorem (Section 3.3.2) is typically derived in the context of Dirac fermion observables. The theorem's conclusion remains the same for Majorana fermions, but it is insightful to confirm this explicitly. Consider the two-point function for a Majorana fermion ψ, with the action of Eq. (6.21).

$$\langle \psi_\alpha^a(x)\psi_\beta^b(y)\rangle = \frac{1}{\mathcal{Z}}\int DU e^{-S_G[U]}\int D\psi \exp\left(-\frac{1}{2}\int d^4x\, d^4y\, \overline{\psi}(x)\mathcal{D}(x,y)\psi(y)\right)\psi_\alpha^a(x)\psi_\beta^b(y). \tag{6.72}$$

The key identity used here is $\overline{\psi} = \psi^T C$, where $C = \gamma_5$ is the charge conjugation matrix. This integral must be explicitly performed to evaluate the base case of Wick's theorem; the rest extends by standard combinatorial arguments. The fermion generating functional with a Majorana fermion source $J_\alpha^a(x)$ is,

$$\mathcal{Z}[J] = \int D\psi \exp\left(-\frac{1}{2}\int d^4x\, d^4y\, \overline{\psi}(x)\,\mathcal{D}(x,y)\,\psi(y) - \int d^4x\, J_\alpha^a(x)\psi_\alpha^a(x)\right). \tag{6.73}$$

This integral is evaluated by completing the square in the integrand,

$$\begin{aligned} -\frac{1}{2}\overline{\psi}\mathcal{D}\,\psi &= -\frac{1}{2}\psi^T Q\psi - J^T\psi = -\frac{1}{2}(\psi^T Q\psi - J^T\psi + \psi^T J) \\ &= -\frac{1}{2}(\psi^T - J^T Q^{-1})Q(\psi + Q^{-1}J) - \frac{1}{2}J^T Q^{-1}J \\ &= -\frac{1}{2}(\psi + Q^{-1}J)^T Q(\psi + Q^{-1}J) - \frac{1}{2}J^T Q^{-1}J \\ &\equiv -\frac{1}{2}\widetilde{\psi}^T Q\widetilde{\psi} - \frac{1}{2}J^T Q^{-1}J. \end{aligned} \tag{6.74}$$

where $J^T\psi = -\psi^T J$, and note that $\overline{\psi}\mathcal{D} = \psi^T C\mathcal{D} = \psi^T Q$ and $Q^T = -Q$ by definition. Here $\widetilde{\psi} \equiv \psi + Q^{-1}J$ is the shifted ψ variable which can now be integrated over:

$$\mathcal{Z}[J] = \int D\psi\, e^{-\frac{1}{2}\overline{\psi}\mathcal{D}\psi - J^T\psi} = \int D\widetilde{\psi}\, e^{-\frac{1}{2}\widetilde{\psi}^T Q\widetilde{\psi} - \frac{1}{2}J^T Q^{-1}J} = \mathrm{Pf}[Q]\exp\left(-\frac{1}{2}J^T Q^{-1}J\right). \tag{6.75}$$

Note that as expected, $\mathcal{Z}[0] = \mathcal{Z} = \mathrm{Pf}[Q]$.

The explicit evaluation of $\mathcal{Z}[J]$ may now be used to compute correlation functions.

Consider the fermion two-point function,

$$\langle \psi^a_\alpha(x)\psi^b_\beta(y)\rangle = \frac{1}{\mathcal{Z}[0]}\frac{\delta}{\delta J^a_\alpha(x)}\frac{\delta}{\delta J^b_\beta(y)}\bigg|_{J=0}\mathcal{Z}[J] = -(Q^{-1})^{ab}_{\alpha\beta}(x,y). \tag{6.76}$$

This yields the correlator,

$$\langle \psi^a_\alpha(x)\overline{\psi}^b_\beta(y)\rangle = \overline{\psi}^a_\alpha(x)\psi^b_\beta(y)\rangle C_{\delta\beta} = -(Q^{-1}C)^{ab}_{\alpha\beta}(x,y) = -(\mathcal{D}^{-1})^{ab}_{\alpha\beta}(x,y), \tag{6.77}$$

which in turn produces an expression for the chiral condensate in terms of the propagator $S(x,y) \equiv \mathcal{D}^{-1}(x,y)$ of the theory,

$$v \equiv \frac{1}{LT}\sum_{x\in\Lambda}\langle\overline{\psi}(x)\psi(x)\rangle = \frac{1}{LT}\sum_{x\in\Lambda}\langle\overline{\psi}^a_\alpha(x)\psi^a_\alpha(x)\rangle = -\frac{1}{LT}\sum_{x\in\Lambda}\mathrm{Tr}\, S(x,x). \tag{6.78}$$

For the numerical calculation, this allows for the extension of the usual LGT machinery to Majorana fermions once the correct configurations are sampled with RHMC (Section 6.4.3). Propagators are the fundamental building blocks of any fermionic observable. In four-dimensional LQCD, entire propagators ("all-to-all propagators") are not computed fully, as they require huge amounts of computation and storage to use (c.f. Section 3.3.3). For the two-dimensional lattices used in this work (Table 6.1), the number of lattice sites is small enough that propagators can be computed and stored directly using matrix inversion routines. The computation size is small enough that this is not prohibitive as it is in $d = 4$. For each ensemble, the Dirac operator is constructed on each configuration (Section 6.3.2) and then inverted. The inverse matrix is stored in memory, and correlation functions may then be computed at will without the need for simplifications.

6.7.2 Local Fermion Bilinears

Spectroscopic calculations are performed to extract the ground-state energies of the scalar and pseudoscalar mesons on the ensembles of Table 6.1. For an overview of the quantum numbers of fermion bilinears in $d = 2$, see Appendix J.3. The quantum numbers of the fermion bilinear $\overline{\psi}\Gamma\psi$ are different in $d = 2$ than in $d = 4$ and given in Table J.1. There are only two classes of states that may be excited– scalar and pseudoscalar– each of which is characterized by its transformation under parity P and charge conjugation C. Scalar states satisfy $PC = ++$ and are excited by the Dirac structures 1 and γ^1, while pseudoscalar states satisfy $PC = --$ and are excited by the structures γ_5 and γ^0.

To excite a mesonic state with the quantum numbers of $\Gamma \in \{1, \gamma_5, \gamma^0, \gamma^1\}$, consider the momentum-projected interpolator,

$$\chi_\Gamma(t;p) = \frac{1}{\sqrt{L}} \sum_x e^{-ipx}\, \overline{\psi}(x,t)\Gamma\psi(x,t). \tag{6.79}$$

Ground-state energies are extracted by constructing the two-point function at $p = 0$ momentum[6],

$$C_2^\Gamma(t;p) = \frac{1}{T} \sum_s \langle \chi_\Gamma(t+s;p)\overline{\chi}_\Gamma(s;p)\rangle. \tag{6.80}$$

This is directly computable on these ensembles by performing all possible Wick contractions (Section 6.7.1),

$$\begin{aligned} C_2^\Gamma(t;p) = \frac{1}{V}\sum_s \sum_{x,y} e^{-ip(x-y)} \Bigg(&\mathrm{Tr}\left[S(y,s;x,t+s)\Gamma S(x,t+s;y,s)\widetilde{\Gamma}\right] \\ &+ \mathrm{Tr}\left[S(x,t+s;x,t+s)\Gamma\right]\ \mathrm{Tr}\left[S(y,s;y,s)\widetilde{\Gamma}\right]\Bigg), \end{aligned} \tag{6.81}$$

where $\widetilde{\Gamma} \equiv \gamma^0\Gamma^\dagger\gamma^0$. Note that in $d = 4$, $\widetilde{\Gamma} = \Gamma$ for $\Gamma = \gamma^\mu$, which may be used to simplify $\widetilde{\Gamma}$; in $d = 2$, this does not necessarily hold (i.e., for $\Gamma = \gamma^1$).

The two-point correlator $C_2^\Gamma(t;0)$ is computed on each of the ensembles in Table 6.1 for each $\Gamma \in \{1, \gamma_5, \gamma^0, \gamma^1\}$. Data for $C_2^\Gamma(t;0)$ is shown in Figure 6.7 on the 20×20 ensemble, plotted on a logarithmic scale against time t. The same data is shown as cosh-corrected effective masses (Eq. (3.45)) in Figure 6.8. Observe that the data for $\Gamma = \gamma_5$ and $\Gamma = \gamma^0$ is nearly degenerate, which indicates that both interpolators excite the same set of states. This is consistent with the analytic structure of these operators, as both operators are expected to excite states with the same quantum numbers, $PC = --$.

[6]Eq. (6.80) is presented at arbitrary p to keep the equation at full generality.

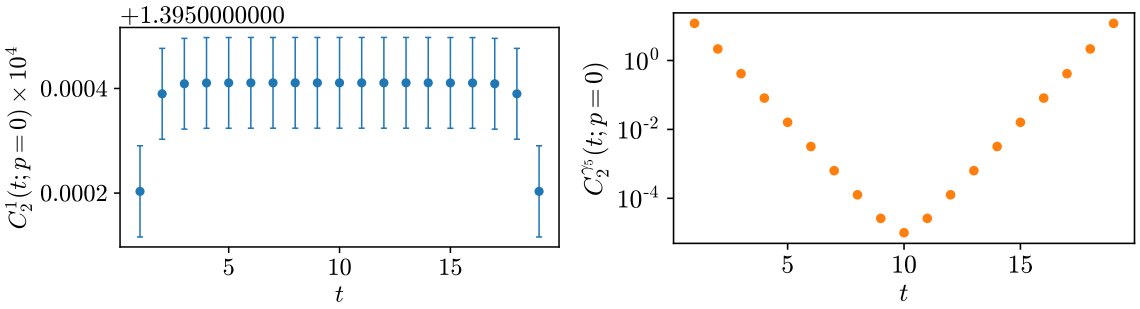

(a) $\Gamma = 1$

(b) $\Gamma = \gamma_5$

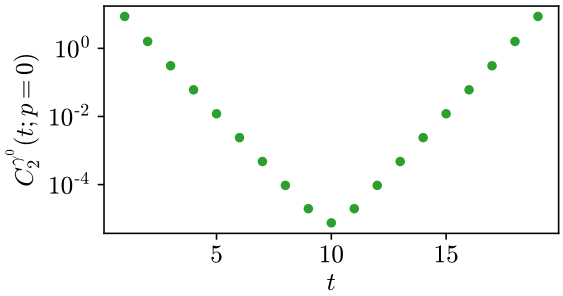

(c) $\Gamma = \gamma^0$

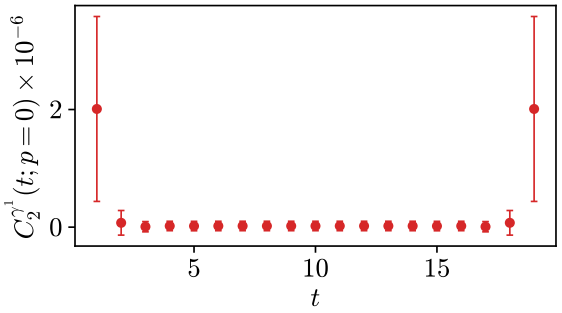

(d) $\Gamma = \gamma^1$

Figure 6.7. Data for the two-point correlator $C_2^\Gamma(t;0)$ plotted on a logarithmic scale against time t in lattice units. Each plot is labeled by its Γ structure. For $\Gamma = 1, \gamma^1$ (blue, red), the correlator data plateaus to a constant, indicating that these interpolators excite the vacuum state $|0\rangle$.

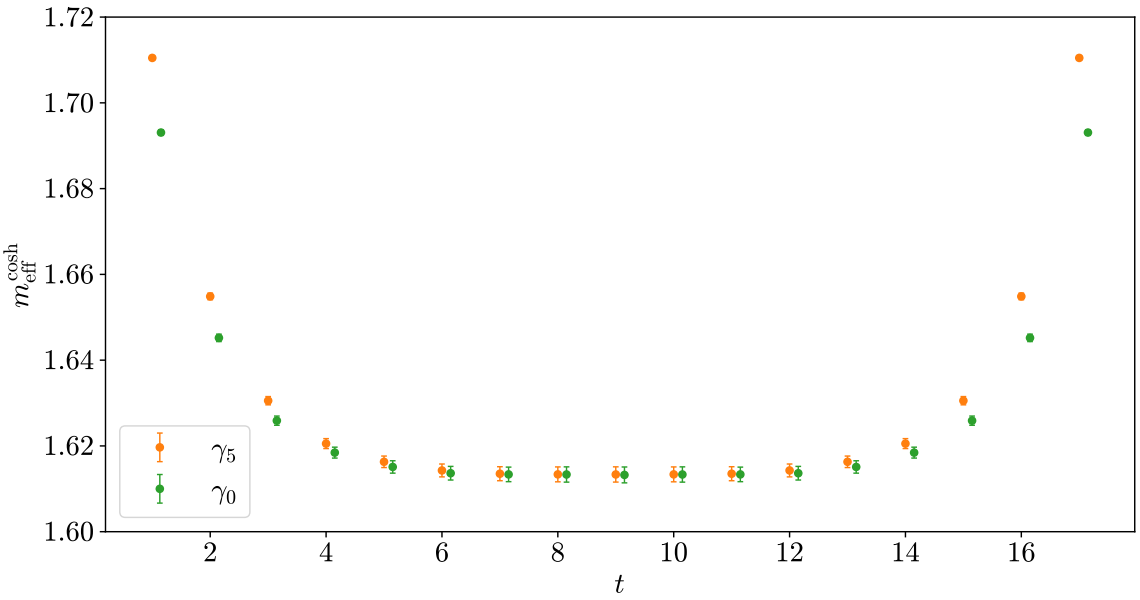

Figure 6.8. Cosh-corrected effective masses on the 20×20 ensemble computed for $\Gamma \in \{\gamma_5, \gamma^0\}$. The data for γ^0 (green) has been offset slightly, as it is nearly degenerate with γ_5 (orange), indicating that the interpolators excite the same ground state. The correlator data for $\Gamma \in \{1, \gamma^1\}$ is consistent with a constant, indicating these operators overlap onto the vacuum state, with an effective mass consistent with zero.

Of particular note is the correlator data for $\Gamma = \gamma^1$, which is observed to have similar behavior on each ensemble in Table 6.1. The correlator data is statistically consistent with zero, shown in Figure 6.7. This is because the interpolator $\chi_{\gamma^1}(t;0)$ has non-zero overlap with the vacuum state $|0\rangle$, which dominates the spectral decomposition. This behavior can be removed by considering the correlator at non-zero momentum $p = \pi/L$. In this case, the correlator is no longer expected to overlap onto the vacuum. Figure 6.9 shows the correlator data at momentum $p = \pi/L$ on a logarithmic scale. The correlator is now exponentially decaying, as is expected for an interpolator that does not overlap onto the vacuum.

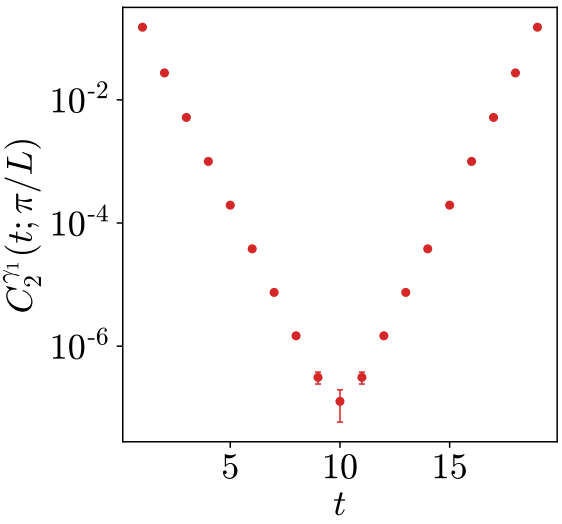

Figure 6.9. Boosted correlator $C_2^{\gamma^1}(t;p)$ at non-zero momentum $p = \pi/L$, plotted on a logarithmic scale. The correlator now shows an exponential decay and no longer overlaps onto the vacuum.

To determine the pseudoscalar ground state m^{PC} in the sector $PC = --$, the correlation function data for $C_2^{\gamma_5}(t;0)$ and $C_2^{\gamma^0}(t;0)$ is fit with two exponential models,

$$f_0(t) = C_0 e^{-m^{PC}t}, \tag{6.82}$$

$$f_1(t) = C_0 e^{-m^{PC}t} + C_1 e^{-(m^{PC}+\delta)t}. \tag{6.83}$$

Here $\delta > 0$ is the energy gap between the ground state and the first excited state, and C_0 and C_1 are the overlap coefficients, which are arbitrary parameters. Data for $C_2^{\gamma_2}(t;0)$ and $C_2^{\gamma_2}(t;0)$ shows that the bilinear operators $\chi_1(t;p)$ and $\chi_{\gamma^1}(t;p)$ overlap onto the vacuum state, so the scalar state with the lowest non-zero energy cannot be extracted without first removing the vacuum contribution. Data for $C_2^{\gamma_5}(t;0)$ and $C_2^{\gamma^0}(t;0)$ are fit with the models of Eqs. (6.82, 6.83) to extract m^{--}[7]. Note that on each ensemble for $\Gamma \in \{\gamma_5, \gamma^0\}$, $C_2^{\Gamma}(t;0)$ and $C_2^{\Gamma}(T-t,0)$ are statistically consistent, hence correlation function data is folded over the midpoint of the lattice to symmetrize

[7]This analysis performs separate fits for $C_2^{\gamma_5}(t;0)$ and $C_2^{\gamma^0}(t;0)$ and verifies that the extracted values of m^{--} are consistent with one another, before determining a final value for m^{--} by averaging both estimates while keeping track of correlations. In the future, a joint fit to both sets of correlation functions to estimate a single value for m^{--} will be performed instead.

the correlators,

$$C_2^{\Gamma}(t;0) \longrightarrow \frac{1}{2}\left(C_2^{\Gamma}(t;0) + C_2^{\Gamma}(T-t,0)\right), \tag{6.84}$$

where $t \in [T/2]$. Correlated fits to both models are performed over ranges $[t_{\text{min}}, t_{\text{max}}]$, where $t_{\text{min}} \in \{2,3,4\}$ and $t_{\text{max}} \in \{T/2-2, T/2-1, T/2\}$ are varied independently. A given fit is accepted only if its p-value is > 0.05, and accepted fits are averaged with the AIC weight [295].

Figure 6.10 shows the result of each series of fits on the 20×20 ensemble, plotted against the effective mass of the correlator. The posterior value of m^{--} is denoted in each panel by the colored band. If any fits to the excited-state model f_1 (Eq. (6.83)) are accepted, the averaged fit band of all accepted fits with model f_1 is shown on the corresponding panel in gray. The extracted value of m^{--} from $C_2^{\gamma_5}(t;0)$ and $C_2^{\gamma^0}(t;0)$ are consistent on all ensembles. Table 6.3 shows the posterior values for the pseudoscalar ground state energy m^{--} on each ensemble in units of σ, where σ is the scale set by the string tension in Section 6.6.

Ensemble	m^{--} $[\sigma]$
10	4.63(29)
12	5.80(19)
14	7.91(15)
16	9.33(15)
18	11.49(18)
20	11.98(14)
22	14.53(21)
24	16.96(21)
26	15.7(8.7)
28	18.55(22)

Table 6.3. Numerical results for the pseudoscalar ground-state energy for each adjoint QCD ensemble in Table 6.1. Data for m^{--} is computed by taking a correlated average of the determinations of this quantity extracted from $C_2^{\gamma_5}$ and $C_2^{\gamma^0}$.

6.7.3 The Two-Point Spectrum

The previous operator construction only enabled access to the lowest-lying states in each sector. To expand on this, the Generalized Eigenvalue Problem (GEVP) is used to access additional low-lying states. Given a set of quantum numbers, one constructs a set of operators consistent with those quantum numbers and the symmetries of the lattice (c.f. Ref. [296, 297] for the construction of $(3+1)d$ lattice operators). Two

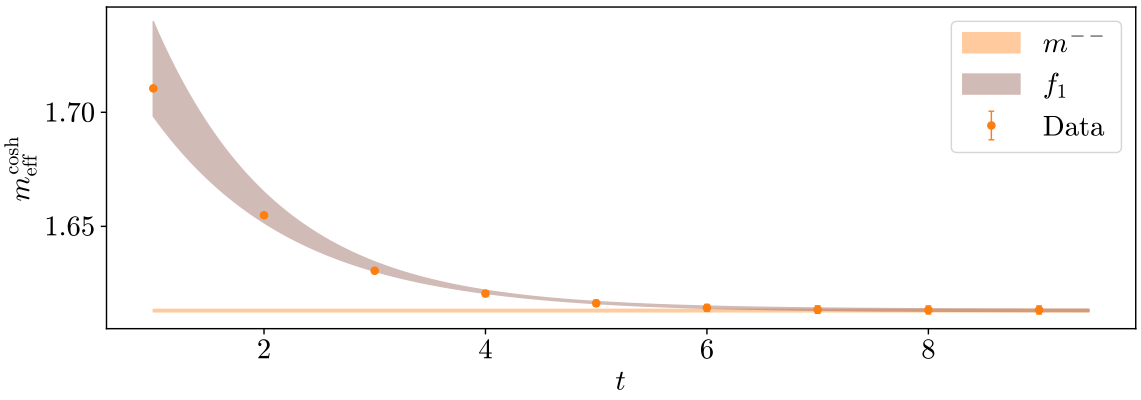

(a) $\Gamma = \gamma_5$

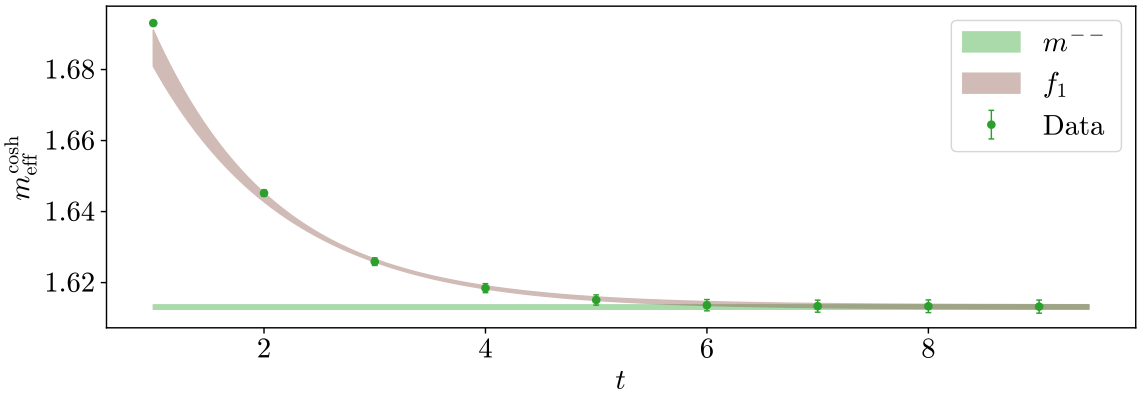

(b) $\Gamma = \gamma^0$

Figure 6.10. Fits to the two-point correlator $C_2^{\Gamma}(t; p = 0)$ on the 20×20 ensemble for $\Gamma \in \{\gamma_5, \gamma^0\}$ with fitting procedure described in the text. Fits are displayed against the corresponding cosh-corrected effective masses. In each panel, the model-averaged posterior for m^{--} is displayed by the colored horizontal band. If any excited-state fits are accepted (model f_1, Eq. (6.83)), the averaged fit band of all accepted fits for this model is displayed in gray. Determinations of m^{--} from $C_2^{\gamma_5}$ and $C_2^{\gamma^0}$ are consistent with one another.

classes of symmetries must be respected: translational symmetry and 1D hypocubic symmetry (rotation and inversion on the lattice). For translational symmetry, correlators are projected to $p = 0$ 1-momentum. Constructing operators that satisfy lattice rotations and translations in 1-dimension is trivial in $(1+1)d$. There is only a single non-trivial symmetry of the 1-dimensional (fixed time) spatial lattice cell, inversion, which is denoted as σ. Thus, the symmetry group is the cyclic group of order 2,

$$\mathbb{Z}/2\mathbb{Z} = \langle \sigma | \sigma^2 = 1 \rangle. \tag{6.85}$$

This group has two conjugacy classes, $\{1\}$ and $\{\sigma\}$, hence two irreducible representations (irreps), both of which are 1-dimensional. The first is denoted A_g and has even parity,

$$A_g(1) = 1 \qquad\qquad A_g(\sigma) = 1. \tag{6.86}$$

The second has odd parity and is denoted A_u,

$$A_u(1) = 1 \qquad\qquad A_u(\sigma) = -1. \tag{6.87}$$

Next, operators are constructed that are consistent with each irrep. The basic building blocks for these operators are the gauge-invariant displaced quark fields,

$$D^{(\eta)}\psi(x) = V_0(x)V_0(x+\hat{0})...V_0(x+(\eta-1)\hat{0})\psi(x+\eta\hat{0}) = W_{\text{Adj}}(x, x+\eta\hat{0})\psi(x+\eta\hat{0}), \tag{6.88}$$

with $\eta \geq 1$, and where conventionally $D^{(0)}\psi(x) \equiv \psi(x)$ and the adjoint Wilson line $W_{\text{Adj}}(x, x+\eta\hat{0})$ is

$$W_{\text{Adj}}(x, x+\eta\hat{0}) = V_0(x)V_0(x+\hat{0})...V_0(x+(\eta-1)\hat{0}), \tag{6.89}$$

which performs parallel transport on the adjoint fermion field from site $x+\eta\hat{0}$ to site x. This is defined similarly to the adjoint Wilson loop $W_{\text{Adj}}(r,t)$ (Eq. (6.69)), but for an open Wilson line. Note that notation will often be abused, and $W_{\text{Adj}}(\boldsymbol{x}, t; \boldsymbol{y}, s) \equiv W_{\text{Adj}}((\boldsymbol{x}, t), (\boldsymbol{y}, s))$. It is also useful to construct the opposite Wilson line,

$$W_{\text{Adj}}(\sigma x - \eta\hat{0}, -x) = V_0(\sigma x - \eta\hat{0})V_0(\sigma x - (\eta-1)\hat{0})...V_0(\sigma x - \hat{0}), \tag{6.90}$$

which performs parallel transport from $-x-\eta\hat{0}$ to $-x$. Note here that $\sigma \in \mathbb{Z}/2\mathbb{Z}$ acts on 2-vectors (x,t) as spatial inversion, $\sigma(x,t) = (-x,t)$.

To construct a bilinear operator, a γ-matrix $\Gamma \in \{1, \gamma^0, \gamma^1, \gamma_5\}$ is inserted between two displaced quark fields,

$$B^{\eta}_{\Gamma}(t) = \sum_{x} \overline{\psi}(x)\Gamma D^{(\eta)}\psi(x) \tag{6.91}$$

$$= \sum_{x} \overline{\psi}(x) W_{\text{Adj}}(x, x+\eta\hat{0})\Gamma\psi(x+\eta\hat{0}) \tag{6.92}$$

$$= \sum_{x} \overline{\psi}(x) V_0(x) V_0(x+\hat{0}) ... V_0(x+(\eta-1)\hat{0})\Gamma\psi(x+\eta\hat{0}), \tag{6.93}$$

with $\eta \in \{0, 1, ..., L-1\}$ (note $\eta = 0$ corresponds to the non-displaced operators of Section 6.7.2). In general, it is unnecessary to compute every displaced operator on the lattice because the GEVP must be solved on a matrix that is the size of the number of displacements. For small lattices, all displacements will be computed, but for larger lattices, the maximum number of displacements is truncated to 8, i.e., $\eta \in \{0, 1, ..., N_{\text{shift}} - 1\}$ where

$$N_{\text{shift}} = \min\{8, L\}. \tag{6.94}$$

Let $B^{\Gamma}_{\eta}(t)$ denote any operator that is gauge invariant and invariant under all spatial rotations, i.e., a 0-momentum projected operator. A projected operator is constructed from B consistent with $G \equiv \mathbb{Z}/2\mathbb{Z}$ symmetry in irrep Λ as

$$\mathcal{B}^{\Lambda,\Gamma}_{\eta}(t) = \frac{d_\Lambda}{|G|} \sum_{g\in G} \Omega_g B^{\Gamma}_{\eta}(t) \Omega^{\dagger}_g, \tag{6.95}$$

where $d_\Lambda = 1$ is the dimension of irrep Λ, $|G| = 2$ is the order of the symmetry group G, and $\Omega_g B^{\Gamma}_{\eta}(t)\Omega^{\dagger}_g$ implements the symmetry operation g on the operator $B^{\Gamma}_{\eta}(t)$. For the elemental displaced operators, this is explicitly:

$$\Omega_g (D^{(p)}_{\hat{0}}\psi)^a_\alpha(x)\Omega^{\dagger}_g = D^{(p)}_{g\hat{0}} S(g)_{\alpha\beta}\psi^a_\beta(gx) \tag{6.96}$$

where the $g\hat{0}$ and gx denote the group action of g on the vector $\hat{0}$ and on the coordinate $x = (\boldsymbol{x}, t)$, i.e.

$$1\hat{0} = \hat{0} \qquad 1x = x \qquad \sigma\hat{0} = -\hat{0} \qquad \sigma x = (-\boldsymbol{x}, t), \tag{6.97}$$

and $S(g)$ denotes the passage of the element $g = e^{i\theta J}$ to the spinor representation.

The only non-trivial element of G is inversion, with $S(\sigma)$ computed in Eq. (J.8),

$$S(\sigma) = S(\pi) = \begin{pmatrix} 0 & 1 \\ -1 & 0 \end{pmatrix}. \tag{6.98}$$

Note that the displaced quark field under parity is (with $\sigma x = (-\boldsymbol{x}, t)$)

$$\begin{aligned} D^{(\eta)}_{\sigma\hat{0}}\psi(\sigma x) &= V_{-\hat{0}}(\sigma x)...V_{-\hat{0}}(\sigma x - \eta\hat{0})\psi(\sigma x - (\eta-1)\hat{0}) \\ &= W_{\text{Adj}}(\sigma x, \sigma x - \eta\hat{0})\psi(\sigma x - \eta\hat{0}) \end{aligned} \tag{6.99}$$

Hence, the elemental displacement operators $B^{\eta}_{\Gamma}(t)$ can be expressed as

$$\Omega_g B^{\eta}_{\Gamma}(t)\Omega^{\dagger}_g = \sum_{\boldsymbol{x}} \overline{\psi}^a_{\alpha}(gx) D^{(\eta)}_{g\hat{0}} S(g)_{\alpha\beta}\psi^a_{\beta}(gx) \tag{6.100}$$

where $x = (\boldsymbol{x}, t)$.

Projectors onto each of the two lattice irreps may now be explicitly computed. The first is trivial and corresponds to symmetrization by parity,

$$\begin{aligned} \mathcal{B}^{A_g,\Gamma}_{\eta}(t) &= \frac{1}{2}\sum_{\boldsymbol{x}} \left(\overline{\psi}(\boldsymbol{x}, t)\Gamma D^{(\eta)}_{\hat{0}}\psi(\boldsymbol{x}, t) + \overline{\psi}(-\boldsymbol{x}, t)\Gamma D^{(\eta)}_{-\hat{0}}\psi(-\boldsymbol{x}, t) \right) \\ &= \frac{1}{2}\sum_{\boldsymbol{x}} \Big(\overline{\psi}(x) W_{\text{Adj}}(x, x+\eta\hat{0})\Gamma\psi(x+\eta\hat{0}) \\ &\qquad + \overline{\psi}(\sigma x) W_{\text{Adj}}(\sigma x, \sigma x - \eta\hat{0})\Gamma\psi(\sigma x - \eta\hat{0}) \Big). \end{aligned} \tag{6.101}$$

The second is the parity-odd sector A_u, where the lattice-projected operators are written in terms of $S(\sigma)$,

$$\begin{aligned} \mathcal{B}^{A_u,\Gamma}_{\eta}(t) &= \frac{1}{2}\sum_{\boldsymbol{x}} \left(\overline{\psi}(\boldsymbol{x}, t)\Gamma D^{(\eta)}_{\hat{0}}\psi(\boldsymbol{x}, t) + \overline{\psi}(-\boldsymbol{x}, t)\Gamma S(\sigma) D^{(\eta)}_{-\hat{0}}\psi(-\boldsymbol{x}, t) \right) \\ &= \frac{1}{2}\sum_{\boldsymbol{x}} \Big(\overline{\psi}(x) W_{\text{Adj}}(x, x+\eta\hat{0})\Gamma\psi(x+\eta\hat{0}) \\ &\qquad + \overline{\psi}(\sigma x) W_{\text{Adj}}(\sigma x, \sigma x - \eta\hat{0})\Gamma S(\sigma)\psi(\sigma x - \eta\hat{0}) \Big). \end{aligned} \tag{6.102}$$

Correlation functions of the lattice projected operators $\{\mathcal{B}^{\Lambda,\Gamma}_{\eta}(t)\}$ are computed for each irrep $\Lambda \in \{A_g, A_u\}$ and each γ structure $\Gamma \in \{1, \gamma^0, \gamma^1, \gamma_5\}$. This is a matrix in

the space of displaced operators, with indices p, q that range from 0 to N_{shift}:

$$C^{\Lambda,\Gamma}_{\eta\zeta}(t) = \frac{1}{T}\sum_{s}\langle \mathcal{B}^{\Lambda,\Gamma}_{\eta}(t+s)(\mathcal{B}^{\Lambda,\Gamma}_{\zeta})^{\dagger}(s)\rangle \tag{6.103}$$

The result is written in terms of 8 possible propagator contractions,

$$C^{\Lambda,\Gamma}_{\eta\zeta}(t) = \frac{1}{4T}\sum_{s}\sum_{\boldsymbol{x},\boldsymbol{y}}\Big(\textcircled{1}+\textcircled{2}+\textcircled{3}+\textcircled{4}+\textcircled{5}+\textcircled{6}+\textcircled{7}+\textcircled{8}\Big), \tag{6.104}$$

where the contraction structures (k) are defined as,

$$
\begin{aligned}
(1) &= \mathrm{Tr}\Big[S(\boldsymbol{y},s;\boldsymbol{x},t+s)W_{\mathrm{Adj}}(\boldsymbol{x},t+s;\boldsymbol{x}+\eta,t+s)\Gamma \\
&\qquad \times S(\boldsymbol{x}+\eta,t+s;\boldsymbol{y}+\zeta,s)W^{\dagger}_{\mathrm{Adj}}(\boldsymbol{y},s;\boldsymbol{y}+\zeta,s)\gamma^0\Gamma^{\dagger}\gamma^0\Big] \\
(2) &= \mathrm{Tr}\Big[S(-\boldsymbol{y},s;\boldsymbol{x},t+s)W_{\mathrm{Adj}}(\boldsymbol{x},t+s;\boldsymbol{x}+\eta,t+s)\Gamma \\
&\qquad \times S(\boldsymbol{x}+\eta,t+s;-\boldsymbol{y}-\zeta,s)W^{\dagger}_{\mathrm{Adj}}(-\boldsymbol{y},s;-\boldsymbol{y}-\zeta,s)\gamma^0\Sigma^{\dagger}_{\Lambda}\Gamma^{\dagger}\gamma^0\Big] \\
(3) &= \mathrm{Tr}\Big[S(\boldsymbol{y},s;-\boldsymbol{x},t+s)W_{\mathrm{Adj}}(-\boldsymbol{x},t+s;-\boldsymbol{x}-\eta,t+s)\Gamma\Sigma_{\Lambda} \\
&\qquad \times S(-\boldsymbol{x}-\eta,t+s;\boldsymbol{y}+\zeta,s)W^{\dagger}_{\mathrm{Adj}}(\boldsymbol{y},s;\boldsymbol{y}+\zeta,s)\gamma^0\Gamma^{\dagger}\gamma^0\Big] \\
(4) &= \mathrm{Tr}\Big[S(-\boldsymbol{y},s;-\boldsymbol{x},t+s)W_{\mathrm{Adj}}(-\boldsymbol{x},t+s;-\boldsymbol{x}-\eta,t+s)\Gamma\Sigma_{\Lambda} \\
&\qquad \times S(-\boldsymbol{x}-\eta,t+s;-\boldsymbol{y}-\zeta,s)W^{\dagger}_{\mathrm{Adj}}(-\boldsymbol{y},s;-\boldsymbol{y}-\zeta,s)\gamma^0\Sigma^{\dagger}_{\Lambda}\Gamma^{\dagger}\gamma^0\Big] \\
(5) &= \mathrm{Tr}\Big[S(\boldsymbol{x}+\eta,t+s;\boldsymbol{x},t+s)W_{\mathrm{Adj}}(\boldsymbol{x},t+s;\boldsymbol{x}+\eta,t+s)\Gamma\Big] \\
&\qquad \times \mathrm{Tr}\Big[S(\boldsymbol{y},s;\boldsymbol{y}+\zeta,s)W^{\dagger}_{\mathrm{Adj}}(\boldsymbol{y},s;\boldsymbol{y}+\zeta,s)\gamma^0\Gamma^{\dagger}\gamma^0\Big] \\
(6) &= \mathrm{Tr}\Big[S(\boldsymbol{x}+\eta,t+s;\boldsymbol{x},t+s)W_{\mathrm{Adj}}(\boldsymbol{x},t+s;\boldsymbol{x}+\eta,t+s)\Gamma\Big] \\
&\qquad \times \mathrm{Tr}\Big[S(-\boldsymbol{y},s;-\boldsymbol{y}-\zeta,s)W^{\dagger}_{\mathrm{Adj}}(-\boldsymbol{y},s;-\boldsymbol{y}-\zeta,s)\gamma^0\Sigma^{\dagger}_{\Lambda}\Gamma^{\dagger}\gamma^0\Big] \\
(7) &= \mathrm{Tr}\Big[S(-\boldsymbol{x}-\eta,t+s;-\boldsymbol{x},t+s)W_{\mathrm{Adj}}(-\boldsymbol{x},t+s;-\boldsymbol{x}-\eta,t+s)\Gamma\Sigma_{\Lambda}\Big] \\
&\qquad \times \mathrm{Tr}\Big[S(\boldsymbol{y},s;\boldsymbol{y}+\zeta,s)W^{\dagger}_{\mathrm{Adj}}(\boldsymbol{y},s;\boldsymbol{y}+\zeta,s)\gamma^0\Gamma^{\dagger}\gamma^0\Big] \\
(8) &= \mathrm{Tr}\Big[S(-\boldsymbol{x}-\eta,t+s;-\boldsymbol{x},t+s)W_{\mathrm{Adj}}(-\boldsymbol{x},t+s;-\boldsymbol{x}-\eta,t+s)\Gamma\Sigma_{\Lambda}\Big] \\
&\qquad \times \mathrm{Tr}\Big[S(-\boldsymbol{y},s;-\boldsymbol{y}-\zeta,s)W^{\dagger}_{\mathrm{Adj}}(-\boldsymbol{y},s;-\boldsymbol{y}-\zeta,s)\gamma^0\Sigma^{\dagger}_{\Lambda}\Gamma^{\dagger}\gamma^0\Big],
\end{aligned}
\tag{6.105}
$$

and the irrep-dependent spinor matrix Σ_Λ is

$$\Sigma_\Lambda \equiv \begin{cases} 1_{2\times 2} & \Lambda = A_g \\ S(\sigma) & \Lambda = A_u \end{cases}. \tag{6.106}$$

Contractions 5-8 are made up of four simpler terms, denoted d_1, d_2, d_3, d_4,

$$\begin{aligned} d_1 &= \mathrm{Tr}\left[S(\boldsymbol{x}+\eta, t+s; \boldsymbol{x}, t+s) W(\boldsymbol{x}, t+s; \boldsymbol{x}+\eta, t+s)\Gamma\right] \\ d_2 &= \mathrm{Tr}\left[S(\boldsymbol{y}, s; \boldsymbol{y}+\zeta, s) W^\dagger(\boldsymbol{y}, s; \boldsymbol{y}+\zeta, s)\gamma^0\Gamma^\dagger\gamma^0\right] \\ d_3 &= \mathrm{Tr}\left[S(-\boldsymbol{x}-\eta, t+s; -\boldsymbol{x}, t+s) W(-\boldsymbol{x}, t+s; -\boldsymbol{x}-\eta, t+s)\Gamma\Sigma_\Lambda\right] \\ d_4 &= \mathrm{Tr}\left[S(-\boldsymbol{y}, s; -\boldsymbol{y}-\zeta, s) W^\dagger(-\boldsymbol{y}, s; -\boldsymbol{y}-\zeta, s)\gamma^0\Sigma_\Lambda^\dagger\Gamma^\dagger\gamma^0\right], \end{aligned} \tag{6.107}$$

and $\textcircled{5} = d_1 d_2$, $\textcircled{6} = d_1 d_4$, $\textcircled{7} = d_3 d_2$, $\textcircled{8} = d_3 d_4$. Note that in $d = 4$, the identity $\gamma^0\Gamma^\dagger\gamma^0 = \Gamma$ may be used to simplify this equation further; however, this identity does not hold in $d = 2$, hence $\gamma^0\Gamma^\dagger\gamma^0$ will be kept explicit. This is the sum of four terms, each with two possible Wick contractions.

6.7.4 The GEVP

From the correlation matrix $C^{\Lambda,\Gamma}_{\eta\zeta}(t)$ of Eq. (6.104), the Generalized Eigenvalue Problem (GEVP) may be solved to determine a variational upper bound on the low-lying spectrum of the theory [215, 298]. $C^{\Lambda,\Gamma}_{\eta\zeta}(t)$ is an $N_{\text{shift}} \times N_{\text{shift}}$ matrix for each $t \in [T]$. One solves the GEVP for the generalized eigenvalues and eigenvectors to perform the variational analysis. For each combination (t, t_0), there is a GEVP for the (at most) N_{shift} eigenvalues $\{\lambda^{(k)}(t, t_0)\}_{k=1}^{N_{\text{shift}}}$ and N_{shift} eigenvectors $\{v_\eta^{(k)}\}_{k=1}^{N_{\text{shift}}}$. That is, for each (t, t_0) and $k \in \{1, ..., N_{\text{shift}}\}$,

$$\sum_{\eta'} C_{\eta,\eta'}(t) v^{(k)}_{\eta'}(t, t_0) = \lambda^{(k)}(t, t_0) \sum_{\eta'} C_{\eta,\eta'}(t_0) v^{(k)}_{\eta'}(t, t_0) \tag{6.108}$$

Suppressing the (η, η') indices makes the structure of this problem more obvious:

$$C(t)\vec{v}^{(k)}(t, t_0) = \lambda^{(k)}(t, t_0) C(t_0)\vec{v}^{(k)}(t, t_0). \tag{6.109}$$

The easiest way to solve the GEVP is to turn it into a standard eigenvalue problem. Note that the correlation matrix $C(t_0)$ can be inverted to obtain

$$C(t_0)^{-1} C(t)\vec{v}^{(k)}(t, t_0) = \lambda^{(k)}(t, t_0)\vec{v}^{(k)}(t, t_0) \tag{6.110}$$

which is the standard eigenvalue problem for the $n \times n$ matrix $C(t_0)^{-1}C(t)$; solving this will give the N_{shift} eigenvalues and eigenvectors $\{\lambda^{(k)}(t,t_0)\}_{k=1}^{N_{\text{shift}}}$ and $\{\vec{v}^{(k)}(t,t_0)\}_{k=1}^{N_{\text{shift}}}$. The GEVP is a standard calculation in most linear algebra libraries: this project uses scipy's scipy.linalg.eigh function to solve the GEVP [299]. The generalized eigenvalues $\{\lambda^{(k)}(t,t_0)\}$ correspond to the low-lying spectrum of the theory,

$$\lambda^{(k)}(t,t_0) \sim e^{-E_k(t-t_0)}, \tag{6.111}$$

where E_k is the variational bound on the k^{th} energy. The energies are extracted from fitting the generalized eigenvalues to this functional form.

When considering statistics, each correlation matrix becomes drawn from a bootstrap sample. That is, for each configuration $i \in \{1, ..., n_{\text{cfgs}}\}$, one computes a sample of the correlation matrix:

$$C^{(i)}_{\eta,\eta'}(t) := \frac{1}{T}\sum_s \langle \mathcal{B}^{\Lambda,\Gamma}_\eta(t+s)(\mathcal{B}^{\Lambda,\Gamma}_\zeta)^\dagger(s)\rangle_{U^{(i)}} \tag{6.112}$$

where $\langle ... \rangle_{U^{(i)}}$ denotes the value of this correlation function with the gauge field $U^{(i)}$. These correlation matrices are then bootstrapped,

$$\{C^{(i)}_{\eta,\eta'}(t)\}_{i=1}^{n_{\text{cfgs}}} \longrightarrow \{C^{b}_{\eta,\eta'}(t)\}_{b=1}^{n_b}, \tag{6.113}$$

and the analysis is run on the bootstrap samples of the correlation matrix. This analysis will thus return a bootstrapped set of generalized eigenvalues and eigenvectors,

$$\{\lambda^{(k)}_b(t,t_0)\}, \qquad\qquad \{\vec{v}^{(k)}_b(t,t_0)\}, \tag{6.114}$$

where $b \in \{1, ..., n_b\}$, $k \in \{1, ..., N_{\text{shift}}\}$, and $t, t_0 \in \{1, ..., T\}$.

6.8 Conclusion

Two-dimensional adjoint QCD is an important theory for understanding the implications that confinement has on gauge theories. The theory confines when the adjoint Majorana fermion is massive and interestingly becomes deconfining when the fermion is made massless. Many different field theoretical techniques have been used over the last 30 years to understand QCD_2 and have led to a deep understanding of the dynamics of the theory in different sectors. In particular, calculations of the k-string tension for small and large m have been performed using non-invertible symmetries,

and the spectrum of the theory for $N = 2, 3, 4$ has been computed using DLCQ. The theory as $N \to \infty$ is well-studied, using 't Hooft's large N expansion, and the spectrum has also been computed in this case.

Non-perturbative input is crucial to improve understanding of QCD_2 in all regions of parameter space, and LGT provides a useful numerical tool that can be used to obtain said input. This is the second study of QCD_2 using lattice Monte Carlo methods. Ensembles have been generated with $N = 2$ colors at ten different values of the lattice size, gauge coupling, and fermion mass, ranging from 10×10 to 28×28 lattices. The static quark potential and fundamental string tension have been computed on each ensemble, and the scale has been set with the string tension. Preliminary spectroscopic calculations have been performed, and the lightest pseudoscalar mass has been computed on each ensemble in units of the string tension. These calculations have shown that the vacuum has the quantum numbers of a scalar meson, as the matrix elements $\langle 0|\chi_1^\dagger(0;0)|0\rangle$ and $\langle 0|\chi_{\gamma^1}^\dagger(0;0)|0\rangle$ are non-zero. Work is ongoing to extend the calculation to $N = 3$ and $N = 4$ colors to study the k-string tension of these theories outside the fundamental representation and to study the low-lying spectrum of the theory using the GEVP.

The calculation of the QCD_2 spectrum presented in this chapter, while still in progress, aims to corroborate the results of Ref. [261] for $N = 2, 3, 4$, and provide a framework to extend the calculation of the low-lying states to higher values of N. Existing calculations have hinted that the N dependence of the spectrum is heavily suppressed and that at $N = 3, 4$, the spectrum is similar to its large-N counterpart. The spectrum is predicted to follow a power-law in N^{-2},

$$M^2(i;N) = \frac{g^2 N}{\pi}\left(a_0(i) + a_1(i)N^{-2} + \mathcal{O}(N^{-4})\right) \tag{6.115}$$

where $M^2(i;N)$ is the energy-squared of the i^{th} bound state with N colors. The coefficients a_0 and a_1 are independent of N and have been computed for the fermionic and bosonic ground states in Ref. [261]. They are observed to obey $a_1 \ll a_0$, indicating the spectrum has light dependence on the number of colors. LGT calculations can precisely map out this statement and verify that this is indeed the case for larger values of $N > 4$.

The calculation performed in this section is performed with the bare Wilson action, Eq. (6.18), and is the first LGT calculation of fermion observables using this action. As discussed in Ref. [300], the four-fermion terms $(\mathrm{Tr}[\overline{\psi}\psi])^2$ and $\mathrm{Tr}[(\overline{\psi}\psi)^2]$ (which are equal in $N = 2$) are not forbidden by any symmetries of the theory. Without

fine-tuning the fermion mass and coupling, these terms will be radiatively generated by the Wilson term, and the physics of the system will be that of the theory with non-zero four-fermion couplings. In the continuum limit, these couplings vanish; hence, although any quantities computed at finite lattice spacing feel the effects of the four-fermion operators, their values must match the theory with no four-fermion couplings after continuum extrapolation. The extrapolation of the spectrum to the continuum limit will provide the first numerical exploration of how the four-fermion couplings postulated in Ref. [301] influence the spectrum and string tension of the theory.

Chapter 7

Conclusion

Quantum Chromodynamics is a beautiful example of a strongly-coupled QFT. The theory is responsible for a rich hadronic spectrum that has been extensively studied in the last 75 years. It is unique compared to the other Standard Model sectors because of its confinement mechanism, prompting abundant research into QCD-like theories. Lattice gauge theory is a tool that is uniquely capable of dealing with the non-perturbative physics found in QCD. It provides a systematically improvable, *ab initio* framework to compute correlation functions and observables in a given theory, regardless of how strongly coupled the theory is. Lattice calculations have been immensely useful in studying QCD, and many theoretical predictions for experimental quantities have come through LQCD calculations.

QCD is the only sector of the Standard Model that is strongly interacting, but strongly-coupled QFTs are useful experimentally not just in the study of QCD, but also in the study of condensed matter theory. Many QFTs found in condensed matter are strongly coupled, finding applications in the study of Bose-Einstein Condensation [302] and chiral spin liquids [303], among other systems. Studying the dynamics of other strongly-coupled QFTs may inform knowledge of QCD and such condensed matter theories. This thesis explores strongly-coupled theories inside and outside of QCD, using LGT as the primary numerical tool to understand said theories.

To better understand such gauge theories, new methods and techniques for LGT can provide novel insights into said theories. In particular, spectral reconstruction problems are ubiquitous in high-energy physics. The spectral density of a theory contains information about all the energy states, resonances, and kinematic thresholds in a theory. It is an object which, if known, illuminates the entire structure of a QFT. Spectral densities underlie the connection between correlation functions, computable with LGT techniques, and the direct physical observables of interest. Most LGT calculations truncate the spectral expansion for a correlation function quickly, retaining

information from only the ground state and possibly a few excited states. Spectral reconstruction techniques aim to holistically reconstruct the entire (smeared) spectral density from a Euclidean correlator. Spectral function reconstruction from LGT data is a notoriously ill-posed method: an infinite number of spectral functions can yield a given set of LGT data. A new method for spectral function reconstruction from LGT data, Nevanlinna-Pick Spectral Reconstruction, is presented in Chapter 4. The NPSR method exploits the analytic structure of the thermal Green's function to reconstruct the smeared spectral density of a theory. A novel feature of the NPSR method absent from other spectral density reconstruction methods is its ability to constrain the full set of smeared spectral densities consistent with the input data (the *Wertevorrat*). The NPSR method is tested through simulation on four input spectral densities, which vary in complexity. Extensions of the NPSR method to handle data with statistical uncertainties are now underway.

Spectral reconstruction methods enable the *ab initio* reconstruction of inclusive cross sections and form factors directly from Euclidean correlator data computed with LGT. Examples of spectral reconstruction problems are the reconstruction of the smeared R-ratio for inclusive electron-positron scattering and the calculation of the axial form factor for neutrino-nucleus scattering. Many smeared spectral densities are experimentally measurable but not directly computable from theory without the existence of a reliable spectral reconstruction method. A particularly important area that would benefit from such a method for spectral reconstruction is upcoming neutrino-nucleon scattering experiments like DUNE, which require knowledge of the nucleon's axial structure functions to constrain the experimental background. The structure functions can only be constrained from neutrino-nucleon scattering, which do not have sufficient statistics to compute the structure functions to meet DUNE's precision benchmarks. The structure functions must hence be computed theoretically, which can be done with LGT. Spectral reconstruction methods can provide access to the behavior of these structure functions in the resonance regime, which current LGT methods [304] cannot access.

The first QFT directly studied in this thesis is the Standard Model EFT (Chapter 5). The SMEFT allows one to study extensions of the Standard Model by instead studying the matrix elements of higher-dimensional operators formed from Standard Model fields. The SMEFT is used to study $0\nu\beta\beta$ decay, a hypothesized BSM process in which two down quarks convert to two up quarks and two electrons. This decay is being searched for worldwide because of the wealth of neutrino physics it would reveal if found. If $0\nu\beta\beta$ decay is ever discovered, non-perturbative input

from QCD and its extensions will be required to understand the data. This thesis details the computation of the short-distance matrix elements that induce the $\pi^- \to \pi^+ e^- e^-$ transition and the calculation of the long- and short-distance matrix elements that induce the $n^0 n^0 \to p^+ p^+ e^- e^-$ decay. The $\pi^- \to \pi^+ e^- e^-$ matrix elements are computed on five domain-wall fermion ensembles, and the renormalized results in $\overline{\text{MS}}$ at 3 GeV are extrapolated to the chiral, continuum, and infinite-volume limit. The $n^0 n^0 \to p^+ p^+ e^- e^-$ matrix elements are computed on a single ensemble of Wilson-Clover fermions at pion mass 806 MeV and are the first calculation of $0\nu\beta\beta$ decay in a nuclear system. The short-distance $n^0 n^0 \to p^+ p^+ e^- e^-$ calculation is ongoing, and results are expected to be published soon.

The calculation of the short-distance $\pi^- \to \pi^+ e^- e^-$ presented in Section 5.3, along with long-distance calculation of Ref. [12], completes the LGT computation of $\pi^- \to \pi^+ e^- e^-$ on the domain wall fermion ensembles in Table 5.2. The short-distance contribution yields the leading-order LECs for χEFT, which can be used to better constrain nuclear many-body models for $0\nu\beta\beta$ decay. These models are currently the only *ab initio* way to study $0\nu\beta\beta$ decay in a nuclear system which can undergo $0\nu\beta\beta$ decay (the lightest of which is ^{48}Ca), as direct LGT calculations are too computationally expensive in such a system. The LO vertex that contributes in χEFT is the nucleon-nucleon vertex $n^0 n^0 \to p^+ p^+ e^- e^-$, Figure 5.7b. There are nine LECs which must be computed for this vertex, corresponding to the five scalar operators $\{\mathcal{O}_k\}$ (Eq. (5.12)) and the four vector operators $\{\mathcal{V}_p^\mu\}$ (Eq. (5.13)). The calculation of the short-distance dinucleon decay in Section 5.4 is the first step on the road towards such a calculation. The presented $n^0 n^0 \to p^+ p^+ e^- e^-$ calculation is performed at finite volume and at heavy pion mass ($m_\pi \approx 806$ MeV), and is the first calculation of short-distance $0\nu\beta\beta$ decay in a nuclear system. It has shown numerically that many of the matrix elements that were suppressed in the $\pi^- \to \pi^+ e^- e^-$ decay (matrix elements of $\mathcal{O}_3$ and the vector operators $\mathcal{V}_p^\mu$) are not necessarily suppressed in the $n^0 n^0 \to p^+ p^+ e^- e^-$ case, and all nine matrix elements must be treated equally. Future calculations must compute the same matrix elements with parameters closer to the physical point in order to have a systematically controlled extrapolation to use as input to χEFT. Such a calculation is increasingly important as next-generation $0\nu\beta\beta$ decay calculations come online and begin to take data, as if $0\nu\beta\beta$ decay is discovered, nuclear inputs will be required to understand the underlying physics of the decay from experimentally measured signals.

This thesis concludes with studying two-dimensional adjoint QCD, the theory of a single Majorana fermion in the adjoint representation coupled to an $SU(N)$

gauge field, in Chapter 6. This theory is strongly interacting and has very interesting physics: in particular, it deconfines when the Majorana fermion is made massless, but confines when the Majorana fermion is massive. Over the last 30 years, QCD_2 has been a playground to study the confinement mechanism in gauge theories. The two-dimensional nature of the theory allows for a wealth of calculations using non-perturbative techniques from QFT to understand the theory, but many of these techniques are not valid over the entire parameter space of the theory. Until very recently [272], a lattice Monte Carlo calculation had not been performed on the theory. Chapter 6 details an in-progress LGT calculation of QCD_2 and presents current preliminary results. The static quark potential and string tension are computed on ten different ensembles with $N = 2$ colors, and the scale is set between ensembles with the string tension. Fermionic observables are considered, and the ground-state energy of the pseudoscalar sector of the theory are computed. Work is ongoing to extend this calculation with the GEVP method, which variationally bounds the low-lying spectrum of the theory.

Knowledge of the low-lying spectrum of QCD_2 would allow for the verification of the results in Ref. [261], which computed the spectrum using DLCQ, and would allow for these results to be extended larger numbers of colors. It would be particularly interesting to compare these results to existing calculations of the glueball spectrum for $SU(N)$ gauge theories in $2+1$ and $3+1$ dimensions. The underlying systems are very different: QCD_2 is constructed in two spacetime dimensions with adjoint matter, while the glueball spectrum is computed in a higher number of spacetime dimensions with only gauge field degrees of freedom. Nonetheless, the spectra of each of these systems share the broad qualitative feature that its dependence on the number of colors is very mild, and they each approach the $N \to \infty$ limit rapidly (for QCD_2, $N = 3$ can be considered "large N" by empirical calculation, as is also true in four-dimensional QCD). The predominant similarity between these two types of theories is that they are confining theories of adjoint fields, and correlations between these theories may have broad implications for the confinement mechanism as a whole.

Appendix A

Abbreviations and Notation

Abbreviation	Meaning	Defined
QFT	Quantum Field Theory	Page 23
QCD	Quantum Chromodynamics	Page 23
EFT	Effective Field Theory	Page 23
BSM	Beyond the Standard Model	Page 23
LGT	Lattice Gauge Theory	Page 23
EWSB	Electroweak Symmetry Breaking	Page 25
vev	vacuum expectation value	Page 25
CKM	Cabibbo-Kobayashi-Maskawa	Page 28
PMNS	Pontecorvo-Maki-Nakagawa-Sakata	Page 39
SNO	Sudbury Neutrino Observatory	Page 39
NH (IH)	normal hierarchy (inverted hierarchy)	Page 40
$0\nu\beta\beta$	Neutrinoless double β	Page 41
MCMC	Markov Chain Monte Carlo	Page 44
HMC	Hamiltonian Monte Carlo	Page 66
NPR	Non-perturbative renormalization	Page 66
AIC	Akaike Information Criterion	Page 71
NPSR	Nevanlinna-Pick Spectral Reconstruction	Page 89
NAC	Nevanlinna Analytical Continuation	Page 108
DUNE	Deep Underground Neutrino Experiment	Page 128
SMEFT	Standard Model EFT	Page 136
(N)LO	(next to) leading-order	Page 136
χEFT	Chiral EFT	Page 136
LEC	low-energy constant	Page 138
QCD_2	Two-dimensional adjoint QCD	Page 173
DLCQ	Discretized Lightcone Quantization	Page 184
RHMC	Rational HMC	Page 192
GEVP	Generalized Eigenvalue Problem	Page 218

Table A.1. Abbreviations defined in this thesis.

Symbol	Meaning	Defined
$\mathbb{C}^+$	The upper half-plane in $\mathbb{C}$	Page 77, Eq. (4.13)
$\mathbb{R}^-$	The negative real axis	Page 81
$\mathbb{I}^+$	The positive imaginary axis	Page 87
$\mathbb{D}$	The (open) unit disk	Page 81, Eq. (4.30)
H^p	The Hardy space H^p, with $p \geq 1$	Page 101

Table A.2. Mathematical symbols defined in this thesis.

Abbreviation	Meaning
$\equiv$	Defined as
$\doteq$	Equals in a given basis
s.t.	Such that
a.e.	Almost everywhere (off a set of measure 0)
TFAE	The following are equivalent
$\overline{A}$	Closure of the set A
$a_n \uparrow a$ ($a_n \downarrow a$)	a_n approaches a from above (below)
Det	Functional determinant
Pf	Functional Pfaffian
$f\|\Omega$	Restriction of f to subdomain Ω
$\sup A$, $\inf A$	Supremum and infimum of a set A
$\operatorname{sgn}(x)$	Sign of $x \in \mathbb{R}$.

Table A.3. Mathematical notation used in this thesis.

Appendix B

Lie Groups, Lie Algebras, and their Representations

Let $\mathbb{K}$ be a field, and let $M_{n\times m}(\mathbb{K})$ denote the set of all $m \times n$ matrices with values in $\mathbb{K}$ (usually here $\mathbb{K}$ will be either $\mathbb{R}$ or $\mathbb{C}$). Group representations will typically be denoted by Π or by D depending on whether the group is a Lie group or finite group, and Lie algebra representations will typically be denoted π. For algebraic objects M and N (by this I mean objects in a category), the set of morphisms between them will be denoted $\mathrm{Hom}(M, N)$.

Let V be a n-dimensional $\mathbb{K}$-vector space. The dual of V is denoted by V^*, and recall for finite dimensional vector spaces there is an isomorphism $V \to V^*$. An **endomorphism** of V is an homomorphism $\phi : V \to V$. If ϕ is invertible (an isomorphism $V \to V$) then ϕ is called an **automorphism**. One denotes the automorphism group of V by $\mathrm{Aut}(V)$ and its endomorphism ring by $\mathrm{End}(V)$. The group $\mathrm{Aut}(V)$ is naturally isomorphic to the group $GL(V) := GL(\mathbb{K}^n)$ of $n \times n$ invertible matrices with values in $\mathbb{K}$[1], and the group $\mathrm{End}(V)$ is naturally isomorphic to $gl(V) := gl(\mathbb{K}^n)$, the set of all $n \times n$ matrices with values in $\mathbb{K}$.

B.1 Lie Groups and Algebras

The theory of Lie groups and algebras is used to describe continuous symmetries. A **Lie group** $(G, \cdot)$ is a group which is also a differentiable manifold, in which the group operation respects the structure of the manifold. Namely, one requires that the maps $\cdot : G^2 \to G$ and $\cdot^{-1} : G \to G$ be smooth. A **Lie algebra** $\mathfrak{g}$ over a field $\mathbb{K}$ is a $\mathbb{K}$-valued vector space equipped with a map $[\cdot, \cdot] : \mathfrak{g} \times \mathfrak{g} \to \mathfrak{g}$, called a **Lie bracket**, such that

[1] Once a basis is chosen for V, invertible linear maps $V \to V$ are in bijection with invertible matrices

the following hold:

1. $[\cdot,\cdot]$ is bilinear.
2. $[\cdot,\cdot]$ is antisymmetric.
3. $[\cdot,\cdot]$ satisfies the **Jacobi identity**, i.e. for $A, B, C \in \mathfrak{g}$:

$$[A,[B,C]] + [B,[C,A]] + [C,[A,B]] = 0. \tag{B.1}$$

In physics, one typically considers matrix Lie groups and algebras, in which case the Lie bracket is simply the commutator, $[A,B] = AB - BA$. In the case of matrix groups, our Lie algebras will also be matrix-valued, so $\mathfrak{g}$ is a matrix-valued vector space. $\mathfrak{g}$ is called an algebra because the map $[\cdot,\cdot]$ gives the vector space an algebra-like structure[2].

The essential idea behind Lie groups is this: Lie groups act on a vector space V as the symmetry operation (for example, the group $SO(3)$ of orthogonal real valued 3×3 matrices with determinant 1 act as rotations in $V = \mathbb{R}^3$). Lie algebras generate the Lie group via the exponential map in the following way: suppose $U \in G$ is an arbitrary element (assume G is path-connected, or at least that U is in the path-component of $1 \in G$). Then, there exists $X \in \mathfrak{g}$ such that:

$$U = \exp(iX). \tag{B.2}$$

The proof of this existence is one of the fundamental theorems of Lie theory. In essence, the Lie algebra parameterizes the Lie group. Let $n = \dim(\mathfrak{g})$. A basis $\{T^a\}_{a=1}^n$ is called a set of **generators** for the Lie group G because an arbitrary element of G can be represented as

$$\exp(iX^aT^a). \tag{B.3}$$

The coordinates X^a thus parameterize the Lie group G (really they parameterize the path-component of 1), thus an element of G is specified by a given set of $\{X^a\}$.

Every Lie algebra is defined by its Lie bracket. Because the Lie bracket $[\cdot,\cdot]$ maps $\mathfrak{g}^2$ into $\mathfrak{g}$, one can expand

$$[T^a,T^b] = if^{abc}T^c \tag{B.4}$$

[2]An algebra is simply a vector space with a ring structure, i.e. with a multiplication $\cdot : \mathfrak{g}\times\mathfrak{g} \to \mathfrak{g}$. However, the axioms that ring multiplication must satisfy are different than those that $[\cdot,\cdot]$ must satisfy.

where f^{abc} is an antisymmetric tensor of numbers known as the **structure constants** of the Lie algebra. Specifying the structure constants of an algebra exactly define the algebra and its Lie bracket. The associated Lie algebra with a Lie group can be defined by taking its tangent space at the identity, and in this way defines a correspondence from Lie groups to Lie algebras, and back.

B.2 Representations

Symmetry operations in the Lie group act on vector spaces via representations. Note that the endomorphism ring $\mathrm{End}(V)$ of a vector space is also a Lie algebra, by allowing the Lie bracket to equal the commutator of operators $A, B \in \mathrm{End}(V)$. A **representation** of a Lie algebra $\mathfrak{g}$ on a vector space V is a Lie algebra homomorphism[3] $\pi : \mathfrak{g} \to \mathrm{End}(V)$. A representation of a Lie group G is a Lie group homomorphism $\Pi : G \to \mathrm{Aut}(V)$. The **dimension** of a representation $\Pi : G \to \mathrm{Aut}(V)$ is the dimension of V. Given a Lie algebra representation $\pi : \mathfrak{g} \to \mathrm{End}(V)$ and the Lie group G associated with $\mathfrak{g}$, if G is simply connected (i.e. $\pi_1(G) \cong \{1\}$), then π induces a Lie group representation,

$$\Pi : G \to \mathrm{Aut}(V) \qquad\qquad \Pi(e^{iX}) \equiv e^{i\pi(X)}. \tag{B.5}$$

The assumption that G is simply connected is essential because Lie groups inherently contain more structure than Lie algebras: the algebra $\mathfrak{g}$ describes the local structure of G near the identity, but does not capture the global structure. Two isomorphic Lie groups must have the same Lie algebra, but the converse is not necessarily true.

Irreducible representations (irreps) are the simplest representations that can be constructed– they are akin to simple groups in standard group theory, or prime ideals in ring theory. Irreps provide the building blocks to form more complicated representations, and understanding the full set of representations of a group is equivalent to understanding its irreps. If $\Pi : G \to \mathrm{Aut}(V)$ is a representation of G, one says that a subspace $W \subset V$ is an **invariant subspace** if $\pi(g)(W) \subseteq W$ for each $g \in G$, i.e. that the group always goes into itself under symmetry transformations. W is a **nontrivial** subspace of V if W is a nonempty proper subspace. If the representation π has no nontrivial invariant subspaces, then one calls π an **irreducible representation**. If $W \subseteq V$ is invariant and if it contains no proper invariant subspaces, then W is an **irreducible subspace** of Π. Note that saying V is an irreducible subspace

[3]Meaning it preserves + and $[\cdot, \cdot]$

of itself is the same as saying that the representation V is irreducible. A representation Π is called **unitary** if $\Pi(g)$ is a unitary operator on V for each $g \in G$. Any finite-dimensional unitary representation of a group is completely reducible, meaning that it is isomorphic to a direct sum of a finite number of irreps.

Irreps in physics are often denoted by their dimension. For example, the adjoint of $SU(3)$ is 8-dimensional, the fundamental and anti-fundamental representations are 3-dimensional, and the singlet (trivial) representation is 1-dimensional. The adjoint is denoted **8**, the fundamental **3**, the anti-fundamental $\overline{\mathbf{3}}$, and the singlet **1**. One will often see equations written out in physics books that look like:

$$\mathbf{3} \otimes \overline{\mathbf{3}} = \mathbf{8} \oplus \mathbf{1}. \tag{B.6}$$

All this means is that if the fundamental with the anti-fundamental representations are tensored together, this product splits as a direct sum of the adjoint plus the singlet.

B.3 Constructions

B.3.1 Sums and Products of Representations

Recall the direct sum $V_1 \oplus V_2$ of two vector spaces V_1 and V_2 is simply a fancy way of writing the Cartesian product $V_1 \times V_2$ after it is given with the canonical vector space structure. Let G be a Lie group with two representations $\pi_1 : G \to V_1$ and $\pi_2 : G \to V_2$. One can form a representation of G on $V_1 \oplus V_2$ in the obvious way:

$$\pi_1 \oplus \pi_2 : G \to \mathrm{Aut}(V_1 \oplus V_2), \tag{B.7}$$

where $\pi_1 \oplus \pi_2(g)$ acts on elements $(v_1, v_2) \in V_1 \oplus V_2$ by:

$$[(\pi_1 \oplus \pi_2)g](v_1, v_2) := ((\pi_1 g)v_1, (\pi_2 g)v_2). \tag{B.8}$$

The sum of two Lie algebra representations is defined in an analogous way. Note that when two representations are summed, their dimensions add because the direct sum adds dimensions of vector spaces:

$$\dim(\pi_1 \oplus \pi_2) = \dim(\pi_1) + \dim(\pi_2). \tag{B.9}$$

Let $\Pi_1 : G \to \mathrm{Aut}(V)$ and $\Pi_2 : H \to \mathrm{Aut}(W)$ be representations of groups G and H. Then the induced canonical representation of $G \times H$ is denoted $\Pi_1 \otimes \Pi_2$, and is defined as

$$\Pi_1 \otimes \Pi_2 : G \times H \to \mathrm{Aut}(V \otimes W) \qquad (g, h) \mapsto (\Pi_1 g) \otimes (\Pi_2 h), \tag{B.10}$$

because $(\Pi_1 g) \otimes (\Pi_2 h)$ is clearly a morphism on the space $V \otimes W$ by its definition.

Suppose that $H = G$, so Π_1 and Π_2 are two representations of V with codomains V and W, respectively. Using the previous construction and embedding G into $G \times G$ via the diagonal map,

$$G \hookrightarrow G \times G \xrightarrow{\Pi_1 \otimes \Pi_2} \mathrm{Aut}(V \otimes W), \tag{B.11}$$

to form a new representation of G, one which acts on $V \otimes W$ as $(\Pi_1 \otimes \Pi_2)(g) = (\pi_1 g) \otimes (\pi_2 g)$. The dimensionality of the new representation is:

$$\dim(\Pi_1 \otimes \Pi_2) = \dim(\Pi_1) \dim(\Pi_2). \tag{B.12}$$

In general, the product of irreducible representations is not reducible, and the factorization of the product of irreps into a sum of irreps is the basis for the Clebsch-Gordan theory often studied in the context of adding angular momentum in quantum mechanics. For example, in $SU(3)$, $\mathbf{3} \otimes \bar{\mathbf{3}}$ (the fundamental times the antifundamental) is reducible, and in fact $\mathbf{3} \otimes \bar{\mathbf{3}} = \mathbf{8} \oplus \mathbf{1}$, the sum of the adjoint 8 and the singlet 1.

There is a corresponding induced representation of the Lie algebra on the tensor product. Given two Lie algebra representations $\pi_1 : \mathfrak{g} \to \mathrm{End}(V)$ and $\pi_2 : \mathfrak{g} \to \mathrm{End}(W)$, the tensor product representation of $\mathfrak{g}$ is the representation:

$$\pi_1 \otimes \pi_2 : \mathfrak{g} \to \mathrm{End}(V \otimes W) \qquad (\pi_1 \otimes \pi_2)(X) = \pi_1(X) \otimes I + I \otimes \pi_2(X) \tag{B.13}$$

This exponentiates to the correct representation of G because $[\pi_1(X) \otimes I, I \otimes \pi_2(X)] = 0$,

$$e^{i(\pi_1 \otimes \pi_2)(X)} = e^{i\pi_1(X) \otimes I + iI \otimes \pi_2(X)} = e^{i\pi_1(X)} \otimes e^{i\pi_2(X)}. \tag{B.14}$$

The direct sum of representations is not equivalent to the direct sum of Lie algebras or Lie groups. While the operation is still defined in this case, it acts on different objects, and can have profound differences. Namely, note that (of course) the direct sum of irreps is not an irrep, because doing this gives an explicit decomposition of the representation. However, if two Lie algebras are summed, then in fact there is a

way to construct an irrep on the direct sum from the individual irreps.

Theorem B.3.1. Let $\mathfrak{g}, \mathfrak{h}$ be two Lie algebras. Then the irreps of $\mathfrak{g} \oplus \mathfrak{h}$ are precisely the tensor products of the irreps of $\mathfrak{g}$ and of $\mathfrak{h}$. In other words, if (π_a, V_a) are the irreps of $\mathfrak{g}$ and (ϕ_b, W_b) are the irreps of $\mathfrak{h}$, then the irreps of $\mathfrak{g} \oplus \mathfrak{h}$ are precisely the tensor products:

$$\{(\pi_a \otimes \phi_b, V_a \otimes W_b)\}_{a,b} \tag{B.15}$$

This theorem is extremely useful in constructing the irreps of the Lorentz group (Section B.4).

B.3.2 Conjugate (dual) representations

Let (π, V) be a complex representation of a Lie algebra $\mathfrak{g}$. Then the **conjugate representation** to (π, V) is the representation $\pi^* : \mathfrak{g} \to End(V^*)$ (where V^* is the dual space of V) defined as:

$$\pi^*(X) := -\pi(X)^T. \tag{B.16}$$

Note that for the case where the generators $\{\pi(X)\}$ are unitary (as in the case of the fundamental representation of $SU(N)$), then $-\pi(X)^T = -\pi(X)^*$ where $*$ is the conjugate, so often one sees this definition instead. For representations of Lie groups (Π, V), this induces a representation $\Pi^* : G \to Aut(V^*)$,

$$\Pi^*(g) = \Pi(g^{-1})^T. \tag{B.17}$$

In physics, one often see the generators of the fundamental representation written with less jargon. If $T_r^a = \pi(X^a)$ are the images of the generators $\{X^a\}$ of a Lie algebra $\mathfrak{g}$ in a representation r, then the generators of the conjugate representation $T_{\bar{r}}^a$ are:

$$(T_{\bar{r}}^a)_{ij} = -(T_r^a)_{ij}^* = -(T_r^a)_{ji}. \tag{B.18}$$

As a point of notation, if $\mathbf{r}$ is denoting a representation of G (i.e. for $SU(3)$ the fundamental is denoted by $\mathbf{3}$) then its conjugate representation is denoted by $\bar{\mathbf{r}}$. The conjugate of the fundamental representation is called the **anti-fundamental** representation. A representation is called **real** if it equals its conjugate representation. In the case of $SU(N)$, for $N > 2$ the fundamental representation is complex. For arbitrary $SU(N)$, the adjoint representation is always a real representation.

B.4 The Lorentz Group $SO(1,3)$ and its Representations

The Lorentz Group $SO(1,3)$ is the group of symmetries of spacetime which preserve the Minkowski metric $\eta \equiv \text{diag}(1,-1,-1,-1)$. The group has corresponding algebra $\mathfrak{so}(1,3)$ which has six generators, denoted $\mathcal{J}_{\mu\nu}$ for $\mu < \nu$. $\mathcal{J}_{\mu\nu}$ is an antisymmetric tensor, hence an arbitrary Lorentz transformation (in the connected component of 1, $SO(1,3)^+$) may be written as

$$\Lambda = \exp\left(-\frac{i}{2}\omega_{\mu\nu}\mathcal{J}^{\mu\nu}\right). \tag{B.19}$$

Note that $\omega_{\mu\nu}$ can be taken to be antisymmetric WLOG, as the symmetric part will vanish when contracted with $\mathcal{J}^{\mu\nu}$. The Lorentz algebra is:

$$[\mathcal{J}_{\mu\nu}, \mathcal{J}_{\rho\sigma}] = i(g_{\mu\sigma}\mathcal{J}_{\nu\rho} + g_{\nu\rho}\mathcal{J}_{\mu\sigma} - g_{\mu\rho}\mathcal{J}_{\nu\sigma} - g_{\nu\sigma}\mathcal{J}_{\mu\rho}) \tag{B.20}$$

The other way the generators of $SO(1,3)$ are conventionally written is as a angular momentum generator J_i and a boost generator K_i for $i \in \{1,2,3\}$. This decomposition comes from separating the time-like parts of $\mathcal{J}_{\mu\nu}$ from the space-like parts of $\mathcal{J}_{\mu\nu}$. The generators are defined as

$$J^i := \frac{1}{2}\epsilon^{ijk}\mathcal{J}_{jk} \qquad\qquad K^i := \mathcal{J}^{0i}. \tag{B.21}$$

In particular, this implies the decomposition,

$$\mathcal{J}_{\mu\nu} = \begin{pmatrix} 0 & K^1 & K^2 & K^3 \\ -K^1 & 0 & J^3 & -J^2 \\ -K^2 & -J^3 & 0 & J^1 \\ -K^3 & J^2 & -J^1 & 0 \end{pmatrix} \qquad \omega_{\mu\nu} = \begin{pmatrix} 0 & \lambda^1 & \lambda^2 & \lambda^3 \\ -\lambda^1 & 0 & \theta^3 & -\theta^2 \\ -\lambda^2 & -\theta^3 & 0 & \theta^1 \\ -\lambda^3 & \theta^2 & -\theta^1 & 0 \end{pmatrix}, \tag{B.22}$$

where the three boost parameters are $\vec{\lambda}$ and the rotation parameters are $\vec{\theta}$. They satisfy the algebra:

$$\begin{aligned} [J_i, J_j] &= i\epsilon_{ijk}J_k \\ [J_i, K_j] &= i\epsilon_{ijk}K_k \\ [K_i, K_j] &= -i\epsilon_{ijk}J_k \end{aligned} \tag{B.23}$$

which makes it clear that the elements J_i generate **rotations** (their algebra is $\mathfrak{so}(3) \cong \mathfrak{su}(2)$) and hence are generators of $SO(3)$.

The boost generators are more complicated, and do not generate anything as simple as $SO(3)$. However, the algebra can be simplified dramatically by taking a specific linear combination of the generators:

$$J_i^{\pm} := \frac{1}{2}(J_i \pm iK_i) \tag{B.24}$$

These $\{J_i^{\pm}\}$ also generate $\mathfrak{so}(1,3)$. More importantly, their algebra is easier to deal than how the Lorentz algebra was previously cast:

$$[J_i^{\pm}, J_j^{\pm}] = i\epsilon_{ijk}J_k^{\pm} \qquad\qquad [J_i^{\pm}, J_j\mp] = 0 \tag{B.25}$$

This makes it explicit that $\{J_i^+\}$ and $\{J_i^-\}$ each generate their own independent $\mathfrak{su}(2)$ subalgebra of $\mathfrak{so}(1,3)$. Because of this, the entire algebra $\mathfrak{so}(1,3)$ has a decomposition as a sum,

$$\mathfrak{so}(1,3) = \mathfrak{su}(2) \oplus \mathfrak{su}(2). \tag{B.26}$$

B.4.1 Representation theory of the Lorentz group

Because the Lorentz group implements Lorentz transformations, understanding its representation theory is crucial. Scalars, vectors, and tensors transform in different representations of the Lorentz group. Consider a vector V_μ. This lives in $\mathbb{R}^4$, and a Lorentz transformation $\Lambda \in SO(1,3)$ acts on the vector as:

$$V^\mu \mapsto \Lambda^\mu_\nu V^\nu. \tag{B.27}$$

Suppressing the indices, this is $V \mapsto D(\Lambda)V$, where $D(\Lambda)$ has the components $\Lambda^{\mu\nu}$, i.e., D is simply the identity. Thus whenever one works with vectors in special relativity, one is simply using the **fundamental representation** of the Lorentz group. Written out explicitly, this representation is $id : SO(1,3) \to \mathrm{Aut}(\mathbb{R}^4)$, $\Lambda \mapsto \Lambda_{\mu\nu}$. Here one views $\Lambda \in SO(1,3)$ as an abstract element of a group (which is defined as a matrix group), and one explicitly views $id(\Lambda)$ as a 4×4 matrix which has components $\Lambda^{\mu\nu}$. The fundamental representation by **4**, its dimension.

In a similar way, scalars and tensors are also representations of the Lorentz group. Scalars live in the singlet representation **1** since a scalar ϕ does not transform, i.e., $D(\Lambda)\phi = \phi$. 2-tensors $T^{\mu\nu}$ live in the tensor product representation $\mathbf{16} = \mathbf{4} \otimes \mathbf{4}$,

because under a Lorentz transformation $\Lambda \in SO(1,3)$ they transform as:

$$T^{\mu\nu} \mapsto \Lambda^{\mu}_{\rho}\Lambda^{\nu}_{\sigma}T^{\rho\sigma}. \tag{B.28}$$

This can be written out as a matrix equation $T \mapsto D(\Lambda)T$, where T is viewed as a 16 dimensional vector and $D(\Lambda) = \Lambda \otimes \Lambda \in \mathrm{Aut}(\mathbb{R}^{16})$ (viewing Λ as a matrix) is a 16×16 dimensional matrix. Thus 2-tensors $T^{\mu\nu}$ live in the representation **16**.

Unlike the representations **1** and **4**, the representation **16** is a reducible representation. Let (D_{16}, V_{16}) be this representation. One defines 3 subspaces of V_{16} as follows:

$$\begin{aligned} W &:= \left\{ \frac{1}{4}T^{\alpha}_{\alpha}g^{\mu\nu} : T^{\mu\nu} \in V_{16} \right\} \\ A &:= \left\{ \frac{1}{2}(T^{\mu\nu} - T^{\nu\mu}) : T^{\mu\nu} \in V_{16} \right\} \\ S &:= \left\{ \frac{1}{2}(T^{\mu\nu} + T^{\nu\mu}) - \frac{1}{4}T^{\alpha}_{\alpha}g^{\mu\nu} : T^{\mu\nu} \in V_{16} \right\} \end{aligned} \tag{B.29}$$

These are respectively the subspaces of traces, antisymmetric tensors, and traceless symmetric tensors. Note that $\dim(W) = 1$, $\dim(A) = 6$, and $\dim(S) = 9$, so they are denoted respectively by **1**, **6**, and **9**.

The space V_{16} of all 2-tensors splits as a direct sum of these subspaces, as each tensor $T^{\mu\nu}$ can be written as a sum of a symmetric and antisymmetric component, and the symmetric component can further be split into a trace part and a traceless part. Thus one has the decomposition:

$$V_{16} = W \oplus A \oplus S \tag{B.30}$$

which is written as $\mathbf{16} = \mathbf{1} \oplus \mathbf{6} \oplus \mathbf{9}$ by denoting each irrep with its dimensionality. Furthermore, each of these subspaces is invariant under the action of the Lorentz group because tensor transformations preserve symmetry and antisymmetry, and trace is a Lorentz singlet. The representation **6** of antisymmetric tensors is the adjoint representation because the Lorentz group has 6 generators. The representation **9** of symmetric traceless tensors is irreducible. **9** plays an important role in QFT, as one often attempts to decompose tensor operators into a sum of tensors which live in irreps of the Lorentz group[4].

[4]In quantum mechanics, this procedure carried out for Euclidean tensors V_{ij} gives a similar decomposition, and the corresponding decomposition of symmetric and traceless tensors gives an irreducible tensor operator for which the Wigner-Eckart theorem can be applied (although because

From the decomposition in Eq. (B.26), one can classify **all** the irreps of $\mathfrak{so}(1,3)$ using the decomposition theorem for irreps of a direct sum, which implies that the irreps of a sum of Lie algebras are exactly the tensor products of their individual irreps. The irreps of $\mathfrak{su}(2)$ are uniquely labeled by a (half) integer $j \in \{0, \frac{1}{2}, 1, \frac{3}{2}, ...\}$, and the corresponding irrep π_j has dimension $2j+1$. Thus, one can label all the irreps of $SO(1,3)$ by a pair:

$$(j_+, j_-) \tag{B.31}$$

with $j_+, j_- \in \{0, \frac{1}{2}, 1, \frac{3}{2}, ...\}$, and (j_+, j_-) denoting the tensor product representation $\pi_{j_+} \otimes \pi_{j_-}$. Note that the irrep (j_+, j_-) has a dimensionality $D^{p,q}$ given by,

$$D^{j_+,j_-} = \dim(\pi_{j_+} \otimes \pi_{j_-}) = (2j_+ + 1)(2j_- + 1), \tag{B.32}$$

and furthermore, that the irrep of dimension **k** is the unique such irrep of that dimension.

The fundamental irrep **4** can be denoted in this convention as $(\frac{1}{2}, \frac{1}{2})$, and the irrep **9** of symmetric traceless tensors is denoted $(1,1)$. If $j_+ + j_-$ is an integer the irrep (j_+, j_-) is called a **tensor representation** and if $j_+ + j_-$ is a half integer one calls the irrep a **spinor representation**. The reason for this comes from QFT. If a field lives in a tensor irrep, then it will have a Lorentz index, which is why a spin 1 particle like the photon A_μ will have a single Lorentz index.

A spinor representation (j_+, j_-) will have spinor indices and not Lorentz indices. The example of this which should come to mind is Dirac spinors. The representations $(\frac{1}{2}, 0)$ and $(0, \frac{1}{2})$ are equivalent the spin $\frac{1}{2}$ representations of $\mathfrak{su}(2)$, and so they are 2 dimensional and J_i^+ and J_i^- are represented on each by either the Pauli matrices, or zero. Physically, these correspond to right and left handed spinors ψ_L and ψ_R, which is why these spinors have 2 components. The **Dirac representation** of $SO(1,3)$ (also called the **bispinor** representation) is the sum $(\frac{1}{2}, 0) \oplus (0, \frac{1}{2})$, and this is the representation that one typically uses to study spin $\frac{1}{2}$ particles in QFT. The basis that shows this decomposition of $(\frac{1}{2}, 0) \oplus (0, \frac{1}{2})$ explicitly is the Weyl basis, which is why Weyl spinors decouple into 2 dimensional left and right spinors.

Of particular interest is the adjoint representation **6**. Although $D^{\frac{1}{2},1} = 6$, it is important to note that $(\frac{1}{2}, 1)$ and **6** are different representations. **6** can be decomposed into a direct sum $\mathbf{6} = (\mathbf{1}, \mathbf{0}) \oplus (\mathbf{0}, \mathbf{1})$, and so in fact 6 is a reducible tensor representation. Physically, this is because the antisymmetric field strength tensor $F_{\mu\nu}$ must live in a tensor representation because it is constructed from the photon field A_μ. One

the dimensions are different this subspace is only 5 dimensional in QM)

can decompose $F_{\mu\nu}$ into this invariant decomposition $(1,0)\oplus(0,1)$ by taking specific linear combinations of $\vec{E}$ and $\vec{B}$ which rotate into themselves under boosts, as these spatial vectors live in the representations $(1,0)$ and $(0,1)$ which each have dimension 3.

To summarize, some of the most common irreps are enumerated in Table B.1.

Name	(j_+, j_-) label	Dimension	Irrep?
Singlet	$(0,0)$	1	Y
Left Weyl (ψ_a)	$(\frac{1}{2},0)$	2	Y
Right Weyl ($\psi^{\dot{a}}$)	$(0,\frac{1}{2})$	2	Y
Dirac (bispinor)	$(\frac{1}{2},0)\oplus(0,\frac{1}{2})$	4	N
Vector (V_μ)	$(\frac{1}{2},\frac{1}{2})$	4	Y
Adjoint (curvature $F_{\mu\nu}$)	$(1,0)\oplus(0,1)$	6	N
—	$(1,\frac{1}{2})$	6	Y
Symmetric Tensor ($S_{\mu\nu}$)	$(1,1)$	9	Y

Table B.1. Low dimensional representations of the Lorentz group.

B.4.2 Weyl Spinors

Spin $\frac{1}{2}$ representations of the Lorentz group are important because they provide an example of spinor representations, which fermions live in. In particular, **the fundamental fermion fields in the Standard Model are all left-handed Weyl or right-handed Weyl spinors**, and so to understand the Standard Model it is important to understand how Weyl spinors work.

Before diving into the indices that will be used to study these representations, a good starting place is to see what Lorentz transformations actually look like in the $D_L := (\frac{1}{2},0)$ and $D_R := (0,\frac{1}{2})$ representations of $SO(1,3)$. For the left handed representation, $j_+ = \frac{1}{2}$ and $j_- = 0$, so,

$$D_L(J_i^+) = \frac{1}{2}\left[D_L(J_i) + iD_L(K_i)\right] = \frac{1}{2}\sigma_i \quad D_L(J_i^-) = \frac{1}{2}\left[D_L(J_i) - iD_L(K_i)\right] = 0. \tag{B.33}$$

This implies that **in the left-handed Weyl irrep**, the generators are mapped to:

$$(J_i)_L = \frac{1}{2}\sigma_i, \qquad (K_i)_L = -i\frac{1}{2}\sigma_i. \tag{B.34}$$

The notation here uses the subscript L to denote that J^i or K^i is in the left-handed Weyl representation, i.e., $J_L^i = D_L(J^i)$, and applies likewise for K^i and right-handed

spinors. This can be extended to show how a left-handed spinor ψ_L transforms under the Lorentz group. In the right handed representation D_R, $D_R(J_i^+) = 0$ and $D_R(J_i^-) = \frac{1}{2}\sigma_i$, so the boost generator flips sign:

$$(J_i)_R = \frac{1}{2}\sigma_i, \qquad (K_i)_R = i\frac{1}{2}\sigma_i. \tag{B.35}$$

To perform a Lorentz transformation on a Weyl spinor in either the D_L or D_R representations, one substitutes how the generators J_i and K_i look in the corresponding representation, and then applies Eq. (**??**). Often these generators are packaged into a tensor form,

$$S_L^{\mu\nu} = D_L(\mathcal{J}^{\mu\nu}) \qquad S_R^{\mu\nu} = D_R(\mathcal{J}^{\mu\nu}), \tag{B.36}$$

and so for an arbitrary Weyl spinor ψ_L or ψ_R, S_L and S_R generate the corresponding Lorentz transformation Λ with parameters $\omega_{\mu\nu}$ as,

$$\psi_L^a(x) \mapsto \exp\left(-\frac{i}{2}\omega_{\mu\nu}S_L^{\mu\nu}\right)_b^a \psi^b(\Lambda^{-1}x) \quad \psi_R^{\dot{a}}(x) \mapsto \exp\left(-\frac{i}{2}\omega_{\mu\nu}S_R^{\mu\nu}\right)_{\dot{b}}^{\dot{a}} \psi^{\dot{b}}(\Lambda^{-1}x). \tag{B.37}$$

Compactly, the generators S_L and S_R in the left/right-handed Weyl irreps are related by negation and conjugation:

$$(S_R^{\mu\nu})_{\dot{a}}^{\dot{b}} = -[(S_L^{\mu\nu})_a^b]^*. \tag{B.38}$$

Conventionally, one uses undotted indices a to denote the $D_L = (\frac{1}{2}, 0)$ representation, and dotted indices $\dot{a}$ to denote the $D_R = (0, \frac{1}{2})$ representation. This is helpful because **a Lorentz invariant can only be formed by contracting the same type of indices**, i.e., if ϕ^a and $\chi_{\dot{b}}$ are a left and right handed spinor respectively then $\phi^a\chi_{\dot{a}}$ is *not Lorentz invariant*. Hermitian conjugation interchanges dotted and undotted indices, that is, it maps left handed spinors to right handed spinors and vice versa. This is because of how the generators are defined as $J_i^{\pm} = \frac{1}{2}(J_i \pm iK_i)$. Since the J_i and K_i are hermitian, $(J_i^{\pm})^\dagger = J_i^{\mp}$, which implies that $\dagger$ maps $(\frac{1}{2}, 0)$ into $(0, \frac{1}{2})$, and vice versa. If ψ_L is a left handed Weyl spinor, then it has an undotted index ψ_L^a. However, its Hermitian conjugate is a right handed spinor, and so has a dotted index, $(\psi_L^\dagger)^{\dot{a}}$.

The Clebsch-Gordan theory for $SU(2)$ carries over to spin 1/2 particles. As an example, consider a tensor $C_{\alpha\beta}$ which has two undotted indices, and therefore lives in

$(\frac{1}{2},0)\otimes(\frac{1}{2},0)$. One wishes to see if this is irreducible, or if it can be decomposed into a sum of terms which each do not mix with one another. Since the first component has the relation $\frac{1}{2}\otimes\frac{1}{2}=0\oplus 1$ in $SU(2)$, this relation follows in the Lorentz algebra. Note that the singlet 0 is antisymmetric and the triplet 1 is symmetric, so that implies that one can decompose any tensor C_{ab} as:

$$C_{ab}=\epsilon_{ab}D+G_{ab} \tag{B.39}$$

where ϵ_{ab} is the totally antisymmetric 2d Levi-Civita symbol:

$$\epsilon^{12}=-\epsilon^{21}=1=\epsilon_{21}=-\epsilon_{12} \tag{B.40}$$

and G_{ab} is a symmetric tensor, i.e. in matrix form:

$$\epsilon^{ab}=\begin{pmatrix}0 & 1\\ -1 & 0\end{pmatrix} \qquad\qquad \epsilon_{ab}=\begin{pmatrix}0 & -1\\ 1 & 0\end{pmatrix}. \tag{B.41}$$

Note that $\epsilon^{ab}=-\epsilon_{ab}$, so it is important to keep the upper and lower indices in mind when working with this symbol. The Levi-Civita symbol ϵ is also used to raise and lower indices on spinors, i.e. $\psi_L^a=\epsilon^{ab}(\psi_L)_b$.

B.4.3 Dirac and Majorana spinors

Although left- and right-handed Weyl spinors are the simplest types of spin $\frac{1}{2}$ objects that can be considered, one often works with different types of fermions and larger dimensional representations. Another spin $\frac{1}{2}$ representation that is frequently used is the **Dirac (bispinor) representation** of $(\frac{1}{2},0)\oplus(0,\frac{1}{2})$. Spinors are often introduced in this representation as it is easier to get here from the physics of quantum mechanics than to start with the representation theory of the Lorentz group. Dirac fermions are most easily expanded in the **Weyl basis**, in which the Dirac spinor is a four-component spinor made by stacking a left-handed and right-handed spinor on top of one another. Consider two left-handed fields, χ_a and ξ_a (note they both start with a lowered index). Then the **Dirac spinor** containing these fields is:

$$\Psi=\begin{pmatrix}\chi_a\\ \xi^{\dagger\dot{a}}\end{pmatrix}. \tag{B.42}$$

Care must be taken when working with these equations in spinor form. Because indices are raised with $\epsilon^{ab} = i\sigma^2$, when explicitly written out in components, this implies the Dirac spinor is formed from χ_a and ξ_a as:

$$\Psi = \begin{pmatrix} \chi_a \\ \epsilon^{\dot{a}\dot{b}}\xi^\dagger_{\dot{b}} \end{pmatrix} = \begin{pmatrix} \chi \\ i\sigma^2\xi^* \end{pmatrix} \tag{B.43}$$

since $\epsilon^{ab} = i\sigma^2$ and $\epsilon_{ab} = -i\sigma^2$. The four γ matrices γ^μ can be encoded as follows:

$$\gamma^\mu = \begin{pmatrix} 0 & \sigma^\mu \\ \overline{\sigma}^\mu & 0 \end{pmatrix} \qquad\qquad \gamma_5 = \begin{pmatrix} -1 & 0 \\ 0 & 1 \end{pmatrix}. \tag{B.44}$$

When working with a Dirac fermion Ψ, one typically does not use the Hermitian conjugate $\Psi^\dagger$, but rather consider the **Dirac conjugate** of Ψ,

$$\overline{\Psi} = \Psi^\dagger\beta, \tag{B.45}$$

where as a matrix, $\beta = \gamma^0$ (β is used here because γ^0 is part of a four vector γ^μ). To see this is used, note that in the Weyl basis, the difference between $\Psi^\dagger$ and $\overline{\Psi}$ is a swapping of chiral components:

$$\overline{\Psi} = \begin{pmatrix} \xi^a & \chi^\dagger_{\dot{a}} \end{pmatrix} \qquad\qquad \Psi^\dagger = \begin{pmatrix} \chi^\dagger_{\dot{a}} & \xi^a \end{pmatrix}. \tag{B.46}$$

This implies that $\chi^\dagger$ and χ cannot be contracted, and one cannot form a Lorentz invariant from them,

$$\Psi^\dagger\Psi = \chi^\dagger\chi + \xi^\dagger\xi = (\chi^\dagger)_{\dot{a}}\chi_a + \xi^a\xi^{\dagger\dot{a}}, \tag{B.47}$$

as can be clearly seen because χ and $\chi^\dagger$ have different indices, one dotted and one undotted. Consider instead $\overline{\Psi}$. In this case, the correct left- and right-handed Weyl spinors are contracted with one another, i.e., the dotted and undotted indices agree:

$$\overline{\Psi}\Psi = \xi^a\chi_a + \chi^\dagger_{\dot{a}}\xi^{\dagger\dot{a}}. \tag{B.48}$$

When added to the Lagrangian, this is called the **Dirac mass** term. The full Lagrangian for a Dirac field is

$$\mathcal{L}_{\text{Dirac}} = \overline{\Psi}(i\gamma^\mu\partial_\mu - m)\Psi. \tag{B.49}$$

When written in the Weyl basis, Eq. (B.49) splits into the two Weyl Lagrangians, one for the left-handed field and another for the right-handed field.

Because most computational tools are for Dirac spinors, one often projects Dirac spinors onto a state of definite chirality. This allows one to embed two-component Weyl spinors into four-component Dirac spinors. Projectors onto the left- and right-handed subspaces are given by,

$$P_L = \frac{1}{2}(1 - \gamma_5) \qquad\qquad P_R = \frac{1}{2}(1 + \gamma_5). \tag{B.50}$$

For Standard Model calculations, these projectors will always be inserted in front of the fermion fields that are being used since the Standard Model only contains Weyl fermions. Using $\{\gamma_\mu, \gamma_5\} = 0$, one can rearrange the projectors, as $\gamma^\mu P_L = P_R \gamma^\mu$, and this self-consistently connects spinors with the correct handedness as dictated by the indices.

In the Dirac representation, the generators of the Lorentz group $\mathcal{J}^{\mu\nu}$ may be expanded using the $\sigma_{\mu\nu}$ matrices:

$$\sigma^{\mu\nu} = \frac{i}{2}[\gamma^\mu, \gamma^\nu]. \tag{B.51}$$

The generator $J^{\mu\nu}$ in the bispinor representation can be expressed as,

$$D_{\text{bispinor}}(\mathcal{J}^{\mu\nu}) = \frac{1}{2}\sigma^{\mu\nu}, \tag{B.52}$$

which explains why $\sigma^{\mu\nu}$ plays such an important role in Dirac algebra computations. This generator of the bispinor representation can also be related to the two generators of the left- and right-handed representations,

$$\frac{1}{2}\sigma^{\mu\nu} = \begin{pmatrix} (S_L^{\mu\nu})_a^c & 0 \\ 0 & -(S_R^{\mu\nu})_{\dot{c}}^{\dot{a}} \end{pmatrix}. \tag{B.53}$$

Weyl spinors can form mass terms as well. When one discusses massive chiral fermions, one often uses**Majorana spinors**, which allows one to embed a chiral Weyl fermion into the bispinor representation. Given a left-handed Weyl fermion ψ, the spinor $\psi^\dagger_{\dot{a}}$ is right-handed. The associated Majorana spinor Ψ is then constructed as a Dirac spinor using ψ and $\psi^\dagger$:

$$\Psi = \begin{pmatrix} \psi_a \\ \psi^{\dagger\dot{a}} \end{pmatrix} = \begin{pmatrix} \psi \\ i\sigma^2\psi^*. \end{pmatrix} \tag{B.54}$$

This is exactly how the Dirac spinor was defined, but the right-handed component is $\psi^{\dagger\dot{a}} = \epsilon^{\dot{a}\dot{b}}\psi^\dagger_{\dot{b}} = \epsilon\psi^*$. A Majorana fermion has **two degrees of freedom and four components**, because it is in the bispinor representation but corresponds exactly to a chiral Weyl fermion with 2 components. From a Majorana spinor, one can form a mass term conventionally called a **Majorana mass**,

$$m\left(\psi\psi + \psi^\dagger\psi^\dagger\right) = m\left(\epsilon^{ab}\psi_a\psi_b + \epsilon^{\dot{a}\dot{b}}\psi^\dagger_{\dot{a}}\psi^\dagger_{\dot{b}}\right) = m\left(\psi^T i\sigma^2\psi + \psi^{*T} i\sigma^2\psi^*\right). \tag{B.55}$$

To determine if a Dirac spinor is Majorana, one can see if it satisfies the **reality constraint**: a Dirac spinor Ψ is Majorana if and only if it equals its charge conjugate,

$$\Psi = \Psi^{\mathrm{C}}. \tag{B.56}$$

Charge conjugation will be defined rigorously in Appendix B.4.4, and essentially switches the corresponding left- and right-handed fields inside the Dirac spinor. For now, it suffices to observe that for a Dirac spinor made up of left-handed Weyl spinors χ and ξ:

$$\Psi = \begin{pmatrix} \chi_a \\ \xi^{\dagger\dot{a}} \end{pmatrix}, \tag{B.57}$$

its charge conjugate Ψ^{C} is:

$$\Psi^{\mathrm{C}} = \begin{pmatrix} \xi_a \\ \chi^{\dagger\dot{a}} \end{pmatrix}. \tag{B.58}$$

A Dirac spinor is hence Majorana iff $\chi = \xi$, i.e., if it is composed of the same spinor. If Ψ is not Majorana, then its upper and lower components correspond to different particles, and not simply conjugates of the same particle.

B.4.4 Spinor indices and invariant symbols

The Levi-Civita tensor is also called an **invariant symbol** of the Lorentz group, because under boosts it does not change, i.e. for $\Lambda \in SO(1,3)$,

$$D_L(\Lambda)^c_a D_L(\Lambda)^d_b \epsilon_{cd} = \epsilon_{ab}, \tag{B.59}$$

just as the metric does not change under Lorentz transformations in the fundamental, i.e. $\Lambda^\rho_\mu\Lambda^\sigma_\nu g_{\rho\sigma} = g_{\mu\nu}$. The close relation of ϵ to the metric g means that one can use the ϵ tensor to raise and dotted and undotted indices. In general, an invariant symbol is a tensor which lives in the singlet representation. To find invariant symbols

for specific representations / tensors, one can look at the Clebsch-Gordan decomposition. Common invariant symbols that one will find and the corresponding tensor decompositions are given in Table B.2; note the existence of an invariant symbol is a direct result of the decomposition containing the singlet $(0,0)$. Because each invariant symbol lives in a singlet representation, there is a generalized version of Eq. (B.59) for each corresponding invariant, which one can use it to change indices with impunity because the symbol will not change under Lorentz transformation.

Symbol	Tensor decomposition
ϵ_{ab}	$(\frac{1}{2},0)\otimes(\frac{1}{2},0) = (0,0)_A \oplus (1,0)$
$\epsilon_{\dot{a}\dot{b}}$	$(0,\frac{1}{2})\otimes(0,\frac{1}{2}) = (0,0)_A \oplus (0,1)$
$g_{\mu\nu}$	$(\frac{1}{2},\frac{1}{2})\otimes(\frac{1}{2},\frac{1}{2}) = (0,0)_S \oplus (0,1)\oplus(1,0)\oplus(1,1)$
$\epsilon_{\mu\nu\alpha\beta}$	$(\frac{1}{2},\frac{1}{2})^{\otimes 4} = (0,0)_A \oplus \ldots$
$\sigma^{\mu}_{a\dot{b}}$	$(\frac{1}{2},0)\otimes(0,\frac{1}{2})\otimes(\frac{1}{2},\frac{1}{2}) = (0,0)\oplus\ldots$

Table B.2. Some common invariant symbols used in spinor analysis. Note that the representation $(\frac{1}{2},\frac{1}{2})$ is the fundamental vector representation of the Lorentz group. The subscripts A and S on the representations mean that they are either "antisymmetric" or "symmetric".

As an example, the fundamental representation **4** is the same representation as $(\frac{1}{2},\frac{1}{2})$. So, one should be able to translate the components of a four vector V_μ into components of a tensor $V_{a\dot{a}}$. This is done with the invariant symbol $\sigma^{\mu}_{a\dot{b}}$, and simply contracting it with V_μ gives the desired components:

$$V_{a\dot{a}} = \sigma^{\mu}_{a\dot{a}} V_\mu. \tag{B.60}$$

This is an explicit decomposition of the four-vector V_μ into components in the $(\frac{1}{2},\frac{1}{2})$ representation of the Lorentz group.

Explicitly, the invariant symbol $\sigma^{\mu}_{a\dot{a}}$ is given by the σ^μ tensor, and has a counterpart in the $\overline{\sigma}$ tensor,

$$\sigma^\mu = \begin{pmatrix} 1 & \sigma^i \end{pmatrix}, \qquad \overline{\sigma}^\mu = \begin{pmatrix} 1 & -\sigma^i \end{pmatrix}, \tag{B.61}$$

$$\sigma^{\mu}_{a\dot{a}} = \sigma^\mu, \qquad \sigma^{\mu\dot{a}a} = \overline{\sigma}^\mu. \tag{B.62}$$

The generators $\mathcal{J}_{\mu\nu}$ in the $(\frac{1}{2},0)$ and $(0,\frac{1}{2})$ irreps can be covariantly expressed in terms of σ and $\overline{\sigma}$ as,

$$(S_L^{\mu\nu})^b_a = \frac{i}{4}(\sigma^\mu\overline{\sigma}^\nu - \sigma^\nu\overline{\sigma}^\mu)^b_a, \qquad (S_R^{\mu\nu})^{\dot{b}}_{\dot{a}} = -\frac{i}{4}(\overline{\sigma}^\mu\sigma^\nu - \overline{\sigma}^\nu\sigma^\mu)^{\dot{b}}_{\dot{a}}. \tag{B.63}$$

B.4.5 Discrete symmetries

Because parity does not respect handedness, parity does not exist for Weyl spinors. To include parity in a theory, one must consider the Dirac representation of $(\frac{1}{2},0)\oplus(0,\frac{1}{2})$. The parity operator in the bispinor representation is just equal to γ^0, since this connects $\psi_L \mapsto \psi_R$ and $\psi_R \mapsto \psi_L$,

$$D_{\text{bispinor}}(P) = \gamma^0 = \begin{pmatrix} 0 & 1 \\ 1 & 0 \end{pmatrix}. \tag{B.64}$$

Charge conjugation C is another symmetry that must be discussed. There are a few ways to implement this symmetry. First, one can suppress all Dirac indices and use spinor notation. On a bispinor Ψ, charge conjugation acts as:

$$\Psi \xrightarrow{C} -i\gamma^2\Psi^* =: \Psi^{\mathrm{C}}. \tag{B.65}$$

If one instead uses spinor indices for Ψ, it is clear what this incredibly opaque definition is doing,

$$\Psi = \begin{pmatrix} \chi_a \\ \xi^{\dagger\dot{a}} \end{pmatrix} \mapsto \begin{pmatrix} 0 & -i\sigma^2 \\ i\sigma^2 & 0 \end{pmatrix} \begin{pmatrix} \chi^* \\ \xi^{\dagger *} \end{pmatrix} = \begin{pmatrix} -i\sigma^2\xi^a \\ i\sigma^2\chi^* \end{pmatrix} = \begin{pmatrix} \epsilon_{ab}\xi^b \\ \epsilon_{\dot{a}\dot{b}}\chi^{\dagger\dot{b}} \end{pmatrix} \tag{B.66}$$

as $\epsilon^{ab} = i\sigma^2 = -\epsilon_{ab}$. The easiest way to remember this symmetry is through its action on spinor indices. From this point of view, **charge conjugation acts by interchanging the left- and right-handed pieces inside Ψ and raising and lowering the appropriate indices**,

$$\begin{pmatrix} \chi_a \\ \xi^{\dagger\dot{a}} \end{pmatrix} \xrightarrow{C} \begin{pmatrix} \xi_a \\ \chi^{\dagger\dot{a}} \end{pmatrix}. \tag{B.67}$$

Note that as a matrix, $-i\gamma^2$ appears because it contains the ϵ tensors,

$$-i\gamma^2 = \begin{pmatrix} 0 & -i\sigma^2 \\ i\sigma^2 & 0 \end{pmatrix} = \begin{pmatrix} 0 & \epsilon_{ab} \\ \epsilon^{ab} & 0 \end{pmatrix}. \tag{B.68}$$

Conventionally, charge conjugation can also be defined as $\Psi \mapsto C\overline{\Psi}^T$, where C is essentially the same matrix as $-\gamma^2$, just block-diagonal, as in this definition the upper and lower components of Ψ have already been flipped through Dirac conjugation.

Explicitly:

$$C = \begin{pmatrix} \epsilon_{ab} & 0 \\ 0 & \epsilon^{ab} \end{pmatrix}. \tag{B.69}$$

Appendix C

Gamma Matrices in $d = 4$

C.1 Gamma Matrix Conventions

The Euclidean γ matrices are the set of 4×4 matrices in spin space $\{\gamma^0, \gamma^1, \gamma^2, \gamma^3\}$ are constructed to satisfy the Dirac algebra,

$$\{\gamma^\mu, \gamma^\nu\} = 2\,\delta^{\mu\nu} \tag{C.1}$$

where there is an implicit multiplication by the matrix $1_{4\times4}$ on the right-hand side of Eq. (C.1). There are a number of bases that one can express γ^μ in; our work will use the Weyl (chiral) basis,

$$\gamma^0 \doteq \begin{pmatrix} 0 & i\sigma^1 \\ -i\sigma^1 & 0 \end{pmatrix} \quad \gamma^1 \doteq \begin{pmatrix} 0 & -i\sigma^2 \\ i\sigma^2 & 0 \end{pmatrix} \quad \gamma^2 \doteq \begin{pmatrix} 0 & i\sigma^3 \\ -i\sigma^3 & 0 \end{pmatrix} \quad \gamma^3 \doteq \begin{pmatrix} 0 & 1 \\ 1 & 0 \end{pmatrix}, \tag{C.2}$$

defined in terms of the 2×2 identity matrix 1 and the Pauli matrices,

$$\sigma^1 = \begin{pmatrix} 0 & 1 \\ 1 & 0 \end{pmatrix} \qquad \sigma^2 = \begin{pmatrix} 0 & -i \\ i & 0 \end{pmatrix} \qquad \sigma^3 = \begin{pmatrix} 1 & 0 \\ 0 & -1 \end{pmatrix}, \tag{C.3}$$

unless otherwise specified. We use the notation $\doteq$ to denote "equal to in a basis", in this case in the basis of Eq. (C.2). Note that in other conventions, γ^0 is often expressed as γ_4. We also will not specify between upper and lower indices in Euclidean spacetime, as the metric $\delta^{\mu\nu}$ is trivial.

Chiral transformations are implemented by the Dirac matrix

$$\gamma_5 \equiv i\gamma^0\gamma^1\gamma^2\gamma^3 \tag{C.4}$$

which, in the basis of Eq. (C.2), is

$$\gamma_5 \doteq \begin{pmatrix} 1 & 0 \\ 0 & -1 \end{pmatrix}. \tag{C.5}$$

Observe that the Weyl basis is chosen to make γ_5 diagonal. From γ_5, we construct left- and right-handed projectors,

$$P_L \equiv \frac{1-\gamma_5}{2} \doteq \begin{pmatrix} 0 & 0 \\ 0 & 1 \end{pmatrix} \qquad P_R \equiv \frac{1+\gamma_5}{2} \doteq \begin{pmatrix} 1 & 0 \\ 0 & 0 \end{pmatrix} \tag{C.6}$$

which projects a Dirac spinor $\psi(x)$ onto its left- and right-handed components.

Given a Dirac fermion $\psi(x)$, the charge-conjugate of $\psi(x)$ is the field,

$$\psi^c(x) \equiv C\overline{\psi}^T(x) \qquad C = -i\gamma_0\gamma_2. \tag{C.7}$$

Charge conjugation is discussed in greater depth in Appendix B.4. The operation essentially evaluates $\psi^*(x)$ in such a way that $\psi^c(x)$ has the proper Dirac fermion structure. This is simplest to see in the index notation introduced in Appendix B.4, as the index notation makes it clear what spinor quantities are Lorentz covariant: it is rather opaque as formulated in Eq. (C.7).

C.2 Dirac Bilinears

We adopt the QDP convention for the basis of all Dirac matrix bilinears in $d = 4$ Euclidean spacetime dimensions [305],

$$\Gamma_a = \gamma_0^{a_0}\gamma_1^{a_1}\gamma_2^{a_2}\gamma_3^{a_3} \tag{C.8}$$

where $a \in \{0, 1, 2, ..., 15\}$ is written in binary as $(a)_{\text{base 2}} = a_3a_2a_1a_0$ in terms of the one-bit variables $a_i \in \{0, 1\}$. For convenience, we list the γ matrix basis explicitly in Table C.1 in terms of the bilinears

$$S = 1 \qquad P = \gamma_5 \qquad V^\mu = \gamma^\mu \qquad A^\mu = \gamma^\mu\gamma_5 \qquad T^{\mu\nu} = \frac{1}{2}[\gamma^\mu, \gamma^\nu] = \gamma^\mu\gamma^\nu. \tag{C.9}$$

Γ_a	Dirac Bilinear
Γ_0	S
Γ_1	V^0
Γ_2	V^1
Γ_3	T^{01}
Γ_4	V^2
Γ_5	T^{02}
Γ_6	T^{12}
Γ_7	$-A^3$

Γ_a	Dirac Bilinear
Γ_8	V^3
Γ_9	T^{03}
Γ_{10}	T^{13}
Γ_{11}	A^2
Γ_{12}	T^{23}
Γ_{13}	$-A^1$
Γ_{14}	A^0
Γ_{15}	P

Table C.1. Basis of Dirac bilinears $\{\Gamma_a\}_{a=0}^{15}$, listed in terms of the bilinear structures S, P, V, A, and T with the QDP++ γ-matrix conventions [305].

Appendix D

Fierz Identities

Fierz identities allow one to relate different combinations of indices of Dirac matrices to one another in a linear fashion. Recall that in $d = 4$ spacetime dimensions, there are 16 independent Dirac bilinears $\{\Gamma_a\}_{a=0}^{15}$ that may be written in terms of the γ matrices $\{\gamma^0, \gamma^1, \gamma^2, \gamma^3\}$ (Appendix C.2). We define a skew-symmetric 2-form on the space $\{\Gamma_a\}_{a=0}^{15}$ as

$$g_{ab} \equiv \mathrm{Tr}\left[\Gamma_a \Gamma_b\right]. \tag{D.1}$$

We will treat $g_{\alpha\beta}$ as a metric to raise and lower tensor indices on this space, but note that it is more similar to a symplectic form than to a proper metric. The Dirac Fierz identities [306] state that

$$(\Gamma_a)_{ij}(\Gamma_b)_{k\ell} = \sum_{cd} C_{ab}{}^{cd}(\Gamma_c)_{i\ell}(\Gamma_d)_{kj} \tag{D.2}$$

where the tensor $C_{ab}{}^{cd}$ essentially acts as a curvature is defined as

$$C_{ab}{}^{cd} = g^{ce} g^{df} C_{abef}, \qquad C_{abcd} \equiv \mathrm{Tr}\left[\Gamma_a \Gamma_b \Gamma_c \Gamma_d\right]. \tag{D.3}$$

These coefficients $C_{ab}{}^{cd}$ can be precomputed with standard Dirac algebra manipulations and explicitly used to convert between these two configurations of indices on Dirac bilinears.

There are additional color Fierz identities that play a similar role in rewriting the indices of products of $SU(3)$ generators. Let $t^a \in \mathfrak{su}(3)$ denote the 8 generators of the algebra. The color Fierz identities state that [306]

$$t^a_{ik} t^a_{j\ell} = \frac{1}{2}\left(\delta_{i\ell}\delta_{jk} - \frac{1}{3}\delta_{ik}\delta_{j\ell}\right), \tag{D.4}$$

and can be used to simplify color algebra.

In this work, Fierz identities have played a important role in simplifying operator bases used in the renormalization of short-distance $0\nu\beta\beta$ decay operators (Section 5.5).

For the vector operators $\mathcal{V}^\mu_{1'}$ and $\mathcal{V}^\mu_{2'}$ (Eq. (**??**)), the color Fierz identities are first applied to rewrite t^a in terms of open and closed Takahashi brackets:

$$\begin{aligned}
\mathcal{V}^\mu_{1'} &= \frac{1}{2}(\overline{u}\gamma^\mu P_L d][\overline{u}P_R d) - \frac{1}{6}(\overline{u}\gamma^\mu P_L d)[\overline{u}P_R d] + (L \leftrightarrow R) \\
&= \frac{1}{4}\left((V^\mu][S) - (A^\mu][P)\right) - \frac{1}{12}\left(V^\mu S - A^\mu P\right), \\
\mathcal{V}^\mu_{2'} &= \frac{1}{2}(\overline{u}\gamma^\mu P_L d][\overline{u}P_L d) - \frac{1}{6}(\overline{u}\gamma^\mu P_L d)[\overline{u}P_L d] + (L \leftrightarrow R) \\
&= \frac{1}{4}\left((V^\mu][S) + (A^\mu][P)\right) - \frac{1}{12}\left(V^\mu S + A^\mu P\right)
\end{aligned} \tag{D.5}$$

Here a Takahashi bracket around a pair of Dirac bilinears denotes the color and Dirac indices are contracted in a different pattern, for example the contraction $(\Gamma_1][\Gamma_2) = \overline{u}^a_\alpha\,(\Gamma_1)_{\alpha\beta}\,d^b_\beta\,\overline{u}^b_\gamma\,(\Gamma_2)_{\gamma\delta}\,d^a_\delta$. The spinor Fierz transformation may now be applied to compute the color-mixed pieces, which yields

$$\begin{aligned}
(V^\mu][S) &= \frac{1}{2}\left(V^\mu S + \frac{i}{2}\epsilon^{\mu\nu\alpha\beta}A^\nu T^{\alpha\beta}\right), \\
(A^\mu][P) &= \frac{1}{2}\left(A^\mu P - T^{\mu\nu}V^\nu\right).
\end{aligned} \tag{D.6}$$

Appendix E

Mathematical Background for Nevanlinna-Pick Interpolation

E.1 Hardy Spaces

For $1 \leq p \leq \infty$, the **Hardy space** H^p is defined as the set of holomorphic functions on the disk $f : \mathbb{D} \to \mathbb{D}$ such that

$$||f||_p := \sup_{0 \leq r < 1} ||f_r||_{L^p(\mathbb{T})} < \infty, \tag{E.1}$$

where f_r is the angular function defined on the unit circle $\mathbb{T} := \partial\mathbb{D}$ as

$$f_r : \mathbb{T} \to \mathbb{D} \qquad\qquad f_r(e^{i\theta}) := f(re^{i\theta}). \tag{E.2}$$

The Hardy spaces $(H^p, ||\cdot||_p)$ are Banach spaces. The $L^p(\mathbb{T})$-norm $||\cdot||_{L^p(\mathbb{T})}$ for complex-valued functions $g : \mathbb{T} \to \mathbb{C}$ on $\mathbb{T}$ is defined for $1 \leq p < \infty$ as

$$||g||_{L^p(\mathbb{T})} := \left(\int_{\mathbb{T}} |g|^p dm\right)^{\frac{1}{p}} = \left(\frac{1}{2\pi}\int_0^{2\pi} |g(e^{i\theta})| d\theta\right)^{\frac{1}{p}}, \tag{E.3}$$

where m is the normalized Lebesgue measure on $\mathbb{T}$, i.e. $dm(\theta) = d\theta/2\pi$. For $p = \infty$, the ∞-norm is defined as the essential supremum of $|g|$,

$$||f||_{L^\infty(\mathbb{T})} := \operatorname{ess\,sup}_{\mathbb{T}} |g|, := \inf\{a \in \mathbb{R} : |g| \leq a \text{ a.e.}\} \tag{E.4}$$

where the essential supremum acts as a supremum except on sets of measure zero.

For $1 \leq p \leq \infty$, the definition (Eq. E.1) of H^p implies that for any $f \in H^p$, the

radial limit of f,

$$\tilde{f}(\theta) := \lim_{r\uparrow 1} f(re^{i\theta}) \tag{E.5}$$

exists a.e. as a map $\tilde{f} : \mathbb{T} \to \mathbb{D}$ and is finite, with $L^p(\mathbb{T})$ norm

$$||\tilde{f}||_{L^p(\mathbb{T})} = ||f||_p. \tag{E.6}$$

The function f may be obtained from its radial limit $\tilde{f}$ by convolution,

$$f(re^{i\theta}) = P_r * \tilde{f} := \int_{\mathbb{T}} P_r(t-\theta)\tilde{f}(e^{it})\, dm(t) = \frac{1}{2\pi}\int_0^{2\pi} P_r(t-\theta)\tilde{f}(e^{it})\, dt, \tag{E.7}$$

where $P_r(\theta)$ is the **Poisson kernel**,

$$P_r(\theta) := \frac{1-r^2}{|1-re^{i\theta}|^2}. \tag{E.8}$$

Note that because the map $[1,\infty] \ni p \mapsto ||f||_p$ is non-decreasing for any $f \in \mathrm{Hol}(\mathbb{D})$, we have the increasing tower $H^\infty \subseteq H^p \subseteq H^q \subseteq H^1$ for any $1 \leq q \leq p \leq \infty$.

E.2 Matrix-vector notation for continued fractions

The continued fractions expansion used in Chapter 4 are often denoted with a matrix-vector multiplication, and it remains to show that this notation is well-defined. Let $a, b, c, d, g : \mathbb{D} \to \mathbb{D}$ be analytic functions, and define $f : \mathbb{D} \to \mathbb{D}$ via the continued fractions expansion,

$$f(\zeta) = \frac{a(\zeta)g(\zeta)+b(\zeta)}{c(\zeta)g(\zeta)+d(\zeta)} =: F(\zeta)g(\zeta) \qquad F(\zeta) := \begin{pmatrix} a(\zeta) & b(\zeta) \\ c(\zeta) & d(\zeta) \end{pmatrix} \tag{E.9}$$

Note that one may regard $g(\zeta)$ in the above equation as the column vector $g(\zeta) \to \begin{pmatrix} g(\zeta) \\ 1 \end{pmatrix}$. This notation is degenerate in that scalar multiplication of a matrix $F(\zeta)$ by $a \neq 0$ does not change its action on functions. If $F(\zeta) \to aF(\zeta)$, this multiplies both the numerator and the denominator of the resulting matrix-vector product by a, which cancels out. For example, in the definition of $U_n(\zeta)$ in Eq. (4.81), the normalization of the matrix by $1/\sqrt{1-\left|w_n^{(n-1)}\right|^2}$ does not affect the final value of any continued fractions expansion containing U_n.

To make this notation well-defined, one shows that matrix-matrix and matrix-

vector products yield the equivalent function compositions, and that matrix inversion corresponds to the inverse function composition.

- As in the case of $g \to \begin{pmatrix} g \\ 1 \end{pmatrix}$, functions g are regarded as column vectors whose top component is their numerator and whose bottom component is their denominator. In this way, matrix-vector multiplication exactly reproduces function composition. To see this, Eq. (E.9) is recast in this notation,

$$\begin{pmatrix} \text{num}(f) \\ \text{denom}(f) \end{pmatrix} = \begin{pmatrix} a(\zeta) & b(\zeta) \\ c(\zeta) & d(\zeta) \end{pmatrix} \begin{pmatrix} g(\zeta) \\ 1 \end{pmatrix} = \begin{pmatrix} a(\zeta)g(\zeta) & b(\zeta) \\ c(\zeta)g(\zeta) & d(\zeta) \end{pmatrix}, \tag{E.10}$$

  which equals $f(\zeta) = \frac{a(\zeta)g(\zeta)+b(\zeta)}{c(\zeta)g(\zeta)+d(\zeta)}$, as desired.

- Matrix-matrix multiplication preserves function composition. Consider expanding $g(\zeta)$ as a continued fraction in terms of $h(\zeta)$.

$$g(\zeta) = \frac{a'(\zeta)h(\zeta) + b'(\zeta)}{c'(\zeta)h(\zeta) + d'(\zeta)} = \begin{pmatrix} a'(\zeta) & b'(\zeta) \\ c'(\zeta) & d'(\zeta) \end{pmatrix} h(\zeta). \tag{E.11}$$

  The expansion of $f(\zeta)$ (Eq. (E.9)) in terms of $h(\zeta)$ is

$$\begin{aligned} f(\zeta) &= \frac{a(\zeta)\frac{a'(\zeta)h(\zeta)+b'(\zeta)}{c'(\zeta)h(\zeta)+d'(\zeta)} + b(\zeta)}{c(\zeta)\frac{a'(\zeta)h(\zeta)+b'(\zeta)}{c'(\zeta)h(\zeta)+d'(\zeta)} + d(\zeta)} \\ &= \frac{a(\zeta)a'(\zeta)h(\zeta) + a(\zeta)b'(\zeta) + b(\zeta)c'(\zeta)h(\zeta) + b(\zeta)d'(\zeta)}{c(\zeta)a'(\zeta)h(\zeta) + c(\zeta)b'(\zeta) + d(\zeta)c'(\zeta)h(\zeta) + d(\zeta)d'(\zeta)}. \end{aligned} \tag{E.12}$$

  For the notation to be well-defined, $F(\zeta)F'(\zeta)h(\zeta)$ must equal this value, where $F'(\zeta) = \begin{pmatrix} a'(\zeta) & b'(\zeta) \\ c'(\zeta) & d'(\zeta) \end{pmatrix}$. Upon computation,

$$\begin{aligned} F(\zeta)F'(\zeta)h(\zeta) &= \begin{pmatrix} a(\zeta) & b(\zeta) \\ c(\zeta) & d(\zeta) \end{pmatrix} \begin{pmatrix} a'(\zeta) & b'(\zeta) \\ c'(\zeta) & d'(\zeta) \end{pmatrix} \begin{pmatrix} h(\zeta) \\ 1 \end{pmatrix} \\ &= \begin{pmatrix} a(\zeta) & b(\zeta) \\ c(\zeta) & d(\zeta) \end{pmatrix} \begin{pmatrix} a'(\zeta)h(\zeta) + b'(\zeta) \\ c'(\zeta)h(\zeta) + d'(\zeta) \end{pmatrix} \\ &= \begin{pmatrix} a(\zeta)a'(\zeta)h(\zeta) + a(\zeta)b'(\zeta) + b(\zeta)c'(\zeta)h(\zeta) + b(\zeta)d'(\zeta) \\ c(\zeta)a'(\zeta)h(\zeta) + c(\zeta)b'(\zeta) + d(\zeta)c'(\zeta)h(\zeta) + d(\zeta)d'(\zeta) \end{pmatrix}, \end{aligned} \tag{E.13}$$

it is clear that this exactly yields Eq. (E.12).

- Matrix inversion: Matrix inversion must correspond to inverting the continued fractions expansion. Upon inverting Eq. (E.9) for $g(\zeta)$,

$$g(\zeta) = \frac{d(\zeta)f(\zeta) - b(\zeta)}{-c(\zeta)f(\zeta) + a(\zeta)}. \tag{E.14}$$

The inverse of the 2×2 matrix (neglecting the scale factor from the determinant) is

$$F(\zeta)^{-1} = \begin{pmatrix} d(\zeta) & -b(\zeta) \\ -c(\zeta) & a(\zeta) \end{pmatrix}, \tag{E.15}$$

which is exactly the matrix representation of Eq. (E.14).

E.3 Blaschke Products

For a given set of points $\{\zeta_k\}$, the Blaschke factors $b_k(z)$ and their product $B_N(z)$,

$$b_k(z) \equiv \frac{|\zeta_k|}{\zeta_k}\frac{\zeta_k - z}{1 - \zeta_k^* z} \qquad\qquad B_N(z) \equiv \prod_{k=1}^{N} b_k(z) \tag{E.16}$$

are interesting to study in their own right [136, 307], as their properties inform many properties of the Nevanlinna coefficients P_N, Q_N, R_N, and S_N. Note that the points where the interpolation problem is fixed, ζ_k, all lie on the real axis in $\mathbb{D}$,

$$\zeta_k = h(i\omega_k) \in \mathbb{D} \cap \mathbb{R} \tag{E.17}$$

since the Matsubara frequencies are purely imaginary. With this simplification, the phase factor can be neglected,

$$b_k(z) = \frac{\zeta_k - z}{1 - \zeta_k z}. \tag{E.18}$$

There are two main regions to consider b_k and B_N: on the real axis of $\mathbb{D}$, and as we approach the boundary of $\mathbb{D}$. In the first case, note that by construction, $b_k(z)$ must vanish as we approach ζ_k, hence we expect $B_N(z)$ to have N zeros at $\{\zeta_k\}_{k=1}^N$. Fig. E.1 shows the Mobiüs transform of the first 20 nonzero Matsubara frequencies, ζ_k, on a lattice with $\beta = 48$, along with the corresponding Blaschke factors b_k and the Blaschke product B_N. Note that each b_k vanishes at the corresponding ζ_k. The

Blaschke product B_N is very small in the bulk of the disk $\mathbb{D}$, but approaches 1 at the boundary of the disk, $\partial\mathbb{D}$.

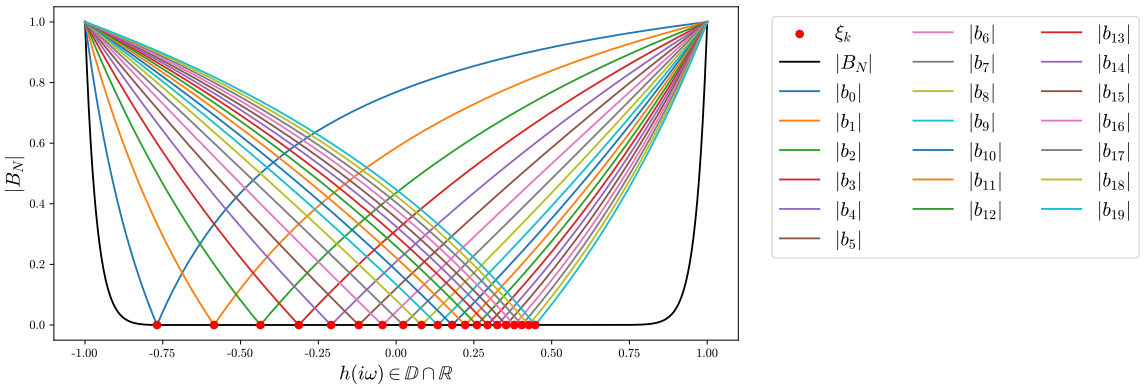

Figure E.1. Evaluation of the Blaschke factors and the Blaschke product on the real axis of the disk, $\mathbb{D} \cap \mathbb{R}$. The Mobiüs transform of the Matsubara frequencies, ζ_k, are shown in red, while the Blaschke product B_N is the black curve, and the colored curves are the corresponding Blaschke factors b_k. The depicted Matsubara frequencies are the first 20 non-zero frequencies on a lattice with temporal extent $\beta = 48$.

The fact that $B_N(z) \to 1$ as $z \to \mathbb{D}$ is not a coincidence, and can be seen by considering the behavior of each Blaschke factor $b_k(z)$ as one approaches $\partial\mathbb{D}$. As $z \to e^{i\alpha} \in \partial\mathbb{D}$, one can expand out the individual Blaschke product $b_k(z)$ as

$$b_k(z) \to \frac{\zeta_k - e^{i\alpha}}{1 - \zeta_k e^{i\alpha}} \left(\frac{1 + \zeta_k e^{-i\alpha}}{1 + \zeta_k e^{-i\alpha}} \right) = e^{-i\alpha} \left(\frac{\zeta_k^2 - 1}{1 - 2\zeta_k \sin\alpha - \zeta_k^2} \right). \tag{E.19}$$

Note that $\alpha = 0$ corresponds to evaluation of the Blaschke factor on the real axis, as in Fig. E.1, and we see that $|b_k(z)| \to 1$ in this case, as is depicted in the data.

What does $B_N(z)$ look like for $\alpha \neq 0$? We can prove a general bound with the (reverse) triangle inequality,

$$|b_k(z)| = \left| \frac{\zeta_k - z}{1 - \zeta_k z} \right| \geq \frac{||z| - |\zeta_k||}{1 + |\zeta_k z|} \xrightarrow{|z| \to 1} \frac{1 - |\zeta_k|}{1 + |\zeta_k|}. \tag{E.20}$$

If we plot the Blaschke factors on an evaluation contour $h(\omega + i\eta)$, we can numerically study its behavior. We see that as we approach $1 \in \mathbb{D}$ (equivalently, $\omega \to \infty$ where $\omega + i\eta \in \mathbb{C}^+$ is the domain of the Matsubara frequencies), the Blaschke factors all approach 1, while as we approach $-1 \in \mathbb{D}$ (equivalently, $\omega \to 0$) the Blaschke factors do not approach 1 at fixed η. However, varying η and sending $\eta \downarrow 0$ sends each Blaschke factor to 1 asymptotically.

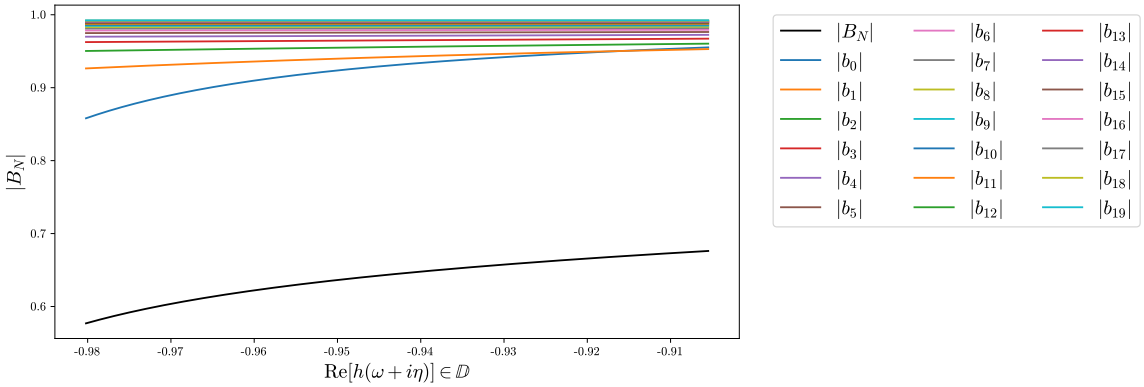

Figure E.2. Blaschke factors evaluated on the evaluation contour $h(\omega + i\eta) \in \mathbb{D}$, for $\omega \in [0, 2]$ and $\eta = 0.01$. The further ζ_k is from the boundary of the disk, the closer b_k remains to 1.

Appendix F

Three-Point Contractions for Short-Distance $\pi^- \to \pi^+ e^- e^-$

The correlation functions of Eq. (5.20) can be written in terms of the following contraction structures,

$$
\begin{aligned}
\textcircled{1}_{\Gamma_1\Gamma_2} &= \sum_{\boldsymbol{x}} \mathrm{Tr}\left[\gamma_5\Gamma_1 S_d(t_- \to x) S_u^\dagger(t_- \to x)\right] \cdot \mathrm{Tr}\left[\gamma_5\Gamma_2 S_d\left(t_+ \to x\right) S_u^\dagger(t_+ \to x)\right] \\
&\qquad + (t_- \leftrightarrow t_+), \\
\textcircled{2}_{\Gamma_1\Gamma_2} &= \sum_{\boldsymbol{x}} \mathrm{Tr}[\gamma_5\Gamma_1 S_d(t_- \to x) S_u^\dagger(t_- \to x) \gamma_5\Gamma_2 S_d(t_+ \to x) S_u^\dagger(t_+ \to x)] + (t_- \leftrightarrow t_+), \\
\textcircled{3}_{\Gamma_1\Gamma_2} &= \sum_{\boldsymbol{x}} \mathrm{Tr_C}[\mathrm{Tr_D}[\gamma_5\Gamma_1 S_d(t_- \to x) S_u^\dagger(t_- \to x)] \cdot \mathrm{Tr_D}[\gamma_5\Gamma_2 S_d(t_+ \to x) S_u^\dagger(t_+ \to x)]] \\
&\qquad + (t_- \leftrightarrow t_+), \\
\textcircled{4}_{\Gamma_1\Gamma_2} &= \sum_{\boldsymbol{x}} \mathrm{Tr_D}[\mathrm{Tr_C}[\gamma_5\Gamma_1 S_d(t_- \to x) S_u^\dagger(t_- \to x)] \cdot \mathrm{Tr_C}[\gamma_5\Gamma_2 S_d(t_+ \to x) S_u^\dagger(t_+ \to x)]] \\
&\qquad + (t_- \leftrightarrow t_+),
\end{aligned}
\tag{F.1}
$$

where Γ_1, Γ_2 are arbitrary Dirac matrices, $\mathrm{Tr_C}$ ($\mathrm{Tr_D}$) denotes a color (spin) trace, $\mathrm{Tr} = \mathrm{Tr_C} \circ \mathrm{Tr_D}$ denotes a full trace, and $x = (\boldsymbol{x}, t_x)$. Propagators $S(t_{\mathrm{src}} \to x)$ are computed with a zero three-momentum wall source at time $t_{\mathrm{src}} \in \{t_-, t_+\}$ and a point sink at time t_x,

$$
S(t_{\mathrm{src}} \to x) \equiv \sum_{\boldsymbol{y}} S((\boldsymbol{y}, t_{\mathrm{src}}) \to (\boldsymbol{x}, t_x)). \tag{F.2}
$$

With the definitions of Eq. (F.1), the correlation functions are evaluated as

$$\begin{aligned}
\mathcal{C}_1(t_-,t_x,t_+) &= -\frac{1}{4}\left[\textcircled{1}_{VV} - \textcircled{2}_{VV} - \textcircled{1}_{AV} + \textcircled{2}_{AV} + \textcircled{1}_{VA} - \textcircled{2}_{VA} - \textcircled{1}_{AA} + \textcircled{2}_{AA}\right], \\
\mathcal{C}_2(t_-,t_x,t_+) &= -\frac{1}{2}\left[\textcircled{1}_{SS} - \textcircled{2}_{SS} + \textcircled{1}_{PP} - \textcircled{2}_{PP}\right], \\
\mathcal{C}_3(t_-,t_x,t_+) &= -\frac{1}{2}\left[\textcircled{1}_{VV} - \textcircled{2}_{VV} + \textcircled{1}_{AA} - \textcircled{2}_{AA}\right], \\
\mathcal{C}_{1'}(t_-,t_x,t_+) &= -\frac{1}{4}\left[\textcircled{3}_{VV} - \textcircled{4}_{VV} - \textcircled{3}_{AV} + \textcircled{4}_{AV} + \textcircled{3}_{VA} - \textcircled{4}_{VA} - \textcircled{3}_{AA} + \textcircled{4}_{AA}\right], \\
\mathcal{C}_{2'}(t_-,t_x,t_+) &= -\frac{1}{2}\left[\textcircled{3}_{SS} - \textcircled{4}_{SS} + \textcircled{3}_{PP} - \textcircled{4}_{PP}\right],
\end{aligned} \tag{F.3}$$

where $S = 1$, $P = \gamma_5$, $V = \gamma^\mu$, and $A = \gamma^\mu\gamma_5$.

Appendix G

Effective Matrix Elements for Short-Distance $\pi^- \to \pi^+ e^- e^-$

Figs. (G.1)-(G.4) display the remaining fits to the effective matrix elements (Eq. (5.22)) that were not depicted in Fig. (5.8). The fit procedure is described in Section 5.3.1 of the main text. The number of gauge field configurations per ensemble used in each matrix element extraction, n_{cfgs}, and the corresponding bare matrix elements in lattice units, Eq. (5.21), are shown in Table G.1.

Ensemble	am_ℓ	n_{cfgs}	$a^4\langle\pi^+\|\mathcal{O}_1\|\pi^-\rangle$	$a^4\langle\pi^+\|\mathcal{O}_2\|\pi^-\rangle$	$a^4\langle\pi^+\|\mathcal{O}_3\|\pi^-\rangle$	$a^4\langle\pi^+\|\mathcal{O}_{1'}\|\pi^-\rangle$	$a^4\langle\pi^+\|\mathcal{O}_{2'}\|\pi^-\rangle$
24I	0.01	52	-0.005804(41)	-0.010023(91)	0.0003442(16)	-0.01794(13)	0.002445(22)
	0.005	53	-0.004891(38)	-0.00834(11)	0.0001742(14)	-0.01533(12)	0.002043(26)
32I	0.008	33	-0.001862(17)	-0.002917(34)	0.00008286(58)	-0.005791(53)	0.0007248(86)
	0.006	42	-0.001644(16)	-0.002587(36)	0.00005600(40)	-0.005145(50)	0.0006445(87)
	0.004	47	-0.001482(15)	-0.002331(31)	0.00003391(40)	-0.004669(47)	0.0005822(78)

Table G.1. Determination of bare matrix elements $a^4\langle\pi^+|\mathcal{O}_k(\boldsymbol{p}=\mathbf{0})|\pi^-\rangle$ on each ensemble for each operator $\mathcal{O}_k(x)$ in the BSM basis, Eq. (5.12), extracted from fits to the effective matrix elements (Eq. (5.22)) as described in the text. The effective matrix elements are computed on n_{cfgs} configurations on the respective ensemble.

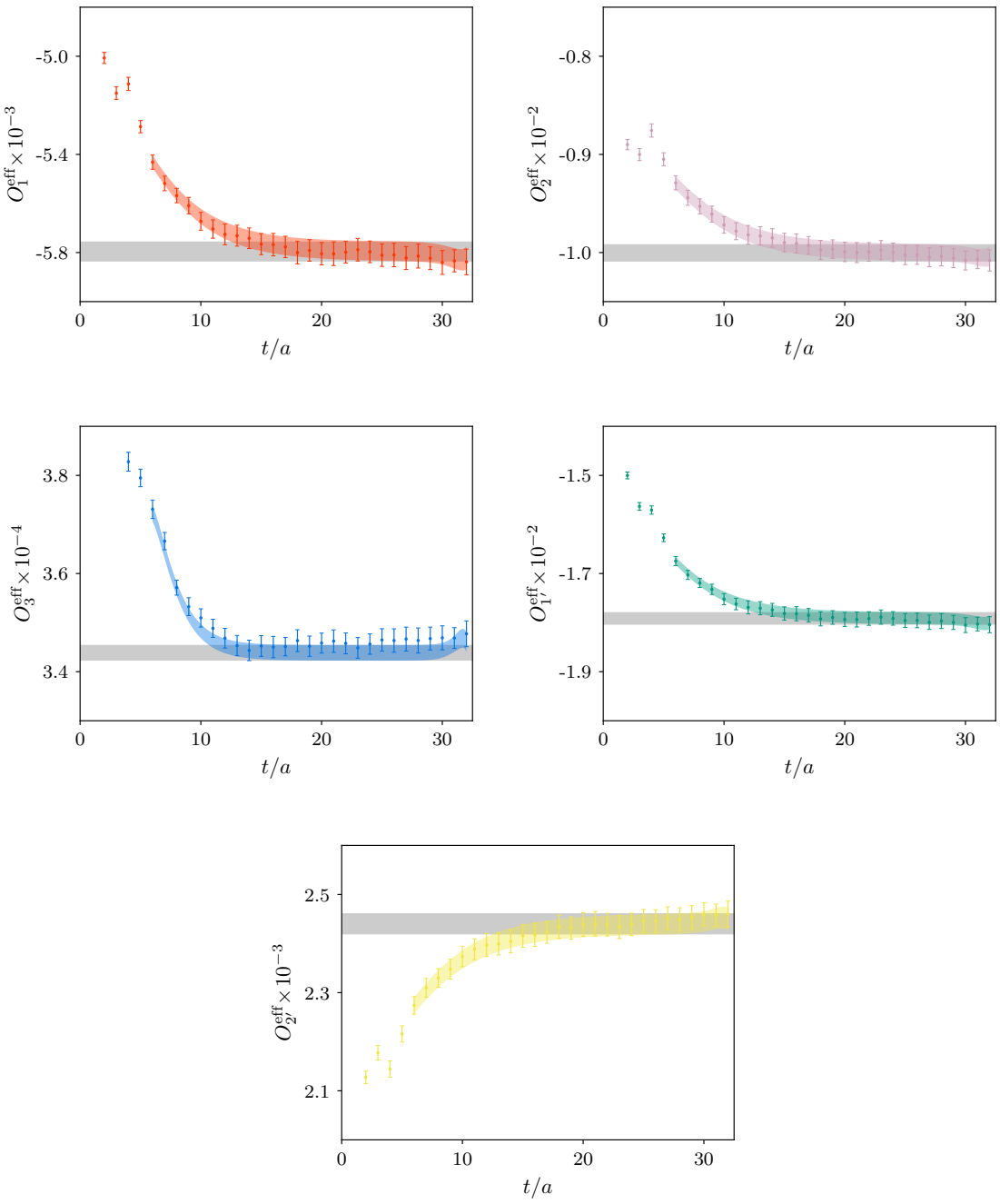

Figure G.1. Effective matrix elements, Eq. (5.22), for the operators $\mathcal{O}_k(\boldsymbol{p} = \boldsymbol{0})$ on the 24I, $am_\ell = 0.01$ ensemble. The constant grey band denotes the fit results for each bare, dimensionless matrix element $a^4\langle\pi^+|\mathcal{O}_k(\boldsymbol{p} = \boldsymbol{0})|\pi^-\rangle$, and the colored data points and colored band denote the effective matrix element data and extrapolation band, respectively. The fit procedure is detailed in Section 5.3.1.

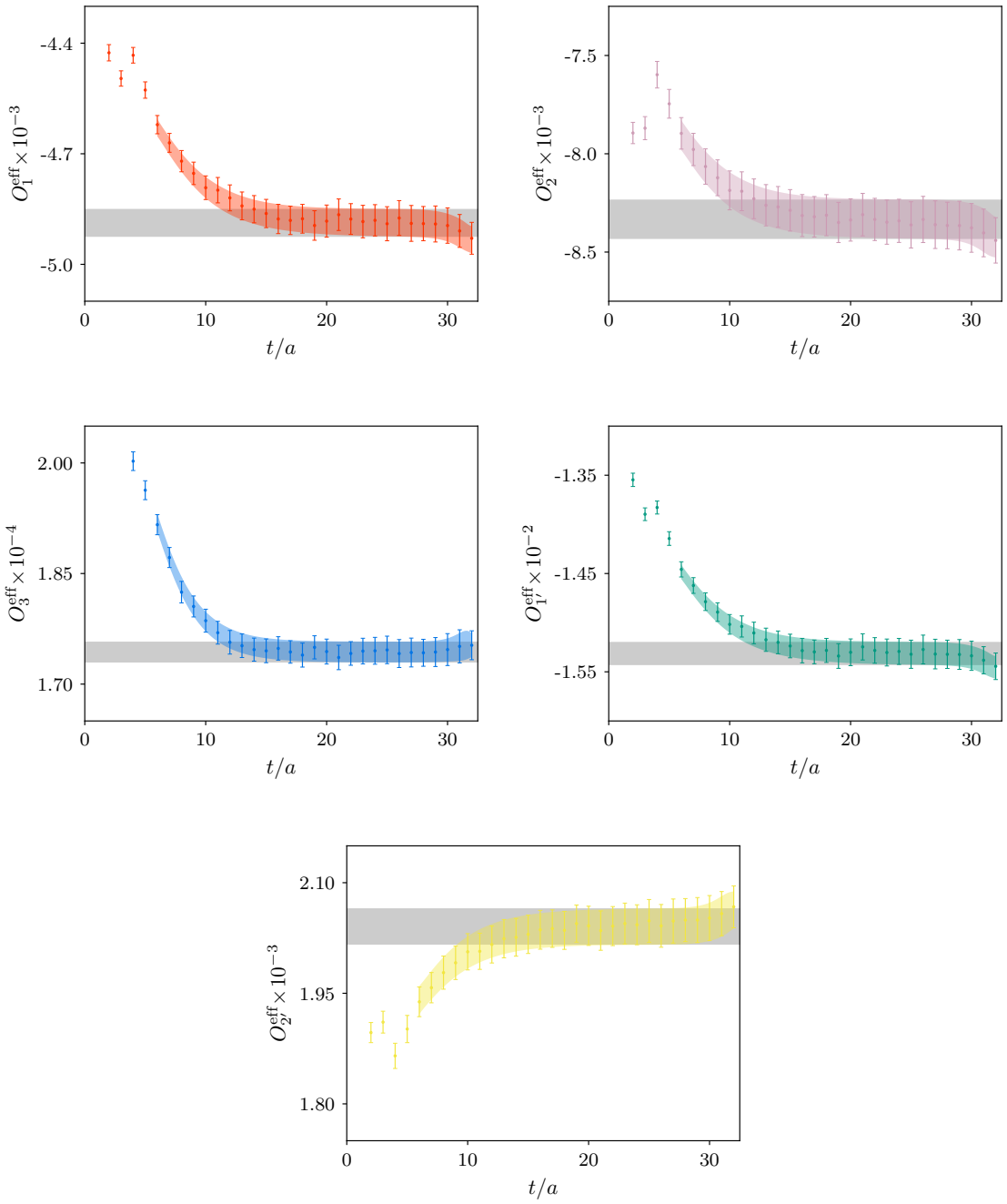

Figure G.2. As in Fig. (G.1), for the 24I, $am_\ell = 0.005$ ensemble.

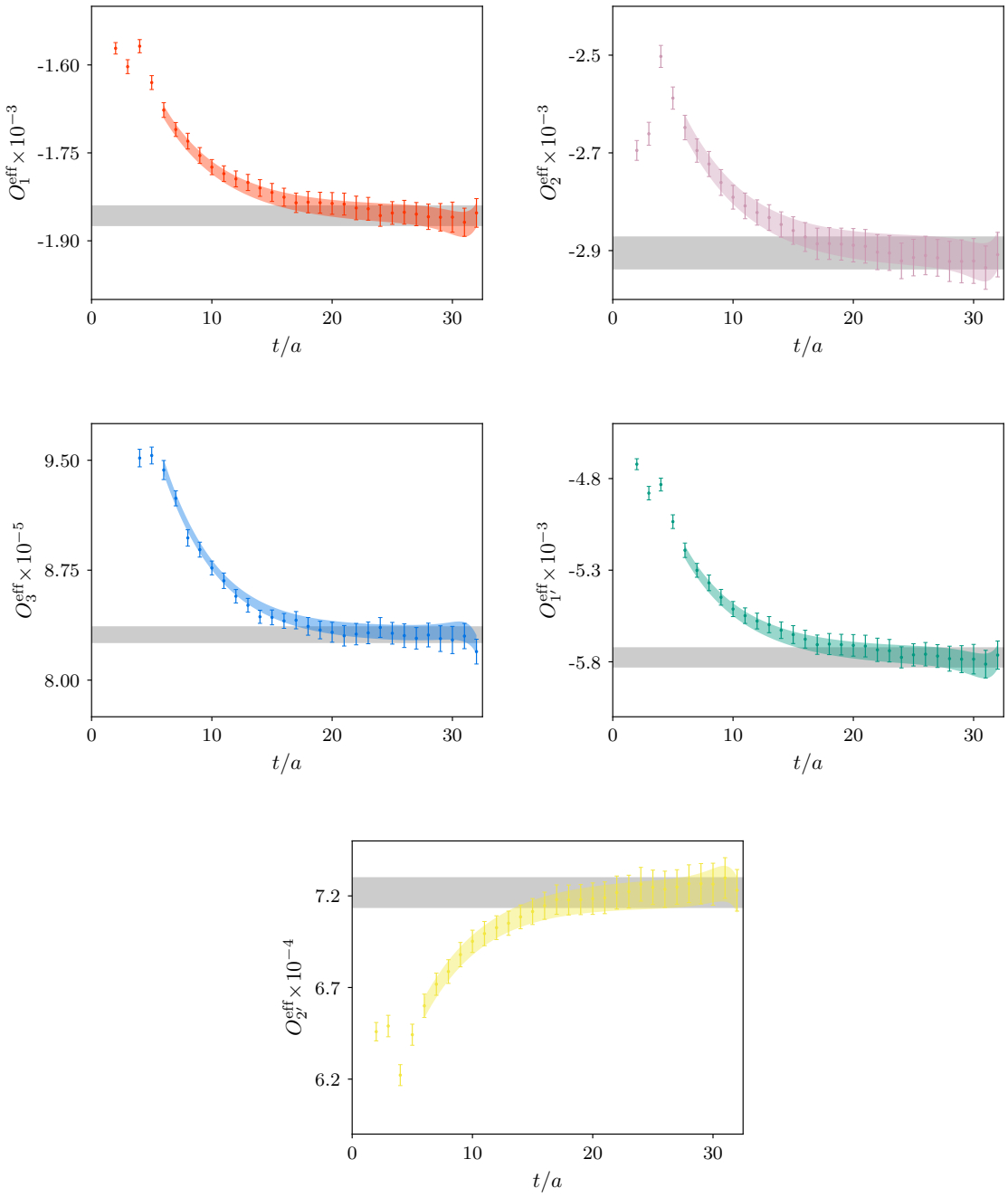

Figure G.3. As in Fig. (G.1), for the 32I, $am_\ell = 0.008$ ensemble.

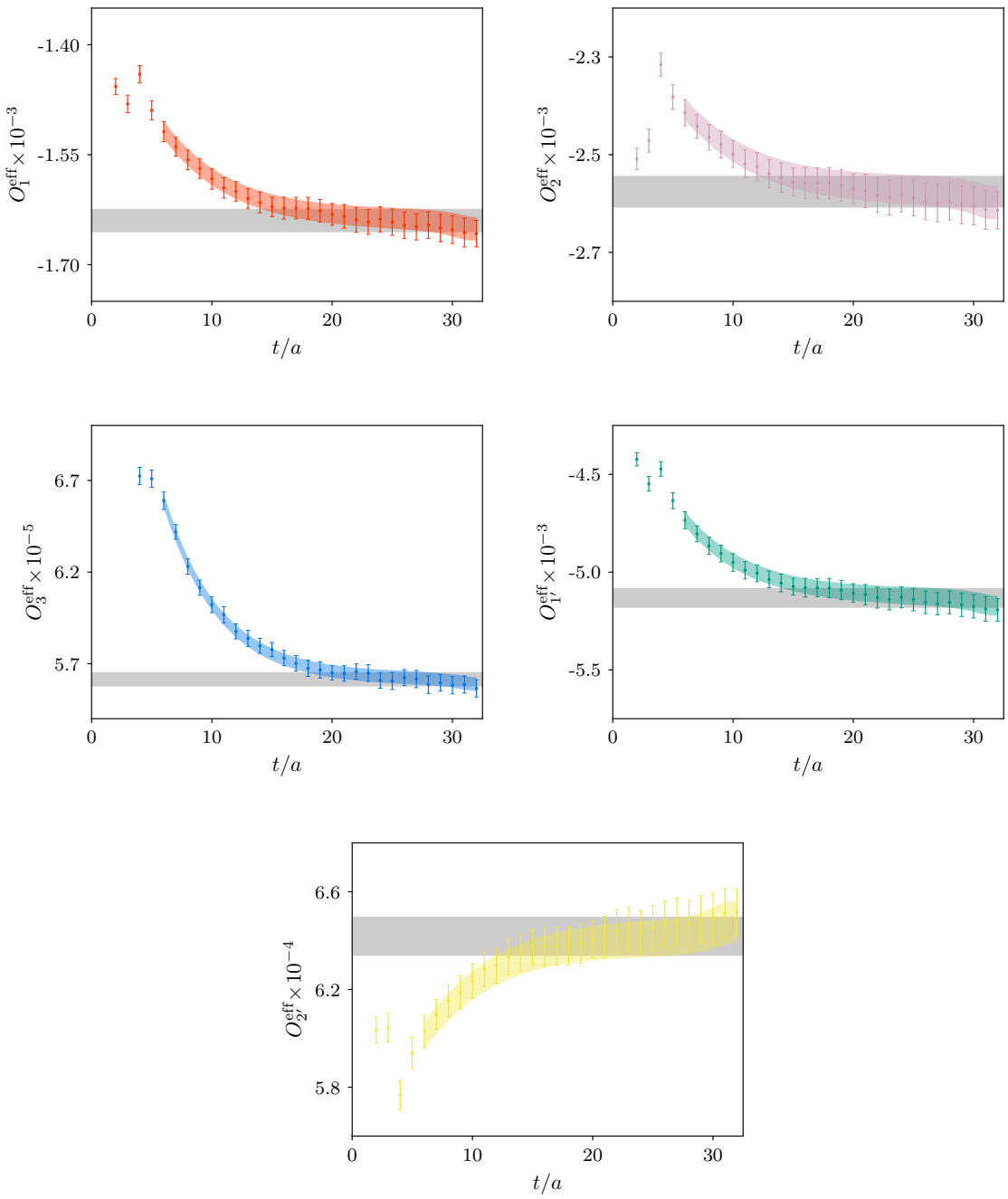

Figure G.4. As in Fig. (G.1), for the 32I, $am_\ell = 0.006$ ensemble.

Appendix H

Vector and Axial-Vector Renormalization Coefficients for Short-Distance $\pi^- \to \pi^+ e^- e^-$

Calculation of the scale and scheme-independent vector and axial-vector-current renormalization coefficients $\mathcal{Z}_j(a)$, with $j \in \{V, A\}$, proceeds through the vector (Eq. (5.56)) and axial-vector three-point functions,

$$G_A^\mu(q; a, m_\ell) = \frac{1}{V} \sum_{x, x_1, x_2} e^{i(p_1 \cdot x_1 - p_2 \cdot x_2 + q \cdot x)} \langle 0 | u(x_1) A^\mu(x) \overline{d}(x_2) | 0 \rangle, \tag{H.1}$$

where $A^\mu(x) = \overline{u}(x) \gamma^\mu \gamma_5 d(x)$. The momenta p_1, p_2, and q are subject to the symmetric constraint, Eq. (5.46), and parameterized identically to the modes used in the calculation of the four-quark operator renormalizations (Eq. (5.47)) with $k \in \{2, 3, 4, 5\}$. The lattice spacing dependence is made explicit in this section. The amputated three-point functions

$$\Lambda_j^\mu(q; a, m_\ell) = S^{-1}(p_1; a, m_\ell) G_j^\mu(q; a, m_\ell) S^{-1}(p_2; a, m_\ell), \tag{H.2}$$

with $j \in \{V, A\}$, are used to compute the renormalization coefficients,

$$\begin{aligned} \frac{1}{12\tilde{q}^2} \frac{\mathcal{Z}_V(\mu^2; a, m_\ell)}{\mathcal{Z}_q^{\mathrm{RI/sMOM}}(\mu^2; a, m_\ell)} \mathrm{Tr}\left[\tilde{q}_\mu \Lambda_V^\mu(q; a, m_\ell) \not{\tilde{q}}\right] \Big|_{\mathrm{sym}} &= 1, \\ \frac{1}{12\tilde{q}^2} \frac{\mathcal{Z}_A(\mu^2; a, m_\ell)}{\mathcal{Z}_q^{\mathrm{RI/sMOM}}(\mu^2; a, m_\ell)} \mathrm{Tr}\left[\tilde{q}_\mu \Lambda_A^\mu(q; a, m_\ell) \gamma_5 \not{\tilde{q}}\right] \Big|_{\mathrm{sym}} &= 1, \end{aligned} \tag{H.3}$$

where $\tilde{p}_\mu = \frac{2}{a}\sin(\frac{a}{2}p_\mu)$ is the lattice momentum. Note that the quark-field renormalization in Eq. (H.3) is defined in the RI/sMOM scheme [211],

$$\mathcal{Z}_q^{\mathrm{RI/sMOM}}(\mu^2; a, m_\ell)\Big|_{p^2=\mu^2} = \frac{i}{12\tilde{p}^2}\mathrm{Tr}[S^{-1}(p; a, m_\ell)\not{\tilde{p}}]\Big|_{p^2=\mu^2}, \tag{H.4}$$

which differs from the RIγ scheme [212] of Eq. (5.55); $\mathcal{Z}_V$ and $\mathcal{Z}_A$ are scheme-independent, hence may be computed in any scheme. The chiral limits $\mathcal{Z}_V(\mu^2; a)$ and $\mathcal{Z}_A(\mu^2; a)$ of $\mathcal{Z}_V(\mu^2; a, m_\ell)$ and $\mathcal{Z}_A(\mu^2; a, m_\ell)$ are evaluated by a joint, correlated linear extrapolation of $\{\mathcal{Z}_q^{\mathrm{RI/sMOM}}, \mathcal{Z}_V, \mathcal{Z}_A\}$ in m_ℓ, identical to the procedure used in the $am_\ell \to 0$ extrapolation of $\{\mathcal{Z}_q^{\mathrm{RI}\gamma}/\mathcal{Z}_V, F_{nm}\}$, as described in Section 5.5 of the text (Eqs. (5.50)-(5.57)).

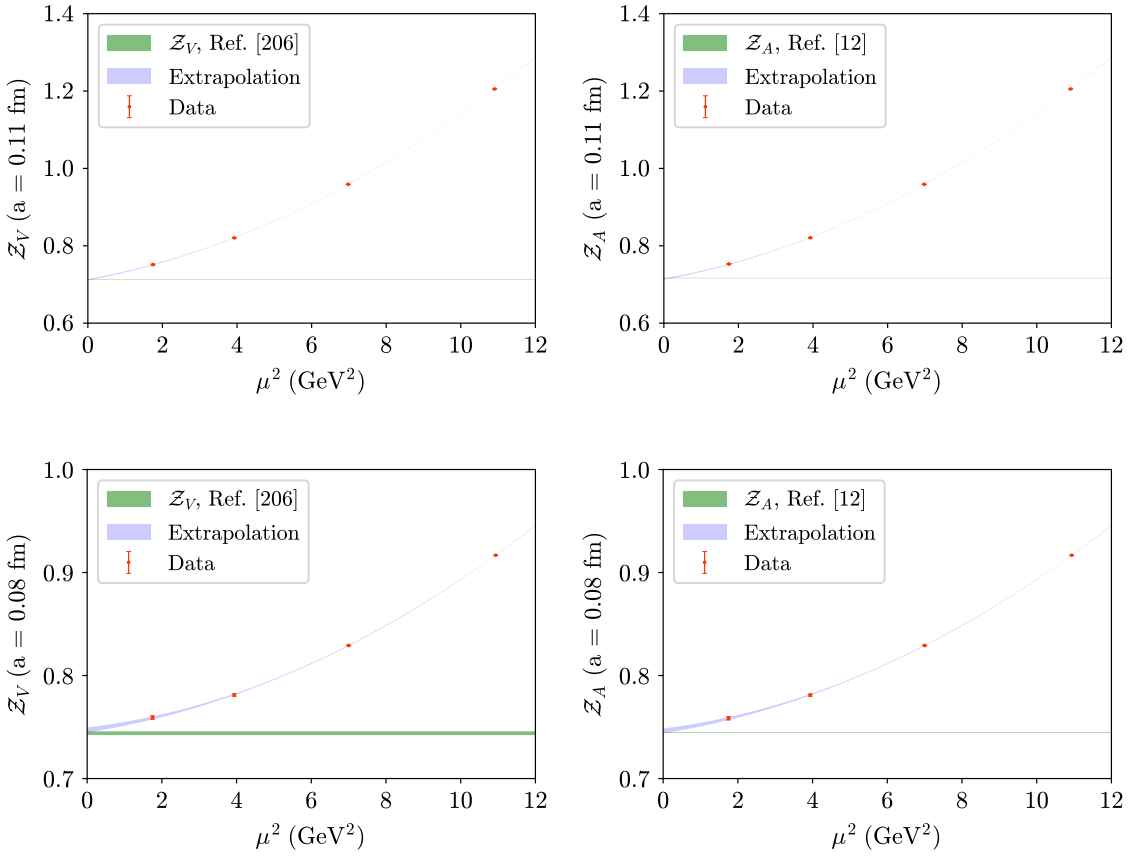

Figure H.1. Vector and axial-vector renormalization coefficients computed by the procedure described in the text, and extrapolated to $\mu^2 = 0$ with the model given in Eq. (H.5). The red data points are the computed data, Eq. (H.3), the blue bands show the extrapolation to $\mu^2 \to 0$, and the green bands denote the chiral limit value of $\mathcal{Z}_A$ and $\mathcal{Z}_V$ computed in Refs. [12, 206].

Although the renormalization coefficients $\mathcal{Z}_V$, $\mathcal{Z}_A$ are scale-independent, the RI procedure introduces scale-dependence from the kinematic setup (Eq. (5.46)). This scale-dependence is removed by fitting $\mathcal{Z}_j(\mu^2; a)$ to a power series in μ^2 and taking the $\mu^2 \to 0$ limit as described in Ref. [1], with fit model:

$$\mathcal{Z}_j(\mu^2; a) = \mathcal{Z}_j(a) + c_j^{(1)}(a)\mu^2 + c_j^{(2)}(a)\mu^4. \tag{H.5}$$

Here $\mathcal{Z}_j(a), c_j^{(1)}(a)$, and $c_j^{(2)}(a)$ are coefficients which are determined by correlated χ^2 minimization. The fits are shown in Fig. (H.1). The fits have χ^2/dof ranging between 0.15 and 0.71. The best-fit value of $\mathcal{Z}_j(a)$ is the value that is taken for the renormalization factor, and it is determined that

$$\begin{aligned} \mathcal{Z}_V(0.11\text{ fm}) &= 0.7119(20) & \mathcal{Z}_V(0.08\text{ fm}) &= 0.7472(24) \\ \mathcal{Z}_A(0.11\text{ fm}) &= 0.7137(19) & \mathcal{Z}_A(0.08\text{ fm}) &= 0.7462(23). \end{aligned} \tag{H.6}$$

The results show that $\mathcal{Z}_V = \mathcal{Z}_A$ within statistical precision as expected. The determination presented in this work is consistent with the determination of $\mathcal{Z}_V$ in Ref. [206] for the $a = 0.08$ fm and $a = 0.11$ fm ensembles, and with $\mathcal{Z}_A$ in Ref. [12] for the $a = 0.08$ fm ensembles, although $\mathcal{Z}_A$ differs from the $a = 0.11$ fm value in that work by about one standard deviation. This deviation may be due to discrepancies in the procedure used to extract $\mathcal{Z}_A$, as the fit model (Eq. (H.5)) does not capture all the discretization artifacts present in the data.

Appendix I

Renormalization coefficient $am_\ell \to 0$ extrapolation

Figures (I.1)-(I.8) display the $am_\ell \to 0$ extrapolations of $\mathcal{Z}_q^{\mathrm{RI}\gamma}/\mathcal{Z}_V$ and F_{nm}, as described in Section 5.5 of the text. Each renormalization coefficient is evaluated at $q = \frac{2\pi}{L}(4,4,0,0)$, which is the lattice momentum corresponding to the scale $\mu = \mu_4$. In each of Figures (I.1)-(I.8), the μ dependence of $(\mathcal{Z}_q^{\mathrm{RI}\gamma}/\mathcal{Z}_V)(\mu^2;a)$ and the q dependence of $F_{nm}(q;a)$ has been suppressed for clarity. The data is observed to have very mild dependence on am_ℓ.

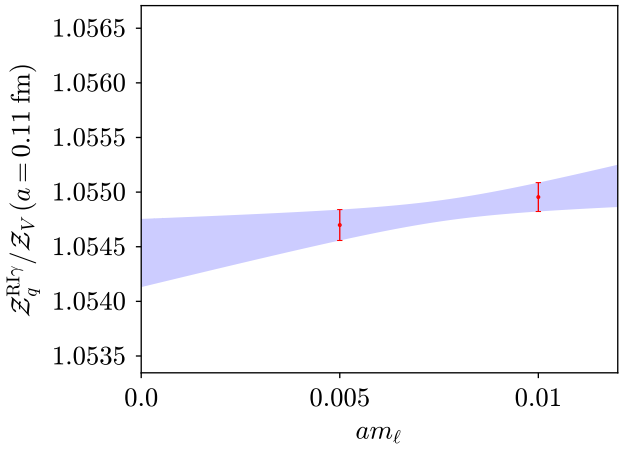

Figure I.1. The $am_\ell \to 0$ extrapolation for the RI quark-field renormalization $\mathcal{Z}_q^{\mathrm{RI}\gamma}/\mathcal{Z}_V$, Eq. (5.55), computed on the $a = 0.11$ fm ensembles at $q = \frac{2\pi}{aL}(4,4,0,0)$ and extrapolated to the chiral limit via a joint correlated linear extrapolation in am_ℓ (Eq. (5.57)). The data is depicted in red, and the shaded band denotes the extrapolation.

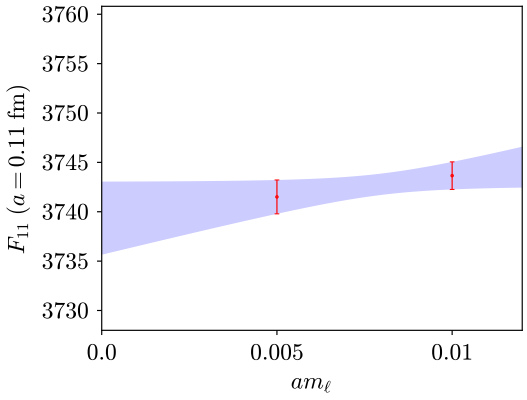

Figure I.2. As in Figure (I.1), $am_\ell \to 0$ extrapolation for F_{nm} on the first irreducible chiral subspace $\{F_{11}\}$, for the $a = 0.11$ fm ensembles.

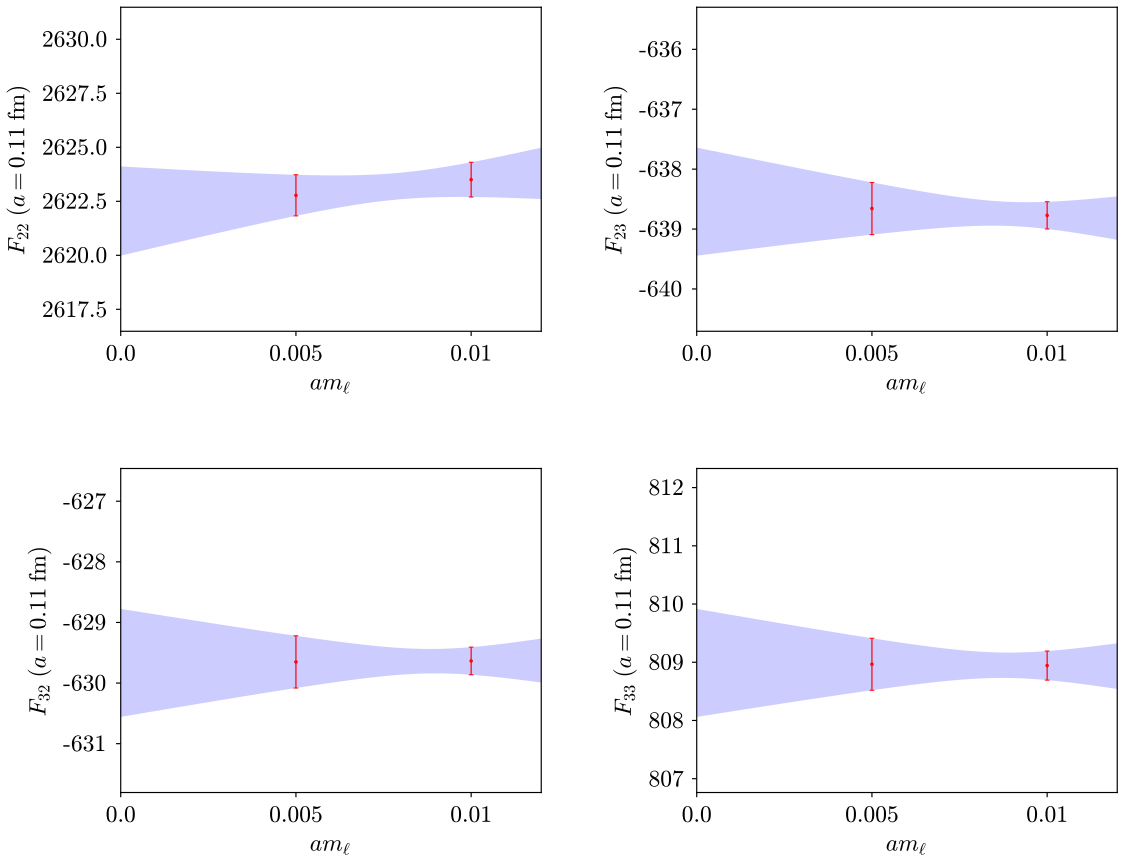

Figure I.3. As in Figure (I.1), $am_\ell \to 0$ extrapolation for F_{nm} on the second irreducible chiral subspace $\{F_{22}, F_{23}, F_{32}, F_{33}\}$, for the $a = 0.11$ fm ensembles.

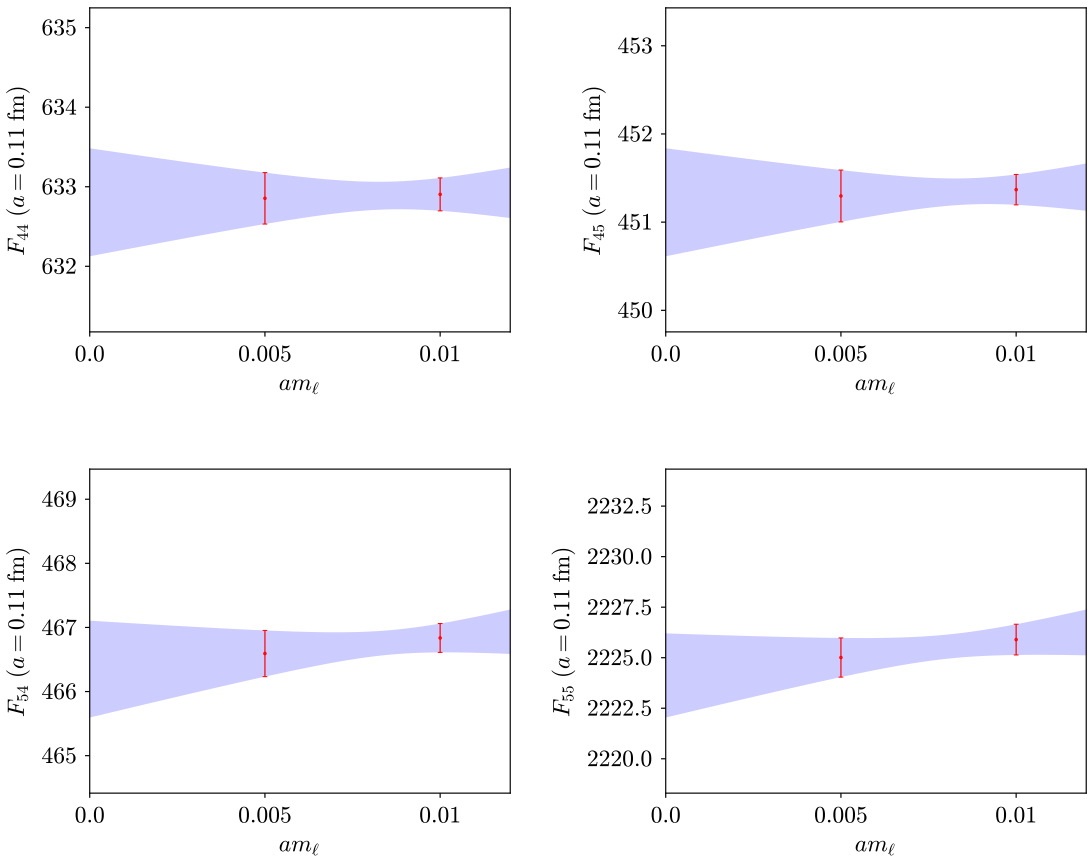

Figure I.4. As in Figure (I.1), $am_\ell \to 0$ extrapolation for F_{nm} on the third irreducible chiral subspace $\{F_{44}, F_{45}, F_{54}, F_{55}\}$, for the $a = 0.11$ fm ensembles.

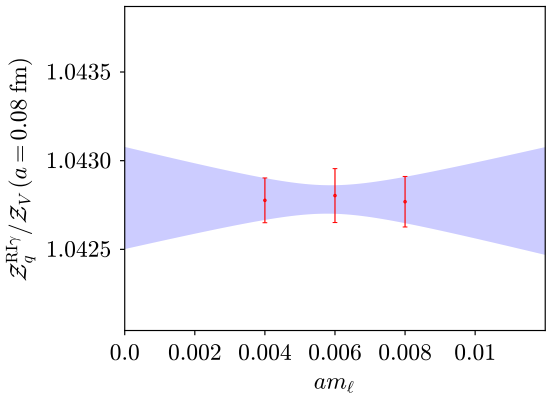

Figure I.5. As in Figure (I.1), $am_\ell \to 0$ extrapolation for $\mathcal{Z}_q^{\mathrm{RI}\gamma}/\mathcal{Z}_V$, for the $a = 0.08$ fm ensembles.

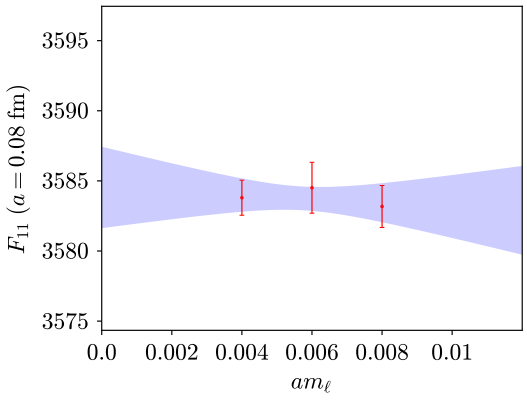

Figure I.6. As in Figure (I.1), $am_\ell \to 0$ extrapolation for F_{nm} on the first irreducible chiral subspace $\{F_{11}\}$, for the $a = 0.08$ fm ensembles.

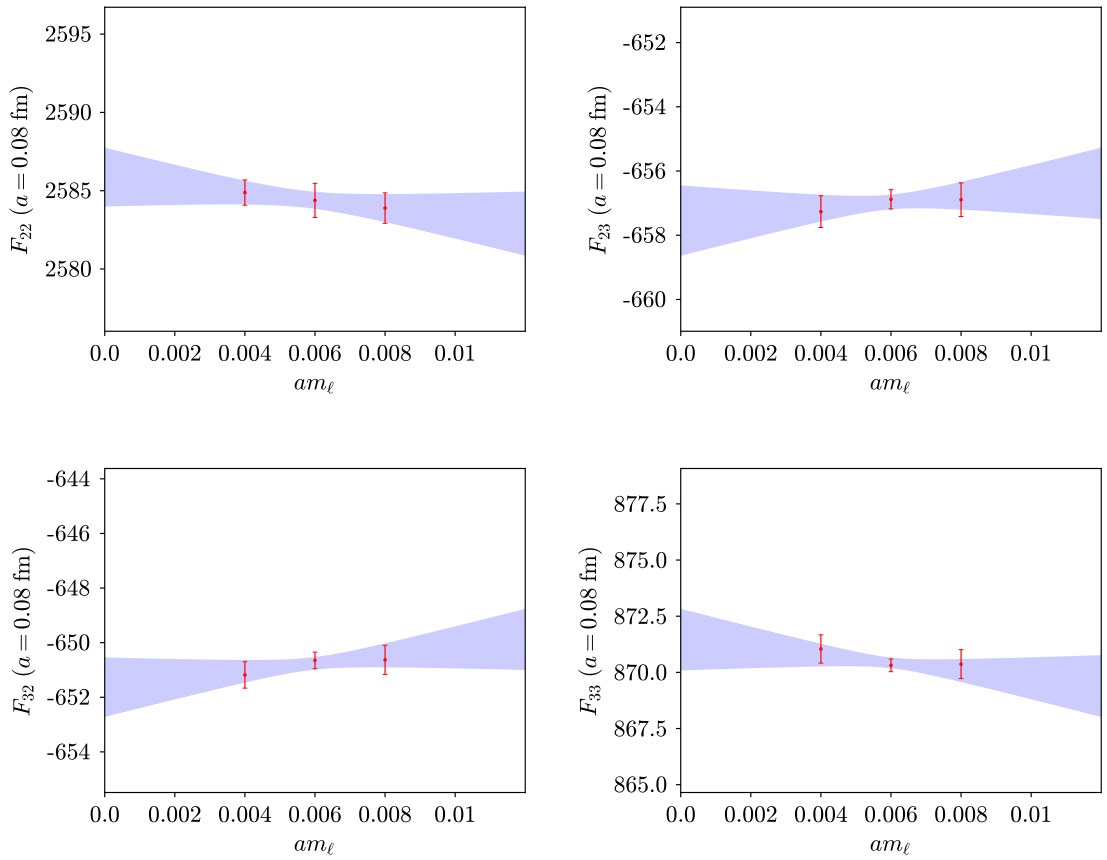

Figure I.7. As in Figure (I.1), $am_\ell \to 0$ extrapolation for F_{nm} on the second irreducible chiral subspace $\{F_{22}, F_{23}, F_{32}, F_{33}\}$, for the $a = 0.08$ fm ensembles.

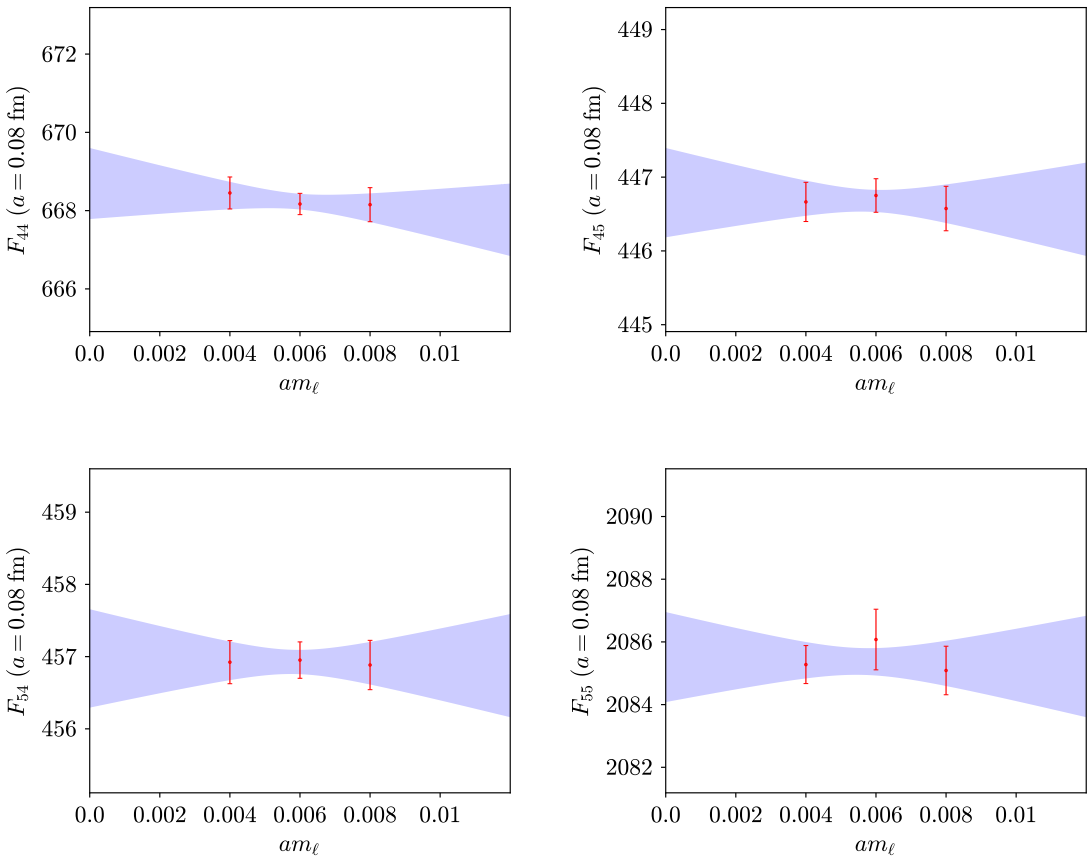

Figure I.8. As in Figure (I.1), $am_\ell \to 0$ extrapolation for F_{nm} on the third irreducible chiral subspace $\{F_{44}, F_{45}, F_{54}, F_{55}\}$, for the $a = 0.08$ fm ensembles.

Appendix J

Spinors in $d = 2$

J.1 Bispinors in $d = 2$

Recall that the Lorentz group in d dimensions is generated by a $d \times d$ antisymmetric tensor $\mathcal{J}^{\mu\nu}$ and parameterized by a $d \times d$ antisymmetric tensor $\omega_{\mu\nu}$. In two dimensions, this reduces to a single generator and parameter,

$$\mathcal{J}^{\mu\nu} = \begin{pmatrix} 0 & J \\ -J & 0 \end{pmatrix} \qquad \omega_{\mu\nu} = \begin{pmatrix} 0 & \theta \\ -\theta & 0 \end{pmatrix} \tag{J.1}$$

In Euclidean space, J is the generator of rotations in $\mathbb{R}^2$, and θ is the rotation angle. A general Lorentz transformation can be expressed as

$$\Lambda(\omega) = \Lambda(\theta) = e^{-\frac{i}{2}\omega_{\mu\nu}\mathcal{J}^{\mu\nu}} = e^{-i\theta J}, \tag{J.2}$$

which is simply rotation in $\mathbb{R}^2$ by the angle θ.

In d dimensions, the (Euclidean space) Dirac γ-matrices satisfy the defining anti-commutation relation[1],

$$\{\gamma^\mu, \gamma^\nu\} = 2\delta^{\mu\nu}. \tag{J.3}$$

A particular basis which satisfies this relation is the Weyl basis,

$$\gamma^1 = \sigma_1 = \begin{pmatrix} 0 & 1 \\ 1 & 0 \end{pmatrix} \quad \gamma^2 = \sigma_3 = \begin{pmatrix} 1 & 0 \\ 0 & -1 \end{pmatrix} \quad \gamma_5 = i\gamma^1\gamma^2 = i \begin{pmatrix} 0 & -1 \\ 1 & 0 \end{pmatrix} = \sigma_2. \tag{J.4}$$

[1]The Minkowski space γ matrices can be found in David Tong's lecture notes [308] and are $\gamma^0 = \sigma_1$, $\gamma^1 = i\sigma^2$, and $\gamma_5 = -\gamma^0\gamma^1 = \sigma_3$

We have the usual identities,

$$\{\gamma^\mu, \gamma^\nu\} = 2\delta^{\mu\nu} \qquad \{\gamma^\mu, \gamma_5\} = 0 \qquad \gamma_\mu^\dagger = \gamma_\mu, \gamma_5^\dagger = \gamma_5. \tag{J.5}$$

Any representation of the Lorentz group is specified by where J is sent to. Recall that in 4 dimensions, the bispinor representation is characterized as

$$S^{d=4}_{\text{bispinor}}(\mathcal{J}^{\mu\nu}) = \frac{1}{2}\sigma^{\mu\nu} \qquad \sigma^{\mu\nu} = \frac{i}{2}[\gamma^\mu, \gamma^\nu]. \tag{J.6}$$

By the analogy to the four-dimensional case, in $d = 2$ the rotation generator J is sent to

$$S^{d=2}_{\text{bispinor}}(J) = S^{d=2}_{\text{bispinor}}(\mathcal{J}^{01}) = \frac{i}{4}[\gamma^0, \gamma^1] = \frac{i}{2}\gamma^0\gamma^1 = \frac{1}{2}\gamma_5. \tag{J.7}$$

Thus, Lorentz transformations with angle θ act on bispinors as

$$\psi \xrightarrow{\theta} e^{i\theta S(J)} = e^{\frac{i}{2}\theta\gamma_5} \doteq \begin{pmatrix} \cos(\theta/2) & \sin(\theta/2) \\ -\sin(\theta/2) & \cos(\theta/2) \end{pmatrix} \tag{J.8}$$

which is simply a rotation matrix with angle θ.

J.2 Majorana Spinors in $d = 2$

The two-component Dirac fermion ψ can be split into two Weyl components, which act as Majorana spinors. In this basis, the two-component Majorana fermion is represented as[2]

$$\psi^a = \begin{pmatrix} \psi_1^a \\ \psi_2^a \end{pmatrix}. \tag{J.9}$$

These are related to the chiral components $\psi_\pm^a$ by the usual projection formulas,

$$P_\pm = \frac{1}{2}(1 \pm \gamma) \qquad \psi_\pm^a = P_\pm \psi^a. \tag{J.10}$$

The other important thing to consider is charge conjugation. Charge conjugation is defined to satisfy the relation,

$$C\gamma_\mu^T C^{-1} = -\gamma_\mu. \tag{J.11}$$

[2]Note that in this basis, the matrix γ is not diagonal. This is the $d = 2$ version of the Dirac basis, while the Weyl basis can be determined by diagonalizing γ, resulting in $\gamma = \sigma_3$. In the Weyl basis the Dirac fermion splits as $\psi^a = \begin{pmatrix} \psi_+^a \\ \psi_-^a \end{pmatrix}$.

The simplest way to satisfy this is by choosing

$$C = \gamma_5 = \sigma_2. \tag{J.12}$$

Note that this also satisfies $C\gamma_5 C = \gamma_5$, since $\gamma_5^2 = 1$. One also has the identity,

$$\overline{\psi} = \psi^\dagger \gamma^0 = \begin{pmatrix} \psi_2 \\ \psi_1 \end{pmatrix} = \psi^T C(i\gamma^2). \tag{J.13}$$

J.3 Dirac Bilinears in $d = 2$

This section closely follows Artur Avkhadiev's notes [**?**]. In $d = 4$, the Dirac algebra $\{\Gamma^{(d=4)}\}$ contains 16 elements. Each of the 16 elements is characterized by its quantum numbers, and has the quantum numbers of either a scalar, pseudoscalar, vector, axial-vector, or tensor (the explicit decomposition is given in Appendix C.2). In $d = 2$, a similar story holds, but the transformation properties of each bilinear are different. In this case, there are four elements of the Dirac algebra, $\{\Gamma\} = \{1, \gamma_5, \gamma_0, \gamma_1\}$. Each element of this algebra is characterized by its transformation properties under parity and charge conjugation,

$$P = \gamma^0 \qquad\qquad C = \gamma_5. \tag{J.14}$$

One determines the quantum numbers P and C of an element of the Dirac algebra by transforming the corresponding Dirac bilinear $\overline{\psi}\Gamma\psi$ with the transformation, and noting the incurred sign. The quantum numbers for each bilinear are found in Table J.1. Note that in $d = 2$, angular momentum $J = 0$, and there are no vector, axial-vector, or tensor states: the only two states are scalar ($PC = ++$) and pseudoscalar ($PC = --$). Interestingly enough, the different components of γ^μ excite different states: γ^0 maps to the pseudoscalar, and γ^1 maps to the scalar.

Γ	1	γ_5	γ^0	γ^1
PC	$++$	$--$	$--$	$++$

Table J.1. Transformation properties for the Dirac algebra in $d = 2$.

Appendix K

Computation of the QCD_2 Driving Forces

K.1 The Gauge Force

This section computes the gauge derivative $\frac{\delta S_g[\omega]}{\delta \omega_\mu^a(n)}$ (Eq. (6.56)), where $S_g[U]$ is the Wilson gauge action (Eq. (3.13)),

$$S_g = \beta \sum_{x\in\Lambda} \left(1 - \frac{1}{N}\mathrm{Re}\,\mathrm{Tr}\,P(x)\right) = \beta|\Lambda| - \frac{\beta}{2N}\sum_{x\in\Lambda}\mathrm{Tr}\left[P(x) + P^\dagger(x)\right] \tag{K.1}$$

where the plaquette $P(x) = P_{01}(x) = U_0(x)U_1(x+\hat{0})U_0^\dagger(x+\hat{1})U_1^\dagger(x)$ (Eq. (3.11)) only has one independent ordering, which is in the $(0,1)$ plane. The derivative of this is the staple in the corresponding direction of differentiation:

$$\begin{aligned}
(F_g)_\mu^a(n)[\omega] = \frac{\partial S_g}{\partial \omega_\mu^a(n)} &= -\frac{\beta}{2N}\frac{\partial}{\partial \omega_\mu^a(n)}\sum_{x\in\Lambda}\mathrm{Tr}\left[P(x) + P(x)^\dagger\right] \\
&= -\frac{\beta}{2N}\frac{\partial}{\partial \omega_\mu^a(n)}\sum_{x\in\Lambda}\mathrm{Tr}\left[U_\rho(x)A_\rho(x) + A_\rho^\dagger(x)U_\rho^\dagger(x)\right] \\
&= -\frac{\beta}{2N}\mathrm{Tr}\left[(it^a)U_\mu(n)A_\mu(n) + A_\mu^\dagger(n)U_\mu^\dagger(n)(-it^a)\right] \\
&= -\frac{i\beta}{2N}\mathrm{Tr}\left[t^a U_\mu(n)A_\mu(n) - A_\mu^\dagger(n)U_\mu^\dagger(n)t^a\right]
\end{aligned} \tag{K.2}$$

where here $A_\mu(n)$ is the staple formed from removing the link $U_\mu(n)$ from the sum on plaquettes $\sum_{x\in\Lambda} P(x)$, which is given by Eq. 4.20 in Ref. [78],

$$\begin{aligned} A_\mu(n) &= [U_\nu(n+\hat{\mu})U_{-\mu}(n+\hat{\mu}+\hat{\nu})U_{-\nu}(n+\hat{\nu}) + U_{-\nu}(n+\hat{\mu})U_{-\mu}(n+\hat{\mu}-\hat{\nu})U_\nu(n-\hat{\nu})]\Big|_{\nu\neq\mu} \\ &= \left[U_\nu(n+\hat{\mu})U_\mu^\dagger(n+\hat{\nu})U_\nu^\dagger(n) + U_\nu^\dagger(n+\hat{\mu}-\hat{\nu})U_\mu^\dagger(n-\hat{\nu})U_\nu(n-\hat{\nu})\right]\Big|_{\nu\neq\mu}. \end{aligned} \tag{K.3}$$

It is useful to re-express Eq. (K.2) in the algebra $\mathfrak{su}(N)$ using the following trick. Let $c^a t^a \in \mathfrak{su}(N)$, where c^a are coefficients given by $c^a = \mathrm{Tr}[t^a\zeta]$ and $\zeta \in \mathfrak{su}(N)$ is some other element of the algebra. Expanding $\zeta = \zeta^b t^b$, one obtains:

$$c^a t^a = \mathrm{Tr}[t^a\zeta]t^a = \mathrm{Tr}[\zeta^b t^a t^b]t^a = \left(\frac{1}{2}\zeta^b\delta^{ab}\right)t^a = \frac{1}{2}\zeta. \tag{K.4}$$

This implies that the coefficients c^a can be brought back to the algebra after the trace, as this simply induces a factor of $\frac{1}{2}$. Cycling the t^a factors to the front of Eq. (K.2) reveals the expression for the algebra-valued force,

$$(F_g)_\mu(n)[\omega] = (F_g)^a_\mu(n)[\omega]t^a = -\frac{i\beta}{4N}\left(U_\mu(n)A_\mu(n) - A^\dagger_\mu(n)U^\dagger_\mu(n)\right). \tag{K.5}$$

K.2 The Pseudofermion Force

The pseudofermion force is significantly more complicated to compute than the gauge force. Recall the pseudofermion force is,

$$(F_{\mathrm{pf}})^a_\mu(n) = \Phi^\dagger \frac{\delta K[\omega]^{-1/4}}{\delta\omega^a_\mu(n)}\Phi, \tag{K.6}$$

which after applying the rational approximation (Eq. (6.46)), becomes

$$K^{-1/4}[\omega]\Phi \approx r^{(-1/4)}(K[\omega])\Phi = \alpha_0^{(-1/4)}\Phi + \sum_{i=1}^{P}\alpha_i^{(-1/4)}(K+\beta_i^{(-1/4)})^{-1}\Phi. \tag{K.7}$$

For a Lie derivative,

$$\frac{\partial}{\partial\omega}A^{-1} = -A^{-1}\frac{\partial A}{\partial\omega}A^{-1}, \tag{K.8}$$

which implies that

$$\begin{aligned}\frac{\partial}{\partial\omega_\mu^a(n)}K^{-1/4}\Phi &= \frac{\partial}{\partial\omega_\mu^a(n)}\left(\alpha_0^{(-1/4)}\Phi + \sum_{i=1}^{P}\alpha_i^{(-1/4)}\left(K+\beta_i^{(-1/4)}\right)^{-1}\Phi\right) \\ &= -\sum_{i=1}^{P}\alpha_i^{(-1/4)}\left(K+\beta_i^{(-1/4)}\right)^{-1}\frac{\partial K}{\partial\omega_\mu^a(n)}\left(K+\beta_i^{(-1/4)}\right)^{-1}\Phi.\end{aligned} \tag{K.9}$$

Next $\partial K/\partial\omega$ must be evaluated, which is done by exploiting the hermiticity of Q:

$$\begin{aligned}\frac{\partial K}{\partial\omega_\mu^a(n)} &= \frac{\partial}{\partial\omega_\mu^a(n)}Q^\dagger Q = \frac{\partial Q^\dagger}{\partial\omega_\mu^a(n)}Q + Q^\dagger\frac{\partial Q}{\partial\omega_\mu^a(n)} \\ &= \frac{\partial Q}{\partial\omega_\mu^a(n)}Q + Q^\dagger\frac{\partial Q^\dagger}{\partial\omega_\mu^a(n)} \\ &= 2\mathrm{Re}\left[Q\frac{\partial Q}{\partial\omega_\mu^a(n)}\right].\end{aligned} \tag{K.10}$$

Putting this together shows that,

$$\begin{aligned}(F_{\mathrm{pf}})_\mu^a(n) &= -2\sum_{i=1}^{P}\alpha_i^{(-1/4)}\mathrm{Re}\left[\psi_i^\dagger Q[\omega]\frac{\partial Q[\omega]}{\partial\omega_\mu^a(n)}\psi_i\right] \\ &= -2\sum_{i=1}^{P}\alpha_i^{(-1/4)}\mathrm{Re}\left[(Q[\omega]\psi_i)^\dagger\frac{\partial Q[\omega]}{\partial\omega_\mu^a(n)}\psi_i\right] \\ &= -2\sum_{i=1}^{P}\alpha_i^{(-1/4)}\mathrm{Re}\left[(\mathcal{D}[\omega]\psi_i)^\dagger\frac{\partial\mathcal{D}[\omega]}{\partial\omega_\mu^a(n)}\psi_i\right]\end{aligned} \tag{K.11}$$

where (note that $(K+\beta_i^{(-1/4)})^{-1}$ is Hermitian),

$$\psi_i = \left(K+\beta_i^{(-1/4)}\right)^{-1}\Phi. \tag{K.12}$$

The variables ψ_i may be computed with a conjugate gradient (CG) solver [**?**].

The remaining piece to compute is $\partial\mathcal{D}[\omega]/\partial\omega_\mu^a(n)$. Note that,

$$\begin{aligned}\frac{\partial}{\partial\omega_\mu^a(n)}V_\nu^{bc}(x) &= 2\frac{\partial}{\partial\omega_\mu^a(n)}\mathrm{Tr}\left(U_\nu^\dagger(x)t^bU_\nu(x)t^c\right) \\ &= 2i\delta_{nx}\delta_{\mu\nu}\mathrm{Tr}\left(-t^aU_\nu^\dagger(x)t^bU_\nu(x)t^c + U_\nu^\dagger(x)t^bt^aU_\nu(x)t^c\right) \\ \frac{\partial}{\partial\omega_\mu^a(n)}(V_\nu^{bc})^T(y) &= 2i\delta_{ny}\delta_{\mu\nu}\mathrm{Tr}\left(-t^aU_\nu^\dagger(y)t^cU_\nu(y)t^b + U_\nu^\dagger(y)t^ct^aU_\nu(y)t^b\right).\end{aligned} \tag{K.13}$$

Applying these identities to the Wilson-Dirac operator $\mathcal{D}_W[\omega]$ (Eq. (6.21)) yields,

$$\begin{aligned}\frac{\partial}{\partial\omega_\mu^a(n)}\mathcal{D}^{bc}_{\beta\gamma}(x,y) &= -\kappa\sum_{\nu=1}^{2}\frac{\partial}{\partial\omega_\mu^a(n)}\left[V_\nu^{bc}(x)(1-\gamma_\nu)_{\beta\gamma}\delta_{x+\hat{\nu},y} + (V_\nu^T)^{bc}(y)(1+\gamma_\nu)_{\beta\gamma}\delta_{x-\hat{\nu},y}\right] \\ &= 2i\kappa\Big[\delta_{nx}\mathrm{Tr}\left(t^c t^a U_\mu^\dagger(x) t^b U_\mu(x) - t^b t^a U_\mu(x) t^c U_\mu^\dagger(x)\right)(1-\gamma_\mu)_{\beta\gamma}\delta_{x+\hat{\mu},y} \\ &\qquad + \delta_{ny}\mathrm{Tr}\left(t^b t^a U_\mu^\dagger(y) t^c U_\mu(y) - t^c t^a U_\mu(y) t^b U_\mu^\dagger(y)\right)(1+\gamma_\mu)_{\beta\gamma}\delta_{x-\hat{\mu},y}\Big]\end{aligned} \tag{K.14}$$

Upon acting this expression on ψ_i, one obtains,

$$\begin{aligned}\left(\frac{\partial\mathcal{D}_W}{\partial\omega_\mu^a(n)}\psi_i\right)^b_\beta(x) &= \sum_y\frac{\partial}{\partial\omega_\mu^a(n)}(D_W)^{bc}_{\beta\gamma}(x,y)\psi^c_\gamma(y) \\ &= 2i\kappa\Big[\delta_{nx}\mathrm{Tr}\left(t^a\left(U_\mu^\dagger(n)t^b U_\mu(n)t^c - U_\mu(n)t^c U_\mu^\dagger(n)t^b\right)\right)(1-\gamma_\mu)_{\beta\gamma}\psi^c_\gamma(n+\hat{\mu}) \\ &\qquad + \delta_{n+\hat{\mu},x}\mathrm{Tr}\left(t^a\left(U_\mu^\dagger(n)t^c U_\mu(n)t^b - U_\mu(n)t^b U_\mu^\dagger(n)t^c\right)\right)(1+\gamma_\mu)_{\beta\gamma}\psi^c_\gamma(n)\Big]\end{aligned} \tag{K.15}$$

This equation is simplified using the tensor,

$$\mathcal{W}_\mu^{ab} \equiv U_\mu^\dagger(n)t^a U_\mu(n)t^b - U_\mu(n)t^b U_\mu^\dagger(n)t^a \qquad \mathrm{Tr}\,\mathcal{W}_\mu^{ab} = \frac{1}{2}(V_\mu^{ab} - V_\mu^{ab}) = 0. \tag{K.16}$$

Note that $\mathcal{W}_\mu^{ab}$ also has fundamental color indices, $(\mathcal{W}_\mu^{ab})_{ij}(n)$. This definition simplifies the expression for $\partial\mathcal{D}_W/\partial\omega$ after acting on ψ_i,

$$\begin{aligned}\left(\frac{\partial\mathcal{D}_W}{\partial\omega_\mu^a(n)}\psi_i\right)^b_\beta(x) = 2i\kappa\Big[&\delta_{nx}\mathrm{Tr}\left(t^a\mathcal{W}_\mu^{bc}(n)\right)(1-\gamma_\mu)_{\beta\gamma}\psi^c_\gamma(n+\hat{\mu}) \\ &+ \delta_{n+\hat{\mu},x}\mathrm{Tr}\left(t^a\mathcal{W}_\mu^{cb}(n)\right)(1+\gamma_\mu)_{\beta\gamma}\psi^c_\gamma(n)\Big].\end{aligned} \tag{K.17}$$

The best way to compute this is thus to precompute the traceless quantity $\mathcal{W}_\mu$, then form the appropriate tensor contractions. The result in Eq. (K.17) has been confirmed numerically with the autodifferentiation library JAX in Python.

This section concludes with a bit of bookkeeping, combining the previous results

and making indices explicit:

$$\begin{aligned}(F_{\mathrm{pf}})^a_\mu(n) &= -2\sum_{i=1}^{P}\alpha_i^{(-1/4)}\mathrm{Re}\left[(\mathcal{D}[\omega]\psi_i)^\dagger\frac{\partial\mathcal{D}[\omega]}{\partial\omega^a_\mu(n)}\psi_i\right]\\ &= -2\sum_{i=1}^{P}\alpha_i^{(-1/4)}\sum_x\mathrm{Re}\left[\left((\mathcal{D}[\omega]\psi_i)^\dagger\right)^b_\beta(x)\left(\frac{\partial\mathcal{D}[\omega]}{\partial\omega^a_\mu(n)}\psi_i\right)^b_\beta(x)\right]\\ &= -4iK\sum_{i=1}^{P}\alpha_i^{(-1/4)}\sum_x\mathrm{Re}\Big[\left((\mathcal{D}[\omega]\psi_i)^\dagger\right)^b_\beta(x)\Big[\delta_{nx}\mathrm{Tr}\left(t^a\mathcal{W}^{bc}_\mu(n)\right)(1-\gamma_\mu)_{\beta\gamma}\psi^c_\gamma(n+\hat\mu)\\ &\qquad\qquad +\delta_{n+\hat\mu,x}\mathrm{Tr}\left(t^a\mathcal{W}^{cb}_\mu(n)\right)(1+\gamma_\mu)_{\beta\gamma}\psi^c_\gamma(n)\Big]\Big].\end{aligned}\tag{K.18}$$

Simplifying the sum yields the following result for the pseudofermion force:

$$\begin{aligned}(F_{\mathrm{pf}})^a_\mu(n) = -4i\kappa\sum_{i=1}^{P}\alpha_i^{(-1/4)}\mathrm{Re}\Big[&\left((\mathcal{D}\psi_i)^\dagger\right)^b(n)\,\mathrm{Tr}\left(t^a\mathcal{W}^{bc}_\mu(n)\right)(1-\gamma_\mu)\psi^c(n+\hat\mu)\\ &+\left((\mathcal{D}\psi_i)^\dagger\right)^b(n+\hat\mu)\,\mathrm{Tr}\left(t^a\mathcal{W}^{cb}_\mu(n)\right)(1+\gamma_\mu)\psi^c(n)\Big].\end{aligned}\tag{K.19}$$

Bibliography

[1] William Detmold, Marc Illa, David J. Murphy, Patrick Oare, Kostas Orginos, Phiala E. Shanahan, Michael L. Wagman, and Frank Winter. Lattice qcd constraints on the parton distribution functions of ^{3}He. *Phys. Rev. Lett.*, 126:202001, May 2021. doi: 10.1103/PhysRevLett.126.202001. URL `https://link.aps.org/doi/10.1103/PhysRevLett.126.202001`.

[2] W. Detmold, W. I. Jay, D. J. Murphy, P. R. Oare, and P. E. Shanahan. Neutrinoless double beta decay from lattice qcd: The short-distance $\pi^- \to \pi^+ e^- e^-$ amplitude. *Phys. Rev. D*, 107:094501, May 2023. doi: 10.1103/PhysRevD.107.094501. URL `https://link.aps.org/doi/10.1103/PhysRevD.107.094501`.

[3] Thomas Bergamaschi, William I. Jay, and Patrick R. Oare. Hadronic structure, conformal maps, and analytic continuation. *Phys. Rev. D*, 108(7):074516, 2023. doi: 10.1103/PhysRevD.108.074516.

[4] Daniel C. Hackett, Patrick R. Oare, Dimitra A. Pefkou, and Phiala E. Shanahan. Gravitational form factors of the pion from lattice QCD. *Phys. Rev. D*, 108(11):114504, 2023. doi: 10.1103/PhysRevD.108.114504.

[5] Zohreh Davoudi, William Detmold, Zhenghao Fu, Anthony V. Grebe, William Jay, David Murphy, Patrick Oare, Phiala E. Shanahan, and Michael L. Wagman. Long-distance nuclear matrix elements for neutrinoless double-beta decay from lattice qcd. *Phys. Rev. D*, 109:114514, Jun 2024. doi: 10.1103/PhysRevD.109.114514. URL `https://link.aps.org/doi/10.1103/PhysRevD.109.114514`.

[6] Kenneth G. Wilson. The Origins of lattice gauge theory. *Nucl. Phys. B Proc. Suppl.*, 140:3–19, 2005. doi: 10.1016/j.nuclphysbps.2004.11.271.

[7] Michael Creutz. Lattice gauge theory: A Retrospective. *Nucl. Phys. B Proc. Suppl.*, 94:219–226, 2001. doi: 10.1016/S0920-5632(01)00958-6.

[8] Daniel Göschl, Christof Gattringer, Alexander Lehmann, and Christoph Weis. Simulation strategies for the massless lattice Schwinger model in the dual formulation. *Nucl. Phys. B*, 924:63–85, 2017. doi: 10.1016/j.nuclphysb.2017.09.006.

[9] Georg Bergner and Simon Catterall. Supersymmetry on the lattice. *Int. J. Mod. Phys. A*, 31(22):1643005, 2016. doi: 10.1142/S0217751X16430053.

[10] Joel Giedt, Anthony W. Thomas, and Ross D. Young. Dark matter, the CMSSM and lattice QCD. *Phys. Rev. Lett.*, 103:201802, 2009. doi: 10.1103/PhysRevLett.103.201802.

[11] Jiani Fei, Chia-Nan Yeh, and Emanuel Gull. Nevanlinna analytical continuation. *Physical Review Letters*, 126(5):056402, 2021.

[12] W. Detmold and D. J. Murphy. Neutrinoless Double Beta Decay from Lattice QCD: The Long-Distance $\pi^- \to \pi^+ e^- e^-$ Amplitude. 4 2020.

[13] G. Arnison, A. Astbury, B. Aubert, et al. Experimental observation of isolated large transverse energy electrons with associated missing energy at $\sqrt{s} = 540$ gev. *Physics Letters B*, 122(1):103–116, 1983. ISSN 0370-2693. doi: https://doi.org/10.1016/0370-2693(83)91177-2. URL `https://www.sciencedirect.com/science/article/pii/0370269383911772`.

[14] G. Arnison et al. Experimental Observation of Lepton Pairs of Invariant Mass Around 95-GeV/c^2 at the CERN SPS Collider. *Phys. Lett. B*, 126:398–410, 1983. doi: 10.1016/0370-2693(83)90188-0.

[15] S. Abachi et al. Observation of the top quark. *Phys. Rev. Lett.*, 74:2632–2637, 1995. doi: 10.1103/PhysRevLett.74.2632.

[16] Y. Fukuda et al. Evidence for oscillation of atmospheric neutrinos. *Phys. Rev. Lett.*, 81:1562–1567, Aug 1998. doi: 10.1103/PhysRevLett.81.1562. URL `https://link.aps.org/doi/10.1103/PhysRevLett.81.1562`.

[17] A. Arbey and F. Mahmoudi. Dark matter and the early Universe: a review. *Prog. Part. Nucl. Phys.*, 119:103865, 2021. doi: 10.1016/j.ppnp.2021.103865.

[18] A. D. Sakharov. Violation of CP Invariance, C asymmetry, and baryon asymmetry of the universe. *Pisma Zh. Eksp. Teor. Fiz.*, 5:32–35, 1967. doi: 10.1070/PU1991v034n05ABEH002497.

[19] Peter W. Higgs. Broken symmetries and the masses of gauge bosons. *Phys. Rev. Lett.*, 13:508–509, Oct 1964. doi: 10.1103/PhysRevLett.13.508. URL https://link.aps.org/doi/10.1103/PhysRevLett.13.508.

[20] Georges Aad et al. Observation of a new particle in the search for the Standard Model Higgs boson with the ATLAS detector at the LHC. *Phys. Lett. B*, 716: 1–29, 2012. doi: 10.1016/j.physletb.2012.08.020.

[21] F. Englert and R. Brout. Broken symmetry and the mass of gauge vector mesons. *Phys. Rev. Lett.*, 13:321–323, Aug 1964. doi: 10.1103/PhysRevLett.13.321. URL https://link.aps.org/doi/10.1103/PhysRevLett.13.321.

[22] R. Brout and F. Englert. Spontaneous symmetry breaking in gauge theories: A Historical survey. In *1997 Europhysics Conference on High Energy Physics*, pages 3–10, 2 1998.

[23] Sheldon L. Glashow. Partial-symmetries of weak interactions. *Nuclear Physics*, 22(4):579–588, 1961. ISSN 0029-5582. doi: https://doi.org/10.1016/0029-5582(61)90469-2. URL https://www.sciencedirect.com/science/article/pii/0029558261904692.

[24] K.S. Kumar, Sonny Mantry, W.J. Marciano, and P.A. Souder. Low-energy measurements of the weak mixing angle. *Annual Review of Nuclear and Particle Science*, 63(1):237–267, 2013. doi: 10.1146/annurev-nucl-102212-170556. URL https://doi.org/10.1146/annurev-nucl-102212-170556.

[25] Y. Fukuda et al. Measurements of the solar neutrino flux from super-kamiokande's first 300 days. *Phys. Rev. Lett.*, 81:1158–1162, Aug 1998. doi: 10.1103/PhysRevLett.81.1158. URL https://link.aps.org/doi/10.1103/PhysRevLett.81.1158.

[26] P. A. Zyla et al. Review of Particle Physics. *PTEP*, 2020(8):083C01, 2020. doi: 10.1093/ptep/ptaa104.

[27] Nicola Cabibbo. Unitary symmetry and leptonic decays. *Phys. Rev. Lett.*, 10: 531–533, Jun 1963. doi: 10.1103/PhysRevLett.10.531. URL https://link.aps.org/doi/10.1103/PhysRevLett.10.531.

[28] Makoto Kobayashi and Toshihide Maskawa. CP-Violation in the Renormalizable Theory of Weak Interaction. *Progress of Theoretical Physics*, 49(2):

652–657, 02 1973. ISSN 0033-068X. doi: 10.1143/PTP.49.652. URL https://doi.org/10.1143/PTP.49.652.

[29] C.P. Burgess and G.D. Moore. *The Standard Model: A Primer*. Cambridge University Press, 2006. ISBN 9780511256523. URL https://books.google.com/books?id=o32xAQAACAAJ.

[30] H.B. Nielsen and Masao Ninomiya. The adler-bell-jackiw anomaly and weyl fermions in a crystal. *Physics Letters B*, 130(6):389–396, 1983. ISSN 0370-2693. doi: https://doi.org/10.1016/0370-2693(83)91529-0. URL https://www.sciencedirect.com/science/article/pii/0370269383915290.

[31] R. P. Feynman. Space - time approach to quantum electrodynamics. *Phys. Rev.*, 76:769–789, 1949. doi: 10.1103/PhysRev.76.769.

[32] Julian Schwinger. Quantum electrodynamics. i. a covariant formulation. *Phys. Rev.*, 74:1439–1461, Nov 1948. doi: 10.1103/PhysRev.74.1439. URL https://link.aps.org/doi/10.1103/PhysRev.74.1439.

[33] S. Tomonaga. On a relativistically invariant formulation of the quantum theory of wave fields. *Prog. Theor. Phys.*, 1:27–42, 1946. doi: 10.1143/PTP.1.27.

[34] E. Fermi. An attempt of a theory of beta radiation. 1. *Z. Phys.*, 88:161–177, 1934. doi: 10.1007/BF01351864.

[35] H. David Politzer. Reliable perturbative results for strong interactions? *Phys. Rev. Lett.*, 30:1346–1349, Jun 1973. doi: 10.1103/PhysRevLett.30.1346. URL https://link.aps.org/doi/10.1103/PhysRevLett.30.1346.

[36] Abdus Salam. Weak and Electromagnetic Interactions. *Conf. Proc. C*, 680519: 367–377, 1968. doi: 10.1142/9789812795915_0034.

[37] P. W. Anderson. Plasmons, gauge invariance, and mass. *Phys. Rev.*, 130:439–442, Apr 1963. doi: 10.1103/PhysRev.130.439. URL https://link.aps.org/doi/10.1103/PhysRev.130.439.

[38] G. S. Guralnik, C. R. Hagen, and T. W. B. Kibble. Global conservation laws and massless particles. *Phys. Rev. Lett.*, 13:585–587, Nov 1964. doi: 10.1103/PhysRevLett.13.585. URL https://link.aps.org/doi/10.1103/PhysRevLett.13.585.

[39] M. Banner et al. Observation of Single Isolated Electrons of High Transverse Momentum in Events with Missing Transverse Energy at the CERN anti-p p Collider. *Phys. Lett. B*, 122:476–485, 1983. doi: 10.1016/0370-2693(83)91605-2.

[40] David J. Gross and Frank Wilczek. Ultraviolet behavior of non-abelian gauge theories. *Phys. Rev. Lett.*, 30:1343–1346, Jun 1973. doi: 10.1103/PhysRevLett.30.1343. URL `https://link.aps.org/doi/10.1103/PhysRevLett.30.1343`.

[41] David J. Gross and Frank Wilczek. Asymptotically free gauge theories. i. *Phys. Rev. D*, 8:3633–3652, Nov 1973. doi: 10.1103/PhysRevD.8.3633. URL `https://link.aps.org/doi/10.1103/PhysRevD.8.3633`.

[42] T. Blum et al. Working Group Report: Lattice Field Theory. In *Snowmass 2013: Snowmass on the Mississippi*, 10 2013.

[43] Roman Pasechnik and Michal Šumbera. Phenomenological Review on Quark–Gluon Plasma: Concepts vs. Observations. *Universe*, 3(1):7, 2017. doi: 10.3390/universe3010007.

[44] S. Aoki, G. Boyd, R. Burkhalter, S. Ejiri, M. Fukugita, S. Hashimoto, Y. Iwasaki, K. Kanaya, T. Kaneko, Y. Kuramashi, K. Nagai, M. Okawa, H.P. Shanahan, A. Ukawa, and T. YoshiÃľ. The static quark potential in full qcd. *Nuclear Physics B - Proceedings Supplements*, 73(1):216–218, 1999. ISSN 0920-5632. doi: https://doi.org/10.1016/S0920-5632(99)85027-0. URL `https://www.sciencedirect.com/science/article/pii/S0920563299850270`.

[45] K. Schilling and G. S. Bali. The Static quark - anti-quark potential: A 'Classical' experiment on the connection machine CM-2. *Int. J. Mod. Phys. C*, 4:1167–1177, 1993. doi: 10.1142/S0129183193000926.

[46] Robert Feger, Thomas W. Kephart, and Robert J. Saskowski. LieART 2.0 – A Mathematica application for Lie Algebras and Representation Theory. *Comput. Phys. Commun.*, 257:107490, 2020. doi: 10.1016/j.cpc.2020.107490.

[47] Bastian B. Brandt and Marco Meineri. Effective string description of confining flux tubes. *Int. J. Mod. Phys. A*, 31(22):1643001, 2016. doi: 10.1142/S0217751X16430016.

[48] Michele Caselle. Effective String Description of the Confining Flux Tube at Finite Temperature. *Universe*, 7(6):170, 2021. doi: 10.3390/universe7060170.

[49] N. D. Hari Dass. Strings to Strings: Yang-Mills Flux Tubes, QCD Strings and Effective String Theories. *Lect. Notes Phys.*, 1018:pp., 2023. doi: 10.1007/978-3-031-35358-1.

[50] Sourav Chatterjee. Yang-mills for probabilists, 2018.

[51] Pedro Jimenez-Delgado and Ewald Reya. Delineating parton distributions and the strong coupling. *Phys. Rev. D*, 89(7):074049, 2014. doi: 10.1103/PhysRevD.89.074049.

[52] S. Alekhin, J. Blümlein, S. Moch, and R. Placakyte. Parton distribution functions, α_s, and heavy-quark masses for LHC Run II. *Phys. Rev. D*, 96(1):014011, 2017. doi: 10.1103/PhysRevD.96.014011.

[53] Tie-Jiun Hou et al. New CTEQ global analysis of quantum chromodynamics with high-precision data from the LHC. *Phys. Rev. D*, 103(1):014013, 2021. doi: 10.1103/PhysRevD.103.014013.

[54] T. Cridge, L. A. Harland-Lang, A. D. Martin, and R. S. Thorne. An investigation of the α_S and heavy quark mass dependence in the MSHT20 global PDF analysis. *Eur. Phys. J. C*, 81(8):744, 2021. doi: 10.1140/epjc/s10052-021-09533-7.

[55] Florian Herren and Matthias Steinhauser. Version 3 of RunDec and CRunDec. *Comput. Phys. Commun.*, 224:333–345, 2018. doi: 10.1016/j.cpc.2017.11.014.

[56] Manfred F. Gari and N. G. Stefanis. Determination of the Scale Parameter Λ (QCD) From Elastic Electron Proton Scattering at High Q^2. *Phys. Lett. B*, 187:401–404, 1987. doi: 10.1016/0370-2693(87)91118-X.

[57] S. M. Bilenky. Neutrino in Standard Model and beyond. *Phys. Part. Nucl.*, 46 (4):475–496, 2015. doi: 10.1134/S1063779615040024.

[58] Marco Drewes. The Phenomenology of Right Handed Neutrinos. *Int. J. Mod. Phys. E*, 22:1330019, 2013. doi: 10.1142/S0218301313300191.

[59] Tsutomu Yanagida. Horizontal Symmetry and Masses of Neutrinos. *Progress of Theoretical Physics*, 64(3):1103–1105, 09 1980. ISSN 0033-068X. doi: 10.1143/PTP.64.1103. URL `https://doi.org/10.1143/PTP.64.1103`.

[60] J. W. F. Valle. Neutrino physics overview. *J. Phys. Conf. Ser.*, 53:473–505, 2006. doi: 10.1088/1742-6596/53/1/031.

[61] Zhi-zhong Xing. Naturalness and Testability of TeV Seesaw Mechanisms. *Prog. Theor. Phys. Suppl.*, 180:112–127, 2009. doi: 10.1143/PTPS.180.112.

[62] Masaki J. S. Yang. Conditions of naturalness and fine-tuning for the type-I seesaw mechanism with four-zero texture. *PTEP*, 2022(4):043B05, 2022. doi: 10.1093/ptep/ptac054.

[63] Steven Weinberg. Baryon and Lepton Nonconserving Processes. *Phys. Rev. Lett.*, 43:1566–1570, 1979. doi: 10.1103/PhysRevLett.43.1566.

[64] Armen Tumasyan et al. Probing Heavy Majorana Neutrinos and the Weinberg Operator through Vector Boson Fusion Processes in Proton-Proton Collisions at s=13 TeV. *Phys. Rev. Lett.*, 131(1):011803, 2023. doi: 10.1103/PhysRevLett.131.011803.

[65] B. Pontecorvo. Inverse beta processes and nonconservation of lepton charge. *Zh. Eksp. Teor. Fiz.*, 34:247, 1957.

[66] Ziro Maki, Masami Nakagawa, and Shoichi Sakata. Remarks on the unified model of elementary particles. *Prog. Theor. Phys.*, 28:870–880, 1962. doi: 10.1143/PTP.28.870.

[67] B. Pontecorvo. Neutrino Experiments and the Problem of Conservation of Leptonic Charge. *Zh. Eksp. Teor. Fiz.*, 53:1717–1725, 1967.

[68] G. Bellini, L. Ludhova, G. Ranucci, and F. L. Villante. Neutrino oscillations. *Adv. High Energy Phys.*, 2014:191960, 2014. doi: 10.1155/2014/191960.

[69] S. Bilenky. Neutrino oscillations: From a historical perspective to the present status. *Nuclear Physics B*, 908:2–13, 2016. ISSN 0550-3213. doi: https://doi.org/10.1016/j.nuclphysb.2016.01.025. URL `https://www.sciencedirect.com/science/article/pii/S0550321316000353`. Neutrino Oscillations: Celebrating the Nobel Prize in Physics 2015.

[70] Q. R. Ahmad et al. Direct evidence for neutrino flavor transformation from neutral current interactions in the Sudbury Neutrino Observatory. *Phys. Rev. Lett.*, 89:011301, 2002. doi: 10.1103/PhysRevLett.89.011301.

[71] Gabriel D. Orebi Gann, Kai Zuber, Daniel Bemmerer, and Aldo Serenelli. The Future of Solar Neutrinos. *Ann. Rev. Nucl. Part. Sci.*, 71:491–528, 2021. doi: 10.1146/annurev-nucl-011921-061243.

[72] T. K. Gaisser and M. Honda. Flux of atmospheric neutrinos. *Ann. Rev. Nucl. Part. Sci.*, 52:153–199, 2002. doi: 10.1146/annurev.nucl.52.050102.090645.

[73] M. C. Gonzalez-Garcia, Michele Maltoni, Jordi Salvado, and Thomas Schwetz. Global fit to three neutrino mixing: critical look at present precision. *JHEP*, 12:123, 2012. doi: 10.1007/JHEP12(2012)123.

[74] X. Qian and P. Vogel. Neutrino Mass Hierarchy. *Prog. Part. Nucl. Phys.*, 83: 1–30, 2015. doi: 10.1016/j.ppnp.2015.05.002.

[75] G. Burgers, F. Karsch, A. Nakamura, and I. O. Stamatescu. QCD ON ANISOTROPIC LATTICES. *Nucl. Phys. B*, 304:587–600, 1988. doi: 10.1016/0550-3213(88)90644-X.

[76] N.H. Christ, R. Friedberg, and T.D. Lee. Gauge theory on a random lattice. *Nuclear Physics B*, 210(3):310–336, 1982. ISSN 0550-3213. doi: https://doi.org/10.1016/0550-3213(82)90123-7. URL `https://www.sciencedirect.com/science/article/pii/0550321382901237`.

[77] Kenneth G. Wilson. Confinement of quarks. *Phys. Rev. D*, 10:2445–2459, Oct 1974. doi: 10.1103/PhysRevD.10.2445. URL `https://link.aps.org/doi/10.1103/PhysRevD.10.2445`.

[78] Christof Gattringer and Christian B. Lang. *Quantum chromodynamics on the lattice*, volume 788. Springer, Berlin, 2010. ISBN 978-3-642-01849-7, 978-3-642-01850-3. doi: 10.1007/978-3-642-01850-3.

[79] H.B. Nielsen and M. Ninomiya. A no-go theorem for regularizing chiral fermions. *Physics Letters B*, 105(2):219–223, 1981. ISSN 0370-2693. doi: https://doi.org/10.1016/0370-2693(81)91026-1. URL `https://www.sciencedirect.com/science/article/pii/0370269381910261`.

[80] David B. Kaplan. A Method for simulating chiral fermions on the lattice. *Phys. Lett. B*, 288:342–347, 1992. doi: 10.1016/0370-2693(92)91112-M.

[81] David B. Kaplan. Chiral Symmetry and Lattice Fermions. In *Les Houches Summer School: Session 93: Modern perspectives in lattice QCD: Quantum field theory and high performance computing*, pages 223–272, 12 2009.

[82] B. Sheikholeslami and R. Wohlert. Improved Continuum Limit Lattice Action for QCD with Wilson Fermions. *Nucl. Phys. B*, 259:572, 1985. doi: 10.1016/0550-3213(85)90002-1.

[83] S. Basak, R. Edwards, R. Fiebig, George Tamminga Fleming, U. M. Heller, C. Morningstar, D. Richards, I. Sato, and Stephen J. Wallace. Baryon operators and spectroscopy in lattice QCD. *Nucl. Phys. B Proc. Suppl.*, 128:186–192, 2004. doi: 10.1016/S0920-5632(03)02476-9.

[84] S. Brooks, A. Gelman, G. Jones, and X.L. Meng. *Handbook of Markov Chain Monte Carlo*. ISSN. CRC Press, 2011. ISBN 9781420079425. URL `https://books.google.ch/books?id=qfRsAIKZ4rIC`.

[85] G. C. Wick. The evaluation of the collision matrix. *Phys. Rev.*, 80:268–272, Oct 1950. doi: 10.1103/PhysRev.80.268. URL `https://link.aps.org/doi/10.1103/PhysRev.80.268`.

[86] Jonathan R Shewchuk. An introduction to the conjugate gradient method without the agonizing pain. Technical report, USA, 1994.

[87] Tomasz Korzec. Introduction to scale setting in qcd, 2020.

[88] Szabolcs Borsányi, Stephan Dürr, Zoltán Fodor, Christian Hoelbling, Sándor D. Katz, Stefan Krieg, Thorsten Kurth, Laurent Lellouch, Thomas Lippert, and Craig McNeile. High-precision scale setting in lattice QCD. *JHEP*, 09:010, 2012. doi: 10.1007/JHEP09(2012)010.

[89] R. Sommer. A New way to set the energy scale in lattice gauge theories and its applications to the static force and α_s in SU(2) Yang-Mills theory. *Nucl. Phys. B*, 411:839–854, 1994. doi: 10.1016/0550-3213(94)90473-1.

[90] Rainer Sommer. Scale setting in lattice QCD. *PoS*, LATTICE2013:015, 2014. doi: 10.22323/1.187.0015.

[91] Martin Lüscher. Properties and uses of the Wilson flow in lattice QCD. *JHEP*, 08:071, 2010. doi: 10.1007/JHEP08(2010)071. [Erratum: JHEP 03, 092 (2014)].

[92] Yuji Ito. Invariant measures for markov processes. *Transactions of the American Mathematical Society*, 110(1):152–184, 1964. ISSN 00029947. URL `http://www.jstor.org/stable/1993641`.

[93] Simon Duane, A.D. Kennedy, Brian J. Pendleton, and Duncan Roweth. Hybrid monte carlo. *Physics Letters B*, 195(2):216–222, 1987. ISSN 0370-2693. doi: https://doi.org/10.1016/0370-2693(87)91197-X. URL `https://www.sciencedirect.com/science/article/pii/037026938791197X`.

[94] Michael Betancourt. A conceptual introduction to hamiltonian monte carlo, 2018.

[95] Larry Wasserman. *All of Statistics A Concise Course in Statistical Inference*. Springer, 2004.

[96] B. Efron. Bootstrap Methods: Another Look at the Jackknife. *The Annals of Statistics*, 7(1):1 – 26, 1979. doi: 10.1214/aos/1176344552. URL `https://doi.org/10.1214/aos/1176344552`.

[97] Rupert G. Miller. The jackknife–a review. *Biometrika*, 61(1):1–15, 1974. ISSN 00063444. URL `http://www.jstor.org/stable/2334280`.

[98] Philip R Bevington and D Keith Robinson. *Data reduction and error analysis for the physical sciences; 3rd ed.* McGraw-Hill, New York, NY, 2003. URL `https://cds.cern.ch/record/1305448`.

[99] C. M. Bouchard, G. Peter Lepage, Christopher Monahan, Heechang Na, and Junko Shigemitsu. $B_s \to k\ell\nu$ form factors from lattice qcd. *Phys. Rev. D*, 90: 054506, Sep 2014. doi: 10.1103/PhysRevD.90.054506. URL `https://link.aps.org/doi/10.1103/PhysRevD.90.054506`.

[100] Peter Lepage and Christoph Gohlke. gplepage/lsqfit: lsqfit version 13.0.1. May 2023. doi: 10.5281/zenodo.7931361.

[101] Rene Andrae, Tim Schulze-Hartung, and Peter Melchior. Dos and don'ts of reduced chi-squared, 2010.

[102] H. Akaike. A new look at the statistical model identification. *IEEE Transactions on Automatic Control*, 19(6):716–723, 1974. doi: 10.1109/TAC.1974.1100705.

[103] T. Aoyama et al. The anomalous magnetic moment of the muon in the Standard Model. *Phys. Rept.*, 887:1–166, 2020. doi: 10.1016/j.physrep.2020.07.006.

[104] David Bernecker and Harvey B. Meyer. Vector Correlators in Lattice QCD: Methods and applications. *Eur. Phys. J. A*, 47:148, 2011. doi: 10.1140/epja/i2011-11148-6.

[105] M. Davier, A. Hoecker, B. Malaescu, and Z. Zhang. A new evaluation of the hadronic vacuum polarisation contributions to the muon anomalous magnetic moment and to $\boldsymbol{\alpha(m_Z^2)}$. *Eur. Phys. J. C*, 80(3):241, 2020. doi: 10.1140/epjc/

s10052-020-7792-2. Published under the terms of the Creative Commons CC-BY license, [Erratum: Eur.Phys.J.C 80, 410 (2020)].

[106] Harvey B. Meyer. Transport Properties of the Quark-Gluon Plasma: A Lattice QCD Perspective. *Eur. Phys. J. A*, 47:86, 2011. doi: 10.1140/epja/i2011-11086-3.

[107] Hiroshi Shinaoka, Junya Otsuki, Masayuki Ohzeki, and Kazuyoshi Yoshimi. Compressing green's function using intermediate representation between imaginary-time and real-frequency domains. *Phys. Rev. B*, 96:035147, Jul 2017. doi: 10.1103/PhysRevB.96.035147. URL `https://link.aps.org/doi/10.1103/PhysRevB.96.035147`.

[108] Junya Otsuki, Masayuki Ohzeki, Hiroshi Shinaoka, and Kazuyoshi Yoshimi. Sparse modeling approach to analytical continuation of imaginary-time quantum monte carlo data. *Phys. Rev. E*, 95:061302, Jun 2017. doi: 10.1103/PhysRevE.95.061302. URL `https://link.aps.org/doi/10.1103/PhysRevE.95.061302`.

[109] Etsuko Itou and Yuki Nagai. Sparse modeling approach to obtaining the shear viscosity from smeared correlation functions. *JHEP*, 07:007, 2020. doi: 10.1007/JHEP07(2020)007.

[110] Junya Otsuki, Masayuki Ohzeki, Hiroshi Shinaoka, and Kazuyoshi Yoshimi. Sparse modeling in quantum many-body problems. *Journal of the Physical Society of Japan*, 89(1):012001, 2020. doi: 10.7566/JPSJ.89.012001. URL `https://doi.org/10.7566/JPSJ.89.012001`.

[111] Jia Li, Markus Wallerberger, Naoya Chikano, Chia-Nan Yeh, Emanuel Gull, and Hiroshi Shinaoka. Sparse sampling approach to efficient ab initio calculations at finite temperature. *Phys. Rev. B*, 101:035144, Jan 2020. doi: 10.1103/PhysRevB.101.035144. URL `https://link.aps.org/doi/10.1103/PhysRevB.101.035144`.

[112] Maxwell T. Hansen, Harvey B. Meyer, and Daniel Robaina. From deep inelastic scattering to heavy-flavor semileptonic decays: Total rates into multihadron final states from lattice QCD. *Phys. Rev. D*, 96(9):094513, 2017. doi: 10.1103/PhysRevD.96.094513.

[113] Martin Hansen, Alessandro Lupo, and Nazario Tantalo. Extraction of spectral densities from lattice correlators. *Phys. Rev. D*, 99(9):094508, 2019. doi: 10.1103/PhysRevD.99.094508.

[114] Fritz Carlson. Sur une classe de séries de taylor. URL `https://api.semanticscholar.org/CorpusID:116984101`.

[115] Steven G. Krantz, editor. *The Green's Function and the Poisson Kernel*, pages 169–183. Birkhäuser Boston, Boston, MA, 2006. ISBN 978-0-8176-4440-6. doi: 10.1007/0-8176-4440-7_8. URL `https://doi.org/10.1007/0-8176-4440-7_8`.

[116] M. J. Lighthill. *An Introduction to Fourier Analysis and Generalised Functions*. Cambridge Monographs on Mechanics. Cambridge University Press, 1958.

[117] Rolf Nevanlinna. Zur Theorie der Meromorphen Funktionen. *Acta Mathematica*, 46(1-2):1 – 99, 1925. doi: 10.1007/BF02543858. URL `https://doi.org/10.1007/BF02543858`.

[118] P. Emig and R. Nevanlinna. *Analytic Functions*. Grundlehren der mathematischen Wissenschaften. Springer Berlin Heidelberg, 2013. ISBN 9783642855900. URL `https://books.google.com/books?id=gYLqCAAAQBAJ`.

[119] Raoul Bott and Loring W. Tu. *Differential forms in algebraic topology*. Springer, 1995.

[120] G. H. Hardy. On two theorems of F. Carlson and S. Wigert. *Acta Mathematica*, 42(none):327 – 339, 1920. doi: 10.1007/BF02404414. URL `https://doi.org/10.1007/BF02404414`.

[121] E. M. Stein. Functions of exponential type. *Annals of Mathematics*, 65(3):582–592, 1957. ISSN 0003486X. URL `http://www.jstor.org/stable/1970066`.

[122] Steven Weinberg. *The Quantum Theory of Fields*. Cambridge University Press, 1995.

[123] L. A. Rubel. Necessary and sufficient conditions for carlson's theorem on entire functions. *Transactions of the American Mathematical Society*, 83(2):417–429, 1956. ISSN 00029947. URL `http://www.jstor.org/stable/1992882`.

[124] Y. Burnier, M. Laine, and L. Mether. A Test on analytic continuation of thermal imaginary-time data. *Eur. Phys. J. C*, 71:1619, 2011. doi: 10.1140/epjc/s10052-011-1619-0.

[125] Gianaurelio Cuniberti, Enrico De Micheli, and Giovanni Alberto Viano. Reconstructing the thermal Green functions at real times from those at imaginary times. *Commun. Math. Phys.*, 216:59–83, 2001. doi: 10.1007/s002200000324.

[126] M Razavy. *An Introduction to Inverse Problems in Physics*. WORLD SCIENTIFIC, 2020. doi: 10.1142/11860. URL `https://www.worldscientific.com/doi/abs/10.1142/11860`.

[127] R. G. Newton. Inverse problems in physics. *SIAM Review*, 12(3):346–356, 1970. ISSN 00361445. URL `http://www.jstor.org/stable/2028553`.

[128] Dhruv V. Patel, Deep Ray, and Assad A. Oberai. Solution of physics-based bayesian inverse problems with deep generative priors. *Computer Methods in Applied Mechanics and Engineering*, 400:115428, October 2022. ISSN 0045-7825. doi: 10.1016/j.cma.2022.115428. URL `http://dx.doi.org/10.1016/j.cma.2022.115428`.

[129] Nick Antipa, Patrick Oare, Emrah Bostan, Ren Ng, and Laura Waller. Video from stills: Lensless imaging with rolling shutter. In *2019 IEEE International Conference on Computational Photography (ICCP)*, pages 1–8, 2019. doi: 10.1109/ICCPHOT.2019.8747341.

[130] Jiani Fei, Chia-Nan Yeh, Dominika Zgid, and Emanuel Gull. Analytical continuation of matrix-valued functions: Carathéodory formalism. *Phys. Rev. B*, 104:165111, Oct 2021. doi: 10.1103/PhysRevB.104.165111. URL `https://link.aps.org/doi/10.1103/PhysRevB.104.165111`.

[131] R. Nevanlinna. Über beschränkte Funktionen die in gegebenen punkten vorgeschriebene Werte annehmen. *Ann. Acad. Sci. Fenn. Ser. A*, 13(1), 1919.

[132] R. Nevanlinna. Über beschränkte analytische Funktionen. *Ann. Acad. Sci. Fenn. Ser. A*, 32(7), 1929.

[133] G. Pick. Über die Beschränkungen analytischer Funktionen, welche durch vorgegebene Funktionswerte bewirkt werden. *Math. Ann.*, 77:7–23, 1915. doi: 10.1007/BF01456817.

[134] A. Nicolau. The Nevanlinna-Pick Interpolation Problem. In J. Gröhn, J. Heittokangas, R. Korhonen, and J. Rättyä, editors, *Proceedings of the Summer School in Complex and Harmonic analysis, and related topics*, number 22. Publications of the University of eastern Finland, 2016. https://mat.uab.cat/∼artur/data/nevanlinna-pick.pdf.

[135] J. Agler and J.E. McCarthy. *Pick Interpolation and Hilbert Function Spaces*. American Mathematical Society, 2002.

[136] S.R. Garcia, J. Mashreghi, and W.T. Ross. *Finite Blashke Products and Their Connections*. Springer, 1 edition, May 2018.

[137] Jiani Fei, Chia-Nan Yeh, and Emanuel Gull. Nevanlinna analytical continuation. *Phys. Rev. Lett.*, 126:056402, Feb 2021. doi: 10.1103/PhysRevLett.126.056402. URL `https://link.aps.org/doi/10.1103/PhysRevLett.126.056402`.

[138] Nikolaï Nikolski. *Hardy Spaces*. Cambridge Studies in Advanced Mathematics. Cambridge University Press, 2019. doi: 10.1017/9781316882108.

[139] J.B. Conway. *Functions of One Complex Variable I*. Functions of One Complex Variable. Springer, 1978. ISBN 9780387903286. URL `https://books.google.co.uk/books?id=9LtfZr1snG0C`.

[140] Issai Schur. Über potenzreihen, die im innern des einheitskreises beschränkt sind. *Journal für die reine und angewandte Mathematik (Crelles Journal)*, 1918 (148):122–145, 1918. doi: doi:10.1515/crll.1918.148.122. URL `https://doi.org/10.1515/crll.1918.148.122`.

[141] A. N. Tikhonov. On the stability of inverse problems. *Proceedings of the USSR Academy of Sciences*, 39:195–198, 1943. URL `https://api.semanticscholar.org/CorpusID:202866372`.

[142] Donald E. Hilt and Donald W. Seegrist. *Ridge, a computer program for calculating ridge regression estimates*, volume no.236. Upper Darby, Pa, Dept. of Agriculture, Forest Service, Northeastern Forest Experiment Station, 1977, 1977. URL `https://www.biodiversitylibrary.org/item/137258`. https://www.biodiversitylibrary.org/bibliography/68934.

[143] Joseph I. Kapusta and Edward V. Shuryak. Weinberg type sum rules at zero and finite temperature. *Phys. Rev. D*, 49:4694–4704, 1994. doi: 10.1103/PhysRevD.49.4694.

[144] Alexander A. Rusakov, Jordan J. Phillips, and Dominika Zgid. Local Hamiltonians for quantitative Green's function embedding methods. *The Journal of Chemical Physics*, 141(19):194105, 11 2014. ISSN 0021-9606. doi: 10.1063/1.4901432. URL `https://doi.org/10.1063/1.4901432`.

[145] Marvin Rosenblum and James Rovnyak. Topics in hardy classes and univalent functions. 1994. URL `https://api.semanticscholar.org/CorpusID:118701369`.

[146] Artur Nicolau and Arne Stray. Nevanlinna's coefficients and Douglas algebras. *Pacific Journal of Mathematics*, 172, February 1996. doi: 10.2140/pjm.1996.172.541.

[147] Nacho Monreal Galán and Artur Nicolau. Extremal solutions of Nevalinna-Pick problems and certain classes of inner functions, May 2014. URL `http://arxiv.org/abs/1405.3578`. arXiv:1405.3578 [math].

[148] Alan F. Beardon. *Möbius transformations*, pages 254–283. Cambridge University Press, 2005.

[149] Kosuke Nogaki and Hiroshi Shinaoka. Bosonic Nevanlinna Analytic Continuation. *J. Phys. Soc. Jap.*, 92:035001, 2023. doi: 10.7566/JPSJ.92.035001.

[150] Kosuke Nogaki, Jiani Fei, Emanuel Gull, and Hiroshi Shinaoka. Nevanlinna.jl: A julia implementation of nevanlinna analytic continuation, 2023.

[151] Sz. Borsanyi et al. Leading hadronic contribution to the muon magnetic moment from lattice QCD. *Nature*, 593(7857):51–55, 2021. doi: 10.1038/s41586-021-03418-1.

[152] B. Chakraborty et al. Strong-Isospin-Breaking Correction to the Muon Anomalous Magnetic Moment from Lattice QCD at the Physical Point. *Phys. Rev. Lett.*, 120(15):152001, 2018. doi: 10.1103/PhysRevLett.120.152001.

[153] Sz. Borsanyi et al. Hadronic vacuum polarization contribution to the anomalous magnetic moments of leptons from first principles. *Phys. Rev. Lett.*, 121(2):022002, 2018. doi: 10.1103/PhysRevLett.121.022002.

[154] T. Blum, P. A. Boyle, V. Gülpers, T. Izubuchi, L. Jin, C. Jung, A. Jüttner, C. Lehner, A. Portelli, and J. T. Tsang. Calculation of the hadronic vacuum polarization contribution to the muon anomalous magnetic moment. *Phys. Rev. Lett.*, 121(2):022003, 2018. doi: 10.1103/PhysRevLett.121.022003.

[155] D. Giusti, V. Lubicz, G. Martinelli, F. Sanfilippo, and S. Simula. Electromagnetic and strong isospin-breaking corrections to the muon $g-2$ from Lattice QCD+QED. *Phys. Rev.*, D99(11):114502, 2019. doi: 10.1103/PhysRevD.99.114502.

[156] Eigo Shintani and Yoshinobu Kuramashi. Study of systematic uncertainties in hadronic vacuum polarization contribution to muon $g-2$ with 2+1 flavor lattice QCD. *Phys. Rev.*, D100(3):034517, 2019. doi: 10.1103/PhysRevD.100.034517.

[157] C. T. H. Davies et al. Hadronic-vacuum-polarization contribution to the muon's anomalous magnetic moment from four-flavor lattice QCD. *Phys. Rev.*, D101 (3):034512, 2020. doi: 10.1103/PhysRevD.101.034512.

[158] Antoine Gérardin, Marco Cè, Georg von Hippel, Ben Hörz, Harvey B. Meyer, Daniel Mohler, Konstantin Ottnad, Jonas Wilhelm, and Hartmut Wittig. The leading hadronic contribution to $(g-2)_\mu$ from lattice QCD with $N_\mathrm{f} = 2+1$ flavours of O(a) improved Wilson quarks. *Phys. Rev.*, D100(1):014510, 2019. doi: 10.1103/PhysRevD.100.014510.

[159] Christopher Aubin, Thomas Blum, Cheng Tu, Maarten Golterman, Chulwoo Jung, and Santiago Peris. Light quark vacuum polarization at the physical point and contribution to the muon $g-2$. *Phys. Rev.*, D101(1):014503, 2020. doi: 10.1103/PhysRevD.101.014503.

[160] D. Giusti and S. Simula. Lepton anomalous magnetic moments in Lattice QCD+QED. *PoS*, LATTICE2019:104, 2019. doi: 10.22323/1.363.0104.

[161] Andreas Enge, Mickaël Gastineau, Philippe Théveny, and Paul Zimmermann. *mpc: A library for multiprecision complex arithmetic with exact rounding*. INRIA, 1.3.0 edition, December 2022. `http://www.multiprecision.org/mpc/`.

[162] S.G. Krantz. *Handbook of Complex Variables*. Birkhäuser Boston, 1999. ISBN 9780817640118. URL `https://books.google.com/books?id=aYU2AdF_0dIC`.

[163] Constantia Alexandrou et al. Probing the Energy-Smeared R Ratio Using Lattice QCD. *Phys. Rev. Lett.*, 130(24):241901, 2023. doi: 10.1103/PhysRevLett.130.241901.

[164] Alexander Keshavarzi, Daisuke Nomura, and Thomas Teubner. $g-2$ of charged leptons, $\alpha(M_Z^2)$, and the hyperfine splitting of muonium. *Phys. Rev. D*, 101: 014029, Jan 2020. doi: 10.1103/PhysRevD.101.014029. URL `https://link.aps.org/doi/10.1103/PhysRevD.101.014029`.

[165] Elizabeth J. Beise. The Axial form-factor of the nucleon. *Eur. Phys. J. A*, 24S2: 43–46, 2005. doi: 10.1140/epjad/s2005-04-009-y.

[166] R. Acciarri et al. Long-Baseline Neutrino Facility (LBNF) and Deep Underground Neutrino Experiment (DUNE): Conceptual Design Report, Volume 2: The Physics Program for DUNE at LBNF. 12 2015.

[167] M. V. Diwan, V. Galymov, X. Qian, and A. Rubbia. Long-Baseline Neutrino Experiments. *Ann. Rev. Nucl. Part. Sci.*, 66:47–71, 2016. doi: 10.1146/annurev-nucl-102014-021939.

[168] L. Alvarez Ruso et al. Theoretical tools for neutrino scattering: interplay between lattice QCD, EFTs, nuclear physics, phenomenology, and neutrino event generators. 3 2022.

[169] Véronique Bernard, Latifa Elouadrhiri, and Ulf-G MeiÃ§ner. Axial structure of the nucleon. *Journal of Physics G: Nuclear and Particle Physics*, 28(1):R1, nov 2001. doi: 10.1088/0954-3899/28/1/201. URL `https://dx.doi.org/10.1088/0954-3899/28/1/201`.

[170] Dalibor Djukanovic, Georg von Hippel, Jonna Koponen, Harvey B. Meyer, Konstantin Ottnad, Tobias Schulz, and Hartmut Wittig. Isovector axial form factor of the nucleon from lattice qcd. *Phys. Rev. D*, 106:074503, Oct 2022. doi: 10.1103/PhysRevD.106.074503. URL `https://link.aps.org/doi/10.1103/PhysRevD.106.074503`.

[171] Aaron S. Meyer, André Walker-Loud, and Callum Wilkinson. Status of lattice qcd determination of nucleon form factors and their relevance for the few-gev neutrino program. *Annual Review of Nuclear and Particle Science*, 72 (Volume 72, 2022):205–232, 2022. ISSN 1545-4134. doi: https://doi.org/10.

1146/annurev-nucl-010622-120608. URL https://www.annualreviews.org/content/journals/10.1146/annurev-nucl-010622-120608.

[172] Aaron S. Meyer, Minerba Betancourt, Richard Gran, and Richard J. Hill. Deuterium target data for precision neutrino-nucleus cross sections. *Phys. Rev. D*, 93:113015, Jun 2016. doi: 10.1103/PhysRevD.93.113015. URL https://link.aps.org/doi/10.1103/PhysRevD.93.113015.

[173] Xin-Yu Tuo, Xu Feng, and Lu-Chang Jin. Long-distance contributions to neutrinoless double beta decay $\pi^- \to \pi^+ ee$. *Phys. Rev. D*, 100:094511, Nov 2019. doi: 10.1103/PhysRevD.100.094511. URL https://link.aps.org/doi/10.1103/PhysRevD.100.094511.

[174] A. Nicholson et al. Heavy physics contributions to neutrinoless double beta decay from qcd. *Phys. Rev. Lett.*, 121:172501, Oct 2018. doi: 10.1103/PhysRevLett.121.172501. URL https://link.aps.org/doi/10.1103/PhysRevLett.121.172501.

[175] Stefano Dell'Oro, Simone Marcocci, and Francesco Vissani. New expectations and uncertainties on neutrinoless double beta decay. *Phys. Rev. D*, 90:033005, Aug 2014. doi: 10.1103/PhysRevD.90.033005. URL https://link.aps.org/doi/10.1103/PhysRevD.90.033005.

[176] Michael Duerr, Manfred Lindner, and Alexander Merle. On the Quantitative Impact of the Schechter-Valle Theorem. *JHEP*, 06:091, 2011. doi: 10.1007/JHEP06(2011)091.

[177] Gary Prézeau. Light neutrino and heavy particle exchange in $0\nu\beta\beta$-decay. *Physics Letters B*, 633(1):93–97, 2006. ISSN 0370-2693. doi: https://doi.org/10.1016/j.physletb.2005.11.048. URL https://www.sciencedirect.com/science/article/pii/S0370269305016278.

[178] J.A Grifols, E Massó, and R Toldrà. Majorana neutrinos and long range forces. *Physics Letters B*, 389(3):563–565, 1996. ISSN 0370-2693. doi: https://doi.org/10.1016/S0370-2693(96)01304-4. URL https://www.sciencedirect.com/science/article/pii/S0370269396013044.

[179] Jenni Kotila, Jacopo Ferretti, and Francesco Iachello. Long-range neutrinoless double beta decay mechanisms. 10 2021.

[180] Frank F. Deppisch, Lukas Graf, Francesco Iachello, and Jenni Kotila. Analysis of light neutrino exchange and short-range mechanisms in $0\nu\beta\beta$ decay. *Phys. Rev. D*, 102:095016, Nov 2020. doi: 10.1103/PhysRevD.102.095016. URL `https://link.aps.org/doi/10.1103/PhysRevD.102.095016`.

[181] V. Cirigliano, W. Dekens, J. de Vries, M. L. Graesser, and E. Mereghetti. Neutrinoless double beta decay in chiral effective field theory: lepton number violation at dimension seven. *JHEP*, 12:082, 2017. doi: 10.1007/JHEP12(2017)082.

[182] Werner Rodejohann. Neutrino-less Double Beta Decay and Particle Physics. *Int. J. Mod. Phys. E*, 20:1833–1930, 2011. doi: 10.1142/S0218301311020186.

[183] S. M. Bilenky and C. Giunti. Neutrinoless Double-Beta Decay: a Probe of Physics Beyond the Standard Model. *Int. J. Mod. Phys. A*, 30(04n05):1530001, 2015. doi: 10.1142/S0217751X1530001X.

[184] Lukas Graf, Frank F. Deppisch, Francesco Iachello, and Jenni Kotila. Short-range neutrinoless double beta decay mechanisms. *Phys. Rev. D*, 98:095023, Nov 2018. doi: 10.1103/PhysRevD.98.095023. URL `https://link.aps.org/doi/10.1103/PhysRevD.98.095023`.

[185] V. Cirigliano, A. Kurylov, M. J. Ramsey-Musolf, and P. Vogel. Neutrinoless double beta decay and lepton flavor violation. *Phys. Rev. Lett.*, 93:231802, Dec 2004. doi: 10.1103/PhysRevLett.93.231802. URL `https://link.aps.org/doi/10.1103/PhysRevLett.93.231802`.

[186] G. Prézeau, M. Ramsey-Musolf, and Petr Vogel. Neutrinoless double β decay and effective field theory. *Phys. Rev. D*, 68:034016, Aug 2003. doi: 10.1103/PhysRevD.68.034016. URL `https://link.aps.org/doi/10.1103/PhysRevD.68.034016`.

[187] K. S. Babu and R. N. Mohapatra. New vector - scalar contributions to neutrinoless double beta decay and constraints on R-parity violation. *Phys. Rev. Lett.*, 75:2276–2279, 1995. doi: 10.1103/PhysRevLett.75.2276.

[188] Amand Faessler, Sergey Kovalenko, Fedor Šimkovic, and Joerg Schwieger. Dominance of pion exchange in R-parity-violating supersymmetric contributions to neutrinoless double beta decay. *Phys. Rev. Lett.*, 78:183–186, Jan

1997. doi: 10.1103/PhysRevLett.78.183. URL https://link.aps.org/doi/10.1103/PhysRevLett.78.183.

[189] Enrico Fermi. Tentativo di una teoria dei raggi β. *Il Nuovo Cimento (1924-1942)*, 11(1):1–19, Jan 1934. ISSN 1827-6121. doi: 10.1007/BF02959820. URL https://doi.org/10.1007/BF02959820.

[190] Chen Ning Yang. Fermi's beta-decay theory. *Int. J. Mod. Phys. A*, 27:1230005, 2012. doi: 10.1142/S0217751X12300050.

[191] Samoil Bilenky. *Introduction to the Physics of Massive and Mixed Neutrinos*, volume 947. Springer, 2018. ISBN 978-3-319-74801-6, 978-3-319-74802-3. doi: 10.1007/978-3-319-74802-3.

[192] Ilaria Brivio and Michael Trott. The Standard Model as an Effective Field Theory. *Phys. Rept.*, 793:1–98, 2019. doi: 10.1016/j.physrep.2018.11.002.

[193] Vincenzo Cirigliano, William Detmold, Amy Nicholson, and Phiala Shanahan. Lattice QCD Inputs for Nuclear Double Beta Decay. 3 2020. doi: 10.1016/j.ppnp.2020.103771.

[194] V. Cirigliano, W. Dekens, J. de Vries, M. L. Graesser, and E. Mereghetti. A neutrinoless double beta decay master formula from effective field theory. *JHEP*, 12:097, 2018. doi: 10.1007/JHEP12(2018)097.

[195] Stefan Scherer. Introduction to chiral perturbation theory. *Adv. Nucl. Phys.*, 27:277, 2003.

[196] R. N. Mohapatra and J. W. F. Valle. Neutrino Mass and Baryon Number Nonconservation in Superstring Models. *Phys. Rev. D*, 34:1642, 1986. doi: 10.1103/PhysRevD.34.1642.

[197] Gary Prezeau. Light neutrino and heavy particle exchange in neutrinoless double beta decay. *Phys. Lett. B*, 633:93–97, 2006. doi: 10.1016/j.physletb.2005.11.048.

[198] R.N. Mohapatra. Particle physics implications of neutrinoless double beta decay. *Nuclear Physics B - Proceedings Supplements*, 77(1):376–385, 1999. ISSN 0920-5632. doi: https://doi.org/10.1016/S0920-5632(99)00447-8. URL https://www.sciencedirect.com/science/article/pii/S0920563299004478.

[199] Stefano Dell'Oro, Simone Marcocci, Matteo Viel, and Francesco Vissani. Neutrinoless double beta decay: 2015 review. *Adv. High Energy Phys.*, 2016:2162659, 2016. doi: 10.1155/2016/2162659.

[200] C. Allton, D. J. Antonio, Y. Aoki, T. Blum, P. A. Boyle, N. H. Christ, et al. Physical results from $2+1$ flavor domain wall qcd and su(2) chiral perturbation theory. *Phys. Rev. D*, 78:114509, Dec 2008. doi: 10.1103/PhysRevD.78.114509. URL `https://link.aps.org/doi/10.1103/PhysRevD.78.114509`.

[201] Y. Aoki, R. Arthur, T. Blum, P. A. Boyle, D. Brömmel, N. H. Christ, et al. Continuum limit physics from $2+1$ flavor domain wall qcd. *Phys. Rev. D*, 83: 074508, Apr 2011. doi: 10.1103/PhysRevD.83.074508. URL `https://link.aps.org/doi/10.1103/PhysRevD.83.074508`.

[202] Yigal Shamir. Chiral fermions from lattice boundaries. *Nucl. Phys. B*, 406: 90–106, 1993. doi: 10.1016/0550-3213(93)90162-I.

[203] Y. Iwasaki and T. Yoshié. Renormalization group improved action for su(3) lattice gauge theory and the string tension. *Physics Letters B*, 143(4):449–452, 1984. ISSN 0370-2693. doi: https://doi.org/10.1016/0370-2693(84)91500-4. URL `https://www.sciencedirect.com/science/article/pii/0370269384915004`.

[204] P. A. Boyle et al. Low energy constants of SU(2) partially quenched chiral perturbation theory from N_f=2+1 domain wall QCD. *Phys. Rev. D*, 93(5): 054502, 2016. doi: 10.1103/PhysRevD.93.054502.

[205] P. A. Boyle, N. H. Christ, N. Garron, C. Jung, A. Jüttner, C. Kelly, R. D. Mawhinney, G. McGlynn, D. J. Murphy, S. Ohta, A. Portelli, and C. T. Sachrajda. Low energy constants of $su(2)$ partially quenched chiral perturbation theory from $N_f = 2+1$ domain wall qcd. *Phys. Rev. D*, 93:054502, Mar 2016. doi: 10.1103/PhysRevD.93.054502. URL `https://link.aps.org/doi/10.1103/PhysRevD.93.054502`.

[206] T. Blum, P. A. Boyle, N. H. Christ, J. Frison, N. Garron, R. J. Hudspith, et al. Domain wall qcd with physical quark masses. *Phys. Rev. D*, 93:074505, Apr 2016. doi: 10.1103/PhysRevD.93.074505. URL `https://link.aps.org/doi/10.1103/PhysRevD.93.074505`.

[207] V. Cirigliano, W. Dekens, M. Graesser, and E. Mereghetti. Neutrinoless double beta decay and chiral $SU(3)$. *Phys. Lett. B*, 769:460–464, 2017. doi: 10.1016/j.physletb.2017.04.020.

[208] S. R. Beane, E. Chang, S. D. Cohen, W. Detmold, H. W. Lin, T. C. Luu, K. Orginos, A. Parreño, M. J. Savage, and A. Walker-Loud. Light nuclei and hypernuclei from quantum chromodynamics in the limit of su(3) flavor symmetry. *Phys. Rev. D*, 87:034506, Feb 2013. doi: 10.1103/PhysRevD.87.034506. URL `https://link.aps.org/doi/10.1103/PhysRevD.87.034506`.

[209] M. Lüscher and P. Weisz. Computation of the action for on-shell improved lattice gauge theories at weak coupling. *Physics Letters B*, 158(3): 250–254, 1985. ISSN 0370-2693. doi: https://doi.org/10.1016/0370-2693(85)90966-9. URL `https://www.sciencedirect.com/science/article/pii/0370269385909669`.

[210] R. J. Dowdall, B. Colquhoun, J. O. Daldrop, C. T. H. Davies, I. D. Kendall, E. Follana, T. C. Hammant, R. R. Horgan, G. P. Lepage, C. J. Monahan, and E. H. Müller. The upsilon spectrum and the determination of the lattice spacing from lattice qcd including charm quarks in the sea. *Phys. Rev. D*, 85:054509, Mar 2012. doi: 10.1103/PhysRevD.85.054509. URL `https://link.aps.org/doi/10.1103/PhysRevD.85.054509`.

[211] C. Sturm, Y. Aoki, N. H. Christ, T. Izubuchi, C. T. C. Sachrajda, and A. Soni. Renormalization of quark bilinear operators in a momentum-subtraction scheme with a nonexceptional subtraction point. *Phys. Rev. D*, 80:014501, 2009. doi: 10.1103/PhysRevD.80.014501.

[212] Peter A. Boyle, Nicolas Garron, Renwick J. Hudspith, Christoph Lehner, and Andrew T. Lytle. Neutral kaon mixing beyond the Standard Model with $\mathrm{n}_f = 2 + 1$ chiral fermions. Part 2: non perturbative renormalisation of the $\Delta F = 2$ four-quark operators. *JHEP*, 10:054, 2017. doi: 10.1007/JHEP10(2017)054.

[213] Boram Yoon, Yong-Chull Jang, Rajan Gupta, Tanmoy Bhattacharya, Jeremy Green, Bálint Joó, Huey-Wen Lin, Kostas Orginos, David Richards, Sergey Syritsyn, and Frank Winter. Isovector charges of the nucleon from $2 + 1$-flavor qcd with clover fermions. *Phys. Rev. D*, 95:074508, Apr 2017. doi: 10.1103/PhysRevD.95.074508. URL `https://link.aps.org/doi/10.1103/PhysRevD.95.074508`.

[214] S. R. Beane, E. Chang, S. D. Cohen, W. Detmold, H. W. Lin, T. C. Luu, K. Orginos, A. Parreño, M. J. Savage, and A. Walker-Loud and. Light nuclei and hypernuclei from quantum chromodynamics in the limit of SU(3) flavor symmetry. *Physical Review D*, 87(3), feb 2013. doi: 10.1103/physrevd.87.034506. URL https://doi.org/10.1103%2Fphysrevd.87.034506.

[215] Saman Amarasinghe, Riyadh Baghdadi, Zohreh Davoudi, William Detmold, Marc Illa, Assumpta Parreño, Andrew V. Pochinsky, Phiala E. Shanahan, and Michael L. Wagman. Variational study of two-nucleon systems with lattice QCD. *Physical Review D*, 107(9), may 2023. doi: 10.1103/physrevd.107.094508. URL https://doi.org/10.1103%2Fphysrevd.107.094508.

[216] Evan Berkowitz, Thorsten Kurth, Amy Nicholson, Bálint Joó, Enrico Rinaldi, Mark Strother, Pavlos M. Vranas, and André Walker-Loud. Two-nucleon higher partial-wave scattering from lattice QCD. *Physics Letters B*, 765:285–292, feb 2017. doi: 10.1016/j.physletb.2016.12.024. URL https://doi.org/10.1016%2Fj.physletb.2016.12.024.

[217] Ben Hörz, Dean Howarth, Enrico Rinaldi, Andrew Hanlon, Chia Cheng Chang, Christopher Körber, Evan Berkowitz, John Bulava, M. A. Clark, Wayne Tai Lee, Colin Morningstar, Amy Nicholson, Pavlos Vranas, and André Walker-Loud. Two-nucleon s-wave interactions at the $SU(3)$ flavor-symmetric point with $m_{ud} \simeq m_s^{\text{phys}}$: A first lattice QCD calculation with the stochastic Laplacian Heaviside method. *Physical Review C*, 103(1), jan 2021. doi: 10.1103/physrevc.103.014003. URL https://doi.org/10.1103%2Fphysrevc.103.014003.

[218] Christoph Lehner and Christian Sturm. Matching factors for $\Delta s = 1$ four-quark operators in ri/smom schemes. *Phys. Rev. D*, 84:014001, Jul 2011. doi: 10.1103/PhysRevD.84.014001. URL https://link.aps.org/doi/10.1103/PhysRevD.84.014001.

[219] M. Göckeler, R. Horsley, Y. Nakamura, H. Perlt, D. Pleiter, P. E. L. Rakow, et al. Perturbative and nonperturbative renormalization in lattice qcd. *Phys. Rev. D*, 82:114511, Dec 2010. doi: 10.1103/PhysRevD.82.114511. URL https://link.aps.org/doi/10.1103/PhysRevD.82.114511.

[220] R. Arthur and P. A. Boyle. Step Scaling with off-shell renormalisation. *Phys. Rev. D*, 83:114511, 2011. doi: 10.1103/PhysRevD.83.114511.

[221] R. Arthur, P. A. Boyle, N. Garron, C. Kelly, and A. T. Lytle. Opening the rome-southampton window for operator mixing matrices. *Phys. Rev. D*, 85: 014501, Jan 2012. doi: 10.1103/PhysRevD.85.014501. URL `https://link.aps.org/doi/10.1103/PhysRevD.85.014501`.

[222] Mauro Papinutto, Carlos Pena, and David Preti. On the perturbative renormalization of four-quark operators for new physics. *Eur. Phys. J. C*, 77(6):376, 2017. doi: 10.1140/epjc/s10052-017-4930-6. [Erratum: Eur.Phys.J.C 78, 21 (2018)].

[223] W. Detmold, D. J. Murphy, A. V. Pochinsky, M. J. Savage, P. E. Shanahan, and M. L. Wagman. Sparsening algorithm for multihadron lattice QCD correlation functions. *Physical Review D*, 104(3), aug 2021. doi: 10.1103/physrevd.104.034502. URL `https://doi.org/10.1103%2Fphysrevd.104.034502`.

[224] Anthony Valenti Grebe. *Probing the Frontiers of the Standard Model with Lattice QCD*. PhD thesis, MIT, 2022.

[225] Zohreh Davoudi and Saurabh V. Kadam. The path from lattice QCD to the short-distance contribution to $0\nu\beta\beta$ decay with a light Majorana neutrino. *Physical Review Letters*, 126(15), apr 2021. doi: 10.1103/physrevlett.126.152003. URL `https://doi.org/10.1103%2Fphysrevlett.126.152003`.

[226] H. W. Hammer, S. König, and U. van Kolck. Nuclear effective field theory: status and perspectives. *Rev. Mod. Phys.*, 92(2):025004, 2020. doi: 10.1103/RevModPhys.92.025004.

[227] David B. Kaplan, Martin J. Savage, and Mark B. Wise. A New expansion for nucleon-nucleon interactions. *Phys. Lett. B*, 424:390–396, 1998. doi: 10.1016/S0370-2693(98)00210-X.

[228] David B. Kaplan, Martin J. Savage, and Mark B. Wise. Two nucleon systems from effective field theory. *Nucl. Phys. B*, 534:329–355, 1998. doi: 10.1016/S0550-3213(98)00440-4.

[229] Zohreh Davoudi and Saurabh V. Kadam. Path from Lattice QCD to the Short-Distance Contribution to $0\nu\beta\beta$ Decay with a Light Majorana Neutrino. *Phys. Rev. Lett.*, 126(15):152003, 2021. doi: 10.1103/PhysRevLett.126.152003.

[230] S. R. Beane, E. Chang, S. D. Cohen, William Detmold, H. W. Lin, T. C. Luu, K. Orginos, A. Parreno, M. J. Savage, and A. Walker-Loud. Light Nuclei

and Hypernuclei from Quantum Chromodynamics in the Limit of SU(3) Flavor Symmetry. *Phys. Rev. D*, 87(3):034506, 2013. doi: 10.1103/PhysRevD.87.034506.

[231] S. R. Beane et al. Nucleon-Nucleon Scattering Parameters in the Limit of SU(3) Flavor Symmetry. *Phys. Rev. C*, 88(2):024003, 2013. doi: 10.1103/PhysRevC.88.024003.

[232] Michael L. Wagman, Frank Winter, Emmanuel Chang, Zohreh Davoudi, William Detmold, Kostas Orginos, Martin J. Savage, and Phiala E. Shanahan. Baryon-baryon interactions and spin-flavor symmetry from lattice quantum chromodynamics. *Phys. Rev. D*, 96:114510, Dec 2017. doi: 10.1103/PhysRevD.96.114510. URL `https://link.aps.org/doi/10.1103/PhysRevD.96.114510`.

[233] Evan Berkowitz, Thorsten Kurth, Amy Nicholson, Balint Joo, Enrico Rinaldi, Mark Strother, Pavlos M. Vranas, and Andre Walker-Loud. Two-Nucleon Higher Partial-Wave Scattering from Lattice QCD. *Phys. Lett. B*, 765:285–292, 2017. doi: 10.1016/j.physletb.2016.12.024.

[234] Saman Amarasinghe, Riyadh Baghdadi, Zohreh Davoudi, William Detmold, Marc Illa, Assumpta Parreno, Andrew V. Pochinsky, Phiala E. Shanahan, and Michael L. Wagman. Variational study of two-nucleon systems with lattice QCD. *Phys. Rev. D*, 107(9):094508, 2023. doi: 10.1103/PhysRevD.107.094508.

[235] Ben Hörz, Dean Howarth, Enrico Rinaldi, Andrew Hanlon, Chia Cheng Chang, Christopher Körber, Evan Berkowitz, John Bulava, M. A. Clark, Wayne Tai Lee, Colin Morningstar, Amy Nicholson, Pavlos Vranas, and André Walker-Loud. Two-nucleon s-wave interactions at the su(3) flavor-symmetric point with $m_{ud} \approx m_s^{\text{phys}}$: A first lattice qcd calculation with the stochastic laplacian heaviside method. *Phys. Rev. C*, 103:014003, Jan 2021. doi: 10.1103/PhysRevC.103.014003. URL `https://link.aps.org/doi/10.1103/PhysRevC.103.014003`.

[236] A. Francis, J. R. Green, P. M. Junnarkar, Ch. Miao, T. D. Rae, and H. Wittig. Lattice qcd study of the h dibaryon using hexaquark and two-baryon interpolators. *Phys. Rev. D*, 99:074505, Apr 2019. doi: 10.1103/PhysRevD.99.074505. URL `https://link.aps.org/doi/10.1103/PhysRevD.99.074505`.

[237] Vincenzo Cirigliano, Wouter Dekens, Jordy de Vries, Martin Hoferichter, and Emanuele Mereghetti. Determining the leading-order contact term in neutrinoless double β decay. *JHEP*, 05:289, 2021. doi: 10.1007/JHEP05(2021)289.

[238] Davide Trotta. The cupid neutrinoless double-beta decay experiment. *Nuclear Instruments and Methods in Physics Research Section A: Accelerators, Spectrometers, Detectors and Associated Equipment*, 1066:169657, 2024. ISSN 0168-9002. doi: https://doi.org/10.1016/j.nima.2024.169657. URL `https://www.sciencedirect.com/science/article/pii/S0168900224005837`.

[239] N. Abgrall et al. The Large Enriched Germanium Experiment for Neutrinoless $\beta\beta$ Decay: LEGEND-1000 Preconceptual Design Report. 7 2021.

[240] Marek Gaździcki and Mark I. Gorenstein. *Hagedorn's Hadron Mass Spectrum and the Onset of Deconfinement*, pages 87–92. 2016. doi: 10.1007/978-3-319-17545-4_11.

[241] L. D. Faddeev. Mass in quantum yang-mills theory, 2009.

[242] Andreas Athenodorou and Michael Teper. The glueball spectrum of SU(3) gauge theory in 3 + 1 dimensions. *JHEP*, 11:172, 2020. doi: 10.1007/JHEP11(2020)172.

[243] Andreas Athenodorou and Michael Teper. SU(N) gauge theories in 3+1 dimensions: glueball spectrum, string tensions and topology. *JHEP*, 12:082, 2021. doi: 10.1007/JHEP12(2021)082.

[244] L. D. Faddeev. Mass in Quantum Yang-Mills Theory: Comment on a Clay Millenium problem. 11 2009.

[245] J. Greensite. The Confinement problem in lattice gauge theory. *Prog. Part. Nucl. Phys.*, 51:1, 2003. doi: 10.1016/S0146-6410(03)90012-3.

[246] L. Del Debbio, Manfried Faber, J. Greensite, and S. Olejnik. Casimir scaling versus Abelian dominance in QCD string formation. *Phys. Rev. D*, 53:5891–5897, 1996. doi: 10.1103/PhysRevD.53.5891.

[247] Manfried Faber, J. Greensite, and S. Olejnik. Casimir scaling from center vortices: Towards an understanding of the adjoint string tension. *Phys. Rev. D*, 57:2603–2609, 1998. doi: 10.1103/PhysRevD.57.2603.

[248] J. Ambjørn, P. Olesen, and C. Peterson. Stochastic confinement and dimensional reduction (ii). three-dimensional su(2) lattice gauge theory. *Nuclear Physics B*, 240(4):533–542, 1984. ISSN 0550-3213. doi: https://doi.

org/10.1016/0550-3213(84)90242-6. URL https://www.sciencedirect.com/science/article/pii/0550321384902426.

[249] A. Armoni and M. Shifman. On k string tensions and domain walls in N=1 gluodynamics. *Nucl. Phys. B*, 664:233–246, 2003. doi: 10.1016/S0550-3213(03)00409-7.

[250] Davide Gaiotto, Anton Kapustin, Nathan Seiberg, and Brian Willett. Generalized Global Symmetries. *JHEP*, 02:172, 2015. doi: 10.1007/JHEP02(2015)172.

[251] Pedro R. S. Gomes. An introduction to higher-form symmetries. *SciPost Phys. Lect. Notes*, 74:1, 2023. doi: 10.21468/SciPostPhysLectNotes.74.

[252] Lakshya Bhardwaj, Lea E. Bottini, Ludovic Fraser-Taliente, Liam Gladden, Dewi S. W. Gould, Arthur Platschorre, and Hannah Tillim. Lectures on generalized symmetries. *Phys. Rept.*, 1051:1–87, 2024. doi: 10.1016/j.physrep.2023.11.002.

[253] A. K. Halder, Andronikos Paliathanasis, and P. G. L. Leach. Noether's Theorem and Symmetry. *Symmetry*, 10(12):744, 2018. doi: 10.3390/sym10120744.

[254] A.M. Polyakov. Compact gauge fields and the infrared catastrophe. *Physics Letters B*, 59(1):82–84, 1975. ISSN 0370-2693. doi: https://doi.org/10.1016/0370-2693(75)90162-8. URL https://www.sciencedirect.com/science/article/pii/0370269375901628.

[255] Oliver Jahn and Owe Philipsen. The Polyakov loop and its relation to static quark potentials and free energies. *Phys. Rev. D*, 70:074504, 2004. doi: 10.1103/PhysRevD.70.074504.

[256] David J. Gross, Akikazu Hashimoto, and Igor R. Klebanov. The Spectrum of a large N gauge theory near transition from confinement to screening. *Phys. Rev. D*, 57:6420–6428, 1998. doi: 10.1103/PhysRevD.57.6420.

[257] Alexander A. Migdal. Recursion Equations in Gauge Theories. *Sov. Phys. JETP*, 42:413, 1975.

[258] David J. Gross, Igor R. Klebanov, Andrei V. Matytsin, and Andrei V. Smilga. Screening versus confinement in (1+1)-dimensions. *Nucl. Phys. B*, 461:109–130, 1996. doi: 10.1016/0550-3213(95)00655-9.

[259] Zohar Komargodski, Kantaro Ohmori, Konstantinos Roumpedakis, and Sahand Seifnashri. Symmetries and strings of adjoint QCD_2. *JHEP*, 03:103, 2021. doi: 10.1007/JHEP03(2021)103.

[260] Joshua Boorstein and David Kutasov. Symmetries and mass splittings in QCD in two-dimensions coupled to adjoint fermions. *Nucl. Phys. B*, 421:263–277, 1994. doi: 10.1016/0550-3213(94)90328-X.

[261] Ross Dempsey, Igor R. Klebanov, Loki L. Lin, and Silviu S. Pufu. Adjoint Majorana QCD_2 at finite N. *JHEP*, 04:107, 2023. doi: 10.1007/JHEP04(2023)107.

[262] Clay Córdova and Thomas T. Dumitrescu. Candidate Phases for SU(2) Adjoint QCD_4 with Two Flavors from $\mathcal{N} = 2$ Supersymmetric Yang-Mills Theory. 6 2018.

[263] A. V. Smilga. Two-dimensional instantons with bosonization and physics of adjoint two-dimensional qcd. *Phys. Rev. D*, 54:7757–7773, Dec 1996. doi: 10.1103/PhysRevD.54.7757. URL `https://link.aps.org/doi/10.1103/PhysRevD.54.7757`.

[264] Gerard 't Hooft. A Planar Diagram Theory for Strong Interactions. *Nucl. Phys. B*, 72:461, 1974. doi: 10.1016/0550-3213(74)90154-0.

[265] Gyan Bhanot, Kresimir Demeterfi, and Igor R. Klebanov. (1+1)-dimensional large-n qcd coupled to adjoint fermions. *Phys. Rev. D*, 48:4980–4990, Nov 1993. doi: 10.1103/PhysRevD.48.4980. URL `https://link.aps.org/doi/10.1103/PhysRevD.48.4980`.

[266] S. Dalley. Adjoint QCD in two-dimensions and the nonAbelian Schwinger mechanism. *Phys. Lett. B*, 418:160–166, 1998. doi: 10.1016/S0370-2693(97)01474-3.

[267] Tatsuo Azeyanagi, Masanori Hanada, Mithat Ünsal, and Ran Yacoby. Large-n reduction in qcd-like theories with massive adjoint fermions. *Phys. Rev. D*, 82:125013, Dec 2010. doi: 10.1103/PhysRevD.82.125013. URL `https://link.aps.org/doi/10.1103/PhysRevD.82.125013`.

[268] Meseret Asrat. $(1 + 1)$D qcd with heavy adjoint quarks. *Phys. Rev. D*, 107:106022, May 2023. doi: 10.1103/PhysRevD.107.106022. URL `https://link.aps.org/doi/10.1103/PhysRevD.107.106022`.

[269] Ross Dempsey, Igor R. Klebanov, and Silviu S. Pufu. Exact symmetries and threshold states in two-dimensional models for QCD. *JHEP*, 10:096, 2021. doi: 10.1007/JHEP10(2021)096.

[270] Andreas Athenodorou and Michael Teper. SU(N) gauge theories in 2+1 dimensions: glueball spectra and k-string tensions. *JHEP*, 02:015, 2017. doi: 10.1007/JHEP02(2017)015.

[271] Piotr Korcyl and Mateusz Koren. Preliminary study of two-dimensional SU(N) Yang-Mills theory with adjoint matter by Hybrid Monte Carlo approach. *PoS*, LATTICE2011:071, 2011. doi: 10.22323/1.139.0071.

[272] Georg Bergner, Stefano Piemonte, and Mithat Ünsal. Investigating two-dimensional adjoint QCD on the lattice. 4 2024.

[273] Luigi Del Debbio, Haralambos Panagopoulos, Paolo Rossi, and Ettore Vicari. k string tensions in SU(N) gauge theories. *Phys. Rev. D*, 65:021501, 2002. doi: 10.1103/PhysRevD.65.021501.

[274] F. Antonuccio and S. Pinsky. On the transition from confinement to screening in QCD(1+1) coupled to adjoint fermions at finite N. *Phys. Lett. B*, 439:142–149, 1998. doi: 10.1016/S0370-2693(98)01023-5.

[275] Istvan Montvay. Majorana fermions on the lattice. 8 2001.

[276] Block compressed row format (bsr). URL `https://scipy-lectures.org/advanced/scipy_sparse/bsr_matrix.html`.

[277] T. Muir and W.H. Metzler. *A Treatise on the Theory of Determinants*. Dover phoenix editions. Dover Publications, 2003. ISBN 9780486495538. URL `https://books.google.com/books?id=ZGLIHQ0TPTAC`.

[278] Simon Catterall, Richard Galvez, Anosh Joseph, and Dhagash Mehta. On the sign problem in 2D lattice super Yang-Mills. *Journal of High Energy Physics*, 2012(1):108, January 2012. ISSN 1029-8479. doi: 10.1007/JHEP01(2012)108. URL `http://link.springer.com/10.1007/JHEP01(2012)108`.

[279] David Schaich and Thomas DeGrand. Parallel software for lattice N = 4 supersymmetric Yang-Mills theory. *Computer Physics Communications*, 190: 200–212, May 2015. ISSN 00104655. doi: 10.1016/j.cpc.2014.12.025. URL `https://linkinghub.elsevier.com/retrieve/pii/S0010465515000132`.

[280] David Schaich. Lattice studies of supersymmetric gauge theories. *The European Physical Journal Special Topics*, 232(3):305–320, April 2023. ISSN 1951-6355, 1951-6401. doi: 10.1140/epjs/s11734-022-00708-1. URL https://link.springer.com/10.1140/epjs/s11734-022-00708-1.

[281] Anyi Li, Andrei Alexandru, and Keh-Fei Liu. Reweighting method in finite density lattice QCD. *PoS*, LAT2006:030, 2006. doi: 10.22323/1.032.0030.

[282] Jacob Finkenrath, Francesco Knechtli, and Björn Leder. One flavor mass reweighting in lattice QCD. *Nucl. Phys. B*, 877:441–456, 2013. doi: 10.1016/j.nuclphysb.2013.10.019. [Erratum: Nucl.Phys.B 880, 574–575 (2014)].

[283] Shinji Ejiri. Remarks on the multiparameter reweighting method for the study of lattice qcd at nonzero temperature and density. *Phys. Rev. D*, 69:094506, May 2004. doi: 10.1103/PhysRevD.69.094506. URL https://link.aps.org/doi/10.1103/PhysRevD.69.094506.

[284] Gert Aarts. Introductory lectures on lattice qcd at nonzero baryon number. *Journal of Physics: Conference Series*, 706(2):022004, apr 2016. doi: 10.1088/1742-6596/706/2/022004. URL https://dx.doi.org/10.1088/1742-6596/706/2/022004.

[285] Martin Luscher. Computational Strategies in Lattice QCD. In *Les Houches Summer School: Session 93: Modern perspectives in lattice QCD: Quantum field theory and high performance computing*, pages 331–399, 2 2010.

[286] A.D. Kennedy. Approximation theory for matrices. *Nuclear Physics B - Proceedings Supplements*, 128:107–116, 2004. ISSN 0920-5632. doi: https://doi.org/10.1016/S0920-5632(03)02466-6. URL https://www.sciencedirect.com/science/article/pii/S0920563203024666. Proceedings of the 2nd Cairns Topical Workshop on Lattice Hadron Physics.

[287] Andreas Stathopoulos and James R. McCombs. Primme: Preconditioned iterative multimethod eigensolver methods and software description. *ACM Trans. Math. Softw.*, 37(2), apr 2010. ISSN 0098-3500. doi: 10.1145/1731022.1731031. URL https://doi.org/10.1145/1731022.1731031.

[288] M. A. Clark and A. D. Kennedy. Accelerating dynamical fermion computations using the rational hybrid Monte Carlo (RHMC) algorithm with multiple pseud-

ofermion fields. *Phys. Rev. Lett.*, 98:051601, 2007. doi: 10.1103/PhysRevLett.98.051601.

[289] M. A. Clark. The Rational Hybrid Monte Carlo Algorithm. *PoS*, LAT2006:004, 2006. doi: 10.22323/1.032.0004.

[290] S. Duane, A. D. Kennedy, B. J. Pendleton, and D. Roweth. Hybrid Monte Carlo. *Phys. Lett. B*, 195:216–222, 1987. doi: 10.1016/0370-2693(87)91197-X.

[291] Haruo Yoshida. Construction of higher order symplectic integrators. *Physics Letters A*, 150(5):262–268, 1990. ISSN 0375-9601. doi: https://doi.org/10.1016/0375-9601(90)90092-3. URL `https://www.sciencedirect.com/science/article/pii/0375960190900923`.

[292] Albert Reuther et al. Interactive supercomputing on 40,000 cores for machine learning and data analysis. In *2018 IEEE High Performance extreme Computing Conference (HPEC)*, pages 1–6. IEEE, 2018.

[293] Alan D. Sokal. Monte carlo methods in statistical mechanics: Foundations and new algorithms note to the reader. 1996. URL `https://api.semanticscholar.org/CorpusID:14817657`.

[294] Michael Wimmer. Efficient numerical computation of the pfaffian for dense and banded skew-symmetric matrices. *ACM Transactions on Mathematical Software (TOMS)*, 38(4):1–17, 2012.

[295] William I. Jay and Ethan T. Neil. Bayesian model averaging for analysis of lattice field theory results. *Phys. Rev. D*, 103:114502, 2021. doi: 10.1103/PhysRevD.103.114502.

[296] John M. Bulava, Robert G. Edwards, Eric Engelson, Justin Foley, Bálint Joó, Adam Lichtl, Huey-Wen Lin, Nilmani Mathur, Colin Morningstar, David G. Richards, and Stephen J. Wallace. Excited state nucleon spectrum with two flavors of dynamical fermions. *Phys. Rev. D*, 79:034505, Feb 2009. doi: 10.1103/PhysRevD.79.034505. URL `https://link.aps.org/doi/10.1103/PhysRevD.79.034505`.

[297] S. Basak, R. G. Edwards, G. T. Fleming, U. M. Heller, C. Morningstar, D. Richards, I. Sato, and S. Wallace. Group-theoretical construction of extended baryon operators in lattice qcd. *Phys. Rev. D*, 72:094506, Nov 2005. doi:

10.1103/PhysRevD.72.094506. URL https://link.aps.org/doi/10.1103/PhysRevD.72.094506.

[298] Benoit Blossier, Michele Della Morte, Georg von Hippel, Tereza Mendes, and Rainer Sommer. On the generalized eigenvalue method for energies and matrix elements in lattice field theory. *JHEP*, 04:094, 2009. doi: 10.1088/1126-6708/2009/04/094.

[299] Pauli Virtanen, Ralf Gommers, Travis E. Oliphant, Matt Haberland, Tyler Reddy, David Cournapeau, Evgeni Burovski, Pearu Peterson, Warren Weckesser, Jonathan Bright, Stéfan J. van der Walt, Matthew Brett, Joshua Wilson, K. Jarrod Millman, Nikolay Mayorov, Andrew R. J. Nelson, Eric Jones, Robert Kern, Eric Larson, C J Carey, İlhan Polat, Yu Feng, Eric W. Moore, Jake VanderPlas, Denis Laxalde, Josef Perktold, Robert Cimrman, Ian Henriksen, E. A. Quintero, Charles R. Harris, Anne M. Archibald, Antônio H. Ribeiro, Fabian Pedregosa, Paul van Mulbregt, and SciPy 1.0 Contributors. SciPy 1.0: Fundamental Algorithms for Scientific Computing in Python. *Nature Methods*, 17:261–272, 2020. doi: 10.1038/s41592-019-0686-2.

[300] Aleksey Cherman and Maria Neuzil. Beta functions of 2d adjoint qcd. *Phys. Rev. D*, 109:105014, May 2024. doi: 10.1103/PhysRevD.109.105014. URL https://link.aps.org/doi/10.1103/PhysRevD.109.105014.

[301] Aleksey Cherman, Theodore Jacobson, Yuya Tanizaki, and Mithat Ünsal. Anomalies, a mod 2 index, and dynamics of 2d adjoint QCD. *SciPost Phys.*, 8 (5):072, 2020. doi: 10.21468/SciPostPhys.8.5.072.

[302] Takafumi Kita. Quantum field theory of correlated bose einstein condensates: I. basic formalism. *Journal of the Physical Society of Japan*, 90(2):024001, February 2021. ISSN 1347-4073. doi: 10.7566/jpsj.90.024001. URL http://dx.doi.org/10.7566/JPSJ.90.024001.

[303] Poetri Sonya Tarabunga, Giuliano Giudici, Titas Chanda, and Marcello Dalmonte. Classification and emergence of quantum spin liquids in chiral rydberg models. *Phys. Rev. B*, 108:075118, Aug 2023. doi: 10.1103/PhysRevB.108.075118. URL https://link.aps.org/doi/10.1103/PhysRevB.108.075118.

[304] Aaron S. Meyer, Evan Berkowitz, Chris Bouchard, Chia Cheng Chang, M. A. Clark, Ben Hörz, Dean Howarth, Christopher Körber, Henry Monge-Camacho,

Amy Nicholson, Enrico Rinaldi, Pavlos Vranas, and André Walker-Loud. Nucleon axial form factor from domain wall on hisq, 2021. URL https://arxiv.org/abs/2111.06333.

[305] Robert G. Edwards and Balint Joo. The Chroma software system for lattice QCD. *Nucl. Phys. B Proc. Suppl.*, 140:832, 2005. doi: 10.1016/j.nuclphysbps.2004.11.254.

[306] V. I. Borodulin, R. N. Rogalyov, and S. R. Slabospitskii. CORE 3.2 (COmpendium of RElations, Version 3.2). 2 2017.

[307] Stephan Ramon Garcia, Javad Mashreghi, and William T. Ross. Finite Blaschke products: a survey, July 2016. URL http://arxiv.org/abs/1512.05444. arXiv:1512.05444 [math].

[308] David Tong. David tong: Lectures on gauge theory, 2018. URL https://www.damtp.cam.ac.uk/user/tong/gaugetheory.html.